Numerical Modeling of the Special Light Source with Novel R-FEM Method

E. Kadlecova and P. Fiala
Department of Theoretical and Experimental Electrical Engineering
Brno University of Technology, Kolejni 4, 612 00 Brno, Czech Republic

Abstract— This paper presents information about new directions in the modelling of lighting systems, and an overview of methods for the modelling of lighting systems. The novel R-FEM method is described, which is a combination of the Radiosity method and the Finite Elements Method. The paper contains modelling results and their verification by experimental measurements and by the Matlab simulation for this R-FEM method.

1. INTRODUCTION

The paper contains information about verification of the design of the special light sources by the numerical simulation of the R-FEM method and verification by experimental measurements.

2. THE R-FEM METHOD

The R-FEM method is a new direction in the modelling of lighting systems. It utilizes the similarity between physical models. This paragraph demonstrates the usage of analogy between different physical models for the modelling of light problems. The R-FEM method is able to solve tasks that fulfill the condition $\lambda_S \ll \max(D) \wedge \lambda_S < 10 \cdot \max(D)$, where λ_S is the source of light wavelength and D is one of the geometrical dimensions of the modelling task. It can be used for to model more complicated physical problems than the methods mentioned up to now. An example of a more complicated physical problem, which we can solve by the R-FEM method, is the modelling of light intensity distribution in interior or exterior spaces with non-homogeneous environment, where the light has passed through some impure air (e.g., filled with smoke, fog, mist, vapour, dust, etc.).

3. THE DESIGN BY R-FEM METHOD

In technical praxis we often encounter conjugate problems. A necessary part of the design process during the development and measurement of light sources is the modelling and experimental verification of results. The most accurate mathematical models of the sources of light include models based on the radiation principle. One possibility is to use standard one-purpose programs while another possibility offers the usage of sophisticated numerical methods, among them the finite element method, for example the ANSYS program.

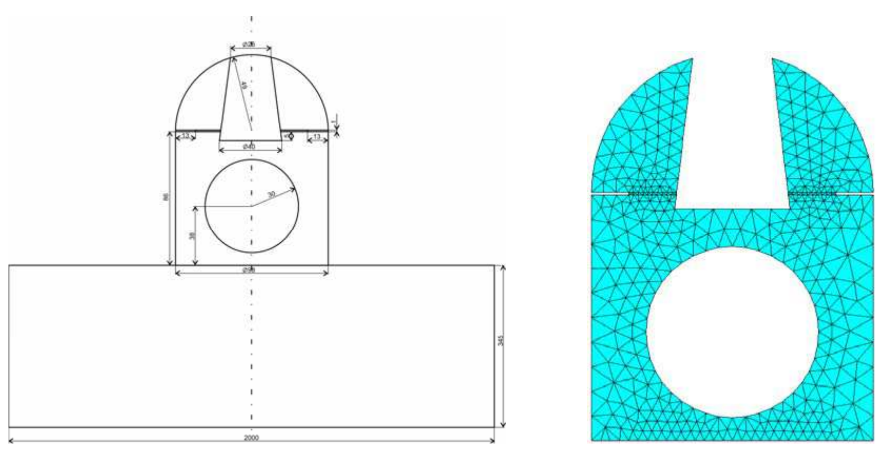

Figure 1: Geometrical configuration of the special light source.

The ANSYS program uses standard program tools such as modelling, discretization into a net of elements, solvers, evaluation, and interpretation of the results. The crux of the whole problem lies in the transformation of thermal field quantities into optical quantities. In the following text the basics of modelling the primitive light problem are described. The verification of the model of light source is done via experiment and then it continues to the hollow light guide problems and it was also verified by experiment. The geometrical situations that were modeled and verified is shown in the Fig. 1.

4. BUILDING THE NUMERICAL MODEL

The formulation of the basic thermal model is based on the first law of thermodynamics

$$q + \rho\, c\, \boldsymbol{v} \cdot divT - div(k\ \mathrm{grad}T) = \rho c \left(\frac{\partial T}{\partial t}\right) \tag{1}$$

where q is the specific heat, ρ is the specific weight, c is the specific solidification heat, T is the temperature, t is the time, k is the coefficient of calorific conduction, v is the the velocity of flow. This model can, with respect to the application of Snell's principles and according to the Stefan-Boltzmann principles, heat transfer by way of radiation between surfaces with relative indexes i, j is formulated as be simplified into the form

$$q_{ri} = \sigma \varepsilon_i A_{i,j} S_i \left(T_i^4 - T_j^4\right) \tag{2}$$

where q_{ri} is the specific heat transferring from surface with index i, σ is the Stefan-Boltzmann constant, ε_i is the emissivity of surface, $A_{i,j}$ is the projection factor of surface with index i to surface with index j, S_i is the area of surface with index i, T_i, T_j are the temperature of surfaces i, j. When the projection factor is determined, it is possible to use the Gallerkin principles for converting this problem into model (1). Marginal and initial conditions must be respected.

$$[K]\{T\} = \{Q\} \tag{3}$$

where K is the coefficients matrix, T is the columnar matrix of sought temperatures, Q is the columnar matrix of heat sources. Thermal flow T_f is determined from temperature T as

$$T_f = -(k\ \mathrm{grad}T) \tag{4}$$

By the radiation principle, the elements of column matrix of heat sources Q and adjusting for mathematical model yields

$$Q_{i,j} = \overbrace{S_i A_{i,j} \varepsilon_i \sigma \left(T_i^2 - T_j^2\right)(T_i + T_j)}^{K} (T_i - T_j) \tag{5}$$

The heating model will be used for the modelling of light problem using the Snell principles in optics. Light source with lighting intensity $E(lx)$ corresponds to equivalent heat quantity density of heat flow q'', light flow $\Phi(lm)$ corresponds to equivalent quantity of heat flow q'. The resulting light flow is defined by Equation (6).

$$\Phi_e = \frac{T_{f,e}}{S_{n,e}} \tag{6}$$

where Φ_e is the flow of light on the element, $T_{f,e}$ is the equivalent of the thermal flow through the element, $S_{n,e}$ is the normal surface to the element. The result of modeling by the R-FEM method is shown in the Fig. 2.

5. VERIFICATION OF THE R-FEM

The results of the verification of the R-FEM via experiments is given in Fig. 3. There are differences between the values obtained by modelling and experimental measurement, ranging from 5–15%, depending on the distribution of the net of elements. When the elements of the net are of a lower density, the differences are also lower. This problem requires the net of elements to be optimized.

6. ADVANTAGES OF THE R-FEM

One of the biggest advantages of this method is the wide spectrum of its usage. We can design the interior and also exterior scenes with its specifications in the materials quality, climatic dissimilarities and geometrical dimension varieties. We can use all types of sources of light with their diversity of the colour distribution in the light spectrum. The designers are not limited by the geometrical

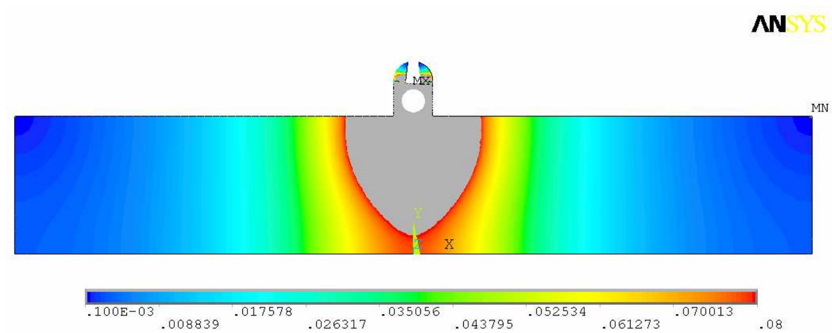

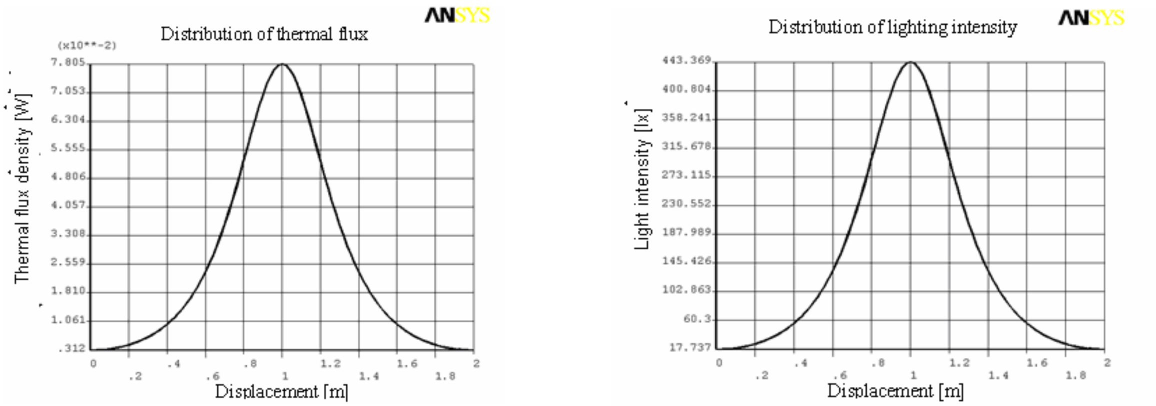

(a) (b)

Figure 2: (a) The result of the R-FEM method Cthermal flux, module of vector, distribution on central line. (b) The result of the R-FEM method-lighting intensity $E(lx)$.

dimension varieties, colour distribution in the light spectrum, material qualities or climatic dissimilarities. The other advantage is that the method is very accurate. The degree of accuracy can be chosen by choosing the method of generating nets of elements and the solution algorithm because all this is provided by the ANSYS standard program tools.

7. THE FULL FEM WAVE SOLUTION

FEM is the short form for the Finite Elements Method modelling. The light problems that fulfill the condition $\lambda_S \ll \max(D) \wedge \lambda_S < 10 \cdot \max(D)$, where λ_S is the source of light wavelength and D is one of the geometrical dimensions of the modelling assignment, will be solved by the FEM using the full wave equation, which was used to define light emissions. This method of the solution yields highly accurate results, but is demanding as regards geometrical declaration, and time-consuming (for example, for incoherent sources of light the calculation is too long). The Full FEM wave solution is suitable for a specific purpose.

8. VERIFICATION THE R-FEM BY TWO EXPERIMENTS AND MATLAB SIMULATION

Matlab simulation is the modeling of lighting systems which combines the EPM and ray tracing methods and then approximation by the principle of radiation follows. The algorithm is created by combining the ray tracing method and the EPM method as a geometrical simulation in the Matlab and then the approximation of the light intensity by the principle of radiation is used. It gives the right behavior of the light intensity distribution. This method was designed for second verification of the lighting systems modeling and it is given in the Fig. 3. The results of the verification of the R-FEM via two experiments are given in Figs. 4 and 5. Experimental measurements were used as first verification. The main advantages of the Matlab simulation are the simplicity of the submission for the initial figures and the high speed of the calculations for the simple assignments. This modeling is suitable for the verification of the results, which are received from other type of the modeling method. The comparison modeling and experimental values is given in Fig. 6.

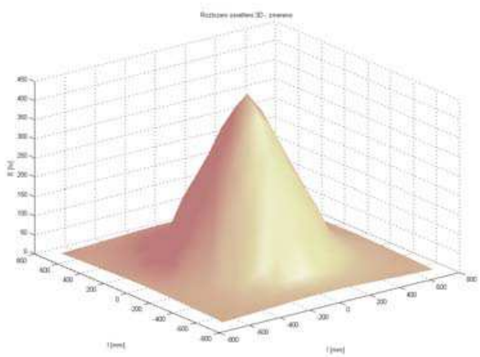

Figure 3: The results of the modeling by the Matlab-Lighting intensity $E[lx]$.

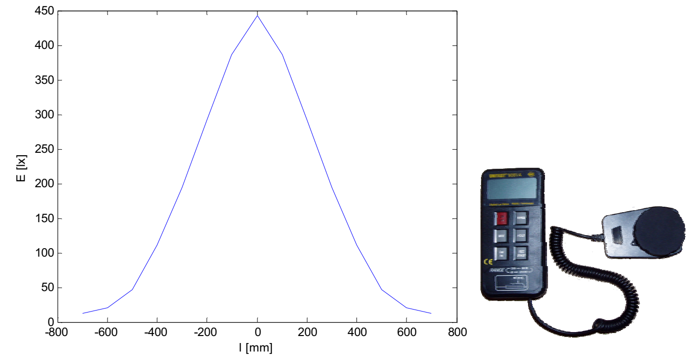

Figure 4: Results of the light intensity by the experiment with the luxmeter.

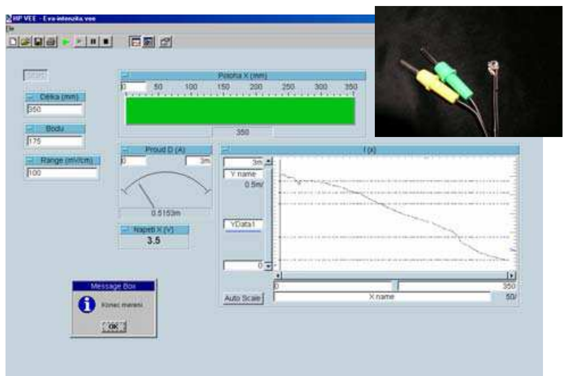

Figure 5: The shape of distribution of the light intensity by experiment with the LED.

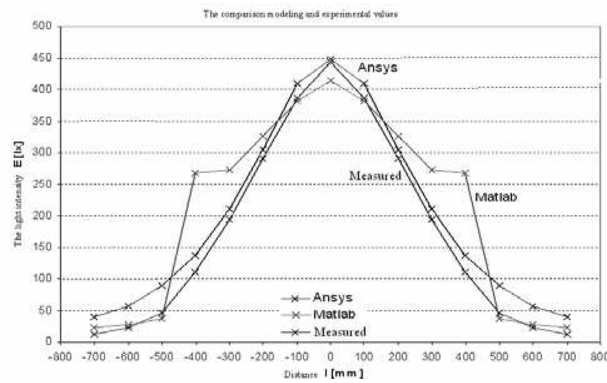

Figure 6: The comparison modeling and experimental values.

9. CONCLUSION

This article describes novel numerical methods (R-FEM) of modelling lighting problems, which are used in Computer Graphics and in Lighting Engineering. Main novel described method exploits FEM ANSYS system for partial solution. Article also describes the R-FEM method, which has been verified and found to be a great asset for the modern trends in modelling lighting problems. It can solve specific light problems that up to now have only been solved by using many simplifications.

ACKNOWLEDGMENT

The research described in the paper were financially supported by FRVŠ by research plan No. MSM 0021630516 and grant GAAV No. B208130603.

REFERENCES

1. http://www.lighting-technologies.com/Products/Photopia/Photopia2_pod.htm.
2. Kadlecová, E., M. Bernard, and P. Fiala, "Illumination of interiors by the Hollow Light Guides," *14th International Conference Light 2003*, Bratislava, ISBN 80-233-0488-7, 2003.
3. Kadlecová, E. and P. Fiala, "Light guide modeling," *Energy Forum 2004*, Sofia, Technical University - Sofia, Bulgaria, 338–341, ISBN 80-986-1619-1, 2004.
4. Kadlecová, E., "Automated system of calculation of reflecting surface of light sources," Ph.D. thesis, VUT v Brně, FEKT, Brno srpen, 2004.

Numerical Modeling of Accuracy of Air Ion Field Measurement

K. Bartušek[1, 2], **P. Fiala**[2], **T. Bachorec**[2], **and E. Kadlecová**[2]

[1]Institute of Scientific Instruments, Academy of Sciences of the Czech Republic
Královopolská 147, 612 64 Brno, Czech Republic
[2]Department of Theoretical and Experimental Electrical Engineering
Brno University of Technology, Kolejni 4, 612 00 Brno, Czech Republic

Abstract— An analysis of the electric state of air shows the presence of various ion sorts. The therapeutic effect of negative high-mobility ions of proper concentration is known. This positive effect was observed in caves that are used for speleotherapy. This article presents the capability of methods for measuring ion concentration and for ion spectral analysis.

1. INTRODUCTION

Air ion concentration and composition belong to the frequently monitored parameters of the atmosphere [5]. Their influence on living organisms has been the subject of intensive studies. Earlier research has demonstrated the positive influence of light negative ions and air cleanness on human health. The Department of the Theoretical and Experimental Electrical Engineering of Brno University of Technology and the Institute of Scientific Instruments of the Academy of Sciences of the Czech Republic are involved in the research of ion field in office and living spaces. The objective is to increase the concentration of light air ions in these spaces. Another task is to set up a simulated therapy room, with conditions similar to speleotherapy caves. It sets the requirements for accurate measurement of ion field with good repeatability. The article deals with the design of gerdien condenser and peripheral measuring devices. An optimal design is important for eliminating the inaccuracy of ion concentration measurement.

2. MEASURING METHOD

Several methods are currently used to measure air ion fields: the dispersion method, the ionspectrometer method, the Faraday cage method, and the gerdien condenser method, whose principle is shown in Figure 1. Here is $d1$ — inner electrode diameter, $d2$ — outer electrode diameter, l — length of gerdien condenser, M — air flow volume rate, v — air flow velocity, e — elementary charge of electron, $\oplus$ positive air particle (ion), $\ominus$ negative air particle (ion). The gerdien condenser consists of two electrodes. There is an electric field between the inner electrode (the collector) and the outer electrode. The field is imposed by voltage source U. Air ions flow from the fan through the gerdien condenser. Negative ions in the electric field impact the collector, and the current produced is measured by a pA-meter. The current measured is proportional to air ion concentration. The model of the measuring system is shown in Figure 2. The values measured carry systematical measurement errors. This is due to leakage currents and parasitic capacitances (modeled by I_{LEAK} in Figure 2) [6]. We have to consider leakage resistances R_{AK} of gerdien condenser, leakage resistances and capacitance of the pA-meter input (R_{EH}, C_{EH}, R_{EL}, C_{EL}), insulation resistance (R_V) of the collector voltage source. The current measured is further affected by the input resistance of pA-meter and the input resistance of voltage source (R_U, C_U). To minimize the measurement error, R_{AK} ,and R_V should be much larger than R_I, and R_{EH}, and R_{EL} should also be much larger than R_{OUT}. Time constant R_UC_U has to be much larger than the measuring time.

3. NEW DESIGN OF GERDIEN CONDENSER

The inner and outer electrodes are elliptical in shape. This shape ensures that the flow of air is laminar. Air flow turbulence can distort the accuracy of measurement. The surface of the electrodes is required to be as smooth as possible. These aspects make the design of gerdien condenser quite demanding (fine grinding, lapping, etc.). The new design of gerdien condenser is shown in Figure 3.

Since in the measurement of air ion concentration very small currents are detected, it is necessary to eliminate the influence of ambient electric charge. The influence of magnetic fields has to be minimized too.

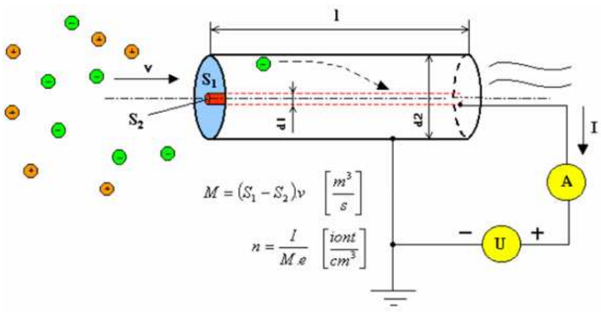

Figure 1: Principle of gerdien condenser method.

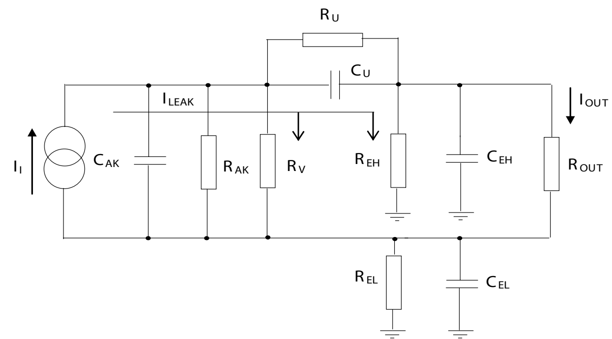

Figure 2: Model of a system for measuring air ion concentration — the gerdien condenser method.

Figure 3: New gerdien condenser.

4. WEAK CURRENT AMPLIFIER

The current flowing through the gerdien condenser is due to the ion concentration. Current intensity depends on polarization voltage, on the dimension and parameters of gerdien condenser, and on ion concentration. The specific current range for the designed gerdien condenser is 10^{-10}A–10^{-13}A. For the following measurement it is suitable to convert the current to voltage. Because the current is very weak, it is suitable to do this near the gerdien condenser. The low-level amplifier is realized with INA 116 — Figure 4. The INA 116 has a very low input bias current $I_{b,\max} = 100$ fA. The design of the amplifier is shown in Figure 5. The gain of INA 116 is set by resistor R_{10}.

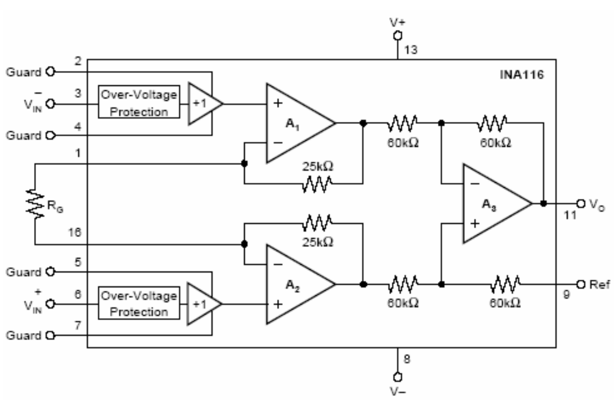

Figure 4: Principal scheme of INA 116.

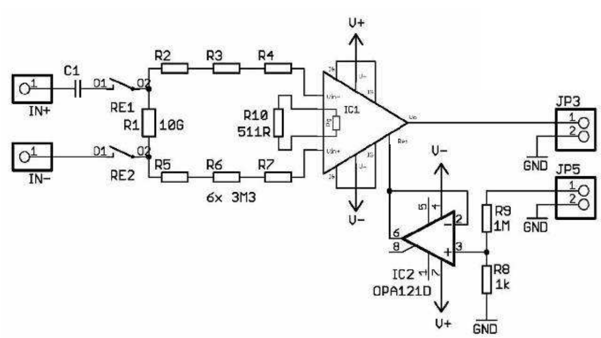

Figure 5: Design of low-level amplifier.

5. NUMERICAL MODELING

It is possible to carry out analysis of a MG model as a numerical solution by help of Finite element method (FEM). The electromagnetic part of the model is based on the solution of full Maxwell's equations. It was solved like simply electrostatic field , SOLID123. Solution is showed in Figure 6. In postprocessor was simulated many cases of ion position and its moving. This results showed to new facts in gerdien condenser design. The new knowledge were tested in many experiments and our measurement system had approximately 50% better characteristics. In Figure 7 is showed one effect of light negative ion inside of gerdien condenser. There are showed the non-primitive moving of one electron. Therefore the sensor has higher noise then sensor with filter.

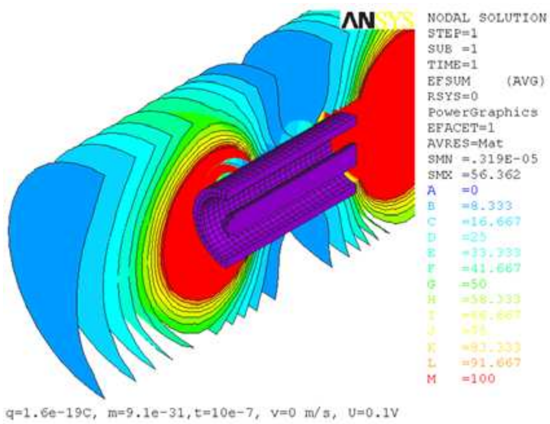

Figure 6: Result — intensity of electric field E.

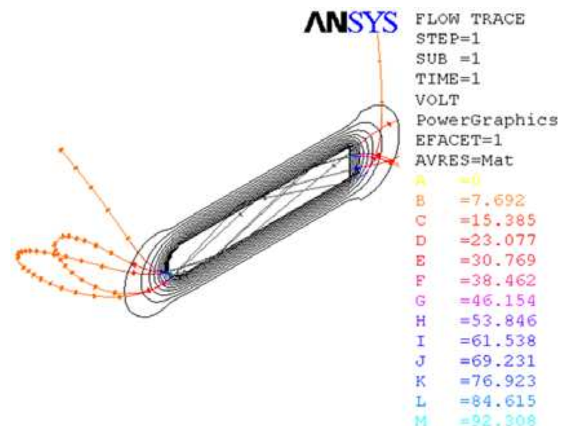

Figure 7: Result — particle moving, trajectory of light negative particle.

New design of gerdien condenser was made with filter for the specific particles. Result of new experiments are showed in Figure 8.

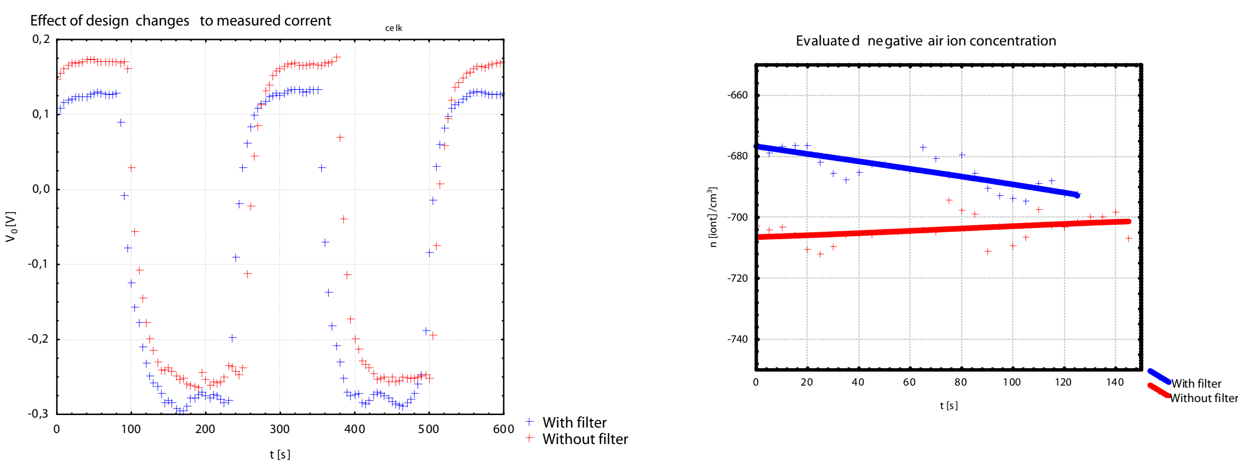

(a) (b)

Figure 8: (a) Result — characteristics of gerdien condenser with filter, time depend. (b) Result — characteristics of gerdien condenser with filter.

6. COMPARISON OF GERDIEN CONDENSERS

The gerdien condenser of new design was compared with two others. Gerdien condenser configuration and parameters are shown in Figures 9–11. Measurement results of condenser are shown in Figure 12. Very low leakage currents were achieved in the new design of gerdien condenser. It allows higher sensitivity measurement. A long-term research task is to create an environment with suitable ion concentration and humidity in living spaces. The ion distribution in the environment will be simulated.

Figure 9: Gerdien condenser [5] ($M = 10.62\,\mathrm{dm}^3$, $v = 4.3\,\mathrm{ms}^{-1}$, $I_{leak} = 0.4\,\mathrm{pA}$ @ 150 V).

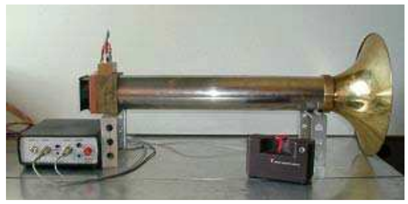

Figure 10: Gerdien condenser [5] ($M = 12.14\,\mathrm{dm}^3$, $v = 3.75\,\mathrm{ms}^{-1}$, $I_{leak} = 0.3\,\mathrm{pA}$ @ 150 V).

Figure 11: New design of gerdien condenser ($M = 0.75\,\mathrm{dm}^3$, $v = 0.8\,\mathrm{ms}^{-1}$, $I_{leak} = 0.05\,\mathrm{pA}$ @ 150 V).

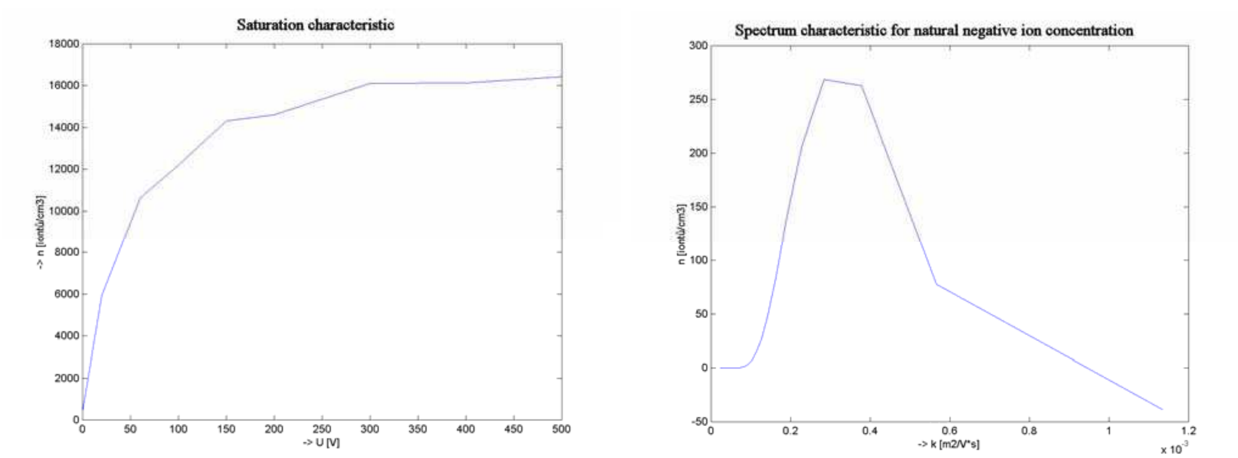

Figure 12: Results of measurement gerdien condenser.

7. CONCLUSION

The new design of gerdien condenser and the optimization of peripheral measuring devices have minimized the systematic error of measurement. The new system allows measuring air ion concentration with a sensitivity $> 100\,\mathrm{ions/cm}^3$. The ion mobility is in the interval 0.3–100 $\mathrm{cm}^2\mathrm{V}^{-1}\mathrm{s}^{-1}$. The system will be used to measure ion field distribution in living and office spaces.

ACKNOWLEDGMENT

The paper were prepared within the framework of VUT Brno of the Czech Republic and with the support of the research plan MSM 0021630516 and grant GAAV No. B208130603.

REFERENCES

1. Bartušek, K., "Měření speleoterapeutických parametrů jeskyní pro lékařské účely," *Interní Text UPT AV ČR*, 1997.
2. Buřival, Z., "Vliv prostorového náboje v atmosféře na znečištění vzduchu v technologických provozech," *Knižnice Odborných a Věeckých Spisů*, VUT, Brno.
3. Spurny, Z., *Atmosferická Ionizace*, Praha. Academia, 1985.
4. Puškeilerová, L., "Nové poznatky o měření volných záorných iontů v laboratorním prostředí," *Příspěvek k VŠTČ FEI*, Brno, 2000.
5. Israël, H., *Atmosphärische Elektrizität*, Akademische Verlagsgesellschaft, Leipzig, 1957.
6. Smutný, T., "Vliv obvodových prvků na přesnost měření iontových polí," *Diplomová Práce 2004*, VUT, Brno.
7. Kafka, V., "Saturační a spektrální charakteristika iontového pole," *Diplomová Práce 2004*, VUT, Brno.

Microwave Applications in Growth and Physical Property Measurements of Nanomaterials

J. T. Lue[1], **L. W. Chang**[2], **and H. Y. Miao**[3]

[1]Department of Physics, Tsing Hua University, Hsin Chu, Taiwan, China
[2]Department of Electrical Engineering, Tsing Hua University, Hsin Chu, Taiwan, China
[3]Department of Mechanical Engineering, Kaohsiung University of Applied Sciences
Kaohsiung, Taiwan, China

Abstract— Low-power microwave spectrometer and electron spin resonance spectrometer have long been exploited in analyzing the strcture of specified moleculars and free radicals contained in gas, and solid materials. High-power microwave sources have recently expected to stimulate many innovative applications in generation new materials and/or in performing surface modification. Diamond carbon films and carbon nanotubes (CNT) were succesfully grown by the microwave plasma enhanced chemical vapor deposition (MPECVD). Aligned CNTs and a single CNT tube across a nickle bridge can be grown providing electron field emission and the 1D conductivity investigation. The real and imaginary parts of the complex dielectric constant of metallic nanoparticles at various microwave frequencies of the TM_{010} mode can be determined from the resonant frequency and the quality factor, respectively, of the transmission resonance spectrum. The real parts of the dielectric constants of single wall CNTs are negative behaving metqallic. The imaginary parts are small at high frequency and largely increase at low frequencies which satisfically agree with the Drude free electron model. Microwave microstrips made of conducting magnetic films also intriguing an exploration of the frequency and temperature dependence on the conductivity of good and not good conducting films. Conventional ferromagnetic resonance for magnetic thin films is found to be co-existed with the transmission resonance of a T-type microwave micro-strip at certain applied magnetic fields. The conductivity, the magnetization, and the magnetic anisotropic field of magnetic films can be evolved eventually from the measured resonance frequency and the quality Q factor of the resonance spectra. This work provides a closely scrutinized method to delineate the magnetic and electric properties of the deposited magnetic films succinctly.

Microwave enhanced chemical vapor deposition is extensively implemented to growth high quality, high adhesion and high-hardness films such as carbon nitride, diamond, diamond-like and carbon nanotubes. We have used microwave assistance in chemical dissociation of a radio-frequency-field-assisted hot-filament chemical vapor deposition (RFCVD) system [1] as shown in Fig. 1 to grow well-aligned carbon nanotubes exploited a self-dc-bias induced by rf-field. With the usually deposited catalyst films on the silicon surface replaced by polished Cu-Ni and Cu-Ni-Fe-Co bulk alloys as substrates, we can grow the well-aligned carbon nanotubes featured in Fig. 2.

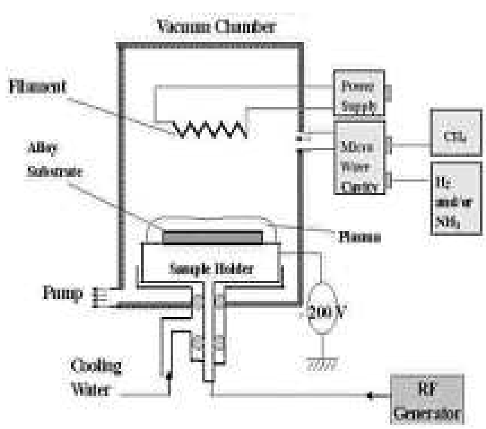

Figure 1: The radio-frequency-field-assisted hot-filament chemical vapor deposition (RFCVD) system.

We have also constructed an impedance-matched microwave plasma enhanced CVD system as shown in Fig. 3 where the microwave field from the TE_{100} wave guide is fed to the TM_{100} circular

Figure 2: The as-grown well-aligned multi-wall carbon nanotubes.

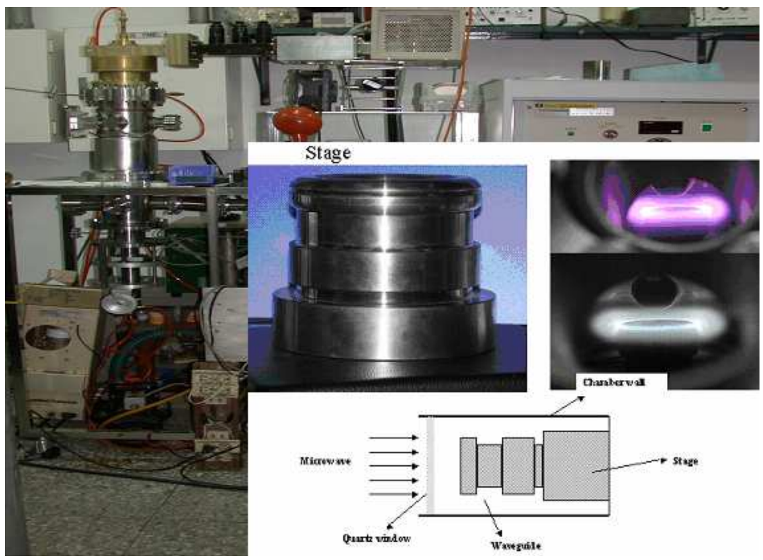

Figure 3: The Impedance-matched microwave plasma enhanced chemical vapor deposition system.

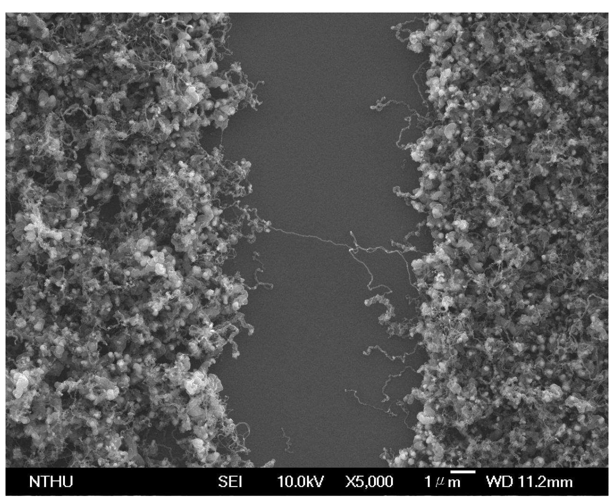

Figure 4: A solo carbon nano wire is grown on the catalyst electrodes.

resonator with the impedance is matched by the cylindrical block stage as illustrated in the inset [2]. With an introduction of carbon dioxide prior to the CNTs growth period, the plasma ball can be easily built above the substrate surface thereby evoking the CNT growth at low input power emanating a direct growth single carbon nanowire on the catalyst electrodes as shown if Fig. 4. This sample provides the one dimensional transport measurement at high currents to justify the quantum theory of Luttinger liquid.

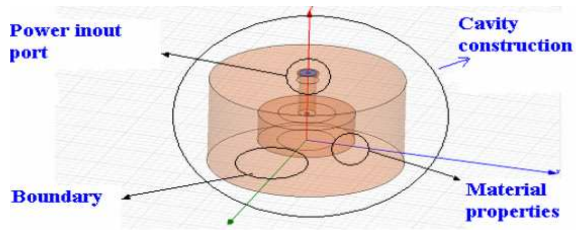

Figure 5: Microwave cylindrical dielectric resonator providing the measurement of dielectric constant of metallic powders.

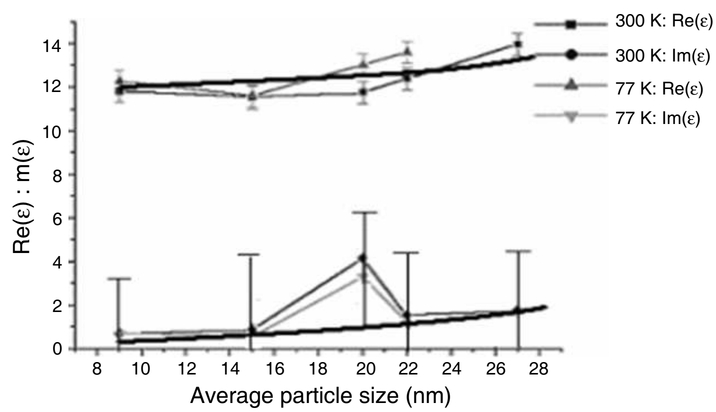

$$\lim_{\omega\to 0, q\to 0} \varepsilon(q,\omega) = \varepsilon_0 - 0.1061(k_F a_0)[R/a_0]^2 + i\, 0.1061(k_F a_0)[R/a_0]^2$$

Figure 6: The real and imaginary parts of the dielectric constant of silver at various sizes and temperatures, the solid curves ate simulated from the classical size effect.

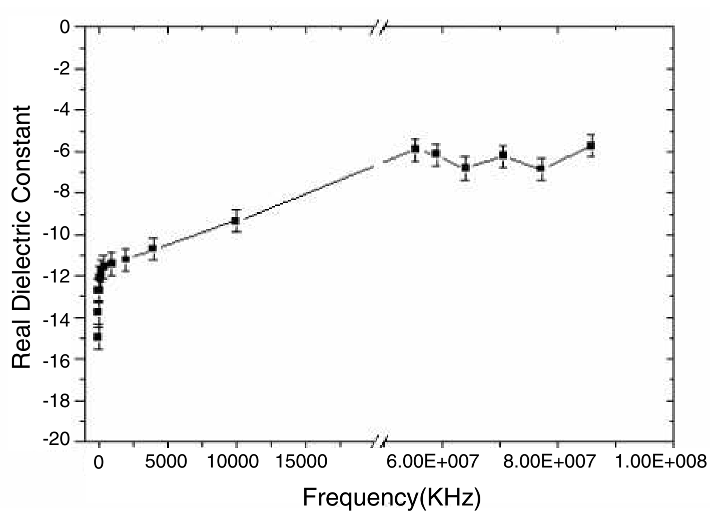

Figure 7: The real dielectric constant of SWCNTs at various frequencies from dc to microwave.

A cylindrical rod composed of a uniform mixture of metallic nanoparticles and alumina powder as dissolved in pareffin was inserted at the center of a cylindrical microwave cavity as sketched in Fig. 5. The real and imaginary parts of the complex dielectric constant of metallic nanoparticles at various microwave frequencies can be retrieved from the resonant frequency and quality factors, respectively, of the transmission resonance spectrum. The admixture of paraffin with metalic powders emunizes from moisture absorption and air filling within the rod resulting in a higher accuracy and stability in the determination of experimerntal values than the dielectric double-cavity method [3]. The dielectric constants of metallic nanoparticles is deduced from the effective medium approximation for the mixture system. In this work, we have measured the real and imaginary parts of silver nanoparticles of various particle sizes at room and liquid nitrogen temperatures as shown in Fig. 6. The real part of the dielectric constant for single wall carbon nanotubes is also illustrated in Fig. 7.

The frequency dependence of the conductivity and magnetic properties of magnetic films can also measured by the coexistence of ferromagnetic and structure mode resonance of a microwave T-type microstrips (MSMR) designed in Fig. 8 where the resonance dips are changed with the applied magnetic fields as shown in Fig. 9. We can derive the physical constants from this measurement.

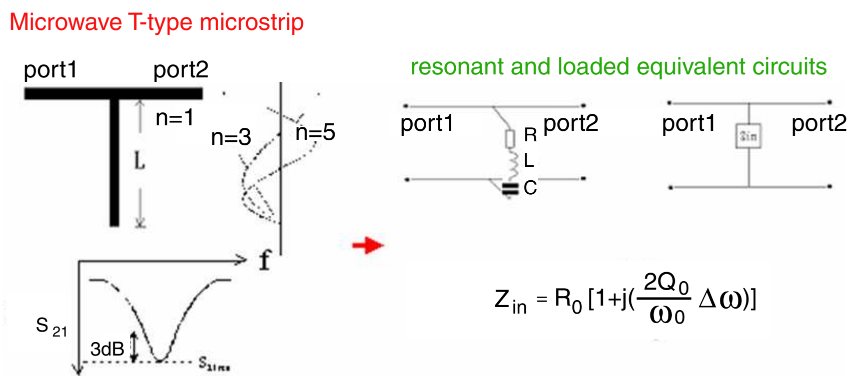

Figure 8: The construction of the microwave T-type microstrips providing the FMR and MSMR resonance.

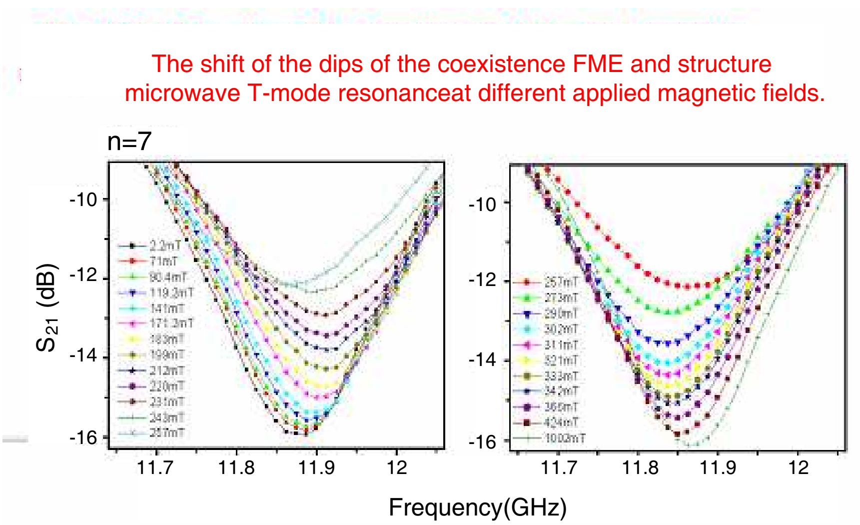

Figure 9: The shift of the resonance dips at various applied magnetic fields.

REFERENCES

1. Che, S. Y., H. Y. Miao, and J. T. Lue, *J. Phys. D: Appl. Phys.*, Vol. 37, 273, 2004.
2. Che, S. Y., L. W. Chang, H. Y. Miao, and J. T. Lue, *J. Nonoscience* & *Nanotech*, Vol. 5, 1887, 2005.
3. Liu, J. H., C. L. Chen, H. T. Lue, and J. T. Lue, *IEEE Microwave Wireless Components*, Vol. 13, 181, 2003.

Complex Dielectric Measurement Using TM_{010} Cylindrical Cavity

Jing Li and C. Richard Liu
Department of ECE, University of Houston, 4800 Calhoun Rd. Houston, TX 77204, USA

Abstract— Electrical properties are important parameters in characterizing materials. For example, in electrical logging, dielectric constant and conductivity are used to characterize oil and gas reservoirs. At high frequencies, dielectric parameters are difficult to measure in lossy materials. In this paper, an automated dielectric constant measurement system using TM_{010} cylindrical cavity is developed, which can measure the electrical properties of rock samples with different water and oil saturation levels and borehole fluids. Operating software was programmed using LabVIEW for equipment control, sample measurement and data processing. Easy-to-use software interface was also provided. After sample measurement and data processing, the relative dielectric constant and the conductivity of the test sample can be displayed graphically. By implementing the automatic measurement systems, the procedure for sample measurement and data processing are simplified and much more efficient.

1. TM_{010} RESONANT CAVITY TECHNIQUE

A TM_{010} resonant cavity has been used to measure the complex dielectric permittivity of the core samples at 1.1 GHz. The cavity was assumed to be made of perfect conductors for theoretical analysis [1, 2]. The cavity with a sample placed at the middle in the cylindrical coordinate is shown in Fig. 1 [1–3].

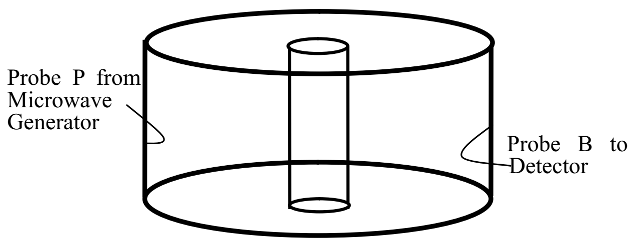

Figure 1: Cylindrical cavity in cylindrical coordinate with the core sample in the middle.

By investigating the fields inside the cavity, the mathematical expression of the relative dielectric constant of the core sample can be expressed as [3–7]:

$$\varepsilon_1 = \frac{2\sqrt{\varepsilon_2}}{\omega\sqrt{\mu_0\varepsilon_0}R_1}A \tag{1}$$

where:
ε_1=relative dielectric constant of the sample;
ε_2=relative dielectric constant of the sample holder;
ω=resonant frequency of the cavity;
R_1=radius of the sample.
A is a coefficient which can be expressed by Bessel functions.

2. MEASUREMENT APPARATUS

The automatic measurement system consists of a LabVIEW software package, HP8510C Network Analyzer and a TM_{010} resonant cavity. The HP8510C network analyzer is used to measure S parameters of the resonant cavity. A block diagram of the automatic measurement system is shown in Fig. 2. A photo of this system is shown in Fig. 3.

The computer control program is developed using LabVIEW 7.0. The operations, such as equipment control, sample measurement, data acquisition and processing, parameter calculation, and results display are accomplished using LabVIEW. One user friendly interface is also provided as shown in Fig. 4. The operator selects the proper test signal from the user interface. The relative dielectric constant and conductivity of the core sample will be displayed and S-parameters measured by HP8510C will be plotted on computer screen in real time.

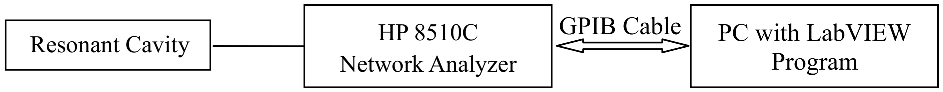

Figure 2: Block diagram of the resonant cavity measurement system.

Figure 3: Workstation of the resonant cavity technique.

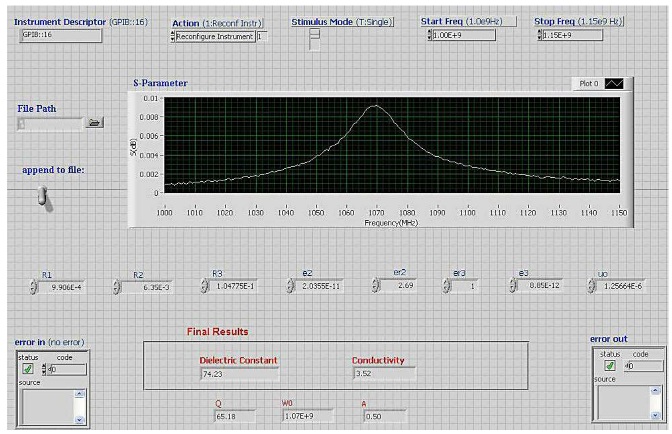

Figure 4: User interface of the cavity technique.

3. MEASUREMENTS AND RESULTS

The measurement system is first calibrated when the sample holder is empty. In this case, the relative dielectric constant measured is calibrated as 1. When distilled water is filled in the sample holder, the measured relative dielectric constant is verified as 81.03. The results are in good consistent with the unknown values. Then measurements for various samples can be performed.

3.1. Saline Solutions with Different Salinities

In order to test the measurement accuracy of the resonant cavity measurement system, saline solutions with different salinities have been measured. The solutions were prepared using deionized water and sodium chloride with less than 0.013 percent of other ions and impurities [3]. The salinity was in units of kppm (kiloparts per million by weight). The diameter of the sample holder is 1 mm. The water level is a little bit convex to the top of the sample holder in order to have good contact between the sample solution and the cavity cover.

The relative dielectric constant and conductivity of the saline solutions were measured with salinities ranging from 5 to 20 kppm at the room temperature. The differences between the current experimental data and the previous data [2, 3] are less than 5 percent as shown in Table 1. It shows that the resonant cavity measurement system has satisfied accuracy.

Table 1: Measured data of saline solutions.

Saline solutions	Measurement Data		Reference Data [3]		Difference
(kppm)	ε_r (F/m)	σ (S/m)	ε_r (F/m)	σ (S/m)	ε_r/σ (%)
5	80.2000	1.3020	79.1000	1.2460	1.3720/4.3010
8	76.6500	1.7470	76.5200	1.7190	0.1700/1.6030
10	77.9300	1.9810	77.0400	2.0760	1.1420/4.5760
13	78.8600	2.5360	76.7000	2.7160	2.7390/6.6270
15	78.0300	3.0700	75.3200	3.0600	3.4730/0.3260
20	76.1400	3.6030	73.0800	3.7860	4.0190/4.8340

3.2. Asphalt and Mortar Sand with Different Moisture Contents

Using the resonant cavity, samples of other materials were also measured. The radius of these samples is 0.383 inches, height is 1.000 inch; radius of sample holder is 0.501 inches, and height is 1.0000 inch. The measurement data of asphalt material is: $\varepsilon_r = 4.3000\,\mathrm{F/m}$ and $\sigma = 0.0060\,\mathrm{S/m}$ at the room temperature.

The mortar sand sample was prepared by using $Quikrete^R$ Mortar Mix No.1102. The mix was placed into the sample holder and compressed tightly. The sample became drier with time because both evaporation and cement hydration. The water left in the sample were free water and structural water which was not sensitive to the dielectric constant measurements. The dielectric constant measurement may be more sensitive to the change of free water.

The mortar sample with different moisture contents was tested. The sample was measured in one hour period. Due to the evaporation of water, time in the figure is inversely proportional to the moisture contents. Measured data of the mortar sample with different moisture contents at the room temperature are shown in Figs. 5 and 6.

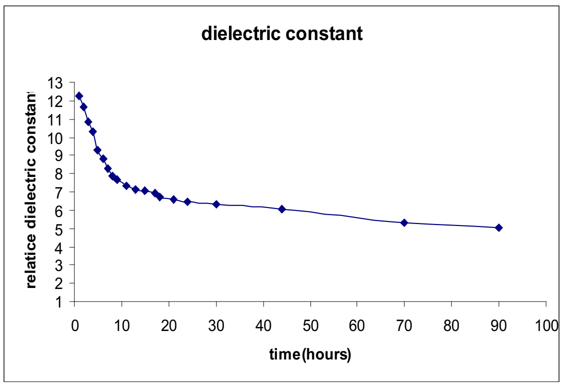

Figure 5: Relative dielectric constant of mortar sand with different moisture contents.

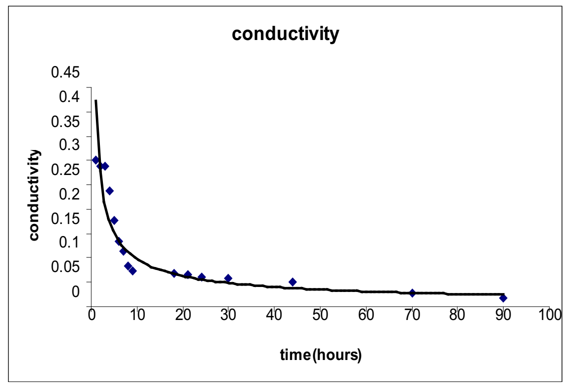

Figure 6: Conductivity of mortar sand with different moisture contents.

4. ERROR ANALYSIS

The main errors are system errors and operating errors. The system errors result from the limitation of the resonant cavity, sample preparation, sample holder and instruments, which can directly influence accuracy of measurements [8]. The operating error, which is generated when samples are handled during the measurement, is an indication of the repeatability of the measurement. The volume error of saline solutions can be avoided by using a syringe to carefully inject it into the sample holder in order to avoid air bubbles. The water level must be a little bit convex to the top of the sample holder to make sure good contact. The measurement errors can be reduced by repeating measurement couples of times. The operating errors are much greater than the system errors and are considered to be the main factor in determining measurement accuracy.

5. CONCLUSIONS

The automatic measurement system was established at 1.1 GHz to measure complex dielectric constant of rock samples and borehole fluids. The instrument control and data processing program was developed using LabVIEW. Easy-to-use software interfaces was also provided. By implementing the automatic measurement system, sample measurement and data processing procedures were simplified.

The system was established by using the resonant cavity, HP8510C Network Analyzer, and LabVIEW computer control program. Measurement accuracy of the automatic measurement system was proved from measurement results of saline solutions with different salinities. Asphalt and mortar samples and their sample holders were designed and tested. The relative dielectric constant and conductivity of mortar with different moisture contents, which are not available in existing literature, were presented.

REFERENCES

1. Li, J., "Electrical property measurement of rocks in the range of 10 KHz to 1.1 GHz," Master Thesis, University of Houston, 2005.

2. Zhao, X. and R. C. Liu, "Numerical analysis of a TM_{010} cylindrical cavity for dielectric measurement," *IEEE Transaction on Microwave Theory and Techniques*, Vol. 40, No. 10, University of Houston, 1991.
3. Zhao, X., "Measurement of samples in a TM_{010} cylindrical cavity at 1.1 GHz," Master Thesis, University of Houston, 1991.
4. Harrington, R. F., *Time-harmonic Electromagnetic Fields*, McGraw-Hill, Inc., 1961.
5. Shen, L. C. and J. A. Kong, *Applied Electromagnetism*, Third Edition, PWS Publishing Company, 1995.
6. Pozar, D. M., *Microwave Engineering*, Third Edition, John Wiley & Sons, Inc., Hoboken, NJ, 2003.
7. McQuarrie, D. A., *Mathematical Methods for Scientists and Engineers*, University Science Books, Sausalito, California, 2003.
8. Su, S. M., "Measurement of dielectric constant and conductivity of petroleum reservoir rocks at microwave frequencies," Master Thesis, University of Houston, 1982.

Spectroscopic Characterization of $Ba(Mg_{1/3}Ta_{2/3})O_3$ Dielectrics for the Application to Microwave Communication

Hsiu-Fung Cheng[1], **Chia-Ta Chia**[1], **Hsiang-Lin Liu**[1], **Mei-Yu Chen**[1]
Yuan-Tai Tzeng[1], **and I-Nan Lin**[2]

[1]Department of Physics, National Taiwan Normal University, Taipei, Taiwan 116, Taiwan, China
[2]Department of Physics, Tamkang University, Taipei, Taiwan 251, Taiwan, China

Abstract— The lattice vibrational modes of the $Ba(Mg_{1/3}Ta_{2/3})O_3$ materials, possessing dielectric constants $K = 22.2$–25.5 and quality factor $Q \times f = 182,600$–$248,000$ GHz, were characterized by Raman and FTIR spectroscopies. The high-Q materials possess sharpest vibrational modes, viz., smallest full-width-at-half-maximum (FWHM) value for Raman peaks and smallest damping coefficient γ_j value for FTIR peaks and vice versa.

1. INTRODUCTION

Complex perovskite compounds with the chemical formula $Ba(B'_{1/3}B''_{2/3})O_3$, where B' is Zn, Mg, Ni, or Mn and B'' is Nb or Ta, exhibit ultra-low dielectric losses at microwave frequencies [1–3], when the materials possess B'–B'' 1:2 ordered arrangement with a structural symmetry described by the $P\underline{3}m1\,(D^3_{3d})$ space group [4]. Since the dielectric properties at microwave range follow mainly from ionic polarization, the phonon vibration spectra of $Ba(B'_{1/3}B''_{2/3})O_3$ have been of particular interest [5–8]. H. Tamura et al. [5] first analyzed the vibration of 1:2 ordered $Ba(Zn_{1/3}Ta_{2/3})O_3$ normal modes, and I. G. Siny et al. [6] investigated the Raman spectra of several complex perovskites, proposing the existence of short-range 1:1 order in $Ba(Mg_{1/3}Ta_{2/3})O_3$ (BMT). Recently, C. T. Chia et al. [7] studied the Raman phonons in $Ba(Mg_{1/3}Ta_{2/3})O_3$ and correlates the lattice vibration characteristics with the dielectric properties of the materials. In this study, the Raman and FTIR spectra of $Ba(Mg_{1/3}Ta_{2/3})O_3$ were used to investigate the correlation between the phonon properties with the ordering phenomenon of the materials, so as to understand the mechanism influencing the microwave dielectric properties of the materials.

2. EXPERIMENTS

BMT ceramic samples were prepared by a conventional mixed oxide process. As shown in Table 1 BMT samples were sintered at 1600°C in air for 4–200 h and then cooled at the different rates (2–200°C/h). The dielectric properties were measured by the TE011 resonant cavity method using an HP 8722 network analyzer, near 6 GHz [9]. Far-infrared and mid-infrared reflectance spectra were obtained at room temperature using a Bruker IFS 66v FTIR spectrometer. The modulated light beam from the spectrometer was focused onto either the sample or an Au reference mirror, and the reflected beam was directed onto a 4.2-K bolometer detector $\sim$30–600 cm^{-1} and a B-doped Si photoconductor $\sim$450–4000 cm^{-1}. The different sources, beam splitters, and detectors used in

Table 1: The dielectric properties of the $Ba(Mg_{1/3}Ta_{2/3})O_3$ materials processed by different conditions, where the dielectric properties were either measured by resonance cavity method at 6 GHz or were deduced from FTIR spectroscopy at 1 THz.

Sample	Ordering parameters (S)	Processing[a]		Microwave Properties		FTIR Properties	
		time (h)	rate (°C/h)	$K_{6\,\mathrm{GHz}}$	$Q \times f$ (GHz)	K_{FTIR}	$Q \times f$ (THz)
A	1.000	200	2	22.2	248,000	26.3	15.2
B	0.995	20	20	22.3	205,700	26.2	11.0
C	0.966	4	200	25.5	182,600	26.1	9.4

[a]time: sintering time at 1600 °C; rate: cooling rate (°C/h) after sintering.

these studies provided substantial spectral overlap, and the reflectance mismatch between adjacent spectral ranges was less than 1%. The optical properties were calculated from a Kramers-Kronig analysis of the reflectance data [10]. These transformations were performed by extrapolating the reflectance at both low and high frequencies. The low-frequency extensions were determined by using the Lorentz model. Raman measurements were taken at room temperature, and the signals were recorded by a DILOR XY-800 triple-grating Raman spectrometer, equipped with a liquid-nitrogen-cooled CCD. The 10-mW output of the 514.5-nm line of an Ar ion laser was used as the excitation source. The obtained Raman spectra exhibited a resolution approximately $0.5\,\mathrm{cm}^{-1}$.

3. RESULTS AND DISCUSSION

3.1. Characteristics of Raman Spectra

The Raman spectra of the three BMT materials are shown in Fig. 1(a), indicating that the Raman peaks are very sharp, a characteristic for the high-Q materials. Among the major Raman peaks, the A_{1g}(O) mode at $796\,\mathrm{cm}^{-1}$ varies more markedly among the samples. Detailed analyses show that the characteristics of this Raman resonance peak are closely related with the microwave dielectric properties of the materials. Figure 2(a) reveals that the Raman peak shift is largest for the sample C, which possesses largest dielectric constant ($K_C = 25.5$), and is smallest for sample A, which owns smallest K value ($K_A = 22.2$). However, the change is very modest. In contrast, Fig. 2(b) illustrates that the Raman peak width (full-width- at-half-maximum, FWHM) is narrowest ($(\mathrm{FWHM})_A = 14.55\,\mathrm{cm}^{-1}$) for sample A, which possesses highest quality factor ($(Q \times f)_A = 248,000\,\mathrm{GHz}$), and is broadest ($(\mathrm{FWHM})_C = 15.16\,\mathrm{cm}^{-1}$) for sample C, which has lowest $Q \times f$ value ($(Q \times f)_C = 182,600\,\mathrm{GHz}$) (Table 1).

While the characteristics of the Raman resonance peak of BMT materials correlate with the microwave dielectric properties of these materials very well, what is the genuine factor altering these Raman characteristics is still not clear. Detailed analysis on the Raman spectra reveals the presence of the Raman peaks corresponding to *1:2-order-phonon* in frequency regime of 150–$300\,\mathrm{cm}^{-1}$ (Fig. 1(a)). The relative intensity, which is defined as the ratio of integral intensity of E_g(O), E_g(Ta) and A_{1g}(Ta) Raman peaks associating with the *non-ordering* of the A1g(Ba) Raman peak at $105\,\mathrm{cm}^{-1}$, *non-ordering phonons*, was calculated. Figure 1(b) shows that the relative intensities of the *1:2-order-phonon* Raman peaks are larger for the samples with higher quality factor ($Q \times f$). In fact, the relative intensity of the three *1:2-order-phonon* Raman peaks with respective to other non-ordering Raman peaks, such as E_g(Ba) at $103\,\mathrm{cm}^{-1}$, A_{1g}(O) at $384\,\mathrm{cm}^{-1}$, or E_g(O) at $431\,\mathrm{cm}^{-1}$, also leads to the similar trend (not shown).

3.2. Characteristics of Infrared Spectra

While the Raman spectroscopy correlates with the microwave dielectric properties of the materials very well, it cannot explain directly the dielectric response of the materials, since the Raman resonance is not a polar mode. In contrast, the Fourier transform infrared (FTIR) spectroscopy is the response of polarization of the materials with respect to the electromagnetic field (infrared). However, although the FTIR spectroscopy relates to the dielectric properties of the materials more

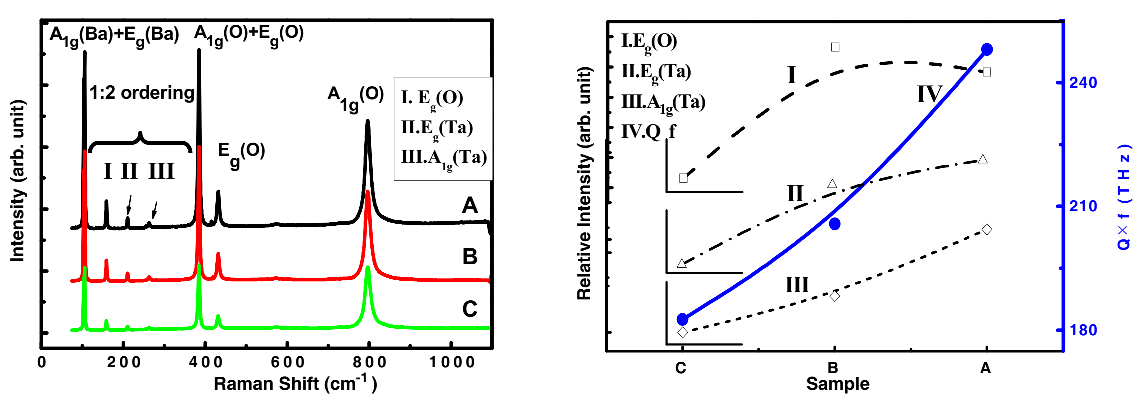

(a) (b)

Figure 1: (a) Typical Raman spectra of the $\mathrm{Ba(Mg_{1/3}Ta_{2/3})O_3}$ materials and (b) variation of relative intensity of *1:2-order-phonon* modes for three BMT samples : (I) $\mathrm{E}_g(\mathrm{O})/\mathrm{A}_{1g}(\mathrm{Ba})$, (II) $\mathrm{E}_g(\mathrm{Ta})/\mathrm{A}_{1g}(\mathrm{Ba})$, (III) $\mathrm{A}_{1g}(\mathrm{Ta})\mathrm{A}_{1g}(\mathrm{Ba})$, and (IV) quality factor ($Q \times f$).

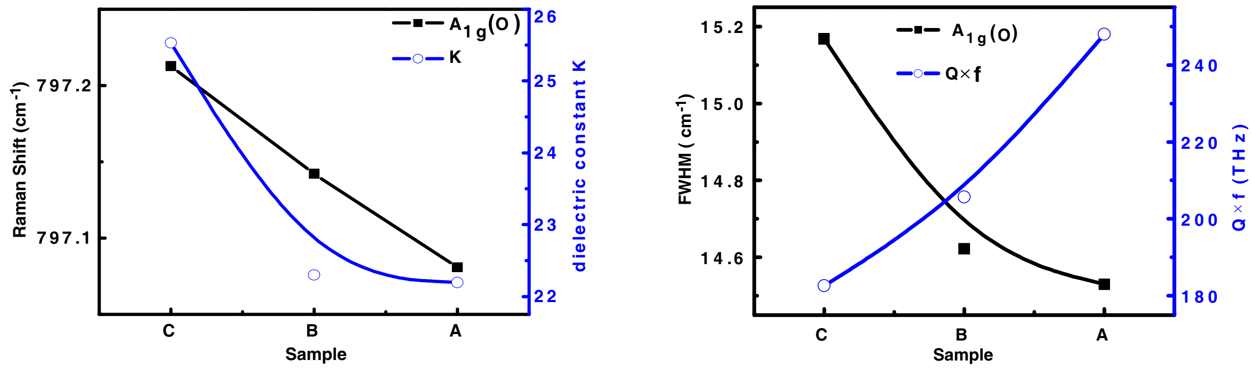

(a) (b)

Figure 2: Variations of (a) Raman shift and dielectric constant, (b) full-width-at-half-maximum (FWHM) of the $A_{1g}(O)$ modes and quality factor ($Q \times f$) among the three $Ba(Mg_{1/3}Ta_{2/3})O_3$ materials with different microwave dielectric properties.

directly, the analysis on the FTIR spectra is complicated. Figure 3(a) shows reflection spectra of the the BMT samples measured in the range of 30–6500 cm^{-1}, along with the fitted data (dotted lines). The reflection spectra were analyzed using Kramers-Kronig (K-K) relationship [10], in which the Lorentz distribution of the TO modes is used for fitting the spectra, i. e.,

$$\omega\varepsilon_2 = \sum_j \left(\frac{4\pi e^2 N_j}{mV}\right) \cdot \frac{\gamma_j \omega^2}{\left(\omega_{0j}^2 - \omega^2\right)^2 + \gamma_j^2 \omega^2} \tag{1}$$

The factor analysis indicates that among the normal modes for BMT materials of P$\underline{3}$m1 symmetry, $4A_{1g}$[Ba, Ta or O] + A_{2g} + $5E_g$ [Ba, Ta or O] + $2A_{1u}$ + $7A_{2u}$ [Ba, Mg, Ta or O] + $9E_u$ [Ba, Mg, Ta or O], the $7A_{2u}$ + $9E_u$ modes are IR active. Figure 3(b) shows the $\omega\varepsilon_2$ dispersion of BMT materials deduced from the reflection spectra using K-K analysis. The important dispersion parameters, including resonance frequency (ω_{oj}), the damping coefficient (γ_j), and resonance strength ($4\pi\rho_j$) of the jth mode resonator, corresponding to Figure 3(b) are listed in Tables 2(a) and 2(b). It should be noted that in these tables, only the ω_{oj}, γ_j, and $4\pi\rho_j$ of the major resonance peaks including $A_{2u}(O_{II})$ at 244 cm^{-1} and $E_u(O_{II})$ at 224 cm^{-1} are listed, since previous reports[11] indicated that these FTIR normal modes are of larger resonance strength ($4\pi\rho_j$) and are the most important modes, influencing the dielectric properties of the materials.

The dielectric properties at lower microwave frequency regime can be calculated using dispersion equations[10],

$$\varepsilon_1 = \varepsilon_\infty + \sum_j \left(\frac{4\pi e^2 N_j}{mV}\right) \cdot \frac{1}{\omega_{0j}^2} = \varepsilon_\infty + \sum_j 4\pi\rho_j, \tag{2}$$

$$\frac{1}{Q} = \sum_j \tan\delta_j = \sum_i \frac{4\pi\rho_j \gamma_j \omega}{\omega_{0j}^2 \varepsilon_1}. \tag{3}$$

The calculated dielectric properties at $\sim$30 cm^{-1} (K_{FTIR}&$Q \times f_{\mathrm{FTIR}}$) are also listed in Table 1. The dielectric constant derived from FTIR spectra ($K_{\mathrm{FTIR}} \sim 26.3$) is similar to as that measured at microwave frequency regime ($K_{6\,\mathrm{GHz}} \sim 22.2$), indicating that there is no vibrational resonance mode in between microwave frequency and the terahertz regime (6 GHz–1 THz). This is an important factor for a high-Q material, as the vibrational resonance modes occurred at low frequency regime usually quite lossy and will lead to low Q-value for the materials. Moreover, the $Q \times f_{\mathrm{FTIR}}$-values calculated from FTIR spectra vary among the BMT samples in a manner the same as the way that the $Q \times f_{6\,\mathrm{GHz}}$-values measured by TE011 resonant cavity technique [9] change with the samples, that is, the samples with larger $(Q \times f)_{6\,\mathrm{GHz}}$-values at microwave frequency regime also possess larger $(Q \times f)_{\mathrm{FTIR}}$-values in tetrahertz frequency regime.

The resonance frequency (ω_{oj}) of the vibrational modes relates to the strength of Ta-O (or Mg-O) bonds, which, in turn, relates to the polarizability of the Ta-O (or Mg-O) dipoles and hence correlates with the dielectric constant (K) of the materials. Table 2 shows that the resonance

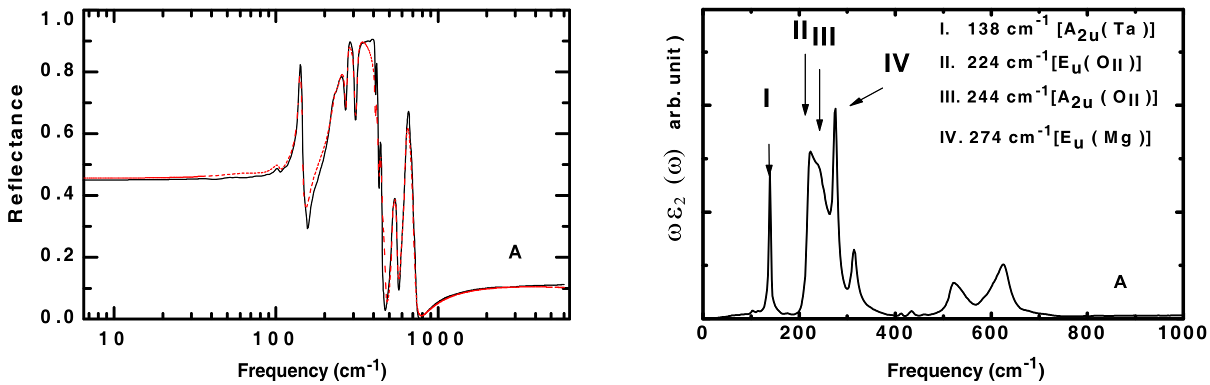

(a) (b)

Figure 3: Typical FTIR spectrum: (a) reflection spectra, (b) dielectric dispersion ($\omega\varepsilon_2$) of BMT sample A.

frequencies of the two major vibrational modes vary insignificantly among the three BMT materials, which is in accordance with the fact that the K values for these samples are similar with one another. In contrast, damping coefficient (γ_j) of the vibrational modes relates to the coherency of lattice vibration, which, in turn, relates to the dielectric loss factor of the materials, as indicated in Eq. (3). The larger the γ_j-value is, the higher the dielectric loss (smaller Q factor). Table 2 shows that the damping coefficient of the $A_{2u}(O_{II})$ modes varies most markedly, whereas that of the $E_{2u}(O_{II})$ modes changes least appreciably, among the samples. The damping coefficient of $A_{2u}(O_{II})$ modes is smallest ($(\gamma_j)_A = 29.2\,\text{cm}^{-1}$) for sample A, which possesses the largest $Q \times f$-value (248,000 GHz), and is the largest ($(\gamma_j)_C = 36.0\,\text{cm}^{-1}$) for sample C, which possesses the smallest $Q \times f$-value (182,600 GHz).

Table 2: The dispersion parameters (resonance frequency, ω_{oj}, damping coefficient, γ_j, and resonance strength, $4\pi\rho_j$) of the major resonance peaks derived from Lorentz simple-harmonic model for the three BMT materials.

(a) $A_{2u}(O_{II})$ at $244\,\text{cm}^{-1}$			
	ω_{oj} (cm^{-1})	γ_j (cm^{-1})	$4\pi\rho_j$
A	245.0	29.2	10.57
B	243.9	34.0	9.38
C	244.0	36.0	8.46

(b) $E_u(O_{II})$ at $244\,\text{cm}^{-1}$			
	ω_{oj} (cm^{-1})	γ_j (cm^{-1})	$4\pi\rho_j$
A	230.5	20.9	9.19
B	227.8	20.1	6.61
C	224.5	20.0	6.21

The above-described results imply that the coherency of the $A_{2u}(O_{II})$ vibrational mode is very sensitive, whereas the characteristics of $E_u(O_{II})$ vibrational mode is relatively insensitive, to the ordering of the Ta- and Mg-cations. The possible explanation for such a phenomenon is that the O_{II}-layer is the layer sandwiched in between two Ta-layers. The $A_{2u}(O_{II})$ mode is the vibration of O_{II}-layer out of plane, towarding the Ta-layer, and is more sensitive to the Ta-O bonding strength. In contrast, the $E_u(O_{II})$ mode is the vibration of O_{II}-layer in plane and is relatively insensitive to the Ta-O bonding strength. Substituting some Mg-ions for Ta-ions due to the change in the ordering of cations disturbs the uniformity of the Ta-O bonding and the coherency of O_{II}-layer vibration, as it is the layer sandwiched in between two Ta-layers. Therefore, such a substitution degrades the coherency of $A_{2u}(O_{II})$ FTIR vibrational modes, and hence leads to larger damping coefficient (γ_j) of these modes, decreasing the quality factor ($Q \times f$-value) of the materials. Restated, the characteristics of FTIR vibrational modes vary among the BMT samples in a similar trend with the characteristics of Raman vibrational modes, and correlate very well with the crystal structure parameters, the *ordering parameter* (S in Table 1) of the materials.

4. CONCLUSION

The lattice vibrational modes of the BMT materials with different microwave dielectric properties were characterized by Raman and FTIR spectroscopies. These characteristics were correlated with the microwave dielectric properties of the materials, which, in turn, is related to the crystal structure parameters, such as *ordering parameters* of the materials. The Raman-shift ($\Delta\omega_{oj}$) of the Raman peaks and the resonance frequency (ω_{oj}) of the FTIR peaks vary insignificantly, whereas the full-width-at-half-maximum (FWHM) of the Raman peaks and the damping coefficient (γ_j) of the FTIR peaks vary markedly, among the samples. Such a behavior correlates very well with the phenomenon that the K values for these materials are similar with one another and the $Q \times f$-values vary markedly for the samples.

ACKNOWLEDGMENT

The authors would like to thank the National Science Council in Taiwan, China for financial supporting this research under Contract No. NSC 95-2112-M-003-018-MY2.

REFERENCES

1. Nomura, S., K. Toyama, and K. Kaneta, *Jpn. J. Appl. Phys.*, Part 2, Vol. 21, L642, 1982.
2. Guo, R., A. S. Shalla, and L. E. Cross, *J. Appl. Phys.*, Vol. 75, 4704, 1994.
3. Nomura, S., T. Konoike, Y. Sakabe, and K. Wakino, J., Am. Ceram. Soc., Vol. 67, 59, 1984.
4. Galasso, F. S., *Properties and Preparation of Perovskite-type Compounds in Structure*, 13–15, Pergamon, Oxford, 1969.
5. Tamura, H. D., A. Sagala, and K. Wakino, *Jpn. J. Appl. Phys.*, Part 1, Vol. 25, 787, 1986.
6. Siny, I. G., R. W. Tao, R. S. Katiyar, R. A. Guo, and A. S. Bhalla, *J. Phys. Chem. Solids*, Vol. 59, 181, 1998.
7. Chia, C. T., Y. C. Chen, H. F. Cheng, and I. N. Lin, *J. Appl. Phys.*, Vol. 94, 3360, 2003.
8. Cheng, H. F., Y. C. Chen, and I. N. Lin, *J. European Ceram. Soc.* Vol. 26, 1801, 2006.
9. Kajfez, D. and P. Guillon, *Dielectric Resonators*, Chap. 6, Artech House, Norwood, MA, 1986.
10. Spitzer, W. G., R. C. Miller, D. A. Kleinman, and L. E. Howarth, *Phys. Rev.*, Vol. 126, 1710, 1962.
11. Chen, Y. C., H. F. Cheng, H. L. Liu, C. T. Chia, and I. N. Lin, *J. Appl. Phys.*, Vol. 94, 3365, 2003.

Improving the Characteristics of $Ba_2Ti_9O_{20}$ Materials by Using Pre-reacted Ba-Ti-O Compounds

I-Nan Lin
Department of Physics, Tamkang University, Tamsui 251, Taiwan, China

Chi-Ben Chang and Keh-Chyang Leou
Department of Engineering and System Science
Tsing-Hua University, Hsinchu, Taiwan 300, China

Abstract— The effect of starting materials Ba-Ti-O compound mixture, $2BaTiO_3$+$7TiO_2$ (type A) or $BaTi_4O_9$+$BaTi_5O_{11}$ (type B), on the characteristics of the $Ba_2Ti_9O_20$ materials was investigated. Both materials can be sintered to the same high density (>96% T. D.) with the same large dielectric constant ($K = 35\sim38$). While the microwave dielectric constant (K) of the materials are not sensitive to detailed microstructure of the samples, the $Q\times f$-value of the materials correlates with the microstructure of the samples closely and therefore varies appreciably with the processing details. Comparing with the "two-step densification processes", the "one-step densification processes" improved pronouncedly the characteristics of the type B materials, but degraded markedly those of the type A materials. The possible explanation for such a phenomenon is that direct sintering of type A mixture requires complicated reaction steps to form the Hollandite-like phase and thus leads to non-uniformed microstructure, which results in inferior microwave properties.

$Ba_2Ti_9O_{20}$ phase was first reported by Jonker and Kwestroo in BaO-TiO_2-SnO_2 ternary system [1] and was observed to possess marvelous microwave dielectric properties, including high dielectric constant and large quality factor, by O'Bryan et al. [2]. Although increasing the calcinations temperature can result in pure Hollandite-like $Ba_2Ti_9O_{20}$ phased powders and circumvent the deleterious effect of the preferentially formed $BaTi_4O_9$ or $BaTi_5O_{11}$ phases on the microstructure uniformigy of the Hollandite-like structured $Ba_2Ti_9O_{20}$ materials. Low activity and anisotropic growth of the $Ba_2Ti_9O_{20}$ particulates along c-axis will hinder the densification of the samples. Therefore, in conventional mixed oxide process for preparing the $Ba_2Ti_9O_{20}$ materials [3–7], the powders were always calcined at a temperature lower than that is needed to completely transform the powders into Hollandite-like $Ba_2Ti_9O_{20}$ phase, resulting in multiple phased powders. Therefore, the occurrence of reactions among the phases during the sintering process is inevitable and the processing reliability in the preparation of $Ba_2Ti_9O_{20}$ materials is thus not satisfactory. In this paper, the reactions among the constituents in the sintering process was carefully controlled by using pre-reacted Ba-Ti-O compounds, viz. either $2BaTiO_3 + 7TiO_2$ or $BaTi_4O_9 + BaTi_5O_{11}$ mixtures. The characteristics of the Ba2Ti9O20 materials thus obtained will be described and the possible mechanism will be discussed.

The $Ba_2Ti_9O_{20}$ materials were synthesized via the conventional mixed oxide process, using nano-sized $BaTiO_3$ (~50 nm) and anatase TiO_2 (~50 nm) as starting materials. Two types of mixture were used for preparing the $Ba_2Ti_9O_{20}$ samples. In type A materials, $2BaTiO_3$ and $7TiO_2$ powders were mixed thoroughly, whereas, in type B materials, the $BaTi_4O_9$ and $BaTi_5O_{11}$ powders were first prepared by calcining the $BaTiO_3$+$3TiO_2$ and $BaTiO_3$+$4TiO_2$ mixture at 1000°C/4 h, pulverized, and then thoroughly mixed. Two densification processes were adopted for synthesizing the $Ba_2Ti_9O_{20}$ materials. In the "two-step densification" process, both of the type A and type B of mixtures were first calcined at 1000°C for 4 h (in air), followed by a 3-dimensional milling process to disintegrate the agglomerates. These powders were then pressed into pellets and were sintered at 1250~1400°C for 4 h (in air). In the "one-step densification" process, the $2BaTiO_3 + 7TiO_2$ (type A) and $BaTi_4O_9 + BaTi_5O_{11}$ (type B) powder mixtures were pulverized, pelletized and then sintered directly. The temperature was increased to 1000°C, held for 6 h and then was directly increased to 1300~1410°C, soaked for 4 h. The microstructure of the sintered samples was examined using scanning electron microscopy (Jeol 6700F). The crystal structure of the calcined powders and sintered samples was examined using x-ray diffractometry (Rigaku D/max-II). The density of the sintered materials was measured using Archimedes method. The microwave dielectric constant (K) and quality factor ($Q \times f$) of the $Ba_2Ti_9O_{20}$ samples were measured using a cavity method at 7–8 GHz [8].

1. $Ba_2Ti_9O_{20}$ MATERIALS PREPARED FROM TYPE A MIXTURE

Pure Hollandite-like structure is obtained for the 1250∼1350°C sintered type A samples, regardless of the densification process used for preparing the materials. However, the XRD peaks of the "one-step processed" samples are slightly broaden, which could be due to the incomplete reaction of $BaTiO_3$ & TiO_2 phases or the partial dissociation of $Ba_2Ti_9O_{20}$ phase (not shown). Both processes densify the materials efficiently, such that the samples achieve a density higher than 96% T. D. (theoretical density) when sintered at a temperature higher than 1250°C/4 h in air. The sintered density increased moderately with the sintering temperature and reached 97.8% T. D. when 1350°C/4 h (air)-sintered (Table 1(a)), regardless of the densification process.

Table 1: The characteristics of the type A $Ba_2Ti_9O_{20}$ materials, which were prepared from $2BaTiO_3$+$7TiO_2$ compound mixture and were sintered by "one-step densification routes" or "two-step densification routes".

Characteristics \ Process[a]	Two-step Process			One-step Process		
	1300°C	1350°C	1400°C	1300°C	1350°C	1400°C
(a) Density (%T. D.)	98.1	98.0	-	97.0	97.8	-
(b) Dielectric Constant (K)	39.3	38.8	-	37.5	38.2	-
(c) Quality factor ($Q \times f$, GHz)	26,000	28,000	-	29,200	30,000	-

[a] One-step process: the pellets were pre-reacted at 1000°C for 6 h and then sintered at 1300∼1400°C for 4 h; Two-step process: the powder mixture were calcined at 1000°C for 6 h and cooled to room temperature; pelletized and then sintered at 1300∼1400°C for 4 h.

The densification process imposes pronounced effect on the microwave dielectric properties of the materials. The microwave dielectric constant (K) and the quality factor ($Q \times f$) of the materials increased moderately with the sintering temperature and is around $K = 38.8$ for 1350°C/4 h-sintered type A samples. The microwave dielectric constant (K) of "one-step processed" samples is about 2∼3% lower that that of "two-step processed" ones (Table 1(b)), whereas the $Q \times f$-value of the "one-step processed" type A materials is about 7∼8% higher than that of the "two-step processed" ones (Table 1(c)). For the samples sintered at 1350°C/4 h, the quality factor is $(Q \times f)_{A1} = 30,000$ GHz for "one-step processed" materials and is $(Q \times f)_{A2} = 28,000$ GHz for "two-step processed" ones.

The SEM microstructure of these samples was examined in order to understand the genuine factor resulting in better Oxf-value for "one-step processed" samples. Figure 1(a) shows that the granular structure of the "two-step processed" type A materials is quite uniform and the grains are of rod-shaped geometry with small aspect ratio (length/diameter around 2∼3). The grains, which are of roundish-geometry with very small size (3×1 µm) for 1250°C-sintered samples, grows monotonously with temperature to about 7×1.8 µm in size, with the geometry of the grains transformed into faceted-one for 1350°C-sintered samples. Such a result implies that better development of the microstructure is possibly the factor resulting in the higher $Q \times f$-value for the 1350°C-sintered type A samples, as compared with those sintered at lower temperature, since all the samples possess the same high density (>96%T. D.) and are of pure Hollandite-like phase. However, detailed examination indicates that there exists some abnormally grown grains in these materials (circled, Fig. 1(a)). Moreover, SEM micrographs in Fig. 1(b) illustrate that "one-step process" results in even more complicated microstructure for the 1350°C-sintered type A materials. Most of the grains are of small rods-geometry with large aspect-ratio (4×1.4 µm) and there exists large proportion of large rod-shaped grains with small aspect-ratio. Direct sintering these materials at 1400°C results in even more complicated microstructure. There exists long-rods (12.0×2.0 µm), short rod (2.8×1.4 µm) and equi-axis (~ 1.2 µm) grains.

Previous studies [7] revealed that, for the type A materials ($2BaTiO_3$+$7TiO_2$), the perovskite $BaTiO_3$ first reacted with anatase TiO_2 to form $BaTi_4O_9$ phase at 950°C. The $BaTi_4O_9$ phase partially reacted with TiO_2 to form $BaTi_5O_{11}$ phase at 1050°C, instead of directly transformed into $Ba_2Ti_9O_{20}$ Hollandite-like phase. It takes 1100°C to complete the phase transformation process for the formation of $Ba_2Ti_9O_{20}$ Hollandite-like phase. In contrast, there is no marked reaction occurred for type B materials ($BaTi_4O_9 + BaTi_5O_{11}$) calcined at a temperature lower than 1000°C, but the phase transformation process is completed at 1025°C, forming Hollandite-like phase.

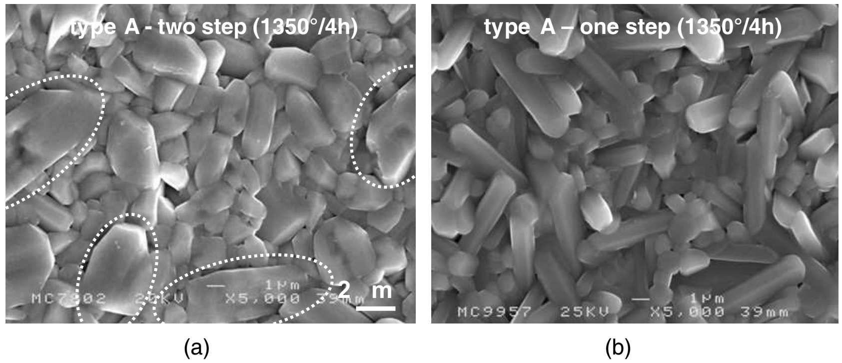

Figure 1: SEM micrographs of the type A $Ba_2Ti_9O_{20}$ materials sintered by (a) "two-step densification routes" and (b) one-step densification routes at 1350°C/4 h. The materials were prepared from type A ($2BaTiO_3$ $+7TiO_2$) compound mixture.

The reaction sequence during sintering of the type A materials are schematically depicted in Fig. 2(a), which shows that the 1000°C-calcined powders used for pelletizing the type A samples still contain large proportion of $BaTiO_3$, TiO_2 and $BaTi_4O_9$ phases, in addition to the partially transformed $Ba_2Ti_9O_{20}$ phases. These mixture will experience many reaction steps, including the formation of Hollandite-like phase at 1100°C, before starting the densification process. The complicated reaction process occurred in type A materials usually induces the non-uniformity in chemical composition and possibly formed the residual TiO_2 and $BaTi_4O_9$ aggregates (Fig. 2(b)). Therefore, local melting phenomenon is expected due to the peritectic reaction between TiO_2 and $Ba_2Ti_9O_{20}$ phases [9, 10], when the type A materials were fired at too high temperature (e.g., 1400°C).

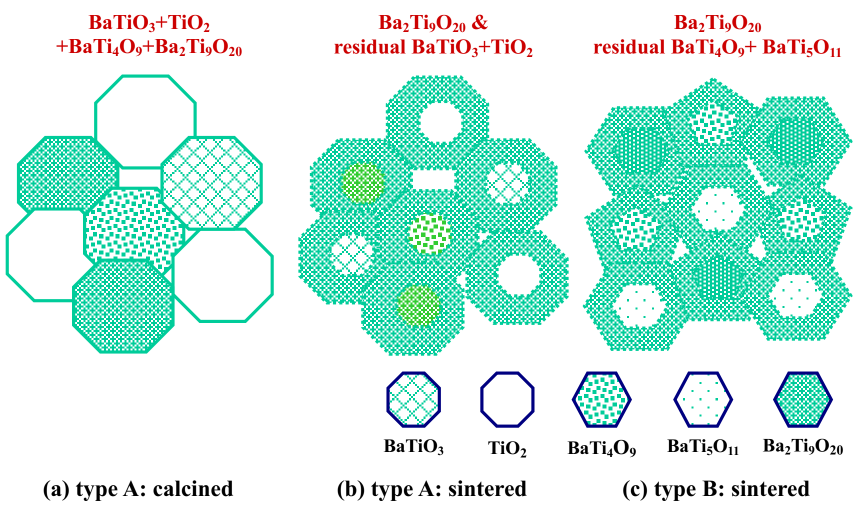

Figure 2: Schematics showing the phases constituents of type A materials ($2BaTiO_3 + 7TiO_2$) after (a) calcinations at 1000°C/4 h and (b) sintering at 1350°C/4 h; (c) those of type B materials ($BaTi_4O_9$ + $BaTi_5O_{11}$) after sintering at 1350°C/4 h, in the "two-step densification process".

In contrast, the type B powders, which are mixture of $BaTi_4O_9$ and $BaTi_5O_{11}$, are readily forming the $Ba_2Ti_9O_{20}$ phase at 1025°C (Fig. 2(c)). Therefore, the initial stage of sintering process, i.e., necking of particulates, is expected to occur slightly earlier for the type B materials and the grains grow slightly larger after sintering, as compared with those for type A materials. Moreover, the chemical composition for type B materials is much more uniform and can withstand higher sintering temperature, since there is no complicated reaction occurred before the onset of densification process among the $BaTi_4O_9$, $BaTi_5O_{11}$ and $Ba_2Ti_9O_{20}$ phases.

2. $Ba_2Ti_9O_{20}$ MATERIALS PREPARED FROM TYPE B MIXTURE

The above described results indicate that reaction among phase constituents during sintering is inevitable for synthesizing the $Ba_2Ti_9O_{20}$ Hollandite-like materials. The reaction sequence between the $BaTi_4O_9$ and $BaTi_5O_{11}$ compounds (type B compounds) is much more simpler than the type A compounds and is expected to be able to improve the characteristics of the $Ba_2Ti_9O_{20}$ materials. The $BaTi_4O_9$ and $BaTi_5O_{11}$ mixtures were thus utilized, in lieu of the type A compound, for preparing the $Ba_2Ti_9O_{20}$ Hollandite-like materials. Basically, Hollandite-like phase was resulted for the type B materials, no matter whether they were synthesized by "one-step process" or by "two-step process" (not shown). No secondary phase or peak broadening occurs for these samples due to the simplification of reaction sequence.

The characteristics of the type B $Ba_2Ti_9O_{20}$ materials prepared by "one-step process" and "two-step process" are shown in Table 2. Both processes densify the type B materials efficiently, such that all the samples possess very high density and large dielectric constant, i.e., $D > 97\%$ T. D. and $K > 38.5$ (Tables 2(a) & 2(b)), regardless of the densification process. However, "one-step process" leads to markedly better $Q \times f$-value for the type B $Ba_2Ti_9O_{20}$ materials, as compared with the conventional "two-step process" ones. Table 2(c) shows that the $Q \times f$-value for "two-step processed" type B materials increases from $(Q \times f)_{\mathrm{B}\,1300} = 28,000$ for 1300°C-sintered samples to $(Q \times f)_{\mathrm{B}\,1350} = 30,500$ for 1350°C-sintered ones and decreases slightly to $(Q \times f)_{\mathrm{B}\,1400} = 28,000$ for the 1400°C-sintered ones. In contrast, the $Q \times f$-value for "one-step processed" type B materials increases monotonously with sintering temperature, reaching a $Q \times f$-value as high as $(Q \times f)_{\mathrm{B}\,1400} = 33,800$ for 1400°C-sintered type B materials (Table 2(c)).

Table 2: The characteristics of the type B $Ba_2Ti_9O_{20}$ materials, which were prepared from $BaTi_4O_9$ $+BaTi_5O_{11}$ compound mixture and were sintered by "one-step densification routes" or "two-step densification routes".

Process[a] / Characteristics	Two-step Process			One-step Process		
	1300°C	1350°C	1400°C	1300°C	1350°C	1400°C
(a) Density (%T. D.)	98.2	98.3	98.1	97.2	97.2	98.1
(b) Dielectric Constant (K)	39.2	38.9	38.2	37.9	38.2	38.2
(c) Quality factor ($Q \times f$, GHz)	28,000	30,500	28,000	29,600	31,000	33,800

[a] One-step process: the pellets were pre-reacted at 1000°C for 6 h and then sintered at 1300∼1400°C for 4 h; Two-step process: the powder mixture were calcined at 1000°C for 6 h and cooled to room temperature; pelletized and then sintered at 1300∼1400°C for 4 h.

Figure 3(a) shows that the granular structure for the type B materials is markedly more uniform than that for type A materials. The grains are also of rod-shaped geometry with small aspect ratio and the grain size increases moderately with sintering temperature, which correlates very well with the increase of $Q \times f$-value with the sintering temperature for the type B materials. For the samples sintered at 1350°C/4 h, the grains of the type B materials are about the same size as that of type A materials ($\sim 3.0 \times 1.5\,\mu$m). But abnormally grown grains, which occurred to type A materials, was not observable for type B ones. SEM micrographs in Fig. 3(b) illustrates that "one-step process" improves profoundly the uniformity of granular structure for type B materials. The 1350°C-sintered materials contain grains of short-rod geometry with small aspect-ratio ($3.0 \times 1.5\,\mu$m). But no abnormal grain growth phenomenon was induced even for 1400°C-sintered samples (not shown), except that the average grain size of the samples increases slightly, to $7.0 \times 3.0\,\mu$m. These results imply that "one-step sintering process" results in superior microstructure for the type B materials, although it leads to inferior granular structure for the type A materials, as compared with those prepared by "two-step sintering process".

The above-described results support the argument that the improvement in granular structure of the samples, rather than the higher sintered density, is the prime factor resulting in superior quality factor ($Q \times f$-value) for the type B materials. However, the attempt to improve the granular structure of the materials by sintering the samples at higher temperature (1400°C/4 h) is not successful. The type A materials melted (not shown), such that, the K- and $Q \times f$-properties of the materials are seriously degraded and are not measurable. For type B materials prepared by "two-step process", the samples were not melted but there appears large proportion of abnormally grown grains (not shown). Both phenomena result in deleterious effect on the microwave dielectric properties for the type B materials. In contrast, for type B materials prepared by "one-step process", the samples still preserve uniform granular structure even when they were sintered at

1400°C/4 h and, thereafter, leads to superior $Q \times f$-factor to the other samples ($Q \times f = 33,800$ GHz, Table 2(c)).

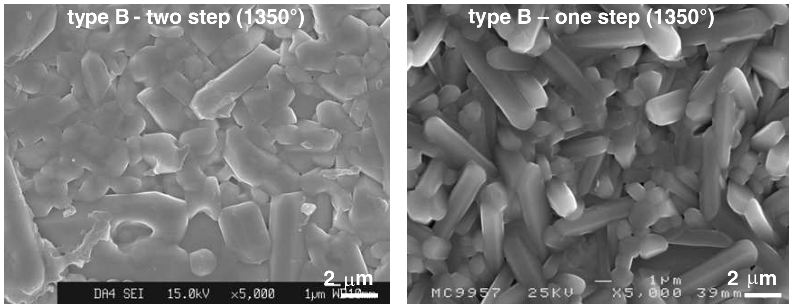

Figure 3: SEM micrographs of the type B — $Ba_2Ti_9O_{20}$ materials sintered by "two-step densification routes" at (a) 1350°C/4 h and (b) 1400°C/4 h. Those of the materials sintered by "one-step densification routes" at (c)1350°C/4 h and (d)1400°C/4 h. The materials were prepared from type B ($BaTi_4O_9 + BaTi_5O_{11}$). mixture.

In summary, effect of starting compound mixtures on the characteristics of $Ba_2Ti_9O_{20}$ materials were systematically investigated. Both the materials prepared from the $2BaTiO_3 + 7TiO_2$ (type A) and $BaTi_4O_9$ +$BaTi_5O_{11}$ (type B) mixtures can be densified to a high density (≧96%), possessing high microwave dielectric constant ($K = 35 \sim 38$), regardless of whether they were prepared by "1-step densification" or "2-step densification" processes. The type B materials show most uniform microstructure and exhibit the highest $Q \times f$-value ($Q \times f = 33,800$ GHz). It is ascribed to the simplicity in reaction routes for the formation of the $Ba_2Ti_9O_{20}$ Hollandite-like phase from $BaTi_4O_9$ + $BaTi_5O_{11}$ mixture, which results in better granular structure for the materials.

ACKNOWLEDGMENT

The authors gratefully thank the financial support of the National Science Council, R. O. C. for this research through the project No. NSC 95-2112-M032-005.

REFERENCES

1. Jonker, G. H. and W. Kwestroo, "Ternary system BaO-TiO_2-SnO and BaO-TiO_2-ZrO_2," *J. Amer. Ceram. Soc.*, Vol. 41, No. 10, 390–394, 1958.
2. O'Bryan, H. M., J. Thomson, Jr, and J. K. Plourde, "A new BaO-TiO_2 compound with temperature-stable high permittivity and low microwave loss," *J. Amer. Ceram. Soc.*, Vol. 57, No. 10, 450–453, 1974.
3. Fang, T. T., J. T. Shiue, and S. C. Liou, "Formation mechanism and sintering behavior of $Ba_2Ti_9O_{20}$," *J. Euro. Ceram. Soc.*, Vol. 22, No. 1, 79–85, 2002.
4. Cerchez, L. and A. Ciupeiu, "Preparation and sintering of $Ba_2Ti_9O_{20}$-based ceramics and their properties for dielectric resonators," *Ceram. Internation*, Vol. 26, No. 1, 99–103, 2000.
5. Lin, W. Y., R. A. Gerhardt, R. F. Speyer, et al., "Thermal processing and properties of $BaTi_4O_9$ and $Ba_2Ti_9O_{20}$ dielectric resonators," *J. Mater. SCI.*, Vol. 34, No. 12, 3021–3025, 1999.
6. Negas, T., G. Yeager, S. Bell, et al., "$BaTi_4O_9$/$Ba_2Ti_9O_{20}$-based ceramics — resurrected for — modern microwave applications," *Amer. Cerem. Soc. Bull.*, Vol. 72 No. 1, 80–89, 1993.
7. Chu, L. W., G. H. Hsiue, I. N. Lin, and Y. C. Chen, "Novel reaction mechanism for the synthesis of $Ba_2Ti_9O_20$ materials prepared from nano-sized oxides," *Nanotechnology*, Vol. 17, 185–191, 2006.
8. Hakki, W. and P. D. Coleman, *IEEE Trans. Mirowave Theory Tech.*, MTT-18, 402, 1980.
9. Roth, R. S., C. J. Rawn, C. G. Lindsay, et al., "Phase-equilibria and crystal-chemistry of the binary and ternary barium polytitanates and crystallography of the barium zinc polytitanates," *J. Solid State Chem.*, Vol. 104, No. 1, 99–118, 1993.
10. O'Bryan, H. M. and J. Thomson, "$Ba_2Ti_9O_{20}$ phase-equilibria," *J. Amer. Ceram. Soc.*, Vol. 66, No. 1, 66–68, 1983.

Low-temperature Crystallization of Lead Zirconate Titanate Thin Films Using 2.45 GHz Microwaves

T. H. Chang[1], **Ankam Bhaskar**[1], **H. Y. Chang**[2], **and S. Y. Cheng**[2]

[1]Department of Physics, Tsing Hua University, Hsinchu, Taiwan, China
[2]Material and Chemical Research Laboratories, Industrial Technology Research Institute
Hsinchu, Taiwan, China

Abstract— Lead zirconate titanate (PZT) thin films of thickness 420 nm were deposited on $Pt/Ti/SiO_2/Si$ substrate using a spin coating sol-gel precursor solution, and then annealed using 2.45 GHz microwaves at a temperature of 450°C for 30 min. The film has a high perovskite content and high crystallinity with a full width at half maximum of 0.35°. Well-saturated ferroelectric properties were obtained with a remanent polarization of 46.86 $\mu C/cm^2$ and coercive field of 86.25 kV/cm. The film also exhibited excellent dielectric properties with a dielectric constant of 1140 and a dissipation factor of 0.03. These properties are superior to those obtained by conventional annealing at a temperature of 700°C for 30 min.

Microwave processing of ceramics has attracted considerable attention in recent years [1] for its volumetric heating, which is capable of uniform sintering, lower processing temperature, shorter processing time, and thus better properties [2]. Microwaves have been utilized for both the synthesis and the sintering of a wide variety of materials, especially oxides [3, 4]. It also has been adopted to anneal thin films [5, 6]. Song et al. [6], using a multimode cavity of 2.45 GHz microwaves, completed the formation of perovskite-phase PZT thin films at a lower temperature (600°C) than that of conventionally annealed PZT thin films (700°C).

Pb $(Zr_xTi_{1-x})O_3$ films have excellent ferroelectric, optical, piezoelectric, and pyroelectric properties [7]. Formation of the ferroelectric perovskite phase in PZT films generally requires temperature of about 600°C which makes it difficult to integrate the films with silicon monolithic circuits. Therefore, decreasing the processing temperature of the PZT thin films has been goal of researchers. However, low temperature processing (< 500°C) of PZT thin films using 2.45 GHz microwaves has not been reported. This study reports the low-temperature processing of $Pb_{1.1}$ $(Zr_{0.53}Ti_{0.47})O_3$ (PZT) thin films deposited on $Pt/Ti/SiO_2/Si$ substrate using a single-mode cavity of 2.45 GHz microwaves. The crystal structure, the surface morphology, and the electrical properties of PZT thin films were investigated. The effects of 2.45 GHz microwaves on PZT thin films (450°C/30 min) are compared to those of conventional annealing of PZT thin films (700°C/30 min).

Figure 1 shows that the conventional annealing of PZT thin films at 450°C yields a broad diffraction peak of (2 2 2) planes of the pyrochlore phase. No peak of the perovskite phase was detected in the thin film because the temperature of the PZT thin film was not high enough for the reaction to occur among the Pb, Ti, Zr, and O. The microwave annealed PZT thin film (450°C) yields a prominent diffraction peak of the perovskite phase (1 1 0) planes, and no peak of the pyrochlore phase was detected in this film. The conventionally annealed PZT thin film at 700°C yielded an XRD pattern that was similar to that of the PZT thin film annealed using 2.45 GHz microwaves. The peak with the highest intensity in the X-ray diffraction pattern of the PZT thin film was indexed as (1 1 0) planes, indicating that the thin film was mostly randomly oriented.

Figure 2 shows the P–E hysteresis loops of microwave and conventionally annealed PZT thin films. The microwave-annealed PZT thin film (450°C) has a square hysteresis loop, a remanent polarization P_r of 46.86$\mu C/cm^2$ and a coercive field E_c of 86.25 kV/cm. An attempt was also made to measure the hysteresis loop of a PZT thin film conventionally annealed at 450°C, but no hysteresis loop was obtained, since it contained only the pyrochlore phase, as revealed by the XRD pattern (Fig. 1). The PZT thin film conventionally annealed at 700°C exhibits a reasonably square hysteresis loop; the value of P_r is lower about 39.40$\mu C/cm^2$; E_c is 101.21 kV/cm, higher 250°C than that of the microwave annealed PZT thin film. Microwave-sintered PZT ceramics yielded similar results [8]. The shape of the hysteresis loop reflected the difference between the crystallinity of the PZT thin films. Notably the low value of E_c is an advantage in device applications, since the power losses are minimized and the switching voltages reduced. Hence, microwave-annealed PZT thin films are better than conventionally annealed PZT thin films. The P_r for this film was higher than the reported values for microwave-annealed thin films [6].

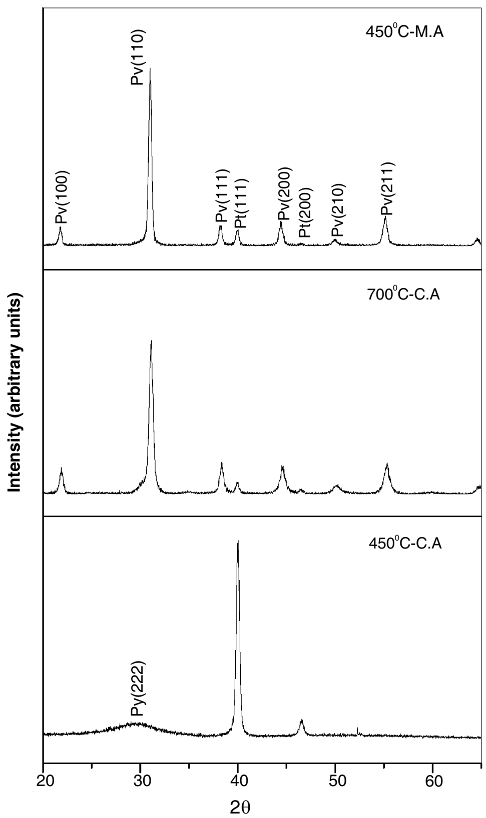

Figure 1: XRD patterns of PZT thin films annealed by microwave annealing (M.A), and conventional annealing (C.A)

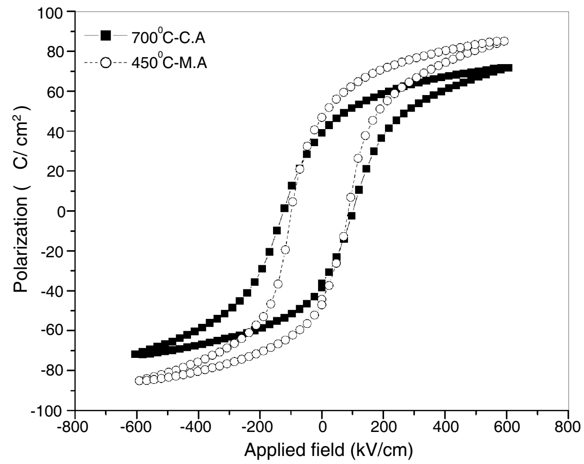

Figure 2: Polarization-electric field hysteresis loops of PZT thin films annealed by microwaves (M.A) and conventionally (C.A).

REFERENCES

1. Roy, R., D. Agrawal, J. Cheng, and S. Gedevanishvili, "Full sintering of powdered-metal bodies in a microwave field," *Nature*, Vol. 399, 668, 1999.
2. Agrawal, D. K., "Microwave processing of ceramics," *Curr. Opin. Solid State Mater. Sci.*, Vol. 3, 480, 1998.
3. Ramesh, P. D., D. Brandon, and L. Schachter, "Use of partially oxidized SiC particle bed for microwave sintering of low loss ceramics," *Mater. Sci. Eng. A*, Vol. 266, 211, 1999.
4. Cheng, J. P., D. K. Agarwal, S. Komarneni, M. Mathis, and R. Roy, "Microwave processing of WC-Co composites and ferroic titanates," *Mater. Res. Innovations*, Vol. 1, 44, 1997.
5. Hart, J. N., Y. B. Cheng, G. P. Simon, and L. Spiccia, "Challenges of producing TiO_2 films by microwave heating," *Surf. Coat. Technol.*, Vol. 198, 20, 2005.
6. Song, S., X. Fu, H. Tan, M. Tao, L. Chen, L. Wang, and C. Lin, "Microstructure of PZT/PT thin films prepared by sol-gel process and microwave annealing," *Phys. Status Solidi A*, Vol. 164, 779, 1997.
7. Scott, J. F., and C. A. Paz de Araujo, "Ferroelectric memories," *Science*, Vol. 246, 1400, 1989.
8. Sharma, P. K, Z. Ounaies, V. V. Vardan, and V. K. Varadan, "Dielectric and piezoelectric properties of microwave sintered PZT," *Smart Mater. Struct*, Vol. 10, 878, 2001.

Raman Interpretation of Microwave Properties of $x\mathrm{Ba(Mg_{1/3}Ta_{2/3})O_3}+(1-x)\mathrm{Sr(Mg_{1/3}Ta_{2/3})O_3}$ Ceramics

C.-T. Chia[1], **P.-J. Chang**[1], **I.-N. Lin**[2], **and L.-J. Lin**[3]

[1]Department of Physics, Taiwan Normal University, Taipei 116, Taiwan, China
[2]Department of Physics, Tamkang University, Tamsui Taipei 251, Taiwan, China
[3]Material and Chemical Research Laboratories
Industrial Technology Research Institute, Chutung Hsinchu 310, Taiwan, China

Abstract— The complex perovskites, $x\mathrm{Ba(Mg_{1/3}Ta_{2/3})O_3}+(1-x)$ $\mathrm{Sr(Mg_{1/3}Ta_{2/3})O_3}$ with $x = 0$, 0.125, 0.25, 0.375, and 0.5 were investigated by Raman scattering and the microwave dielectric measurements. The Raman result shows a dominance of 1 : 2 ordered structure for $x \leqq 0.5$. The microwave dielectric constant linearly increases and $Q \times f$ value decreases with Sr concentrations. The microwave performance is mainly caused by the Sr substitution that induces the rigidity of oxygen-octahedral network, as evidenced by the blue shift and wide width of the $\mathrm{A_{1g}(O)}$ phonon near $800\,\mathrm{cm^{-1}}$, i.e., the stretching mode of oxygen-octahedron.

1. INTRODUCTION

Due to the excellent microwave properties of the perovskite ceramics, such as low loss, high dielectric constant (20–100) and a small temperature coefficient, the microwave materials have attracted much attentions for industrial applications [1–3]. Especially, the 1 : 2 ordered structure perovskite ceramics possesses the known highest $Q \times f$ value and dielectric constant [4]. Recently the optical methods were used to probe the B-site effect on the microwave properties, such as Raman scattering, FTIR measurements [5–9]. On the other hand, relatively several works were published concerning the A-site effect on the microwave properties and phase transformation [10, 11]. During studying of $x\mathrm{Ba(Mg_{1/3}Ta_{2/3})}$ $\mathrm{O_3}+(1-x)\mathrm{Sr(Mg_{1/3}Ta_{2/3})O_3}$, dielectric constant and the sample length as function of temperature calculate from new way and $\mathrm{TC}_f < 0$ the materials are the low-temperature phase at room temperature [12, 13]. The tilting of oxygen octahedral in the perovkite is the important factor to cause structure change that also reflected to a additional infrared active, numerous additional peaks in Raman scattering and new electron microscopic diffraction spots [14, 15]. In this paper, we report the Raman investigation of the $x\mathrm{Ba(Mg_{1/3}Ta_{2/3})O_3}+(1-x)$ $\mathrm{Sr(Mg_{1/3}Ta_{2/3})O_3}$ (hereafter refer to xBMT+$(1-x)$SMT), and phonon lineshape variation around $800\,\mathrm{cm^{-1}}$ due to Sr substitution is discussed. A strong correlation of the oxygen-octahedral property with the microwave properties is found. The variation of dielectric constant and $Q \times f$ value due to Sr substitution are explained based on the Raman results.

2. EXPERIMENT

$x\mathrm{Ba(Mg_{1/3}Ta_{2/3})O_3}+(1-x)\mathrm{Sr(Mg_{1/3}Ta_{2/3})O_3}$ (hereafter refer to xBMT+$(1-x)$SMT) ceramic samples with $x = 0$, 0.125, 0.25, 0.375, and 0.5 were prepared by conventional mixed oxide process. The powder samples were calcined at 1200°C and sintered at 1650°C for 10 h each time. The dielectric properties were measured by the $\mathrm{TE_{011}}$ resonant cavity method using an HP 8722 network analyzer, near 6 GHz [16, 17]. The Raman measurements were taken at room temperature, and the signals were recorded by a DILOR XY-800 triple-grating Raman spectrometer, equipped with a liquid-nitrogen-cooled CCD. The 10 m-W output of the 514.5-nm line of $\mathrm{Ar^+}$ ion laser was used as the excitation source. The obtained Raman spectra exhibited a resolution approximately $0.5\,\mathrm{cm^{-1}}$.

3. RESULTS AND DISCUSSION

The four dominant Raman features of 1 : 2 ordered perovskite ceramics, i.e., A-site vibration near $105\,\mathrm{cm^{-1}}$, 1 : 2 ordered phonons, O-layer related vibrations and stretching mode of oxygen octahedra, are plotted in Fig. 1. A detail analysis of the lineshape of $\mathrm{A_{1g}(O)}$ phonon near $800\,\mathrm{cm^{-1}}$ (i.e., the stretching mode of oxygen octahedra) and the microwave properties are shown in Fig. 2 and Fig. 3. For $x \leqq 0.5$, the 1 : 2 ordered structure is preserved and the width of the $\mathrm{A_{1g}(O)}$ phonon increases with the Sr concentration, and the $Q \times f$ value decreases with the Sr substitution, as found in Fig. 2. In Fig. 3, the blueshifted phonon energy is accompanied by the increasing dielectric constant for $x < 0.5$. This result clearly indicates the stiffness of oxygen-cage increases

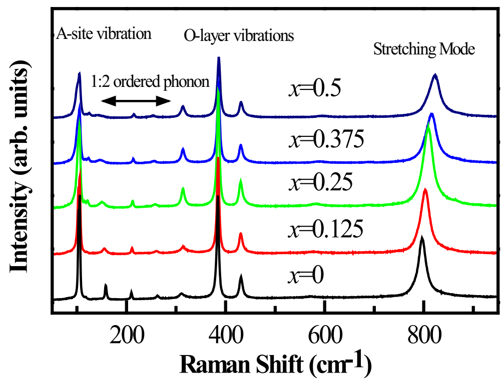

Figure 1: Raman spectra of Ba(Mg$_1$/3Ta$_2$/3)O$_3$+(1-x)Sr(Mg$_1$/3Ta$_2$/3)O$_3$ ceramics.

with the Sr concentration, and this causes the increase of the phonon frequency. However, the small size of Sr ions also induces the degrading of the 1 : 2 order, which may induce the slight twist and distortion of the oxygen octahedras. Our result is similar to the recent publish of Chia et al. [5]. They have shown that the microwave dielectric property is strongly correlated to the stretching mode of oxygen cages for B"-site substitution of 1 : 2 ordered ceramics. In our case, the rigid B"O$_6$ oxygen-octahedral network is due to the antiphase tilting of the oxygen octahedra and also found by Raman measurement. This is the reason that causes dielectric constant increasing with Sr doping, and the degrading of the quality factor. When the Sr replaces Ba (i.e., A-site of 1 : 2 ordered structure), we think the rigid oxygen octahedra is due to small size and the larger electronegativity of Sr. The small Sr^{2+} have plenty space to oscillate with electric field of the propagating microwaves, and this causes the dielectric constant to increase in $0 \leqq x \leqq 0.5$ range. On the other hand, the large space for small Sr^{2+} ion indicates that the A-site structure is slightly loosen and oxygen octahedra is slightly twisted. Therefore, the degrading of the Q factor is expected.

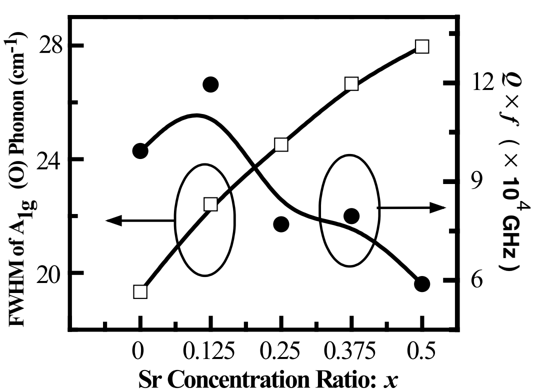

Figure 2: Correlation of A$_{1g}$(O) FWHM with the $Q \times f$ value are plotted as function of x.

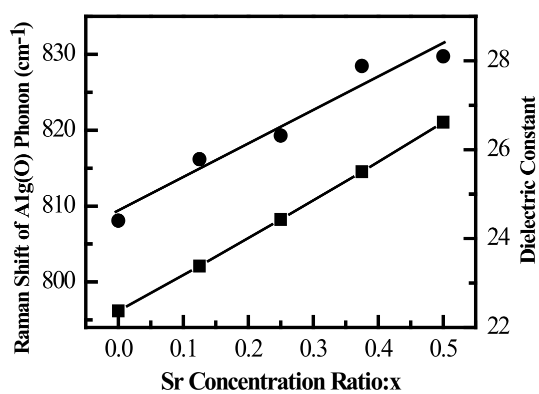

Figure 3: Correlation of A$_{1g}$(O) shift with the microwave dielectric constant are plotted as function of Sr concentrations.

4. CONCLUSION

We have perform the Raman and microwave measurement of xSMT+$(1-x)$BMT ceramics. Sr-concentration dependence of the characteristics of A$_{1g}$(O) phonon and the microwave properties of xSMT+$(1-x)$BMT ceramics were discussed. For $x \leqq 0.5$, the 1 : 2 ordered structure is still preserved for xSMT+$(1-x)$BMT, and the dielectric constant increases and the $Q \times f$ value decreases with increasing Sr substitution. The properties of oxygen octahedra are strongly correlated with the microwave properties.

ACKNOWLEDGMENT

The authors would like to thank the National Science Council, Taiwan, China, for financially supporting this research under Contract Nos. NSC 92-2112-M-003-017 and NSC 93-2112-M-003-012.

REFERENCES

1. Nomura, S., K. Toyama, and K. Kaneta, "$Ba(Mg_{1/3}Ta_{2/3})O_3$ ceramics with temperature-stable high dielectric constant and low microwave loss," *Jpn. J. Appl. Phys.*, Part 2, Vol. 21, L642–626, 1982.
2. Guo, R., A. S. Shalla, and L. E. Cross, "$Ba(Mg_{1/3}Ta_{2/3})O_3$ single crystal fiber grown by the laser heated pedestal growth technique," *J. Appl. Phys.*, Vol. 75, 4704–4708, 1994.
3. Fang, Y., A. Hu, S. Ouyang, and J. J. Oh, "The effect of calcination on the microwave dielectric properties of $Ba(Mg_{1/3}Ta_{2/3})O_3$," *J. Eur. Ceram.*, 2745–2750, Vol. 21, 2001.
4. Siny, I. G., R. W. Tao, R. S. Katiyar, R. A. Guo, and A. S. Bhalla, "Raman spectroscopy of Mg-Ta order-disorder in $BaMg_{1/3}Ta_{2/3}O_3$," *J. Phys. Chem. Solids*, Vol. 59, 181–195, 1998.
5. Chia, C.-T., Y.-C. Chen, and H.-F. Cheng, "Correlation of microwave dielectric properties and normal vibration modes of $x Ba(Mg_{1/3}Ta_{2/3})O_3 - (1-x)\ Ba(Mg_{1/3}Nb_{2/3}O_3)$ ceramics I," *J. Appl. Phys.*, Vol. 94, 3360–3364, 2003.
6. Chen, Y.-C., H.-F. Cheng, H.-L. Liu, and C.-T. Chia, "Correlation of microwave dielectric properties and normal vibration modes of $x Ba(Mg_{1/3}Ta_{2/3})O_3 - (1-x)\ Ba(Mg_{1/3}Nb_{2/3}O_3)$ ceramics II," *J. Appl. Phys.*, Vol. 94, 3365–3370, 2003.
7. Moreira, R. L., F. Matinaga, and A. Dias, "Raman-spectroscopic evaluation of the long-range order in $Ba(B'_{1/3}\ B''_{2/3})O_3$ ceramics," *Appl. Phys. Lett.*, Vol. 78, 428–430, 2001.
8. Iwata, M., H. Hoshino, H. Orihara, H. Ohwa, N. Yasuda, and Y. Ishibashi, Raman scattering in $(1-x)\ Pb(Zn_{1/3}Nb_{2/3})O_3 - xPbTiO_3$ mixed crystal system," *Jpn. J. Appl. Phys.*, Vol. 39, 5691–5696, 2002.
9. Ohwa, H., M. Iwata, H. Orihara, N. Yasuda, and Y. Ishibashi, "Raman scattering in $(1-x)Pb(Mg_{1/3}\ Nb_{2/3})O_3 - xPbTiO_3$," *J. Phys. Soc. Jpn.*, Vol. 70, 3149–3154, 2001.
10. Galasso, F. and J. Pyle, "Preparation and study of ordering in $A(B'_{0.33}Nb_{0.67})O_3$ perovskite-type compounds," *J. Phys. Chem.*, Vol. 67, 1561–1562, 1963.
11. Onoda, M., J. Kuwata, K. Kaneta, K. Toyama, and S. Nomura, "$Ba(Zn_{1/3}Nb_{2/3})O_3$–$Sr(Zn_{1/3}Nb_{2/3})O_3$ solid solution ceramics with temperature-stable high dielectric constant and low microwave loss," *Jpn. J. Appl. Phys.*, Vol. 21, 1707–1710, 1892.
12. Nagai, T., T. Inuauka, and M. Sugiyama, "Contribution of dielectric constant to change in temperature coefficient of resonant frequency in $(Ba_{1-x}Sr_x)(Mg_{1/3}Ta_{2/3})O_3$ compounds," *Jpn. J. Appl. Phys.*, Vol. 31, 3132–3135, 1992.
13. Sugiyama, M. and T. Nagai, "Anomaly of dielectric constant of $(Ba_{1-x}Sr_x)(Mg_{1/3}Ta_{2/3})O_3$ solid solution and its relation to structure change," *Jpn. J. Appl. Phys.*, Vol. 32, 4360–4363, 1993.
14. Nagai, T., M. Sugiyama, M. Sando, and K. Niihara, "Structural change in $Ba(Sr_{1/3}Ta_{2/3})O_3$-type Perovskite compounds upon tilting of oxygen octahedra," *Jpn. J. Appl. Phys.*, Vol. 36, 1146–1153, 1997.
15. Nagai, T., M. Sugiyama, M. Sando, and K. Niihara, "Anomaly in the infrared active phonon modes and its relationship to the dielectric constant of $(Ba_{1-x}Sr_x)(Mg_{1/3}Ta_{2/3})O_3$ compound," *Jpn. J. Appl. Phys.*, Vol. 35, 5163–5167, 1996.
16. Lin, I. N., C. T. Chia, H. L. Liu, H. F. Cheng, and C. C. Chi, "Dielectric properties of $xBa(Mg_{1/3}\ Ta_{2/3})O_3 - (1-x)Ba(Mg_{1/3}Nb_{2/3})O_3$ complex perovskite ceramics," *Jpn. J. Appl. Phys.*, Part 1, Vol. 41, 6952–6956, 2002.
17. Kajfez, D. and P. Guillon, *Dielectric Resonators*, Chap. 6, Artech House, Norwood, MA, 1986.

Image Subtraction Analysis for Finger Color Variation

I. Fujieda[1], **A. Hori**[1], **and K. Tai**[2]

[1]Ritsumeikan University, Japan
[2]A'SYCK Co. Ltd., Japan

Abstract— If a fingerprint sensor can evaluate our health conditions, health-monitoring and data-logging will be quick and easy. We record fingerprint images during an input action, process them by means of subtraction analysis and quantify variations in color and area of the fingerprint. Based on the analogy to an electric circuit, an index related to blood vessel stiffness (resistance) is extracted from the color changes (blood flow) and the area changes (voltage). Analysis on the 150 input trials taken by 50 apparently-healthy subjects shows a correlation coefficient of 0.51 between this index and their ages.

1. INTRODUCTION

Fingerprints identification systems are slowly replacing passwords in personal computers, cell telephones, etc. In order to make a fingerprint sensor replica-proof, we have been studying color changes in a series of fingerprint images acquired during an input action [1]. Finger deformation induces blood movement and the resultant color variation can be used as a signature of a living finger. The configuration of the fingerprint sensor used here is illustrated in Fig. 1. Because it detects both fingerprint images and the light scattered inside a finger simultaneously, it is well suited for this purpose. We have proposed and evaluated various indices in an effort to distinguish artificial fingers from genuine ones. Our initial sensor system with a white LED performed reasonably well for a small number of replicas [2]. Its reliability has been improved by replacing the white LED with the dual LED that enhances the color changes [3]. We have also shown that the dual-LED system is adequately robust against the temperature fluctuation of a finger and that it can be used under an illumination level of 3000 lux [4].

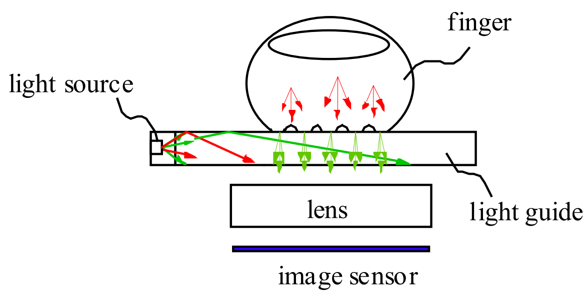

Figure 1: A fingerprint sensor based on scattered-light detection.

If health conditions of an individual were evaluated based on the information extracted from a finger-tip simultaneously, we could record such information automatically every time we log on to the Internet. Health-monitoring and data-logging will be quick and easy. Conventional technologies that evaluate health conditions from a finger-tip include accelerated plethysmography [5] and laser Doppler perfusion imaging [6]. In case of the accelerated plethysmography, a relatively large correlation coefficient of 0.70 has been reported between an index extracted from pulse waveforms and the age of the subjects. However, there are two problems in these methods if we were to adopt them in a personal computer peripheral device. First, in accelerated plethysmography, it takes at least several seconds to detect pulses reliably. Therefore, it is not possible to apply this technique in conjunction with fingerprint identification. Second, in case of the laser Doppler perfusion imaging, expensive extra components (a high-speed CMOS camera and a laser diode) are needed and this increases the size of the system as well as its manufacturing cost.

Previously, we considered a model based on an electric circuit [1]. The blood flow inside a finger was regarded as the current in an electric circuit and the force applied to the finger was related to the voltage. Therefore, the resistance represented the blood vessel stiffness. We analyzed 152 input trails taken by 36 people and correlated the results with their ages. The stiffness index and the age of the subjects were only weakly correlated and the correlation coefficient was 0.21. Since then, we have improved our sensor hardware for more reliable liveliness detection. In this paper, we report a higher correlation coefficient obtained with the dual-LED system and image subtraction analysis.

2. ANALYSIS

The image acquisition apparatus used in this study is exactly the same one as described in Ref. [3]. We apply digital subtraction analysis for the fingerprint images in order to enhance the color variations. The flow of this analysis is as below. First, a color fingerprint image is divided into the three images (R, G and B), each corresponding to each of the color sensors of the image sensor. Second, pixel values in the R and G images are normalized by the following equations. Third, we subtract G_n from R_n. This process is repeated for every pixel.

$$\begin{aligned} R_n &= \frac{R}{R+G} \\ G_n &= \frac{G}{R+G} \end{aligned} \tag{1}$$

In an attempt to extract a signal related to the amount of the residual blood, we define an index b_r as follows. First, the area signal A is defined as the number of pixels exceeding a certain threshold value in the processed image. Second, we set a number b equal to the number of pixels whose $R_n - G_n$ values exceed a pre-determined value in the processed image. This number b is a measure of the amount of blood remaining inside the finger. Finally, we set $b_r = b/A$.

When we plot this index b_r with respect to A, it shows remarkably different behaviors, depending on the ages of the subjects. An example is illustrated in Fig. 2(a). Here, the area signal A is normalized by its maximum value $A_{\max}$ in order to compensate the individual variations in the finger size. The spacing between the markers corresponds to the time interval between the subsequent images, namely 1/15 second in the experiment described in this paper. The index b_r obtained from a 22 year-old male decreases to about 0.2 when the finger deformation reaches maximum. On the other hand, for a 62 year-old male, the index only decreases to about 0.7. Another point to be noted is that the trajectories of b_r do not coincide during the pressing period and the releasing period. The same data are plotted as a function of the time for the input action in Fig. 2(b). Again, the difference between the young and old subjects is clear. These behaviors of this index reflect the ease of the blood movement inside a finger and they may be utilized for evaluating our conditions of blood vessels. Next, we will define such an index, blood vessel stiffness R_b.

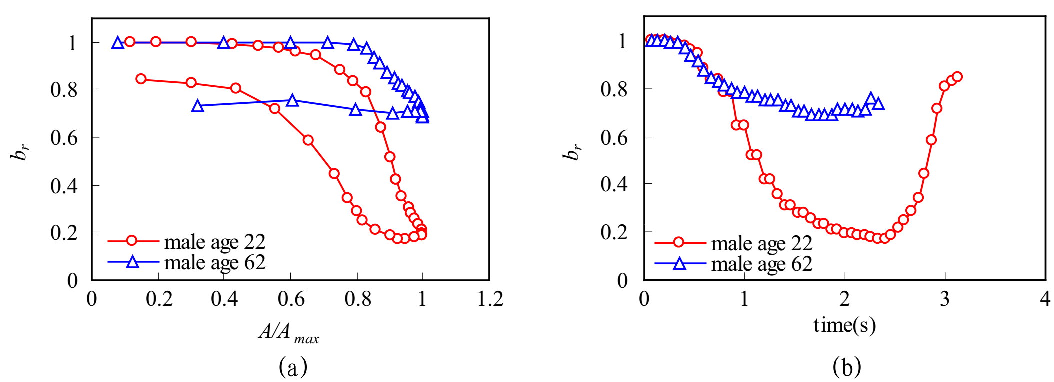

Figure 2: The index b_r shows markedly different behaviors for a young subject and an old subject.

The plot of b_r versus the area signal A shows characteristic behaviors as schematically illustrated in Fig. 3(a). Focusing on the finger-pressing duration, we can identify the point (A_d, 0.9) when b_r takes the value of 0.9. When b_r is not exactly equal to 0.9, we can always extrapolate the nearby data points. Next, in Fig. 3(b), we look at the negative gradient of the curve for the finger-pressing duration. Here, current is defined as $I = dQ/dt$ where Q is the amount of electric charge and t is time. When we regard the residual blood inside the finger as Q, the blood movement or flow is regarded as the current. Therefore, the gradient of the curve in the plot of b_r vs. t should be

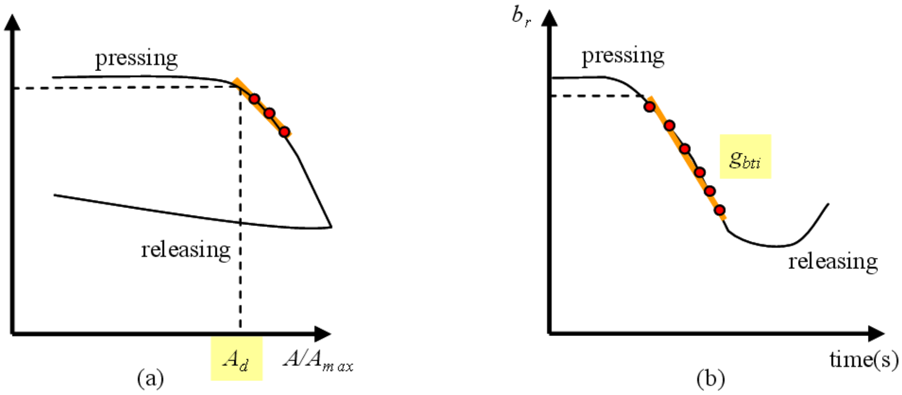

Figure 3: The index b_r shows behaviors unique to individuals.

related to the blood flow. We express this gradient as g_{bti}. Based on the model, we define an index R_b for the blood vessel stiffness by the following equation.

$$R_b = \frac{A_d}{g_{bti}} \tag{2}$$

We evaluated the index R_b from the 150 input trail data taken by 50 healthy participants. The relationship between R_b and their ages showed a positive correlation as depicted in Fig. 4. This means that blood mobility or blood vessel conductivity becomes smaller as we get older. For calculating the correlation coefficient, some data indicated by the circles in Fig. 4 were removed because the series of fingerprint images corresponding to these input trials showed irregularities, such as the fact that the number of images was too large, indicating that the input duration was longer than three seconds. The resultant correlation coefficient between R_b and the subjects' age was 0.51.

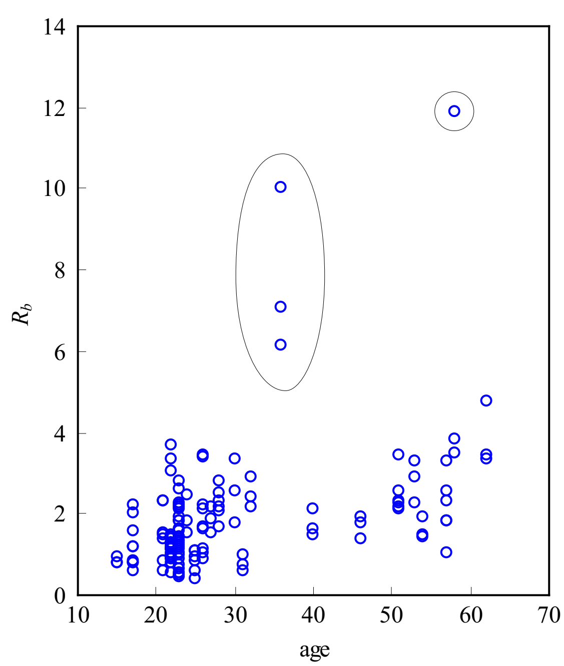

Figure 4: Correlation between the index R_b and the age of the subjects.

3. CONCLUSION

Fingerprints identification systems are gradually accepted in the world. If such a system can measure our health conditions, it can also function as a health monitor. For this purpose, we have proposed to extract a health-related signal from the area and color variations in a series of color fingerprint images recorded during an input action. The acquired fingerprint images are processed by means of digital subtraction analysis. Based on the analogy to a resistor in an electric circuit, an index related to blood vessel stiffness is defined. Using a dual-LED imaging system based on scattered-light detection, we captured 150 input trails taken by 50 healthy volunteers of both sexes and various ages ranging from 15 to 62. Each of the fingerprint images was processed by the subtraction analysis and the signals related to the residual blood were extracted. The resultant index showed behaviors characteristic to the individuals. We defined blood vessel stiffness based on the area changes and the time-derivative of this index. The blood vessel stiffness was correlated with the age of the subjects and the correlation coefficient was 0.51. In the future, we need to address possible improvements in the sensor hardware and more elaborate models for analyzing the blood movement induced by the finger deformation. Correlation with some real health conditions other than the age is also a subject of our future studies.

REFERENCES

1. Fujieda, I., E. Matsuyama, and M. Kurita, "Signatures of live fingers extracted from a series of fingerprint images," *Proceedings of SPIE*, San Jose, CA, U.S.A., Vol. 5677, 177–185, January 2005.
2. Tai, K., M. Kurita, and I. Fujieda, "Recognition of living fingers with a sensor based on scattered-light detection," *Applied Optics*, Vol. 45, No. 3, 419–427, 2006.
3. Tai, K., E. Matsuyama, M. Kurita, and I. Fujieda, "Dual-LED imaging for finger liveliness detection and its evaluation with replicas," *Applied Optics*, Vol. 45, No. 24, 6263–6269, 2006.
4. Fujieda, I., K. Tai, E. Matsuyama, and M. Kurita, "Dual-LED imaging system for secure and robust fingerprint detection," to be published in *Journal of Robotics and Mechatronics*, Vol. 18, No. 6, December 2006.
5. Sano, Y., Y. Kataoka, and T. Ikuyama, "Evaluation of peripheral circulation with accelerated plethysmography and its practical application," *J. Science of Labor*, Vol. 68, 17–25, 1988 (in Japanese).
6. Serov, A. and T. Lasser, "High-speed laser Doppler perfusion imaging using an integrating CMOS image sensor," *Optics Express*, Vol. 13, No. 17, 6416–6428, 2005.

Influence of Micro-particle Surface Roughness on TAOS Patterns: Experimental and Theoretical Studies

Jean-Claude Auger[1], **Gustavo E. Fernandes**[1], **Yong-Le Pan**[1]
Kevin B. Aptowicz[2], **and Richard K. Chang**[1]

[1]Center for Laser Diagnostics and Department of Applied Physics, Yale University
New Haven, CT 06520, USA
[2]Department of Physics, West Chester University, West Chester, PA 19383, USA

Abstract— The relation between surface roughness of aerosol particles and the appearance of islands in their large-angle elastic-light scattering (TAOS) patterns is studied by means of an image processing routine. Measured TAOS patterns of aggregates of polystyrene spheres as well as numerically calculated TAOS patterns based on Chebyshev particles are analyzed and qualitative agreement is obtained.

In recent years, large-angle elastic-light scattering has been investigated as a potential tool for use in the detection and characterization of aerosols in the micrometer range [1–5]. The aim of this work is to study the relation between surface roughness of microparticles and the appearance of islands in their two-dimensional angular optical scattering (TAOS) patterns. We first investigate a series of experimental TAOS patterns collected in the backward hemisphere [1] ($15^\circ < \theta < 95^\circ$) for various polystyrene latex spheres aggregates, which have similar volume but are composed of primary spheres of different sizes. An image analysis routine [2, 6] was applied to each pattern to calculate the mean island size and the mean density of islands appearing in the TAOS patterns. The image processing routine was designed to approximate the way the eye sees the islands by using the gradient of the TAOS patterns in determining the island boundaries, instead of absolute intensities. While the illuminating wavelength of the laser used was $0.532\,\mu\text{m}$, the primary PSL sphere diameters chosen for comparison were $0.202\,\mu\text{m}$, $0.988\,\mu\text{m}$ and $2.9\,\mu\text{m}$ (Fig. 1). The density of islands in the TAOS pattern is observed to increase as the size of the primary particles in the aggregate decreases.

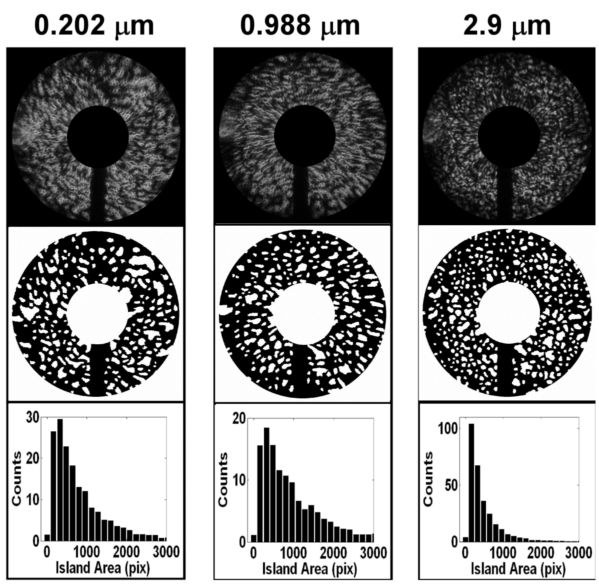

Figure 1: TAOS patterns of aggregates ($\approx 5\,\mu\text{m}$ in diameter) of primary PSL spheres (row 1), black-and-white island profile obtained from image processing (row 2), and island area histograms of each image in the top row (row 3). The primary PSL sphere diameter is shown on top of each column.

The same tendency was observed on theoretical TAOS patterns calculated from Chebyshev [7] particles with different surface roughness. Let us recall that a Chebyshev particle is an axisymmetric given by $r(\theta) = r_0(1 + \xi \cos n\theta)$, where r_0 is the radius of the unperturbed sphere, ξ is the deformation parameter and n is the polynomial order. Fixing r_0 to 3.0 μm, the surface roughness was changed by varying n from 10 to 30 and ξ from 0.01 to 0.06. Calculations of TAOS patterns were performed using the T-matrix formalism [8] in the backward hemisphere ($120° < \theta < 180°$), for various orientations and polarization of the incident wave with respect to the particle's axis of symmetry. The surrounding medium was supposed to be vacuum, the particle's complex index of refraction was set to $1.52 + \mathrm{i}0.0182$ and the incident wavelength to 0.532 μm. Qualitative systematic studies showed that an increase in the number of ridges (n) and the deformation parameter caused the numerically calculated TAOS patterns to exhibit a greater number of islands. We give two examples of this general study.

Figure 3 illustrate TAOS patterns corresponding to $n = 30$, $\xi = 0.0$, 0.02, 0.04 and 0.06 whereas the corresponding surface morphologies are given in Fig. 2. The incident wave vector is parallel to the Oz axis of the laboratory reference frame and polarized in the Oy direction while the particle's axis of symmetry is rotated parallel to the Ox axis. Inspection of Fig. 3 clearly shows variations in the shape, number and density of the islands, starting from the well known rings related to spherical objects ($\xi = 0.0$) to a large number of islands corresponding to particles with rougher surface.

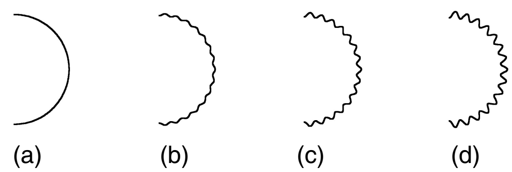

Figure 2: Surface of different Chebyshev particles, $r_0 = 3.0$ micrometers, $n = 30$, as function of increasing surface roughness. (a) $\xi = 0$ (sphere), (b) $\xi = 0.02$, (c) $\xi = 0.04$, (d) $\xi = 0.06$.

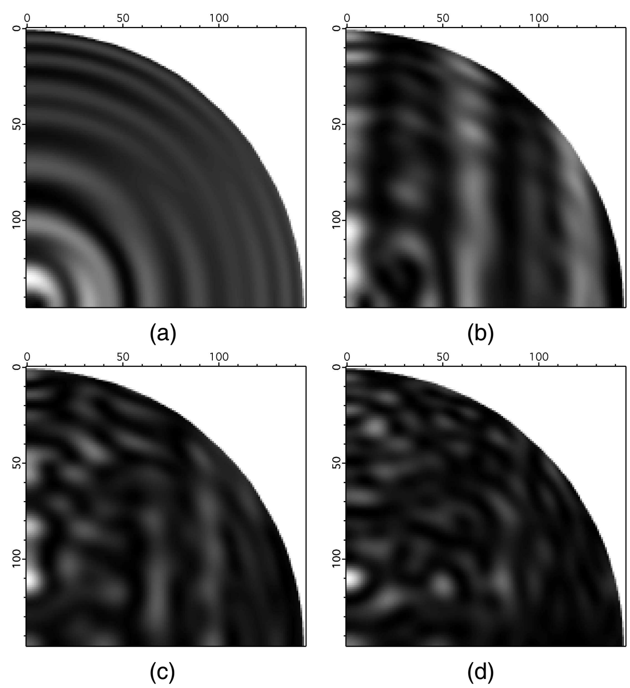

Figure 3: Theoretical backscattering patterns from Chebyshev particles, $r_0 = 3.0$ micrometers, $n = 30$, as function of increasing surface roughness. (a) $\xi = 0$ (sphere), (b) $\xi = 0.02$, (c) $\xi = 0.04$, (d) $\xi = 0.06$.

Figure 4 shows theoretical TAOS patterns calculated from the previous Chebyshev particles but considering a non-polarized incident beam. As expected, the image analysis routine shows that the density of islands in the TAOS pattern increases as the deformation parameter of the particle surface roughness also increases.

Our results suggest that the island structure appearing in the TAOS patterns of certain aerosol aggregates is related to the surface roughness of the aggregates. We hope to be able to use this

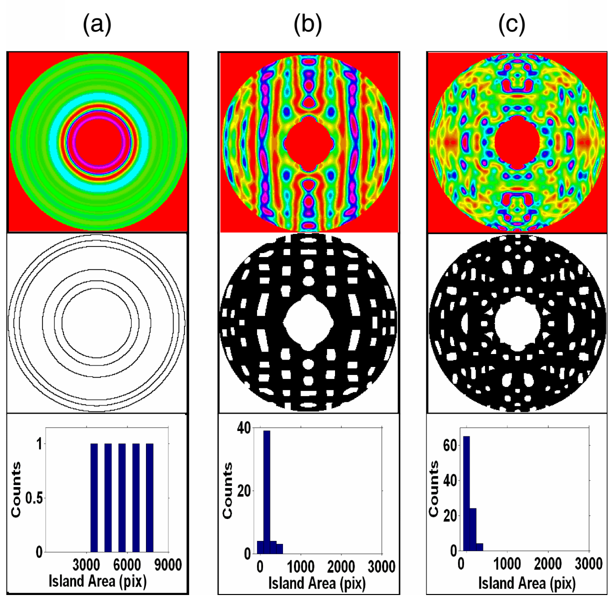

Figure 4: Theoretical backscattering patterns from a Chebyshev particle, $r_0 = 3.0$ micrometers, $n = 30$, as function of increasing surface roughness. (a) $\xi = 0$ (sphere), (b) $\xi = 0.02$, (c) $\xi = 0.06$.

knowledge to obtain insight into the structure of aggregates of aerosol particles from their TAOS patterns.

REFERENCES

1. Pan, Y. L., K. B. Aptowicz, and R. K. Chang, *Opt. Lett.*, Vol. 28, 589, 2003.
2. Aptowicz, K. B., R. G. Pinnick, S. C. Hill, Y. L. Pan, and R. K. Chang, *J. Geophys. Res., C: Oceans Atmos.*, Vol. 111, D12212, 2006.
3. Holler, S., Y. L. Pan, J. R. Bottiger, S. C. Hill, D. B. Hillis, and R. K. Chang, *Opt. Lett.*, Vol. 23, 1489, 1998.
4. Hirst, E., P. H. Kaye, and J. R. Guppy, *Appl. Opt.*, Vol. 33, 7180, 1994.
5. Fernandes, G. E., Y. L. Pan, K. B. Aptowicz, R. G. Pinnick, and R. K. Chang, *Opt. Lett.*, Vol. 31, 20, 2006.
6. Gonzalez, R. C., R. E. Woods, and S. L. Eddins, *Digital Image Processing Using Matlab*, Pearson Prentice Hall, 2004.
7. Mishchenko, M. I., J. W. Hovenier, and L. D. Travis, *Light Scattering by Nonspherical Particles*, Academic Press, 2000.
8. Waterman, P. C., *Phys. Rev. D*, Vol. 3, 825, 1971.

The Quest for Detection and Identification of Bio-aerosols

Richard K. Chang[1], **Gustavo E. Fernandes**[1], **Yong-Le Pan**[1], **Kevin Aptowicz**[2] **and Ronald G. Pinnick**[3]

[1]Department of Applied Physics and Center for Laser Diagnostics, Yale University
New Haven, CT 06520-8284, USA
[2]Department of Physics, West Chester University, West Chester, PA 19383, USA
[3]US Army Research Laboratory, Adelphi, MD 20783, USA

Abstract— A brief review is made of the status of fluorescence techniques to detect and partially identify bio-aerosols. The potential and frustrations in extracting morphology information from the angularly-resolved elastic scattering pattern is summarized. The latest advancements in the measurement of angularly-resolved elastic-light scattering for single aerosol particles on-the-fly are surveyed. Special emphasis is placed on our more recent efforts to simultaneously measure the scattering patterns of aerosol particles in both the forward and backward hemispheres.

In recent years, the quest for bio-aerosol detection and identification has been an active field for research and development. The detected fluorescence spectra, either at two-bands or at 32-bands, and excitation either at one wavelength or two wavelengths, has provided the ability to classify whether an aerosol particle (in the 1–10 μm range) is bio- or not bio- [1]. A number of ambient aerosols have similar or even identical fluorescence spectra of BW particles. Hence, false positive identification occurs, leading to false alarms. There is a real need for additional identification diagnostic, hopefully all optical, techniques. Alternatively, there are biochemical techniques such as specific binding of antibody with antigens or RNA gene sequencing using μ-fluidic cells or lab-on-a-chip.

Among the optical techniques, FTIR and Raman scattering (resonance Raman, surface enhanced Raman, and ordinary Raman) are two hopeful candidates for more specific identification of a suspect particle. However, both these techniques require special substrates to be covered with aerosol samples. Because of their possible interference effect, it is desirable to have only biological samples devoid of non-biological samples such as Arizona road dust or organic soot particles. In this regard, we have developed a sorting technique that enriches the biological aerosol sample to deposit on the surface of the substrate. Cued by the pre-determined fluorescence spectra of a particle as it travels downstream, a puffer sends out a short-duration pulse of air to deflect that particle from the main stream of particles. In order to localize the deflected particle into a small area on the substrate, a pulse aerodynamic localizer (PAL) concentrates the deflected particles. Using a biochemical technique, we could aim the PAL to inject deflected bio-aerosols into the reservoir well of a μ-fluidic cell [2].

It has been frustrating to know that elastic scattering, i. e., angularly resolved elastic scattering intensity pattern, has the strongest signal in any optical technique [1]. Elastic scattering (at some angle averaged over a small range of angles) is mainly used for measuring the aerodynamic equivalent sphere size of any particle regardless of whether the particle is spherical or not. The pioneering work of Paul Kaye and associates [3, 4] made use of the different angular patches of the angular scattering pattern to determine the degree of symmetry, the size, and to some extent the shape. Specially shaped photo detectors were used to provide quasi-real time data on the angularly integrated intensity in different discrete angles. Therefore, Kaye has combined the power of angularly resolved intensity patterns with image processing techniques when he used different shapes of detectors. He progressed further by using an ellipsoidal mirror, thereby capturing the angularly resolved intensity pattern (over a large fraction of 4π solid angle) on a CCD camera.

We went the next step and converted the XY coordinates of the CCD camera to angles θ and ϕ. In this paper we will go into depth on the angularly resolved intensities in the forward and backward hemispheres. However, this cannot be done in real time because it takes too long to read the CCD information into a standard computer as the inversion process is at best tedious and can give rise to particle size restrictions. Compromising on the large number of CCD pixels, a multi-anode photomultiplier (8×8 anodes) may be used to provide 64 channels of angularly integrated intensity patterns. Therefore, we need to give up resolution for speed. Theoretical or computational backing from the image processing and electromagnetic computation communities are essential for the future development of this technique.

The comparison of experimental and theoretical results is frustrating because experimentalists tend to work in larger size parameter domain while theorists tend to work in smaller size parameter domain due to computer time restrictions Therefore, computation on multiple scattering and particle interactions cannot be fully verified by experiments. The inability to control and to know the orientation of the non-spherical particles with respect to laser direction and the cluster geometry makes it nearly impossible to compare theory with experiments. How soon will experiment converge with theory?

In spite of some of the weaknesses and complications of elastic scattering techniques, there is still hope that the angularly resolved scattering intensity patterns can provide some information on a particle's morphology. This additional information gleaned from elastic scattering may prevent many of the causes for false alarms in the present detection instruments. For example, soot and BW agents have similar fluorescence spectra, but very different morphology. We will describe in some detail the experimental information that could be obtained thus far in the hope that theorists will take notice and take interest in this rich informative data set covering almost all 4π solid angle.

Two-dimensional $I_s(\theta, \phi)$ Angular Optical Scattering (TAOS), has been investigated as a possible diagnostic tool for the characterization of aerosols in the respirable range (1–10 µm in diameter) [4, 5]. TAOS has the potential of being useful in rapid characterization of biowarfare and other aerosols, because it is sensitive to a particle's size, morphology and complex index of refraction. Thus TAOS should provide complementary information to that extracted from other real-time aerosol measurement techniques, e. g., single-particle fluorescence, or laser induced breakdown spectroscopy (LIBS). In addition, TAOS can be measured with a CCD camera in quasi real-time even for submicrometer-diameter particles that are illuminated by laser diodes, thus opening the possibility for compact, low-cost particle detection and characterization systems.

Previous studies [3, 5, 6] measured TAOS patterns for a variety of aerosols, including micro fibers, salt and ice crystals, fluid droplets, aggregates of polystyrene-latex (PSL) spheres, bioaerosol particles, and ambient atmospheric aerosols. In these studies, TAOS was measured either in the forward hemisphere alone (Fig. 1(b)) or in the backward hemisphere alone (Fig. 1(c)). It was previously noted [5] that the scattering pattern of large aggregates of aerosols such as BG spores and PSL spheres contained a larger number of high frequency peaks and valleys termed *islands* or *speckles*.

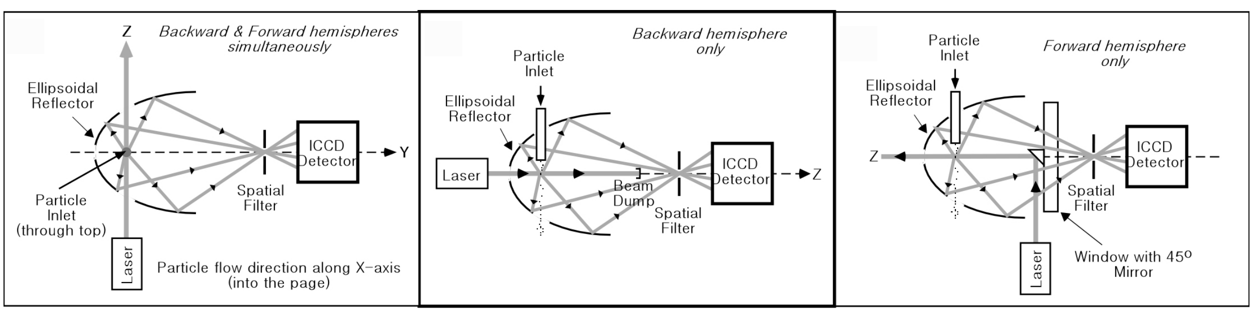

(a) (b) (c)

Figure 1: (a) Top view of the setup used to simultaneously collect the scattered radiation in the TAOS patterns of single aerosols on-the-fly in the forward and backward hemispheres. A single 30 ns laser pulse at 0.532 µm illuminates the particle. (b) and (c) Side view of the setup used in previous experiments that collected TAOS patterns in a single (*backward only* or *forward only*) hemisphere.

In a more recent experiment [7], we measured TAOS patterns of various single aerosols collected *simultaneously* in both the forward and backward hemispheres. A new configuration was used based on the illumination geometry shown in Fig. 1(a). The particle travels along the y-axis and is irradiated by a laser pulse propagating along the z-axis. Unlike previous experiments, the symmetry axis of the ellipsoidal reflector (Opti-Forms), oriented along the x-axis, is *perpendicular* to the direction of laser propagation. The scattering event occurs at the first focal point of the truncated-ellipsoidal reflector. A large portion (63% of the 4π sr) of the light that is scattered by the particle is intercepted by the reflector and projected onto the intensified CCD detector (ICCD)-1024×1024 pixels, Andor iStar. Half of the ICCD detector detects the forward-scattering pattern and the other half detects the backward-scattering pattern.

TAOS is measured for the scattering angles in the range $15° < \theta < 165°$ and for azimuthal angles covering as much as 360° in the near-forward and near-backward scattering. The full range of azimuthal angles ($0° < \phi < 360°$) is collected for all θ except where the reflector has parts removed by truncation of the ellipsoid and five holes drilled through the reflector. The particles enter through the top hole at $\theta = 90°$, $\phi = 270°$, and exit through the bottom hole at $\theta = 90°$, $\phi = 90°$. The laser beam enters through a side hole centered at $\theta = 180°$ and exits through a side hole at $\theta = 0°$. Lastly, there is the fifth hole in the back ($\theta = 90°$, $\phi = 180°$) used for the passage of the trigger laser diode beam.

The TAOS recorded on the ICCD were transformed into $I_s(\theta, \phi)$ in the spherical coordinates θ and ϕ by means of a ray-tracing computer code. As always, the z-axis was defined as the direction of the laser beam as in Fig. 1(a). The Log of the measured intensity $\text{Log}_{10}(I_s(\theta, \phi))$ was plotted into two separate parts, corresponding to the forward $15° < \theta < 90°$, and the backward $90° < \theta < 165°$ hemispheres, as shown in Fig. 2. On the top row of Fig. 2, the recordable angle range of the TAOS patterns is marked for the spherical coordinates. The shaded areas represent the areas that are lost due to open space and the 5 holes.

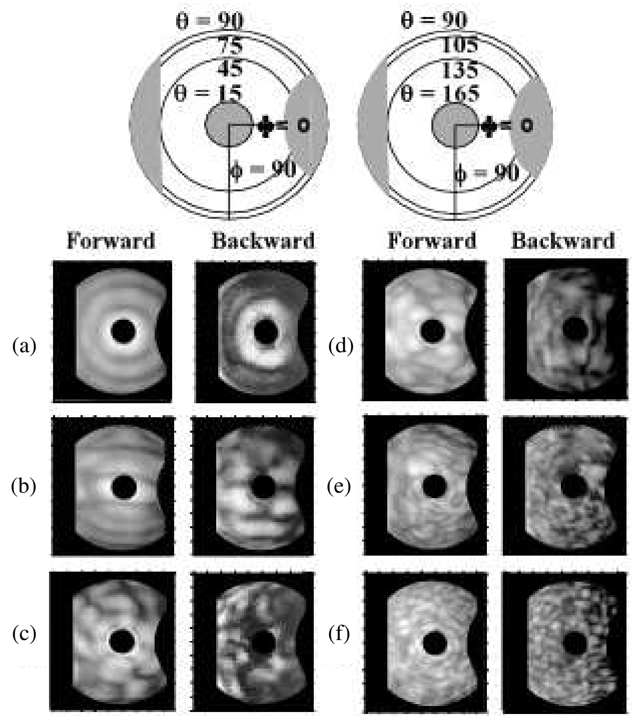

Figure 2: Simultaneously measured forward and backward TAOS patterns for randomly oriented clusters of PSL spheres. The clusters were illuminated by a 30 ns pulse of the second harmonic of an Nd-YAG laser at 0.532 µm. The black circle in the center of each pattern corresponds to holes on the ellipsoidal reflector used for the passage of the illuminating laser beam.

Figure 2 shows the forward and backward TAOS patterns for particles generated by putting 1.44-µm-diameter PSL spheres in the inkjet aerosol generator. Each pair of patterns labeled (a) through (f) correspond to the simultaneously measured forward (left) and backward (right) hemisphere scattering patterns. By varying the concentration of the solutions in the particle generator, the mean number of spheres per cluster was varied from 1 (row a) to 6 particles (row f). The TAOS patterns were generated for random orientations of the particle symmetry axis relative to the beam axis. Thus several different patterns were obtained from a given concentration of PSL spheres placed in the aerosol generator. The patterns displayed here were chosen among the many different patterns obtained in each data sample. An increasing density of islands in the scattering patterns is observed here [5] as the mean number of particles per cluster is increased in the scattering patterns shown in Figs. 2 (a)–(f).

Figure 3 shows the scattering patterns obtained for single *B. subtilis* spores. Because the BG spore has an elongated shape, resembling a small cylinder 1 m in height and 0.5 µm in diameter, its orientation relative to the illuminating laser beam axis affects the scattering pattern. Shown in

Figs. 3 (a)–(d) are measurements of the scattering pattern obtained simultaneously in the forward and backward hemispheres for four random orientations of the BG spore relative to the illuminating laser beam.

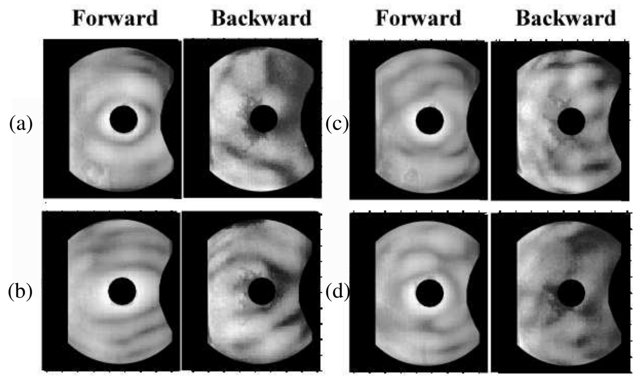

Figure 3: Simultaneously measured forward and backward TAOS patterns from single, randomly oriented, *B. subtilis* spores. The spores were illuminated by a 30 ns pulse of the second harmonic (at 0.532 μm) of a Nd-YAG laser.

The most recent efforts in measuring the angularly-resolved elastic-light scattering (TAOS) pattern of single aerosol particles on-the-fly were surveyed. A new configuration was presented that allows the measurement of TAOS patterns simultaneously in both the forward and the backward hemispheres for aerosols on-the-fly. Results were presented, for single and clusters of polystyrene latex spheres and single *B. subtilis* spores. We expect that this new configuration presented here will lead to a more complete characterization of individual aerosol particles than that could be obtained with TAOS measured over a single hemisphere.

We thank Dr. Burt V. Bronk for his support and Dr. Steven C. Hill for useful scientific discussions. This work was partially supported by the US Air Force Research Laboratory under contract F33615-02-6066.

REFERENCES

1. *Proceedings from NATO Advanced Research Workshop*, Novosibrsk, Russia, Oct. 3–7, 2005, *Optics of Biological Particles*, to be published by Springer 2006, see Fluorescence and Elastic-Scattering chapters.
2. Huang, H., Y. Pan, S. C. Hill, and R. K. Chang, "Deposition of selected airborne particles into a microfluidic flow cytometer for bioanalysis," submitted to Lab-On-A-Chip, 2006.
3. Hirst, E., P. H. Kaye, and J. H. Guppy, "Light scattering from non spherical airborne particles: Experimental and theoretical comparisons," *Appl. Opt.*, 33–30, 1994.
4. Kaye, P. H., K. Alexander-Buckley, E. Hirst, and S. Sauders, "A real-time monitoring system for airborne particle shape and size analysis," *J. Geophys. Res. D*, Vol. 14, 19215, 1996.
5. Pan, Y., K. Aptowicz, and R. K. Chang, "Characterizing and monitoring respiratory aerosols by light scattering," *Opt. Lett.*, 28–8, 2003.
6. Aptowicz, K. B., R. G. Pinnick, S. C. Hill, Y. Pan, and R. K. Chang, "Optical scattering patterns from single urban aerosol particles at Adelphi, Maryland, USA; a classification relating to particle morphologies," *J. of Geophys. Res.-Atmospheres*, Vol. 111, D12212, 2006.
7. Fernandes, G. E., K. Aptowicz, Y. Pan, R. G. Pinnick, and R. K. Chang, "Simultaneous forward- and backward-hemisphere elastic-light-scattering patterns of respirable-size aerosols," *Opt. Lett.*, Vol. 31, 20, 2006.

Angle-resolved Measurement and Simulations of Mueller Matrix Elements of B-cells and HL60 cells

H. Ding[1], **J. Q. Lu**[1], **R. S. Brock**[1], **L. P. Burke**[2], **D. A. Weidner**[3]
T. J. McConnell[4], **and X. H. Hu**[1]

[1]Departments of Physics, East Carolina University, Greenville, NC 27858, USA
[2]Departments of Internal Medicine, Brody School of Medicine, East Carolina University Greenville, NC 27858, USA
[3]Departments of Microbiology & Immunology, Brody School of Medicine, East Carolina University Greenville, NC 27858, USA
[4]Departments of Biology, East Carolina University, Greenville, NC 27858, USA

Abstract— Angle-resolved Mueller matrix elements of B-cell and HL-60 cell suspensions have been measured at three different wavelengths of 442, 633 and 862 nm. A finite-difference-time-domain method has been used to obtain simulated Mueller matrix elements and compared to a coated sphere model to model the experimental results with realistic structures of the B-cells and HL-60 cells reconstructed from confocal images. The comparison between the measured and simulated Mueller matrix elements allows the determination of the intracellular distributions of refractive index at different wavelengths.

The strong correlation between the light scattering signals in the visible and near-infrared regions and cell morphology has been demonstrated by numerous studies [1–3], which laid the foundation for cell sorting with light scattering based flow cytometry techniques [4]. Recent development of accurate modeling tools through numerical simulations significantly improved our ability to understand quantitatively the scattering of polarized light by cells of complex morphology [5–7]. To exploit the full potential of light scatter based detection for cell analysis, however, it is necessary to investigate thoroughly the angle-resolved light scattering process with realistic intracellular distributions of refractive index with experimental measurement and theoretical modeling. Furthermore, the diverse morphology of blood cells requires the availability of a large database on the experimental and modeling data of light scattering property of these cells. In this report, we present the measured and simulated Mueller matrix elements of hydrosol samples of B-cells and HL-60 cells and their angular dependence. The choice of B-cells and HL60 cells for our study is based on their importance in the understanding and diagnosis of lymphomas and leukemia as well as their relative simple morphology. The latter feature enables us to reconstruct their 3D structures from confocal images for Finite-Difference-Time-Domain (FDTD) simulations and comparison with experimental results.

We have developed a goniometer system with a photoelastic modulation scheme to measure the Mueller matrix elements versus the scattering angle [8]. The suspended B-cells in clear culture solutions were used for the measurements. A photoelastic modulator was employed to modulate the birefringence of an incident laser beam so that the polarization of the transmitted beam or the Mueller matrix elements of the modulator varies as functions of time at $f = 50\,\text{kHz}$. Three different lasers have been used to obtain incident beams at three different wavelengths of 442, 633 and 862 nm. The goniometer system was calibrated with a polystyrene microsphere suspension of 1 μm in diameter by determination of three independent Mueller matrix elements for spheres and comparison to the Mie theory calculated values. For accurate determination of optical parameters, the realistic 3D structures of single B-cells and HL60 cells as the scatterer are required for calculations of Mueller matrix elements and comparison with the measured data. We developed an image processing method to automatically reconstruct the 3D structure of a B-cell imaged by a confocal microscope [9].

The hydrosol samples of B-cells and HL60 cells in culture solutions were prepared for the goniometer measurement. To satisfy the single scattering condition, the concentration of the cells in the suspension culture was reduced with 0.9% saline to a level so that the scattering phase function (normalized S_{11}) was determined to a linear function of the concentration. We measured all of the 16 Mueller matrix elements of the hydrosol samples and 2 are presented in Figs. 1 and 2. Each data set represents four measurements of different cell samples harvested at different days with the symbol as the mean value and error bars as the standard deviation.

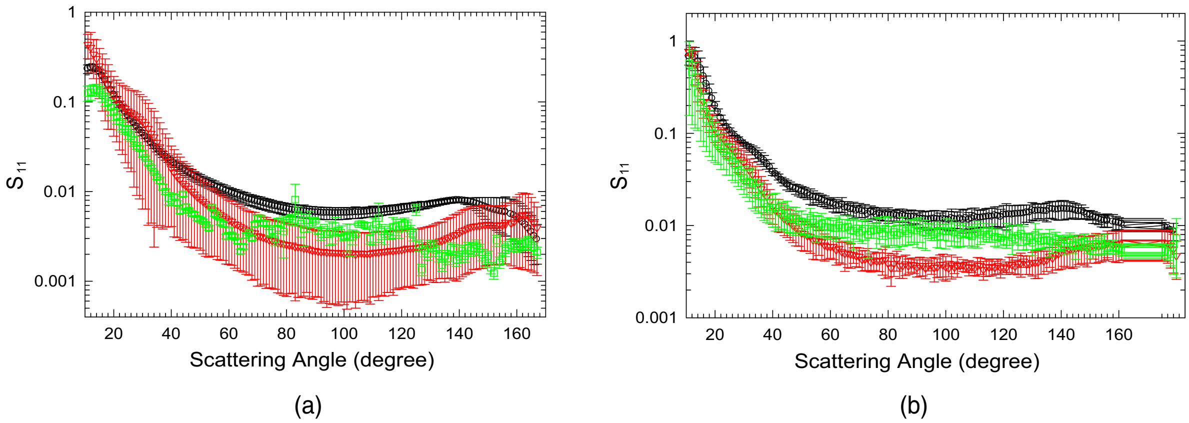

Figure 1: The angular dependence of the S_{11} elements of (a) B-cells and (b) HL-60 cells at three wavelengths: $\lambda = 442$ nm (green square symbols), $\lambda = 633$ nm (red triangle symbols) and $\lambda = 862$ nm (black and circle symbols).

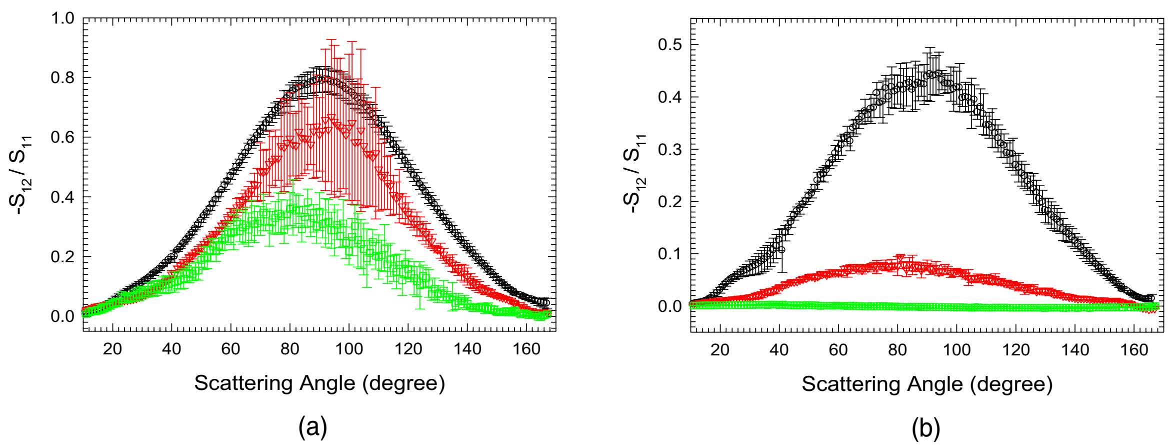

Figure 2: The angular dependence of the $-S_{12}/S_{11}$ elements of (a) B-cells and (b) HL-60 cells at three wavelengths: $\lambda = 442$ nm (green square symbols), $\lambda = 633$ nm (red triangle symbols) and $\lambda = 862$ nm (black and circle symbols).

To account for the complex morphology of biological cells in the modeling, we employed a recently developed method to reconstruct the three-dimensional (3D) structure of cultured B-cells from their confocal images [9]. A parallel FDTD code has been built by our group to obtain the angle-resolved Mueller matrix elements for a single cell [7]. Briefly, the FDTD method discretizes the two curl Maxwell equations with a Yee cell scheme in the near-field region around the scatterer where the optical heterogeneity is described in terms of spatial distribution of refractive index within the cell [10]. The Mueller matrix elements can then be determined from the relation between the incident and scattered light fields [6] as a function of the scattering angles of θ_s and ϕ_s when the cell is oriented along a direction of angle θ_o and ϕ_o relative to the incident beam. In our FDTD calculations, the size of the discretizing grid cell was set at $\lambda/20$. For each B-cell, the matrix elements were obtained as a function of θ_s by averaging over ϕ_s at each of 12 orientations of the cell uniformly distributed among the 4p range of (θ_o, ϕ_o). Another averaging was performed over the 12 orientations for each calculated matrix element to enable the comparison with the measured elements from cells at random orientations in a hydrosol sample. Two examples of simulated elements are shown in Fig. 3 with nuclear index $n_n = 1.400$ and 1.430, cytoplasm index $nc = 1.368$ and 1.380, host medium index $nh = 1.330$ and 1.336 for $\lambda = 862$ nm and 633 nm, respectively. We have also calculated the Mueller matrix elements using a coated sphere model with results shown in Fig. 4. Even thought the coated sphere results have been obtained with averaging over a Gaussian distribution of sphere diameters of 20% variance, one can still see that the angular dependence of the Mueller matrix elements are significantly different.

Based on the measured and simulated Mueller matrix elements and their angular dependence,

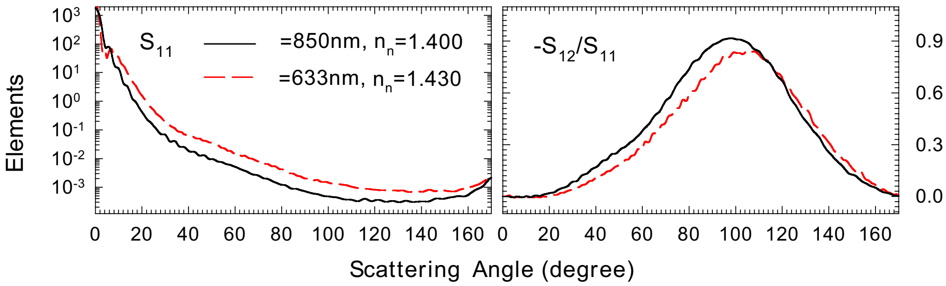

Figure 3: The simulated Mueller matrix elements of B-ells using a FDTD method with confocal reconstructed cell structures.

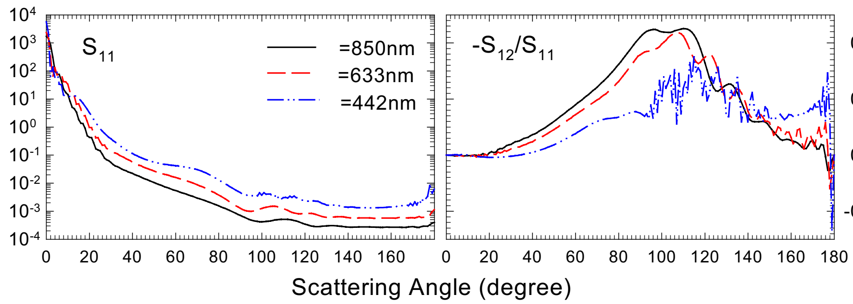

Figure 4: The simulated Mueller matrix elements of B-ells using a coated sphere model with identical nuclear and cytoplasm diameters from the confocal reconstructed cell structures.

we demonstrated the rich information of the light scattering signals. Large-scale simulations are currently in progress to extract the intracellular distribution of refractive index in these two blood cell lines and will be presented.

REFERENCES

1. Salzman, G. C., J. M. Crowell, J. C. Martin, T. T. Trujillo, A. Romero, P. F. Mullaney, and P. M. LaBauve, "Cell classification by laser light scattering: identification and separation of unstained leukocytes," *Acta Cytol*, Vol. 19, 374–7, 1975.
2. Bickel, W. S., J. F. Davidson, D. R. Huffman, and R. Kilkson, "Application of polarization effects in light scattering: a new biophysical tool," *Proc. Nat. Acad. Sci. USA*, Vol. 73, 486–490, 1976.
3. Bickel, W. S. and M. E. Stafford, "Polarized light scattering from biological systems: a technique for cell differentiation," *J. Biol. Phys.*, Vol. 9, 53–66, 1981.
4. Melamed, M. R., T. Lindmo, and M. L. Mendelsohn, *Flow Cytometry and Sorting*, 2nd ed., Wiley-Liss, New York, 1990.
5. Dunn, A. and R. Richard-Kortum, "Three-dimensional computation of light scattering from cells," *IEEE J. Selected Topics Quantum. Electron.*, Vol. 2, 898–890, 1996.
6. Lu, J. Q., P. Yang, and X. H. Hu, "Simulations of Light Scattering from a biconcave red blood cell using the FDTD method," *J. Biomed. Opt.*, Vol. 10, 024022, 2005.
7. Brock, R. S., X. H. Hu, P. Yang, and J. Q. Lu, "Evaluation of a parallel FDTD code and application to modeling of light scattering by deformed red blood cells," *Opt. Express*, Vol. 13, 5279–5292, 2005.
8. Hunt, A. J. and D. R. Huffman, "A new polarization-modulated light scattering instrument," *Rev. Sci. Instrum.*, Vol. 44, 1753–1762, 1973.
9. Brock, R. S., X. H. Hu, D. A. Weidner, J. R. Mourant, and J. Q. Lu, "Effect of detailed cell structure on light scattering distribution: FDTD study of a B-cell with 3D structure constructed from confocal images," *J. Quant. Spectrosc. Radiat. Transfer*, Vol. 102, 25–36, 2006.
10. Taflove, A. and S. C. Hagness, *Computational Electrodynamics: The Finite-Difference Time-Domain Method*, 2nd ed., Artech House, Boston, Mass, 2000.

In Vivo Measurement and Modeling of Multispectral Reflectance Images for Melanoma Diagnosis

C. Chen[1], K. M. Jacobs[1], J. Q. Lu[1], R. E. Cuenca[2], J. Finley[3], and X. H. Hu[1]

[1]Department of Physics, East Carolina University, Greenville, NC 27858, USA
[2]Departments of Surgery, Brody School of Medicine, East Carolina University
Greenville, NC 27858, USA
[3]Departments of Patohlogy, Brody School of Medicine, East Carolina University
Greenville, NC 27858, USA

Abstract— Noninvasive detection of malignant melanoma in early stages is critical to improve patients' prognosis. We acquired *in vivo* reflectance images of dysplastic lesions from 12 patients at 31 wavelengths from 500 to 950 nm. Based on these image data, we developed a parallel Monte Carlo code to simulate reflectance images from a heterogeneous skin tissue model. With this tool, we have investigated the dependence of the lesion contrast in the reflectance image on the heterogeneous distribution of tissue optical parameters. The Monte Carlo model is currently used to generate multispectral reflectance imaging data for multivariate analysis of the *in vivo* imaging data.

It has been estimated that Caucasians may develop up to 50 clinically benign nevi by age 40. Patients with more than 100 nevi were estimated to have a 3-fold to 10-fold increased risk of developing malignant melanomas and pigmented basal cell carcinomas in comparison to the general population [1]. Diagnosis of MM is currently established by histopathology of biopsied tissues from the suspicious-appearing nevi or pigmented lesions. These patients often present a difficult dilemma to primary-care physicians and dermatologists. A physician has to either prescribe painful and costly excision biopsy with likely cosmetic disfigurement with limited information on the lesion or leave untouched with the risk of MM developing in the patients. Therefore, cost-effective pre-biopsy methods of examination could greatly improve patient care and reduce medical cost with better specificity and sensitivity than what are available now. In this report, we present multispectral reflectance image data acquired from 12 patients with dysplastic lesions at 31 wavelengths from 500 to 950 nm and results of numerical studies of reflectance imaging method by a Monte Carlo (MC) code.

A multispectral imaging system employing a thermoelectrically cooled CCD camera has been constructed to acquire polarimetric images [2]. Fig. 1 presents a schematic of the imaging system. We used a xenon fiber optic light source and a collimating lens to produce a parallel light beam of

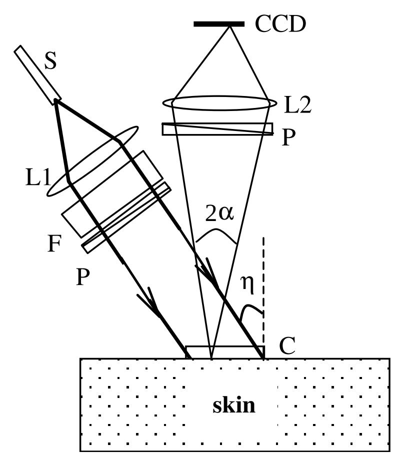

Figure 1: A schematic of the polarimetric multispectral imaging system. S: light source; L1, L2: lenses, F: wavelength filter; P: polarizer; h: incident angle; C: contact window.

25 mm in diameter with wavelengths ranging from 300 to 1100 nm for full-field illumination at the skin surface. The illumination beam was first passed through a long-pass filter with the edge at

500 nm and then one of two liquid-crystal-tunable-filters for selecting a waveband of about 10nm bandwidth between 500 to 950 nm with a stepsize of 15 nm. The illumination arm of the imaging system was at an oblique angle of $\eta = 30°$ from the normal of the skin surface while the imaging arm was oriented along the normal direction to reduce contribution to the image signals by skin surface reflection. Polarimetric images have been acquired from four patients suspected to have dysplastic nevi or MM and prescribed to be removed by their surgical oncologist. All participating patients agreed to be imaged for our study and were required to read and sign an informed consent form with the detailed description of the study before the start of imaging process. The patient study protocol and consent form were approved by the IRB of East Carolina University and followed strictly throughout this study. For each patient, a total of 64 images were acquired at 31 wavelengths from each patient between 500 and 950 nm with two polarimetric images, $I_{\perp}(x, y, \lambda)$ and $I_{//}(x, y, \lambda)$, at each wavelength. Immediately after patient imaging, the same sequence of multispectral images of a certified 40% diffuse reflectance standard was acquired to determine the relative distribution of the incident light at the object plane with the imaging polarizer set parallel to the incidence plane. With these images and the output power of the incident beam measured at each wavelength λ, we obtained the irradiance distribution of the incident light $I_i(x, y, \lambda)$. Examples of the multispectral reflectance image data from one patient at selected wavelengths is shown in Fig. 2.

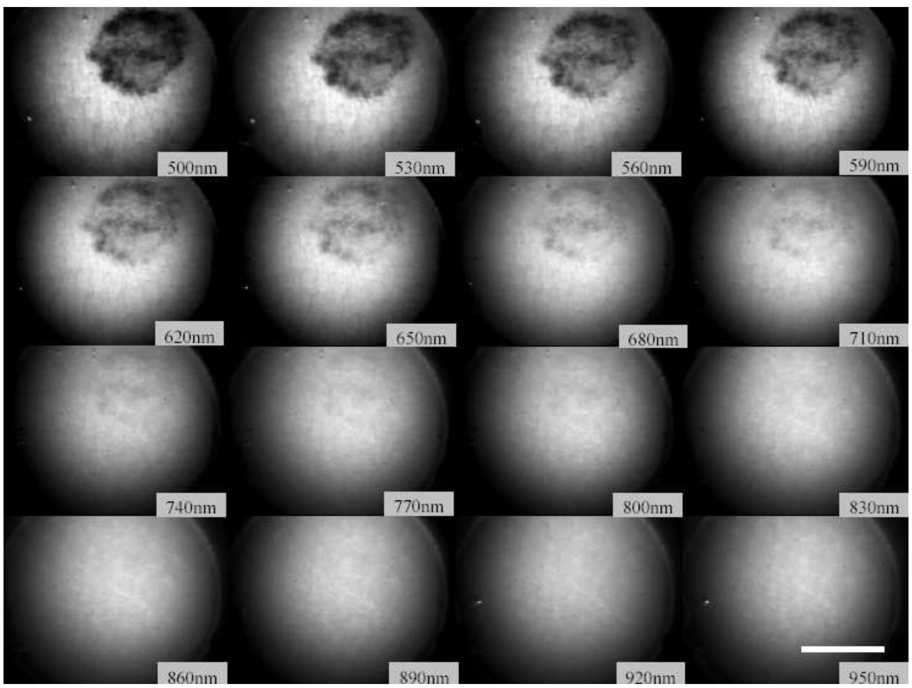

Figure 2: Reflectance images of $R_{//}$ of lesion #4 at 16 selected wavelengths noted at the lower right corner. Bar = 10 mm.

Based on the in vivo imaging data, we have developed a parallel Monte Carlo code that can generate reflectance images by calculation of photon density distribution at the air side of a two-layer heterogeneous skin model, as shown in Fig. 3. The details of the MC algorithm and the skin model have been reported elsewhere [3–5]. In tracking photon in the turbid media of skin tissues, we used the Henyey-Greenstein function as the scattering phase function which is characterized by an anisotropy factor g. A collimated beam of diameter $2w = 25$ mm is incident at a angle of $\eta = 30°$ to the surface normal. In the above defined heterogeneous skin model, we designed a central region of cylindrical shapes of radius r with optical parameters different from the peripheral region in the illuminated area to imitate a pigmented lesion in a normal tissue. The images in Fig. 4 exhibit clear differences in reflectance R between these two regions in which stronger light absorption in the central region leads to smaller R and vice versa. Furthermore, the value of reflectance R depends not only on the optical parameters of the phantom but also on the collection angle α or NA of the imaging system. These can be quantitatively analyzed in Fig. 5 by plotting $R(x, y)$ along the x-axis for different NA. Because of the symmetry, we averaged the photon density along the y-axis over 2 rows of pixels on each side of the x-axis to reduce the fluctuation.

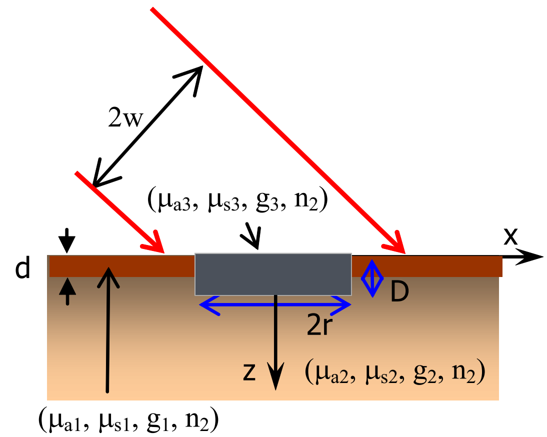

Figure 3: The two-layer skin model with a pigmented lesion at the center. Optical parameters of each layer or region: (μ_{a1}, μ_{s1}, g_1, n_1) for epidermis; (μ_{a2}, μ_{s2}, g_2, n_2) for dermis and (μ_{a3}, μ_{s3}, g_3, n_3) for the lesion.

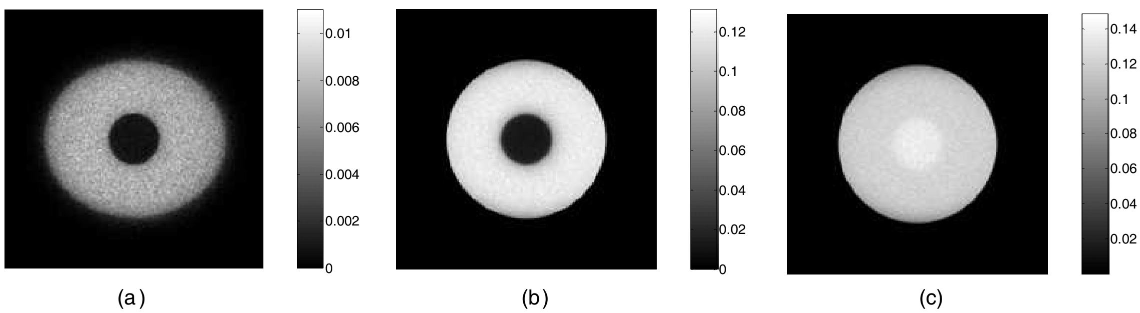

Figure 4: Three gray-scale reflectance images $R(x, y)$ of a semi-infinite heterogeneous phantom with a 201×201 grid over an FOV of 41.2 mm along x- and y-axis: (a) $\mu_{a3} = 2.00\,\text{mm}^{-1}$, $\alpha = 15.0°$; (b) $\mu_{a3} = 2.00\,\text{mm}^{-1}$, $\alpha = 90.0°$; (c) $\mu_{a3} = 0.15\,\text{mm}^{-1}$, $\alpha = 90.0°$. Other parameters are $N_0 = 1.13 \times 10^8$, $r = 12.5\,\text{mm}$, $\theta_0 = 30°$, $d = 0$, $D = 0.75\,\text{mm}$, $r = 4.00\,\text{mm}$. Other parameters are: $\mu_{a2} = 0.20\,\text{mm}^{-1}$, $\mu_{s3} = \mu_{s3} = 4.00\,\text{mm}^{-1}$, $g_2 = g_3 = 80$, $n_{r2} = n_{r3} = 1.50$.

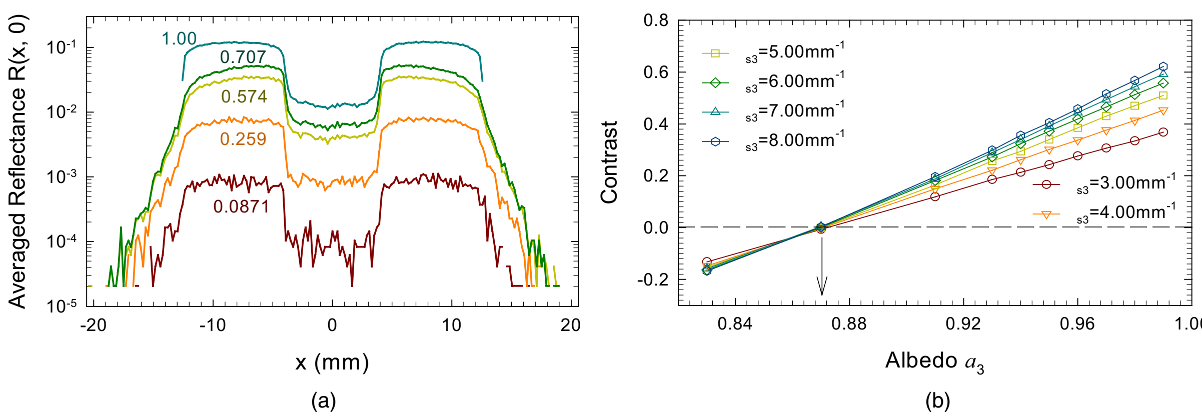

Figure 5: (a) The x-dependence of $R(x, 0)$ with $\mu_{a3} = 2.00\,\text{mm}^{-1}$ at different values of numerical aperture (=sinα) as marked; (b) the contrast versus the albedo a_3 of the central region with $D = 0.75\,\text{mm}$ for different albedo of the peripheral region: $a_2 = 0.870$ and $\mu_{t2} = 6.32\,\text{mm}^{-1}$. The scattering coefficient of the central region are marked in the figures with arrows indicating the a_2 values and the solid lines are visual guides. Other parameters are identical to those in Fig. 4.

From Fig. 5(a), one can see that the reflectance increases as the collection angle α increases to 90°, in which all photons exiting from the phantom surface and within the circular area of the lens contribute to the reflectance image. But the relative differences in R between the two regions remains similar, indicating the portion of the image information that is independent of the imaging system parameters. Based on these results, we define an image contrast C to characterize the relative change in reflectance as

$$C = \frac{< R_c > - < R_p >}{< R_c > + < R_p >}, \quad (1)$$

where $< R_c >$ is the reflectance averaged over a circle concentric with the central region and $< R_p >$ is the reflectance averaged over a concentric ring in the peripheral region of illuminated area outside of the central region. For a central region of radius $r = 4$ mm, the radius of the averaging circle for $< R_c >$ is 3 mm and the inner and outer radii of the averaging ring for $< R_p >$ is 5 and 11 mm, respectively. With the above definition, we fist investigated the effect of collection angle α and the results shows clearly that C has a very weak dependence on α. In the following results, we adopted $\alpha = 90°$ to reduce the output variance in the following results of MC generated $R(x, y)$.

To find the relations between the image contrast C and phantom parameters, we carried out a large number of MC simulations with different sets of optical parameters (μ_a, μ_s, g, n_r) between the two regions. Analysis of these numerical image data demonstrated an interesting relation in that C depends mainly on the single-scattering albedo $a_3 = \mu_{s3}/(\mu_{a3} + \mu_{s3})$ in the central region relative to the albedo a_2 in the peripheral region when $a_2 = a_3$ and $g_2 = g_2$. These results are presented in Fig. 5(b) with the thickness of central region $D = 0.75$ mm. The thickness of the first layer d was set to 0.

The above MC model has been used to generate multispectral reflectance images for development of a principal-component based multivariate algorithm for analysis of the in vivo data [2]. These results will be presented.

REFERENCES

1. Swetter, S. M., "Dermatological perspectives of malignant melanoma," *Surg Clin North Am*, Vol. 83, 77–95, vi, 2003.
2. Lu, J. Q., Y. Feng, R. E. Cuenca, Y. Ti, K. Li, K. M. Jacobs, S. B. Jackson, R. R. Allison, C. H. Sibata, G. H. Downie, and X. H. Hu, "Multivariate analysis of monte carlo generated images for diagnosis of dysplastic lesions," presented at *Proc. SPIE*, 2005.
3. Song, Z., K. Dong, X. H. Hu, and J. Q. Lu, "Monte Carlo simulation of converging laser beams propagating in biological materials," *Appl. Opt.*, Vol. 38, 2944–2949, 1999.
4. Lu, J. Q., X. H. Hu, and K. Dong, "Modeling of the rough-interface effect on a converging light beam propagating in a skin tissue phantom," *Appl. Opt.*, Vol. 39, 5890–5897, 2000.
5. Chen, C., J. Q. Lu, H. Ding, K. M. Jacobs, Y. Du, and X. H. Hu, "A primary method for determination of optical parameters of turbid samples and application to intralipid between 550 and 1630nm," *Opt. Express*, Vol. 14, 7420–7435, 2006.

Treatment of Solid Malignant Tumors with Microwave Balloon Ablation Catheters and Localized Chemotherapy

Giorgio di Palma[1], **Ji-Bin Liu**[4], **Daniel D. Mawhinney**[3], **Ralph Meyer**[1], **Adolph Presser**[3]
Ernest L. Rosato[4], **Arye Rosen**[2], **and Fred Sterzer**[3]

[1]AngioDynamics, Queensbury, NY, USA
[2]Drexel University, Philadelphia, PA, USA
[3]MMTC, Inc., Princeton, NJ, USA
[4]Thomas Jefferson University, Philadelphia, PA, USA

Abstract— The paper describes a new approach to the treatment of solid malignant tumors. In this approach the tumors are thermally ablated with minimally invasive microwave balloon catheters, and the cavities created in the tumors by the balloon catheters are filled with anticancer agents that can be forced through the ablated malignant tissues to the margins of the tumors in order to destroy any remaining viable tumor cells. *In vivo* and *in vitro* experiments are described that illustrate the ability of microwave balloon ablation catheters to rapidly ablate of large volumes of tissues, to create reservoirs for anticancer agents in the ablated (necrosed) tissues, and to force substances with large molecular weights that are introduced into these reservoirs through the ablated tissues to the margins of the ablation.

1. INTRODUCTION

Despite important advances in the treatment of cancer with surgery, radiation therapy, and chemotherapy, and despite the introduction of newer anticancer therapies such as, for example, hyperthermia and monoclonal antibodies, there still remains an urgent need for additional new therapies to help the numerous cancer patients that are failing currently available therapies.

Here we describe a new approach to the treatment of solid malignant tumors. In this approach solid tumors are first thermally ablated (necrosed) with minimally invasive microwave balloon catheters that can produce lesions that conform to the shapes of the tumors. Next the cavities that are created by the balloon catheter in the necrosed tumor tissues are filled with anti-cancer agents that are forced by applied pressure through the necrosed tumor tissues to the margins of the tumors where they can act against any remaining viable malignant cells that if not destroyed could lead to recurrences of the cancer. These agents can be heated to enhance their anti-cancer efficacy. If immunotherapeutic agents are introduced into the cavities it might also be possible to stimulate systemic anticancer effects against distant metastasis.

2. EXPERIMENTAL RESULTS

Microwave balloon ablation catheters were tested *in vitro* in beef liver and *in vivo* in the livers of pigs. The microwave antennas were coaxial gap antennas that were matched at 915 MHz. The catheters were 20 cm long with a diameter of 3 mm and with inflatable balloons at their end. They were cooled with circulating water that was also used to inflate the balloons. The balloons inflated to a predetermined diameter and shape and could produce the radial forces needed to create cavities in necrosed tissues. Tissue temperatures were measured with thermistors and a microwave radiometer. These tests demonstrated the following:

- Cylindrical shaped necrotic lesions with a diameter of 3 cm and length of about $4\frac{1}{2}$ cm can be produced *in vivo* in 3 minutes with 100 watts of 915 MHz microwave power without carbonizing any of the tissues surrounding the balloons. The cavities produced in the ablated tissues closely approximated the shape and size of the cylindrically shaped balloons used that had diameters of 1 cm and length of 6 cm. When fluorescent Dextran with molecular weights as large as 2,000,000 dissolved in saline was introduced into these cavities it could be quickly forced by applied pressure to the margins of the ablated tissues.
- It is possible with balloon catheters that incorporate microwave reflectors to preferentially heat tissues in only one direction. This feature makes it possible to safely ablate malignant tissues that are close to vital healthy tissues.

- Temperatures of ablated tissues can be measured with microwave radiometers by using the coaxial gap heating antennas of the ablation balloon catheters for receiving the microwave noise from the ablated tissues. The microwave radiometers used in the experiments have been described at a previous PIERS meeting [1].

3. DISCUSSION

The experimental results obtained with microwave balloon ablation catheters indicate that this form of thermal ablation has important advantages over thermal ablation using radiofrequencies (RF), an approach that is now in clinical use for ablating surgically unresectable tumors, particularly hepatic tumors [2–4]. Heating with RF tends to be non-uniform sometimes leading to rapid charring or vaporization adjacent to the electrodes which often adhere to the tissues making removal difficult. This non-uniform heating can cause incomplete destruction of the tumors. Increasing the heating power in RF catheters has limitations, because resulting vaporization, carbonization, and boiling increases the RF impedance of the tissues and reduces the distances of heating and therefore the extent of tumor necrosis. In contrast, microwaves can deeply and uniformly penetrate tissues and raise the temperatures of large volumes of these tissues to values that cause necrosis in very short times. This is of great clinical importance such as when ablating large or multiple liver lesions. Microwaves, unlike RF currents, can penetrate necrosed tissues and travel unimpeded through non-adhering plastic balloons, and the microwave antenna used in the balloon catheters can be used to not only transmit heating power into the tissues but also to receive thermal radiation from the heated tissues which can be translated to average tissue temperatures by microwave radiometers.

For the same microwave power and duration, microwave balloon catheters can ablate larger volumes of malignant tissues than similar microwave catheters not equipped with balloons. This is because the expanded balloons compress the malignant tissues resulting in a reduction of blood flow and in the distance microwaves have to travel inside the tumors in order to ablate a given volume of tumor. Heating with balloon catheters is also more uniform because the microwave powers emitted by the antennas spread in the balloons before reaching the tissues that are to be ablated, and because of cooling of tissues adjacent to the balloons. Balloons prevent sticking of the catheter to ablated tissues, can be tailored to ablate special shapes, can ablate tissues omni-directionally as well as in one direction only and most importantly, the expanded balloons create cavities in the ablated malignant tissues that can be filled with anticancer agents for localized chemotherapy.

What are the unique features of the microwave balloon ablation/localized drug delivery approach?

- Technically very simple. The cavities that are automatically created by thermally ablating tumor tissues with microwave balloon catheters serve as reservoirs for drugs for attacking any remaining viable cancer cells at the margins of the tumors and also for stimulating systemic immune responses.
- No limitations on the type of drugs that can be introduced into the reservoirs.
- Different drugs can be introduced either together or sequentially.
- Drugs in the reservoirs can be easily heated. This is a very valuable feature since raising the temperatures of a number of commonly used chemotherapeutic agents above core temperatures significantly increases their anticancer activity. Examples of such agents include bleomycin, adriamycin, and Cis Platinum.
- The margins of the ablation can be kept at elevated temperatures by continuing to heat after the ablation has been completed and the cavity has been filled with drugs. This further increases the local toxicity if agents such as bleomycin are used without increasing systemic toxicity.
- The rate at which drugs are forced through the ablated tumor tissues to the margin of the ablation can be controlled by amount of external pressure that is applied to drugs in liquid solutions.
- Drugs in slow-release form can be used to attack tumor cells over long periods of time. Suitable slow-release substrates would be drug-eluting polymers that are fabricated in biodegradable form.

REFERENCES

1. Stauffer, P. R., et al. "Multifrequency microwave radiometry for thermal monitoring and control of superficial hyperthermia," *PIERS*, Hawaii, October 2003.

2. Ianitty, D. A., "Hepatic radiofrequency ablation," *Arch. Surgery*, Vol. 137, 422–6, April 2002.
3. Shibata, T., "Small hepatocellular carcinoma: Comparison of radio-frequency ablation and percutaneous microwave coagulation therapy," *Radiology*, Vol. 223, 304–7, May 2002.
4. *Special Issue: Thermal Ablation Therapy, International Journal of Hyperthermia*, Vol. 20, November 2004.

Vibrational Medicine: A Closer Look at Homeopathics

S. D. R. Bruell
174 Donald St., Brunswick East, Melbourne, Victoria 3057, Australia

Abstract— This study attempts to explain the mechanism by which homeopathics act to cure disease. It is understood that many homeopathic solutions are diluted to the point where they do not contain any chemical or molecular trace of the original substance they are derived from. Therefore, it is proposed here that the mechanism of action involves the particular electromagnetic vibratory characteristics of the medicine, the body, and the disease state or toxin which resides in the tissue. These vibrations seem to interact in a regular fashion within and between cells, and thus the postulated hypothesis also predicts the communicative nature of electromagnetic waves within living systems in general. These conjectures are currently supported by theoretical evidence, although they may be disproved or validated with further experimentation making use of modern techniques in microscopy and amplification.

1. INTRODUCTION

The central tenet behind the theory of homeopathic medicine is "like cures like". In other words, a substance which can cause particular symptoms in a healthy organism can cure those same symptoms in the sick when applied in smaller doses. This principal has been recognized not only in Hippocratic medicinal traditions going back over 2000 years, but also in much earlier Greek mythology, as an infected wound which was inflicted by Achilles' spear was reported to be healed by a tiny part of that same spear [12]. Samuel Hahnemann (1755–1843) developed the techniques by which homeopathic medicine is still prepared and tested to this day. His method involved the serial dilution and succussion (heavy pounding or shaking) of substances in order to reduce them to their smallest and more powerful potencies, coining the notion of the "infinitesimal dose". He used the principle *similia similibus curentur* to explain the importance of "proving" the various remedies, or testing them on healthy subjects to find out what the specific substances do to cause disease [11]. The symptoms brought about by provings are the same or similar to those which the medicine is normally capable of curing, although there is some variance according to individual sensitivity [3]. Homeopathics have been noted to be deactivated upon exposure to certain forms of electromagnetic radiation as well as various other known carcinogenic substances (Schiff 1994).

Up until now the general view has been that homeopathics work according to a placebo effect, despite a wealth of legitimate scientific literature on the subject, some of which attempts to explain an alternative mechanism of action. Following the completion of a thorough literature review on the subject, I have used the available evidence to further justify the proposed hypothesis and these findings will be summarized in this paper. In addition, some possible methodology to definitively validate, alter or disprove the said suggestions as to the action orchestrated within the body by homeopathic medicine will be discussed.

2. EFFICACY

The efficacy of homeopathics has been challenged continually throughout history despite its widespread usage throughout the world, with the total estimated market being around US$230 million. In the UK alone approximately 20% of the population have used homeopathic products, with sales reported at around £25 million per annum [14]. Many papers and discussions have attempted to ultimately prove the hypothesis that they work due to some kind of placebo effect, brought about not only by people's 'belief' in the drug, but also by the absence of the damaging side effects often associated with traditional medicine. However, a number of reviews have reached conflicting results in these attempts (see [8, 10] for eg.), with the overall impression being that despite the unpopularity of homeopathics in traditional circles, its spread continues unabated and the majority of experimental outcomes do not support the placebo hypothesis. Positive results have been documented in numerous experiments and clinical trials, although repetition has proved difficult in some cases [12]. Experimentation involving plants, animals and humans has been conducted over the past 200 years in various spheres of medicine and science and the results have consistently been sufficient to justify the continued exploration of the drugs, which goes on to this day.

3. CURRENT MODELS

Although many authors have chosen to admit to ignorance as to the actual mechanism of action, various other models have been hypothesized. Current alternatives to the Placebo Effect include the attribution of the medicine to a 'vital' or 'dynamic' force by Paracelsus, Hahnemann and others (see [11]); the suggestion of a molecular or chemical signal being contained in the water molecules surrounding the chemicals due to some magic (or exceptional) property of water, also known as the Memory of Water [5]; some function related to Chaos Theory [3]; and the presence of electric fields within living cells [4]. The proposed hypothesis and rationale contradicts only the Placebo Hypothesis in logical terms, and the Memory of Water seems somewhat implausible, although water can play an integral role in what probably constitutes a fairly complex series of interactions. Chaos is presented more as a way of methodically describing current understanding of certain systems than as an actual hypothesis of action, and it seems relevant in this case (see [3], Chapter 7 and Appendix 2 for relevance to homeopathics and biological systems). The theory regarding the presence of electric fields is identical in essence to the hypothesis under discussion, and it was proposed and explored under the name of "digital biology" by Jacques Benveniste (1999). The biophysical descriptions published by physicists Emilio Del Giudice, Giuliano Preparata and others (summarized in [3]; Schiff 1994) appear to be logical in their fundamental understanding and in their various approaches to the problem. However, they avoid discussing the action at as close a vantage point as is required. Furthermore, this is the first paper that the author is aware of that deals with the concept of the meeting of corresponding electromagnetic vibrations in cellular or intercellular space and the subsequent "canceling out" effect which is thought to be the result. This is called the Vibration Hypothesis. Given the appropriate attention, there exist various means to explore this possibility which are readily available within the infrastructure of today's scientific world.

4. THE VIBRATION HYPOTHESIS

I propose the existence of a mechanism by which a particular vibrational signature, or frequency, is implanted on the homeopathic medium, and the medicine is thus able to interact with corresponding vibrations within the body. If the homeopathic chosen is of the same, or a similar frequency to that exhibited by the disease state then a cancellation effect can occur, such that two equivalent vibrations traveling in opposite directions meet, combine and essentially disappear. Hence both the diseased area and the medicine itself are "silenced". The toxin, having been stripped of its communicative power, could then be isolated within its environment, and it would become easy for the immune system to locate it and clear the affected area, restoring it to health. Due to the fact that the homeopathic resembles the toxin, if the opposite vibration were not present in the subject, the consequent proving which has been documented to occur could be explained by the immune system's automatic response to something it normally associates with a foreign presence. A small and short-lived auto-immunological response could result.

This hypothesis is implicitly supported by a variety of evidence collected by researchers around the world, although it could still be disproved, as is the case with any new theory. Immunologists, physiologists and physicists are among the many authors who have confronted homeopathy (see [2, 5, 7] for eg.). A wide variety of experiments have involved the serial dilution and vigorous pounding (or succussion) of substances, and also the electronic means of producing the drugs which makes use of techniques similar to those found in radionics technology (described in [9], pages 24–26; see also [6]). The scientists then observed the resulting solutions' activities when exposed to various cell surface receptors normally triggered by the given antiserum, such as to induce certain reactions at both the chemical and cellular levels (see [1]; Figures 24–27 for example of cellular activation). In fact, many of the body's immune cells have been seen to activate when exposed to the diluted and succussed solutions. Other solutions have been recorded to inhibit cellular activity, and various observations document the homeopathics' capacity to interact with the substances they were originally derived from [2].

Bellavite and Signorini (2002) state and consider the hypothesis that "a homeopathic drug works by providing information commensurate with the complexity of the organism with which it interacts". This implies that the information carried by homeopathics is "commensurable", or "like" the information already in the body (the presence of certain vibrations within the tissue) and that it can possibly activate the regulatory system in ways very similar to the action of the substance itself in large quantities. The radionics machinery uses electromagnetic waves to program the medium to contain the homeopathic message and therefore it may be the case that electromagnetic radiation is being used to communicate certain messages to the internal structures within the body, which presumably understand the message because they produce a corresponding electromagnetic communication. Indeed there have been experiments which reported luminescence at the point of interaction [2]. However, the field of radionics is also found to be lacking a coherent theory to explain its action, and more research is required to rationalize the actions performed by these machines which can essentially change the vibratory state of a solid or liquid medium to match that of another physical substance according to a list of "rates" which have been calculated experimentally [6]. The idea of electromagnetic involvement was also suggested by Del Giudice and Preparata (in [3]), Benveniste (in Schiff 1994) and quite possibly others before them. However, in the cases of both of the above analyses, the analysts seemed to become sidetracked by the examination of the water itself as the medium which, although valid and interesting, does not reach the heart of the matter at this point, nor does it appear to open the doors to new realms of understanding in quite the same way that the exploration of the vibrations themselves does.

5. FUTURE IMPLICATIONS

The particular vibrational characteristics of various substances, both living and otherwise, can be systematically (and numerically) studied using processes and theories developed in radionics (see www.copenlabs.com), although much work is required before these theories can be based upon clear scientific foundations. Furthermore, Nuclear Magnetic Resonance (NMR), Beta radiation emission and other such techniques have already been used to validate the effect of the potentizing process. It has been suggested that the said process of dilution and succussion creates "holes" in solutions and the emission of an electron (Conté et al., in Winston 1999, pp 457). Many of these concepts have been scientifically explored to some extent, generally with very compelling results [3]. Further experimentation involving the use of modern technologies such as high-powered microscopes, extremely low frequency (ELF) amplifiers and even particle accelerators could see the dramatic improvement of our understanding of the physiological mechanisms behind homeopathy and of the vibratory and communicative systems at work not only in living tissue, but in matter in general. This knowledge could feasibly open doors to new fields of investigation that have never before been within the reach of conventional scientific methodology, and the implications in both modern medicine and in other areas are hard to predict at this point. Of equal importance is the requirement to submit the postulated hypothesis to the possibility of disproving. If the experiments that attempt to observe the meeting of various electromagnetic wavelengths within the microenvironments of cells and tissue show that no such vibrations are present at all, then weight could be lent to the proposition that homeopathics work entirely due to a placebo effect on believers, or alternatively due to some other mechanism as yet undiscovered.

6. CONCLUSION

It is the author's suggestion that with the combination of homeopathy's sensitivity, modern science's expertise and the Vibration Hypothesis we could see the accurate and methodological study of the activity of electromagnetic radiation within living systems, and of the specific vibrational properties of atoms, chemicals and molecules which allow them to release and receive these communicative signals over relatively vast distances. It is probable that clinical results would then be witnessed within a short time for a large variety of ailments in both humans and animals. Although homeopathy is already in widespread use around the world, by revealing its inner secrets we could attempt to use the technology to achieve even greater results, both for the relief of illness and for the extension and growth of mankind's collective intelligence and ingenuity.

REFERENCES

1. Alberts, B., A. Johnson, J. Lewis, M. Raff, K. Roberts, and P. Walter, *Molecular Biology of the Cell 4th ed.*, Garland Science, New York and London, 2002.
2. Bellavite, P., A. Conforti, F. Pontarollor, and R. Ortolani, "Immunology and homeopathy," *Evidence Based Comp. Alt. Medicine*, Vol. 3, No. 1, 13–24, 2006.
3. Bellavite P. and A. Signorini, *The Emerging Science of Homeopathy: Complexity, Biodynamics and Nanopharmacology*, North Atlantic Books, Berkeley, 2002.
4. Benveniste, J., "From water memory to digital biology," *Network*, Vol. 69, 11–14, 1999.
5. Benveniste, J., E. Davenas, F. Beauvais, J. Amara, M. Oberbaum, B. Robinzon, A. Miadonna, A. Tedeschi, B. Pomeranz, P. Fortner, P. Belon, J. Sainte-Laudy, and B. Poitevin, "Human

basophil degranulation triggered by very dilute antiserum against IgE," *Nature*, Vol. 333, 816–818, 1988.
6. Copen, B., *Electronic Homoeopathic Medicine (Rates Listing)*, 17th Revised Edition, Bruce Copen Laboratories, Highfield Laboratories, Sussex, 1996. See also www.copenlabs.com.
7. Del Giudice, E., G. Preparata, and G. Vitiello, "Water as a free electric dipole laser," *Phys. Rev. Lett.*, Vol. 61, No. 9, 1085–1088, 1988.
8. Linde, K., N. Clausius, G. Ramirez, D. Melchart, F. Eitel, L. V. Hedges, and W. B. Jonas, "Are the clinical effects of homoeopathy placebo effects? A meta-analysis of placebo-controlled trials," *The Lancet*, Vol. 350, No. 9081, 834–843, 1997.
9. Schiff, M., *The Memory of Water: Homeopathy and the battle of ideas in the New Science*, Thorsons, London, 1995.
10. Shang, A., K. L. Huwiler-Müntener, L. Nartey, P. Jüni, S. Dörig, J. A. C. Sterne, D. Pewsner, and M. Egger, "Are the clinical effects of homoeopathy placebo effects? Comparative study of placebo-controlled trials of homoeopathy and allopathy," *The Lancet*, Vol. 366, 726–32, 2005.
11. Shepherd, D., *The Magic of the Minimum Dose: Experience and Cases*, Health Science Press, Bradford, England, 1938.
12. Walach, H., W. B. Jonas, J. Ives, R. Van Wijk, O. Weingertner, and P. Nat, "Research on homeopathy: state of the art," *J. Alt. Comp. Med.*, Vol. 11, No. 5, 813–829, 2005.
13. Winston, J., *The Faces of Homeopathy, An Illustrated History of the First 200 Years*, Great Auk Publishing, Tawa, New Zealand, 1999.
14. *Homoeopathy, International Conference of Drug Regulatory Authorities (ICDRA)*, published by the World Health Organization (WHO), http://whqlibdoc.who.int/hq/2003/a79903_(chp14).pdf, 107–110.

Issues in Wireless Intracranial Pressure Monitoring at Microwave Frequencies

U. Kawoos[1], **R. V. Warty**[2], **F. A. Kralick**[3], **M. R. Tofighi**[4], **and A. Rosen**[1]

[1]School of Biomedical Engineering, Drexel University, Philadelphia, PA 19104, USA
[2]Department of Electrical Engineering, Drexel University, Philadelphia, PA 19104, USA
[3]Department of Neurosurgery, Hahnemann University Hospital, Philadelphia, PA 19102, USA
[4]Penn State University, the Capital College, Middletown, PA 17057, USA

Abstract— Intracranial pressure (ICP) monitoring has a significant role in the diagnosis and prognosis of various brain diseases. The most prevalent technique of monitoring ICP is using catheter based systems, which involve risks including infection, brain damage and patient discomfort. A novel wireless epidural pressure sensor unit which can be implanted in a burr hole drilled in the skull is proposed. The unit operates at an ISM band of 2.4 GHz and radiates a microwave signal as a function of pressure. In-vitro and in-vivo tests were performed to study the efficiency of this measurement technique. This paper presents the design issues and experimental results of the prototype devices developed so far.

1. INTRODUCTION

ICP monitoring can assist in the management of patients with brain diseases, head injuries or post cranial surgery monitoring. Cerebrospinal fluid pressure can rise rapidly due to blockage of venous outflow in some pathological conditions. For this reason, it is necessary to have a pressure meter exhibiting stability and reliability to gage the course of pressure variation for at least 5 days [1]. Long term monitoring is required in patients suffering from hydrocephalus, Reye's syndrome, mass occupying lesions in the brain. A post-surgical outpatient monitoring is also desired as a shunt check to monitor the working of a shunt to drain excess fluid from the ventricles. Present techniques of measuring ICP are based on a sensor tipped catheter inserted into the subarachnoid space or ventricle. These methods restrict the monitoring to a hospital setting, pose problems of infection, tissue damage, and patient discomfort. Ideal specifications of an ICP monitoring system have been defined [2]. A few of them are: simplicity , reliability and ability to function efficiently over a long period of time and under a variety of conditions, either continuously or intermittently; causing no significant discomfort or risk to the patient; ease of disconnecting the patient to allow other investigational procedures; must provide maximum information about variations in ICP.

Normal ICP ranges from 0–20 mmHg with an elevation beyond 20 mmHg considered to be significant for immediate action [3]. In most cases, such patients have already undergone a surgery and a small device can be implanted in a burr hole in the skull and left there for monitoring the ICP. This research aims at development of a 2.4 GHz (ISM band) wireless implantable device, which can irradiate through scalp, the signal that carries ICP information. A burr hole dimension of 12 mm has been considered appropriate in terms of neurosurgical procedure. In this regard, since irradiation in lower ISM band requires a larger antenna size, 2.4 GHz seems to be an appropriate frequency of operation. The device can be completely implanted under the scalp and it radiates a microwave signal for pressure measurements. A preliminary analysis was performed to determine the specific absorption rate through the scalp [4], showing that for low mW ($\sim$10 mW) irradiation, the SAR is expected to be sufficiently below 1.6 W/kg of ANSI/IEEE RF safety guidelines. This amount of power would be enough for detection at a distance of close to 1 meter [5], and could be improved by careful antenna design [5].

This device must be small, have insignificant drift over the period of its use, be compatible with modern imaging techniques (CT scan, MRI scan, Ultrasound), be biocompatible and comply with the ANSI/AAMI guidelines. A prototype model of the device is developed, tested in-vitro as well as in-vivo for wireless transmission, drift, and biocompatibility. The device design was modified for power management, improved sensitivity and miniaturization. Tests were performed to compare the device with the present gold standard for monitoring ICP.

2. DEVICE DESIGN AND MODIFICATIONS

The device design was planned in three stages: building up a prototype device with commercially available parts (piezoresistive pressure sensor) to prove the concept and study the biocompatibility issues; modified design for efficient power management and microwave transmission through scalp; and a final MEMS capacitive pressure sensor based design.

2.1. Piezo-resistive Sensor Based Design

Figure 1 shows a block diagram of the design. The device is run at a supply voltage of 2.8 V. A half-closed bridge pressure sensor (absolute) in ceramic packaging is exposed to pressure variations. The full scale range of the sensor is 0–258.33 torr; however the device is designed for 0–100 torr range. An instrumentation amplifier conditions the signal from sensor for noise elimination and scales it to linear operating range (1.2 V–1.75 V) of a 2.4 GHz voltage controlled oscillator (VCO) [5]. VCO output is coupled to a chip antenna. The antenna nominal bandwidth and center frequency are 120 MHz and 2.450 GHz respectively.

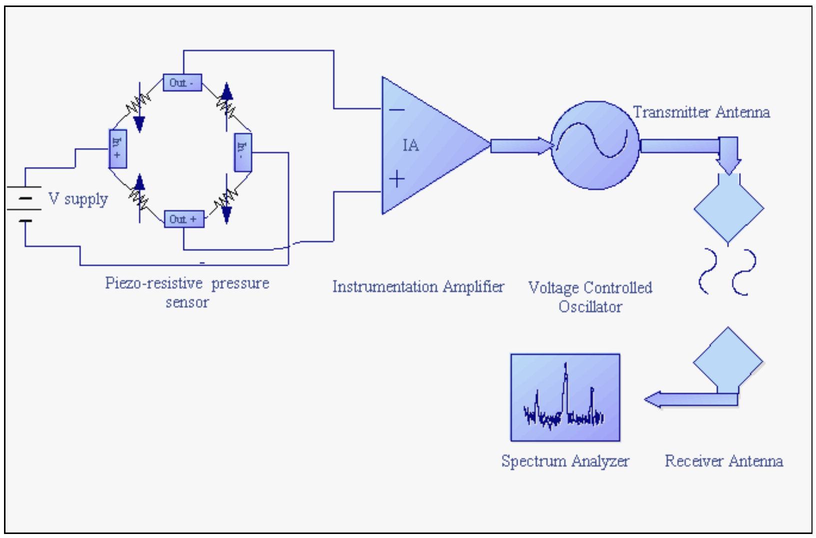

Figure 1: Block diagram showing the basic components of transmitter and receiver system for ICP monitoring.

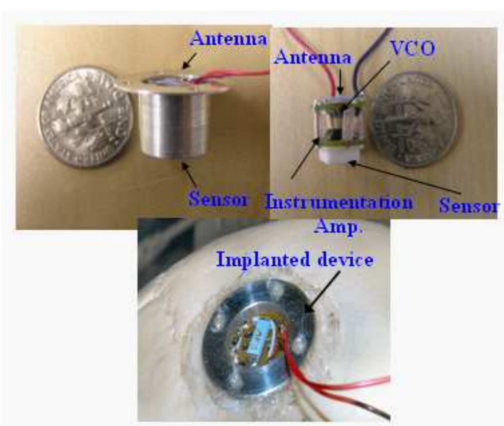

Figure 2: Device placed in a stainless steel case open at top and bottom, figure showing the components of transmitter side, device implanted in a hole in a skull model.

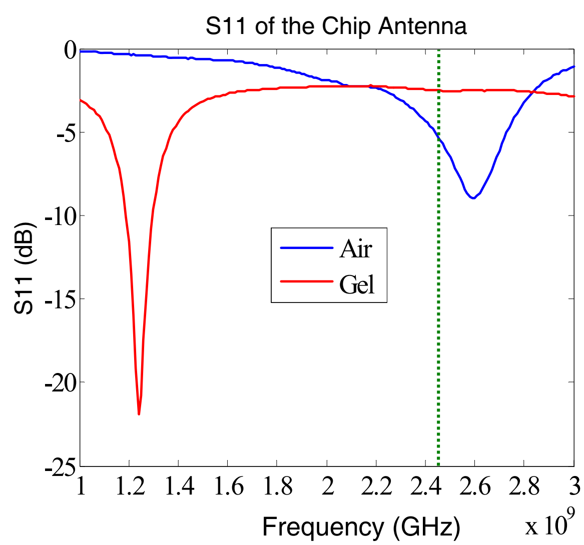

Figure 3: Comparison of the reflection coefficient (S11) of the chip antenna with and without (in air) gel phantom.

The receiver antenna is hooked up to a spectrum analyzer to monitor the frequency shift and the strength of signal obtained due to pressure variations [6]. The device is shown in Figure 2. For biocompatibility and maintaining integrity of this device, a 2.5 μm thick conformal Parylene coating was applied.

Experiments were performed for evaluating the device pressure sensitivity and scalp insertion loss [5, 6]. They demonstrated a measured insertion loss of only about 8–13 dB, i. e., the difference between the received signals with and without the scalp phantom ($\varepsilon_r = 50$ and $\sigma = 2.2\,\mathrm{S/m}$ at 2.45 GHz). The scalp phantom is polyacrylamide gel, 9-mm thick, and its recipe is explained previously [5, 6]. The insertion loss was about 10.5 dB in average. This demonstrated the feasibility of distant monitoring of the pressure information through the scalp at 2.4 GHz. With a receiver sensitivity of −85 dBm [4], the current monitoring range is about 0.8 m [5, 6]. The sensitivity with the pressure change of 0.3 MHz/torr was also obtained.

One reason for limited distance in this setup has been the dielectric loading of the antenna by scalp. Figure 3 illustrates the effect of this loading in the reflection coefficient (S11), with and without (in air) gel phantom. The antenna resonance frequency is shifted to 1.24 GHz through loading by the gel phantom.

2.2. Modified Design

The device design was modified with the inclusion of a power management [4], battery recharging and improved sensitivity. The power consumption is minimized by switching the oscillator on and off at a period of around 10 ms with a pulse width of about 20 µs. The battery is recharged externally and two options are considered. First is charging by an inductive link, which requires the placement of a planar coil on top of the microwave antenna. For MRI compatibility, we are considering optical recharging of the battery as an alternative approach [7]. A die version of the previously used piezo-resistive sensor is being utilized in this device. The sensor was covered by a thin (0.5 mm) layer of silicone followed by 10 µ thick Parylene coating for an interface between the diaphragm and dura. The device case was modified to accommodate a sliding collar for fastening the device in variable skull thickness. Figure 4 shows the device case with threads on the case and set screws to adjust the height.

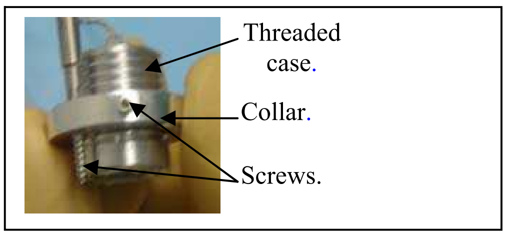

Figure 4: Modified device case.

One of the most important aspects of the modified device is the replacement of the chip antenna with a small planar inverted F (PIFA) antenna for operation in 2.4 GHz, as well as reducing the overall height of the device. Antennas with various sizes were developed and tested. For biocompatibility, they were covered by silicone. Figure 5 illustrates the antenna layout, Ansoft Designer simulation for various antenna thickness, and measurement results of two sample antennas. Since the silicone coating is performed manually, its thickness is not well controlled. However, the figure illustrates a good agreement between the simulation and the measurement.

2.3. Capacitive MEMS Design

The device design is at the third stage, where the piezo-resistive pressure sensor is being replaced by a capacitive MEMS pressure sensor. A capacitive sensor is preferred to the piezo-resistive pressure sensor due to its linearity, in-sensitivity to temperature variations [4], ease of rigging up an oscillator with few additional components unlike the piezo-resistive pressure sensor, resulting in miniaturization.

3. IN-VITRO TESTS

Tests were performed on the prototype devices- basic and modified in a gas pressure chamber at room temperature and a constant power supply. The first prototype went through a series of tests- rigorous in-vitro testing, implantation in a mini-pig for four hours [6], testing the integrity of the device in 0.9 N saline for five weeks and implantation in a canine animal model for five weeks. The last two steps were critical for establishing the integrity of the device in a biological environment.

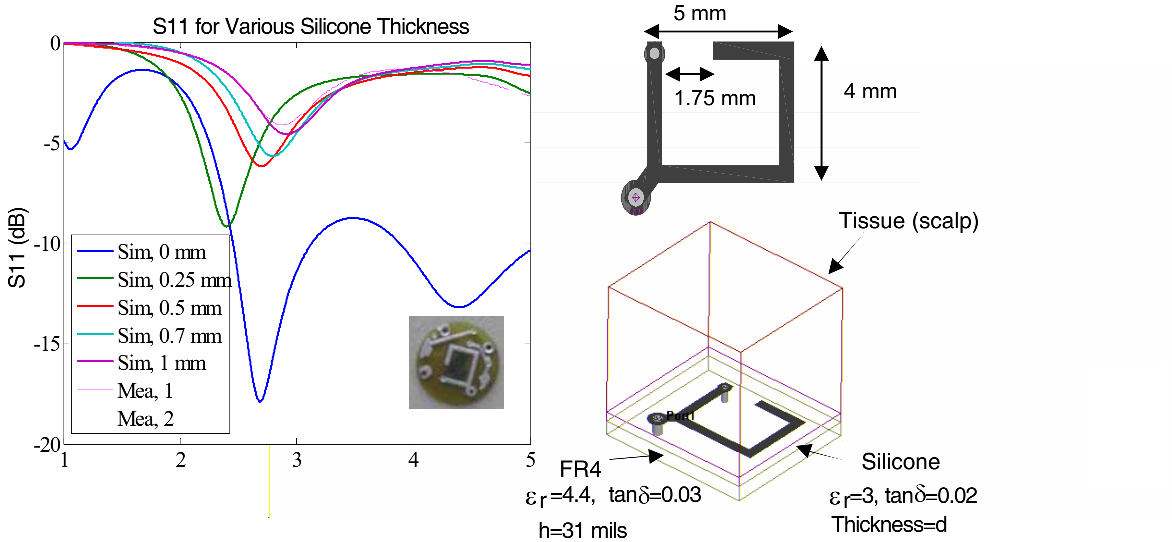

Figure 5: PIFA antenna layout, Ansoft Designer simulation for various antenna thickness, and measurement results of two sample antennas.

4. ANIMAL STUDIES

During each device developmental stage in-vivo studies followed the in-vitro tests as per an IACUC approved protocol. Three successful studies were carried out: implantation of a basic prototype in a miniature swine, implantation of the previously tested device in a dog for a period of five weeks and comparative study between the modified prototype and the standard Camino ICP monitoring catheter, also in a dog model.

In the miniature swine model successful implantation of the permanently implanted device was feasible. It also demonstrated the ability to transmit data through the closed scalp. Recordings and measurements were obtained during a four hour period while the animal was under anesthesia. Maneuvers to alter the physiologic intracranial pressure were instituted. These maneuvers included hypo and hyperventilation to produce increases and decreases in normal ICP respectively. Jugular occlusion was also utilized to raise ICP. The implanted monitor recorded trends in response to these alterations [4]. The results obtained from the swine study of prototype 1 have been discussed earlier [6]. This study established the feasibility of microwave transmission through scalp.

In the subsequent study, the device previously implanted in a swine was reused and implanted in a canine model for a period of five weeks. A good healing of the scalp overlying the device was observed. Figure 6 shows a small protrusion on the dog's head at the site of implantation after

Figure 6: Appearance of protrusion at the implantation site.

one week. This protrusion completely healed over the period of study. The subject was euthanized and three specimens were obtained. The specimens included: 1– reactive scar tissue overlying the device, 2– brain tissue immediately below the device, 3– dura mata immediately below device in continuity with dura mata remote from the device. The device showed abberant performance after the study period. No electrical/signal testing was performed during this experiment. However, alterations to the design of the device casing were made as a result of this study.

In the third study, the modified device (including PIFA antenna and die sensor) was implanted in a dog for a period of 24 hours. A standard ICP monitoring catheter (Camino® 110-4B, Integra Life Sciences, CA) was placed on the other side of the midline for rapid and continuous ICP measurements, and comparison with the wireless measurement. Readings were taken while the dog was anesthetized and being weaned off the ventilator.

5. RESULTS AND DISCUSSIONS

The results of third study exhibited a correlation coefficient of 0.88 between the two modes of measurement (Camino and wireless). The measurements were less erroneous in the pressure range of 10 to 20 torr (+/− 2 torr) and show a slightly higher variation at elevated pressures.

The die version of the pressure sensor exhibits better performance and sensitivity in comparison with the ceramic packaged sensor. This can be explained by an almost direct contact between sensor diaphragm and the dura. Since the sensor was coated with 0.5 mm thick silicone, it did not have a direct contact with the dura. However, prior tests on a silicone coated sensor showed no variations in the sensitivity of the sensor as compared to the bare die. Also, as expected, the replacement of PIFA antenna improved the device operational range (distance).

Further results of the animal study from electrical, histo-pathology and biocompatibility perspective will be discussed in the conference.

ACKNOWLEDGMENT

This research is supported by the National Institutes of Health of the US, grant 1 R21 NS050590-01.

REFERENCES

1. Watson, B. W., J. C. M. Currie, H. C. Riddle, and S. J. Meldrum, "The long term recording of intracranial pressure," *J. Phys. Med. Biol.*, Vol. 19, No. 1, 86–95, 1974.
2. Hulme, A. and R. Cooper, *J. Neurol. Neurosurg. Psychiat.*, Vol. 2, 1549, 1966.
3. Biaha, M. and D. Lazar, "Traumatic brain injury and haemorrhagic complications after intracranial pressure monitoring," *J. Neurol. Neurosurg. Psychaitr.*, Vol. 76, 147, 2005.
4. Kawoos, U., G. K. Mugalodi, M. R. Tofighi, S. Neff, and A. Rosen, "A permanently implantable intracranial pressure monitor," *Proceedings of the IEEE 31st Annual Northeast Bioengineering Conference*, 17–19, April 2005.
5. Tofighi, M. R., U. Kawoos, F. A. Kralick, and A. Rosen, "Wireless intracranial pressure monitoring through scalp at microwave frequencies; preliminary animal study," *Digest of 2006 IEEE International Microwave Symposium*, June 2006.
6. Tofighi, M. R., U. Kawoos, S. Neff, and A. Rosen, "Wireless interacranial pressure monitoring through scalp at microwave frequencies," *Electronics Letteres*, Vol. 42, No. 3, 148–150, Feb. 2006.
7. Goto, K., et al., "An implantable power supply with an optically rechargeable lithium battery," *IEEE Trans. Biomedical Engineering*, Vol. 48, No. 7, 830–833, July 2001.

Simulation of a Wideband Pulsed Radar for Indoor Environments Using FDTD

Rubem G. Farias[1], **Victor Dmitriev**[1]
Francisco Carlos B. F. Müller[1], **and Domingos Savio das Virgens Alves**[2]

[1]Federal University of Para, Belem, Brazil
[2]Institute of Technology of Aeronautics (ITA), San Jose dos Campos, Brazil

Abstract— A numerical simulation of a multistatic radar using the finite-difference time-domain method is performed to identify the presence of intruders inside a residence. The radar operates with ultra-wideband pulses to obtain high resolution. The radar transmits monocycle pulses with maximum amplitude of their spectrum in the frequency of 1 GHz and the half power bandwidth of approximately 1 GHz. One transmitter and three receivers, positioned outside the residence, are used to estimate the target (intruder) location without ambiguity.

1. INTRODUCTION

Finite-difference time-domain (FDTD) method is relatively simple, very versatile and gives a good precision in the calculation of the propagation of ultra wideband (UWB) pulsed signals. These signals are well suited for radar systems and geopositioning systems (GPS). In addition, the UWB pulses are more immune to frequency-selective fading inherent in dense multipath environments such as residences, offices, laboratories and warehouses. Therefore, the use of UWB signals with spread spectrum seems like to be one of the best choices for future indoor communication systems, especially in LANs. The use of spread spectrum in this kind of applications is important since the propagating signal's intensity is below the ambient noise level, so there is virtually no interference with others communication systems. There are systems already in operation using this technology [1].

The transmitter antenna used in our work is omnidirectional. All the six electromagnetic field components are considered in our bidimensional FDTD model (2D-FDTD). Dense multipath environments minimize the coupling effects between the human body and a receiving antenna in close proximity to the body, so that the radiation pattern of the antenna suffers a maximum variation of only 6.8 dB, whereas in an open environment or anechoic chamber a null in the pattern of 23.1 dB for an azimuth angle variation of 360° degrees appears [2]. This fact justifies the kind of radiation pattern adopted in this paper.

The paper is organized as follows. In Section 2, the simulation environment is described, that is, the residence's layout and electrical characteristics of its constituent materials, and essential information about the FDTD method and its accessories: absorbing boundaries in the computational domain, excitation source, ambient additive white Gaussian noise (AWGN) and characterization of the target. Section 3 contains the description of the procedure used in the simulations and in the temporal records of the fields obtained in the receivers. Next, it is shown how the target location estimate is done through the intersection of ellipses defined by the relative location between the transmitter and the three receivers. The results of simulations are described in Section 4, and the conclusions are presented in Section 5.

2. SIMULATION ENVIRONMENT

The environment used for the simulations is a residence whose layout is similar to that of [3]. It is shown in Figure 1. In this residence, there are two distinct kinds of walls, with different electrical properties. The relative electric permittivity of the exterior walls is $\varepsilon_r = 5$, whereas the interior walls have $\varepsilon_r = 4.2$. In both of them, the chosen conductivity is $\sigma = 0.02\,\mathrm{S/m}$. Everywhere else, the relative permittivity is equal to unity except on the absorbing boundaries.

The simulations are performed using a 2D-FDTD method for non-dispersive isotropic media, based on the Yee's formulation [4]. Only perpendicular polarization relative to the plan in Figure 1 is considered in the transmitter antenna. A uniform mesh is used with $(395, 397)$ cells. Each square-shaped cell has 0.03 m width ($\delta_x = \delta_y = \Delta s$) which is equivalent to approximately one tenth of the free space wavelength of the excitation pulse in the reference frequency $f_o = 1\,\mathrm{GHz}$. The time increment is obtained from the spatial ones (cell dimension), in order to assure the numerical stability of the method. The value used in this paper is

$$\delta t = 0.7\frac{\Delta s}{c\sqrt{2}} \tag{1}$$

where c is the light speed in vacuum.

The absorbing boundaries are very important elements in the FDTD mesh. Their purpose is to limit the computational domain and, thus, to simulate propagation in an open environment, with minimum reflection. In order to achieve this, an anisotropic perfectly matched layer-absorbing medium based on a lossy uniaxial medium is used [5]. The parameters of the layer are: the thickness $d = 10$ cells, the maximum conductivity $\sigma_{\max} = 15\,\mathrm{S/m}$ and the order of polynomial variation $m = 4$.

The waveform used as excitation source to scan the environment is the Gaussian monocycle, shown in Figure 2(a). This is the type of pulses used, for example, in the PulsON system [6]. It is obtained from the Gaussian function

$$g(t) = A_0 \exp\left[\frac{-(t-t_0)^2}{\tau^2}\right] \tag{2}$$

where A_0 is the maximum amplitude, t_0 is the time when the maximum amplitude occurs, and τ is the time decay constant. The Gaussian monocycle is the first derivative of this function:

$$p(t) = -A_p\sqrt{\frac{2e}{\tau^2}}\,(t-t_0)\exp\left[-\frac{(t-t_0)^2}{\tau^2}\right] \tag{3}$$

where $e = 2.71828\ldots$ and A_p is the peak amplitude of the monocycle. The relation between A_p and A_0 is as follows:

$$A_0 = A_p\tau\sqrt{\frac{e}{2}} \tag{4}$$

The Gaussian monocycle is an ultra wideband signal, with bandwidth and central frequency depending on the duration of the monocycle. In the frequency domain, the spectrum obtained from its Fourier transform is

$$P(f) = A_p\tau^2\sqrt{\frac{\pi e}{2}}\exp\left[1-(\pi\tau f)^2\right]\exp(-j2\pi t_0 f) \tag{5}$$

and the central frequency of the monocycle can be calculated through the following equation:

$$f_0 = \frac{1}{\sqrt{2\pi^2}}\frac{1}{\tau} \tag{6}$$

The monocycle spectrum is shown in Figure 2(b).

To complete the environment description, the only missing item is the target. It was chosen a cylinder with 0.25 m radius (in fact, only its transversal section since the mesh has two dimensions), attempting to represent a human body. The relative permittivity considered is $\varepsilon_r = 50$ and the conductivity $\sigma = 1.43\,\mathrm{S/m}$ [7].

3. PROCEDURE FOR LOCATION

In this section, the description of the procedure adopted to locate the target is given. The method allows one to determine the position of the target related to the origin of the coordinate system.

Shortly, we can describe the algorithm as follows. The transmitter and the receivers are placed in different positions in order to form a multistatic radar. The pulse is transmitted and the environmental response without target in terms of the electrical field intensity component E_z is recorded. Then, the same is done with the target placed inside the residence. This is the part involving the FDTD method. The rest of the algorithm consists in calculating the difference between the records with and without the target, followed by the normalization of the obtained records and the inclusion of Gaussian noise (AWGN). Finally, the estimate is done using the radar data, and the error of the estimated position of the target is computed.

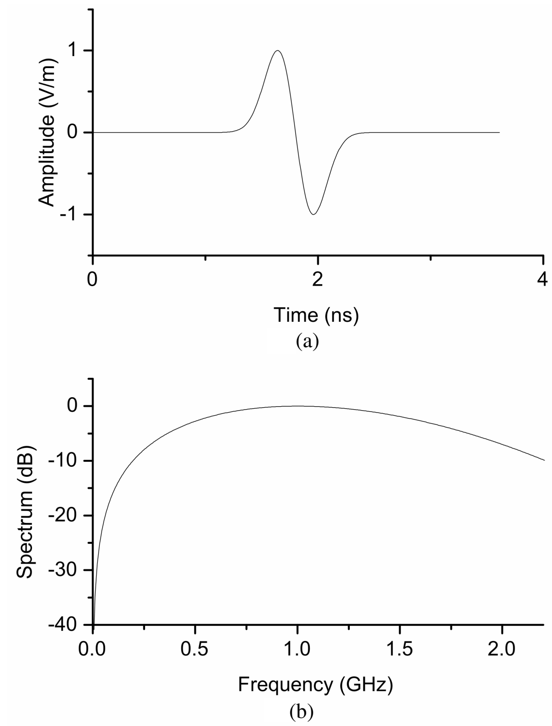

Figure 2: (a) Gaussian monocycle pulse. (b) Gaussian monocycle spectrum.

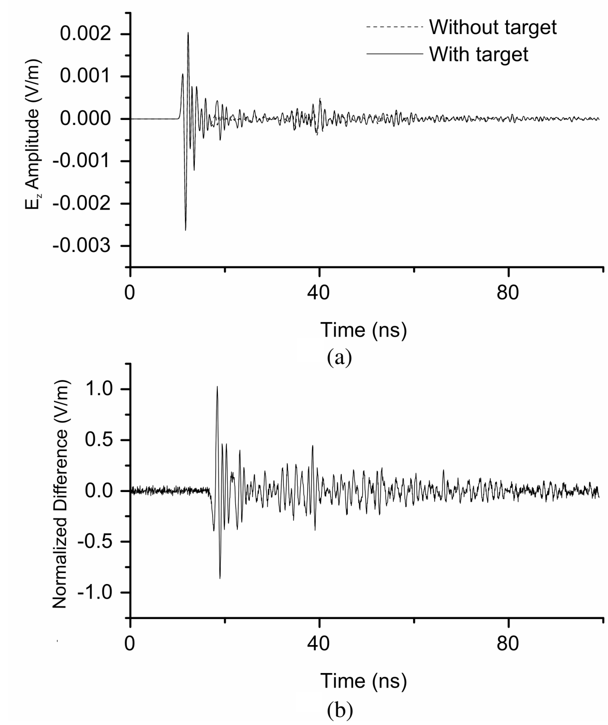

Figure 4: (a) Electrical field intensity record in one of the receivers. (b) Normalized difference between the records of the previous figure, AWGN included.

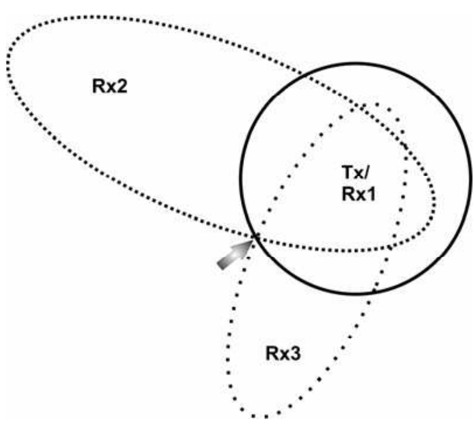

Figure 3: Simplified scheme of the multistatic radar.

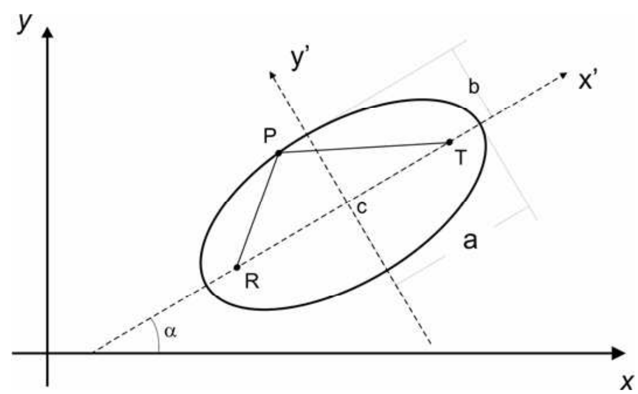

Figure 5: Ellipse with rotated axes and dislocated center.

The multistatic radar used in our simulations consists of one transmitter and three receivers. One of the receivers is located at the point of the transmitter. The geometrical locus obtained in this case is a circle. The other two receiver/transmitter sets possess ellipses as geometrical loci, with the transmitter and one receiver as foci. The combined use of the transmitter and the three receivers allows one to estimate uniquely the position of the target, as illustrated in Figure 3.

The first step in simulating the radar is to produce the intensity field records in time using FDTD. In the computational environment presented in the previous section, the locations of the transmitter, the receivers (three) and the target are chosen as follows. One of the receivers and the transmitter are positioned at the exterior of the residence, close to a wall. The other receivers are placed along another residence's wall, which belongs to the same room, also at the exterior. The target is positioned at the center of one of the residence's rooms. Several arrangements were simulated, but only three of them will be described.

When the intensity field records are obtained, the difference between the records in each receiver with and without the target can be calculated (it is interesting to notice how subtle is the difference between these two records when they are overlapped, as shown in Figure 4(a), but the difference becomes very clear when the subtraction is done, as Figure 4(b) reveals. It also occurs in practical systems [1]). After that, the records are normalized and addictive white Gaussian noise is added, in order to simulate environment and system noise. The standard deviation value relative to the peak values of the normalized differences in each receiver is $\sigma_n = 0.02$.

Figure 5 shows the ellipse and its main parameters. Point T represents the transmitter, point R indicates the receiver location and point P represents the target. The equation of the ellipse, including axis rotation and translation, is given below:

$$F(x,y) = b^2\left[(x-x_c)\cos\alpha + (y-y_c)\sin\alpha\right]^2 + a^2\left[(x-x_c)\cos\alpha - (y-y_c)\sin\alpha\right]^2 - a^2b^2 = 0 \quad (7)$$

where a is the major axis, b is the minor axis, x_c e y_c are the coordinates of the center C and α is the angle between the x-axis and the major axis of the ellipse. The equation is reduced to a circle's one when the positions of the transmitter and receiver coincide (Figure 3). The equation's parameters are all obtained from the known location of the transmitter and the receiver and from the distance traversed by the pulse between transmitter, target and receiver, denoted here as d_{TPR}. In Figure 5, this is the sum of the segments $\overline{TP}$ with $\overline{PR}$. It is obtained from FDTD simulation and the record processing is described below.

The parameter d_{TPR} is calculated from the differences between the electrical field intensities E_z recorded in each receiver. Analyzing Figure 4(b), we see that there is a moment when the difference ΔE_z becomes significant, not being caused only by the system's noise (AWGN), but by the presence of the target in the residence. Assuming the line-of sight propagation as the main propagation mechanism, the time that takes for that difference to appear is equal to the time spent in the pulse propagation between transmitter, target and receiver. To calculate this time, the *threshold* of 0.1 is taken for isolating the noise, and then the first peak exceeding this threshold is detected. Knowing this time and the propagation medium velocity, it is possible to calculate the distance d_{TPR}.

The pulse propagation velocity in the computational environment is obtained from another ad hoc FDTD simulation because there is a significant difference between this velocity and the velocity of light in vacuum. Ignoring this fact would cause significant errors in the calculation of d_{TPR}. In the same computational environment, the residence is taken away and two walls are added (one of the interior kind [$\varepsilon_r = 4.2$] and the other of the exterior kind [$\varepsilon_r = 5$]). The layout is shown in Figure 6, where the direct lines between transmitter and receiver form angles of 0°, 15°, 30° e 45° relative to the x-axis. In this way, the effects of the different media on the velocity and the different propagation velocities in different directions that may arise due to the shape of FDTD cells are taken into consideration. The group velocities between each receiver and the transmitter are calculated, and then a weighted average is obtained using the power defined by the Poynting vector received in each receiver. This average energy velocity is used in the calculation of d_{TPR} and then all the other parameters of the ellipses can be obtained.

With all the parameters of the ellipses and of the circle calculated, the location estimate can be accomplished. First, the system with two the ellipses' equation (7) associated with receivers Rx2 and Rx3 is formed. It generates four possible solutions of the system. Then, we calculate the function $F(x, y)$ for Tx/Rx1, that is, the circle equation, using the four previously found solutions. The solution that makes this function closer to zero is chosen. Finally, the error in the estimated location is calculated.

The type of error parameter used in the paper deserves special attention. We stress that the radar detects the surface of the target, not its center, and that the diameter of the target is significant compared to the dimensions of the environment. Therefore, we consider the following error parameter:

$$e = \frac{d_{sol} - r}{2r} \quad (8)$$

where d_{sol} is the distance between the center of the target and the estimated position and r is the radius of the target.

4. RESULTS

Three cases of simulations for locating the target in the residence are presented below. We have tried to emulate the detection of an intruder inside the residence from its outside. In the first case, the target is positioned at the center of the *Living Room* of the residence, and the transmitter and the receivers are placed around this room, as illustrated in Figure 7. This figure also shows the electrical field intensity in the environment after 19.8 ns from the beginning of the excitation pulse,

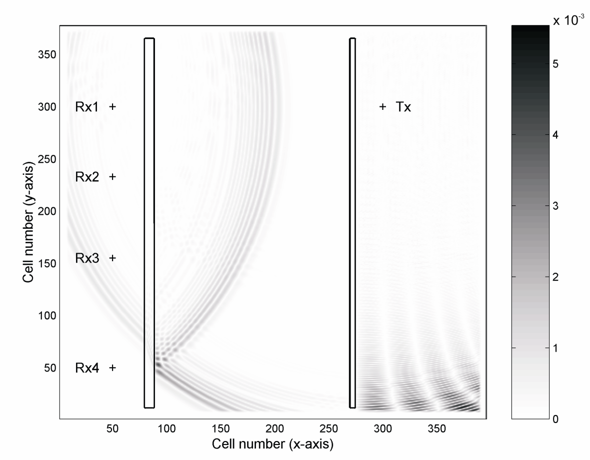

Figure 6: Velocity test environment layout, including the electrical field intensity after 34.7 ns from the beginning of the pulse propagation.

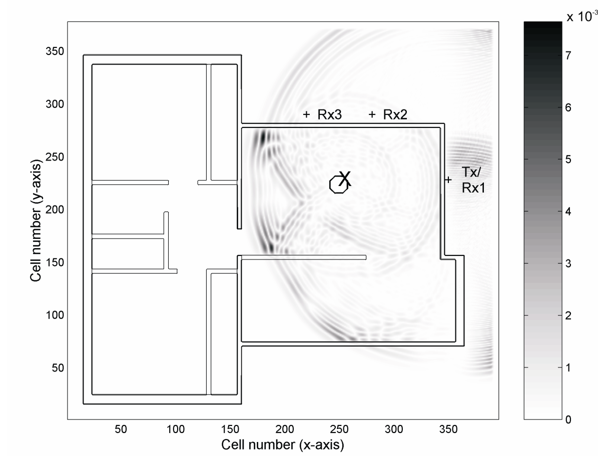

Figure 7: Location of the target estimated by the radar (first case).

and the sign "X" marks the location of the target estimated by the radar. The center of the target location is $(7.5, 6.72)$, in meters (the origin of the coordinate system is in the inferior left corner). The location estimated for the target by the radar is $(7.6631, 6.8646)$. The relative error for this case is 6.4%.

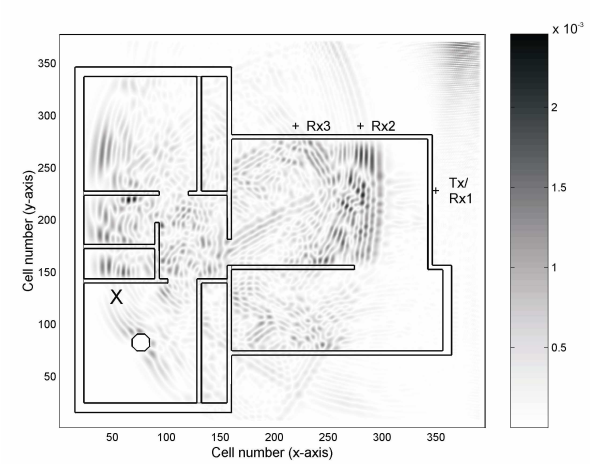

Figure 8: Location of the target estimated by the radar (second case).

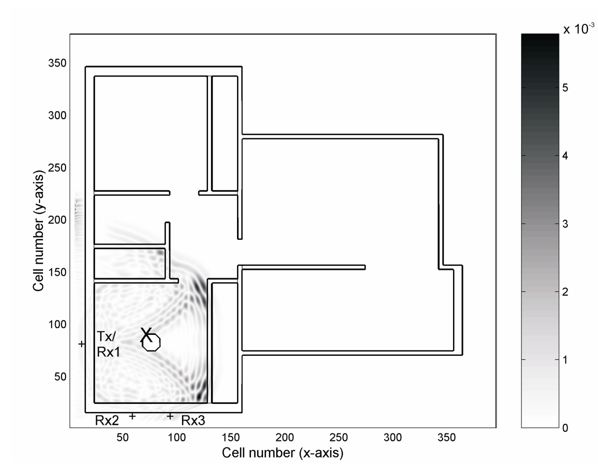

Figure 9: Location of the target estimated by the radar (third case).

For the second case, the positions of the transmitters and the receivers are maintained. The target, however, is placed in the center of *Bedroom 2*, as shown in Figure 8. The field intensity in the figure occurs after 34.67 ns from the beginning of the excitation. The center of the target is $(2.31, 2.49)$, and the calculated estimation is $(1.6289, 3.7794)$. The relative error is increased to 241%. Even with the increase of the quantity of obstacles (walls) and of the distance, the method allows one to predict the presence of the target in the correct room of the residence.

In the next simulation, we change the location of the transmitter and the receivers, placing them around *Bedroom 2*, and keeping the target at the same position. The configuration is shown in Figure 9, with the field intensity after 14.86 ns from the beginning of excitation. With the change, the obtained estimate is $(2.1644, 2.6887)$ and the relative error of calculation is 0.73%, which is a great improvement compared with the previous situation.

Thus the estimate is much better when the receivers are around the same room where the target is present, because there are fewer obstacles (walls) between them. This turns propagation closer to line-of-sight, improving d_{TPR} calculation and therefore the estimate of the target location.

5. CONCLUSIONS

In this paper, we have presented a simulation of a multistatic radar operating with UWB pulses. Our method is based on FDTD technique combined with optical geometry (ellipses). We have described the mathematical procedure and computer technique for solving the problem. Some results of the computer simulations have been presented.

Our results show that FDTD is a useful method to apply for this kind of radar problems. This method can be used to simulate the operation of the multistatic radar in an environment prior to its practical implementation and to develop the signal processing techniques for these radar systems.

ACKNOWLEDGMENT

This paper was partially supported by CNPq and CAPES.

REFERENCES

1. Withington, P. and H. Fluhler e S. Nag, "Enhancing homeland security with advanced UWB sensors," *IEEE Microwave Magazine*, Vol. 4, No. 3, September 2003.
2. Welch, T. B., R. L. Mulsselman, B. A. Emessiene, P. D. Gift, D. K. Choudhury, and D. N. Cassadine e S. M. Yano, "The effects of the human body on UWB signal propagation in an indoor environment," *IEEE Journal on Selected Areas in Commun.*, Vol. 20, No. 9, December 2002.
3. Kondylis, G. D., "On indoor wireless channel characterization and the design of interference aware medium access control protocols for packet swichted networks," University of California, Los Angeles, 2000.
4. Yee, K. S., "Numerical solution of initial boundary value problems involving Maxwell's equations in isotropic media," *IEEE Trans. Antennas Propagat.*, Vol. AP-14, 302–307, May 1966.
5. Gedney, S. D., "An anisotropic perfectly matched layer — Absorbing medium for the truncation of FDTD lattices, *IEEE Trans. Antennas Propagat.*, Vol. AP-44, No. 12, 1630–1639, December 1996.
6. Petroff, A. and P. Withington, "PulsOn technology overview," July, 2001. [Online]. Available: http://www.timedomain.com/Files/downloads/techpapers/PulsONOverview7_01.pdf.
7. Gandhi, O. P., G. Lazzi, and C. M. Furse, "Electromagnetic absorption in the human head and neck for mobile telephones at 835 and 1900 MHz, *IEEE Trans. Microwave Theory and Tech.*, Vol. 44, No. 10, 1884–1897, October 1996.

Propagation of Electromagnetic Waves in Amazon Rain Forest Environment

Domingos Sávio das Virgens Alves[1], **Alberto José de Faro Orlando**[1], **and Victor Dmitriev**[2]

[1]Institute of Technology of Aeronautics, São José dos Campos, Brazil
[2]Federal University of Pará, Belém, Brazil

Abstract— For development of wireless systems for vegetation regions, the detailed knowledge of the involved propagation mechanisms is essential. The physical and geometric parameters of the vegetation are random. Calculating the mean signal amplitude decay, both absorbing and multiple scattering effects must be taken into account. Statistical parameters of rough terrain and vegetation are important but they are not always available. In our investigations, we use a deterministic model for calculation of the losses of point-to-point paths in order to estimate the influence of some of the medium forest parameters on transmission losses.

1. ASPECTS OF THE WAVE PROPAGATION IN FOREST

From the point of view of electromagnetic wave propagation in forest, the Amazon region has some specific features. First of all, it is high humidity. The vegetation and terrain posess dynamic morphology that change in particular, in accordance with periodic annual climatic variations modifying some physical properties. For calculation of electromagnetic waves that propagate in this environment, the vegetation itself should be characterized by some parameters [1], such as (1) type of vegetation: average height, shape and distribution of the elements (trunks, branches and leaves); (2) space density (number of trees per unit of area) (3) vegetation water content: volume of water deposited in the surface of the elements and the interior of the trunks and branches. Another parameter important to consider is the variation of the electric characteristics of the soil with the moisture and salinity [2].

The losses associated with the electromagnetic scattering and absorption in the trunks and branches can be separately calculated considering each element as cylindrical scatterer (absorber) with circular cross-sections of different diameters. The distribution functions of the diameters of the elements in the analysis can be taken into account [3–6]. The foliage can be considered as a uniform media with losses [7, 8].

For the frequency range where the scatterers are small compared with the wavelength, the scattering can be estimated using effective parameters of the media. The dielectric constant can be obtained by theoretical models or by semi-empirical formulas. However, such formulas in many cases possess little versatility, being appropriate for the specific cases (type of vegetation, climatic conditions and range of frequency) for which they have been implemented. The variation of the complex electric permittivity of the vegetation with parameters as frequency, moisture and salinity can be calculated using dielectric mixture models [9, 10]. An example is the approach for dielectric constant proposed by Peake [11]:

$$\varepsilon = m_v\varepsilon_w + (1 - m_v)2.5 \approx m_v\varepsilon_w \tag{1}$$

where $\varepsilon_w = \varepsilon'_w + j\varepsilon''_w$ is the relative complex dielectric constant of water. The dielectric constant of saline water is calculated by the Debye relaxation formulas [9]:

$$\varepsilon'_w = \varepsilon_{w\infty} + \frac{\varepsilon_{ws} - \varepsilon_{w\infty}}{1 + \left(\frac{f}{f_0}\right)^2} \tag{2}$$

$$\varepsilon''_w = \frac{\left(\frac{f}{f_0}\right)(\varepsilon_{ws} - \varepsilon_{w\infty})}{1 + \left(\frac{f}{f_0}\right)^2} + \frac{\sigma}{2\pi\varepsilon_0 f} \tag{3}$$

where
ε_{ws} — static limit of ε'_w
$\varepsilon_{w\infty}$ — high-frequency limit of ε'_w
σ — ionic conductivity of the aqueous solution (S/m), determined by the salinity of the solution.
f — frequency (Hz).

2. PROPAGATION MODEL FOR FOREST ENVIRONMENT

The Amazon rain forest presents a characteristic distribution of vegetation with the peculiarities that can be taken into account to develop a model of electromagnetic propagation in this environment. The model using four dielectric layers, considered by Cavalcante [12], has been adopted in various works [13–16]. However, we shall consider a three layers model [17–19], that is, the forest represented only by one dielectric layer. This is because the Amazon rain forest, in contrast to the Europe and USA forests, is typically dense with the foliage interwining with the trunks, composing only one layer in which the electric characteristics of each constituent (trunks, branches and leaves) should de considered. Thus, our stratified model consists of three horizontal dielectric layers. The first layer is the semi-infinite free space, the second region represents the forest and the last region is the soil.

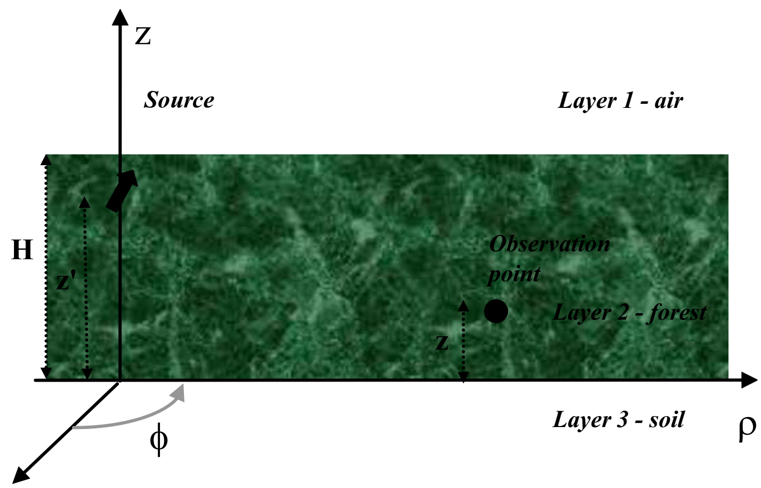

Figure 1: Three layer forest model.

3. MATHEMATIC FORMULATION

The mathematical model, in accordance with Fig. 1, can be implemented using the method of dyadic Green's functions. The following expressions for the electric field in the far zone of the dipole antennas are valid:

$$\bar{E}_2\left(\bar{R}\right) = j\omega\mu_0 \iiint\limits_{V'} \overline{\overline{G}}{}_e^{21}\left(\bar{R}, \bar{R}'\right).\bar{J}\left(\bar{R}'\right)dV' \quad \text{for} \quad H \geq z \geq 0 \tag{4}$$

where

$$\begin{aligned}\overline{\overline{G}}{}_e^{(21)}(\bar{R}, \bar{R}') &= \frac{j}{4\pi}\int\frac{d\lambda}{h_1\lambda}\sum_{n=0}^{\infty}(2-\delta_0).\left[\left(\frac{2h_1}{h_1+h_2}\frac{1}{D^H}\bar{M}(-h_2)+\frac{2h_2}{h_1+h_2}\frac{R_2^H e^{j2h_2H}}{D^H}\bar{M}(h_2)\right)\bar{M}'(h_1)\right.\\&\quad\left.+\left(\frac{2k_2k_1h_1}{k_2^2h_1+k_1^2h_2}\frac{1}{D^V}\bar{N}(-h_2)+\frac{2k_2k_1h_1}{k_2^2h_1+k_1^2h_2}\frac{R_2^V e^{j2h_2H}}{D^H}\bar{N}(h_2)\right)\bar{N}'(h_1)\right] \end{aligned}\tag{5}$$

$$R_2^V = \frac{k_3^2h_2-k_2^2h_3}{k_2^2h_3+k_3^2h_2}; \quad R_2^H = \frac{h_2-h_3}{h_3+h_2}; \quad D^{V,H} = 1+R_1^{V,H}R_2^{V,H}e^{j2h_2H} \tag{6}$$

The vector wave eigenfunctions $\bar{M}$ e $\bar{N}$ are given in [20].

To obtain a compact solution and to reduce the computational efforts, some approximate formula can be deduced from the above expressions. The integral in (4) for example, can be substituted by asymptotical expressions using the method of saddle point and branch cuts integration. In this case, the electromagnetic fields are presented in the form of series of reflections in the dielectric interfaces of the layers. The direct and multireflected waves are obtained by application of the method of saddle point, while the lateral waves are as the results of the integration on branch cuts. Details on the asymptotic methods and procedure of field calculations can be found in references [20–22].

4. NUMERICAL RESULTS

The forest model described above is employed to predict the behavior of the electromagnetic signal of communications systems operating inside the forest.

The transmission loss L for the field radiated by dipole is given by formula:

$$L(\text{dB}) = 32.4 + 20\log_{10}\left[d\,(\text{Km})\right] + 20\log_{10}\left[f\,(\text{MHz})\right] + 20\log_{10}\left|\frac{E_0}{E}\right| \tag{7}$$

where the first three terms defines the free space loss, derived of Friis transmission formula [22]. The horizontal distance between transmitting and receiving antennas d is given in kilometers and the frequency f in MHz. The last term in (7) is the loss associated with the forest layer, where, E_0 is the unattenuated electric field (in the absence of the forest layers), and E is the total field computed by (4).

In the calculation of the total field, the values of the direct wave, multireflected and the lateral wave in the interface between layers 1 (air) and 2 (forest) had been taken into account. The number of the jumps of the multireflected waves which has been taken into account is 40, and the number of the hops of the lateral wave is 6.

Numerical results are computed in this work using the frequency range of 0.2–2 GHz. The parameters of the problem are as follows: the position of the transmitting antenna (dipole) above the ground is $z' = 10$ m, the position of the receiving antenna $z = 1.5$ m, the height of the vegetation layer $H = 25$ m, $\phi = 0°$ and $\alpha = 90°$ (vertical polarization). The effective permittivity of forest layer $\varepsilon_2 = 1.12$ and conductivity $\sigma_2 = 0.12$ mS/m have been adopted. The soil parameters used are, permittivity $\varepsilon_3 = 50$ and conductivity $\sigma_3 = 100$ mS/m.

In Fig. 2, the radio-losses of the total field for 4 different frequencies are presented in function of the radial distance between the transmitter and the receiver antennas. For relatively short distances, the contribution of bigger relevance for composition of the signal is the multireflected waves. For example, for frequency 1.8 GHz, the curve presents a fast growth, that is, the loss levels increase with the increment of the horizontal distance between the transmitter and the receiver until about 2 km. The observed peaks can be explained by multireflected waves that are overlapped. However, for long distances (2–10 Km) the response is flat, where the mechanism of propagation of lateral waves is preponderant.

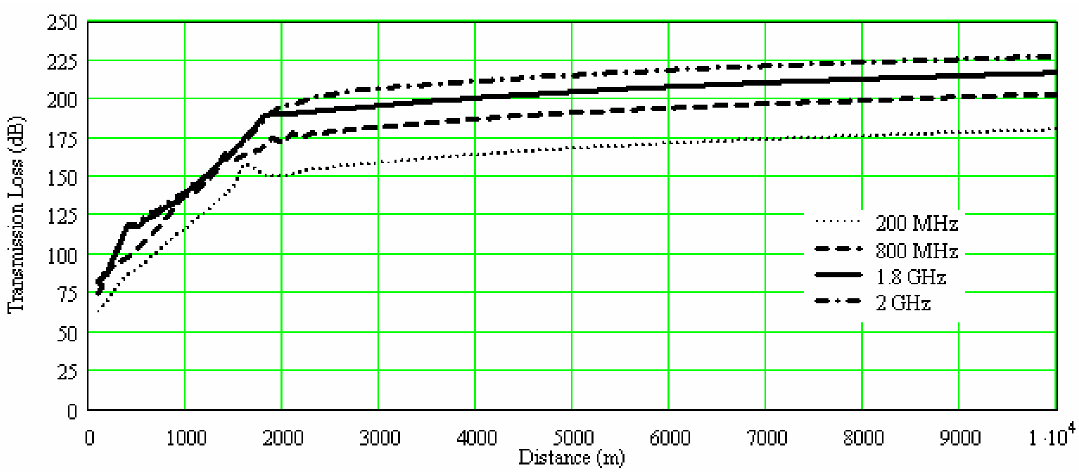

Figure 2: Transmission loss of the total field.

The electric conductivity changes with the variation of the amount of water in each element that constitutes the forest layer. It is known that the Amazon region presents a high moisture index, thus constituting a highly absorbing medium for radiowaves. To verify the variation of the transmission loss in function of the conductivity and concomitant moisture, the curves in Fig. 3 have been plotted. The conductivity range was of 0.01–0.5 mS/m, being the typical extremities, values for dry forests and with high humidity, respectively. The losses have been calculated for distance of 6 km. The observed difference between the levels of reply for the dry forest and the humid one is of the order of 90 dB.

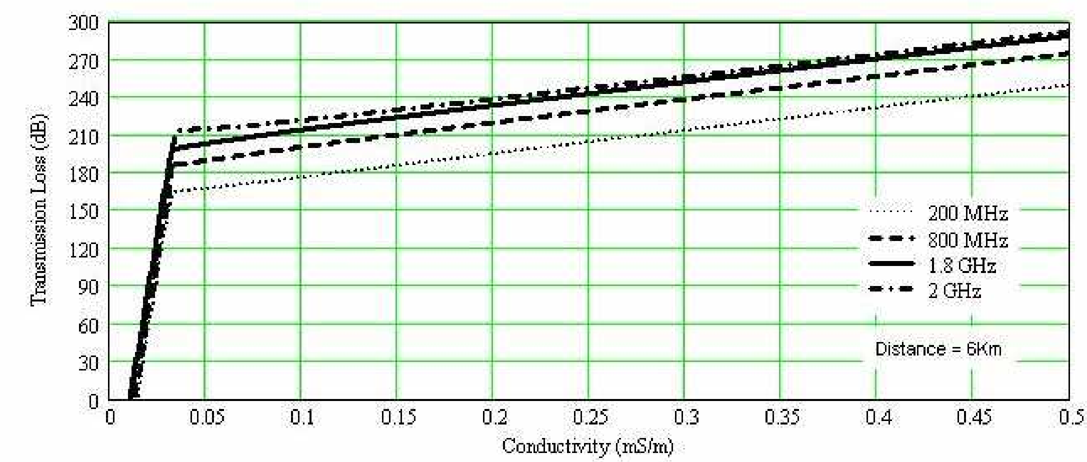

Figure 3: Transmission loss versus conductivity.

For frequency range of 0.2–2 GHz, and the distance between transmitter and receiver in 6 Km, the curves of losses are presented in Fig. 4. The parameters of the forest are the same used in Fig. 2.

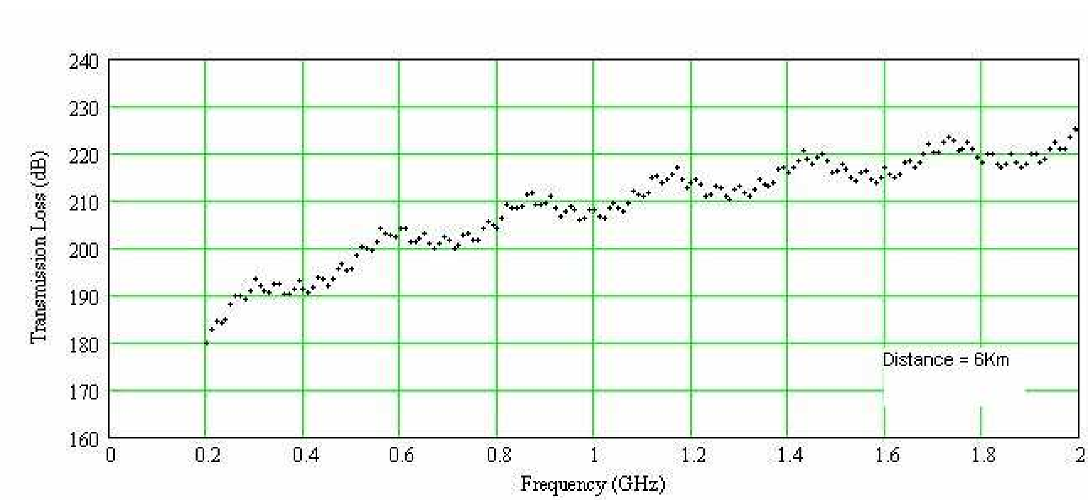

Figure 4: Transmission loss versus frequency.

5. CONCLUSIONS

Using the known mathematical models, we have made in this paper some theoretical predictions of electromagnetic wave propagation losses in Amazon rain forest. The models can be improved using the following methods:

1. Taking into account the anisotropy of the forest layer (trunks).
2. Calculating the effective parameters of the forest layer using the methods of the diffraction theory.
3. To introduce the tensor of permittivity in the model for study of the depolarization.
4. To consider random irregularity in the surfaces of the soil and top of the trees.
5. Using Monte Carlo method for modeling of distribution of the vegetation.
6. Improving the model using techniques of generation of trees as *Honda Tree* and *L-systems*.

REFERENCES

1. Chukhlantsev, A. A., "Microwave emission and scattering from vegetation canopies," *J. Electromagn. Waves Appl.*, Vol. 6, No. 8, 1043, 1992.
2. Peplinski, N. R., F. T. Ulaby, and M. C. Dobson, "Dielectric properties of soils in the 0.3–1.3 GHz Range," *IEEE Trans. Geosci. Remote Sens.*, Vol. 33, No. 3, 803–807, 1995.

3. Suzuki, H., "A statistical model for urban radio propagation," *IEEE Trans. Commun.*, Vol. COM-25, No. 7, 673–680, 1977.
4. Seker, S. S. and A. Schneider, "Stochastic model for pulsed radio transmission through stratified forests," *Proc. Inst. Elect. Eng.*, Vol. 134, pt. H, 361–368, 1987.
5. Seker, S. S., "Radio pulse transmission along mixed paths in a stratified forest," *Proc. Inst. Elect. Eng.*, Vol. 136, pt. H, 13–18, 1989.
6. Li, L. W., "Wave propagation and communication within random in-homogeneous media," Ph.D. dissertation, *Inst. Electron. Acad. Sinica*, Beijing 100080, China, with *China Res. Inst. Radiowave Propagat.*, Xinxiang, Henan, 453003, China, Oct. 1990.
7. Chukhlantsev, A. A., A. M. Shutkoand, and S. P. Golovachev, "Attenuation of electromagnetic waves by vegetation canopies," *J. Comm. Tech. and Electron.*, Vol. 48, No. 11, 1177–1202, 1992.
8. Torrico, S. A. and H. L. Bertoni, "A theoretical investigation of foliage effects on path loss for residential environment," *Proc. IEEE Veh. Tech. Conf.*, 854–858, 1996.
9. Ulaby, F. T. and M. A. El-Rayes, "Microwave dielectric spectrum of vegetation — Part II: dual-dispersion model," *IEEE Trans. Geosci. Remote Sens.*, Vol. 25, 550–557, 1987.
10. Ulaby, F. T. and R. P. Jedlicka, "Microwave dielectric properties of plant materials," *IEEE Trans. Geosci. Remote Sens.*, Vol. GE-22, No. 6, 530–536, 1984.
11. Peak, W. H., *IRE Trans. Antennas Propag.*, Vol. 7, 325, 1959.
12. Cavalcante, G. P. S., D. A. Rogers, and A. J. Giardola, "Radio loss in forests using a model with four layered media," *Radio Sci.*, Vol. 18, 69l–695, 1983.
13. Lian, H. X. and L. Lewin, "UHF radio loss in forest modeled by four layered media with two anisotropic slabs," *IEEE Proc.*, 217–221, 1986.
14. Li, L. W. and P. N. Jiao, "Solution of the electromagnetic field in a forest model with four layered media," *Chinese J. Radio Sci.* (in Chinese) [or *J. Guizhou Univ.-Natural Sci.* (in English)], Vol. 1, No. 2 [or Vol. 6, No. 3 and Vol. 7, No. 1, (in two parts)], 10–25 [or 24–31 and 41–52], 1986 (and 1989 and 1990. respectively).
15. Li, L. W., P. S. Kooi, M. S. Leong, and T. S. Yeo, "Radio waves propagation along mixed paths trough a four-layered model of rain forest: An analytic approach," *IEEE Trans. Antennas Propagat.*, Vol. 46, No. 7, 1098–1111, 1998.
16. Lee, J. K. and J. A. Kong, "Dyadic Green's functions for layered anisotropic medium," *Electromag.*, Vol. 3, 111–130, 1983.
17. Cavalcante, G. P. S. and A. J. Giarola, "Optimization of radio communication in media with three layers," *IEEE Trans. Antennas Propag.*, Vol. AP-31, No. 1, 141–145, 1983.
18. Dunn, J. M., "Lateral wave propagation in a three-layered medium," *Radio Sci.*, Vol. 21, 787, 1986.
19. Chew, W. C., et al, "The layered medium Green's function — A new look," Vol. 31, Issue 4, 251–255, 2001.
20. Ishimaru, A., *Electromagnetic Wave Propagation, Radiation, and Scattering*, Prentice-Hall, Englewood Cliffs, NJ, 1991.
21. Brekhovskikh, L. M., *Waves in Layered Media*, Academic, New York, 1960.
22. Kong, J. A., *Electromagnetic Wave Theory*, Wiley, New York, 1990.

Development of a Methodology for Infrared Aircraft Emission Estimation

R. A. T. Santos, C. G. R. Taranti, F. D. P. Alves, and J. E. B. Oliveira
Instituto Tecnológico de Aeronáutica, Brazil

Abstract— This work discusses the main points of a methodology for the estimation of the infrared emission of aircrafts. It also describes the computational tools that were developed in order to support the work. Softwares for aspect ratio of a flying aircraft measurement, time synchronization, sensor calibration, and atmospheric transmissivity estimation were developed. This work also emphasizes the applications of this technology for civilian aircrafts, increasing the flight safety.

1. INTRODUCTION

There is much concern nowadays with respect to terrorist attacks, and this has brought important changes in the aeronautics industry. Some of these changes can be noticed in changes in the internal layout of the civilian aircraft and the studies on adopting IR defense systems on civilian aircraft. Although one might think about IR missiles as a remote threat for civilian aircrafts, small one-man missiles (MANPADs) pose a somewhat inexpensive and very effective threat to civilian aircrafts. Nowadays, they are accessible even to non-conventional troops [1]. These short-range missiles are designed to be most effective when used against low-altitude aircrafts — this is the case of civilian aircrafts during landings and takeoffs. In order to reduce the vulnerability of the civilian aircrafts when operating inside areas of higher risk, automatic threat detection and automatic defense systems are needed. It is important to point out that the guidance system of most MANPADs will guide them towards the infrared sources of an aircraft. Therefore, the deployment of any defense system against infrared missiles requires a very good knowledge of the characteristics of the infrared radiation emitted by the aircraft, also known as "infrared signature".

Being in use since the 50 s, infrared missiles are hardly a novelty in war scenarios. The increase in efficiency has forced the development of more complex defense systems, based on the knowledge of the IR envelope, scenarios, IR transmission by the atmosphere and the threat. Although complex, the need for this analysis is backed up by the statistics [2]:
in the Falklands War, in 1982, the English Sea-Harriers, were able to shoot down 24 Argentineans aircrafts using IR missiles, while only seven by other means (no Sea-Harrier was shoot down during this period);

- american sources estimate that during the Russian occupation in Afghanistan at least one Russian aircraft was shot down daily by Stinger missiles (IR MANPAD);
- the IR missiles were responsible for 76% of the neutralized aircrafts during the Gulf War (1991); and
- due to the effectiveness of IR missiles, NATO aircrafts were not allowed, in general, to fly bellow 15000 ft during the Kosovo war; even so, a F-117 was shot down by an IR missile.

These numbers lead to several conclusions, such as:

- the technical knowledge of how to use the IR missiles was a key factor in the Falklands war since no English aircraft was shoot down and the Argentineans were in higher number and used equipments of similar capabilities;
- even older-generation equipments may pose a significant threat, reducing the enemy's capability of attack; this was the case in both the Kosovo war and in the Russian occupation in the Afghanistan.

Although this discussion may appear as being of strictly military matter, it is fundamental for s better understanding of asymmetrical conflicts such as guerrilla groups and terrorism, since both tend to use older generation equipment.

The correct usage of an IR missile and the efficient usage of countermeasures depend on the technical knowledge of the radiation sources, atmospheric transmissivity and the properties of the infrared detectors that are used in these missiles.

This work describes the most important points in the development of a methodology for estimating the IR signature of an aircraft. It also describes the tools that were developed in order to support this methodology. The civilian applications of the word are pointed out where appropriate.

In order to accomplish that, the second section discusses the aircraft IR emissions, the radiation behavior when going though the atmosphere and the equipment used for the measures. The tools developed and results are presented in the third section.

2. BACKGORUND

2.1. Aircraft IR Emissions

Although the missile seeker receives the IR radiation from the whole aircraft, it is important to understand that this emission is actually a sum of several different sources and that each one has distinct characteristics and radiates in different wavelengths. The Figure 1 presents the most important IR radiation sources in a jet aircraft. The sections that radiates the most energy are the hot metals of the tailpipe and the plume (formed by the hot gases of the engine exhaust). Also important is the kinetic heating of the airframe, since their emission is usually stronger than the background. The airframe emission's peak is different from the tailpipe and the plume, since the temperature is not as high [3, 4].

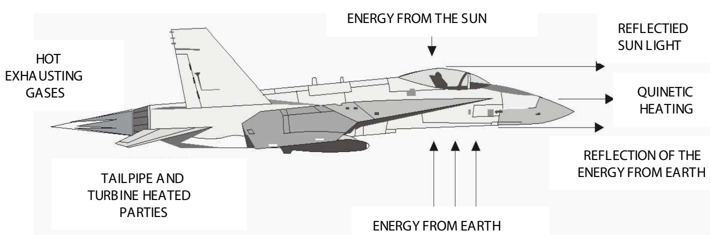

Figure 1: Aircraft's infrared sources [3].

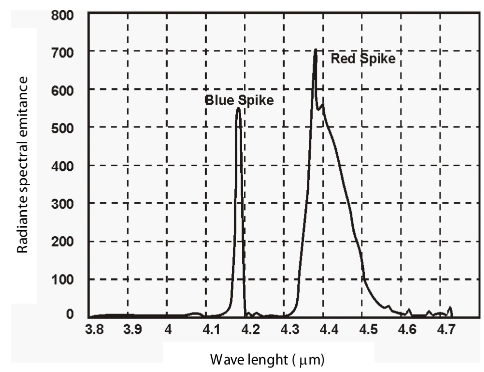

Figure 2: Spectrum of an aircraft's tailpipe after the atmosphere attenuation [3].

It is also important to consider that there are different types of engines, and the emission of each type has different characteristics. The most used types of engines for both civilian and military aircrafts are the turbojet and the turbofan ones. The emission of both takes place roughly in the same IR band, but the energy is spread differently in the 3D space. The response of both types of engine also differ in dynamical behavior when the power is changed.

Due to the temperature of the tailpipe and the plume, the wavelengths of the radiation generated in both the tailpipe and the plume is mostly contained in the 3 to 5 μm. The radiation, after being attenuated by the atmosphere, can be seen in the Figure 2. There are two main spikes: one between 4.17 and 4.20 μm (blue spike) and the other between 4.32 e 4.70 μm (red spike) [3]. The atmosphere has a very important role in this spectrum: some molecules and particles present in the atmosphere filter out the radiation.

2.2. Equipment Used for Detection

A detector with high reliability, high sensitivity, low internal noise and no thermal inertia is needed for the actual testing. No sensor with such characteristics would be available to this work at the time the experiments were to be conducted. Ideally, the sensor would be mountable on an aircraft in order to conduct flight tests. Since no timely COTS solution was available, an actual missile front section was customized in order to use it as a sensor. An actual missile front section was brought to the factory, customized and calibrated. A notebook-based data acquisition system was connected to it, so that all the signals of interest could be recorded. A custom data acquisition software was written in Labview 6.1 in order to complete the system.

3. DEVELOPED TOOLS AND RESULTS

3.1. Experimental Setup

The actual methodology calls for the measurement of the IR emission of an aircraft during its flight. This is not a trivial matter. The first and most obvious difficulty is to maintain the sensor pointed towards the aircraft. The task was easier because the missile front section can actually track the target within its field of view. The missile was then pointed in the general direction of the aircraft and, after it was first acquired, the seeker would track the target autonomously.

In order to perform the static and dynamic tests, a turbofan aircraft (A-1 AMX) was used. This fighter is a single engine, no exposed tailpipe and turbofan.

The static test was composed of measurements of the radiant intensity of the aircraft. These measurements were taken over a range of aspect angles and engine speeds. The behavior of the radiation emitted by the aircraft during engine speed changes was recorded in order to evaluate the dynamic behavior of the IR radiation. Figure 3 shows the actual aircraft during the measurements. The picture was taken from the sensor position.

Figure 3: Aircraft during IR emission measurements.

Figure 4: Different aspect angles of an aircraft during flight [3].

Measuring the IR emissions of a flying aircraft required a more elaborate setup. The first issue was to actually point the missile towards the aircraft. The second issue was to collect data that would enable the estimation of the aspect angle as seen b the sensor and distance from the aircraft to the sensor. In order to do that, the aircraft was fitted with an instrumentation capable of recording Euler angles, attack and sideslip angles and differential GPS. All the data were collected during flight and downloaded afterwards. A synchronization method was used in order to have the aircraft data and the sensor data referred to the same time reference.

The data collected were not usable in raw form. The distance by itself was not useful, since the atmosphere transmissivity was the actual value of interest. The Euler angles, attack angle, sideslip angle and velocity and position were used in order to estimate the presentation angle. Software for estimating the atmospheric transmissivity and aspect angle were developed in MATLAB.

3.2. Aspect Angle Estimation

The energy received from an IR source depends on the emitted energy, the distance from the source to the receiver, and the presentation angle of the source with relation to the receiving point.

When an aircraft cruises at constant power, there is no temperature change on the hot parts of the engine or on the plume. If the irradiance varies, this can only be due to the distance and aspect angle. The changes on the irradiance due to the distance are discussed in Section 3.3. From Figure 4, it is easy to understand how different angles of aspect change the irradiance: in the first picture, no engine parts can be seen. On the two other pictures, the plume is completely visible.

The aspect angle of the aircraft can be estimated using the Euler angles and knowing the position of the aircraft and the position of the sensor. The Euler angles are defined by three angles: pitch (θ), roll (ϕ) and yaw (ψ) (Figure 5).

In order to reconstruct the aspect angle of the flight, one needs to consider the coordinated system in the aircraft and the coordinated system on the sensor. Both are shown in the Figure 6, In order to rotate from the aircraft reference system to the sensor reference system, a standard rotation matrix [3] was used.

The aspect angle (δ) is defined as the angle formed by two vectors:

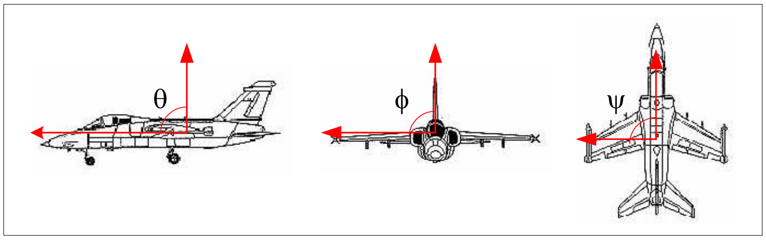

Figure 5: Euler angles [3].

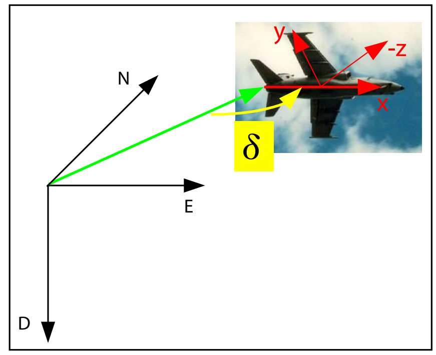

Figure 6: Aspect angle for an aircraft during flight [3].

- the one that connects the origin of the coordinated system at the sensor to the vector that connects the origin of the aircraft coordinated system, and
- the angle of the axial axis of the aircraft.

It is important to note that this presentation angle neglects the roll effect.

A tool was developed in order to take the raw data (Euler angles, aircraft angles, aircraft position, sensor position). This data is fused and post-processed, giving presentation angles and aircraft-sensor distance [3].

3.3. Seeker Calibration

The estimation of the IR signature can not be done with usual spectroradiometers. The main characteristics required are: high reliability, low internal noise, high responsivity and no thermal inertia. Ideally, the equipment should be able to be used on board an aircraft, in a pod. Since no spectroradiometer with the required specifications would be available to this work, an air to air missile seeker was customized and calibrated.

The customization allowed for the direct measurement of signals with information of: IR power density at the dome and elevation angle of the seeker, azimuth angle of the seeker.

The signal that had the information of the IR power density does not relate linearly with the desired information. Therefore, a procedure was developed in order to calibrate the seeker against a known IR source in an optical bench. A MATLAB software was developed in order to convert the voltage signal directly into the IR power density reaching the dome of the seeker.

3.4. Results and Analysis

The first result to be mentioned is the measurement of the plume, as could be verified by the measurements of the lateral sector of the aircraft. This was foreseen in the literature and the results could be used to verify the setup. One important point to be noted is that the absence of thermal inertial allowed the study of the emission during small changes in the engine power. The behavior of the emission can be seen in Figure 7.

The measurements also confirmed that the emissions from the tailpipe are more intense than the ones from the plume for an aircraft flying at low altitude. This behavior was expected from data from the literature. At higher altitudes, the plume emission increases and the atmospheric attenuation decreases.

The confirmation of the previous facts is very important for the development and validation of operational maneuvers for both attack and defense. The behavior of the emission of the turbofan engine is consistent with the measurements take by Santos [5]. The emission is very different from the ones from a turbojet.

Another result from this work was the preliminary measurements of the IR emissions as seen from under the aircraft, by placing the detector on the ground. This result was probably the most important one from this work. The knowledge of the ventral emissions are of prime importance for the development of countermeasures against MANPADs and for planning military missions.

The study of the raw and processed data also resulted in several conclusions of classified nature, providing a deep insight on how the missile actually "sees" the IR radiation. This knowledge is key to the design of countermeasures and also to improve its robustness to the current countermeasures and evasive maneuvers.

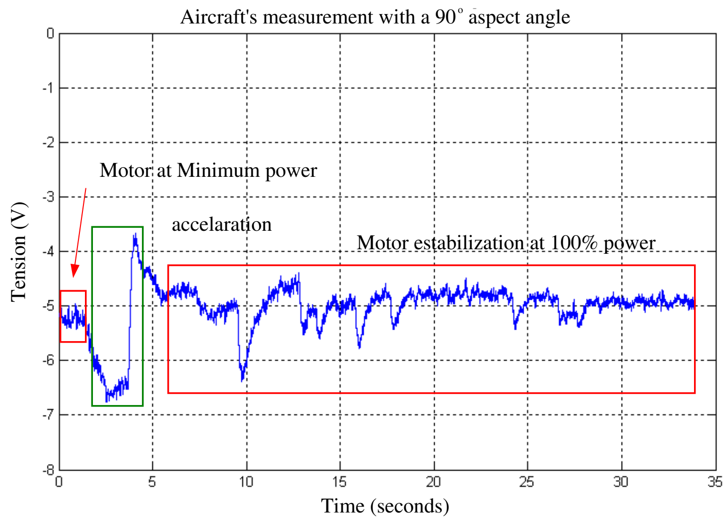

Figure 7: Emission behavior during changes in the engine power [3].

It was also identified that, for a tropical climate, the fuselage emissions due to heating and sun reflections are very important. The fuselage can heat up above 60°C and its large area can generate a large IR signature at some aspect angles.

After presenting the experimental results, it is important to comment the performance of the tools developed for this work. Among these tools, two are the most important: the aspect angle calculation and the atmospheric transition estimation.

The first one is responsible for estimating the aspect angle and the distance at each instant. These estimates must be

4. CONCLUSIONS

It the current days, the threat of being hit by a missile is applicable to both military and civilian aircrafts. The main threat to a civilian aircraft is posed by MANPADs , which are reliable and can be operated by a single man.

The seeker of these missiles works by following the infrared radiation emitted and reflected by an aircraft during its flight. Although new countermeasures and evasive maneuvers are frequently proposed, it is yet to appear one that is effective under all circunstances and against all threats.

In order to select the best alternative, one must:

- be in possession of the IR signature of the aircraft;
- understand the transmissivity of the atmosphere; and
- understand how the missile works and how its affected by the countermeasures.

This work focused mostly on the first and second items, describing the most important steps and tools involved in the determination of the IR signature.

The aircraft's emission of IR radiation was discussed, including the emission of IR by the aircrafts and the transmission of the IR energy through the atmosphere. The most important topics to be considered when estimating the IR signature were pointed out and discussed. A discussion of the custom software tools was also presented.

The knowledge that was generated in this work has already been used in actual flight tests for the estimation of IR signatures of aircrafts by the end of 2005 with excellent results.

REFERENCES

1. *Journal of Electronic Defense*, Disponível em: <http://www.jedonline.com>, Access in 06 Feb., 2004.
2. Nordeen, L. R., "A half-century of jet-fighter combat.," *Journal of Electronic Defense*, Disponible in: <http://www.jedonline.com>, Access em 06 Feb., 2004.
3. Santos, R. A. T., *Proposta de Metodologia Para Estimação do Envelope Infravermelho de Aeronaves*, 161 f. Trabalho de Conclusão de Curso (Mestrado em Engenharia Eletrônica) — Instituto Tecnológico de Aeronáutica, S. José dos Campos., December 2004.
4. Hudson, R. D., *Infrared System Engineering*, John Wiley & Sons, New York, 1969.

5. Santos, R. A. T., *Proposta de Procedimento Para a Medida do Envelope Infravermelho de Aeronaves*, 2001. 92 f. Trabalho de Conclusão de Curso (Especialização em Análise de Ambiente Eletromagnético) — Instituto Tecnológico de Aeronáutica, S. José dos Campos., May 2001.

Measurements of Reflectivity and Complex Permittivities of Radar Absorbing Materials Based on Conducting Polymers

M. Franchitto[1], **A. J. F. Orlando**[2], **R. Faez**[3], **M. C. Rezende**[1], **and I. M. Martin**[2]

[1]Instituto de Aeronáutica e Espaço, Brazil
[2]Instituto Tecnológico da Aeronáutica, Brazil
[3]Universidade do Vale do Paraíba, Brazil

Abstract— The efficiency of recently developed RAM (Radar Absorbing Materials) based on conducting polymers in sheet texture has been investigated at X-band (8 to 12 GHz) scattering measurements and, also by determination of their complex dielectric constant by waveguide method. This paper presents the experimental methodology used to characterize RAM based on conducting polymer called polyaniline. The correlation between the considerable loss tangent of the material and its reflectivity (return loss) suggests its application for aeronautical purposes, for example, to decrease the radar cross section of aircraft.

1. INTRODUCTION

The first reported use of Radar Absorbing Materials was made during World War II, when the Germans applied a mixture of polymeric foam and carbon black on the submarines periscopes to avoid radar detection. Since then, many researches have been conducted with the aim of developing light and practical materials [1]. The purpose of the widely broadcasted "Stealth" technology is the reduction of the aircraft RCS (Radar Cross Section) that is a measure of power scattered in a given direction when a target is illuminated by an incident wave and is an exclusive characteristic of the target [2]. When the question of reducing radar detection is raised one talks about Radar Cross Section Reduction (RCSR). The "Stealth" technology makes use of geometrical means and material engineering in order to develop low reflection and high absorption structures — the so called RAM. The most suitable way of reducing the reflection is by covering the aircraft with a RAM as of paint or polymeric sheet. This work is concerned exclusively with RAM in form of polymeric blend sheets that have been recently developed by CTA/IAE-AMR. An important parameter for the characterization of a RAM is its "reflectivity" that has the same meaning as the return loss in microwave engineering. Absorbing materials can be equally used in telecommunications and data transmission systems, besides in technological installations and other applications. The content of this paper is basically the same of [1] that was presented at SBMO/IEEC/MTT-S/2001.

2. RAM PREPARATION

Radar Absorbing Material preparation involves appropriate mixing of materials so that the final product should yield minimal scattering of waves when illuminated by a power source. Satisfactory results were achieved when conducting polymers, type polyaniline (PAni), were used.

Detailed experimental procedures for the preparation of the RAM are described elsewhere quoted in [1]. Binary polymer blends containing EPDM (ethylene-propylene-diene rubber) and the PAni-DBSA were prepared in an internal mixer coupled to a torque rheometer for different processing time. Flat sheets of 3 mm thick and 15.0 cm×15.0 cm dimension were obtained by compression-molding at 100°C.

3. SCATTERING MEASUREMENTS

As any kind of product, radar absorbers are primarily specified by their intended application. The application with the properties of materials available to fabricate the product, lead to evolution of one or more concepts or structure. Measuring the absorber reflection coefficient is important in order to have an idea on how efficient the RAM is. The electromagnetic wave, traveling in a free space environment, can be partially reflected since there is an impedance difference between two media.

Consider an interface between two semi-infinite media with impedances Z_1 and Z_2, respectively, and a transversal electromagnetic (TEM) wave traveling toward $+x$ direction normally incident to the interface.

The tangential components of electric and magnetic fields must be continuous at the interface and the reflection coefficient, defined as $\rho = \frac{E_r}{E_i}$, is expressed in terms of the impedances.

In a lossless medium, the impedance is expressed by the relative permittivity, ε_r, or dielectric constant, and permeability, μ_r.

If medium 1 is the free-space, the perfect absorber with zero reflection coefficient must have:

$$\frac{\mu_2}{\varepsilon_2} = \frac{\mu_0}{\varepsilon_0} \tag{1}$$

In other words, the perfect absorber would have the relative parameter ε_{r2} equal to μ_{r2}. However, at microwave frequencies, ε_{r2} generally does not approach the magnitude of μ_{r2} [3]. This is one reason for working with loss absorbers. Furthermore, RAM are based on the fact that some materials absorb energy from the electromagnetic fields passing through them. A frequency-dependent impedance including the medium conductivity σ, in the usual way is, therefore, preferable.

The NRL (Naval Research Laboratory) arch free-space measurement method was chosen to validate the absorbing efficiency of the RAM. The NRL arch was widely used initially by the U.S. Navy for research testing purposes, and is a microwave measurement system that can measure the free space radar reflection coefficient. Basically, the NRL arch is a vertical semicircular framework, made of wood, as shown in Figure 1, that allows a pair of horns to be positioned at a constant distance from the material under test [1].

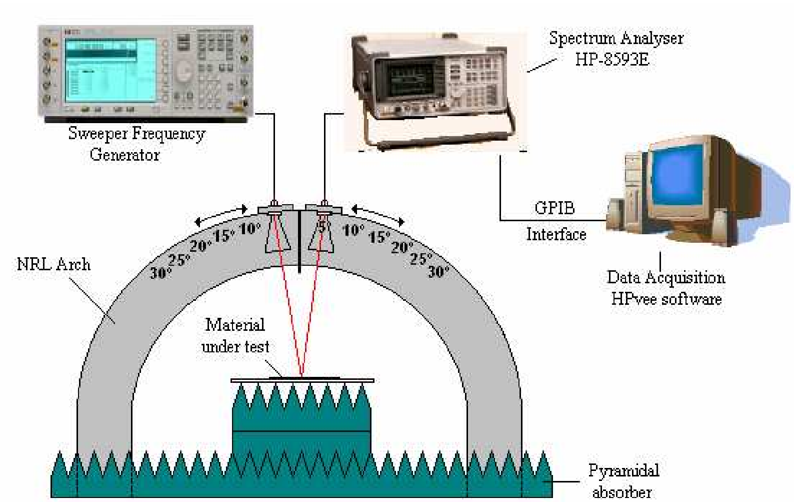

Figure 1: The NRL arch used for radar absorbing materials tests.

On the NRL arch, an antenna is connected to a microwave transmitter and the other to a microwave receiver. Microwave energy is sent by the transmitting horn, reaches the material, is partially absorbed, and the rest is scattered towards the receiving horn. The four samples of RAM prepared for this work were submitted to NRL arch measurements and the upper curves are references from total reflection (metallic plates). Figures 3–6 show the RAM scattering measurements [1].

The electromagnetic aspects of RAM design rest mainly on arrangements of dielectric or magnetic materials that provide appropriate impedance and reduce the scattered wave.

RAM dielectric constant is determined by the two-point method involving the solution of a transcendental equation. An X-band rectangular waveguide with a short circuit termination, was used to measure the voltage minimum in two situations: with and without the RAM sample [4]. An empty short-circuited waveguide is, initially, with a probe located at a voltage minimum D_R, and after, the same waveguide, now containing a RAM sample of length l_ε has the probe located at a new voltage minimum D. The RAM sample is adjacent to the short circuit.

The impedance boundary conditions give:

$$\frac{\tanh \gamma(D_R - D + l_\varepsilon)}{\gamma l_\varepsilon} = \frac{\tanh \gamma_\varepsilon l_\varepsilon}{\gamma_\varepsilon l_\varepsilon} \tag{2}$$

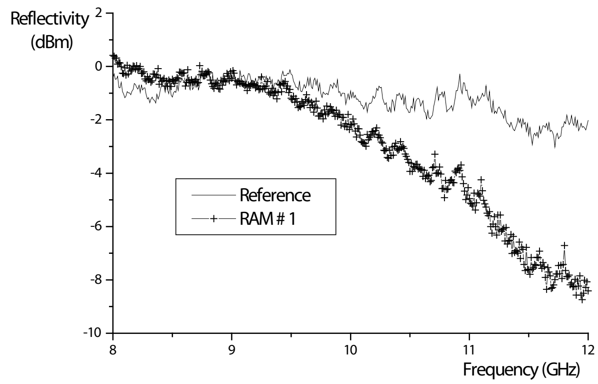

Figure 2: RAM # 1 reflectivity on X-band.

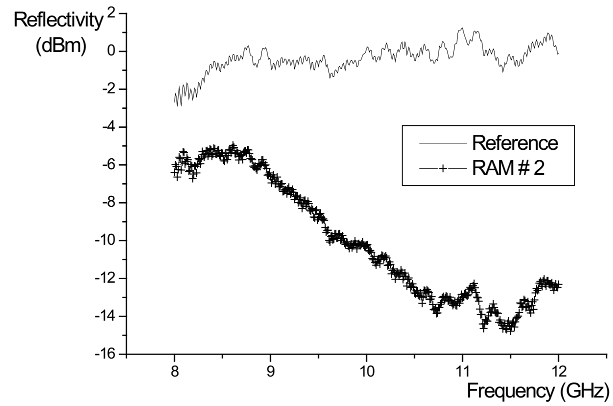

Figure 3: RAM # 2 reflectivity on X-band.

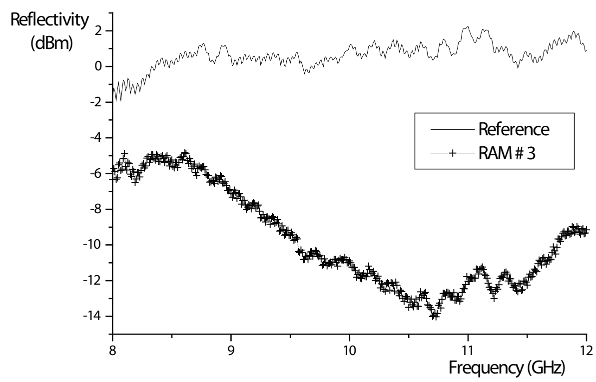

Figure 4: RAM # 3 reflectivity on X-band.

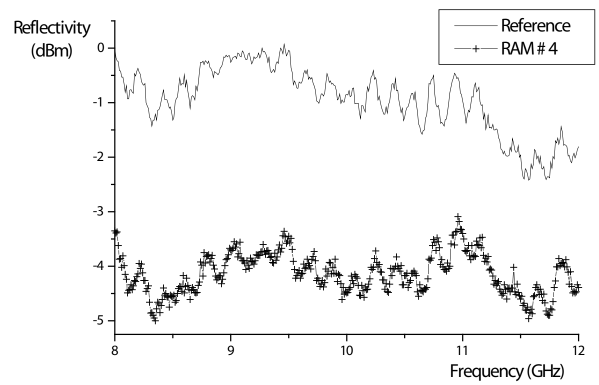

Figure 5: RAM # 4 reflectivity on X-band.

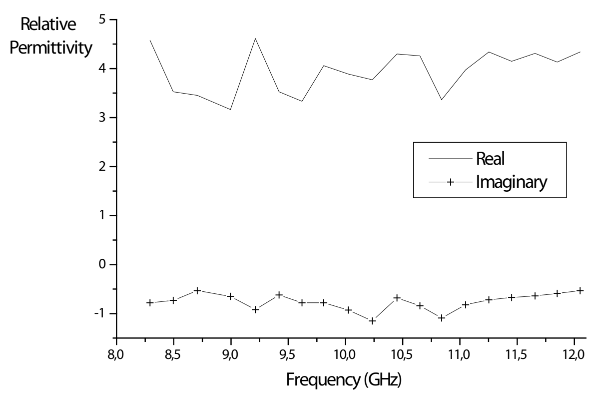

Figure 6: RAM # 1 Dielectric Constant in X-band frequencies.

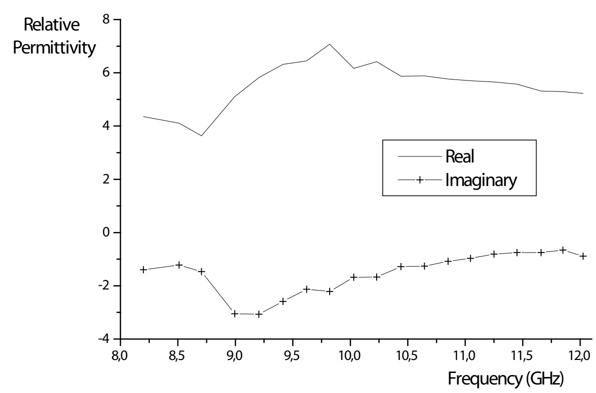

Figure 7: RAM # 2 Dielectric Constant in X-band frequencies.

The dielectric constant is determined by solving the transcendental Equation (2). Both the propagation constant and the dielectric constant are complex quantities that can be written:

$$\gamma_\varepsilon = \alpha_\varepsilon + j\beta_\varepsilon \tag{3}$$
$$\varepsilon_r = \varepsilon' - j\varepsilon'' \tag{4}$$

It must be emphasized that ε'' also includes the conductivity σ and the ratio $\varepsilon''/\varepsilon'$ is called the loss tangent. The real and imaginary parts of the dielectric constant can be found according to [4].

Point to point measurement at X-band frequencies are conducted by taking the voltage minimum position, repeating the process and solving the transcendental equations; one then obtains the frequency variation of the complex dielectric constant of the RAM sample.

Figures 6 to 9 show the frequency behaviors of the four samples of RAM that were synthesized.

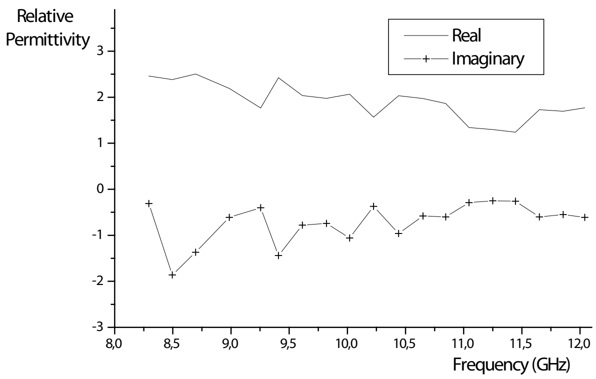

Figure 8: RAM # 3 Dielectric Constant in X-band frequencies.

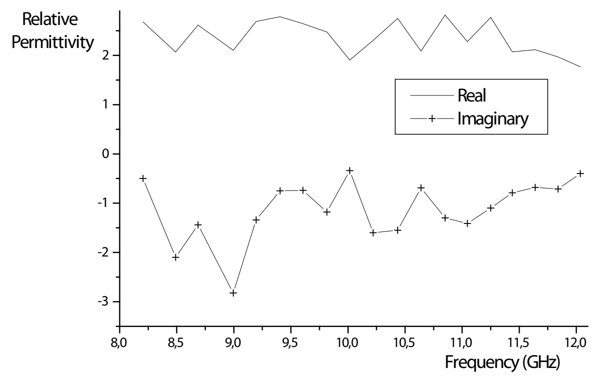

Figure 9: RAM # 4 Dielectric Constant in X-band frequencies.

4. CONCLUSION

Figures 2–5 and there to corresponding Figures 6–9 indicate correlation between RAM efficiency (determined by the NRL arch measurement) and dielectric constant.

Figures 2 and 3 indicate best performance of their samples at 12 and 11.2 GHz, respectively. RAM # 2 shows a −15 dB of reflectivity at 11.2 GHz. This can be explained by the fact that the sheet works as a lossy impedance transformer and at an approximate thickness of $\lambda/4$ matching occurs. Because of the considerable loss tangent ($\varepsilon''/\varepsilon'$), one can expect high absorption. (the RAM thickness was 3 mm in all cases) [5].

On RAM # 3 and RAM # 4, Figures 4 and 5 show a −8 dB and −4 dB, respectively, broadband average reflectivity at X-band frequencies.

As RAM # 1 has a relative real permittivity about 4.2 (See Figure 6) and RAM # 2 has about 5 (See Figure 7), matching frequencies of 12.2 and 11.2 GHz, respectively, can be expected in agreement with the measured values. One can expect matching behavior for RAM # 3 and RAM # 4 at higher frequencies because of the lower real parts of the dielectric constant.

REFERENCES

1. Franchitto, M., R. Faez, A. J. F. Orlando, M. C. Rezende, and I. M. Martin, "Electromagnetic behavior of radar absorbing materials based on conducting polymers," *Proceedings of the 2001 SBMO/IEEE MTT-S International Microwave and Optolectronics Conference*, 137–140, Belem, Brazil, August 2001.
2. Knott, E. F., J. F. Shaeffer, and M. T. Tuley, *Radar Cross Section*, 2nd ed., Artech House, Inc. Norwood, MA, 1993.
3. Johnson, R. N., "Radar absorbing material: A passive role in an active scenario," *The International Countermeasure Handbook*, 11th Edition, Artech House, Inc.
4. Sucher, M. and J. Fox, *Handbook of microwave measurements*, Vol. 3, 3^a Ed., Ed. John Wiley & Sons, New York, 1963.
5. Chatterton, P. A. and M. A. Houlden, *EMC — Electromagnetic Theory to Practical Design*, Ed. John Wiley & Sons. West Sussex, England, 1992.

Practical Aspects of the Characterization of Ferrite Absorber Using One-port Device at RF Frequencies

A. Côrtes[1,2], A. C. C. Migliano[1,2], V. L. O. Brito[1,2], and A. J. F. Orlando[1,2]

[1]Instituto de Estudos Avançados, Brazil
[2]Instituto Tecnolgico de Aeronáutica, Brazil

Abstract— The one-port-circuit impedance method has been used for study and development of novel materials for EW, such as absorbers, in electromagnetic noise suppressors, and current transducers. This method allows the electromagnetic characterization in the frequency range between 100 Hz and 100 MHz. The experimental arrangement implemented in the laboratory was validated using the data obtained from a Ni-Zn ferrite. Based on the expected values for the physical quantities and taking into account the dynamic measuring range of the equipment, it was verified that a limitation of the method is expected for low frequencies. The reliability of both the permeability and permittivity data was certified for frequencies higher than 10 kHz, which was justified from the impedance levels measured on the sample holder used. Discussions are made, about the method and about solutions for using the same in the whole frequency range of the equipment.

1. INTRODUCTION

Due to their magnetic properties in high frequencies and their high resistivity, magnetic ceramics have been widely used in the last decades in applications as RF and microwave absorbers [1], transducers in pulse transformers [2, 3], and noise suppressors [4]. Such materials are among the main constituents of the Measures (SM) and Counter Measures (SCM) Systems employed in Electronic Warfare (EW). Systems for measuring electromagnetic properties of the materials in the operation frequencies of the devices have become indispensable in laboratories that develop technologies or evaluate susceptibility in electromagnetic environment.

The wide-band complex permeability and permittivity spectra of the materials used as transducers or sensors in SM and SCM indicate their quality. As an example, such parameters are used to calculate the reflectivity of an RF absorber. These wide-band measurements, are obtainable by several methods [5–7], highlighting the transmission ones, where the scattering parameters on a two-port sample-holder are measured, and, also, the reflection/impedance ones, in a one-port sample holder.

In order to complement the laboratorial infrastructure for low-frequency measurements ($<$ 100 MHz), an experimental arrangement has been prepared for the evaluation of complex permeability and permittivity of magnetic ceramics in the 100 Hz–100 MHz frequency range. In such arrangement, the one-port sample holder impedance measurement was employed and the validation was made using the measures of a Ni-Zn ferrite. The employed method revealed itself inadequate for frequencies lower than 10 kHz, since the lower frequency that gives valid results is related to the dynamic measurement range of the equipment and the expected values of permeability and permittivity.

Thus, the method for evaluation of the ceramic material is discussed in this work as well as the solutions to enlarge the frequency range of the test, taking into account the operational limits of the experimental arrangement. Permeability and permittivity data of the ferrite are presented for the 50 MHz–1.5 GHz range, being obtained by employing a network analyzer in the experimental arrangement.

2. THEORY

Complex permeability and permittivity measurements may be carried out using the assembly shown in Figure 1, by means of the usual input impedances of a short circuited and open circuited.

The real and imaginary parts of permeability and permittivity of a sample of small electric length are then obtained and given by the following expressions, where superscripts *short* and *open* represent the impedance of the short-ended (0Ω) and open-ended (0S) sample-holder and use is made of the characteristic impedance of the same air-filled transmission line:

$$\mu'_r = \frac{c}{\omega d}\frac{X_{\rm in}^{\rm Short}}{Z_0^{\rm air}} \quad \mu''_r = \frac{c}{\omega d}\frac{R_{\rm in}^{\rm Short}}{Z_0^{\rm air}} \quad \varepsilon'_r = \frac{c}{\omega d}\left(\frac{Z_0^{\rm air}}{X_{\rm in}^{\rm Open}}\right) \quad \varepsilon''_r = \frac{c}{\omega d}\left(\frac{Z_0^{\rm air}}{R_{\rm in}^{\rm Open}}\right)$$

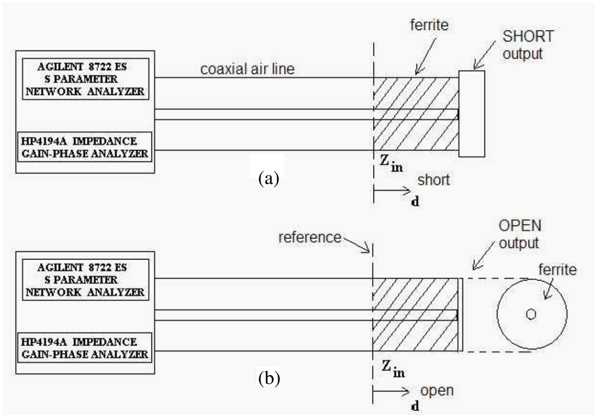

Figure 1: Schematic representation of the assembly used for measuring complex permeability and permittivity. Permeability of the Ni-Zn sample was obtained with the short circuited coaxial line (a) and the permittivity, with the open circuited coaxial line (b).

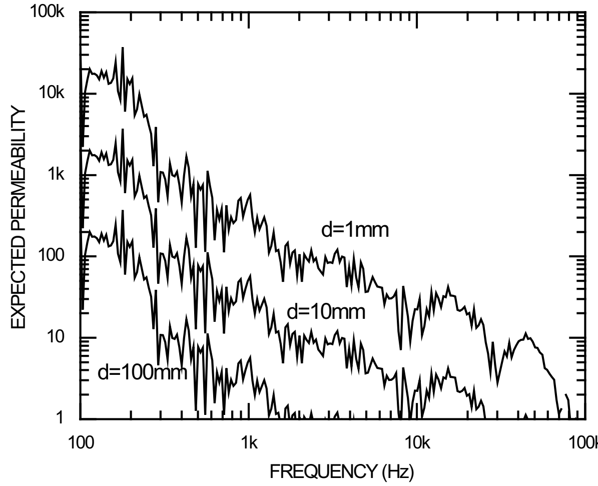

Figure 2: Applicability region of the method employed to evaluate a Ni-Zn ferrite. The solid lines assume $Z_0^{\text{air}} = 50\,\Omega$ and sample thickness of $d = 1\,\text{mm}$, $10\,\text{mm}$, and $100\,\text{mm}$. The area above the lines correspond to the measurement range of the equipment for a given expected permeability.

This set of equations defines the field of applicability of the method, considering the dynamic operation range of the equipment. For example, for 100 Hz to 100 kHz, $Z_0^{\text{air}} = 50\,\Omega$ and $d = 1, 10$ and 100 mm, the limiting curves in Figure 2 are obtained. One can observe that the frequency corresponding to a relative permeability $\mu_r > 200$ (value expected for the real part of the complex permeability) is 300 Hz to $d = 100\,\text{mm}$. To match this value with the limiting operation value of the equipment ($f = 100\,\text{Hz}$), either the sample must be 10 times as thick or one must operate with $X_{\text{in}}^{\text{Short}}$ lower than $0.02\,\text{m}\Omega$.

3. EXPERIMENTAL ARRANGEMENT

The complex permeability and permittivity measurements can be carried out using the assembly represented in Figure 1, considering the input impedance of a short-ended and of an open-ended transmission line. The measurements were performed at two ranges of frequencies-one between 100 Hz and 100 MHz and, the other, between 50 MHz and 1.7 GHz — with two different setups and calibration procedures.

4. RESULTS

Impedance measurements were made with empty circuit and with the same filled by the ferrite sample. These measurements were made both in short (to obtain complex permeability) and in open (to obtain complex permittivity) circuit. The results are shown in Figures 3–7, where the background measure (curve that reflects noise of the input tension of the amplifiers instead of the impedance of the device under test), assumed to be the measurement range of the equipment, is represented by a solid line in Figure 3 and Figure 5. One can observe in Figure 3 that the background is lower than $10\,\text{m}\Omega$ when the sample-holder is empty. When the circuit is short terminated, one can observe that the real part of the impedance (R) overcomes the background in frequencies higher than approximately 100 kHz. When the ferrite sample is part of the circuit, the imaginary part of the impedance (reactance X) overcomes the background for frequencies higher than 5 kHz. In order to obtain permeability measurements with percent error lower than 10%, only the measurements above 5 kHz for X and 100 kHz for R must be considered. As a consequence, well defined permeability results are expected above 5 kHz for the real part and above 100 kHz for the imaginary part.

The solid line represents data of the impedance modulus with empty sample-holder. Other curves represent data of the sample-holder filled with the ferrite: the real part R, imaginary part X, as well as μ' and μ'' obtained from the R and X data.

Figure 4 shows μ' and μ'' curves, where one can observe a well defined behavior in frequencies

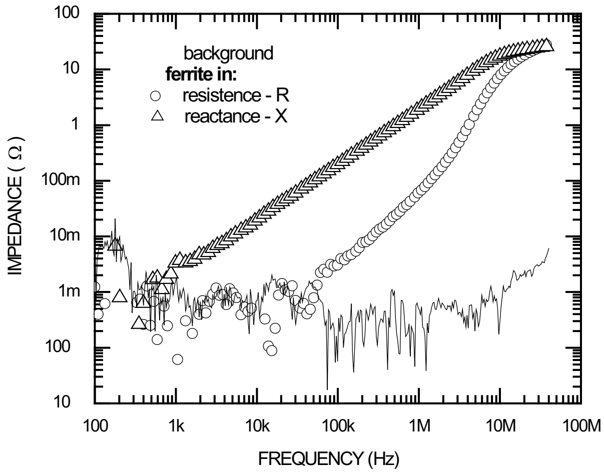

Figure 3: Impedance measurements of the short-ended circuit.

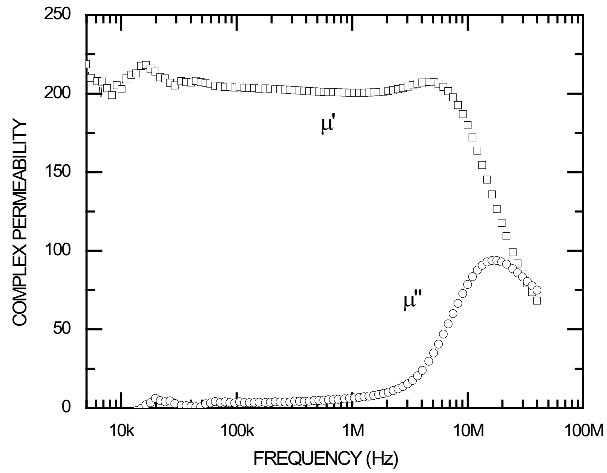

Figure 4: Complex permeability data, μ' and μ'', were obtained from the impedance results.

that give errors lower than 10%. For frequencies lower than 6 MHz the curve showed a flat behavior with μ' of approximately 200 for the ferrite tested. Near 10 MHz, a maximum occurs in μ'', which characterizes resonance due to the movement of magnetic domain walls. This behavior was expected for the ferrite used to validate the system [9].

Figures 5 and 6 show the impedance results with open-termination, with both, filled and empty sample-holder. One can observe that the background level varies with frequency, assuming values around 100 MΩ at 100 Hz and attaining 1 MΩ at 40 MHz. For frequencies lower than 500 Hz, the background level is greater than the signal measured with filled sample-holder.

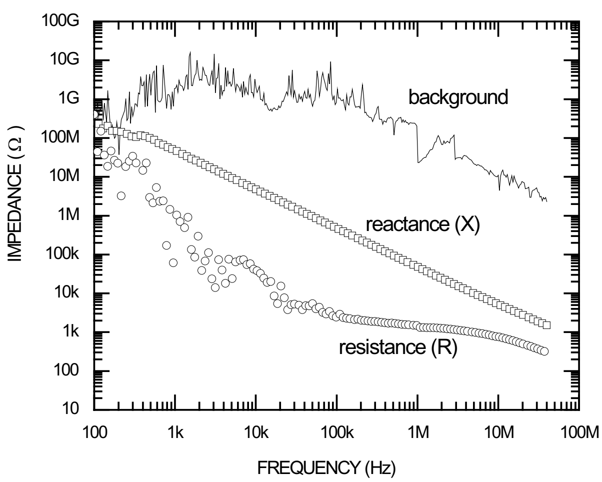

Figure 5: Impedance measurements for the open-terminated sample-holder.

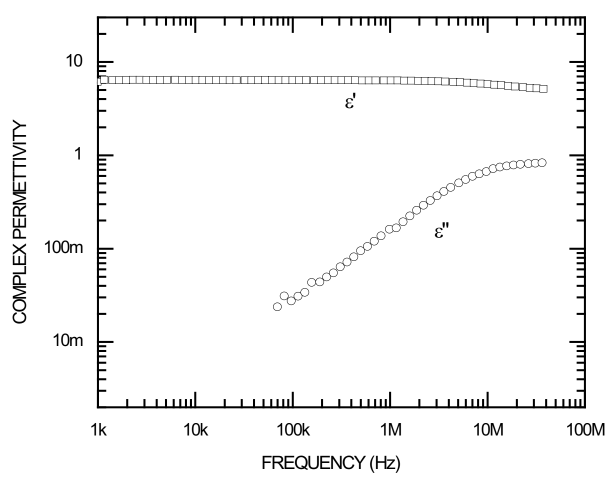

Figure 6: Complex permittivity data (ε' and ε'') obtained from the impedance results.

In the case of open circuit with filled sample-holder, the real part (R) of impedance presented values lower than the background level after 10 kHz. For frequencies higher than 1 kHz, the imaginary part of the impedance (reactance X) is higher than the background. Similarly, it is expected that permittivity assumes well defined values for frequencies higher than 1 kHz for the real part and 10 kHz for the imaginary part.

Figure 6 shows the ε' and ε'' curves, confirming the expected behavior for permittivity. For the ferrite studied, the flat portion of the permittivity curve is located around $\varepsilon' = 6$ up at 10 MHz, where a maximum occurs in the imaginary part.

The solid line represents data of the impedance modulus for the circuit with empty sample-holder. The other curves show the results for the sample-holder filled with the ferrite sample. The real part of the impedance, R, and the imaginary part, X, are closely related to ε'' to ε'', respectively.

Figure 7 shows the complex permeability data, obtained from the input impedance, for frequencies between 50 MHz and 1.5 GHz. In this case, the upper frequency limit imposed by the approximations of the method must be taken into account. To find this so called limit, a maximum value must be established for the angle in these approximations ($\tan\theta \cong \theta$ and $\cot\theta \cong 1/\theta$), where θ is small the electric length of the sample.

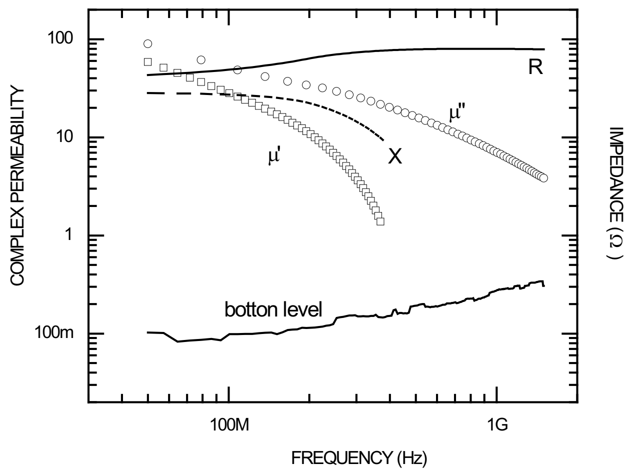

Figure 7: Impedance (R and X) and complex permeability ($\mu'\mu''$) data for frequencies lower than 50 MHz.

The solid line is the impedance modulus of the shorted sample-holder, not filled with the ferrite sample. The dashed line (longer dash) represents the reactance (X) of the shorted sample-holder filled with the sample. The other dashed line (shorter dash) represents the real part of the impedance (R). The squared marks represent the real permeability (μ') and the round marks represent the imaginary part (μ'').

5. CONCLUSIONS

The present paper presents a method of characterization of Ni-Zi ferrites at RF frequencies. The procedure involves input impedances measurements with Network Analyzer and/or Impedance Bridge for a short/open terminated, ferrite filled coaxial line. Considering the approximately linear dependence of this impedance with the frequency, very small values that can be out of the impedance dynamic range of the equipment are possible. This restricts the dynamical range of the method by an inferior frequency limit. There is also a superior frequency limit due the approximation used.

It can be shown that the presented method can be used in the characterization of NiZi, where the experiments were made in the range of 100Hz to 500MHz.

REFERENCES

1. Kim, S. S., D. H. Han, and S. B. Sho, "Microwave absorbing properties of sintered Ni-Zn ferrite," *IEEE Trans. On Magnetics*, Vol. 30, No. 6, 4554–4556, 1994.
2. Vossenberg, E. and G. Grawer, "Wideband precision current transformer for the magnet current of the beam extraction kicker magnet of the large hadron collider," *Power Modulator Symposium, 2004 and 2004 High-Voltage Workshop, Conference Record of the Twenty-Sixth International*, 470–473, 23–26 May 2004.
3. De Polli, Y. C., A. C. C. Migliano, C. R. S. Stopa, S. I. Nabeta, and J. R. Cardoso, "Finite element analysis of impedance of an electron beam current monitor," *IEEE Trans. on Magnetics*, Vol. 35, No. 3, 1833–1836, 1999.
4. Ott, H. W., *Noise Reduction Techniques in Electronic System*, 2nd. Ed., New York, Wiley, 1988.
5. Nicholson, A. M. and G. F. Ross, "Measurement of the intrinsic properties of materials by time domain techniques," *IEEE Trans. Instrum. Meas.*, Vol. IM-19, No. 4, 377–382, 1970.
6. Weir, W. B., "Automatic measurement of complex dielectric Constant and permeability at microwave frequencies," *Proc. IEEE*, Vol. 62, No. 1, 33–36, 1974.
7. Baker-Jarvis, J., M. D. Janezic, J. H. Grosvenor Jr., and R. G. Geyer, "Transmission/Reflection and short-circuit line methods for measuring permittivity and permeability," *NIST Technical Note 1355-R*, December 1993.

8. Chen, C. W., *Magnetism and Metallurgy of Soft Magnetic Materials*, Dover Pub. Inc., Ch6.§2., 1986.
9. Takei, H., H. Tokumasu, H. Rikukawa, and I. Sasaki, "Relationship between thermal characteristics of permeability and microstructure of Ni-Zn ferrites," *IEEE Trans. on Magnetics*, Vol. 23, No. 5, 3080–3082, 1987.

Adaptive Multiple Target Tracking Systems for Airfield Surveillance Radar

H. Deng[1] **and P. F. Wang**[2]

[1]The University of North Texas, Denton, TX 76203, USA
[2]SPAWAR Systems Center, Sand Diego, USA

Abstract— An adaptive multi-target tracking system (AMTT) for airfield surveillance radar is proposed. The core of the AMTT system is an improved multiple hypothesis tracking (MHT) algorithm that is adaptive to the environments and the radar signal processing scheme. The new approach is capable of significantly improving the efficiency of the MHT algorithm for multi-target tracking.

The air strikes by birds and other airfield hazards have caused billions of dollars in damage to aircraft, and led to disruption to air operations and even loss of human life [1]. The airfield surveillance radar is used for search and tracking possible air field hazard objects such as birds to minimize air strike risk. Because of possibility of a large number of simultaneously existing bird targets for the airfield radar to track, the multi-target tracking system is one of the most critical parts of the system [2, 3]. The two essential functions of multi-target tracking are data smoothing and prediction using Kalman filter and detection of data and existing track (data-track) association processing. For slowly-moving bird targets, the data smoothing and prediction become almost a trivial issue; while data-track association for multiple targets becomes very challenging, especially with weak target signals, a relatively low detection threshold and thus a high false target rate. Multiple-Hypothesis Testing (MHT) is widely considered to be the best data-track association algorithm [4, 5]. With an MHT approach, multiple observed data-to-track association hypotheses are formed and evaluated to select the most likely data-track associations and in the meantime identify possible new and false targets. Generally a true target persists in the tracking volume for at least several scans, while the false target due to random noise or clutter does not. Therefore, the MHT method is effective in eliminating the false targets as well as confirming the data-to-track hypotheses through processing multiple scans of detected data. Unfortunately, the computational complexity and memory requirement of MHT grow exponentially with the number of the received data. As a result, with a large number of the detected targets, the tracking system may get saturated and become unworkable. Therefore, the key to the successful application of MHT algorithm to multi-target tracking for airfield radar is how to efficiently implement the algorithm. In this work we propose an innovative MHT, called Adaptive MHT (AMHT) for multi-target tracking. The new algorithm is adapted to the radar environments, the signal processing scheme, and the target types for the best system performance and the maximum efficiency.

In the proposed adaptive multi-target tracking system the Extended Kalman Filtering (EKF) and the Adaptive Multiple Hypothesis Testing (AHMT) tracking interact with each other. Once the track-data association is carried out, the received target data are smoothed by integrating it with the track data to minimize noise effect and the target data for the next scan are predicted subsequently. The predicted target data are sent back to AHMT for performing data-track association for the next scan data. In the HMT algorithm, every detected target in the current scan is assumed to be either a continuing target belonging to one of the existing target tracks, a new target, or a false target due to clutter or noise. Such a complete assumption enables the MHT algorithm to have the capability to identify false targets. Each possible assumption is considered to be a hypothesis with its plausibility measured with a probability. The probability P_i^k of hypothesis Ω_i^k with target data $Z(k)$ received at scan k may be derived using Bayesian method [4]:

$$P_i^k = \frac{1}{C} P_D^{N_{DT}} (1 - P_D)^{(N_{TGT} - N_{DT})} \beta_{FT}^{N_{FT}} \beta_{NT}^{N_{NT}} \left[\prod_{m=1}^{N_{DT}} N(Z_m - f(\hat{\mathbf{x}}(k)), B) \right] P_g^{k-1} \tag{1}$$

P_D : probability of detection β_{FT} : density of false targets β_{NT} : density of new targets
N_{FT} : number of false targets N_{DT} : number of measurements assigned to existing targets
N_{TGT} : number of existing targets M_K : the number of measurements at time k
$F_n(\lambda)$: the poisson probability distribution for n events when the average rate of events is λ
$N(x, B)$: the normal distribution $f(\hat{\mathbf{x}})$: the predicated target state in spherical cooridates
P_g^{k-1} : the probability of the parent hypothesis C : the constant for normlization

Apparently, to calculate hypothesis probabilities in (1), one needs to use the probability of target detection, the density of false targets and the density of new targets in the search areas. These three parameters are directly related to radar operational environments, signal processing schemes and radar target types, and thus are varying from scan to scan. Therefore, to evaluate the hypothesis probability in (1) properly for MHT, we need to estimate the three parameters accurately and apply them to the hypothesis probability calculation accordingly in real time. In the current MHT algorithms implemented in airfield surveillance radars, the probability of detection and densities of false targets and new targets are chosen to be fixed values through the tracking process, which are obviously not correct. Normally inaccurate hypothesis probability estimation results in necessity of more scans of radar data for reliable target tracking or/and inconclusive track-data associations. Therefore, the real-time estimation of detection probability and densities of false targets and new targets included in the proposed Adaptive MHT (AMHT) is necessary for efficient multi-target tracking.

Target detection probability P_D is directly related to the clutter and noise levels and the detection threshold. If there are L range cells at a radar antenna beam position (α, θ), the average detection probability for all the detection cells is:

$$P_D(\alpha, \theta) = \frac{1}{L} \sum_{l=1}^{L} P_D^l(\alpha, \theta) \tag{2}$$

$$P_D^l(\alpha, \theta) = \int_{V_T}^{\infty} \frac{x}{W^l(\alpha, \theta)} \exp\left(-\frac{x^2 + A^l(\alpha, \theta)}{2W^l(\alpha, \theta)}\right) I_0\left(\frac{xA^l(\alpha, \theta)}{W^l(\alpha, \theta)}\right) \mathrm{d}x \tag{3}$$

V_T : detection threshold A : target signal amplitude
W : mean clutter and noise power I_0 : modified zero − order bessel function

Similarly, the average density β_{FT} of false target due clutter and noise at antenna beam position (α, θ) can be estimated from the false alarm rate as follows:

$$\beta_{FT} = P_{FA}(\alpha, \theta) = \frac{1}{L} \sum_{l=1}^{L} P_{FA}^l(\alpha, \theta) \tag{4}$$

$$P_{FA}^l(\alpha, \theta) = \int_{V_T}^{\infty} \frac{x}{W^l(\alpha, \theta)} \exp\left(-\frac{x^2}{2W^l(\alpha, \theta)}\right) \mathrm{d}x = \exp\left(-\frac{V_T^2}{2W^l(\alpha, \theta)}\right) \tag{5}$$

The new target density β_{NT} is determined from historically and empirically collected data for a particular target type (type of birds and their habits). The new target density becomes smaller and steady after the radar operates for an extended period of time. The three parameters are also slightly adjusted based on actual real-time tracking results as:

$$\begin{aligned} P_D &\leftarrow P_D \pm \Delta P_D \\ \beta_{FT} &\leftarrow \beta_{FT} \pm \Delta \beta_{FT} \\ \beta_{NT} &\leftarrow \beta_{NT} \pm \Delta \beta_{NT} \end{aligned} \tag{6}$$

Another innovative technique used in AMHT is the probability ratio approach used to confirm the most likely hypothesis among multiple hypotheses. Most of the current confirmation criteria are based on the absolute probability value. Because the hypothesis probability becomes smaller with more scans of data included in the evaluation, the better approach is to confirm a hypothesis based on the hypothesis probability ration of the largest one to the second-largest.

The scheme of the adaptive target tracking system is shown in Fig. 1. The signal processing and target detection is bypassed if the received data are the detected results. Other non-essential functions of the target tracking system include confirmed track display through Plan Position Indicator (PPI), information fusion processing with information from other sensors and target classification/identification processing.

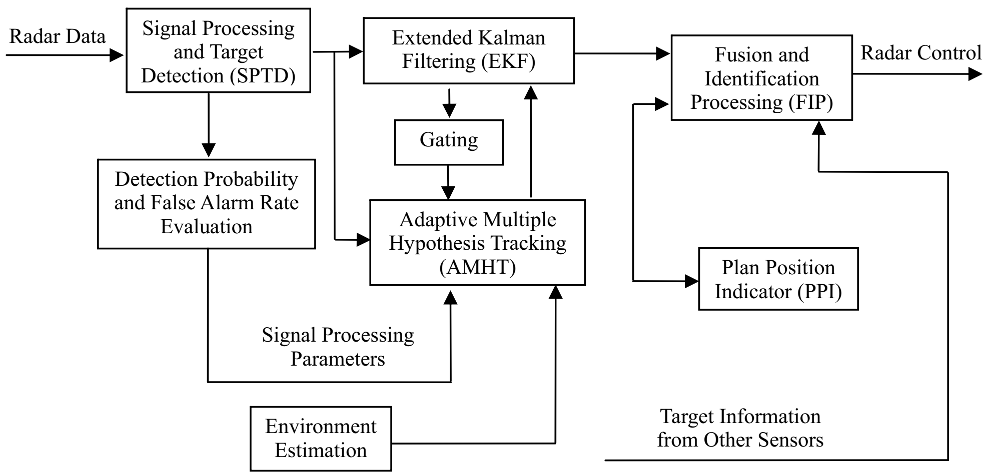

Figure 1: The proposed adaptive target tracking system for airfield surveillance.

The basic idea of adaptive MHT is to adjust the MHT algorithm in real time to significantly reduce the number of the needed hypotheses and thus the computational complexity and computer memory requirements based on the radar operational environments, the signal processing scheme, and the intelligence information about the targets. For example, if the radar is searching certain areas with little clutter and the target strength is expected to be stronger than the white noise, the numbers of the scans and the hypotheses needed for evaluating track quality can be greatly reduced; the similar results are achieved if the signal processing is determined to be effective in clutter rejection. The preliminary simulation results have indicated that with the new approach the radar data needed for reliable hypothesis confirmation can be reduced from 4–6 scans to about 2–3 scans, which generally leads to significant reductions of computation time and memory requirement for implementing MHT algorithm in multi-target tracking.

REFERENCES

1. Cleary, E. C., S. E. Wright, and R. A. Dolbeer, "Wildlife strikes to civil aircraft in the United States in 1991–1997," *Wildlife Aircraft Strike Database*, FDA Report, No. 4, 1998.
2. Nohara, T. J., et al., "Affordable Avian radar surveillance systems for national resource management and BASH applications," *Proc. of 2005 IEEE International Radar Conference*, Arlington, VA, USA, May 2005.
3. Weber, P., et al., "Low-cost radar surveillance of inland waterways for homeland security applications," *Proc. of IEEE National Radar Conference*, Philadelphia, PA, April 2004.
4. Reid, D. R., "An algorithm for tracking multiple targets," *IEEE Trans. Automat. Contr.*, Vol. 22, No. 6, 843–854, Dec. 1979.
5. Blackman, S. S., "Multiple hypothesis tracking for multiple target tracking," *IEEE Aerospace & Elec. Sys. Magazine*, Vol. 19, No. 1, 5–18, Jan. 2004.
6. Kurien, T., "Issues in the design of practical multitarget tracking algorithms," *Multitarget-Multisensor Tracking: Advanced Applications*, Y. Bar-Shalom, Ed., 43–83, Norwood, MA: Artech House, 1990.

The Features of the Angular Spectrum of Scattered Radiation by Turbulent Collisional Anisotropic Magnetized Plasma

G. V. Jandieri, I. B. Shirokov, V. G. Jandieri, and Z. M. Diasamidze

Physics Department, Georgian Technical University, Georgia

Abstract— Statistical characteristics of the angular power spectrum of scattered radiation for power law spectrum of electron density fluctuations in turbulent collisional anisotropic magnetized plasma are considered.

1. INTRODUCTION

Investigation of phase fluctuations of radiowaves in the atmosphere is stimulated by development of interferometric methods of natural and artificial objects' observation. Measurements of correlation lengths of refraction coefficient of the ionosphere using refractometer in both vertical and horizontal directions points out to anisotropy of inhomogeneities in the ionosphere. The irregularities have a variety of sizes and usually are elongated along the magnetic field direction. It has been found that small ($\leq 10\,\mathrm{km}$) F region irregularities are highly elongated along the direction of the magnetic field and large anisotropy could be also expected in case of certain types of plane waves propagating in the ionosphere. On the other hand, large irregularities ($\geq 10\,\mathrm{km}$) may be only weakly anisotropic. Experimental observation of satellite signals shows that a power-law spectrum of ionospheric irregularities gives a better agreement to the data than Gaussian spectrum. The difference between the power-law and Gaussian wavenumber spectra is significant, since different scintillation spectral shapes give different scintillation levels and fluctuation rates. Statistical characteristics of the spatial spectrum of radiation scattered on anisotropic electron density fluctuations for anisotropic Gaussian correlation function have been investigated in [1, 2]. The present paper reports the results of analysis of the angular power spectrum for power law spectrum of electron density fluctuations in the F region of the ionosphere.

2. FORMULATION OF THE PROBLEM

The irregular plasma structure in the scattering medium imposes a random phase on the transmitted radio wave. Analytical expression for correlation function of phase fluctuations of scattered EM waves in a turbulent magnetized collision plasma taking into account both electron density and magnetic field fluctuations has been obtained in [1, 2] using geometrical optic approximation. We will suppose that magnetic field fluctuations in F region of the ionosphere are weaker than electron density fluctuations and therefore, we will utilize autocorrelation function of the phase [1, 2]

$$W_\varphi\left(\rho_x,\,\rho_y,\,z\right) \;=\; 2\pi\sigma_N^2\left(D^2+E^2\right)k_0^2\int\limits_{-\infty}^{\infty}\mathrm{d}\kappa_x\int\limits_{-\infty}^{\infty}\mathrm{d}\kappa_y W_N\left(\kappa_x,\,\kappa_y,\,-b\kappa_y\right)\frac{1}{2a\kappa_y}$$
$$\times\exp\left(i\kappa_x\rho_x+i\kappa_y\rho_y+2a\kappa_y z\right)\left[1-\exp\left(-2a\kappa_y z\right)\right]. \tag{1}$$

Here $\sigma_N^2 \equiv< N_1^2 > /N_0^2$ is the variances of electron density fluctuations, angular brackets denote the statistical average; $W_N(\kappa_x,\,\kappa_y,\,\kappa_z)$ is the 3D spatial power spectrum of the electron density fluctuations, κ_z is the spatial wavenumber component parallel to the geomagnetic field, κ_y is a wavenumber component in direction of cross-field elongation of irregularities, z is the distance the wave has traversed in the turbulent plasma; coefficients in (1) are equal to:

$$a = a_z' a_y'' - a_y' a_z''/a_z'^2, \quad b = a_y'/a_z', \quad D = A_v'/a_z', \quad E = \left(A_v'' a_z' - A_v' a_z''\right)/a_z'^2, \quad a_y = a_y' + i a_y'',$$

$$a_y' = N_* \sin\theta \left[\left(\eta' - n_1^2\right)\left(\eta' + \varepsilon'\right) + \sin^2\theta \cdot n_1^2\left(\varepsilon' - \eta'\right) - \mu''^2\right],$$

$$a_y'' = N_* \sin\theta \left\{\left(\eta' + \varepsilon'\right)\left(n_2^2 - \eta''\right) - \left(\eta' - n_1^2\right)\left(\eta'' + \varepsilon''\right) + \sin^2\theta\left[n_1^2\left(\eta'' - \varepsilon''\right) - n_2^2\left(\varepsilon' - \eta'\right)\right] - 2\mu'\mu''\right\},$$

$$a_z = a_z' + i a_z'', \quad a_z' = N_* \cos\theta\left[2\varepsilon'\left(\eta' - n_1^2\right) + \sin^2\theta \cdot n_1^2\left(\varepsilon' - \eta'\right)\right]$$

$$a_z'' = N_* \cos\theta\left\{2\left[\varepsilon'\left(n_2^2 - \eta''\right) - \varepsilon''\left(\eta' - n_1^2\right)\right] + \sin^2\theta\left[n_1^2\left(\eta'' - \varepsilon''\right) - n_2^2\left(\varepsilon' - \eta'\right)\right]\right\}, \quad A_v = A_v' + A_v'',$$

$$A_v' = \varepsilon'\left(\eta' - n_1^2\right)\left(\eta' - 1\right) + \frac{1}{2}\sin^2\theta n^2 - 1\left(\eta' - 1\right)\left(n_1^2 - 2\eta' + \varepsilon'\right) + \frac{1}{2}\left(n_1^2 - \eta'\right)\left(n_1^2\cos^2\theta - \eta'\right)\left(\varepsilon' - 1\right)$$
$$- \frac{1}{2}\mu''^2\left(\varepsilon' - 1\right) - \mu''^2\left(\varepsilon' - n_1^2\sin^2\theta\right),$$

$$A_v'' = \left[\varepsilon'\left(n_2^2 - \eta''\right) - \varepsilon''\left(\eta' - n_1^2\right)\right]\left(\eta' - 1\right) - \varepsilon'\left(\eta' - n_1^2\right)\eta'' - \frac{1}{2}\sin^2\theta\left\{n_1^2\left(\eta' - 1\right)\left(n_2^2 - 2\eta'' + \varepsilon''\right)\right.$$
$$\left. + \left[n_2^2\left(\eta' - 1\right) + n_1^2\eta''\right]\left(n_1^2 - 2\eta' + \varepsilon'\right)\right\} - \frac{1}{2}\left(n_1^2 - \eta'\right)\left(n_1^2\cos^2\theta - \eta'\right)\varepsilon''$$
$$+ \frac{1}{2}\left(\varepsilon' - 1\right)\left[\left(n_1^2 - \eta'\right)\left(\eta'' - n_2^2\cos\theta\right) + \left(\eta'' - n_2^2\right)\left(n_1^2\cos^2\theta - \eta'\right)\right]$$
$$- \frac{1}{2}\left[\varepsilon''\mu'^2 + 2\mu'\mu''\left(\varepsilon' - 1\right)\right] + \mu'^2\left(n_2^2\sin^2\theta - \varepsilon''\right) - 2\mu'\mu''\left(\varepsilon' - n_1^2\sin^2\theta\right),$$

real η', μ', ε' and imaginary η'', μ'', ε'' components can be easily restored from components of second rank tensor (geomagnetic field is directed along Z-axis and XY plane, which represents the boundary between vacuum and turbulent magnetized plasma) [3]:

$$\varepsilon_{xx} = \varepsilon_{yy} \equiv \tilde{\eta} = 1 - \frac{v(1 - is)}{(1 - is)^2 - u}, \quad \varepsilon_{xy} = -\varepsilon_{yx} \equiv \tilde{\mu} = -i\frac{v\sqrt{u}}{(1 - is)^2 - u}, \quad \varepsilon_{zz} \equiv \tilde{\varepsilon} = 1 - \frac{v}{1 - is}$$
$$\varepsilon_{xz} = \varepsilon_{zx} = \varepsilon_{yz} = \varepsilon_{zy} = 0 \tag{2}$$

and complex refractive index of cold collision magnetized plasma [3]:

$$\tilde{N}^2 \equiv (N_* - iæ)^2 = 1 - \frac{2v(1 - v - is)}{2(1 - is)(1 - v - is) - u\sin^2\theta \pm \sqrt{u^2\sin^4\theta + 4u(1 - v - is)^2\cos^2\theta}}. \tag{3}$$

Signs "+" and "−" refer to the ordinary and extraordinary waves, respectively; æ is absorption coefficient, θ is an angle between the direction of wave propagation $\mathbf{k}$ and the geomagnetic field $\mathbf{H}_0$. $u = \omega_H^2/\omega^2$, $v = \omega_p^2/\omega^2$ and $s = v_{eff}/\omega$ are non-dimensional plasma parameters, v_{eff} is the effective electron collision frequency, $\omega_p^2 = 4\pi e^2 N/m$ is plasma frequency, N is electron concentration, $\omega_H = |e|H/mc$ is electron gyrofrequency, $\omega = 2\pi f$, f is wave frequency, e is electron charge, m is electron mass, c is the light velocity, N and H are functions of the spatial coordinates. $k_0 = \omega/c$ is the wavenumber. We assume that: frequency of the incident wave exceeds plasma frequency; the wavelength is much smaller than the characteristic size of the irregularities. These assumptions enable us to utilize the method of geometrical optics approximation and ignore the interaction between the normal waves. Expression (1) is quite general and could be applied to other types of irregularities in the ionosphere or inter-planetary space.

2.1. The Power-law Spectrum

Measurements of satellite's signal parameters passing through ionospheric layer and measurements aboard of satellite show that in F region of the ionosphere inhomogeneities have power law spectrum with different spatial scales. Observations suggest that the power law spectrum is believed to be the most suitable model of ionospheric irregularities. We will utilize anisotropic power law spectrum of electron density fluctuations for definition of effects caused by large-scale inhomogeneities of the ionosphere. High latitude irregularities are known to be strongly anisotropic [4]. Therefore we shall use a model of 3D anisotropic power law spectrum of irregularities elongated in the direction of geomagnetic field. A generalized correlation function for power-law spectrum by a power-law index

p for electron density irregularities has been proposed in [5]. The corresponding spectral function is:

$$W_N(\mathbf{k}) = \frac{\sigma_N^2}{(2\pi)^{3/2}} \frac{r_0^3 (k_0 r_0)^{(p-3)/2}}{\left(r_0\sqrt{k^2+k_0^2}\right)^{p/2}} \frac{K_{p/2}\left(r_0\sqrt{k^2+k_0^2}\right)}{K_{(p-3)/2}(k_0 r_0)}, \tag{4}$$

where σ_N^2 is a variance of electron density fluctuations, $K_v(x)$ is the modified Bessel function, r_0 is the inner scale of turbulence, $L_0 = 2\pi/k_0$ is the outer scale and, as usual, it is supposed that $k_0 r_0 << 1$. In the interval of wavenumber $k_0 r_0 << k r_0 << 1$ spatial spectrum has the power law form [5]:

$$W_N(k) = \frac{\sigma_N^2}{2\pi} \frac{\Gamma\left(\frac{p}{2}\right)}{\Gamma\left(\frac{3}{2}\right)\Gamma\left(\frac{p-3}{2}\right)} \frac{L_0^3}{(1+L_0^2 k^2)^{p/2}}, \tag{5}$$

Anisotropic case of the spectrum (5) was considered in [6]. Utilizing functional expression for the gamma function Γ [7] $\Gamma(z)\Gamma(1-z) = \pi/\sin(\pi z)$ instead of L_0 we introduce two spatial correlation lengths of electron density fluctuation $\ell_{||}$ and $\ell_\perp$ ($\ell_{||}$ is the scale size of relative elongated irregularities in the direction of geomagnetic field vector $\mathbf{B}$, $\ell_\perp$ is relative elongation of irregularities in a plane perpendicular to the geomagnetic field). Further we will utilize spatial power law spectrum:

$$W_N(\mathbf{k}) = \frac{\sigma_N^2}{2\pi^2} \frac{\Gamma\left(\frac{p}{2}\right)\Gamma\left(\frac{5-p}{2}\right)}{\Gamma\left(\frac{3}{2}\right)} \sin\left[\frac{(p-3)\pi}{2}\right] \frac{\ell_\perp^2 \ell_{||}}{\left[1+\ell_\perp^2\left(k_\perp^2+\chi^2 k_{||}^2\right)\right]^{p/2}}, \tag{6}$$

here $\chi = \ell_{||}/\ell_\perp$ is the anisotropy factor, $p > 3$.

Experimental investigations of Doppler frequency shift of ionospheric signal show that index of the power law spectrum of electron density fluctuations in ionospheric plasma is in the range of $3.8 \leq p \leq 4.6$. Experimental value of the power law spectrum of the ionosphere ($<p> \approx 4$), measured by translucence of the ionosphere by satellite signals [8], is within the limits of p. Experimental investigation of the artificially disturbed ionospheric region by high power HF radio waves based on the reception of backscattered signals shows that a lot of artificial ionospheric irregularities of the electron density are stretched along the geomagnetic field. Power-law spectral index was equal to $p = 1.4 \div 4.8$ in different heating sessions in the probe wave frequency range of $2.6 \div 6$ MHz using "Sura" heating facility in the frequency range of $4.7 \div 9$ MHz (ordinary mode) with the effective radiated power $50 \div 70$ MW beamed vertically upwards [9].

2.2. Statistical Characteristics of Correlation Function of the Phase and the Angular Spectrum

The phase scintillations are often not measured directly, but rather as a difference of scintillations at two points separated by a distance ρ_y. For simplicity we will consider two interferometers in mutually perpendicular directions perpendicular to the radio path. Setting (6) into (1), taking into account smallness of the parameter a and expanding into the series the exponential term, correlation function of the phase has the form:

$$W_\varphi(0, \rho_y, z) = 2^{(4-p/2)}\sigma_N^2\left(D^2+E^2\right) \frac{\Gamma\left(\frac{5-p}{2}\right)}{\Gamma\left(\frac{3}{2}\right)} \sin\left[\frac{(p-3)\pi}{2}\right] \frac{k_0^2 z \ell_{||}\chi^{(p-2)/2}}{(1+b^2\chi^2)^{p/4}} \left(\frac{\rho_y}{\ell_{||}}\right)^{(p-2)/2}$$
$$\times K_{(p-2)/2}\left(\frac{\chi\rho_y}{\ell_{||}\sqrt{1+b^2\chi^2}}\right). \tag{7}$$

The variance of correlation function of the phase at $p > 3$ is given by the following expression:

$$\sigma_\varphi^2 = \frac{1}{\sqrt{\pi}}\sigma_N^2\left(D^2+E^2\right)\Gamma\left(\frac{5-p}{2}\right)\Gamma\left(\frac{p-2}{2}\right)\sin\left[\frac{(p-3)\pi}{2}\right]\frac{k_0^2 z \ell_{||}}{\sqrt{1+b^2\chi^2}}. \tag{8}$$

Knowledge of the correlation function of the phase (1) allows us to calculate the broadening of the angular spectrum of scattered EM waves by electron density fluctuations in turbulent magnetized collisional plasma utilizing well-known expression [1, 10] $< k_x^2 >= -\left[\partial^2 W_\varphi\left(\rho_x,\, \rho_y,\, z\right)/\partial\rho_x^2\right]_{\rho_x=\rho_y=0}$, Integration at $p > 3$ yields:

$$\frac{< k_x^2 >}{k_0^2} = < \sigma_N^2 > \left(D^2+E^2\right) \frac{\Gamma\left(\frac{p}{2}\right)\Gamma\left(\frac{5-p}{2}\right)\Gamma\left(\frac{p-4}{2}\right)}{\Gamma\left(\frac{3}{2}\right)\Gamma\left(\frac{p-3}{2}\right)} \left[\frac{\Gamma\left(\frac{p-3}{2}\right)}{\Gamma\left(\frac{p-2}{2}\right)} - \frac{\Gamma\left(\frac{p-1}{2}\right)}{\Gamma\left(\frac{p}{2}\right)}\right] \sin\left[\frac{(p-3)\pi}{2}\right] \frac{z\chi^2}{\ell_{||}\left(1+b^2\chi^2\right)^{3/2}} \tag{9}$$

Broadening of the angular spectrum in the main plane is equal to $(< k_y^2 > /k_0^2) = (< k_x^2 > /k^2-0)/(1+b^2\chi^2)$. Hence, spatial spectrum of scattered radiation in the main plane is narrowing with an increase of anisotropy factor χ .

The angle-of-arrival variations are simply related to the phase variations using ray-optics method. Utilizing general expression of the angle of arrival of scattered radiation, caused due to electron density fluctuations [2] we have:

$$< \mathbf{g}^2 >= \frac{1}{k_0^2 N_*^2}\left[< \left(\frac{\partial\tilde{\varphi}_1}{\partial x}\right)^2 > +\cos^2\theta < \left(\frac{\partial\tilde{\varphi}_1}{\partial y}\right)^2 > +\sin^2\theta\left(\frac{\partial\tilde{\varphi}_1}{\partial z}\right)^2 >\right]. \tag{10}$$

It could be shown that in case of weak absorption, $a\kappa_y z << 1$, for the power-law spectrum (6) the main contribution in (10) give first and second terms. As a result, formula (10) could be expressed through the normalized broadening of the angular power spectrum $< \mathbf{g}^2 >= \left(< k_x^2 > +\cos\theta < k_y^2 >\right)/k_0^2$.

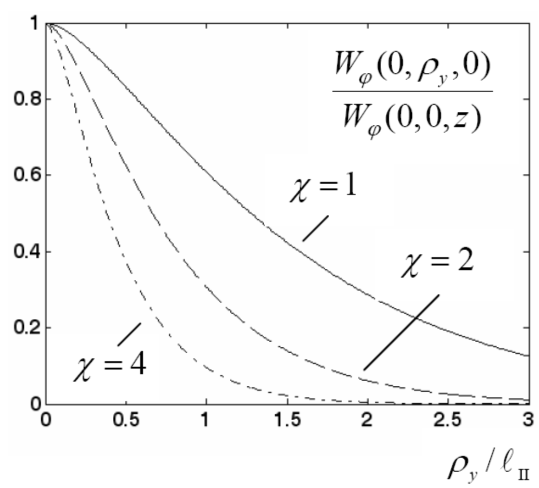

Figure 1: Dependence of the normalized correlation function of the phase of scattered radiation versus normalized distance of the base for different values of anisotropic factor χ.

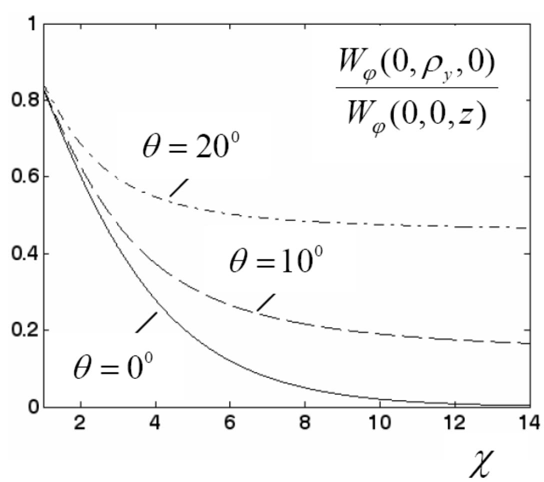

Figure 2: Dependence of the normalized correlation function of the phase of scattered radiation versus anisotropic factor for different values of refraction angle θ.

2.3. Numerical calculations

Calculations have been carried out for F layer of the ionosphere assuming a power-law spectrum at a height 280 km, $k_0\ell_{||} = 10^4$, $\sigma_N^2 = 10^{-4}$ [11] $z/\ell_{||} = 1.5$. Figure 1 shows that normalized correlation function of the phase (NCF) of electron density fluctuations decreases in proportion to a distance ρ_y normalized on the longitudinal scale size of relative elongated irregularities $\ell_{||}$ at $\theta = 10^0$ with an index of $p = 4$. Calculations show that curve smoothly decreases in isotropic case ($\chi = 1$).

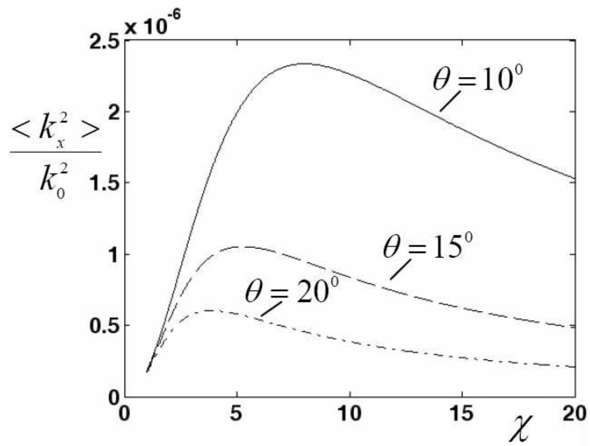

Figure 3: Dependence of the normalized broadening of the angular spectrum versus anisotropic factor for different values of refraction angle θ in XOZ plane.

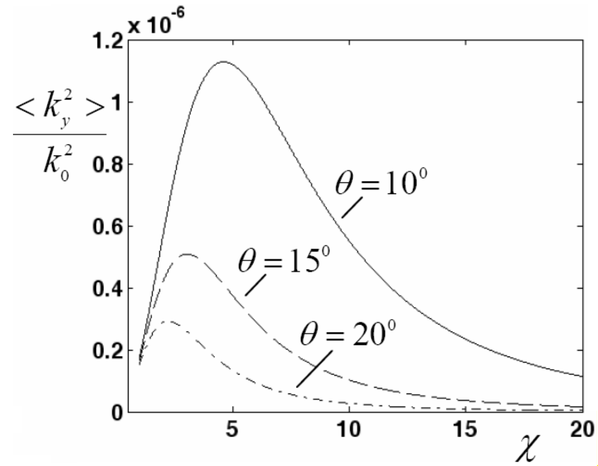

Figure 4: Dependence of the normalized broadening of the angular spectrum versus anisotropic factor for different values of refraction angle θ in YOZ plane.

At small distance of $\rho_y/\ell_{||}$ the curves of NCF sharply decrease inversely proportional to the factor of anisotropy. Figure 2 illustrates the dependence of the NCF versus parameter of anisotropy χ. With increasing of the angle of refraction θ with respect to the external magnetic field, NCF decreases and beginning from $\chi = 13$ tends to saturation (for $\theta = 100$). Anisotropy of electron density inhomogeneities has a substantially effect on the broadening of the angular spectrum of scattered EM waves. Figures 3 and 4 illustrates the broadening of the spatial spectrum at different angles of refraction $\theta = 10^0$, 15^0, , 20^0. Firstly, angular power spectrum of scattered radiation is increasing and then smoothly decreases in proportion to the anisotropy factor of inhomogeneities χ. The reason is that in geometrical optics approximation, in non-absorbing media (neglecting fluctuations) when both amplitude and phase S are real quantities, vector of energy-flux density and vector ∇S are collinear and directed to the normal to the phase front, while in absorptive media the directions of wave propagation ∇S_1 and the direction of fastest dumping of the wave ∇S_2 are not coincided [1]. In particular, in XOZ plane, if $\theta = 10^0$ normalized broadening reaches its maximum at $\chi = 8$; if $\theta = 15^0$ at $\chi = 5$; if $\theta = 20^0$ at $\chi = 4$; in the main plane YOZ if $\theta = 10^0$ normalized broadening reaches its maximum at $\chi = 5$, if $\theta = 15^0$ at $\chi = 3$, if $\theta = 20^0$ at $\chi = 2$. Using the data $\sigma_N^2 = 10^{-12}$, $z/\ell_{||} = 70$ [12], at $p = 4.5$ and $\chi = 5$ the angle-of-arrival $< g^2 >$ in the XOZ plane at $\theta = 5^0$, 10^0, 15^0 is equal to $0.12''$, $0.09''$, $0.06''$, respectively; in YOZ plane at $\theta = 5^0$, 10^0, 15^0 we have $0.11''$, $0.06''$, $0.04''$, respectively, which is in a good agreement with [12].

REFERENCES

1. Jandieri, G. V., V. G. Gavrilenko, A. V. Sorokin, and V. G. Jandieri, "Some properties of the angular power distribution of electromagnetic waves multiply scattered in a collisional magnetized plasma," *Plasma Physics Report*, Vol. 31, No 7, 604–615, 2005.
2. Jandieri, G. V., V. G. Jandieri, Z. M. Diasamidze, and I. N. Jabnidze, "Statistical characteristics of scattered microwaves in gyrotropic medium with random inhomogeneities," *International Journal of Microwave and Optical Technology*, Vol. 1, No. 2, 860–869, 2006.
3. Ginzburg, V. L. *Propagation of Electromagnetic Waves in Plasma*, Gordon and Beach, New York, 1961.
4. Aarons, J., "Global morphology of ionospheric scintillations," *IEEE*, Vol. 70, 360–378, 1982.
5. Shkarofsky, I. P., "Generalized turbulence space-correlation and wave-number spectrum-function pairs," *Canadian Journal of Physics*, Vol. 46, 2133–2153, 1968.
6. Fremov, E. J. and J. A. Secan, "Modelling and scientific application of scintillation results," *Radio Science*, Vol. 19, 687–694, 1984.
7. Abramowitz, M. and I. Stegun, *Handbook of Mathematical Functions*, Dover, 1972.
8. Gailit, T. A., V. D. Gusev, L. M. Erukhimov, and P. I. Shpiro, "On spectrum of phase fluctuations at ionospheric remote sensing," *Radiophysics*, Vol. 26, No. 7, 795–800, 1983 (in Russian).

9. Bakhmet'eva, N. V., V. N. Bubukina, Y. A. Ignat'ev, G. S. Bochkarev, V. A. Eremenko, V. V. Kol'sov, I. V. Krasheninnikov, and Y. N. Cherkashin, "Investigation by backscatter radar irregularities produced in ionospheric plasma heating experiments," *JASTP*, Vol. 59, No. 18, 2257–2263, 1997.
10. Gavrilenko, V. G., A. A. Semerikov, G. V. Jandieri, "On the effect of absorption on multiple wave-scattering in a magnetized turbulent plasma," *Waves Random Media*, Vol. 9. 427–440, 1999.
11. Kravtsov, Y. A., Y. A. Feizulin, and A. G. Vinogradov, "Radio waves propagation through the Earth's atmosphere," *Radio and Communication*, Moscow, 1983 (in Russian).
12. Armand, N. A., I. N. Kibardina, and A. N. Lomakin, "Propagation of radio waves in anisotropic turbulent atmosphere," 5–15, *Electromagnetic Waves in Atmosphere and Cosmic Space*, Nauka, Moscow, 1986 (in Russian).

Occupational Exposure Assessment of the Static Magnetic Flux Density Generated by Nuclear Magnetic Resonance Spectroscopy for Biochemical Purposes

Gilbert Decat
VITO, Belgium

Abstract— The present paper deals with the measurement and evaluation of the static magnetic flux density to which operators are occupationally exposed to. Measurements were performed in normal working and worst case exposure situations. The results show that the exposure levels are conform with the exposure limits for non-wearers of metallic implants like pacemakers, but that wearers of these implants shouldn't work in an NMRS environment.

1. INTRODUCTION

The use of MRI (Magnetic Resonance Imaging) is steadily increasing in medical applications [1] as well as the use of NMRS (Nuclear Magnetic Resonance spectroscopy) in solid physics, biomedical and biochemical applications. Because MRI applications result in the exposure of the patient and the medical staff to static magnetic fields, gradient fields (only during patient scans) and RF (radio frequency) fields [2, 3] and the NMR-spectroscopic exposure is only limited to the exposure of the scientific staff, cleaners and maintenance workers to the static magnetic stray fields, much more attention is given to the MRI research needs [4]. However, by lack of informative exposure data on NMR spectroscopy on the one hand and because the magnet capacity is generally higher in NMR-spectroscopy than in MRI scans on the other there is also a need to assess the static magnetic flux density to which operators of these devices are exposed to. In NMR spectroscopy which is used for physical and biochemical purposes large superconducting magnets ranging up to 22 T can be used. In the present paper we measured and evaluated the B-field exposure of two different types of NMRSs.

2. EXPOSURE LIMITS

Table 1 summarizes the occupational exposure limits for the evaluation of the measured data:

Table 1: Exposure limits.

	Wearers of pacemakers	Exposure limits
Guideline bodies		
NRPB (1993) UK National Radiation Protection Board	-	- 200 mT 24 h average - maximum 2000 mT whole-body exposure - maximum 5000 mT for arms and legs
ACGIH (1994) American Conference of Governmental Industrial Hygienists	0.5 mT	- TLV: 60 mT whole-body exposure - TLV: 600 mT for extremities - Ceiling value: 2 T
ICNIRP (1994) International Commission on Non Ionizing Radiation Protection	0.5 mT	- 200 mT whole working day (TWA) exposure - 5 T for limbs - Ceiling value: 2 T
ICNIRP 1998	-	- refers to ICNIRP (1994)
Directive 2004/40/EC	-	- no recommendations

- TLV: Treshold Limit Values - TWA: time-weighted average

The NRPB (1993) recommends static B-field limits of 200 mT averaged over 24 h, 2 T as a maximum whole-body field and 5 T as a maximum to arms and legs [5].

The ACGIH (1994) recommends threshold limit values (TLV's) to which it is believed that nearly all workers may be repeatedly exposed day after day without adverse health effects [6].

ICNIRP (1994) recommends that whole-body continuous occupational exposure should be limited to a time-weighted average (TWA) less than 200 mT. The ceiling value is 2 T and the limbs exposure restriction is up to 5 T.

Carriers of cardiac pacemakers and implantable defibrillator bearers should avoid locations where the B-field exceeds 0.5 mT (5 G).

When the B-field exceeds 3 mT, precaution should be taken to prevent hazards from flying metallic objects.

Watches, credits cards, magnetic tapes, computer disks may be adversely affected by exposure to 1 mT [7].

ICNIRP (1998) refers to the ICNIRP guidelines of 1994 [8].

Directive 2004/40/EC: by lack of information about medical exposure and risks the directive doesn't contain recommendations for the exposure to static magnetic fields [9].

3. MATERIAL AND METHODS

As shown in Table 2, the exposure of the scientific staff to the static magnetic flux density generated by two different types of NMR-spectrometers was studied. It's important to notice that the first one is a normal shielded 7.5 T and the other one an ultra-shielded 9.39 T spectroscope which are both used for biochemical purposes. Both spectroscopes are installed in the same laboratory at a distance of about 6.5 m from each other.

Table 2: Specifications of both NMR magnets.

Type	**300/67 H**	**400 SB UltraShield**
Frequency (MHz)	300	400
Operating field (T)	7.05	9.39

The B-field has been measured by means of a 3-Axis Hall Teslameter (Metralab) with a precision of ±0.1%. The X-, Y- and Z- field components were measured at the same time.

Table 3 summarizes the worst case exposure situations of the staff when they come closest to the spectroscopes while performing different operations.

Table 3: Worst case exposure situations of spectroscope operators.

Operation	**Operation time**	**Distance (cm) between operator and NMR wall**	
		300 MHz	**400 MHz**
Placement of test tubes in the sample conveyor belt	2–5 minutes per day	10	10
Probe adjustment under NMR	5 minutes per month	5	5
Nitrogen filling operation	10–25 minutes per week	10	10

4. RESULTS

Figure 1 shows the decrease of the B-field as a function or the distance to both NMRS types.

In the worst case situation the operator of the 300 MHz spectroscope will be exposed 5 days a week during 5 minutes to a B-field of 15 mT. With the 400 MHz type the exposure is reduced to about 9 mT. Even in the most unrealistic assumption that the operator should be exposed to the maximum B-field of 30 mT (against the wall of the NMR-300 MHz) for 24 h, according to the interpretation of the exposure limits summarized in table 2 there would be no health effect to be expected.

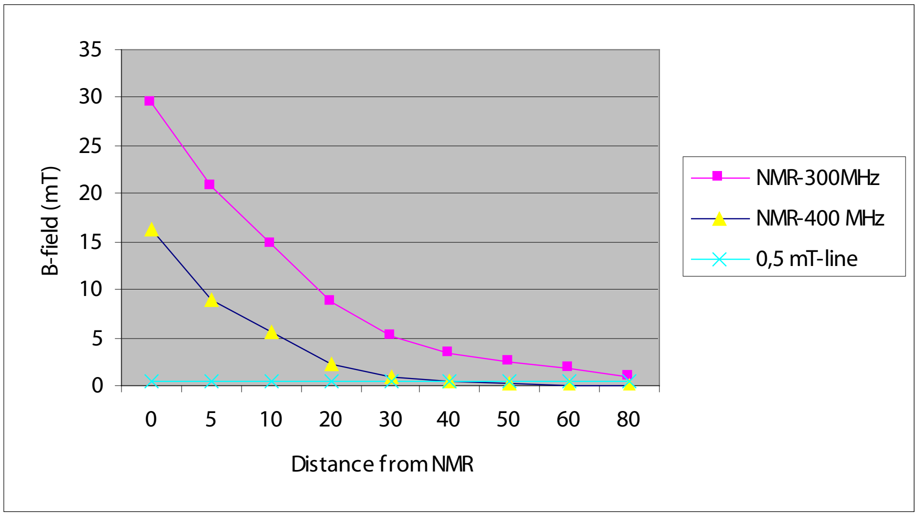

Figure 1: B-field versus distance to the NMRS.

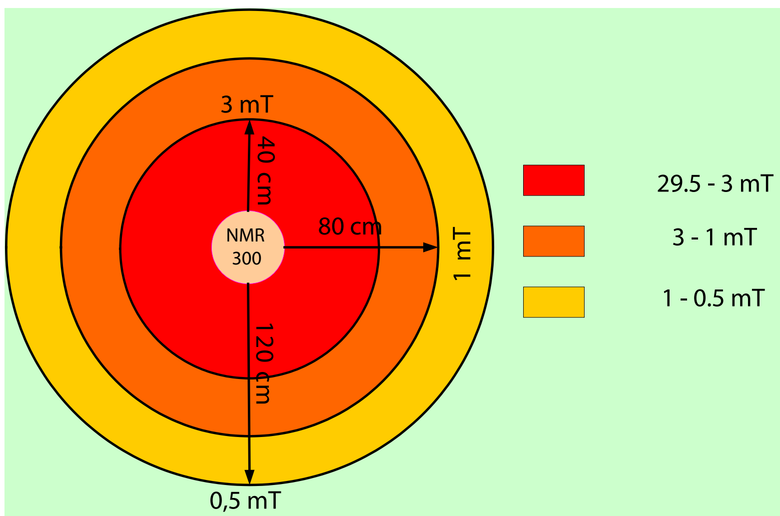

Figure 2: Risk contours of the NMR 300 MHz.

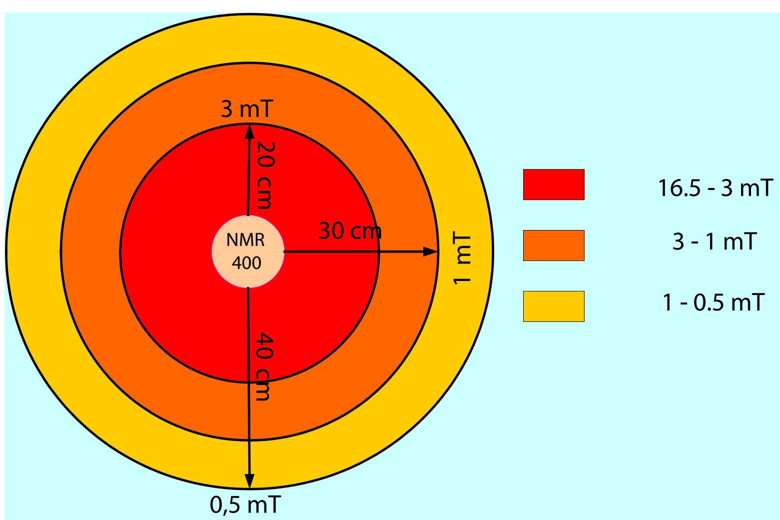

Figure 3: Risk contours of the NMR 400 MHz.

If we focus on the interference between the B-field and metallic implants such as pacemakers, the exposure evaluation gets another interpretation. The Figures 2 and 3 show the radius of the contours at which interference and other possible indirect risks may occur.

Figure 2 shows that carriers of cardiac pacemakers, ferromagnetic and other electronic implants should stay at least about 1.20 m away from the NMR-300 MHz and, because of ultra-shielding only 40 cm from NMR 400 MHz (Figure 3). The risk distances for demagnetization at 1 mT are 80 cm from NMR-300 MHz and 30 cm for NMR 300 MHz. The distance to prevent accidents with strongly attracted flying objects at a B-field threshold of 3 mT lies at 40 cm and 30 cm from the wall of the NMR 300 MHz and 400 MHz respectively.

5. CONCLUSION

The present data show that the magnetic flux density generated by different types of NMR spectroscopes for biomedical applications are even in the worst case situation conform with the exposure limits of ACGIH (1994), NRPB (1993) and ICNIRP (1994). Thus on base of these guidelines/standards, no health effects have to be expected for non-wearers of implanted metallic devices such as pacemakers. Anyway since limits are based on acute effects and not on well-conducted epidemiological or long term animal studies there still exists uncertainty about the long term effects of static magnetic fields. Therefore and since the exposure generated by these devices is about 1000 times the natural B-field background, operators of these devices should limit their exposure to a minimum.

Moreover, since the B-field may interfere with the implants mentioned above wearers of these implants shouldn't operate these spectrometers and have to stay at a safety distance from it.

Passive mitigation by providing ultra-shielding is very efficient, it is to be expected that all new NMR spectroscopes should be designed in this way.

ACKNOWLEDGMENT

The paper has been prepared in the framework of the EMF-NET FP6 Coordination Action: Effects of the exposure to electromagnetic fields from science to public health and safer workplace. Project No SSPE-CT-2004-502173.

REFERENCES

1. WHO, "Electromagnetic fields and public health: Static electric and magnetic fields," *Fact Sheets*, No. 299, March 2006.
2. WHO, "Static Fields," *Environmental Health Criteria 232*, World Health Organization, 2006.
3. Karpowicz, J. and K. Gryz, "Health risk assessment of occupational exposure to a magnetic field from magnetic resonance imaging devices," *Int. J. of Occupational Safety and Ergonomics (JOSE)*, Vol. 12, No. 2, 155–167, 2006.
4. "EMF-NET Committee on research needs," *Environment and Health Implications of Electromagnetic Field Exposure*, Report on Research Needs, August 2005.
5. NRPB, "Restrictions on exposure to static and time-varying electromagnetic fields," National Radiological Protection Board Chilton, Didcot, Oxon OX11 ORQ, UK, 1995.
6. ACGIH, "Threshold limit values for chemical and physical agents and biological exposure indices," *Static Magnetic Fields* 110, *American Conference of Governmental Industrial Hygienists*, 1994–1995.
7. ICNIRP, "Guidelines on the limits of exposure to static magnetic fields," International Commission on Non-ionizing Radiation Protection. *Health Physics*, Vol. 665, No. 1, 100–106, 1994.
8. ICNIRP, "Guidelines for limiting exposure to time-varying electric, magnetic and electromagnetic fields (up to 300 GHz)," International Commission on Non-ionizing Radiation Protection. *Health Physics*, Vol. 74, Nr. 4, April 1998.
9. Directive 2004/40/EC of the European Parliament and of the Council of 29 April 2004 on the minimum health and safety resuirements regarding the exposure of workers to the risks arising from physical agents (electromagnetic fields) (18th individual Directive within the meaning of Article 16(1) of Directive 89/391/EEC), O. J. Nr. L-184 of 24 May, 2004.

A Memory-efficient Strategy for the FDTD Implementation Applied to the Photonic Crystals Problems

Yu Liu, **Ziqiang Yang**, **Zheng Liang**, **and Limei Qi**
College of Physical Electronics, University of Electronic Science and Technology of China
Chengdu 610054, China

Abstract— The Finite Difference Time Domain (FDTD) method is well suited for the computation of the photonic crystals problems. However, this technique has the drawback of high computer memory requirements, when involving complex structures. In this paper, a modified array implementation for the FDTD algorithm, with increased memory efficiency, is presented and applied to studies on the abnormal refraction phenomena of the electromagnetic propagating in the photonic crystals. The novel approach is based on memory-mapped files, which is a mechanism of manipulating memory in Windows or Linux operating system. By using this mechanism, we make use of memory space more availably in allocating and implementing multidimensional arrays for FDTD algorithm. The computed examples are given in the paper to prove the feasibility and accuracy of this strategy. A detailed discussion is presented for the case of the electromagnetic propagating in two-dimensional photonic crystals, formed by parallel air cylinders in a dielectric medium. The results show that some interesting relations can be obtained between the incident and the refraction angles with the group velocity (V_g) and the energy velocity (V_e).

1. INTRODUCTION

The use of the finite difference time domain (FDTD) method is very attractive for the electromagnetic analysis of photonic crystals [1, 2], due mainly to its algorithmic simplicity and flexibility. However, the computational requirements are high, and computer memory can become a limitation for complex or inhomogeneous structures. At the same time, the research also no longer is limited to get only steady transmission spectrum, but pay attention to morely the dynamic process of the interaction between EM wave and the media in photonic crystals, and more information needs to be provided by the FDTD method. This will increase consumedly the memory demand of FDTD simulations. Therefore, for the FDTD implementation in PC, the following problem need to be resolve urgently: how to make use of memory more efficiently.

The foundation of FDTD algorithm is that Maxwell's curl equations are discretized using the central difference approximations in time and space [3]. The express of the space discretization in memory is actually multidimensional arrays, and time discretization behaves as the array iterative operaton step by step in the FDTD method. So the high efficient array realization is starting point of FDTD implementation in PC. In this paper, a modified array realization for the FDTD algorithm, based on memory-mapped files, is presented and applied to studies on the abnormal refraction phenomena of the electromagnetic propagating in the photonic crystals. The computed examples are given to prove the feasibility and accuracy of this strategy.

2. DATA ARRAY REALIZATION OF FDTD ALGORITHM

In the numerical simulation of EM field, there are usually two means for array realization: (1) static array, you can just allocate and access them with operator [ ]. (2) dynamic array, by using the library function. The latter is mostly for use in the EM simulation of electrically-large-size complex structure, and this cause a distinct improvement in memory utilization ratio. However, These array realizations have a few problems, for example, if there exist many times writing hard-disk operation for saving the temporary result in FDTD computation, the algorithm performance descends seriously.

A typical FDTD formula is as follows:

$$\begin{aligned} E_x^{n+1}(i,j,k) &= CA(i,j,k)\cdot E_x^n(i,j,k) \\ &\quad + CB(i,j,k)\cdot\left[\frac{H_z^n(i,j,k)-H_z^n(i,j-1,k)}{\Delta y}-\frac{H_y^n(i,j,k)-H_y^n(i,j,k-1)}{\Delta z}\right] \end{aligned} \tag{1}$$

where $CA(i,j,k)$ and $CB(i,j,k)$ are the characteristic parameters of the media.

With making a data-flow analysis of the FDTD formula, we find, there is a obvious characteristics for the arrays behavior of FDTD computation: no complex memory operation, such as the combination, release and newly allocating of the data arrays. Therefore, to raise performance, the array realization of FDTD algorithm can simplify a series of additive characteristics which relate to the complex memory operation, and is equivalent to allocating a contiguous block of memory.

Furthermore, in the FDTD simulation for the photonic crystals, there exist often many times writing hard-disk operation for saving the temporary result. Hence, for the array realization of the photonic crystals simulation, blocks of memory allocation and the performance of writing hard-disk are two key factors which influence the FDTD implementation. The array realization had better establish a direct link between memory allocating and hard-disk storing.

For general Windows and Unix/Linux system, the layered memory management can be shown in Figure 1 [4–6].

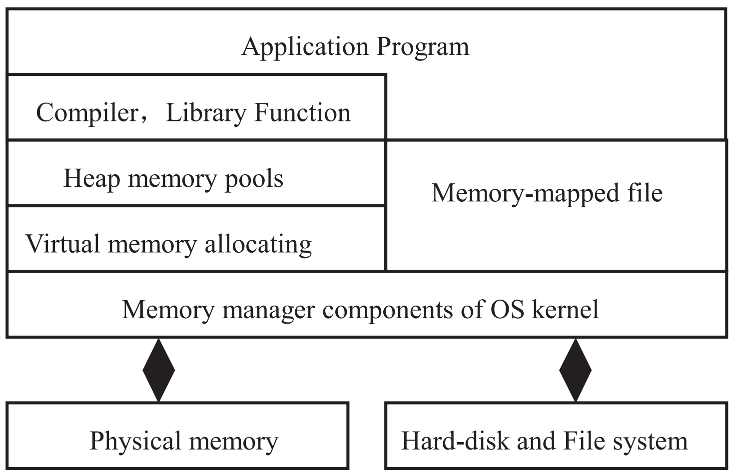

Figure 1: Layered memory management in Windows/Linux.

We find, in the Windows/Linux system memory management, the realization of the static or dynamic array lies on the uppermost layer of the hiberarchy. The additive heap memory pools service of the intermediate layer, such as merging memory fragment, reserving memory space,etc, is in fact unnecessary for FDTD algorithm. Moreover, the memory arrays operating and the results writing hard-disk are two independent processes, and the system need provide a extra buffer for the disk access. These will cause the descent of the computational efficiency. From the Figure 1 can see, there is a particular memory allocating mechanism: memory-mapped file, which can happily combine the array realization and writing disk operation from the system level. Because the physical storage of memory-mapping comes from a file that is already on the disk, this shelters you from performing file I/O operations on the file and from buffering the file's contents. At one time, memory-mapped technique also avoid servicing the heap memory pools, these both improve distinctly the memory efficiency of the FDTD implementation.

By using memory-mapped technique, we get a block of contiguous memory. Memory itself is fundamentally a one-dimensional quantity since memory is ultimately accessed with a single memory address, and the express of the space discretization in FDTD is multidimensional arrays. The distinction between the different dimensions is primarily a question of how we want to think about, and access array elements. For higher-dimensional arrays, we want to specify two, or more, indices to dictate the element of interest. However, regardless of the number of indices, ultimately a single address dictates which memory is being accessed. The translation of multiple indices to a single address can be left to the compiler by using macro definition or that translation is something we can do ourselves.

3. FDTD SIMULATION OF PHOTONIC CRYSTALS

As an application of memory-mapped technique in the array realization, we carry on the FDTD studies on the abnormal refraction phenomena of the electromagnetic propagating in the photonic crystals.

We will consider the two-dimensional photonic crystal slab of a square lattice of identical air cylinders in a dielectric medium with a dielectric constant $\varepsilon = 12$. The lattice constant is denoted by a and the hole radius $r = 0.35a$. TE modes, that is, the magnetic field is kept parallel to the axis of the air cylinders. We scale all length by the lattice constant, and the frequency by $2\pi c/a$ to make the system dimensionless.

The FDTD implementation in form is similar to the general case, the key difference is that EM field arrays are realized by using memory-mapped technique. In Windows system, the main steps are as follows: [5]

1) Create a file on disk using CreateFile( ) function, and open the file flag for read-write access. The length of the file is equal to EM field array.
2) Create a file-mapping object using CreateFileMapping( ) function.
3) Map all of the file-mapping object into the process's address space using MapViewOfFile( ) function, with a pointer which the function return, we can access a data array in memory.

For the multidimensional arrays in FDTD simulation, for example, electric field component $Ez(i, j)$, we can access data in normal manner by using macro definition: $\sharp$ define $Ez(i, j)$ $ez[(i) *$ columns $+ (j)]$, where ez is the pointer which represents electric field component Ez, and columns is the column number of the two-dimensional array.

4. RESULTS AND ANALYSIS

Electromagnetic propagation in photonic crystals structure is very complicated. The real propagation direction of EM wave is the energy velocity (Ve) direciton. In general case, Ve is equal to Vg. Group velocity (Vg) is obtained by the gradient of EFS (Equal Frequency Surface) [7]. The energy velocity (Ve) can be obtained by calculating the Poynting vector.

By FDTD, we compute the electromagnetic propagation and the Poynting vectors in the structure. Here we choose two flat slab sizes. They are $60a \times 9.89a$ and $60a \times 40a$ in terms of lattice constant, and the frequency is 0.195. The Poynting vector is obtained by the cross product of the electric and magnetic field calculated by the FDTD method, and the direction of energy velocity is determined by the following formula [8].

$$V_e = \frac{\frac{1}{A}\int\limits_A (Poynting\ Vector) dS}{\frac{1}{A}\int\limits_A (energy\ density) dS} \tag{2}$$

Figure 2 shows the structure of the PC slab and the intensity distribution of EM wave across the PC slab. A Gaussian beam is incident to the slab with the incident angle of 60 degree with respect to the ΓM direction. The slab measures as 60×40 in terms of lattice constant. The yellow arrow which is the total Poynting vectors in PCs indicates the energy velocity (Ve) directions, and the red arrow indicates the group-velocity (Vg) direction obtained by the gradient of EFS. We found that the relations between the incident angles and the refraction angles are different for the group velocity (Vg) and the energy velocity (Ve).

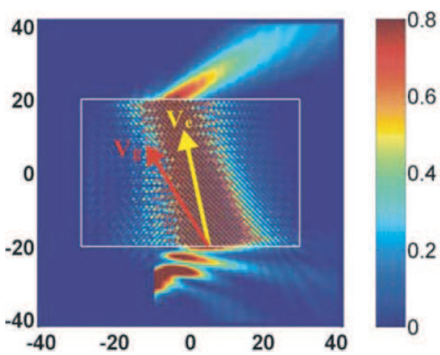

Figure 2: The intensity image of the magnetic fields across a flat photonic crystal slab.

To analysis the directions of the energy velocity (Ve) of the EM wave, we calculated the summation of the poynting vectors inside the slab to get the relation between the incident angles and the refraction angles. The results are shown in Figure 3.

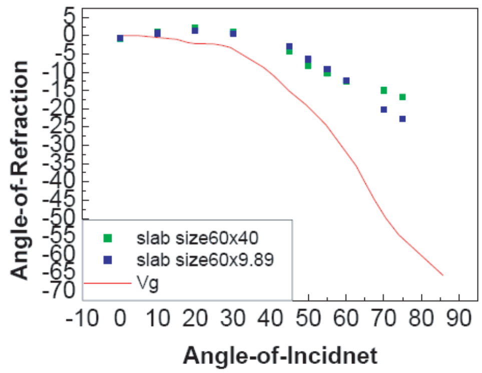

Figure 3: The refraction angles of Vg and Ve respect to the ΓM direction.

Figure 3 shows the refraction angles of Vg and Ve for different incident angles. The results indicate that the thickness of the PC slab hardly effects the propagation direction of Ve. As the incident angle is smaller than 45 degree, the refraction angle of Ve is close to 0 degree, indicating that the energy of the electromagnetic wave propagates along the ΓM direction. This phenomenon has been discussed in Ref. 9, and it originates from the partial bandgap of the PC structure. As the incident angle is larger than 45 degree, a significant difference appears between the refraction angle for Ve and Vg and both Ve and Vg show obviously the abnormal refraction phenomena. However, the refraction angle of Ve is still much smaller than that of Vg. For example, as shown in Figure 2, as the incident angle is 60 degree, the refraction angles for Vg and Ve in the PC slab respect to the ΓM direction are -35 and -11 degrees, respectively.

In a unit cell of the photonic crystal structure, the fact that the group velocity direction is identical to the energy velocity direction is true. However, as the EM wave launched from a media such as air into photonic crystals, the near-field wave scattering effect on the interface may perturb the propagation direction of the wave. This induces that the energy velocity (Ve) direction does not follow the group velocity (Vg) direction predicted by EFS. Therefore, the wave propagation direction is actually the the Poynting vector direction averaged in the whole PC slab.

5. CONCLUSIONS

In this paper, we have introduced a novel array implementation approach based on memory-mapped technique for the FDTD implementation, with increased memory efficiency in allocating and realizing multidimensional arrays. By using this method, we study on the abnormal refraction phenomena in the photonic crystals. The simulation results show that there is difference between the EM wave propagation direction and the group velocity (Vg) direction obtained by the gradient of the EFS, and the real propagation direction of EM wave is the energy velocity (Ve) direciton.

ACKNOWLEDGMENT

Work supported by National Natural Science Foundation of P. R. China (60571020).

REFERENCES

1. Zhu, Z., W. Ye, X. Yuan, et al., "Study of transmission characteristics of 2-D photonic crystals by the finite difference time domain method," *Acta Optica Sinica*, Vol. 23, No. 5, 522–525, 2003.
2. Liu, Y., J. Mao, and D. Yao, "The analysis of the electromagnetic characteristics of planar periodic structures using FDTD method," *Acta Electronica Sinica*, Vol. 28, No. 9, 99–101, 2000.
3. Yee, K. S., "Numerical solution of initial boundary value problems involving Maxwell's equations in isotropic media," *IEEE Trans. Antennas Propagation*, Vol. 17, No. 5, 302–307, 1966.
4. Johnson, M. H., *Windows System Programming*, Third Edition, Anna, Wu Mingjun transl., China Machine Press, Beijing, 88–110, 2006 (in Chinese).

5. Richter, J., *Programming Applications for Microsoft Windows*, Fourth Edition, Microsoft Press, Washington, 299–460, 1999.
6. Bovet, D. P. and M. Cesati, *Understanding the Linux Kernel*, Second Edition, O'Reilly Media, Inc., Cambridge, 436–455, 2003.
7. Foteinopoulou, S. and C. M. Soukoulis, "Negative refraction and left-handed behavior in two-dimensional photonic crystals," *Phys. Rev. B*, Vol. 67, No. 6, 235107-1-5, 2003.
8. Kong, J. A., *Electromagnetic Waves Theory*, 2nd Edition, Wiley-Interscience, New York, 1990.
9. Chien, H. T., H. T. Tang, C. H. Kuo, et al., "Directed diffraction without negative refraction," *Phys. Rev. B*, Vol. 70, No. 9, 113101-1-4, 2004.

Fast Computation of Electromagnetic Wave Propagation and Scattering for Quasi-cylindrical Geometry

Shaolin Liao
Electrical and Computer Engineering, 1415 Engineering Drive
University of Wisconsin, Madison, 53706, USA

Abstract— The cylindrical Taylor Interpolation through FFT (TI-FFT) algorithm for computation of the near-field and far-field in the quasi-cylindrical geometry has been introduced. The modal expansion coefficient of the vector potentials **F** and **A** within the context of the cylindrical harmonics (TE and TM modes) can be expressed in the closed-form expression through the cylindrical addition theorem. For the quasi-cylindrical geometry, the modal expansion coefficient can be evaluated through FFT with the help of the Taylor Interpolation (TI) technique. The near-field on any arbitrary cylindrical surface can be obtained through the Inverse Fourier Transform (IFT). The far-field can be obtained through the Near-Field Far-Field (NF-FF) transform. The cylindrical TI-FFT algorithm has the advantages of $\mathcal{O}(\mathrm{N}\log_2 \mathrm{N})$ computational complexity for $\mathrm{N} = \mathrm{N}_\phi \times \mathrm{N}_z$ computational grid, small sampling rate (large sampling spacing) and no singularity problem.

1. INTRODUCTION

The planar Taylor Interpolation through FFT (TI-FFT) algorithm introduced before [1] has been shown to be efficient in the computation of narrow-band beam propagation and scattering for the quasi-planar geometry. However, cylinder-like geometry is not uncommon in the electromagnetic engineering, e.g., the input mirror system design [2] for the high- power gyrotron application. In such case, the planar TI-FFT algorithm is not efficient and we have developed the cylindrical TI-FFT to solve the problem.

For the cylindrical geometry, the computation is efficient because the electromagnetic field that is expressed in the cylindrical harmonics can be numerically implemented through the FFT. For the quasi-cylindrical geometry, the FFT can still be used, with the help of the Taylor Interpolation (TI) technique. Fig. 1 shows the scheme used to illustrate the cylindrical TI-FFT algorithm and the time dependence $e^{i\omega t}$ ($i \equiv \sqrt{-1}$)is used in this article.

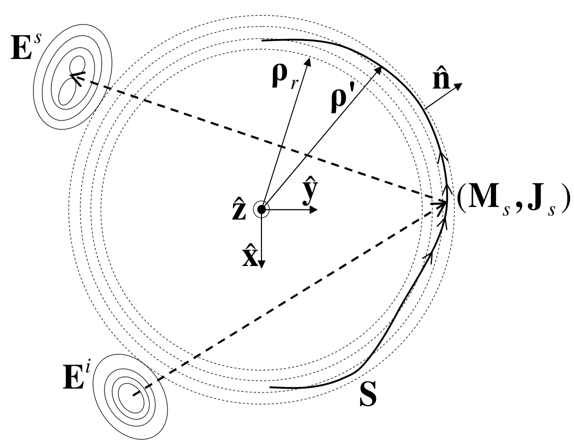

Figure 1: The scattering of the narrow-band beam: the incident field $\mathbf{E}^i$ propagates onto PEC surface S and is back-scattered to $\mathbf{E}^s$. The induced surface currents $(\mathbf{M}_s, \mathbf{J}_s)$ can be obtained through the Method of Moment (MoM) or Physical Optics (PO) approximation if PEC surface S is smooth enough. ρ' is the source coordinate and ρ_r is the radius of the reference cylindrical surface. $\hat{\mathbf{n}}$ is the surface normal to S.

2. THE NEAR-FIELD AND THE FAR-FIELD

In this section, the near-field and the far-field for surface currents ($\mathbf{M}_s$, $\mathbf{J}_s$) are presented within the context of the cylindrical harmonics.

2.1. The Near-field

It can be shown [3] that the vector potential ($\mathbf{F}$, $\mathbf{A}$) due to surface currents ($\mathbf{M}_s$, $\mathbf{J}_s$) for the scattering phenomenon in the region $\rho > \rho'$ can be expressed as

$$\begin{matrix} \mathbf{F}(\mathbf{r}) \\ \mathbf{A}(\mathbf{r}) \end{matrix} = \mathrm{IFT}\left\{ \begin{matrix} \mathbf{f}_m^h \\ \mathbf{g}_m^h \end{matrix} \; H_m^{(2)}(\Lambda\rho) \right\}, \tag{1}$$

$$\begin{matrix} \mathbf{f}_m^h \\ \mathbf{g}_m^h \end{matrix} = \frac{1}{i4} \int\!\!\int_S dS' \; \begin{matrix} \epsilon \mathbf{M}_s(\mathbf{r}') \\ \mu \mathbf{J}_s(\mathbf{r}') \end{matrix} \; H_m^{(1)}(\Lambda\rho) e^{im\phi'} e^{ihz'}, \tag{2}$$

where $H_m^{(1)}(\,\cdot\,)$ and $H_m^{(2)}(\,\cdot\,)$ are Hankel functions of the first kind and the second kind of integer order m respectively. The Inverse Fourier Transform (IFT) has been defined as,

$$\mathrm{IFT}\{\cdot\} = \frac{1}{2\pi} \sum_{m=-\infty}^{\infty} \int_{-\infty}^{\infty} dh \{\,\cdot\,\} \, e^{-im\phi} e^{-ihz}. \tag{3}$$

The electromagnetic field ($\mathbf{E}$, $\mathbf{H}$) is given as

$$\mathbf{E}(\mathbf{r}) = -\frac{1}{\epsilon} \nabla \times \mathbf{F}(\mathbf{r}) - i\omega \mathbf{A}(\mathbf{r}) + \frac{1}{i\omega\epsilon\mu} \nabla' \left[\nabla' \cdot \mathbf{A}(\mathbf{r})\right]. \tag{4}$$

$$\mathbf{H}(\mathbf{r}) = \frac{1}{\mu} \nabla \times \mathbf{A}(\mathbf{r}) - i\omega \mathbf{F}(\mathbf{r}) + \frac{1}{i\omega\epsilon\mu} \nabla' \left[\nabla' \cdot \mathbf{F}(\mathbf{r})\right]. \tag{5}$$

2.2. The Cylindrical Harmonics

The cylindrical TE and TM modes are obtained when the magnetic (electric) surface current has only $\hat{\mathbf{z}}$-component, i.e., $\mathbf{M}_s = \hat{\mathbf{z}}\ \mathrm{M}_{s,z}$ ($\mathbf{J}_s = \hat{\mathbf{z}}\ \mathrm{J}_{s,z}$). From (1)–(5),

$$\mathbf{M}_m^h(\mathbf{r}) = \left[\hat{\boldsymbol{\rho}} \frac{m}{i\rho} H_m^{(2)}(\Lambda\rho) - \hat{\boldsymbol{\phi}} \Lambda \frac{\partial H_m^{(2)}(\Lambda\rho)}{\partial(\Lambda\rho)} \right] e^{-im\phi} e^{-ihz}. \tag{6}$$

$$\mathbf{N}_m^h(\mathbf{r}) = \left[\hat{\boldsymbol{\rho}} \frac{h\Lambda}{ik} \frac{\partial H_m^{(2)}(\Lambda\rho)}{\partial(\Lambda\rho)} - \hat{\boldsymbol{\phi}} \frac{mh}{k\rho} H_m^{(2)}(\Lambda\rho) + \hat{\mathbf{z}} \frac{\Lambda^2}{k} H_m^{(2)}(\Lambda\rho) \right] e^{-im\phi} e^{-ihz}. \tag{7}$$

The electromagnetic field ($\mathbf{E}$, $\mathbf{H}$) can be expressed as the combination of the TE and TM modes,

$$\mathbf{E}(\rho) = \sum_m \left\{ \int_{-\infty}^{\infty} \left[a_m^h \ \mathbf{M}_m^h(\rho) + b_m^h \ \mathbf{N}_m^h(\rho) \right] dh \right\}, \tag{8}$$

$$\mathbf{H}(\rho) = \frac{i}{\eta} \sum_m \left\{ \int_{-\infty}^{\infty} \left[a_m^h \ \mathbf{N}_m^h(\rho) + b_m^h \ \mathbf{M}_m^h(\rho) \right] dh \right\}, \tag{9}$$

$$a_m^h = -\frac{1}{2\pi\epsilon} \mathrm{f}_{m,z}^h, \quad b_m^h = -\frac{iv}{2\pi} \mathrm{g}_{m,z}^h, \tag{10}$$

where $\eta = \sqrt{\frac{\mu}{\epsilon}}$ and $v = \frac{1}{\sqrt{\mu\epsilon}}$ is the electromagnetic wave velocity in the homogeneous medium.

2.3. The Far-field

The far-field can be obtained through the Near-Field Far-Field (NF-FF) transform [4],

$$\mathbf{E}(\mathbf{R}) = -\frac{2k \sin\theta e^{-ikR}}{R} \sum_m i^m e^{-im\phi} \left[\hat{\boldsymbol{\phi}} a_m^h + \hat{\boldsymbol{\theta}} i b_m^h \right], \tag{11}$$

$$\mathbf{H}(\mathbf{R}) = -\frac{2k \sin\theta e^{-ikR}}{\eta R} \sum_m i^m e^{-im\phi} \left[\hat{\boldsymbol{\phi}} i b_m^h - \hat{\boldsymbol{\theta}} a_m^h \right], \tag{12}$$

where $\mathbf{R}$ is the coordinate in the far-field and $R = |\mathbf{R}|$.

3. THE CYLINDRICAL TI-FFT ALGORITHM

For the narrow-band beam and the quasi-cylindrical surface, both the electromagnetic field in (8)–(9) and the modal expansion coefficient in (2) can be expressed in the Taylor series, which facilitates the use of FFT. Due to the similarity, only TE mode will be considered in this article.

3.1. The Electromagnetic Field

Generally, the near-field $\mathbf{E}$ can be expressed in the Taylor series,

$$\mathbf{E}(\rho_r + \delta\rho) = \mathbf{E}(\rho_r) + \sum_{n=1}^{\infty} \frac{1}{n!} \left.\frac{\partial^{(n)}\mathbf{E}}{\partial\rho^{(n)}}\right|_{\rho_r} (\delta\rho)^n, \tag{13}$$

where, ρ_r is the reference cylindrical surface and the Taylor coefficient $\left.\frac{\partial^{(n)}\mathbf{E}}{\partial\rho^{(n)}}\right|_{\rho_r}$ can be expressed in the form of IFT. Take TE mode ($\mathbf{M}_m^h$) as an example, for $\hat{\boldsymbol{\phi}}$-component E_ϕ, from (6) and (8),

$$\mathrm{E}_\phi(\rho) = \mathrm{IFT}\left\{ \frac{\Lambda}{\epsilon} \frac{\partial H_m^{(2)}(\Lambda\rho)}{\partial(\Lambda\rho)} \mathrm{f}_{m,z}^h \right\}, \tag{14}$$

Now, the Taylor coefficient for $\mathrm{E}_\phi(\rho)$ are given as

$$\left.\frac{\partial^{(n)}\mathbf{E}}{\partial\rho^{(n)}}\right|_{\rho_r} = \mathrm{IFT}\left\{ \frac{\Lambda^{n+1}}{\epsilon} \left.\frac{\partial^{(n+1)} H_m^{(2)}(\Lambda\rho)}{\partial(\Lambda\rho)^{(n+1)}}\right|_{\rho_r} \mathrm{f}_{m,z}^h \right\}. \tag{15}$$

Similar argument holds for other electromagnetic field components and TM mode.

3.2. The Modal Expansion Coefficient

Similarly, $H_m^{(1)}(\Lambda\rho')$ in the the modal expansion coefficients ($\mathbf{f}_m^h, \mathbf{g}_m^h$) in (2) can be expanded into the Taylor series,

$$H_m^{(1)}\left(\Lambda\left[\rho_r + \delta\rho'\right]\right) = H_m^{(1)}(\Lambda\rho_r) + \sum_{n=1}^{\infty} \frac{\Lambda^n}{n!} \left.\frac{\partial^{(n)} H_m^{(1)}(\Lambda\rho)}{\partial(\Lambda\rho)^{(n)}}\right|_{\rho_r} (\delta\rho')^n \tag{16}$$

where $\delta\rho' = \rho' - \rho_r$. Now, the modal expansion coefficient in (2) is given as,

$$\begin{matrix}\mathbf{f}_m^h \\ \mathbf{g}_m^h\end{matrix} = \sum_{\triangle S}\sum_{n=0}^{\infty} \mathrm{FT}\left\{ \gamma_m(\Lambda\rho_r) \begin{matrix}\epsilon\tilde{\mathbf{M}}_s(\mathbf{r}') \\ \mu\tilde{\mathbf{J}}_s(\mathbf{r}')\end{matrix} (\delta\rho')^n \right\}\Bigg|_{\triangle S} \tag{17}$$

where the Fourier Transform FT is defined similarly as IFT in (3) and $\triangle S$ is the small surface patch between two adjacent reference cylindrical surfaces; what's more, the following quantities have been defined,

$$\gamma_m(\Lambda\rho_r) = \frac{\pi}{i2} \frac{\Lambda^n \rho'}{n!} \left.\frac{\partial^{(n)} H_m^{(1)}(\Lambda\rho)}{\partial(\Lambda\rho)^{(n)}}\right|_{\rho_r}, \qquad \begin{matrix}\tilde{\mathbf{M}}_s(\mathbf{r}') \\ \tilde{\mathbf{J}}_s(\mathbf{r}')\end{matrix} = \frac{1}{\hat{\mathbf{n}}\cdot\hat{\boldsymbol{\rho}}'} \begin{matrix}\mathbf{M}_s(\mathbf{r}') \\ \mathbf{J}_s(\mathbf{r}')\end{matrix}. \tag{18}$$

$\hat{\mathbf{n}}$ is the surface normal to S.

4. NUMERICAL RESULT

To show the efficiency of the cylindrical TI-FFT algorithm, the direct integration method [1] has been used to make comparison with the cylindrical TI-FFT algorithm. The numerical example used for such purpose is a 110 GHz ($\lambda \sim 2.7$ mm) Fundamental Gaussian Beam (FGB) scattered by a PEC quasi-cylindrical surface with a cosine wave perturbation. The incident FGB is $\hat{\mathbf{x}}$-polarized and propagates at $\hat{\mathbf{z}}$ direction, with symmetrical beam waist radii $w_x = w_y = 8\lambda$. The quasi-cylindrical PEC surface is given as

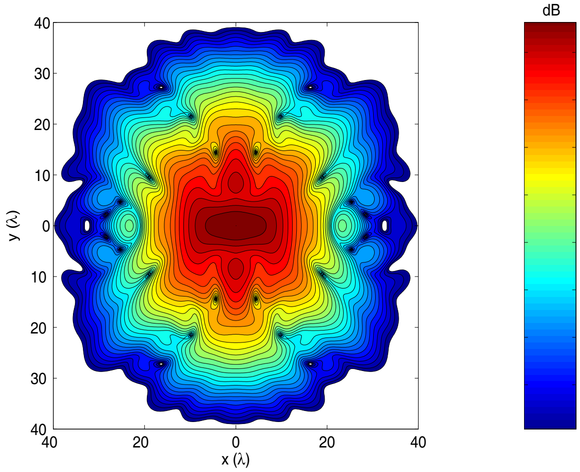

Figure 2: $20\log_{10}|\mathrm{E}_x^s|$.

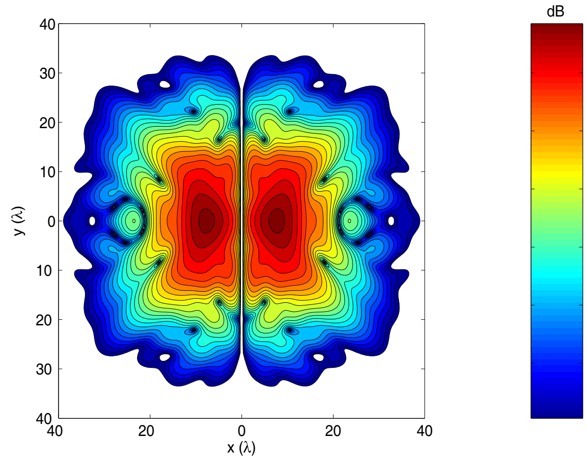

Figure 3: $20\log_{10}|\mathrm{E}_z^s|$.

$$y(x,\,z) \;=\; \sqrt{(80\lambda)^2 - x^2} + 0.1\lambda\cos\left(2\pi\frac{x}{20\lambda}\right)\cos\left(2\pi\frac{z}{20\lambda}\right)$$
$$\rho(x,\,z) = x\cos\phi + y\sin\phi, \quad \phi = \arctan\left[\frac{y}{x}\right] \tag{19}$$

The scattered field $\mathbf{E}^s$ is evaluated on plane $y = 0$ (where the incident FGB starts to propagate). Fig. 2 and Fig. 3 show the magnitude patterns of the x-component E_x^s and the z-component E_z^s of the scattered output field $\mathbf{E}^s$ (y-component E_y^s is small and not shown). The comparison of result obtained from the cylindrical TI-FFT algorithm and that from the direct integration method is given in Fig. 4, for both the magnitude and the real part.

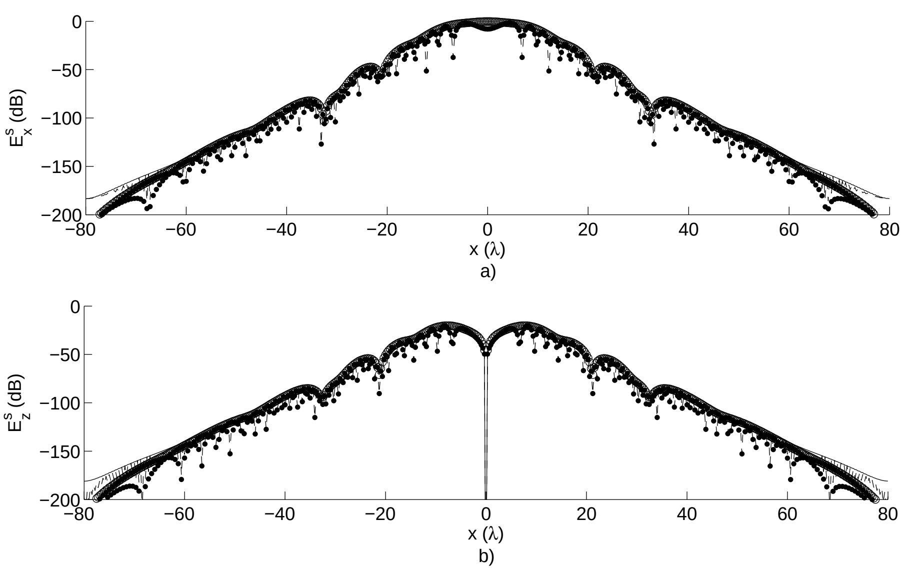

Figure 4: Comparison of the cylindrical TI-FFT algorithm with the direct integration method: a) E_x (dB); and b) E_z (dB). Plots are shown in $\hat{\mathbf{x}}$ direction, across the maximum value point of $|\mathrm{E}_x|$. Solid and dashed lines denote the magnitude and real part obtained from the direct integration method respectively; circles and dots denote the magnitude and real part obtained from the cylindrical TI-FFT algorithm respectively. E_y is small and not shown.

The CPU time for the cylindrical TI-FFT algorithm t_{TI} and the CPU time for the direct integration method t_{DI} are shown in Fig. 5. The ratio $t_{\text{DI}}/\mathrm{t}_{\text{TI}}$ is shown in Fig. 6, for different size of the computational grid ($\mathrm{N} = \mathrm{N}_\phi \times \mathrm{N}_z$). All work was done in Matlab 7.0.1, on a 1.66 GHz PC, with Intel Core Duo and 512 MB RAM.

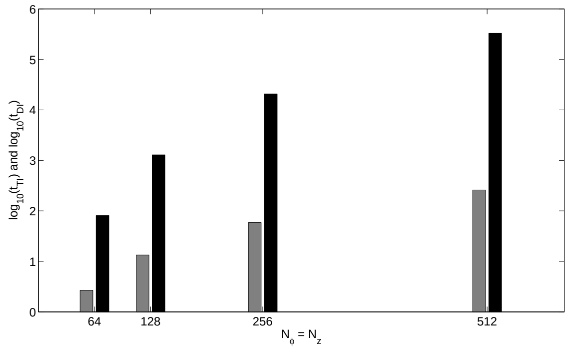

Figure 5: The logarithmic CPU time t_{TI} and t_{DI}.

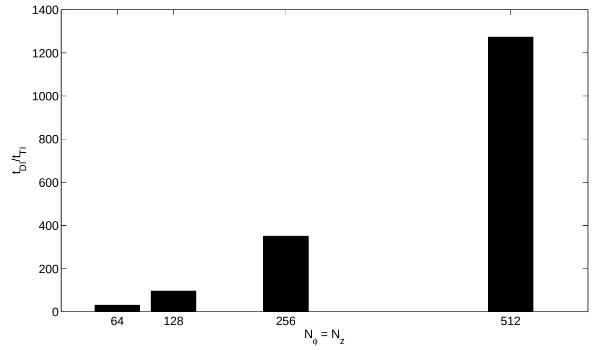

Figure 6: The CPU time ratio of t_{DI}/t_{TI}.

5. CONCLUSION

The cylindrical TI-FFT algorithm for the computation of the electromagnetic wave propagation and scattering has been introduced for the narrow-band beam and the quasi-geometry geometry. The cylindrical TI-FFT algorithm has the complexity of $\mathcal{O}(\mathrm{N}\log_2\mathrm{N})$ for $\mathrm{N} = \mathrm{N}_\phi \times \mathrm{N}_z$ computational grid. The algorithm allows for a low sampling rate (limited the Nyquist sampling rate) and doesn't have the problem of singularity.

ACKNOWLEDGMENT

This work was supported by the U.S. Dept. of Energy under the contract DE-FG02-85ER52122.

REFERENCES

1. Liao, S. and R. J. Vernon, "A new fast algorithm for field propagation between arbitrary smooth surfaces," *The Joint 30th Infrared and Millimeter Waves and 13th International Conference on Terahertz Electronics*, Vol. 2, 606–607, ISBN: 0-7803-9348-1, INSPEC number: 8788764, DOI: 10.1109/ICIMW.2005.1572687, Williamsburg, Virginia, USA, 2005.
2. Liao, S. and R. J. Vernon, "Sub-THz beam-shaping mirror designs for quasi-optical gyrotrons," *Journal of Electromagnetic Waves and Applications*, scheduled for Vol. 21, No. 4, 425–439, 2007.
3. Liao, S., "On the validity of physical optics for narrow-band beam scattering and diffraction from the open cylindrical surface," *PIERS (this conference)*, Mar. 2007.
4. Leach, Jr. W. M. and D. T. Paris, "Probe-compensated near-field measurements on a cylinder," *IEEE Trans. on Antennas and Propagat.*, Vol. 21, Issue 4, 435–445, Jul. 1973.

On the Validity of Physical Optics for Narrow-band Beam Scattering and Diffraction from the Open Cylindrical Surface

Shaolin Liao
Electrical and Computer Engineering, 1415 Engineering Drive, University of Wisconsin
Madison, 53706, USA

Abstract— The exact formulas for the induced electric surface current (in the scattering phenomenon) and the equivalent electric surface current (in the diffraction phenomenon) on the open cylindrical surface due to an arbitrary narrow-band beam have been shown in their closed-form expressions within the context of the cylindrical harmonics, which gives information about the validity of the Physical Optics (PO) approximation. Both the Electric Field Integral Equation (EFIE) and the Magnetic Field Integral Equation (MFIE) are used to find the induced (equivalent) electric surface currents in the context of the cylindrical harmonics. The numerical example of the scattering and diffraction of the Hermite Gaussian beam from the open cylindrical surface is shown. The result is useful for the evaluation of the validity of the PO approximation in the cylinder-like surface.

1. INTRODUCTION

The Physical Optics (PO) approximation has been extensively used as the approximation of the exact solution in many applications, which include microwave imaging, reflector antenna design, and evaluation of Radar Cross Section (RCS) [1–4]. It is helpful to have an analytical formula to predict the behavior of the PO approximation in order to use it effectively. In this article, the exact closed-form expressions will be shown for the induced (equivalent) electric surface currents on the open cylindrical surface, from which the information of the validity of the PO approximation is obtained for the cylinder-like surface. The scheme used to illustrate the problem is given in Fig. 1. The time dependence $e^{i\omega t}$ ($i=\sqrt{-1}$) has been assumed in this article.

2. THE CYLINDRICAL HARMONICS

The cylindrical modal expansion of the vector potential $\mathbf{A}(\mathbf{r})$ for the electric surface current $\mathbf{J}_s(\mathbf{r}')$ on an arbitrary surface in the cylindrical coordinate is given as

$$\begin{aligned}\mathbf{A}(\mathbf{r}) &= \mu\iint_S\left[g(\mathbf{r}-\mathbf{r}')\mathbf{J}_s(\mathbf{r}')\right]dS'\\ &= \frac{\mu}{i8\pi}\iint_S\left[\mathbf{J}_s(\mathbf{r}')\int_{-\infty}^{\infty}H_0^{(2)}\left(\Lambda\left|\boldsymbol{\rho}-\boldsymbol{\rho}'\right|\right)e^{-ih(z-z')}dh\right]dS'\end{aligned} \tag{1}$$

where μ is the permeability of the homogeneous medium. $H_0^{(2)}(\,\cdot\,)$ is Hankel function of the second kind of order 0. The scalar Green's function $g(\,\cdot\,)$ and the transverse wave vector Λ are defined as

$$g(\,\cdot\,)=\frac{e^{-ik|\,\cdot\,|}}{4\pi|\,\cdot\,|},\quad \Lambda=\sqrt{k^2-h^2}. \tag{2}$$

According to the cylindrical addition theorem,

$$H_0^{(2)}\left(\Lambda\left|\boldsymbol{\rho}-\boldsymbol{\rho}'\right|\right)=\sum_{m=-\infty}^{\infty}\begin{cases}H_m^{(2)}(\Lambda\rho)J_m(\Lambda\rho')e^{im(\phi'-\phi)}\Big|_{\rho>\rho'}\\[2ex] J_m(\Lambda\rho)H_m^{(2)}(\Lambda\rho')e^{im(\phi'-\phi)}\Big|_{\rho<\rho'}\end{cases} \tag{3}$$

where $\rho\equiv|\boldsymbol{\rho}|$ is the observation coordinate and $\rho'\equiv|\boldsymbol{\rho}'|$ is the source coordinate. $J_m(\,\cdot\,)$ is Bessel function of the first kind of integer order m and $H_m^{(2)}(\,\cdot\,)$ is Hankel function of the second kind of

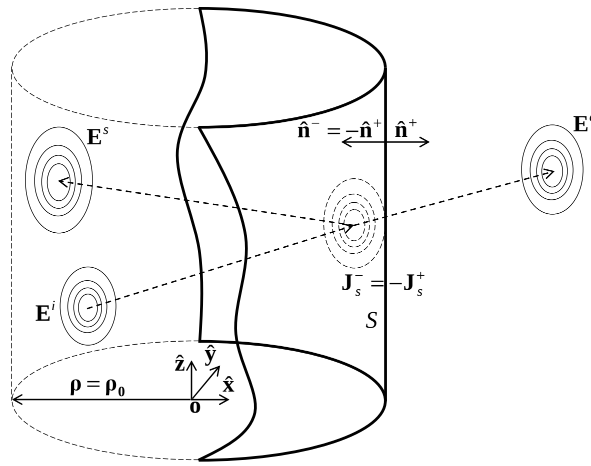

Figure 1: The narrow-band beam scattering and diffraction in the cylindrical geometry: the incident field $\mathbf{E}^i$ propagates onto cylindrical surface S with radius of ρ_0, then it could be back-scattered to $\mathbf{E}^s$ if surface S serves as a PEC scatter, with induced surface current $\mathbf{J}_s^-$; or it may forward-propagate to $\mathbf{E}^d$ if it is a diffraction phenomenon, with equivalent surface current $\mathbf{J}_s^+ = -\mathbf{J}_s^-$. $\hat{\mathbf{n}}^+$ and $\hat{\mathbf{n}}^-$ are the outward and inward unit surface normals to S respectively.

integer order m. Substituting (3) into (1), the cylindrical modal expansion of $\mathbf{A}(\mathbf{r})$ is obtained,

$$
\begin{aligned}
\mathbf{A}_{<}^{>}(\mathbf{r}) &= \mathrm{IFT}\left(\mathbf{g}_{<}^{>}(m,h)\ \begin{matrix} H_m^{(2)}(\Lambda\rho) \\ J_m(\Lambda\rho) \end{matrix}\ \right) \\
\mathbf{g}_{<}^{>}(m,h) &= \frac{\mu}{i4}\iint_S \left[\ \begin{matrix} J_m(\Lambda\rho') \\ H_m^{(2)}(\Lambda\rho') \end{matrix}\ \mathbf{J}_s(\mathbf{r}')e^{i(m\phi'+hz')}\ \right] dS'
\end{aligned}
\tag{4}
$$

where, the the superscript "$>$" denotes $\rho > \rho'$ and the subscript "$<$" denotes $\rho < \rho'$. The Inverse Fourier Transform (IFT) is defined as

$$
\mathrm{IFT}\left(\ \cdot\ \right) = \frac{1}{2\pi}\sum_{m=-\infty}^{\infty}\left\{\int_{-\infty}^{\infty}\left[\left(\ \cdot\ \right)e^{-i(m\phi+hz)}\right]dh\right\}. \tag{5}
$$

The electromagnetic field $(\mathbf{E},\mathbf{H})$ is given as

$$
\mathbf{E}_{<}^{>}(\mathbf{r}) = -i\omega\mathbf{A}_{<}^{>}(\mathbf{r}) + \frac{1}{i\omega\mu\epsilon}\nabla\left[\nabla\cdot\mathbf{A}_{<}^{>}(\mathbf{r})\right], \quad \mathbf{H}_{<}^{>}(\mathbf{r}) = \frac{1}{\mu}\nabla\times\mathbf{A}_{<}^{>}(\mathbf{r}) \tag{6}
$$

3. EXACT FORMULAS FOR INDUCED AND EQUIVALENT ELECTRIC SURFACE CURRENTS

Due to the fact that $\mathbf{J}_s^- = -\mathbf{J}_s^+$ (see Fig. 1), let's consider the scattering phenomenon and express the incident electromagnetic field $(\mathbf{E}^i,\mathbf{H}^i)$ into the cylindrical harmonics,

$$
\mathbf{E}^i(\rho) = \sum_{m=-\infty}^{\infty}\left\{\int_{-\infty}^{\infty}\left[a_m^h\ \mathbf{M}_m^h(\rho) + b_m^h\ \mathbf{N}_m^h(\rho)\right]dh\right\} \tag{7}
$$

$$
\mathbf{H}^i(\rho) = \frac{i}{\eta}\sum_{m=-\infty}^{\infty}\left\{\int_{-\infty}^{\infty}\left[a_m^h\ \mathbf{N}_m^h(\rho) + b_m^h\ \mathbf{M}_m^h(\rho)\right]dh\right\} \tag{8}
$$

$$
\mathbf{M}_m^h(\mathbf{r}) = \left[\hat{\boldsymbol{\rho}}\frac{m}{i\rho}H_m^{(2)}(\Lambda\rho) - \hat{\boldsymbol{\phi}}\Lambda\frac{\partial H_m^{(2)}(\Lambda\rho)}{\partial(\Lambda\rho)}\right]e^{-im\phi}e^{-ihz} \tag{9}
$$

$$
\mathbf{N}_m^h(\mathbf{r}) = \left[\hat{\boldsymbol{\rho}}\frac{h\Lambda}{ik}\frac{\partial H_m^{(2)}(\Lambda\rho)}{\partial(\Lambda\rho)} - \hat{\boldsymbol{\phi}}\frac{mh}{k\rho}H_m^{(2)}(\Lambda\rho) + \hat{\mathbf{z}}\frac{\Lambda^2}{k}H_m^{(2)}(\Lambda\rho)\right]e^{-im\phi}e^{-ihz} \tag{10}
$$

Similarly, express the scattered electromagnetic field $(\mathbf{E}^s, \mathbf{H}^s)$ as

$$\mathbf{E}^s(\rho) = \sum_{m=-\infty}^{\infty} \left\{ \int_{-\infty}^{\infty} \left[c_m^h \ \mathbf{M}_m^h(\rho) + d_m^h \ \mathbf{N}_m^h(\rho) \right] dh \right\} \tag{11}$$

$$\mathbf{H}^s(\rho) = \frac{i}{\eta} \sum_{m=-\infty}^{\infty} \left\{ \int_{-\infty}^{\infty} \left[c_m^h \ \mathbf{N}_m^h(\rho) + d_m^h \ \mathbf{M}_m^h(\rho) \right] dh \right\} \tag{12}$$

Now the induced electric surface current $\mathbf{J}_s^-$ on the cylindrical surface S is given as

$$\begin{aligned} \mathbf{J}_s^-(\rho_0) &= \hat{\mathbf{n}}^- \times \left[\mathbf{H}^i(\rho_0) + \mathbf{H}^s(\rho_0) \right] = \left[\mathbf{H}^i(\rho_0) + \mathbf{H}^s(\rho_0) \right] \times \hat{\boldsymbol{\rho}}_0 \\ &= \frac{i}{\eta} \sum_{m=-\infty}^{\infty} \left\{ \int_{-\infty}^{\infty} \left[\left(a_m^h + c_m^h \right) \mathbf{N}_m^h(\rho_0) \times \hat{\boldsymbol{\rho}}_0 + \left(b_m^h + d_m^h \right) \mathbf{M}_m^h(\rho_0) \times \hat{\boldsymbol{\rho}}_0 \right] dh \right\} \end{aligned} \tag{13}$$

3.1. Electric Field Integral Equation (EFIE)

Let's consider the TM mode ($\mathbf{N}_m^h$ for $\mathbf{E}$ and $\mathbf{M}_m^h$ for $\mathbf{H}$) here. From (9) and (13),

$$\mathbf{J}_s^{-,\text{TM}}(\rho_0) = \hat{\mathbf{z}} \frac{i}{\eta} \sum_{m=-\infty}^{\infty} \left\{ \int_{-\infty}^{\infty} \left(b_m^h + d_m^h \right) \Lambda \left. \frac{\partial H_m^{(2)}(\Lambda\rho)}{\partial(\Lambda\rho)} \right|_{\rho_0} dh \right\} \tag{14}$$

Substituting (14) into (6), the z-component of the scattered electric field $\mathrm{E}_{z,<}^{s,\text{TM}}$ on the cylindrical surface is obtained ($\Lambda_{z,<}^{\text{TM}} \equiv \hat{\mathbf{z}} \cdot \mathbf{A}_<^{\text{TM}}$),

$$\begin{aligned} \mathrm{E}_{<,z}^{s,\text{TM}}(\rho_0) &= -i\omega \left(\frac{\Lambda}{k} \right)^2 \mathrm{A}_{z,<}^{\text{TM}}(\rho_0) \\ &= \frac{\pi\rho_0}{i2k} \sum_{m=-\infty}^{\infty} \left\{ \int_{-\infty}^{\infty} \left(b_m^h + d_m^h \right) \Lambda^3 J_m(\Lambda\rho_0) H_m^{(2)}(\Lambda\rho_0) \left. \frac{\partial H_m^{(2)}(\Lambda\rho)}{\partial(\Lambda\rho)} \right|_{\rho_0} dh \right\} \end{aligned} \tag{15}$$

Note that $\mathrm{E}_{z,<}^{s,\text{TM}}$ is given on the whole cylindrical surface that is just inside (infinitesimally close to) cylindrical surface S, on both the front side and the back side. It can be separated into two parts for the narrow-band beam, which can be seen from the property of Bessel function,

$$J_m(\ \cdot\ ) = \frac{H_m^{(1)}(\ \cdot\ ) + H_m^{(2)}(\ \cdot\ )}{2} \tag{16}$$

The scattered electric field on the front side is thus given as

$$\mathrm{E}_{z,<,f}^{s,\text{TM}}(\rho_0) = \frac{\pi\rho_0}{i4k} \sum_{m=-\infty}^{\infty} \left\{ \int_{-\infty}^{\infty} \left(b_m^h + d_m^h \right) \Lambda^3 H_m^{(1)}(\Lambda\rho_0) H_m^{(2)}(\Lambda\rho_0) \left. \frac{\partial H_m^{(2)}(\Lambda\rho)}{\partial(\Lambda\rho)} \right|_{\rho_0} dh \right\} \tag{17}$$

Now apply the EFIE on the cylindrical surface $\mathrm{E}_{z,<,f}^{s,\text{TM}}(\rho_0) = -\mathrm{E}_z^{i,\text{TM}}(\rho_0)$, from (7) and (17),

$$b_m^h + d_m^h = \frac{2}{\xi} b_m^h, \qquad d_m^h = \left[\frac{2}{\xi} - 1 \right] b_m^h, \qquad \xi \equiv i \frac{\pi}{2} \Lambda\rho_0 H_m^{(1)}(\Lambda\rho_0) \left. \frac{\partial H_m^{(2)}(\Lambda\rho)}{\partial(\Lambda\rho)} \right|_{\rho_0} \tag{18}$$

Note that $\xi \to 1$ for $\rho_0 \to \infty$, which means that $d_m^h \to b_m^h$ and the PO approximation reduces to the exact induced electric surface current.

3.2. Magnetic Field Integral Equation (MFIE)

Let's also take the TM mode ($\mathbf{N}_m^h$ for $\mathbf{E}$ and $\mathbf{M}_m^h$ for $\mathbf{H}$) as an example. From (6) and (14), the ϕ-component of the scattered magnetic field $\mathrm{H}_{\phi,<,f}^{s,\text{TM}}(\rho_0)$ on the front side of the cylindrical surface is found as

$$\mathrm{H}_{\phi,<,f}^{s,\text{TM}}(\rho_0) = \frac{i}{\eta} \sum_{m=-\infty}^{\infty} \left\{ \int_{-\infty}^{\infty} \left[\frac{\xi^*}{2} \left(b_m^h + d_m^h \right) \ \mathbf{M}_m^h(\rho) \right] dh \right\} \tag{19}$$

Now apply the MFIE on the cylindrical surface $\mathrm{H}^{s,\mathrm{TM}}_{\phi,<,f}(\rho_0) + \mathrm{H}^{i,\mathrm{TM}}_{\phi}(\rho_0) = -\mathrm{J}^{-,\mathrm{TM}}_{s,z}(\rho_0)$,

$$b^h_m + d^h_m = \frac{2}{2-\xi^*} b^h_m, \qquad d^h_m = \frac{\xi^*}{2-\xi^*} b^h_m \tag{20}$$

It is not difficult to show that (18) and (20) are equivalent by using the Wronskian relation,

$$H^{(2)}_m(\Lambda\rho)\frac{\partial H^{(1)}_m(\Lambda\rho)}{\partial(\Lambda\rho)} - H^{(1)}_m(\Lambda\rho)\frac{\partial H^{(2)}_m(\Lambda\rho)}{\partial(\Lambda\rho)} = \frac{i4}{\pi\Lambda\rho} \tag{21}$$

3.3. The Induced and Equivalent Electric Surface Currents

Following the similar procedure, the induced electric surface current for the TE mode ($\mathbf{M}^h_m$ for $\mathbf{E}$ and $\mathbf{N}^h_m$ for $\mathbf{H}$) is given as

$$a^h_m + c^h_m = \frac{2}{\xi^*} a^h_m, \qquad c^h_m = \left[\frac{2}{\xi^*} - 1\right] a^h_m \tag{22}$$

Substituting (18) and (22) into (13), the total induced and equivalent electric surface currents are obtained,

$$\mathbf{J}^-_s(\rho_0) = -\mathbf{J}^+_s(\rho_0) = \frac{i2}{\eta}\sum_{m=-\infty}^{\infty}\left\{\int_{-\infty}^{\infty}\left[a^h_m \frac{\mathbf{N}^h_m(\rho_0)\times\hat{\boldsymbol{\rho}}_0}{\xi^*} + b^h_m \frac{\mathbf{M}^h_m(\rho_0)\times\hat{\boldsymbol{\rho}}_0}{\xi}\right] dh\right\} \tag{23}$$

From (23), it is clear that the exact induced and equivalent electric surface currents only deviate from the PO approximation by a factor of $\frac{1}{\xi}$ for TM mode and $\frac{1}{\xi^*}$ for TE mode.

4. NUMERICAL CONFIRMATION: THE HERMITE GAUSSIAN BEAM

The incident Hermite Gaussian beam (TEM_{00} and TEM_{10}) has been used to test the result given in (23). The TEM_{mn} Hermite Gaussian beam is given as

$$\mathbf{E}_{mn} = \hat{\mathbf{z}}\sqrt{\frac{\eta}{\pi 2^{m+n-2} m! n! w_y(x) w_z(x)}}\mathrm{H}_m\left(\sqrt{2}\frac{y}{w_y(x)}\right)\mathrm{H}_n\left(\sqrt{2}\frac{z}{w_z(x)}\right) e^{-\left[y^2\left(\frac{1}{w_y^2(x)}+\frac{ik}{2R_y(x)}\right)+z^2\left(\frac{1}{w_z^2(x)}+\frac{ik}{2R_z(x)}\right)\right]} e^{-i\left[kx-\left(m+\frac{1}{2}\right)\arctan\left(\frac{x}{\mathrm{L}_y}\right)-\left(n+\frac{1}{2}\right)\arctan\left(\frac{x}{\mathrm{L}_z}\right)\right]}, \tag{24}$$

where $\mathrm{H}_{m,n}$ is the Hermite polynomial and the following quantities have been defined,

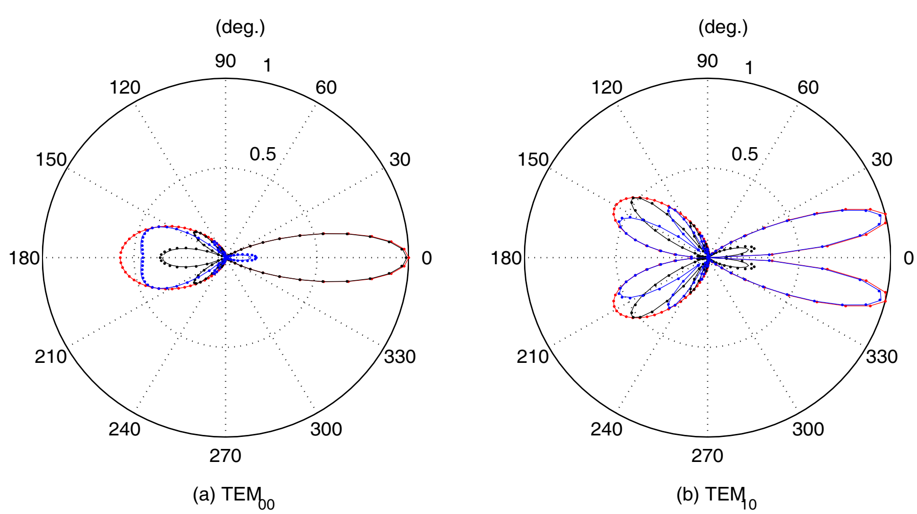

Figure 2: The PO approximation (dots) Vs. result (lines) from MoM: (a) TEM_{00}; and (b) TEM_{10}. Red is for the magnitude; blue is for the real part; and black is for the imaginary part. Results have been normalized.

$$w_\tau(x) = w_{0\tau}\left[1+\frac{x}{\mathrm{L}_\tau}\right]^{\frac{1}{2}}, \qquad R_\tau(x) = x + \mathrm{L}_\tau^2/x, \qquad \mathrm{L}_\tau = \frac{kw_{0\tau}^2}{2}, \qquad \tau = y, z \tag{25}$$

In our numerical computation, both TEM_{00} and TEM_{10} Hermite Gaussian beams are $\hat{\mathbf{z}}$-polarized (TM mode only in the cylindrical coordinate). The symmetrical waist radii have been set as $w_{0y} = w_{0z} = 1\lambda$. The radius of the scattering (diffracting) cylindrical surface is $\rho_0 = 3\lambda$ and the radius of the observation cylindrical surface is $\rho = 20\lambda$.

The scattered electric field E_z^s ($\phi \in \left[\frac{\pi}{2}, \frac{3\pi}{2}\right]$) and the diffracted electric field E_z^d ($\phi \in \left[-\frac{\pi}{2}, \frac{\pi}{2}\right]$) calculated from the PO approximation have been plotted (dots) in Fig. 2, together with the result (lines) obtained from the Method of Moment (MoM). Also, the theoretical induced (equivalent) current given in (23) has been used to calculate the scattered electric field E_z^s and the diffracted electric field E_z^d, which is shown in Fig. 3 (dots), with good agreement with the result from the MoM (lines). All plots are for results on the observation cylindrical surface with radius $\rho = 20\lambda$.

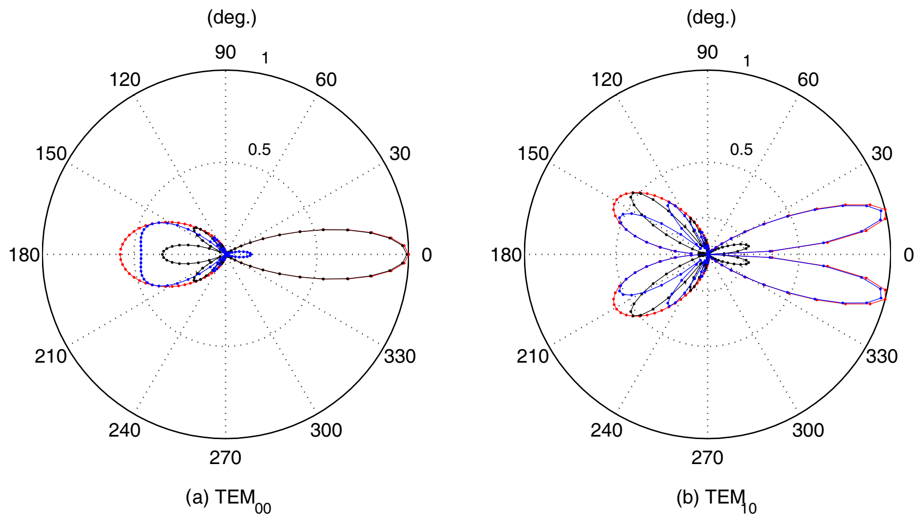

Figure 3: Result (dots) obtained from Eq. (23) Vs. result (lines) from MoM: (a) TEM_{00} and (b) TEM_{10}. Red is for the magnitude; blue is for the real part; and black is for the imaginary part. Results have been normalized.

5. CONCLUSION

The exact formulas for the induced electric surface current in the scattering phenomenon and the equivalent electric surface current in the diffraction phenomenon have been derived, which gives helpful information of the PO approximation in the cylinder-like surface.

ACKNOWLEDGMENT

This work was supported by the U.S. Dept. of Energy under the contract DE-FG02-85ER52122.

REFERENCES

1. Lin, D.-B. and T.-H. Chu, "Bistatic frequency-swept microwave imaging: principle, methodology and experimental results," *IEEE Transactions on Microwave Theory and Techniques*, Vol. 41, No. 5, 855–861, May 1993.
2. Schlobohm, B., F. Amdt, and J. Kless, "Direct PO optimized dual-offset reflector antennas for small earth stations and for millimeter wave atmospheric sensors," *IEEE Transactions on Microwave Theory and Techniques*, Vol. 40, No. 6, 1310–1317, June 1992.
3. Hestilow, T. J., "Simple formulas for the calculation of the average physical optics RCS of a cylinder and a flat plate over a symmetric window around broadside," *IEEE Antennas and Propagation Magazine*, Vol. 42, No. 5, 48–52, Oct. 2000.
4. Liao, S. and R. J. Vernon, "A new fast algorithm for field propagation between arbitrary smooth surfaces," In: *the joint 30th Infrared and Millimeter Waves and 13th International Conference on Terahertz Electronics*, Williamsburg, Virginia, USA, 2005, ISBN: 0-7803-9348-1, INSPEC number: 8788764, DOI: 10.1109/ICIMW.2005.1572687, Vol. 2, 606–607, 2005.

Beam-shaping PEC Mirror Phase Corrector Design

Shaolin Liao

Department of Electrical and Computer Engineering
1415 Engineering Drive, University of Wisconsin, Madison 53706, USA

Abstract— The Perfect Electric Conductor (PEC) mirror phase corrector plays an important role in the beam-shaping mirror system design for Quasi-Optical (QO) mode converter (launcher) in the sub-THz high-power gyrotron. In this article, both the Geometry Optics (GO) method and the phase gradient method have been presented for the PEC mirror phase corrector design. The advantages and disadvantages are discussed for both methods. An efficient algorithm has been proposed for the phase gradient method.

1. INTRODUCTION

The PEC mirror phase corrector is essential to shape the input beam from the QO mode converter (launcher) into the desired Fundamental Gaussian Beam (FGB) in the sub-THz high-power gyrotron [1–6]. Fig. 1 shows the diagram of such beam-shaping mirror system, in which the 4 pieces of PEC mirrors (M_1, M_2, M_3 and M_4) serve as the phase correctors, aiming at shaping the input beam from the QO launcher into the desired FGB output beam. During the iterative beam-shaping mirror system design [1, 6], phase unwrapping is commonly required in the PEC mirror phase corrector design, which can effectively suppress the edge diffraction due to the discontinuities if otherwise the wrapped phase is used. In this article, both the GO method and the phase gradient method are discussed. An FFT-based efficient algorithm is also proposed to speed up the PEC mirror phase corrector design for the phase gradient method. The time dependence $e^{i\omega t}$ is assumed.

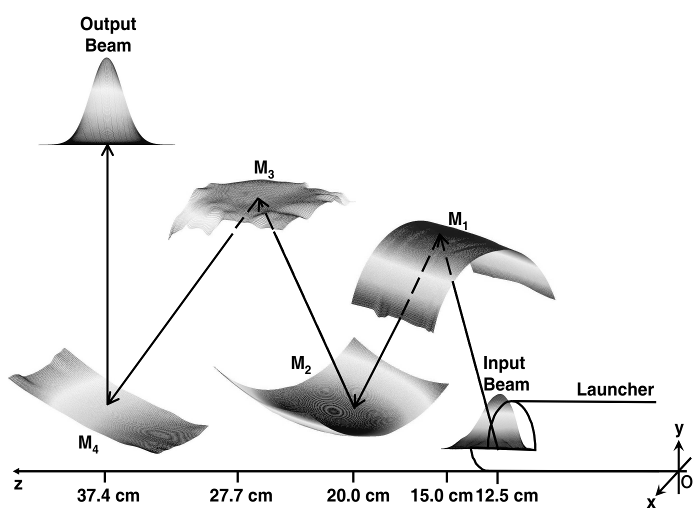

Figure 1: The diagram of the beam-shaping mirror system consisting of 4 pieces of PEC mirrors to shape the input beam from the QO launcher into the desired FGB output beam. The approximate $\boldsymbol{z}$ coordinates of the 4 pieces of PEC mirrors have been marked on $\boldsymbol{z}$ axis.

2. THE PROBLEM OF PHASE UNWRAPPING

The phase correction requires the knowledge of the unwrapped 2-Dimensional (2D) phases of the incident electric field and the reflected electric field (θ^i, θ^r). However, the phase obtained from the electric field $\mathbf{E}$ through $\breve{\theta} = \arctan\left[\frac{\Im(\mathbf{E})}{\Re(\mathbf{E})}\right]$ ($\Re$ and $\Im$ denote the real part and the imaginary part respectively) is the wrapped 2D phase, which contains discontinuities of $2n\pi$ (n is an integer). So, in order to ensure the smoothness of the PEC mirror surface, the wrapped 2D phases ($\breve{\theta}^i$, $\breve{\theta}^r$) must be unwrapped through the 2D phase unwrapping methods [7, 8].

Mathematically, in the ideal situation where there is no residues in the wrapped 2D phase $\check{\theta}$, the discreet phase gradient $\nabla\theta = \nabla\check{\theta}$ (assuming that $\nabla\theta < \pi$) and the 2D phase unwrapping can be expressed as,

$$\theta = \int_C \nabla\check{\theta} \cdot d\mathbf{r} + \theta(\mathbf{r}_0) \tag{1}$$

where, θ denotes the 2D unwrapped phase along the integration path C and r_0 denotes the starting point of the path integration. Note that the unwrapped phase θ obtained through (1) should not depend on the integration path C. However, due to the residues in practice, the discrete phase gradient should be written as $\nabla\check{\theta} = (\nabla g + \nabla\times\mathbf{R})$ and the unwrapped phase θ is obtained as follows,

$$\theta = \int_C (\nabla g + \nabla \times \mathbf{R}) \cdot d\mathbf{r} + \theta(\mathbf{r}_0) \tag{2}$$

From (2), it can be seen that $\nabla\times\mathbf{R} \neq 0$ is caused by the existence of residues and the unwrapped phase θ depends on the integration path C. There are many 2D phase unwrapping algorithms to deal with the residues in the literatures [7, 8]. For example, the path following algorithm (e. g., "quality-guided" method and "mask-cut" method) gives faithful congruent unwrapped phase (with $2n\pi$ difference from the wrapped phase). However, path following algorithm is time-consuming and the unwrapped phase contains many discontinuities due to the existence of residues. Another commonly-used algorithm, the minimum norm method unwraps the wrapped phase by minimizing the r-norm phase difference between the gradients of the wrapped phase and the desired unwrapped phase [8],

$$Q = \sum_X \sum_Z \left[w_x \left| \frac{\partial\theta}{\partial x} - \frac{\partial\check{\theta}}{\partial x} \right|^r + w_z \left| \frac{\partial\theta}{\partial z} - \frac{\partial\check{\theta}}{\partial z} \right|^r \right] \tag{3}$$

where, w_x and w_z are weights for $\hat{\mathbf{x}}$ and $\hat{\mathbf{z}}$ directions respectively. When $r = 2$, it is called the Least Mean Square (LMS) method.

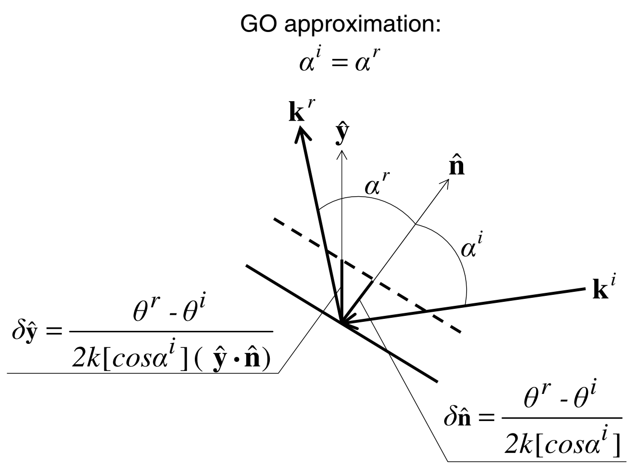

Figure 2: The PEC mirror surface correction in the sub-THz QO regime: $\mathbf{k}^i$ and $\mathbf{k}^r$ are wave vectors for the local incident beam (with incident angle α^i) and the local reflection beam (with reflected angle α^r). $\delta_{\hat{\mathbf{n}}}$ is the PEC mirror surface correction in $\hat{\mathbf{n}}$ direction and $\delta_{\hat{\mathbf{y}}}$ is the PEC mirror surface correction in $\hat{\mathbf{y}}$ direction.

3. THE GO METHOD

In the sub-THz QO regime, it is reasonable to assume that the intensity or magnitude of the electric field is locally constant and the local phase change can be evaluated through the GO method, as shown in Fig. 2. For fixed computational grid given on x-z plane (in favor of FFT operation), $\delta_{\hat{\mathbf{y}}}$ is preferred, which is rewritten as follows ($\cos\alpha^i = \frac{\mathbf{k}^i \cdot \hat{\mathbf{n}}}{k}$),

$$\delta_{\hat{\mathbf{y}}} = \frac{\delta\theta}{2\left(\mathbf{k}^i \cdot \hat{\mathbf{n}}\right)\left(\hat{\mathbf{y}} \cdot \hat{\mathbf{n}}\right)}, \quad \delta\theta = \theta^r - \theta^i \tag{4}$$

There are two approaches to calculate the local wave vector $\mathbf{k}$ (incident wave vector $\mathbf{k}^i$ and reflected wave vector $\mathbf{k}^r$), i. e., 1) the Poynting vector approach; and 2) the phase gradient approach. The Poynting vector approach assumes that the local beam propagates in the direction given by the Poynting vector,

$$\mathbf{k} \propto \mathbf{E} \times (\mathbf{H})^* \propto \mathbf{E} \times \nabla \times (\mathbf{E})^* \tag{5}$$

The phase gradient approach approximates the local wave vector as the gradient of the phase,

$$\mathbf{k} \propto \nabla\theta \tag{6}$$

It is not difficult to show that the two approaches are equivalent in the far-field limit.

4. THE PHASE GRADIENT METHOD

Instead of (4), the expression of the PEC mirror surface correction $\delta_{\hat{\mathbf{y}}}$ in the phase gradient method is given as

$$\delta_{\hat{\mathbf{y}}} = \frac{\delta\theta}{\nabla(\delta\theta)} = \frac{\delta\theta}{\nabla\theta^r - \nabla\theta^i} \tag{7}$$

The phase gradient $\nabla\theta$ for the electric field $\mathbf{E} = |\mathbf{E}|e^{i\theta}$ can be found as

$$\begin{aligned} \nabla\mathbf{E} &= \nabla\left\{|\mathbf{E}|e^{i\theta}\right\} \\ &= \nabla\{|\mathbf{E}|\}\, e^{i\theta} + |\mathbf{E}|\nabla\left\{e^{i\theta}\right\} \\ &= \left[\nabla\{|\mathbf{E}|\} + i|\mathbf{E}|\nabla\theta\right] e^{i\theta} \end{aligned} \tag{8}$$

$$\begin{aligned} \rightarrow \nabla\theta &= \Im\left[\frac{\nabla\mathbf{E}}{\mathbf{E}}\right] = \Im\left[\nabla \ln \mathbf{E}\right] \\ \rightarrow \nabla\{|\mathbf{E}|\} &= \Re\left[\nabla\mathbf{E}e^{-i\theta}\right] \end{aligned} \tag{9}$$

From (8) and (9), the expression for $\nabla(\delta\theta)$ in (7) is obtained,

$$\nabla(\delta\theta) = \Im\left[\frac{\nabla\mathbf{E}^r}{\mathbf{E}^r} - \frac{\nabla\mathbf{E}^i}{\mathbf{E}^i}\right] = \Im\left[\nabla \ln \frac{\mathbf{E}^r}{\mathbf{E}^i}\right] \tag{10}$$

5. AN EFFICIENT ALGORITHM FOR PHASE GRADIENT METHOD

By slicing the PEC mirror phase corrector into many subdomains, as shown in Fig. 3, the FFT can be used [3, 6] to compute the electric field $\mathbf{E}$ and it's derivatives,

$$\mathbf{E}(y) = \mathrm{IFT}\left\{\mathbf{F}(k_x,k_z)e^{-ik_y y}\right\}, \quad \mathbf{F}(k_x,k_z) = \mathrm{FT}\left\{\mathbf{E}(y=0)\right\} \tag{11}$$

$$\frac{\partial\mathbf{E}(y)}{\partial v} = \mathrm{IFT}\left\{-ik_v\mathbf{F}(k_x,k_z)e^{-ik_y y}\right\}, \quad v = x, z \tag{12}$$

where, the Fourier Transform (FT) and the Inverse Fourier Transform (IFT) are defined as follows,

$$\mathrm{FT}\{\cdot\} \equiv \frac{1}{2\pi}\int_{-\infty}^{\infty} dx e^{ik_x x}\int_{-\infty}^{\infty}\{\cdot\}\, e^{ik_z z}dz \tag{13}$$

$$\mathrm{IFT}\{\cdot\} \equiv \frac{1}{2\pi}\int_{-\infty}^{\infty} dk_x e^{-ik_x x}\int_{-\infty}^{\infty}\{\cdot\}\, e^{-ik_z z}dk_z \tag{14}$$

The wrapped phase difference $\delta\check{\theta} = \left(\check{\theta}^i - \check{\theta}^r\right)$ is obtained from (11). Due to similarity, only x-component $\hat{\mathbf{x}}\mathrm{E}_x$ is considered here,

$$\delta\check{\theta}_x = \arctan\left[\frac{\Im\left(\mathrm{IFT}\left\{\ \mathrm{F}_x^r(k_x,k_z)e^{-ik_y y}\right\}\right)}{\Re\left(\mathrm{IFT}\left\{\ \mathrm{F}_x^r(k_x,k_z)e^{-ik_y y}\right\}\right)}\right] - \arctan\left[\frac{\Im\left(\mathrm{IFT}\left\{\ \mathrm{F}_x^i(k_x,k_z)e^{-ik_y y}\right\}\right)}{\Re\left(\mathrm{IFT}\left\{\ \mathrm{F}_x^i(k_x,k_z)e^{-ik_y y}\right\}\right)}\right] \tag{15}$$

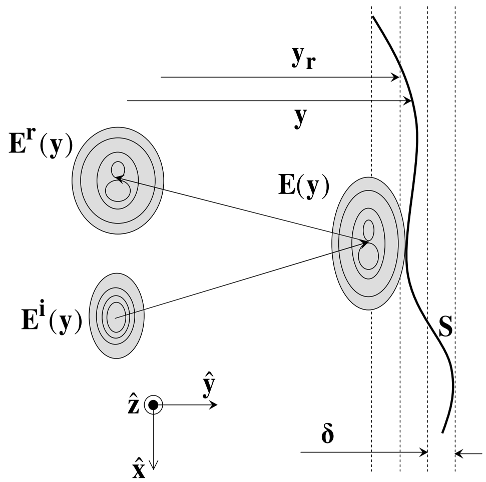

Figure 3: Illustration of the FFT-based efficient algorithm for the phase gradient method. $\mathbf{E}^i$ and $\mathbf{E}^r$ are the incident electric field and reflected electric field respectively. S is the PEC mirror phase corrector. y is the coordinate of the PEC mirror phase corrector and y_r is the coordinate of the slicing reference plane. δ is the spacing between two adjacent slicing reference planes.

With the help of (11)–(14), the gradient of the phase difference $\nabla(\delta\theta_x)$ on the slicing reference plane y_r in Fig. 3 can be obtained from (10),

$$\nabla(\delta\theta_x) = \nabla\left(\delta\check{\theta}_x\right) = \Re\left[\frac{\mathrm{IFT}\left\{\mathbf{k}\ \mathrm{F}_x^i(k_x,k_z)e^{-ik_y y}\right\}}{\mathrm{IFT}\left\{\ \mathrm{F}_x^i(k_x,k_z)e^{-ik_y y}\right\}} - \frac{\mathrm{IFT}\left\{\mathbf{k}\ \mathrm{F}_x^r(k_x,k_z)e^{-ik_y y}\right\}}{\mathrm{IFT}\left\{\ \mathrm{F}_x^r(k_x,k_z)e^{-ik_y y}\right\}}\right] \tag{16}$$

To obtain the PEC mirror surface correction $\delta_{\hat{\mathbf{y}}}$ through (7), $\delta\check{\theta}_x$ has to be unwrapped. Here, an FFT-based phase unwrapping algorithm is presented for the r-norm minimum problem given in (3). Suppose that $\delta\theta_x$ can be expressed in the Fourier series,

$$\delta\theta_x = \mathrm{IFT}\{f(k_x,k_z)\} \tag{17}$$

Then

$$\frac{\partial(\delta\theta_x)}{\partial v} = \mathrm{IFT}\{-ik_v f(k_x,k_z)\}, \quad v = x, z \tag{18}$$

To obtain $\delta\theta_x$, the Fourier coefficient $f(k_x,k_z)$ is chosen to minimize the cost function Q given in (3), with $w_x = w_z = 1$. For LMS method where $r = 2$, it can be shown that $f(k_x,k_z)$ takes the following form,

$$\frac{Q(f+\delta f) - Q(f)}{\delta f} = 0 \to f(k_x,k_z) = i\frac{k_x \mathrm{FT}\left\{\nabla\left(\delta\check{\theta}_x\right)\cdot\hat{\mathbf{x}}\right\} + k_z \mathrm{FT}\left\{\nabla\left(\delta\check{\theta}_x\right)\cdot\hat{\mathbf{z}}\right\}}{k_x^2 + k_z^2} \tag{19}$$

Now, the PEC mirror surface correction $\delta_{\hat{\mathbf{y}}}$ can be obtained from (7), with the help of (16)–(19).

6. DISCUSSION

It has been shown that both the GO method and the phase gradient method can be used in the PEC mirror phase corrector design. Both methods have their advantages and disadvantages, e. g., the GO method is simple and easy to use, but it is time-consuming; the phase gradient method is efficient (due to the use of FFT), but it's application is limited by the sampling theorem. In general, the GO method is suitable for problems of significant side lobes; and the phase gradient method is suitable for problems of smooth phase front with negligible side lobes.

7. CONCLUSIONS

In this article, both the GO method and the phase gradient method have been presented for the PEC mirror phase corrector design. The FFT-based efficient algorithm has been proposed for the phase gradient method to speed up the design procedure.

ACKNOWLEDGMENT

This work was supported by the U.S. Dept. of Energy under the contract DE-FG02-85ER52122.

REFERENCES

1. Cao, R. and R. J. Vernon, "Improved performance of three-mirror beam-shaping systems and application to step-tunable converters," *The 30th Int. Conf. on Infrared and Millimeter Waves*, 616–617, Williamsburg, Virginia, USA, Sep. 19–23, 2005.
2. Perkins, M. P. and R. J. Vernon, "Iterative design of a cylinder-based beam-shaping mirror pair for use in a gyrotron internal quasi-optical mode converter," *The 29th Int. Conf. on Infrared and Millimeter Waves*, Karlsruhe, Germany, Sep. 27–Oct. 1, 2004.
3. Liao, S.-L. and R. J. Vernon, "A new fast algorithm for field propagation between arbitrary smooth surfaces," *The Joint 30th Infrared and Millimeter Waves and 13th International Conference on Terahertz Electronics*, Vol. 2, 606–607, Williamsburg, Virginia, USA, 2005, ISBN: 0-7803-9348-1, INSPEC number: 8788764, DOI: 10.1109/ICIMW.2005.1572687.
4. Liao, S.-L. and R. J. Vernon, "The near-field and far-field properties of the cylindrical modal expansions with application in the image theorem," *The Joint 31st Infrared and Millimeter Waves and 14th International Conference on Terahertz Electronics*, Shanghai, China, IEEE MTT, Catalog Number: 06EX1385C, ISBN: 1-4244-0400-2, Sep. 18–22, 2006.
5. Liao, S.-L. and R. J. Vernon, "The cylindrical Taylor-interpolation FFT algorithm," *The Joint 31st Infrared and Millimeter Waves and 14th International Conference on Terahertz Electronics*, Shanghai, China, IEEE MTT, Catalog Number: 06EX1385C, ISBN: 1-4244-0400-2, Sep. 18–22, 2006.
6. Liao, S.-L. and R. J. Vernon, "Sub-THz beam-shaping mirror designs for quasi-optical mode converter in high-power gyrotrons", *J. Electromagn. Waves and Appl.*, scheduled for Vol. 21, No. 4, 425–439, 2007.
7. Gerchberg, R. and W. Saxton, "A practical algorithm for the determination of phase from image and difraction plane pictures," *Optik*, 237–246, Vol. 35, No. 2, 1972.
8. Ghiglia, D. and M. Pritt, *Two-dimensional Phase Unwrapping Theory*, Algorithms, and Software, John Wiley & Sons, New York, 1998.

A Novel Time-domain Integration Method for Transient Analysis of Nonuniform Transmission Lines

M. Tang, J. F. Mao, and X. C. Li

Department of Electronic Engineering, Shanghai Jiao Tong University, Shanghai, China

Abstract— This paper presents a precise time-step integration method for transient analysis of lossy nonuniform transmission lines. The spatial discretization in this method is the same to the finite difference time domain (FDTD) algorithm. However, in order to eliminate the Courant condition constraint, the precise integration method is utilized in the time-domain calculation. It gives quasi-exact solutions in time domain for the spatial discretized Telegrapher's equations. Since the exponential matrix is calculated precisely, large time step can be adopted in the integration process to achieve accurate results efficiently. A numerical example is presented to demonstrate the accuracy and stability of the proposed method.

1. INTRODUCTION

The finite difference time domain (FDTD) method is widely used in solving various kinds of electromagnetic problems. It is also a common way to obtain transient responses of lossy multiconductor transmission lines (MTL) [1, 2]. Due to its simplicity and flexibility, it doesn't need to decouple MTL in the modeling and is straightforward to be used in nonuniform transmission line cases. In recent past, it has been successfully extended in analyzing transmission lines with frequency-dependent parameters by means of recursive convolutions [3]. Despite its virtues, this method is restricted by the Courant condition to ensure its stability. Thus, both spatial and temporal segments must be small enough to achieve satisfying accuracy, which in turn leads to time-consuming calculation.

In this paper, a precise time-step integration method for the transient analysis of lossy MTL is presented. In contrast to the FDTD method, this approach only discretizes the spatial derivatives in the Telegrapher's equations, while the temporal derivatives remain unchanged. In this way, a semi-discrete model can be obtained. Subsequently, this model is solved using the precise integration method [4]. Unlike FDTD, the spatial and temporal step in this approach is not constrained by the Courant condition. Large time steps can be used in the integration process. Since the exponential matrix is calculated precisely, it can give quasi-exact solutions for nonuniform MTL in the time domain. Similar to the FDTD algorithm, the process of decoupling is not needed in this method. Thus, MTL with arbitrary coupling status can be easily dealt with. A numerical example is presented to illustrate the application of the proposed method, and the results are compared with those obtained with the FDTD method.

2. DEVELOPMENT OF THE SEMI-DISCRETE MODEL

Consider N-coupled transmission lines represented by the Telegrapher's equations as

$$\frac{\partial}{\partial x}\boldsymbol{V}(x,t) = -\boldsymbol{R}(x)I(x,t) - \boldsymbol{L}(x)\frac{\partial}{\partial t}\boldsymbol{I}(x,t) \tag{1}$$

$$\frac{\partial}{\partial x}\boldsymbol{I}(x,t) = -\boldsymbol{G}(x)\boldsymbol{V}(x,t) - \boldsymbol{C}(x)\frac{\partial}{\partial t}\boldsymbol{V}(x,t) \tag{2}$$

where $\boldsymbol{R}(x)$, $\boldsymbol{L}(x)$, $\boldsymbol{C}(x)$, and $\boldsymbol{G}(x)$ are the per-unit-length (p.u.l.) parameter matrices of transmission lines.

It is assumed that the lines are divided into M segments with equal length Δx. As the FDTD algorithm, we interlace the $M+1$ voltage points $(\boldsymbol{V}_1, \boldsymbol{V}_2, \ldots, \boldsymbol{V}_{M+1})$, and the M current points $(\boldsymbol{I}_1, \boldsymbol{I}_2, \ldots, \boldsymbol{I}_M)$. The current points at two ends are $\boldsymbol{I}_0$ and $\boldsymbol{I}_{M+1}$. Each voltage and adjacent current solution point is separated by $\Delta x/2$. Next, the spatial derivatives of voltage and current points are approximated by central differences. At the two end points, forward and backward difference schemes are used. The resulting semi-discrete equations can be given in the matrix form:

$$\frac{d\boldsymbol{X}}{dt} = \boldsymbol{H}\boldsymbol{X} + \boldsymbol{F} \tag{3}$$

3. COMPUTATION WITH TIME-STEP INTEGRATION METHOD

The terminal networks of the transmission lines are usually characterized using the state-variable formulation, which is compatible to the form of (3). Therefore, the state-variable equations can be easily combined into (3), and the resulting equation is given by

$$\frac{d\boldsymbol{X}_1}{dt} = \boldsymbol{H}_1\boldsymbol{X}_1 + \boldsymbol{F}_1 \tag{4}$$

where $\boldsymbol{X}_1$, $\boldsymbol{H}_1$ and $\boldsymbol{F}_1$ are the modified matrices of (3). Note that only the variables associated with the inputs of circuits consist in $\boldsymbol{F}_1$ for linear terminal networks. The solution of equation (4) can be written as

$$\boldsymbol{X}_1(t) = \exp\left(\boldsymbol{H}_1 \cdot t\right)\boldsymbol{X}_1(0) + \int_0^t \exp\left[\boldsymbol{H}_1 \cdot (t-\zeta)\right]\boldsymbol{F}_1(\zeta)d\zeta \tag{5}$$

Assuming that $\boldsymbol{F}_1$ is linear within a time step (t_j, t_{j+1}), where $t_j = j\tau(j = 0, 1, 2, \ldots)$. It can be written as

$$\boldsymbol{F}_1 = \boldsymbol{r}_0 + \boldsymbol{r}_1\left(t - t_j\right) \tag{6}$$

where $\boldsymbol{r}_0$ and $\boldsymbol{r}_1$ are known vectors. It is worthy noting that the inputs of high-speed circuits are generally characterized in the piecewise-linear form (e. g., trapezoidal pulses), this assumption is therefore quite reasonable for the practical application. Thus, (5) can be transformed into the time-step integration form:

$$\boldsymbol{X}_1^{j+1} = \boldsymbol{T}\left[\boldsymbol{X}_1^j + \boldsymbol{H}_1^{-1}\left(\boldsymbol{r}_0 + \boldsymbol{H}_1^{-1}\boldsymbol{r}_1\right)\right] - \boldsymbol{H}_1^{-1}\left(\boldsymbol{r}_0 + \boldsymbol{H}_1^{-1}\boldsymbol{r}_1 + \boldsymbol{r}_1 \cdot \tau\right) \tag{7}$$

where $\boldsymbol{X}_1^j = \boldsymbol{X}_1(j\tau)$ and $\boldsymbol{T} = \exp\left[\boldsymbol{H}_1 \cdot \tau\right]$. Consequently, when the initial value is given, $\boldsymbol{X}_1$ can be calculate in this recursive way. Note that unlike the time-difference approximation implemented in the FDTD algorithm, (7) gives a quasi-exact solution provided that we can calculate the exponential matrix $\boldsymbol{T}$ at a precise value. Details on the precise computation of the exponential matrix are given in [4].

4. NUMERICAL RESULTS

This example is a two-coupled nonuniform transmission line system as shown in Fig. 1. The input voltage source is a 1-V pulse with a 0.5-ns rise/fall time and a width of 3 ns.

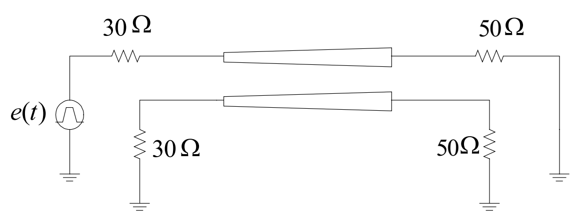

Figure 1: Circuit of nonuniform transmission lines.

The transient response at far end of the active line is depicted in Fig. 2. It is assumed that the nonuniform lines are divided into 20 segments in the length and the time step is chosen to be 10 ps in both the proposed method and FDTD method. The results are described by the dotted line and solid line, respectively. For the proposed method, the CPU time on Pentium IV PC (3.0 GHz) is 0.08 s. In order to improve the computational efficiency, the time step should be enlarge. In this method, the time step will not affect the accuracy of results. Accurate results with $\tau = 250$ ps ('star' symbol) is also depicted in Fig. 2. The CPU time is then reduced to 0.015 s. As an extreme scenario, we can even choose the time step equal to the rise time of the input voltage (500 ps). By contrast, constrained by the Courant condition, the results of the FDTD method become not convergent as the time step increases (e. g., $\tau = 20$ ps in this example).

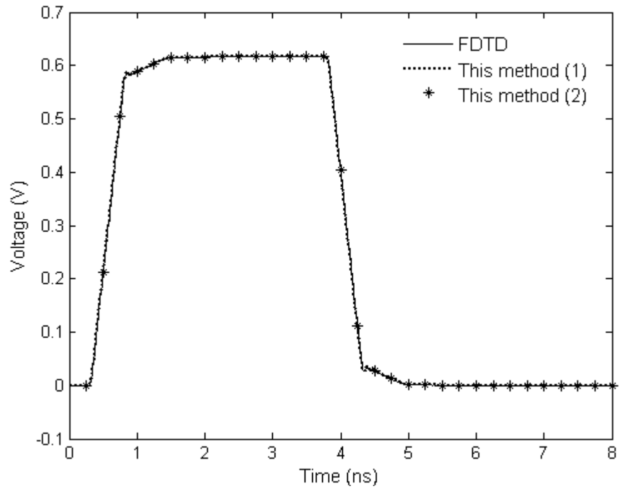

Figure 2: Transient response at far end of the active line.

5. CONCLUSIONS

In this paper, a precise time-step integration method is presented for solving the transient response of lossy transmission lines. The method doesn't need to decouple MTL and is straightforward to be used in modeling nonuniform MTL as it dose for the uniform cases. The stability and accuracy of the results is independent of the size of time step, which contributes to the high efficiency of the proposed method.

ACKNOWLEDGMENT

This work was supported by National Science Fund for Creative Research Groups (60521002), Shanghai AM Foundation (0401), and the Grant of Doctoral Research Foundation from the Ministry of education, China (20040248034).

REFERENCES

1. Paul, C. R., "Incorporation of terminal constraints in the FDTD analysis of transmission lines," *IEEE Trans. Electromagn. Compat.*, Vol. 36, No. 2, 388–399, 1996.
2. Roden, J. A., C. R. Paul, W. T. Smith, and S. D. Gedney, "Finite-Difference, time-domain analysis of lossy transmission lines," *IEEE Trans. Electromagn. Compat.*, Vol. 38, No. 1, 15–24, 1996.
3. Coperich, K. M., J. Morsey, V. Okhmatovski, A. C. Cangellaris, and A. E. Ruehli, "Systematic development of transmission line models for interconnects with frequency-dependent losses," *IEEE Trans. Microwave Theory Tech.*, Vol. 49, No. 10, 1677–1685, 2001.
4. Zhong, W. X. and F. W. Williams, "A high precise time step integration method," *J. Mech. Eng. Sci.*, Vol. 208, 427–430, 1994.

Building Optimal Statistical Models with the Parabolic Equation Method

M. Le Palud

CREC St-Cyr Telecommunications Department (LESTP), Guer, France

Abstract— In this paper, we present a new application of electromagnetic propagation modeling methods like Parabolic Equation (PE) algorithms: these tools can be used to obtain optimal statistical propagation models i. e., best-fitted statistical model for a given propagation environment. Statistical propagation models are widely used because of their convenience to make predictions that are valid for different types of propagation environments and operation conditions. However their accuracy is often questionable because they are obtained either empirically with a limited amount of experimental data collected in few propagation environments or deduced using rough and general theory. As a result the model doesn't square satisfactorily with real operation. Our goal is to improve the preceding process by designing a method that would give an optimized statistical model (OSM) for a given environment. The process that leads to the OSM for a particular application involves several steps that are described in detail in the paper. Sample results are also given and comparisons between OSM and standard statistical models are discussed.

1. INTRODUCTION

For several years strong interest has been shown for the study of ground propagation and transmission in urban as well as in rural and forested environments. An accurate characterization of the propagation channel is needed in digital communication systems as well as in RADAR systems in order to minimize error rates and to optimize system costs. In previous works, we have described a method, based on a Parabolic Equation (PE) algorithm, which allows complete computation of characteristics of stationary determinist channels. We have applied this method in various types of situations, including canonical problems and real radio links over irregular terrain with or without vegetal coverage. However, we have observed that a fully deterministic approach gives often deceiving results since it is most of the time almost impossible in practice to fully implement the features of real propagation environments, considering its high complexity (i. e., for instance: inaccurate localization and characterization of vegetation and man-made obstacles). A more basic and widely used approach is based on the use of standard statistical/empirical propagation models which gives the advantages of more simplicity and convenience but also lowers significantly prediction accuracy targets because standard statistical models will not correctly reflect the actual propagation environments.

In this paper we propose an intermediate approach that is based on the following idea: the goal is to build statistical models that fit at best the actual propagation environments by using deterministic modeling tools.

The first part of the paper gives a general presentation of standard statistical/empirical models. The second part of the paper gives a description of the approach used to build optimized statistical models (OSM). This is illustrated with sample results and also with comparisons and discussions in the third part before some conclusions.

2. STANDARD STATISTICAL MODELS

Statistical models are mainly used for path loss prediction. They are usually elaborated using significant amount of experimental data, collected during long and costly campaigns, together with some theoretical considerations. Some other models that give field distribution predictions or correlation laws for random and/or time-dependent channels may also be ranked among statistical models (i. e., for example, Rayleigh and Rice distributions for random channel).

Statistical models are dedicated to be used with restricted types of propagation environments and operational conditions but this context isn't precisely defined which may lead to important deviations. This last point is illustrated with Fig. 1 where three models (EGLI, ITS and Modified Plane Earth) used for terrestrial propagation over weakly undulating terrain with sparse vegetation are compared. It can be noticed that important discrepancies exist between predicted values of path loss and also between rates of increase with range.

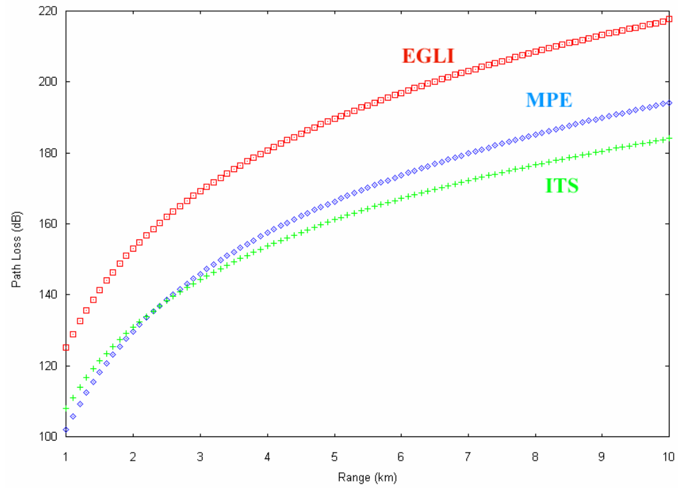

Figure 1: Plots of path loss versus range for 3 standard statistical models (EGLI, ITS and Modified Plane Earth) used for terrestrial propagation over weakly undulating terrain with sparse vegetation ($f = 50$ MHz).

Another important point, which is illustrated on Fig. 2, is that statistical models may be incorporated in various ways inside a modeling strategy. In level-2, the model will replace the real environment with an "effective" flat ground takes globally into account both vegetation coverage and terrain irregularities while statistical models can be used at each step of multiple point-to-point propagation modeling (i. e., for example knife-edge diffraction algorithm) in level-1.

This level-1 approach can give very efficient propagation prediction tools; it is notably used by the well-known TIREM software [1].

Considering Fig. 1 plots, it can be concluded that standard statistical models generally misestimate the lack of knowledge and the uncertainties of propagation environments. This means consequently that the propagation channel is often underutilized and that things will be improved if the model is optimized for the actual propagation environment.

3. BUILDING AN OPTIMIZED STATISTICAL MODEL (OSM)

In order to correct the shortcomings of standard statistical models mentioned above, we propose the following approach to obtain optimized statistical models (OSM) i. e., models that fit at best the actual propagation environments by handling electromagnetic propagation with deterministic tools.

3.1. Parabolic Equation Algorithm

Our choice has been to use a Parabolic Equation (PE) algorithm as the "heart" of the method that's to say as the piece of software that handles electromagnetic propagation. The PE method [2] is a full-wave method used for solving some continuous-wave propagation problems in acoustics and electromagnetism and, in particular, ground propagation of radiowaves over irregular terrain. One of the main limitations of the method is the fact that back scattering is entirely neglected, only one-way propagation off the transmitter is taken into account. The PE equation itself applies to a field function $u(x, z)$, where x is range and z is height, which is related to the amplitude of the horizontal component of the magnetic field (TM polarization case) or of the electric field (TE polarization case). This equation allows approximate computation of the field in the conditions mentioned above when the amplitude is a slow-varying function of range. In its simplest form, it can be written as:

$$\frac{\partial u}{\partial x} = -\frac{1}{2jk}\left[\frac{\partial^2 u}{\partial z^2} + k^2\left(n^2 - 1\right)\right] \tag{1}$$

Our PE algorithm has been tested in canonical CW situations and its results have been compared with exact solutions with good agreement. We have also achieved computations for links over real irregular rural and forested terrain and we have made comparisons with experimental data, obtaining satisfactory agreement.

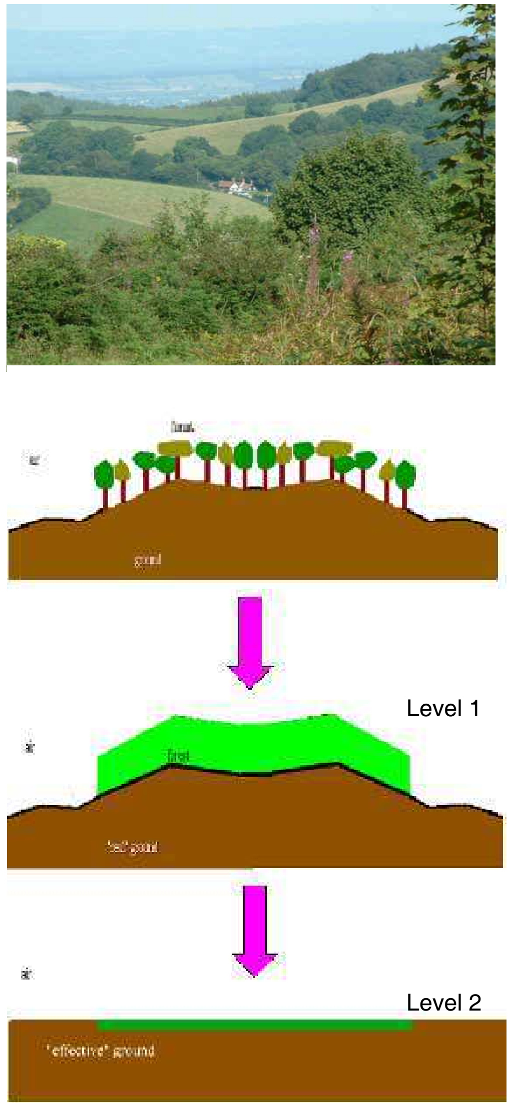

Figure 2: This diagram illustrates different levels of complexity in terrestrial propagation modeling using statistical models.

3.2. OSM Processing

Three steps are necessary to create an optimized statistical model. The global flowchart of the process is summarized on Fig. 3. The first step, which is often the trickiest and the most difficult part of the job, consists in replacing the actual propagation environment, which is generally randomly defined, by an optimal set of deterministic ones that is its statistical equivalent (i. e., a set of possible realizations of terrain and troposphere that gives the same statistical averages, standard deviations, etc. of observable electromagnetic properties). Of course this equivalent set is a theoretical limit and is out of reach in practice but the idea is to obtain a reasonably sized set, sufficiently close to that limit. In order to build an optimized statistical model, one must carefully see that all specific features of the actual terrain are faithfully reflected in this optimal set. The main useful tools at this stage are Monte Carlo techniques and statistical processing.

During the second step of the process, deterministic propagation model is iterated for each element of the previous optimal set and for all required values of the parameters (i. e., frequency, transmitter height, etc.).

Last, statistical processing is performed to obtain the desired results that may be fitted to simple algebraic functions of the parameters: this gives the final product of the OSM procedure.

3.3. Sample Results

We show sample results in order to illustrate the interests of our approach. First of them concern path loss predictions for radio links with geometry shown in Fig. 4: transmitting and receiving

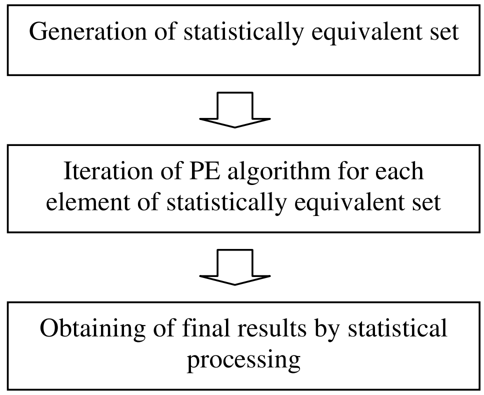

Figure 3: Global flowchart for OSM processing.

antennas are located above the ground surface which presents sinusoidal irregularities of period L and peak-to-peak amplitude H. In our present computations, L was the only random parameter and was supposed to be uniformly distributed on an interval of width $\Delta L = 300\,\text{m}$ around the central value L_c.

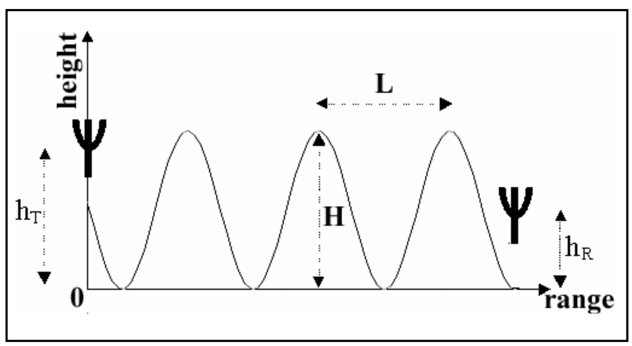

Figure 4: Geometry of radio links for sample results.

A 70 MHz frequency and corresponding standard values of electromagnetic constants for dry ground were taken for the computation. It can be observed in Fig. 5 that global tendencies of OSM plots and also of Modified Plane Earth model are rather close to each other but that noticeable deviations exist between the 4 plots. These results also demonstrate the sensitivity of OSM results to parameters of propagation environments, the most influent parameters being here the heights of antennas and terrain undulation amplitude.

4. SAMPLE COMPARISONS

Experimental path loss data for CW radio link at 61 MHz have been collected between fixed 6mhigh transmitter and mobile 4.7 m-high receiver. The terrain of the experiments was weakly undulating and covered with sparse vegetation. A statistically equivalent set for the terrain was generated following the process described in Fig. 3; for reasons of simplicity, we presumed sinusoidal modulation of ground height versus range (see Fig. 4) for each element of the set and uniform distribution of random parameters. Rough estimations of terrain parameters give: $L_c = 500\,\text{m}$ (mean value of L) $\Delta L = 300\,\text{m}$ and similarly for H, which was also treated as a random parameter $H_c = 75\,\text{m}$ (mean value of H) $\Delta H = 25\,\text{m}$. The 2 continuous curves on Fig. 6 correspond to max and min path loss values in the statistically equivalent set at a given range; they are separated by a gap of the order of 20dB. The global tendency of the experiments and of the 2 curves is found to fit rather well. It can also be observed that most of the experimental dots are located inside the region delimited by these 2 curves, which means that the obtained statistically equivalent set represents rather accurately the actual propagation environment.

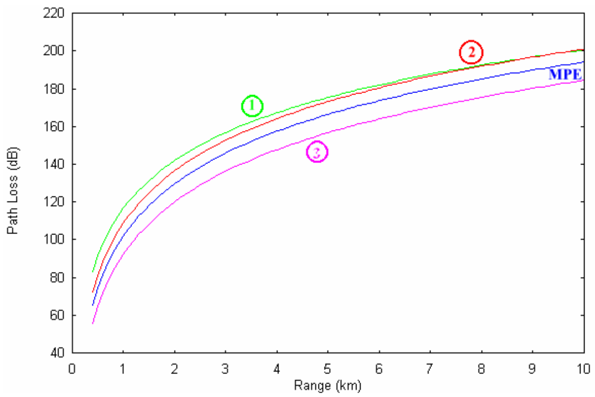

Figure 5: Plots of path loss versus range: plot 1: OSM $h_R = h_T = 0\,\text{m}$ $H = 8\,\text{m}$ $L_c = 500\,\text{m}$ plot 2: OSM $h_R = h_T = 0\,\text{m}$ $H = 8\,\text{m}$ $L_c = 700\,\text{m}$ plot 3: OSM $h_R = h_T = H = 8\,\text{m}$ $L_c = 500\,\text{m}$ blue line: modified plane earth model.

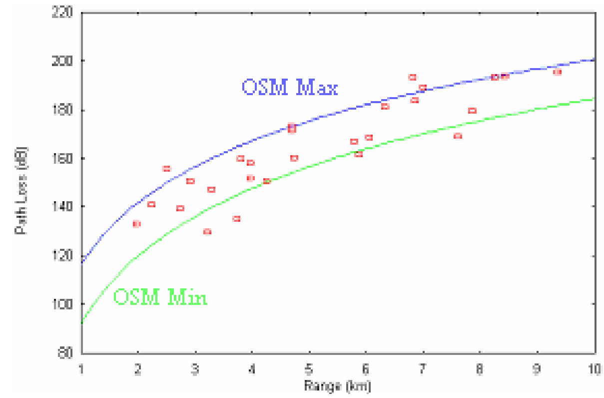

Figure 6: Path loss versus range; red dots are experimental data; upper blue curve and lower green curve give respectively max and min path loss values in the statistically equivalent set at a given range ($f = 61\,\text{MHz}$).

5. CONCLUSION

In this paper, we have presented a novel application of electromagnetic propagation modeling methods algorithms like the PE algorithm: these tools can be used to obtain optimal statistical propagation models i.e. bestfitted statistical model for a given propagation environment. The process that leads to the OSM for a particular application involves several steps that have been described and illustrated with sample results. Comparisons between OSM and standard statistical models have been discussed. We have also displayed some results and comparisons focussed on CW radio propagation in rural environment that showed good agreement with experimental data. We will shortly apply this method to obtain better modeling of radio channels in this type of environment with application to OFDM modulated transmissions. We will also soon be able to obtain results with a hybrid model that mixes OSM together with deterministic processing, following the same approach as the well-known TIREM software [1].

REFERENCES

1. Eppink, D. and W. Kuebler, *TIREM/SEM Handbook*, Department of Defense, Electromagnetic Compatibility Analysis Center ECAC-HDBK-93-076, U. S., Mar. 1994.
2. Barrios, A. E., "A terrain parabolic equation model for propagation in the troposphere," *IEEE Trans. on Ant. and Prop.*, Vol. 42, No. 1, 90–98, 1994.

Echo Extraction Method for a Ground Penetrating Radar

Yiwei He and Hiroshi Mitsumoto
Osaka Electro-Communication University, 18-8 Hatus-cho, Neyagawa, 572-8530, Japan

Zhongquan Ren
Xi'an University of Science and Technology, 58 Yantazhonglu, 710054, China

Abstract— The dielectric permittivity of the ground and the radius of a buried cylindric pipe can be estimated from the echo profile of a ground penetrating radar by using pattern recognition technique. In the practical detection, the echo profile of a specific cylindric pipe is usually mixed with the reflection from some nearby objects. In this research, the echo profile of a specific cylindric pipe is extracted from GPR image base on F-K migration method and its inverse transform. Some numerical simulations are carried out to show the validity of the proposed method.

1. INTRODUCTION

The ground penetrating radar(GPR) has been studied and developed to detected the buried objects such as water and gas pipes, electric cables, historic ruins and so on. Different from the conventional radar, the targets of GPR are buried in an inhomogenous lossy medium, and a GPR is expected to be able to estimate sharps of the targets as well as their locations. The efforts have been made to improve the resolution of GPR system by developing wideband antennas and imaging algorithms.

The estimation of the dielectric constant of the ground is another hard problem in GPR. Some attempts have been made to estimate the dielectric constant and the radius of a cylindric pipe from the echo profile of GPR by using pattern recognition technique [1]. It is noted that the precision of the estimation is very sensitive to the quality of the echo profile. In the practical detections, the echo profile of a specific cylindric pipe is mixed with the reflections from some nearby objects. In this research, the echo profile of a specific cylindric pipe is extracted base on F-K migration method [2] and its inverse transform.

2. THEORY

Figure 1 is the geometry of a GPR. $u(x, y, t)$ is the scattering electromagnetic wave by buried objects, whereas $u(x, 0, t)$ means the scattering electromagnetic wave on the ground surface. $u(x, 0, t)$ can be measured with a receiving antenna moving along the ground surface. An ideal 2D echo image $u(x, 0, t)$ from a single cylindric pipe is a hyperbola like curve, however, because it widely

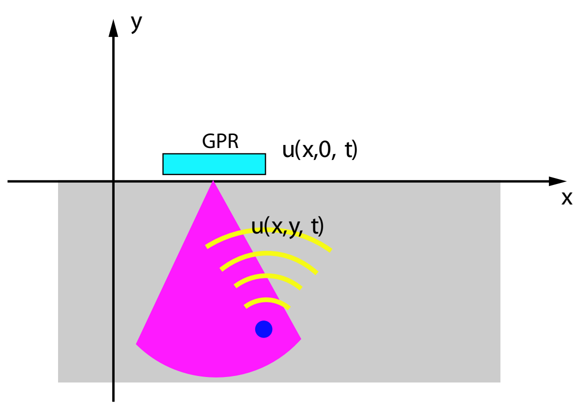

Figure 1: The geometry of the problem.

spreads in a practical 2D echo image of a GPR, the echo profile usually is mixed with the reflections of other nearby buried objects. In order to separate the scattering wave of individual buried objects, a 2D spatial distribution of the scattering electromagnetic wave $u(x, y, t)$ is firstly deduce from $u(x, 0, t)$, then, it is migrated to the initial state. A concentrated distribution of the scattering wave is available with this F-K migration method. For convenience of the explanation of the inverse F-K migration transform, a brief principle of F-K migration is shown hereafter.

It is well know that the scattering electromagnetic wave must be satisfied the following wave equation,

$$\frac{\partial^2 u}{\partial x^2}+\frac{\partial^2 u}{\partial y^2}-\frac{1}{v^2}\frac{\partial^2 u}{\partial t^2}=0 \tag{1}$$

where, v is the light velocity in the ground. A 2D Fourier transform of above equation with respect to x and t gives a following result,

$$\frac{\partial^2 U(\xi,y,\omega)}{\partial y^2}+\left(\frac{\omega^2}{v^2}-\xi^2\right)U(\xi,y,\omega)=0 \tag{2}$$

where, $U(\xi,y,\omega)$ is a 2D Fourier transform of scattering electromagnetic wave $u(x,y,t)$ with respect to x and t. Above differential equation is a standard second-order homogeneous differential equation and its solution is given as follows,

$$U(\xi,y,\omega)=\exp\left(jy\sqrt{\frac{\omega^2}{v^2}-\xi^2}\right)U(\xi,0,\omega) \tag{3}$$

where, $U(\xi,0,\omega)=U(\xi,y,\omega)|_{y=0}$ can be obtained by Fourier transform of the scattering wave $u(x,0,t)$ that is measured on the ground surface. An initial state of the scattering wave is given by an inverse Fourier transform of above equation. The result is shown as fellows,

$$u(x,y,0)=\frac{1}{(2\pi)^2}\iint\exp\left(jy\sqrt{\frac{\omega^2}{v^2}-\xi^2}\right)U(\xi,0,\omega)\exp(j\xi x)d\xi d\omega \tag{4}$$

If a short pulse is used as a transmitting signal, 2D image $u(x,y,0)$ represents the reflection area on the buried object. Because the velocity of light is unknown, a roughly estimated velocity is usually substituted in the F-K migration computation.

In a practical migration computation, a variable transform is substituted into above equation, and fast Fourier transform is performed in order to reduce processing time as follows,

$$\eta = \sqrt{\frac{\omega^2}{v^2}-\xi^2} \tag{5}$$

$$u(x,y,0) = \frac{1}{(2\pi)^2}\iint\frac{1}{\sqrt{1+\frac{\xi^2}{\eta^2}}}U\left(\xi,0,v\eta\sqrt{1+\frac{\xi^2}{\eta^2}}\right)\exp(j(\xi x+\eta y))d\xi d\eta \tag{6}$$

With above imaging processing, the scattering wave from the individual buried object are well separated in spatial domain. The scattering wave of a specific buried object can be extracted easily by an appropriately designed spatial window function as shown in Equation 7. In this research, a circulare Hanning window is utilized.

$$u'(x,y,0)=u(x,y,0)w\left(\sqrt{(x-x_0)^2+(y-y_0)^2}\right),\qquad w(r)=\begin{cases}\frac{1}{2}\left(1+\cos\pi\frac{r}{r_0}\right) & r\le r_0\\ 0 & r>r_0\end{cases} \tag{7}$$

where, $u'(x,y,0)$ is extracted scattering wave, (x_0,y_0) and r_0 are the center coordinate and the radius of the window function, respectively.

The reconstruction of a extracted echo profile is an inverse process of F-K migration. Taking an inverse Fourier transform of Equation 6, following results is available,

$$U'(\xi,0,\omega)=\frac{1}{\sqrt{1-\frac{\xi^2v^2}{\omega^2}}}\tilde{u}'\left(\xi,\sqrt{\frac{\omega^2}{v^2}-\xi^2}\right) \tag{8}$$

where,

$$\tilde{u}'(\xi,\eta)=\iint u'(x,y,0)\exp(-j(\xi x+\eta y))dxdy \tag{9}$$

The extracted echo profile $u'(x,0,t)$ is a Fourier transform of $U'(\xi,0,\omega)$ that is given by Equation 8.

3. NUMERICAL SIMULATIONS

Figure 2 shows the model of numerical simulation. Three cylindric metal pipes are buried in the ground with depths of 0.8 m, 1.0 m and 1.2 m, and their diameter are 10 cm, 20 cm and 10 cm, respectively. The interval of neighboring pipes is 50 cm. Fig. 3 is the image of buried objects computed by F-K migration method. Fig. 4 is an example of the extraction of a specific buried object. Figs. 5(a)–(c) show the results of reconstructed profiles of three buried pipes. Fig. 5(d) shows the original radar echo profile.

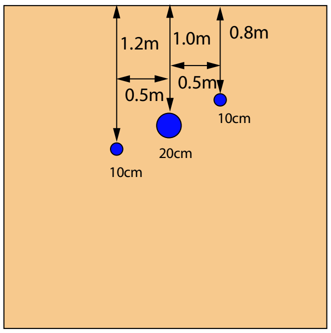

Figure 2: Model of simulation.

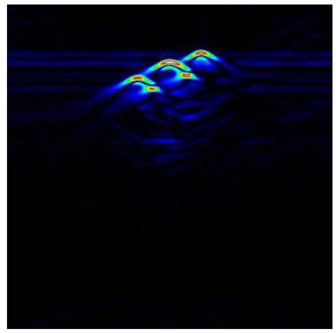

Figure 3: Image of F-K migration.

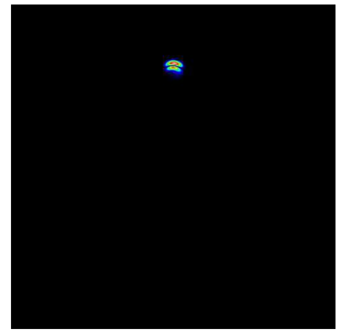

Figure 4: Extracted Image.

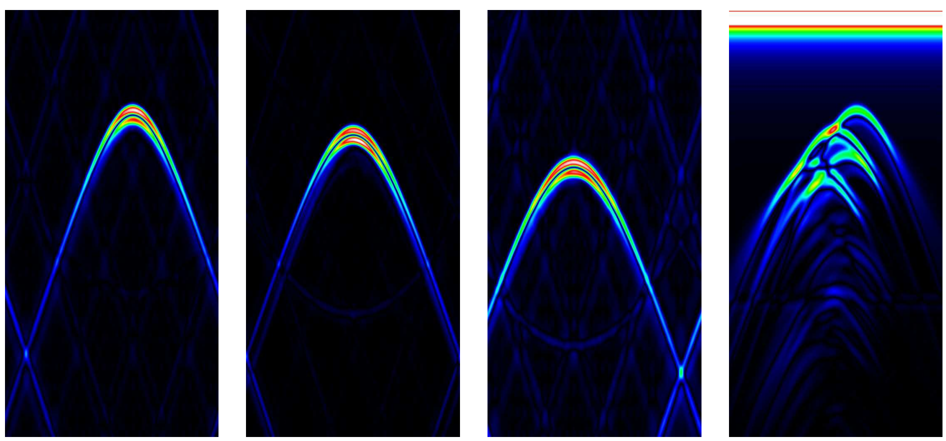

(a) (b) (c) (d)

Figure 5: Echo profile of buried objects.

4. CONCLUSIONS

The extraction of GPR echo for a specific target is proposed based F-K migration method and its inverse transform. Some numerical experiments are carried out to show the validity of the method. The estimation of the permittivity and the radius of buried cylindric pipe from the extracted echo profile will be verified in the future works.

REFERENCES

1. Masaru, M., H. Mitsumoto, and M. Kominami, "Aperture estimation of the underground pipes by ellipse estimation from ground penetrating radar image," Technical Report of IEICE, Vol. 103, No. 300, 1–5, 2003.
2. Stolt, R. H., "Migration by Fourier transform," *Geophisics*, Vol. 43, No. 1, 23–48, 1978.

Reaction Sintering Process for Improving the Microwave Dielectric Properties of $Ba_2Ti_9O_{20}$ Materials

Ya-Ju Chu and I-Nan Lin
Department of Physics, Tamkang University, Tamsui 251, Taiwan, China

Abstract— The effect of processing parameters on the characteristics of the reaction-sintered $Ba_2Ti_9O_{20}$ materials was investigated. The characteristics of the A-series samples, which were prepared from $2BaTiO_3$+$7TiO_2$ mixture, vary markedly with the pre-reacting process, whereas those of the B-series samples, which were prepared from $BaTi_4O_9$+$BaTi_5O_{11}$ mixture, are in sensitive to this process. The possible explanation is that the B-series mixture forms the $Ba_2Ti_9O_{20}$ Hollandite-like phase in one step, which is much simpler than the direct sintering of A-series mixture. The best microwave dielectric properties obtained are $K = 38.2$ and $Q \times f = 36,000$ for B-series $Ba_2Ti_9O_{20}$ materials, which were pre-reacted at 1000℃ for 6 h and sintered at 1410℃ for 4 h by "one-step densification processes".

$Ba_2Ti_9O_{20}$ phase was first reported by Jonker and Kwestroo [1] in BaO-TiO_2-SnO_2 ternary system and was observed to possess marvelous microwave dielectric properties, including high dielectric constant and large quality factor, by O'Bryan et al. [2]. However, the reported results are quite controversial, which is mainly due to the difficulty in forming single phase Hollandite-like structured $Ba_2Ti_9O_{20}$ material. Secondary phases, such as $BaTi_4O_9$ or $BaTi_5O_{11}$, are observed to form preferentially in the calcinations of $BaCO_3$-TiO_2 mixture [3–6] that hinder the formation of Hollandite-like phase for the $Ba_2Ti_9O_{20}$ phase. In this paper, nano-sized starting powders were used to enhance the reaction kinetics and the reaction-sintering technique was adopted to simplify the densification process. How such a non-conventional synthesizing process influences the characteristics of the $Ba_2Ti_9O_{20}$ materials will be described and the possible mechanism will be discussed.

The $Ba_2Ti_9O_{20}$ materials were synthesized via the conventional mixed oxide process, using nano-sized $BaTiO_3$ (~ 50 nm) and anatase TiO_2 (~ 50 nm) as starting materials. Two types of mixture were used for preparing the $Ba_2Ti_9O_{20}$ samples. In A-series materials, $2BaTiO_3$ and $7TiO_2$ powders were mixed thoroughly, using ball milling technique. The B-series materials used the $BaTi_4O_9$ and $BaTi_5O_{11}$ mixture as starting materials, which were pulverized using 3-dimensional milling (3DM, Model 2C, Willy A Bachofen AG, Switzerland) technique, where the $BaTi_4O_9$ and $BaTi_5O_{11}$ powders were first prepared by calcining the $BaTiO_3$+$3TiO_2$ and $BaTiO_3$+$4TiO_2$ mixture at 1000℃/4 h. The $2BaTiO_3$+$7TiO_2$ (A-series) or $BaTi_4O_9$+$BaTi_5O_{11}$ (B-series) powder mixtures were pelletized and then sintered directly, that is, the temperature was increased slowly (3℃/min) to 1000℃, held for 0–12 h, which is designated as pre-reaction process. The temperature was then directly increased again (3℃/min) to $1300 \sim 1410$℃, soaked for 4 h and then cooled slowly (2℃/min), viz. the samples were directly sintered without experiencing the calcinations process. The microstructure of the sintered samples was examined using scanning electron microscopy (Jeol 6700F). The crystal structure of the samples was examined using x-ray diffractometry (Rigaku D/max-II). The density of the sintered materials was measured using Archimedes method. The microwave dielectric constant (K) and quality factor ($Q \times f$) of the $Ba_2Ti_9O_{20}$ samples were measured using a cavity method at 7–8 GHz [7].

Figures 1(a) and 1(b) show the variation of microwave dielectric constant (K) and quality factor ($Q \times f$), respectively, for the A-series materials, indicating that these characteristics of the samples vary markedly with the processing parameters. Generally, the microwave dielectric constand (K) increases monotonically with sintering temperature and reached a K-value higher than 38 for those sintered at a temperature higher than 1300℃/4 h, provided that the samples were pre-reacted at 1000℃ for sufficient long ($t_r > 6$ h) during the heating process. The K-value of the samples pre-reacted at 1000℃ for too short period ($t_r < 3$ h) is appreciably smaller ($K < 36$). The microwave qualify factor ($Q \times f$) of the samples vary with the pre-reaction process even more markedly. The best properties achieved are dielectric constant $K = 38$ and qualify factor $Q \times f = 29,200$ GHz, which were obtaineded for the samples pre-reacted at 1000℃ for 6–12 h and sintered at 1350℃ for 4 h.

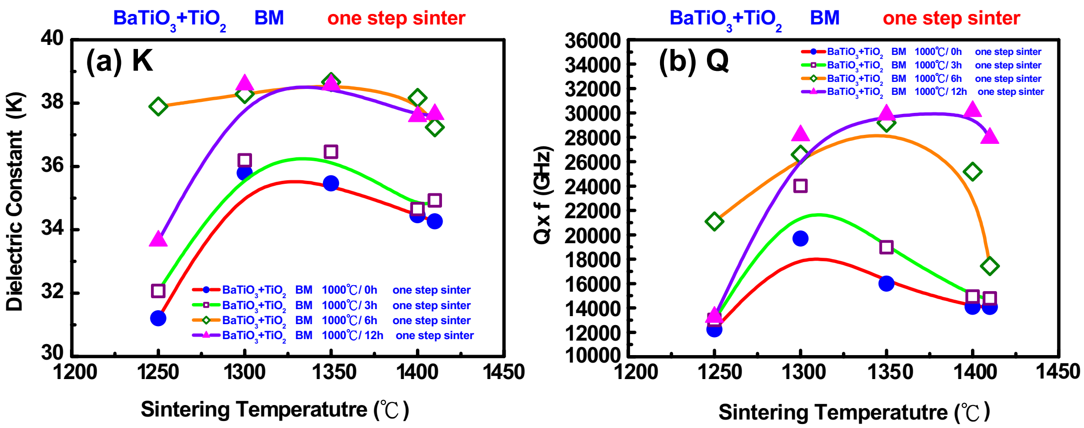

Figure 1: The characteristics of the A-series $Ba_2Ti_9O_{20}$ materials sintered by "one-step densification routes": (a) microwave dielectric constant, K, and (b) microwave dielectric quality factor, Q; where the pellets made of $2BaTiO_3$+$7TiO_2$ mixture were pre-reacted at 1000℃ for 0–12 h and then sintered at 1250 $\sim$ 1400℃ for 4 h.

SEM micrographs in Fig. 2 reveals that, when sintered at 1350℃/4 h, increasing the pre-reaction time interval at 1000℃ improves markedly the uniformity of the granular structure for the materials. For the samples experiencing no pre-reacting process ($t_s = 0$ h, samples A_0, Fig. 2(a)), the microstructure is extremely complicated. There exists abnormally grown extra-large rod-shaped grains about hundreds of micron in size, in addition to the small rod-shaped grains ($30 \times 10\,\mu$m)

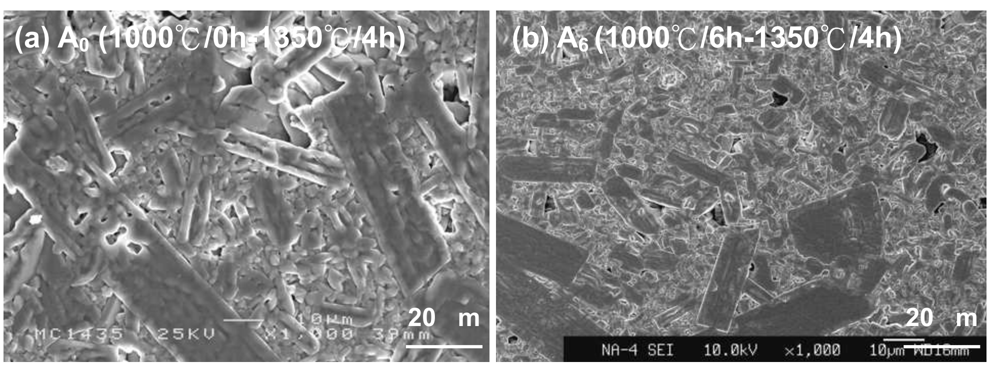

Figure 2: SEM micrographs of the A-series $Ba_2Ti_9O_{20}$ materials sintered by "one-step densification routes"; where the pellets made of $2BaTiO_3$+$7TiO_2$ mixture were pre-reacted at 1000℃ for (a) 0 h, A_0 samples, and (b) 6 h, A_6 samples and then sintered at 1350℃ for 4 h.

and equi-axed grains about ($2\,\mu$m). The number density and size of the abnormally grown grains decrease as the pre-reacting period increases. For the samples experienced 1000℃/6 h pre-reacting process (sample A_6, Fig. 2(b)), only the rod-shaped grains about $10 \times 5\,\mu$m in size co-exist with the equi-axed grains ($\sim 2\,\mu$m in size) and there is no extra-large rod-shaped grains. Fig. 3(a) shows that pure Hollandite-like phase was obtained for the materials, regardless of the sintering temperature, when pre-reacted at 1000℃ for long enough period (> 6 h), whereas Fig. 3(b) indicates that for those pre-reacted at 1000℃ for too short period (< 3 h), the diffraction peaks were pronouncedly broaden, implying that the phase transformation process for the formation of Hollandite-like phase has not been completed.

It is apparent that improving the homogeneity of the powder mixture and simplifying the reaction among the constituents in the mixture during sintering process in necessary to improve the homogeneity of the granular structure for the $Ba_2Ti_9O_{20}$ materials, so as to improve the microwave dielectric properties of these materials. For this purpose, $BaTi_4O_9$+$BaTi_5O_{11}$ mixture was used to replace for the $2BaTiO_3$+$2TiO_2$ mixture as starting materials for preparing the $Ba_2Ti_9O_{20}$ materials. Moreover, 3-dimensional milling technique (3DM, Model 2C, Willy A Bachofen AG, Switzerland) was adopted for pulverizing the mixtures into submicron size ($\sim 0.8\,\mu$m), which is

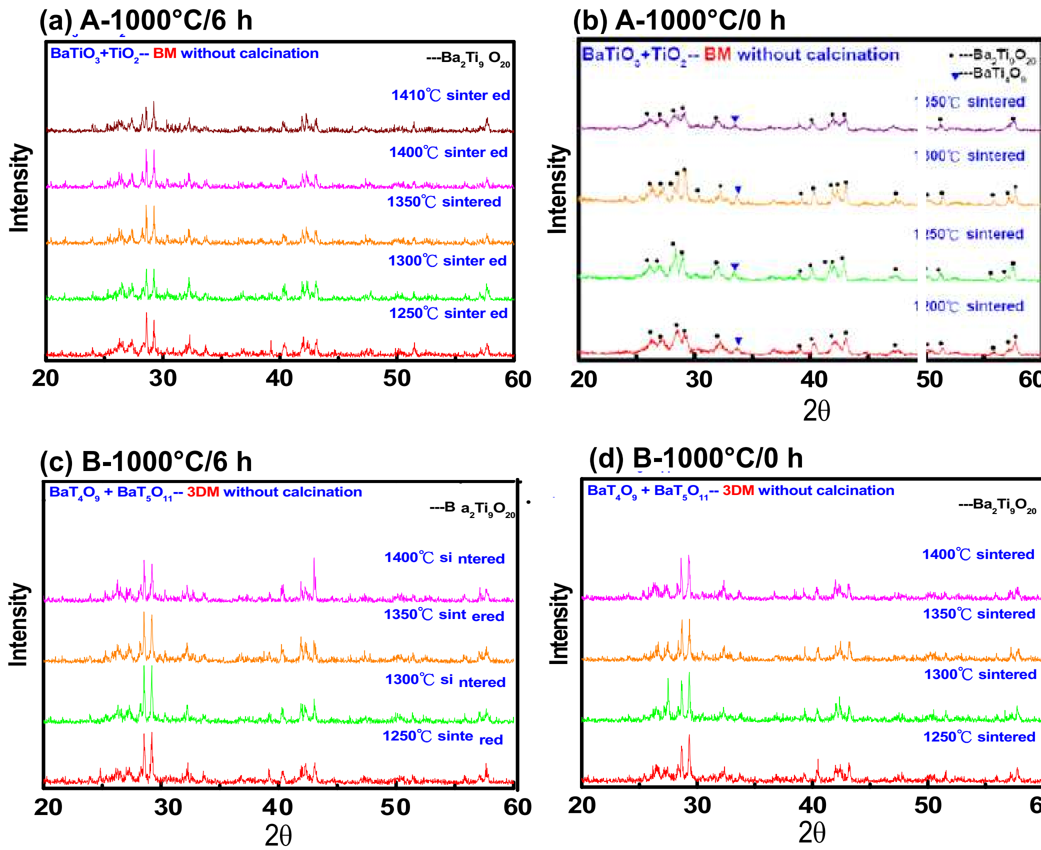

Figure 3: X-ray diffraction patterns of the reaction sintered A-series $Ba_2Ti_9O_{20}$ materials, where the pellets made of $2BaTiO_3$+$7TiO_2$ mixture were pre-reacted at 1000℃ for (a) 6 h and (b) 0 h; Those of the reaction sintered B-series $Ba_2Ti_9O_{20}$ materials, where the pellets made of $BaTi_4O_9$+$BaTi_5O_{11}$ mixture were pre-reacted at 1000℃ for (c) 6 h and (d) 0 h. The samples were sintered at 1250–1400℃/4 h after pre-reaction process.

designated as B-series materials. Fig. 4 shows that the consistency of material's characteristics is significantly improved. The microwave dielectric constant (K) and the dielectric quality factor ($Q \times f$) of the B-series materials also increases monotonously with sintering temperature. The K-value is essentially not varying with the pre-reacting period (Fig. 4(a)), but the $Q \times f$-value varies appreciably with the pre-reacting process (Fig. 4(b)). However, the the extend of variation is much less than that for the A-series materials (cf. Fig. 1(b)).

Figures 3(c) and 3(d) illustrate that, for the type B materials sintered at 1250–1400℃ for 4 h, the XRD peaks are all very sharp, indicating that all of them are of pure Hollandite-like structure, containing no secondary phase, no matter whether they have experienced the pre-reacting process or not. The phase transformation kinetics for B-series materials is pronouncedly higher than those for A-series ones. SEM micrographs shown in Fig. 5 reveals that the microstructure of the B-series materials is much more uniform than that for the type A materials. For the B-series samples sintered at 1350℃/4 h, the abnormal grain growth phenomenon occurs only in the non-prereacted samples (B_0, Fig. 5(a)), whereas the samples pre-reacted at 1000℃ for 6 h contain grains of uniform size (B_6, Fig. 5(b)). These results imply clearly that the superior quality factor for the B_6 samples, as compared with the B_0-series samples, is owing to the improvement on the uniformity of the granular structure for the B_6 samples.

For the samples sintered at 1350℃/4 h, the K-values are $K_A = 35-38$ for A-series materials and are $K_B = 37.6-38$ for B-series materials, whereas the $Q \times f$-values are $Q \times f_A = 16,000-30,000$ GHz for A-series materials and are $Q \times f_B = 29,300-32,000$ GHz for B-series materials. Moreover, the B-series materials can by sintered at higher temperature without inducing the abnormal grain growth phenomenon such that they can reach $Q \times f_B^{1400} = 34,000$ GHz and $Q \times f_B^{1410} = 36,000$ GHz for the samples sintered at 1400℃/4 h and 1410℃/4 h, respectively, which is markedly superior to the

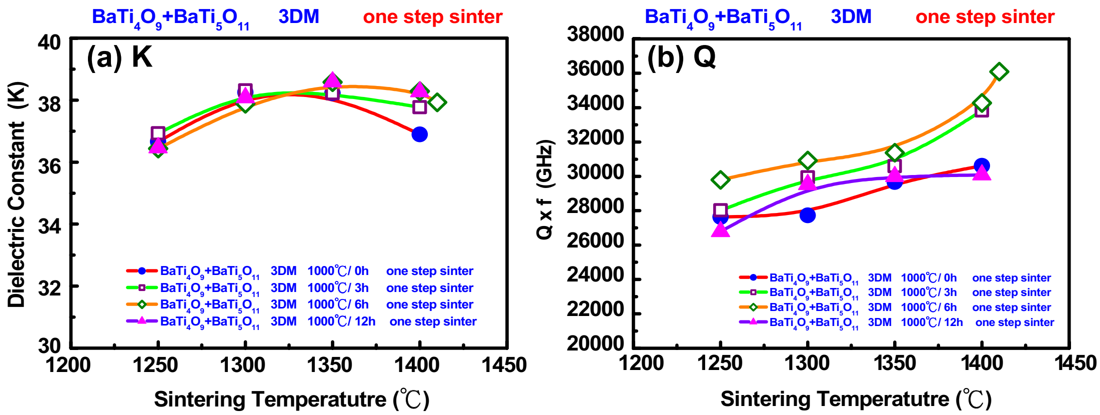

Figure 4: The characteristics of the B-series $Ba_2Ti_9O_{20}$ materials sintered by "one-step densification routes": (a) microwave dielectric constant, K, and (bc) microwave dielectric quality factor, Q; where the pellets made of $BaTi_4O_9$+$BaTi_5O_{11}$ mixture were pre-reacted at 1000℃ for 0–12 h and then sintered at 1250 $\sim$ 1400℃ for 4 h.

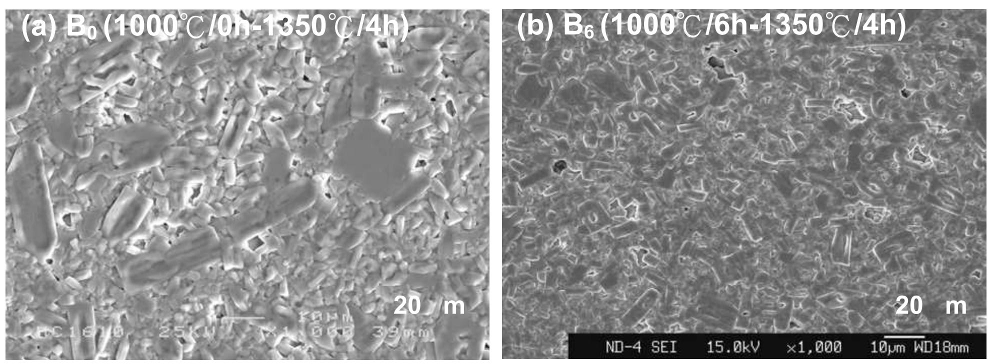

Figure 5: SEM micrographs of the B-series $Ba_2Ti_9O_{20}$ materials sintered by "one-step densification routes"; where the pellets made of $BaTi_4O_9$+$BaTi_5O_{11}$ mixture were pre-reacted at 1000℃ for (a) 0 h, B_0 samples and (b) 6 h, B_6 samples and then sintered at 1350℃ for 4 h.

A-series materials (cf. Figs. 1 and 4). The factor resulting in better microwave dielectric properties for B-series materials is apparently owing to the overwhelmingly better granular structure of these materials, as compared with the microstructure for the A-series materials.

In summary, the effect of starting materials and densification routes on the characteristics of $Ba_2Ti_9O_{20}$ materials were systematically investigated. The K-value of the $Ba_2Ti_9O_{20}$ materials is insensitive to the granular structure of the samples, whereas the $Q \times f$-value of the materials varies markedly with the microstructure, which, in turn, is determined by the processing details. The B-series materials, which were pre-reacted at 1000℃ for 6 h or longer and were sintered at 1400℃ or higher temperature, show most uniform microstructure and exhibit the highest $Q \times f$-value ($Q \times f = 36,000$ GHz). It is ascribed to the simplicity in reaction routes for the formation of the $Ba_2Ti_9O_{20}$ Hollandite-like phase from $BaTi_4O_9$+$BaTi_5O_{11}$ mixture, which results in better granular structure for the materials.

ACKNOWLEDGMENT

The authors gratefully thank the financial support of the National Science Council, R. O. C. for this research through the project No. NSC 95-2112-M032-005.

REFERENCES

1. Jonker, G. H. and W. Kwestroo, "Ternary system BaO-TiO_2-SnO and BaO-TiO_2-ZrO_2," *J. Amer. Ceram. Soc.*, Vol. 41, No. 10, 390–394, 1958.
2. O'Bryan, H. M., J. Thomson, Jr, and J. K. Plourde, "A new BaO-TiO_2 compound with temperature-stable high permittivity and low microwave loss," *J. Amer. Ceram. Soc.*, Vol. 57, No. 10, 450–453, 1974.

3. Wu, J. M. and H. W. Wang, "Factor affecting the formation of $Ba_2Ti_9O_{20}$," *J. Amer. Ceram. Soc.*, Vol. 71, No. 10, 869–873, 1988.
4. Chu, L. W., G. H. Hsiue, I. N. Lin, and Y. C. Chen, "Novel reaction mechanism for the synthesis of $Ba_2Ti_9O_{20}$ materials prepared from nano-sized oxides," *Nanotechnology*, Vol. 17, 185–191, 2006.
5. Chu, L. W., G. H. Hsiue, Y. J. Chiang, K. S. Liu, and I. N. Lin, "Ultra-fine $Ba_2Ti_9O_{20}$ microwave dielectric materials synthesized by chemical process," *J. Euro. Ceram. Soc.*, Vol. 24, No. 6, 1781, 2004.
6. Negas, T., G. Yeager, S. Bell, et al., "$BaTi_4O_9/Ba_2Ti_9O_{20}$-based ceramics — resurrected for — modern microwave applications," *Amer. Cerem. Soc. Bull.*, Vol. 72, No. 1, 80–89, 1993.
7. Hakki, B. W. and P. D. Coleman, P.D., *IEEE Trans. Mirowave Theory Tech.*, Vol. MTT-18, 402, 1980.

The Study on Anti-jamming Capability of UTP Applied in Vehicle CAN Bus

Longshan Yang[1], **Junzhi Zhang**[2], **and Lifang Wang**[1]

[1]Institute of Electrical Engineering, Chinese Academy of Sciences, China
[2]State key laboratory of Automotive Safety and Energy, Tsinghua University, China

Abstract— With the wide application of the CAN bus in the vehicle, the good anti-jamming capability of communication medium is the key factor to make the CAN bus work normally. Through analysis of the single line coupling with UTP, the paper points out several factors affecting the anti-jamming capabilities of the UTP used in the CAN bus. According to the standard of FORD automotive company about the immunity from conductive transients for the data bus, we established the system test platform to test the anti-jamming capability of the communication medium of CAN bus, and compared it with several different parameters of UTP and validated the conclusion of the study.

1. INTRODUCTION

CAN bus designed to solve the data exchanging among the controlling and testing equipments by BOSCH automotive company, has been applied widely by virtue of many advantages in vehicle and regarded one of the most promising field buses.

The medium of the CAN bus can be twisted-pair, coaxial cable or optical fiber. Compared with the latter two medium, the cost of twisted-pair is lower and it is easier to implement. So it has been widely applied in vehicles and industry. However, CAN bus used in vehicles may be interfered by the electric controlling module in the vehicle and the outside electromagnetic environment changing from low frequency to the high frequency at the result of the mobility of the car. The reliability of the CAN bus will be the problem. In the aspect of data transmission, ISO and famous automotive companies have put forward test requirements to test the anti-jamming capability of the data transmission. According to the ISO11898-2 [1], CAN bus should satisfy the 3a and 3b test pulses of ISO7637-3. DaimlerChrysler [2], FORD [3], GM [4] and other automotive companies also have their test requirements in the data transmission aspect.

From above all, we can see the reliability of the data transmission line has been noticed widely. As one kind of data transmissions, the medium of the CAN bus with good anti-electromagnetic interference characteristics is one of the key factors affecting its reliability.

2. MECHANISMS ANALYSIS OF THE SINGLE PAIR COUPLED WITH UTP

In order to analyze the mechanism of the single wire coupled with UTP, we can analyze the mechanism of the single pair coupled with non-shield balanced wire pair first. Figure 1 shows the circuit diagram of the non-shield balanced wire pair coupled with single pair. Figure 2 shows the equivalent circuit diagram of Figure 1.

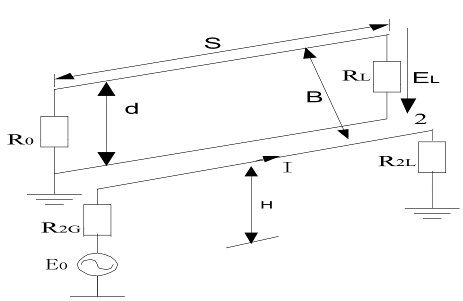

Figure 1: Non-shield balanced wire pair coupling with single pair circuit diagram.

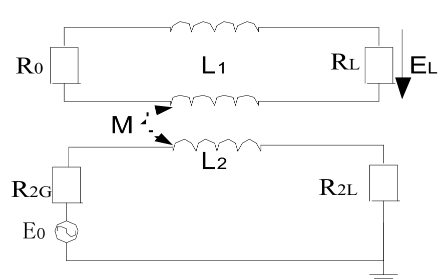

Figure 2: The equivalent circuit diagram.

From the Figure 2, we can get the interference voltage in the interferenced circuit as follows:

$$V_2 = j\omega M \cdot S \cdot I \tag{1}$$

where: M is mutual inductive of the unit length, namely:

$$M = \frac{\mu}{4\pi}\text{In}[(d/B)^2 + 1] \ \ [\text{H/m}] \tag{2}$$

I is the current of the interference circuit, namely

$$I = E_0/(R_{2G} + R_{2L} + j\omega L_2 \cdot S) \tag{3}$$

So the interference voltage E_L generated in the terminal of the interferenced circuit is as follows:

$$E_L = \frac{R_L}{R_0 + R_L + j\omega L_1 \cdot S} \times V_2 = \frac{j\omega R_L M \cdot S}{R_0 + R_L + j\omega L_1 \cdot S} \cdot \frac{E_0}{(R_{2G} + R_{2L} + j\omega L_2 \cdot S)} \tag{4}$$

For the magnetic coupling analysis of the twisted wire pair, we only need add one amended factor [5] to the Equation (4). Therefore, the interference voltage of the single wire coupled with the twisted wire pair is:

$$E_{LT} = \frac{1}{N}\frac{\sin(\frac{N\theta}{2})}{\cos(\frac{\theta}{2})}E_L \frac{1}{N}\frac{\sin(\frac{N\theta}{2})}{\cos(\frac{\theta}{2})}\frac{\omega R_L M \cdot S \cdot E_0}{(R_0 + R_L + j\omega L_1 S)(R_{2G} + R_{2L} + j\omega L_2 S)} \tag{5}$$

where: θ is phase angle between the current in adjacent twist loops, namely

$$\theta = 2\pi d/\lambda = 2\pi S/(N\lambda) \tag{6}$$

N is the number of twists;
S is the length of wire pair (meters)
d is the twist loop length(meters)(pitch of twist)
Substitute Equation (6) into Equation (5), we can get the following equation:

$$E_{LT} = \frac{1}{N}\frac{\sin(\frac{\pi S}{2})}{\cos(\frac{\pi S}{N\lambda})}E_L \frac{1}{N}\frac{\sin(\frac{\pi S}{2})}{\cos(\frac{\pi S}{N\lambda})}\frac{\omega R_L M \cdot S \cdot E_0}{(R_0 + R_L + j\omega L_1 S)(R_{2G} + R_{2L} + j\omega L_2 S)} \tag{7}$$

Therefore, from the equation above, we can know: the larger N is, the weaker E_{LT} is, namely: the weaker interference voltage in the CAN bus is, the stronger the anti-jamming capability of the bus is.

3. INTRODUCTION OF CAN BUS SYSTEM TEST PLATFORM FOR THE ANTI-JAMMING CAPABILITY OF THE COMMUNICATION MEDIUM

Taking the standard of FORD automotive company about the immunity from conductive transients for the data bus as reference, we choose two CAN bus nodes which can send their own messages and receive the other node's messages. When the temperature of the environment is $23° + / -5°$, the CAN nodes are put on the insulation panels whose insulation factor $\varepsilon_r <= 1.4$ and thickness is 50 mm. CAN nodes are made of 51 microcontroller P89C58BA, CAN controller SJA1000 and CAN transceiver PCA82C250. The type of the relay is KUP-14A15-12 (P&B) which is designated by FORD. The relay should be powered by vehicle battery and should be changed by a new one after 100 hours of usage. The negative electrode of the CAN node and that of the battery should be connected to the ground plate. The distance from CAN nodes ECU, test equipment CANoe respectively to the edge of the ground plate should be longer than 10 cm. S, the length of the CAN bus is 1.7 m. Single wire connected with relay should couple with the medium of the CAN bus in the middle and be on top of the medium with the length of 1 m.

4. THE RESULT AND ANALYSIS OF THE TEST

According to Figure 3, we test several different parameter non-shield twist wire pairs on the test platform and get the Figure 4 about their anti-jamming capabilities. These three mediums we choose are the same except the number of twists in the unit length. From Figure 4, we can see that under the same interference situation, the anti-jamming capability of non-shield twist wire pair 2

Figure 3: CAN bus system test platform for the anti-jamming capability of the communication medium.

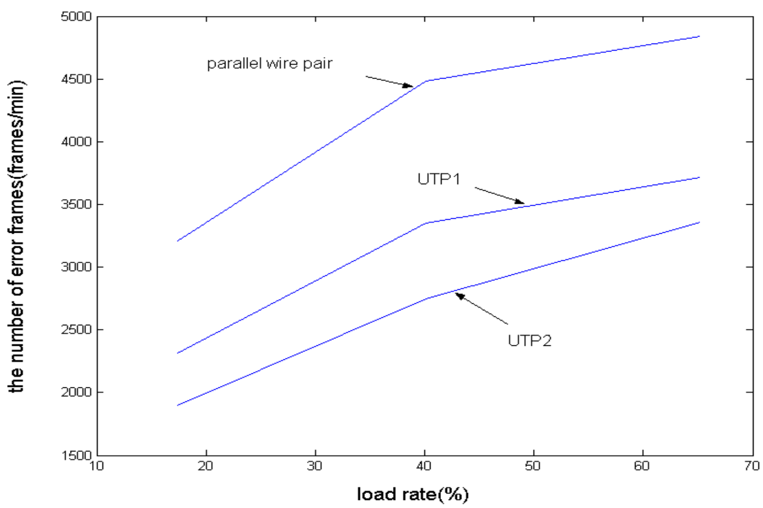

Figure 4: Comparison of anti-jamming capability of different non-shield transmission lines.

is the best, the non-shield twist wire pair 1 is the better and the parallel wire pair is the worst. According to the former mechanisms analysis of the single pair coupled with UTP, the reason is that the less the number of the twists in the unit length is, the better the capability of anti-magnetic field is. Therefore, the number of error frames in the CAN bus is less. However, because UTP doesn't have the anti-electric field capability, there are still many error frames in the CAN bus. As for the parallel wire pair, it doesn't have the anti-electric or magnetic field, so the number of the error frames is the most.

Table 1: Parameter table of three non-shield transmission mediums.

Transmission medium	Number of twistsper meter
UTP 1	50
UTP 2	60
Parallel wire pair	0

In addition, from Figure 4, we can also see that although under the same interference situation, the same CAN communication medium has a different number of error frames in CAN bus at different load rates. The more the load rate is, the more the probability of the bus different voltage level affected validly by interference is. So the number of the error frames is more.

5. CONCLUSION

Through mechanisms analysis of the single pair coupled with UTP, we can get the conclusion as follows: when UTP is used in the CAN bus, the more the number of the twists in the unit length is. The stronger the capability of the anti-jamming is; the higher the load rate is and the more the probability of the bus different voltage level affected validly by interference is, the more the number of error frames is. Taking FORD automotive company standard about the immunity from conductive transients for the data bus as a reference, the conclusion of the paper is validated through testing different non-shield twisted and parallel wire pairs. Therefore, when the non-shield twisted wire pair is chosen as the communication medium of CAN bus, the paper provides a valid selecting principle.

ACKNOWLEDGMENT

The paper is funded by the National "863" plan — the research on the test of the anti-jamming capability of the CAN bus applied in electrical vehicle (2005AA501670), so here I thank our country.

REFERENCES

1. Road vehicles — Interchange of digital information — Controller area network (CAN) for high-speed communication, ISO 11898, International Standardization Organization, 1993.
2. Daimler Chrysler Corporation Performance Standard, No.: PF-10540, 05 December 2001.
3. FORD Motor Company, ES-XW7T-1A278-AC, 10 October 2003.
4. GM World Wide Engineering Standards, GMW3097, GMW3100, August 2001.
5. Hartal, O., *Electromagnetic Compatibility by Design*, R & B Enterprises, March 1993.

The Quasi-elliptic Bandpass Filter Using Quarter-wavelength Stepped Impedance Resonators

Yu-Wei Chen, Yen-Ju Liu, and Min-Hua Ho
Graduate Institute of Communication Engineering and Department of Electronic Engineering
Changhua University of Education, Taiwan, China

Abstract— A bandpass filter is designed using two end-connected quarter-wavelength stepped impedance resonators. The quarter-wavelength stepped impedance resonators are implemented by a half-wavelength stepped impedance resonator with its middle shorting to ground. Hence, the modes that the $\lambda/4$ stepped impedance resonator supports are the $(1+2n)/4$ which also occur on the branches of a combline. An enhanced U-shape coupling feed is adopted in the filter design to reduce the insertion losses as well as suppressing the harmonics. The proposed filter has a quasi-elliptic frequency response. An equivalent circuit model is developed and the experiments are conducted for circuit design verification.

1. INTRODUCTION

For recent microwave component developments, microstrip involves low cost, light weight, and simple design method should remain the most desired structure for most of microwave circuits even if numerous prescient technologies have been proposed [1, 2]. Among these circuits, especially for the microstrip filter designs, the issue of circuit miniaturization has attracted researchers' attention for a long time. In microstrip filter configurations, one considers a quarter-wavelength microstrip resonator more space conservative while compared with the conventional half-wavelength microstrip resonator. Among the diverse configurations of the microstrip resonators, such as a straight uniform-line, a hairpin, and the stepped impedance resonator (SIR), the latter might be the most popular candidate for the filter design for its smaller size and the controllable second harmonic [3]. Plenty of researches in filters are reported using various variations of SIR configurations [4–6]. They are creditable for the efforts made in minimizing the circuit size or in suppressing the harmonics. The resonators used in their filter designs belong to the half-wavelength type which might be limited in further size reduction. In [7], quarter-wavelength resonators in conjunction with half-wavelength ones are successfully implemented in filter design. Their filter design is brilliant which processes multiple harmonics suppression, but the combined structure is somewhat complicated and needs to be fine adjusted to achieve good performance.

In this paper, we propose a bandpass filter (BPF) design using two connected quarter-wavelength-SIRs with the joint shorting to the ground. These connected SIRs can be easily built by a half-wavelength three-sectioned SIR with its middle point shorting to ground through a metallic via hole. The shorting via, which also serves as an impedance inverter between the $\lambda/4$ SIRs, can be equalized by an equivalent shunt inductance in a circuit model. The three-sectioned SIR is bended to a hairpin shape to save the space, and a capacitively coupling structure is employed in the feed which together with the former lend the filter a quasi-elliptic frequency response. This filter's quasi-elliptic response is attributed to the cross-coupling between the input and output. Such frequency response might grand the filter a sharp roll-off of the passband edges and high signal selectivity. In addition, the two connected $\lambda/4$ SIRs feature the circuit a two-staged filter. In order to verify the performance of the proposed circuit, the experiments are conducted and good conformance is well-kept between simulation and measurement.

2. DESIGN OF THE QUARTER-WAVELENGTH SIR FILTER

In view of having the same central frequency, the typical half — (with one shorting end) and quarter-wavelength SIR (with both ends open) shown in Fig. 1(a) are taken into consideration for building a reduced size BPFs. Shown in Fig. 1(b) is the equivalent circuit model of Fig. 1(a). These mentioned $\lambda/2$ SIR is formed by two identical microstrip lines sandwiching an unequal width microstrip line. The SIR is bent to a hairpin shape for saving the circuit space. The SIR is then split up into two $\lambda/4$ SIRs by shorting its middle point to ground through a metallic via hole. For a half-wavelength uniform width resonator, the spurious responses should occur around $(n+1)f_0$, where $n = 1, 2, 3, \ldots$. On the contrary, the spurious responses of quarter-wavelength one will arise

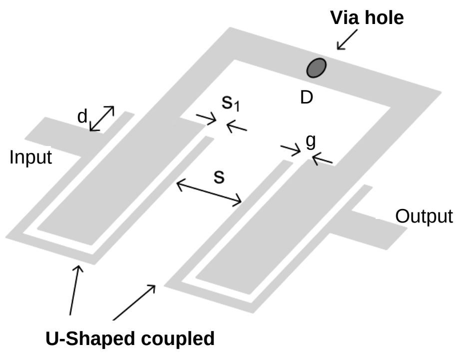

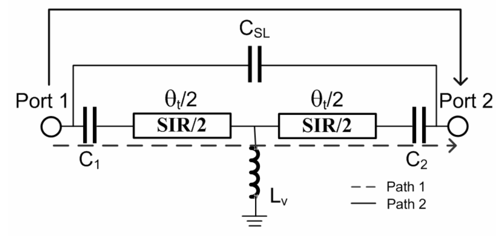

Figure 1: (a) the structure of the quarter-wavelength SIRs BPF and (b) its equivalent circuit model.

at $(2n+1)f_0$. The later one seizes more attractions with its wider rejection bandwidth accounting for the first spurious that appears at $3f_0$, which results in a wider stopband bandwidth.

Shown in Fig. 1(a), the U-shape enhanced coupling feed, which has a better coupling effect and lower insertion losses than those of the conventional parallel-coupled lines. The separation space (denoted by s) between the two U-shape structures can provide a direct coupling between the input and output ports. The strength of the direct coupling (also called a cross-coupling) can be managed by adjusting the separation distance s. This cross-coupling together with the via hole result in the quasi-elliptic response of the proposed filter. The dimension of the via diameter is founded to be inversely proportional to the value of the shunt inductance in Fig. 1(b), and can be used to tune the coupling between the two connected $\lambda/4$ SIRs. The tapping position, d, should be carefully chosen to match the circuit's loaded Q factor, and it is also fine tuned to eliminate the filter's spurious response. Three transmission zeros can be created and predicted by the equivalent circuit model. The first two zeros are allocated by each side of the passband to enhance the filter's signal selectivity.

The positions of these created zeros are primarily dominated by the lumped elements C_1, C_2, and C_{SL} of Fig. 1(b), which physically count for the coupling capacitances between each U-shape structure and the SIR, and the coupling one between the two U-shape structures. Shown in Fig. 2 are the simulated frequency responses obtained from using the equivalent circuit model of Fig. 1(b) and the full wave electromagnetic simulator, IE3D. The lumped elements in Fig. 2 have the values of $C_1 = C_2 = 0.16\,\text{pF}$, $C_{SL} = 0.0175\,\text{pF}$, and $L_v = 0.08134\,\text{nH}$. The electrical length θ_t is equal to 168°. It is observed that this equivalent model can exactly simulate the filter's frequency response and predict the filter's characteristics.

3. SAMPLE RESULTS

The proposed circuit is fabricated on a 0.635-mm-thick RT/duroid 6010 substrate along with dielectric constant 10.2 and loss tangent 0.0023. The impedances are 48 and 40 ohm, respectively,

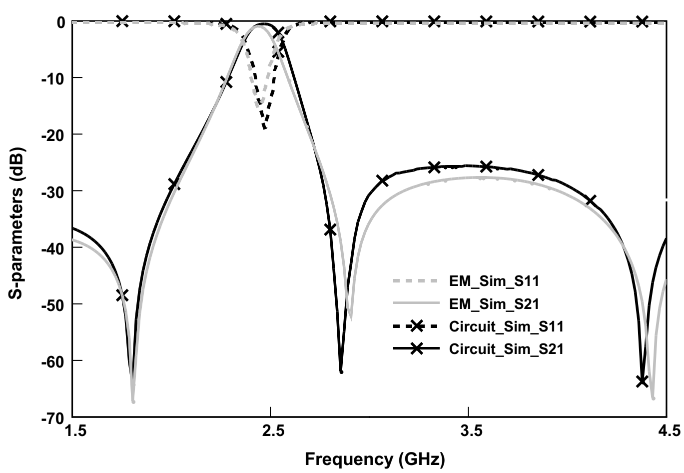

Figure 2: Simulated frequency responses for the structure of Fig. 1 using the equivalent circuit model and IE3D.

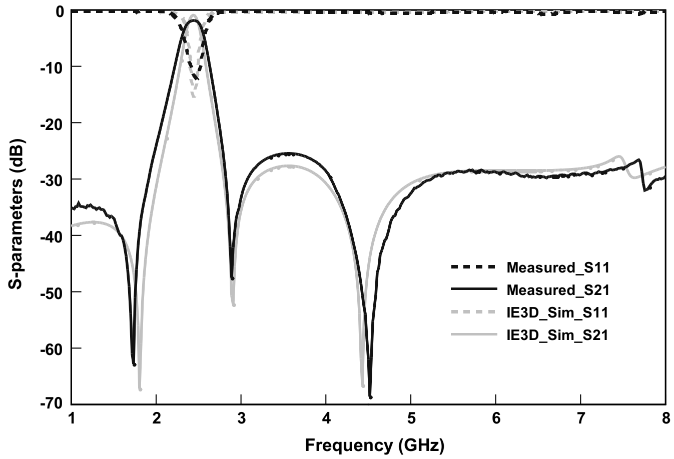

Figure 3: Comparison of simulated and measured results of the proposed quasi-elliptic BPF.

for the corresponding sections of the SIR in Fig. 1(a). The $\lambda/4$ SIR's different width sections have the same electrical length to be 42°. The shorting via's diameter is 0.5 mm. The other dimensions are $s = 1.2$ mm, $s_1 = 0.18$ mm, $g = 0.2$ mm, and $d = 2.6$ mm. The passband bandwidth is targeted at 7.5% while central frequency is selected at 2.4 GHz within 3% tolerance of frequency shift during fabrication samples. Three implanted transmission zeros are measured with the dips depth more than 47.5 dB at 1.735, 2.89 and 4.51 GHz with little excursion from the simulation. In addition to reduce the insertion losses, the U-shape coupling can also effectively suppress the first spurious response, which is predicted at around $3f_0$, occurred at 7.8 GHz. As the result, the upper rejection bandwidth is obtained from 2.735 GHz to the region beyond the measured upper scope of 8 GHz; all are over 20 dB band rejections. And the measured minimal passband insertion loss is about 1.87 dB at 2.435 GHz with a 9.5% passband bandwidth. The discrepancy between simulated and measured curves is mainly due to the tolerance of fabrication. The simulated and measured frequency responses exhibit great agreement for this design. Shown in Fig. 4 is the photograph of proposed BPF.

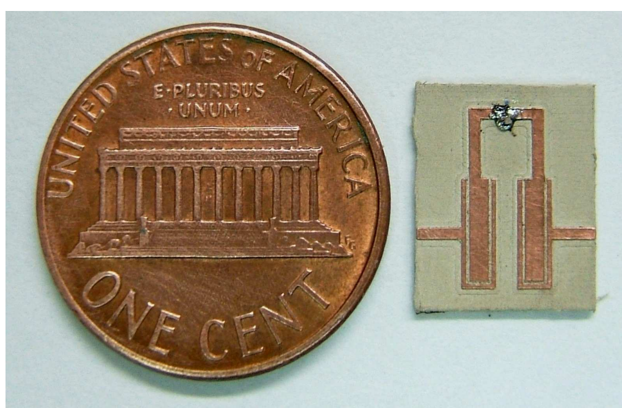

Figure 4: The photograph of experimental circuit.

4. CONCLUSIONS

We have successfully demonstrated a quasi-elliptic BPF built by simple but rather small size quarter-wavelength SIRs. The proposed BPF exhibits good selectivity, wide rejection bandwidth, and size reduction benefit. An inductive via together with the coupling feed gives the filter a quasi-elliptic frequency response. In addition, the U-shape enhanced coupling feed suppress the filter's first spurious response and thus effectively extend the stopband bandwidth. The simple but effective design methodology is presented, and the experimental results are in good agreements with the simulations. It is believed that the proposed filter should find many applications in commercial communication systems.

ACKNOWLEDGMENT

The authors wish to acknowledge the support of the Science Committee of Taiwan. under the research project contract No. NSC 94-2213-E-018-003. The valuable comments provided by Dr. C.-I G. Hsu of Da-Yeh University and Dr. C.-H. Lee of Changhua University of Education are also appreciated.

REFERENCES

1. Rajesh, M., I. Bahl, and P. Bhartia, *RF and Microwave Coupled-line Circuits*, Chs. 4, 9, and 10, Artech House, Boston, 1999.
2. Hong, J. S. and M. J. Lancaster, *Microstrip Filters for RF/Microwave Applications*, Chs. 5, 8, and 10, John Wiley & Sons, New York, 2001.
3. Makimoto, M. and S. Yamashita, *Microwave Resonators and Filters for Wireless Communication*, Chs. 2 and 4, Springer, Berlin, 2000.
4. Chen, C.-F., T.-Y. Huang, and R.-B. Wu, "Design of microstrip bandpass filters with multiorder spurious-mode suppression," *IEEE Trans. Microwave Theory Tech.*, Vol. 53, No. 12, 3788–3793, Dec. 2005.
5. Chen, C.-F., T.-Y. Huang, and R.-B. Wu, "Novel compact net-type resonators and their applications to microstrip bandpass filter," *IEEE Trans. Microwave Theory Tech.*, Vol. 54, No. 2, 755–762, Feb. 2006.
6. Kuo, J.-T., M.-J. Maa, and P.-H. Lu, "A microstrip elliptic function filter with compact miniaturized hairpin resonator," *IEEE Microw. Guided Wave Lett.*, Vol. 10, No. 3, 94–95, Mar. 2000.
7. Lin, S.-C., Y.-S. Lin, and C.-H. Chen, "Extended-stopband bandpass filter using both half- and quarter-wavelength resonators," *IEEE Microw. and Wireless Compon. Lett.*, Vol. 16, No. 1, 43–45, Jan. 2006.

New Type Piezomagnetic Ferrite Materials and Their New Applications

Quanlu Li[1] **and Yuan Li**[2]
[1]Institute of Applied Acoustics, School of Physics and Information Technology
Shaanxi Normal University, Xi'an 710062, China
[2]Department of Health Service, School of Prevention Medicine
Fourth Military Medical University, ♯17, Changlexi Street, Xi'an 710033, China

Abstract— This paper briefly reports on the classification, the basic chemical composition, the method of preparation of the ferrite materials firstly, gave emphasis to the new type piezomagnetic ferrite materials and their new applications in this study.

1. INTRODUCTION

Multifunctional electronic materials and integrated intelligent devices are needed in the development of advanced technologies, especially mechano-electronic integrative units. This work describes the preparation of new type piezomagnetic ferrite materials and acoustical transducers and vibration control devices (combining multipurpose ferrites and magnetorheological fluids) and their new applications in this study. Piezomagnetic materials could be used as reversible electroacoustical or electromechanical transducing etc. acoustical devices by piezomagnetic effect [1, 2]. This paper briefly reports on the classification, the basic chemical composition, the method of preparation of the ferrite materials firstly, gave emphasis to the new type piezomagnetic ferrite materials, and their new applications.

2. CHEMICAL COMPOSITION AND THE APPLICALILITY OF THE IEZOMAGNETIC FERRITES

2.1. The Classification of Piezomagnetic Materials in General

There are many materials exhibiting the piezomagnetic effect, such as nickel, Ni-Fe alloy, V-Fe alloy, Fe-Co-Ni alloy, Ni-Cr-V alloy, (Fe, Cu system) Monel alloy, etc.; nickel ferrite, ickel-copper ferrite, nickel-zinc ferrite, etc.. Various composition systems including magnesium-manganese ferrite, nickel-cobalt ferrite and these systems with aluminum substitutions have been investigated for some important applications. The acoustical transducers made from these materials, which they are capable of producing coherent pulses of ultrasound over a very wide frequency range and have been applied in temperatures such as, for example, the Curie point of nickel (385°C), quartz (576°C), or PZT (lead zirconat-titanate ceramics, generally at 310°C or so). They are likely to remain in common use, but since only a limited range of dielectrics are piezoelectric and only a few metals and ferrites are ferromagnetic, these transducers have to be acoustically bonded in most instances to material under investigation.

In general ceramic processing techniques are modified and adapted to the fabrication of test specimens. Such as, parameters of chemical state and particle size of the reactants, method of mixing, forming process, and heat-treatment must be considered.

Chemical, physical and structural measurements are made and correlated to the fabrication variables. X-ray diffraction, metallurgical microscopy and chemical analysis are employed in making these measurements. The fabrication and physicochemical parameters are studied in connection with structure-sensitive microwave properties such as Faraday rotation (in this paper, the irrelevant between the measurement method and performance parameters are omitted).

The usefulness of a piezomagnetic ferrite as electromechanical transducing devices is influenced by the chemical and physical properties of the material, which in turn are dependent on the chemical composition and method of preparation. Based on we long-term research into ferrites which summed up as follows: The first part of this paper will be concerned with the composition; the second part is with methods of preparation; and their new applications.

2.2. Chemical Compositions of Ferrite Materials of Present Work

Ferrites are the inorganic salts of the formula to be MF_eO_4, where M represents a bivalent metal [3]. Such is the basis of molecular design of all new type ferrite. Almost all of these materials are magnetic materials. Certain of these compounds are ferromagnetic, and posses in addition other properties, which render them valuable for use in circuit components operating at high frequencies. On a functional basis, ferrites can be divided into five groups: (1) soft ferrites, (2) hard ferrites, (3) square-loop ferrites, (4) piezomagnetic ferrites, and (5) microwave ferrites etc.. This paper only researches piezomagnetic ferrite materials and their applications. Piezomagnetic ferrite materials are magnetic materials which can use their piezo-magnetic effect (piezomagnetic materials are linear relation between strain and magnetic field) to design and make of the acoustcal devices. Then, piezomagnetic materials have highly magnetostriction constant which it is produced mechanical vibration. The term literally implies magnetic contraction, but is generally understood to include a number of closely allied phenomena relating to ferromagnetic substances under magnetic influence. Magnetostriction has been put to practical use in the magnetostrictive resonator, essentially a ferrite rod maintained in longitudinal elastic vibration by a high-frequency current in a helix wound upon it, and used; through the joint operation of the Joule and Villari effects, to control the frequency of the current; somewhat after the manner of the familiar piezoelectric (crystal) resonator, as is applied in magnetostriction delay line, etc. acoustical devices.

In this work, the formula for the new multifunctional piezomagnetic ferrite material.

FER_1 is expressed as:

$$Ba_{6-x}R_{2x}(Nb_{1-x}Fe_{2+x})O_3 \text{ (in there R stands for the rare−earth elements) } (x = 0.25 \sim 0.5) \quad (1)$$

FER_2 is expressed as:

$$Bi_{2-x}Fe_xO_3 \ (x = 0.35 \sim 0.65) \quad (2)$$

2.3. The Applicability of Some Piezomagnetic Ferrite Materials in Gengeral

In present work, some piezomagnetic ferrite materials and their chemical composition, and important applicability are listed in Table 1.

Table 1: Chemical composition and its applicability of some piezomagnetic ferrite materials.

Name	Molecular composition	Applicability
Mn-Zn ferrite	$[Mn_yZn_{1-y}]_{1-x}Fe_{2+x}O_4$	$\mu_i = 40000$, $\mu Q = 1.25 \times 10^5$ (at 100 kHz), $B_s = 50000$ Gs; use as magnetic core of inductor, transformer, pulse transformer filter, etc., and antenna bar, magnetic head etc..
Ni-Zn ferrite	$[Zn_yNi_{1-y}]_{1-x}Fe_{2+x}O_4$	high resistivity, (at 1∼300 MHz) use as magnetic core of tunable transformer, magnetic head, short wave antenna, tuning inductance-reactance, and magnetic saturation amplifier, etc..
ferroxplana	$Co_2Zn(Ba_3Co_2Fe_{24}O_{41})$	at 2000 MHz, $\mu Q = 200$, use as tuning inductor, wide-band transformer, scanning frequency magnetic core, etc..
Ni-Co ferrite	$[Ni_yCo_{1-y}]_{1-x}Fe_{2+x}O_4$	the materials are suitable for all piezomagnetic devices.
Ni-Cu ferrite	$Ni_{1-y}Cu_yFe_2O_4$	the materials are suitable for all piezomagnetic devices.
Ni-Mg ferrite	$Ni_{1-y}Mg_yFe_2O_4$	the materials are suitable for all piezomagnetic devices.
Ni-Cu-Zn ferrite	$Ni_{1-x-y}Cu_xZn_yFe_2O_4$	the materials are suitable for all piezomagnetic devices.
...		

3. PREPARING METHOD OF THE NEW PIEZOMAGNETIC FERRITES

Preparation of piezomagnetic ferrite materials can divided into polycrystalline ferrite and ferrite single-crystal pulling technique, in present we together describe them below.

3.1. General Methods

General ceramic processing methods for pure oxide materials (or, applied thermal decomposition of salts to obtain oxides, e.g., with sulphate, oxalate, carbonate, hydroxide, etc.) are applied with very little modification by many investigators, in preparing ferrites particularly in those industry. When close tolerances in electronic properties are required, as with ferrites for some concrete applications, extreme care must be exercised to maintain purity and homogeneity of the material throughout the processing.

For procuring the desired ferrite properties, selection of the firing schedule is preceded in importance only by selection of the composition. The firing schedule can influence chemical composition (oxygen content); phase relations; amount, size, and shape of pores; grain parameters; and strains. All of these can affect the electronic properties.

The shapes must be heated gradually during the low temperature range of the firing cycle to slowly volatilize any organic additives. Also, at temperatures where considerable sintering (i.e., reaction and crystallization) occurs, the rate of heating should be slow.

The preceding discussion has dealt mainly with conventional ceramic techniques as adopted for ferrite preparation. A few specialized processing methods are discussed in the following.

3.2. Thermal Decomposition of Salts

In many case a compound can be broken down into simpler compounds or the component elements. This is usually accomplished by heating or by applying of an electric current. In present work, we adopted the thermal decomposition of some carbonates and sulphates etc. to gain the possessing active oxidetes of the ferrite powder. Then, multipurpose ferrites can be used for preparation.

3.3. Hot Pressing Sintering (When Sintering is Applied Press to the Ferrite Sample)

In this method, sintering and forming are in progress at the same time. The powders of ferrite or the prepressing compact (that was pressed 300 kg·cm^{-2} to form powder compacts of 10 mm thick and 36 mm in diameter) is sintered at applied force by the hot pressing installation at 900°C∼1300°C (the temperature is low than sintering temperature of the general method) at a heating rate to maintaned temperature of 2°C·min^{-1} and maintained temperature time is 2.5 h. The hot pressing sintering has the advantage of controlling the structure and increasing compactibility of ferrite products. This method can obtain ferrite samples of the theoretical density to be 99.7% [3]. Preparation of hot pressing is compared with the general method which it has three conditions:

3.3.1. Constant Press Method

In the whole process of raising temperature and melting sintering of the ferrite compact is applied a predetermined greatest pressure by the hot pressing installation. The press is from small to large, then, to 250 kg·cm^{-2} final, to hold there for some time, then, to cancel the pressure, cooling to room temperature.

3.3.2. High Temperature Applied Press Method

When the sintering temperature is come to predetermined highest point, the hot pressing installation applied a greatest press to the ferrite compact. The greatest pressure is 250 kg·cm^{-2}.

3.3.3. Continuous Applied Press Method

At lower sintering temperature the hot pressing installation applied smaller pressure, when the sintering temperature come to predetermined the highest temperature, applied a predetermined greatest pressure to the compact of ferrite powder, and, to hold there for some time after, to cancel

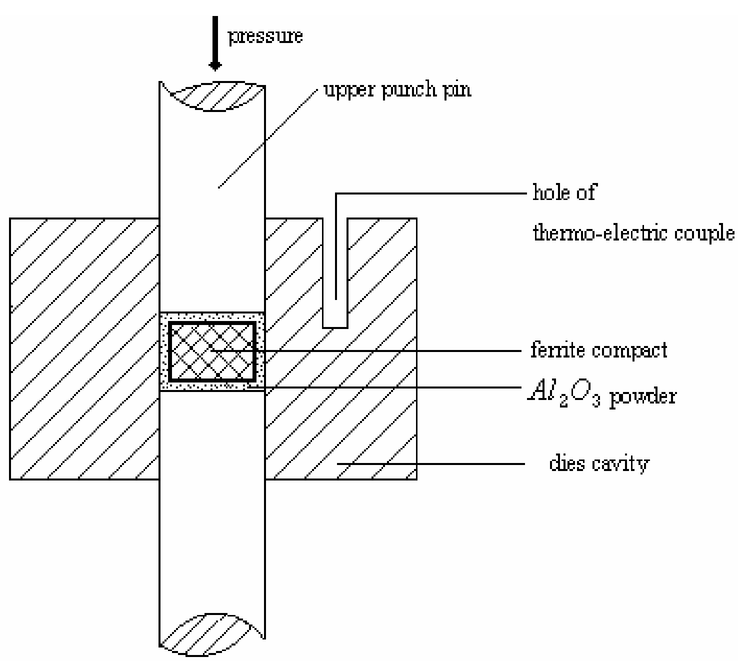

Figure 1: Schematic diagram of charging of hot-press sintering.

the pressure, soon after, continuous to raise temperature, to maintain temperature and cooling to room temperature. General greatest pressure is $250\,\mathrm{kg{\cdot}cm^{-2}}$.

The equipments of the hot pressing installation main consists of three parts, as shown in Fig. 1.

(1) Installation of applied pressure, such as liquid press or spiral press and pressure gauge etc.;
(2) Heating devices, such as tubular electrothermal appliance, or high frequency induction heating devices, etc.;
(3) The dies of hot pressing: Except heat-resisting and pressure-resisting, the material of die should do not possess reacts chemically with compacting materials at high temperature, and, suitably used as material of die which that have graphite, stainless steel, pure corundum (Al_2O_3) and zirconium dioxide (ZrO_2), etc.. Fig. 2 is a schematic diagram of charging of hot-press sintering.

3.4. Chemical Coprecipitation

That is wet method. The method do not use as raw materials with oxides directly, which it added the some precipitating agent to the mixed solution of soluble salts of raw materials of the piezomagnetic ferrite, then, to control appropriate conditions of the chemical reaction (i.e., temperature, acidity, and alkality etc.) of a few metal ions which they are precipitated, and finally the precipitating materials are stoved in oven. This method can get homogeneous mixed piezomagnetic ferrite powders, then, to pass the technological process of forming, sintering etc. to be prepared the piezomagnetic ferrites. In coprecipitation, with the soluble salts are sulphate, nitrate, and chlorate etc.. Sodium hydroxide, ammonium hydroxide, oxalate, and carbonate etc. are used as the precipitating agent. The chemical coprecipitation has the advantage of fine powder, strong activity, homogeneous composition, simple technological process and by this way can get high quality piezomagnetic ferrites. But, in the wet method of ferrite, which it should appropriately, regulated content of iron of formula, which can get better results [4].

4. BROADLY APPLICATIONS OF THE NEW PIEZOMAGNETIC FERRITES IN THIS STUDY

Piezomagnetic ferrite materials was as piezomagnetic element to apply in wave filters initially, recently, applied field of piezomagnetic ferrite materials have greater development, which classify

Table 2: Classification of applied fields of some new type piezomagnetic ferrite materials.

Applied fields	Give examples for applications of the piezomagnetic ferrite materials
the devices of ultrasonics & underwater acoustics	ultrasonic generators, ultrasonic receiver, ultrasonic flaw detector, bit of ultrasonic drilling, ultrasonic cleaning, ultrasonic welding, ultrasonic dispersion, ultrasonic motor, ultrasonic therapy equipment etc.; sonar, underwater acoustic transducer; echo sounding apparatus, acoustic echo repeater; electro-mechanical integrated intelligent devices, magnetostrictiv delay line and microwave, ultrasound generator, etc..
telecommunication devices	filters, frequency regulator, harmonic generator, harmonic filter, microphone, oscillator, and loudspeaker, etc..
devices of electronic computer & automatic control	magnetic memory of ultrasonic delay line, memory of twister, magnetic-core memory, magnetic rod memory, magnetoacoustic memory, integrated magnetic-core memory, and magnetic pickup, integrated intelligent structure — a new type actuator combining piezomagnetic ferrite and magnetorheological fluids, and magnetic levitation technique, etc..
measuring devices	instrument of viscosity, instrument of high-frequency elastic fatigue, vibration measurement, ferrite antenna, and microwave detector, etc..
medical apparatus & instruments	clinical mini-robots, tooth grafting, magnetic therapy equipments, and solid acid catalyst in chemical industry, etc..

for the principal applied field (including the acoustical transducers and vibration control devices combining multipurpose ferrites and magnetorheological fluids, etc.) given in Table 2.

REFERENCES

1. Li, Q., "Research and applications of high-powered acoustoelectric transducing materials," *Technical Acoustics*, Vol. 17, No. 1, 26, 1998, (in Chinese).
2. Nathaway, K. B. and A. E. Clark, "Magnetostrctive materials," *MRS Bulletin*, Vol. 18, No. 4, 34, 1993.
3. Li, Q., "Research and applications of piezoelectric and piezomagnetic acoustoelectric transducer materials," *Piezoelectrics* & *Acoustooptics*, Vol. 17, No. 2, 43, 1995, (in Chinese).
4. Flores, A. G., V. Raposo, and L. Torres, "Ferrimagnetic resonance of manganes ferrites with iron excess," *Appl. Phys. A, Matter. Sci. Process*, Vol. A73, No. 3, 372, 2001, (Germany).

Debye Series Analysis of Forward Scattering by a Multi-layered Sphere

Renxian Li and Xiang'e Han

Xidian University, P. O. Box 270, Xi'an 710071, China

Abstract— A formula of Debye series for forward scattering by a multi-layered sphere is presented. The Debye series expansion allows for the decomposition of the global scattering process in a series of local interactions, and clarifies the physical origins of many effects that occur in electromagnetic scattering. The forward-scattering pattern contains many information about the properties, and the method is widely used for determining such properties on the basis of forward-scattering pattern. In the paper, the Debye series is employed to the study of forward scattering by a multi-layered sphere, which is of great importance to the study of characteristics of particles.

For many practical applications such as combustion, environmental control, fluid mechanics, and chemical reaction, we need to measure the properties of particles such as size and refractive index-temperature ratio quickly and precisely. The forward-scattering pattern contains many information about the properties, and it is widely used for determining such properties on the basis of forward-scattering pattern.

The scattering of a plane electromagnetic wave by a single multilayered spherical particle has been extensively discussed within a theoretical framework similar to the Lorenz-Mie Theory (LMT) in many areas of theoretical and applied research, such as combustion, chemical engineering, remote sensing, communication, biology, and medicine [1]. The Mie theory is a rigorous solution of the Maxwell equations and contains all effects that contribute to the scattering [2, 3]. But it gives few clues to the various physical processes that are responsible for the scattering [2–4]. Full geometrical optics theory can be used with reasonable accuracy for forward direction light scattering computations related to particle sizing and characterization [5], and has been extended to forward scattering by coated particles [6]. But as soon as the scatters are complicated, for instance multi-layered sphere, the construction of the geometrical optics approximation formula is very difficult.

The Debye series writes each term of the Mie series as another infinite series, and clarifies the physical origins of many effect that occur in electromagnetic scattering [2, 3], which is of great importance in the study of characteristics of electromagnetic scattering. The Debye series was originally formulated for scattering of a normally incident plane wave by a cylinder [7] and has been subsequently extended to scattering by a sphere [8, 9], the internal fields [10], scattering by a coated sphere [11], scattering of a plane wave diagonally incident on a cylinder [12], and scattering by a multilayered sphere [2] and a spherical Bragg grating [13].

We consider an l-layered dielectric sphere whose refractive index of any layer j is m_j (region j) and whose radius a is embedded in a dielectric medium of refractive index m_{l+1} (region $l+1$), as shown in Fig. 1. When the sphere is illuminated by a monochromatic plane wave of wavelength λ, the classic Mie coefficients a_n^l and b_n^l can be expanded in the Debye series [2]

$$\left.\begin{matrix} a_n^l \\ b_n^l \end{matrix}\right\} = \frac{1}{2}(1 - Q_n^l) \tag{1}$$

where Q_n^j for region j can be written as:

$$Q_n^j = R_n^{j+1,j,j+1} + T_n^{j+1,j} Q_n^{j-1} T_n^{j,j+1} \sum_{p=1}^{\infty} (R_n^{j,j+1,j} Q_n^{j-1})^{p-1}, \tag{2}$$

The coefficients $R_n^{j+1,j,j+1}$, $T_n^{j+1,j}$, $T_n^{j,j+1}$, $R_n^{j,j+1,j}$ are depicted in Fig. 1, and have the same definitions as in Ref. [2]. P is the mode of refraction, and depicted by Fig. 1 in Ref. [2]. When summed over n, the first term 1/2 in Eq. (1) corresponds to diffraction, and the second term $-1/2R_n^{j+1,j,j+1}$ to the reflection waves. The third term is a series that describes the contributions of all modes of

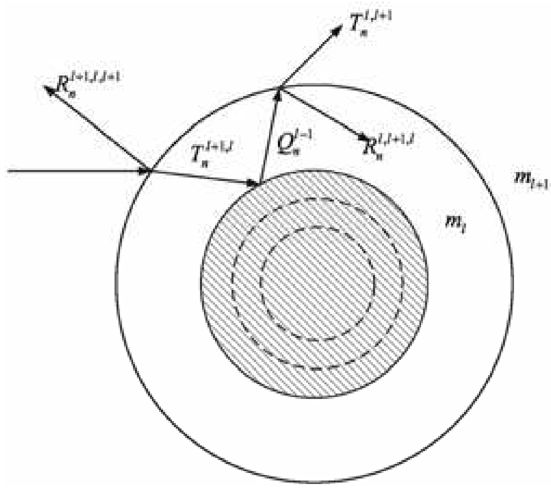

Figure 1: Debye model of scattering by an l-layer sphere.

refraction. Each term in the series represents the contribution of that mode that has undergone $p-1$ internal reflections and then emerged from the sphere. The main advantage of Debye series is to isolate the single mode.

As shown in Ref. [14], upward of 99.5% of the total forward-scattered light for both polarizations emerges from the first interface after simple reflection and from the second interface after twofold refraction. For the forward scattering, the each partial-wave scattering amplitude can be written as a sum of diffraction of the partial wave, its external reflection from the sphere surface, and direct transmission through the sphere. Mathematically speaking, with the help of Debye series, the scattering coefficients a_n^l and b_n^l can be written as

$$\left.\begin{matrix} a_n^l \\ b_n^l \end{matrix}\right\} = \frac{1}{2}(1 - R_n^{j+1,j,j+1} - T_n^{j+1,j} Q_n^{j-1} T_n^{j,j+1}) \tag{3}$$

When summed over n, the first term 1/2 in Eq. (3) corresponds to diffraction, the second term $-1/2R_n^{j+1,j,j+1}$ to the reflection ray, and the third term $-1/2T_n^{j+1,j}Q_n^{j-1}T_n^{j,j+1}$ to the ray penetrating the sphere and emerging from the sphere without internal reflection.

For clarity in the figure, we consider a sphere of relatively small radius ($a = 10\,\mu m$) stratified in 100 layers illuminated by a plane wave of wavelength $\lambda = 632.8$ nm. The refractive index profile of the sphere is depicted in Fig. 2.

It is depicted in Fig. 3 the scattered intensities of diffraction, diffraction including reflection, diffraction including reflection and direct transmission, as well as the Mie scattered intensity. The refractive index of the sphere is depicted in Fig. 2.

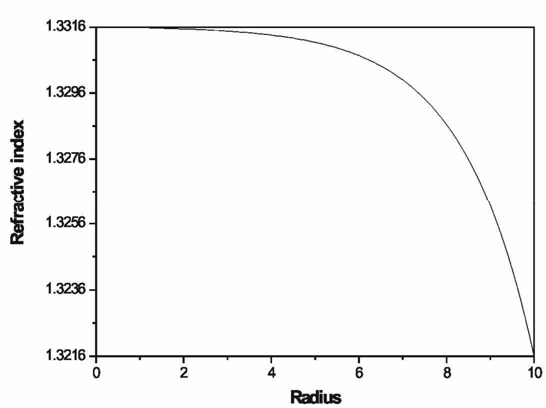

Figure 2: Refractive index distribution.

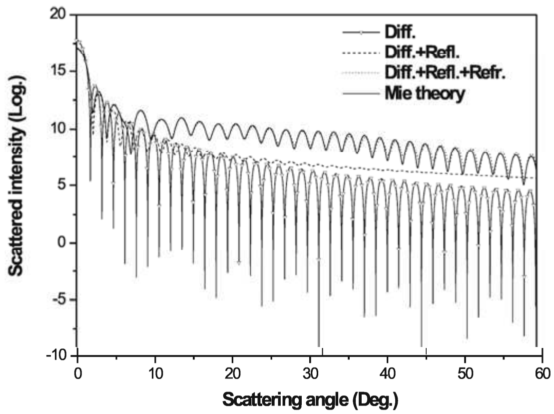

Figure 3: Scattered intensity for a 100 layered sphere of radius 10 μm with refractive profile described by Fig. 2

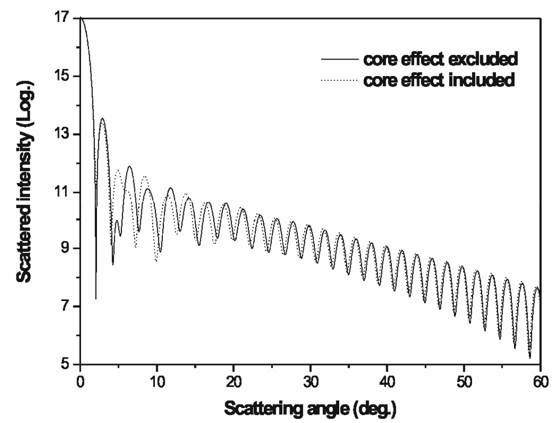

Figure 4: Influence of the core on the composite sphere scattering.

From Fig. 3, we can find that diffraction of incident wave around the sphere is the main fraction of forward scattered intensity, and in the very small angle region, the intensity of pure diffraction or diffraction including external reflection agrees with Mie scattered intensity well. But with the angle increasing, the difference between them increases. Pure diffraction intensity or the interference intensity of diffraction including external reflection is not sufficient. If the wave of direct transmission through the sphere is considered additionally, the intensity agrees with that by Mie theory well in a wider range of angles.

Q_n^{j-1} in Eq. (3) gives the influence of the whole core (from center to region $j-1$) on the composite sphere scattering. If Eq. (3) is written as

$$\left.\begin{matrix} a_n^l \\ b_n^l \end{matrix}\right\} = \frac{1}{2}(1 - R_n^{j+1,j,j+1} - T_n^{j+1,j} T_n^{j,j+1}) \tag{4}$$

then such influence of the core is excluded. It is depicted in Fig. 4 the comparison of scattered intensity simulated by Eq. (3) with that by Eq. (4). From the figure, we can find that if the influence of the core is included, a shift of angle position appears between two curves. This is because if the influence of the core is excluded, the sphere can be considered as a homogeneous sphere whose refractive index equals to the refractive index of layer l. Once the influence is included, the refractive index profile of sphere changes, and a shift of angle position will appear.

The forward-scattering pattern contains much information about the properties, and the separation of such information is of great practice. Debye series has the advantage of the decomposition of global scattering process in a series of local interaction, and can be employed to the simulation of scattered intensity of single mode or interference intensity of many modes. In this paper, a formula of Debye series expansion of forward scattering by multi-layered sphere is presented, and is employed to the study of forward scattering by multi-layered sphere. The construction of forward scattered intensity is studied on the use of Debye series, and the influence of the core on composite sphere scattering is discussed as well.

ACKNOWLEDGMENT

Supported by Project supported by the Research Foundation from Ministry of Education of China (Grant No. 106149).

REFERENCES

1. Wu, Z. S., et al., *Appl. Opt.*, Vol. 36, 5188, 1997.
2. Li, R. X., X. E. Han, H. F. Jiang, and K. F. Ren, *Appl. Opt.*, Vol. 45, 1260, 2006.
3. Li, R. X., X. E. Han, H. F. Jiang, and K. F. Ren, *Appl. Opt.*, Vol. 45, 6255, 2006.
4. Honenac, E. A., *J. Opt. Soc. Am. A*, Vol. 9, 781, 1992.
5. Lock, J. A., J. M. Jamison, and C.-Y. Lin, *Appl. Opt.*, Vol. 33, 4677, 1994.

6. Ungut, A., G. Grehan, and G. Gouesbet, *Appl. Opt.*, Vol. 20, 2911, 1981.
7. Xu, F., X. S. Cai, and K. F. Ren, *Appl. Opt.*, Vol. 43, 1870, 2004.
8. Debye, P., *Phys. Z.*, Vol. 9, 775, 1980.
9. Nussenzveig, H. M., *J. Math. Phys.*, Vol. 10, 82, 1969.
10. Nussenzveig, H. M., *J. Math. Phys.*, Vol. 10, 125, 1969.
11. Lock, J. A., *J. Opt. Soc. Am. A*, Vol. 5, 2032, 1988.
12. Lock, J. A., *Appl. Opt.*, Vol. 33, 4677, 1994.
13. Lock, J. A., *J. Opt. Soc. Am. A*, Vol. 14, 1316, 1997.
14. Lock, J. A., *Appl. Opt.*, Vol. 44, 5594, 2005.
15. Ross, O. N. and S. G. Bradley, *Appl. Opt.*, Vol. 41, 5130, 2002.

Comparison of Two Drain Modulator for Multi-mode Multi-band Transmitters Employing EER Technique

G. Filice[1] **and V. Ferrara**[2]

[1] Electronic Engineering, University of Rome, La Sapienza, Italy
[2] Department of Elettronic Engineering, University of Rome, La Sapienza, Italy

Abstract— This paper compares two types of Amplitude Modulator and their applicability in High Power Amplifiers (HPA) with Envelope Elimination and Restoration (EER) technique and Low Voltage supply for the use of multi-mode multi-band terminals: a very flexible terminal plays a key role in the worldwide telecommunications coverage. First of all a HPA with drain efficiency of 88% that operates at 1.95 GHz was tested with a typical drain modulator, then is shown that a different modulator can achieve a better drain efficiency but it is going to operate with lower values of modulation index (m_a).

1. INTRODUCTION

The Consumer Area of the electronic market has always had an imperative: to offer products with high performance at low cost. The realization of the System On Chip (SoC) in integrated technology at low cost as the Complementary Metal Oxide Semiconductor (CMOS) allows in reducing costs, but it's not over. A mobile terminal, e.g., a mobile phone, should demonstrate a high operative autonomy; improving the efficiency of the Radio Frequency (RF) transmitter inside itself allow to reduce the dimension and the weight of the batteries and the cost itself, a part from the operative temperature consequences. The modern requirement to have a worldwide coverage of telecommunications, intended as the possibility of communicating wireless towards and to every place on the earth, contemplates the interoperability among different kind of terminals. For this reason an important goal is represented by the realization of mobile terminals that have a RF section able to manage FM and AM signals, or both, in a very large frequency band. Besides the high increase in the Bit Rate of the modern system of telecommunications required the introduction of modulation schemes with a greater spectral efficiency with signal modulation to transmit both in phase and in amplitude, these signals could be transmitted only with linear transmitters that typically show a low value for efficiency. From many years on many linearization techniques were studied to make high efficiency amplifier, but strongly non-linear, which could be use in these applications.

2. EER TECHINQUE AND HIGH EFFICIENCY PA

The introduction of the EER is not recent, with its utilization we can achieve the amplification of non constant envelope signals and great drain efficiency. The principle of the EER technique is depicted in Figure 1. The input signal, both modulated in phase and in amplitude, is passed in a limiter that removes the envelope variations, then this signal feeds a switching PA. In the second path of the signal the signal envelope itself is extracted and then utilized to varying the bias supply of the PA. In practice the realization of an EER amplifier has a lot of drawback, particularly for what concern the Intermodulation Products (IMD) produced by many factors, such as the wrong synchronization between the two signal paths. The first goal of this paper is to verify if it's possible the design of EER amplifiers with very high drain efficiency in CMOS technology.

A switching PA is conceptually different from a traditional one, the active device doesn't act as a voltage-controlled current generator but as a switch. In a switch, in theory, the voltage to current product on its terminals always has a zero value, so if the behavior of the active device is similar with the one of a switch, we can achieve a very high efficiency in the DC-RF power conversion.

For behavioral simulation was designed a dual stage switching PA. The final is a class E PA, in this PA the drain (or collector) tension waveform is shaped by a reactive network to have null slope in the moment in which the tension falls to zero, such network moreover acts as a filter on the signal and supplies at the output a sinusoidal one. The efficiency can catches up the theoretical limit of 100% if such PA is droved with a square wave. Therefore the driver is designed in class F in Third Harmonic Peaking (THP) configuration that, thanks to the elimination of the second harmonic term at the output, exhibits a tension waveform very similar to a square wave with a very simply circuitry.

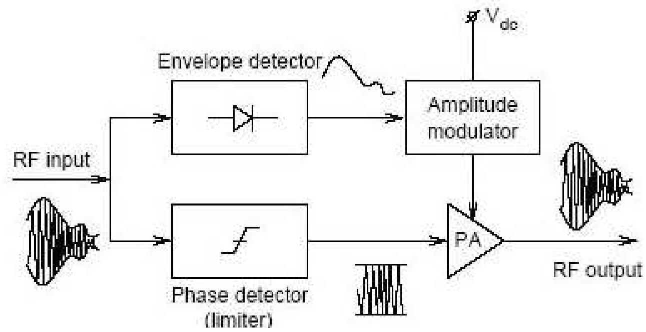

Figure 1: Block diagram of a EER PA.

In Figure 2 is depicted the block diagram of the PA connected to a generic drain modulator and in the continuation used in the tests.

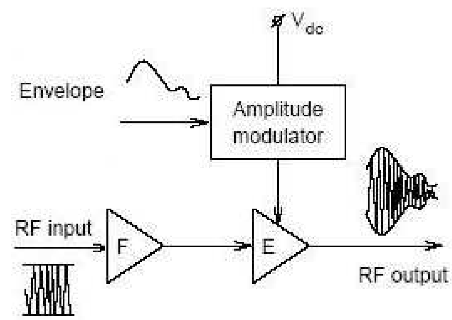

Figure 2: Block diagram of the tested EER PA.

The PA was designed in 0.18 μm MOS on Custom IC Design Tools by Cadence© and BSIM3 models for MOS devices. After the necessary optimizations the PA has exhibited a drain efficiency of 88% and a P_{out} of 22 dBm on a 50 Ω load.

3. MODULATORS SCHEMES

In Figure 3 is depicted the connection of a typical modulator of drain to a PA in class E. Its implementation in Low Voltage IC applications introduces at least two serious problems. First, the stage in class E is designed in order to work with one determined V_{DD}, in this paper 1.2 V, and therefore it must be biased from the modulator with an DC value equals just to 1.2 V. But the PMOS in Figure 3 is the final stage, with output on the drain, of a base-band amplifier, V_{DD} must therefore be increased so that its drain can have a swing sufficient to guarantee the depth of modulation demanded from the application without to sending in triode the PMOS. In our case with $V_{DD} = 1.8$ V such modulator has been able to impose an index of amplitude modulation of the carrier approximately of 0.43. It depends by the fact that the entity of the currents with which works the PA in class E does not change, from the V_{DD} increase is from previewing one remarkable reduction of the efficiency.

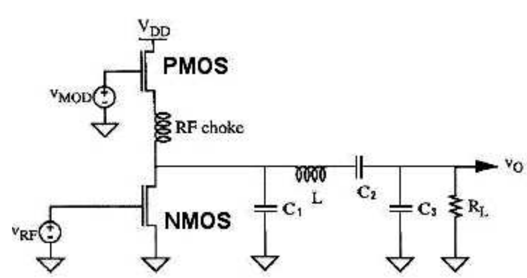

Figure 3: Diagram of a typical drain modulator (simplified).

The second problem is connected to the value of the polarization RFC, as in every RF PA its value must be sufficiently large to allow the drain a swing of tension equal to the double of its DC bias tension, but in an application as the one in Figure 3 its value must be sufficiently small so that at the frequency of the modulating signal its impedance is negligible and the bias of the drain of the PA can therefore be varied dynamically.

In Figure 4 it is depicted as for values of RFC under of 10 nH the efficiency and the P_{out} decreases quickly, for values over of 20 nH the efficiency stretches to become stabilized around to 58% with one P_{out} little inferior to the 22 dBm. Clearly RFC with the values demands from the application is not realizable in integrated technology and must be externally connected to the chip. Putting in evidence like the efficiency of drain is lasting from 88% to 58% for the introduction of the modulator but above all because of the V_{DD} increase. The merits of such circuit they are the elevated value of usable index modulation and the possibility to use a low frequency modulating signal thanks to the DC coupling of the modulator with the PA.

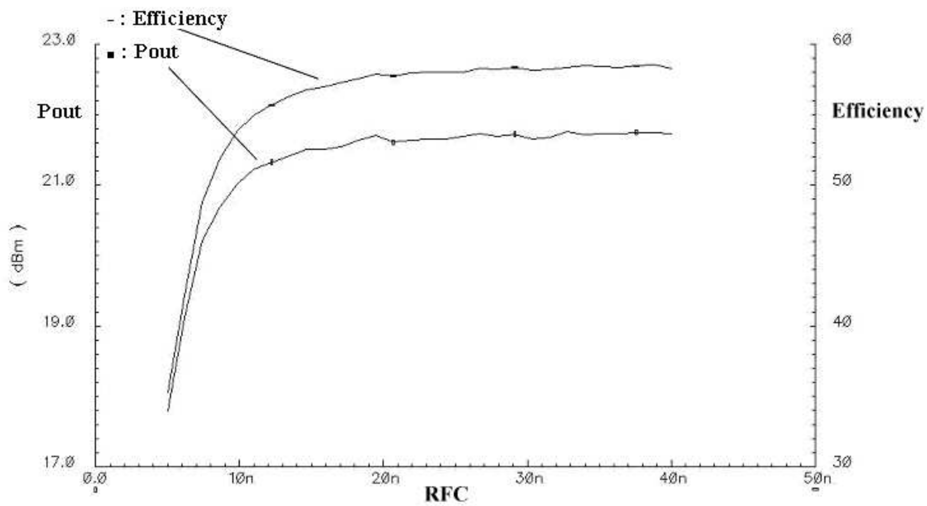

Figure 4: Simulated Efficiency and P_{out} vs. RFC value.

A different type of modulator can be used in order to improve the efficiency of drain. In Figure 5(b) a modified version of the classic modulation Heising scheme is represented. In this circuit V_{DD} remains equal to 1.2 V and the modulator (outlined as a buffer of tension) is coupled to PA through one BFC. The modulator can be assimilated to an OPerational Amplifier (OPA) with output stage in class B push-pull configuration, the OPA has the output tension fixed to $V_{DD}/2$ and exactly for this reason it cannot be connected in continuous to the PA. As moreover typical of the OPA Low Voltage with final stage in class B the swing of the output tension it is much limiting, for this reason this modulator is capable only of a low amplitude modulation index.

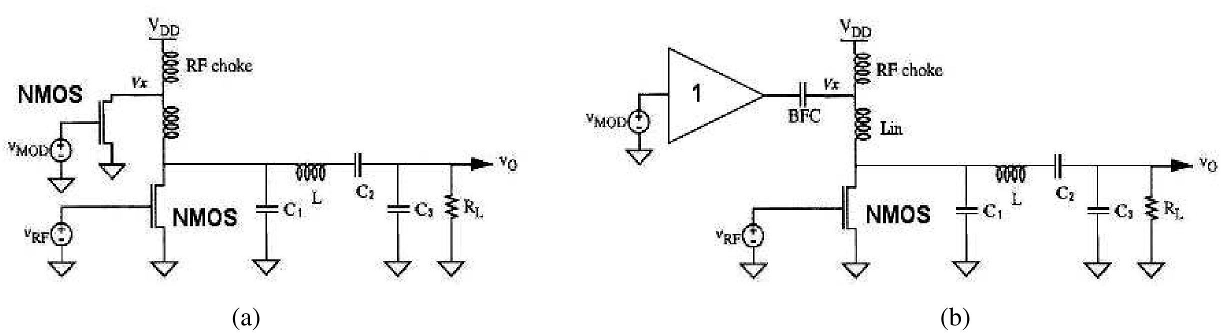

Figure 5: (a) Typical Heising modulation scheme, (b) Modified Heising modulation scheme.

Also in this circuit there are problems of integration of RFC, moreover if it is necessary that the modulator works at very low frequencies also the BFC must be realized externally to the chip.

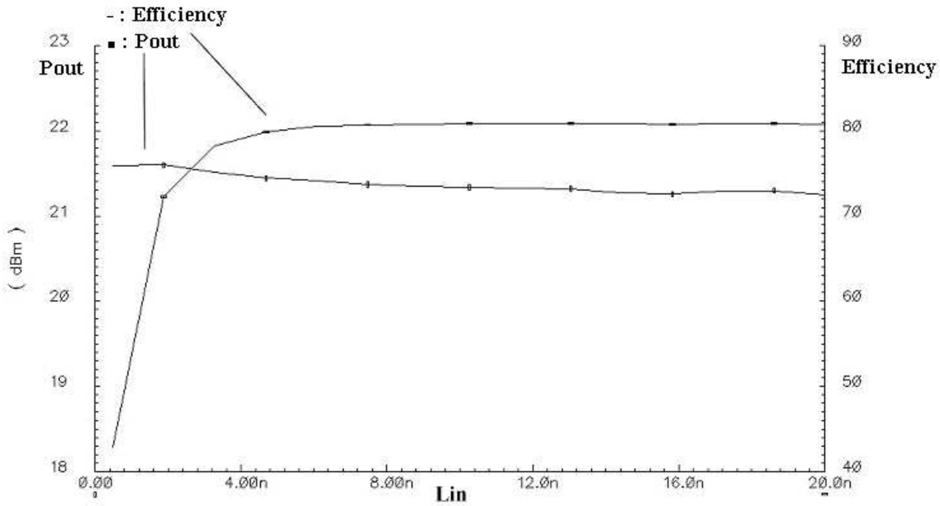

Figure 6: Simulated efficiency and P_{out} vs. Lin value.

The merit of such modulator is shown in Figure 6 where the efficiency and the P_{out} are represented to varying of the value of second inductor Lin in correspondence of the maximum modulation index (approximately 0.24), it is shown clearly as they are obtainable elevate values of the efficiency, also in the order of 80%, joined to one sufficient output power. For typically realizable values of Lin through bondwire it is possible to maintain the efficiency over of 73%.

4. CONCLUSIONS

Two different kinds of modulators have been tested with a switching PA with drain efficiency of 80%, and they have shown their differences. If the application does not demand an elevated index of modulation it has been shown that a modulator can be used, this modulator reduces the efficiency total only 8% to forehead of 30% of a typical modulator.

REFERENCES

1. Sokal, N. O., "Class E-A new class of high-efficiency tuned single-ended switching power amplifiers," *IEEE Journal of Solid-state Circuits*, Vol. SC-10, No. 3, 168–176, 1975.
2. Milosevic, D., J. van der Tang, and A. van Roermund, "On The feasibility of application of class E RF power amplifiers in UMTS," *Proceedings of the 2003 International Symposium on Circuits and Systems ISCAS'03*, Vol. 1, I-149-I152, May 2003.
3. Kahn, L. R., "Single sideband transmission by envelope elimination and restoration," *Proc. IRE*, Vol. 40, No. 7, 803–806, July 1952.
4. Raab, H. and D. J. Rupp, "High-efficiency single-sideband HF/VHF transmitter based upon envelope elimination and Restoration," *Proceedings HF Radio Systems and Techniques*, 4–7 July, 1994, IEE, 1994.

Electronic Structure as a Function of Temperature for Si δ-doped Quantum Wells in GaAs

L. M. Gaggero-Sager, **N. Moreno-Martinez**, **I. Rodriguez-Vargas**
R. Pérez-Alvarez, **V. V. Grimalsky**, **and M. E. Mora-Ramos**

Facultad de Ciencias, Universidad Autónoma del Estado de Morelos
Av. Universidad 1001, Col. Chamilpa 62210 Cuernavaca, Morelos, México

Abstract— The electronic structure of a delta-doped quantum well of Si in GaAs matrix is studied at different temperatures. The calculation is carried out self-consistently in the framework of the Hartree approximation. The energy levels and the occupation numbers of the discrete states are reported.

The doping of semiconductors down to atomic resolution (δ doping) has recently become possible as a natural development of the increasing precision of modern MBE growth techniques. Work on δ-doped systems was primarily on n-type structures [1–6].

The knowledge of the energy level structure is important in the theoretical aspects as well as for potential device applications [7, 8]. In this particular, the B δ-doped Si QW has been recently investigated [9–13]. In Ref. [13], the authors study the effect of the temperature in the electronic structure of this system. From the results of that work it is concluded that this effect qualitatively changes the energy structure.

In this paper, we are going to present the first self-consistent calculation of the electronic energy structure for the Si δ-doped QW in GaAs in which the temperature effect in the statistical distribution of charges is considered.

The calculation is performed within the framework of the Effective Mass Theory and one band Envelope Function Approximation (EFA). Thus, the corresponding wave equation is

$$-\frac{\hbar^2}{2m^*}\frac{d^2}{dz^2}F_i(z)+V(z)F_i(z)=E_iF_i(z). \tag{1}$$

$F_i(z)$ is the z-dependent envelope function, E_i is the i-th energy level and m^* is the effective mass.

The spatial band bending is described by the solution of the Poisson equation. We take the energy origin at $z=0\,(V(0)=0)$ with the electric field tending to zero when z tends to infinity. Integrating twice and using the Fubini-Lebesgue theorem to change the order of integration, the Poisson equation adopts a simple form, i.e.,

$$V(z)=\frac{4\pi e}{\epsilon_r}\int_0^z(z-\chi)\rho_e(\chi)d\chi+\frac{2\pi e^2}{\epsilon_r}n_{2D}|z|, \tag{2}$$

n_{2D} is the two-dimensional impurity concentration ($\rho_{imp}=n_{2D}\delta(z)$), ρ_e is the free charge density in the well region, and ϵ_r is the dielectric constant. The charge density, $\rho_e(z)$, is given by

$$\rho_e(z)=-\frac{em^*k_BT}{\pi\hbar^2}\sum_i\ln\left[1+\exp\left(\frac{E_F-E_i}{k_BT}\right)\right]|F_i(z)|^2 \tag{3}$$

where E_F is the Fermi level and n is the occupation number. For non-zero temperatures, all levels are, in principle, occupied. Nevertheless, if the system is locally neutral, the continuous part of the spectrum may be considered empty. Then, the sum in (3) is extended only up to the value of the occupation number in the band. At the same time, the charge neutrality requires that $en_{2D}=-\int_{-\infty}^{\infty}\rho_e(\chi)d\chi$ Consequently, the Fermi level is given implicitly by:

$$en_{2D}=\frac{em^*k_BT}{\pi\hbar^2}\sum_{i=1}^{n}\ln\left[1+\exp\left(\frac{E_F-E_i}{k_BT}\right)\right], \tag{4}$$

These calculations, which consist of the simultaneous solution of the Schrödinger and Poisson equations, tend to be rather awkward and furthermore, on occasion present divergence. They are carried out in an iterative manner, that is, using in each step an input potential, the charge density is calculated and with this, what we call output potential. The input potential of the following iteration will be a mixture of the input and output potentials from the step of the previous iteration. One of the key issues in obtaining the quickest convergence, and of course, non-divergence, is this mixture. In this section, we will discuss a method which we have developed for the mixture after some experience in self-consistent calculations [14]. The ideal self-consistent calculation is that in which the input and output potentials are identical. Let us imagine that we construct a twodimensional space formed by input potential at point z on the x-axis and the output potential at the same point z on the y-axis, the self-consistent solution would be when the point were exactly above the line with slope 1. If $V^{m\,in}(z)\,(V^{m\,out}(z))$ is the input (output) potential in step m of self-consistency, in general the point in the space will not be above the line with slope 1, we will construct a straight line with the two points from the previous steps and with the intersection of these points on the said line, we will obtain the following input potential. In what follows, we will suppose that the zero of energies is placed at the origin. The mixture was made in the following manner.

$$V^{(m+1)i}(z) = A(z)V^{m\,in}(z) + (1 - A(z))V^{m\,out}(z) \tag{5}$$

where

$$A(z) = \left\{ \begin{array}{ll} \dfrac{V^{m\,out}(z) - V^{(m-1)\,out}(z)}{V^{m\,out}(z) - V^{(m-1)\,out}(z) - V^{m\,in}(z) + V^{(m-1)\,in}(z)} & \text{if } \Delta V^{m}(z)\Delta V^{(m-1)}(z) \leq 0 \\ \dfrac{\left|V^{m\,in(z)}\right|}{V^{m\,in}_{\max}(\infty)}\beta & \text{in other case} \end{array} \right\} \tag{6}$$

where $V^{m\,in}_{\max}(\infty)$ is the absolute value of the maximum value of the input potential in step m, $\beta = 1 - \frac{m}{n_{\max}}$, where $n_{\max}$ is the maximum number of iterations proposed to be carried out, it changes, but is usually $n_{\max} \sim 200$ and $\Delta V^{m}(z) = V^{m\,in}(z) - V^{m\,out}(z)(\Delta V^{(m-1)}(z) = V^{(m-1)\,in}(z) - V^{(m-1)\,out}(z))$. The first part of the equation for $A(z)$, demands that both points (that corresponding to step m and that corresponding to step $m-1$) be on both sides of the line in order to avoid divergence. The second part of the equation for $A(z)$, at the origin, $V^{(m+1)\,i}(0) = V^{m\,out}(0)$, so that the input potential of step $m+1$ slowly begins to differentiate itself from the output potential from step m as it distances distances itself from the origin.

We have used the following values as input parameters: $m^* = 0.067m_0$; m_0 being the free electron mass, $\epsilon_r = 12.5$, and $n_{2D} = 5 \times 10^{12}\,\text{cm}^{-2}$. As a convergence criteria we have taken the depth of the well to vary less than 0.01 meV for two consecutive steps.

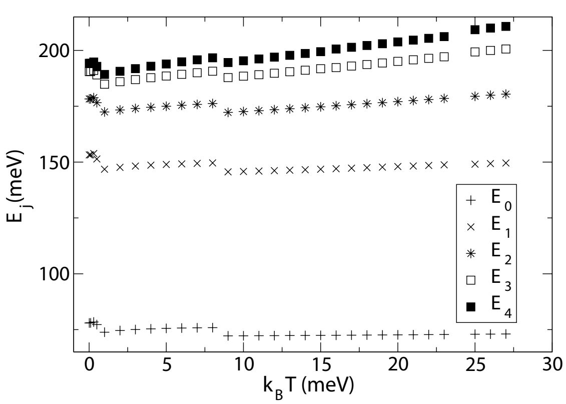

Figure 1: Energy levels (meV) versus k_BT (meV) of Si δ-doped GaAs quantum wells. The energies are measured with respect to the bottom of the conduction band.

In Figure 1, the energy levels are shown between $T = 0$ K and $k_BT = 24$ meV (300 K). The energies are measured with respect to the bottom of the conduction band. Increasing the temperature, the number of levels do not change, the Fermi level shifts 30 meV from the band bottom and the levels are also shifted between them. For example, $E1 - E4$ varies from 116 meV at $T = 0$ K to 133 meV at $k_BT = 23$ meV. In Figure 2 the eigenvalues measured with respect to the Fermi level are depicted.

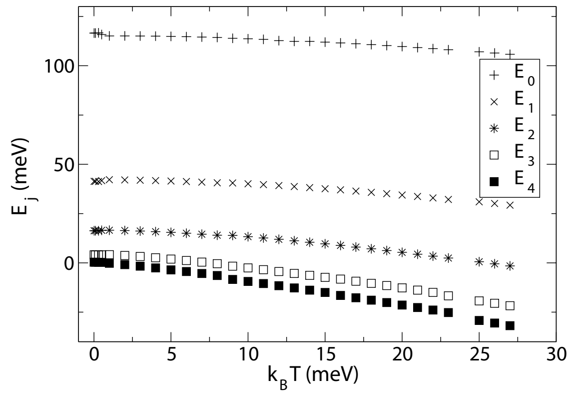

Figure 2: Energy levels (meV) versus k_BT (meV) of Si δ-doped GaAs quantum wells. The energies are measured with respect to the Fermi energy.

In the introduction of this paper we talk about the B δ-doped Si QW. On the contrary to what might be supposed, these two systems (the only ones in which the dependence of the energy levels upon temperature has been self-consistently calculated) bear a qualitatively different behavior. In the case of the B δ-doped Si QW the energy levels structure radically changes with T. At the concentration reported, the number of levels goes from 7 to 13. That is, at room temperature the QW localizes almost the double of levels compared with $T = 0$ K. Meanwhile, in the system here studied the number of levels remains unaltered. While in the B δ-doped Si QW the Fermi level dropped 70 meV at room temperature, in our system it only reduces in less than a half of that quantity (30 meV). The distance between the ground level and the first excited level increases in both cases. In ours the increment at room temperature is almost negligible. Finally, the well bottom rises in both cases just that in our system, this rising is much more smaller than in the B δ-doped Si QW.

Therefore, this system bears a temperature-related behavior which is notably different to previously studied systems, in spite of the similarities between them (because they are both resulting from a planar doping). This suggests that -contrary to the intuition- it can not be asserted that the particular behavior of certain quantum wells can be extended to describe the finite temperature energy spectrum of some other ones even with the existence of strong likenesses in common. Rather, everything seems to indicate that each kind of quantum wells will exhibit a specific behavior with respect to the temperature.

REFERENCES

1. Headrick, R. L., B. E. Weir, A. F. J. Levi, D. J. Eaglesham, and L. C. Feldman, "Si(100)-(2x1) boron reconstruction: Self-limiting monolayer doping," *Appl. Phys. Lett.*, Vol. 57, 2779, 1990.
2. Ni, W.-X., G. V. Hansson, J.-E. Sundgren, L. Hultman, L. R. Wallenberg, J.-Y. Yao, L. C. Markert, and J. E. Greene, "δ-function-shaped Sb-doping profiles in Si(001) obtained using a low energy accelerated-ion source during molecular-beam epitaxy," *Phys. Rev. B*, Vol. 46, No. 12, 7551–7558, 1992.
3. Gossmann, H.-J., C. S. Rafferty, A. M. Vredenberg, H. S. Luftman, F. C. Unterwald, D. J. Eaglesham, D. C. Jacobson, T. Boone, and J. M. Poate, "Time dependence of dopant diffusion in δ-doped Si films and properties of Si point defects," *Appl. Phys. Lett.*, Vol. 64, No. 3, 312–314, 1994.
4. Weir, B. E., L. C. Feldman, D. Monroe, H.-J. Gossmann, R. L. Headrick, and T. R. Hart, "Electrical characterization of an ultrahigh concentration boron delta-doped layer," *Appl. Phys. Lett.*, Vol. 65, No. 6, 737–739, 1994.
5. Scolfaro, L. M. R., D. Beliaev, P. Enderlein, and J. R. Leite, "Electronic structure of n-type δ-doping multiple layers and superlattices in Silicon," *Phys. Rev. B*, Vol. 50, No. 12, 8699–8705, 1994.
6. Wang, Y., R. J. Hamers, and E. Kaxiras, "Atomic structure and bonding of boron induced reconstruction on Si(001)," *Phys. Rev. Lett.*, Vol. 74, No. 3, 403–406, 1995.
7. Schubert, E. F., A. Fischer, and K. Ploog, "The delta-doped field effect transistor (δFET)," *IEEE Transactions on Electron Devices*, Vol. 33, No. 5, 625–632, 1986.

8. Gaggero-Sager, L. M. and R. Péerez-Alvarez, "A simple model for delta-doped field-effect transistor electronic states," *J. Appl. Phys.*, Vol. 78, No. 7, 4566–4569, 1995.
9. Van Gorkum, A. A., K. Nakagawa, and Y. Shiraki, "Controlled atomic layer doping and ALD MOSFET fabrication in Si," *Jpn. J. Appl. Phys.*, Vol. 26, No. 12, L1933–L1936, 1987.
10. Wang, K. L., R. P. G. Karunasiri, and J. S. Park, "Intersubband absorption in $Si_{1-x}Ge_x/Si$ and δ-dope Si multiple quantum wells," *Surf. Sci.*, Vol. 267, No. 1–3, 74–78, 1992.
11. Karunasiri, G., "Intersubband transition in Si-based quantum wells and application for infrared photodetectors," *Jpn. J. Appl. Phys.*, Vol. 33, No. 4B, 2401–2411, 1994.
12. Zhu, J.-H., D.-W. Gong, B. Zhang, F. Lu, C. Sheng, H.-H. Sun, and X. Wang, "Admittance spectroscopy studies of boron δ-doped Si quantum wells," *Phys. Rev. B*, Vol. 52, No. 12, 8959–8963, 1995.
13. Gaggero-Sager, L. M. and R. Péerez-Alvarez, "Electronic structure of delta-doped quantum well as a function of temperature," *Appl. Phys. Lett.*, Vol. 70, No. 2, 212–213, 1997.
14. Vlaev, S. J. and L. M. Gaggero-Sager, *Some Contemporary Problems of Condensed Matter Physics*, Nova Science Publishers Inc., New York, 2000.

p-n-p δ-doped Quantum Wells in GaAs

L. M. Gaggero-Sager and I. Rodriguez-Vargas
Facultad de Ciencias, Universidad Autónoma del Estado de Morelos
Av. Universidad 1001, Col. Chamilpa 62210, Cuernavaca, Morelos, México.

Abstract— We present the electronic structure and relative mobility of a n-type δ-doped quantum well in GaAs surrounded with potential barriers created by p-type δ-doping. The Thomas-Fermi and the effective mass theory has been applied to obtain an analytical expression for the confining potential, and the electron spectrum, respectively. The electron energy levels and the relative mobility have been analyzed as a function of the impurity density in the nand p-type planes as well as the distance between them. We have paid special attention to the relative mobility, obtaining an increase in this by a factor of 2 with respect to a single δ-doped well without barriers. So, the p-n-p δ system can be interesting for applications in high speed and high power devices.

The basic parameters of all semiconductor systems are the free carrier density and the carrier mobility. The δ-doping technique provides the highest carrier density in these systems, however, the carrier mobility is not the optimal due to the strong interaction between the carriers and the impurity centers. One way to improve the transport properties in δ-doped systems is to couple two δ-doped layers (*DDD*) of the same type of impurities [1, 2]. Although the mobility in *DDD* QW's is not greater than in single δ-doped (*SDD*) QW's the conductivity improves 20–30% for temperatures 77–300 K [2], which is attractive for technological applications [3–6]. From the theoretical point of view the double δ-doped systems has been studied — for different materials and type of dopants-within the lines of the envelope function (*EFA*) approximation [7, 8]. In these works the electronic structure is described in detail and the optimal parameters — interwell distance and impurity density — for the maximum mobility are given. The implemented formula for the relative mobility is a key element for the study and it depends on the most important dispersion mechanism at low temperature (the interaction between carriers and impurities) and also on the statistical weight of the carriers (the electronic structure).

In the present work we undertake the study of the electronic properties and the relative mobility in p-n-p δ-doped quantum wells (*pnpDD*) in GaAs. We take advantage from the methodology previously proposed and applied to the case of double δ-doped quantum wells [7, 8] in order to investigate the effect of the surrounded p-type barriers onto the electronic structure and specially onto the carrier mobility.

For a single n-type δ-doped quantum well centered in $z = a$ the confining potential can be written as [9],

$$V^*_{Hn}(z) - \mu^*_n = -\frac{\beta^2}{(\beta|z-a| + z_{0n})^4}, \tag{1}$$

with $\beta = \frac{2}{15\pi}$ and $z_{0n} = \left(\frac{\beta^3}{\pi n_{2D}^{au}}\right)^{1/5}$. $V^*_{Hn} = V_{Hn}/R^*_{yn}$, $\mu^* = \mu/R^*_{yn}$ are given in units of the effective Bohr radius and effective Rydberg, $a^*_{0n} = \frac{\epsilon_r \hbar}{m^* e^2}$ and $R^*_{yn} = \frac{e^2}{2\epsilon_r a^*_{0n}}$.

In the case of a single p-type δ-doped quantum well centered in $z = b$ the confining potential can be written as [10],

$$V^*_{Hp}(z) - \mu^*_p = \frac{\alpha^2}{(\alpha|z-b| + z_0)^4}, \tag{2}$$

with $\alpha = \frac{2m_a^{3/2}}{15\pi}$ and $z_{0p} = \left(\frac{\alpha^3}{\pi p_{2D}^{au}}\right)^{1/5}$. $V^*_{Hp} = V_{Hp}/R^*_{yp}$, $\mu^*_p = \mu/R^*_{yp}$ are given in units of the effective Bohr radius and effective Rydberg, $a^*_{0p} = \frac{\epsilon_r \hbar}{m^*_{hh} e^2}$ and $R^*_{yp} = \frac{e^2}{2\epsilon_r a^*_{0p}}$.

The next step is the construction of the *pnpDD* potential well, so, if we consider the same impurity density in both p-type wells the system is symmetric with respect to the middle of the n-type one, then we can restrict ourself to the half of the plane ($z \leq 0$) and the potential can be written as

$$V^*_H(z) = -\frac{\beta^2}{(\beta|z| + z_{0n})^4} + \frac{\alpha^2}{(\alpha|z+l| + z_0)^4} \tag{3}$$

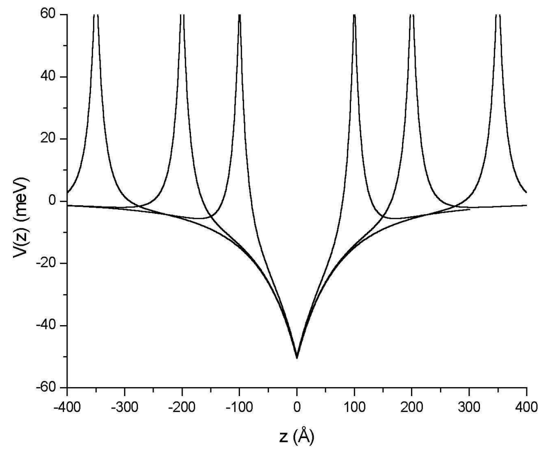

Figure 1: Potential profile of $pnpDD$ QW's for different interwell distances with $n_{2D} = 1 \times 10^{12}\,\mathrm{cm}^{-2}$ and $p_{2D} = 1 \times 10^{13}\,\mathrm{cm}^{-2}$.

where a and b have been taken as 0 and l.

The latter equation summarized the model for the conduction band bending profile. Instead of carrying out numerically troublesome self-consistent calculations, we simply solve the Schrödinger-like effective mass equation at the zone center $\mathbf{k} = \mathbf{0}$, Eq. (4), thus obtaining the corresponding subband electron levels.

$$\left[-\frac{\hbar^2}{2m^*}\frac{d^2}{dz^2} + V_H(z)\right] F_n(z) = E_n F_n(z). \tag{4}$$

For the mobility calculations we adopt the relative mobility formula [7, 8] and applied it to the case of $pnpDD$ quantum wells,

$$\mu_{rel}^{\delta} = \frac{\mu_{pnp}DD}{\mu_{SDD}} = \frac{\iint \rho_e^{\delta}(z')\rho_{imp}^{\delta}(z)|z-z'|dzdz'}{\iint \rho_e^{pnp\delta}(z')\rho_{imp}^{pnp\delta}(z)|z-z'|dzdz'}, \tag{5}$$

where ρ_e^{δ} and ρ_{imp}^{δ} ($\rho_e^{pnp\delta}$ and $\rho_{imp}^{pnp\delta}$) represent the density of electrons and impurities of SDD (of $pnpDD$), respectively. Substituting the density of electrons and impurities and integrating over z we obtain,

$$\mu_{rel}^{\delta} = \frac{\sum_i \int \left|F_e^{\delta}(z')\right|^2 \left(k_F^{\delta} - E_i^{\delta}\right)|z'|dz'}{\sum_i \int \left|F_e^{pnp\delta}(z')\right|^2 \left(k_F^{pnp\delta} - E_i^{pnp\delta}\right)|z'|dz'}, \tag{6}$$

where $F_e^{\delta}(z')$, k_F^{δ} and E_i^{δ} ($F_e^{pnp\delta}(z')$, $k_F^{pnp\delta}$ and $E_i^{pnp\delta}$ are the envelope function, the Fermi level and the ith level respectively of the SDD (of $pnpDD$).

The input parameters for the δ-doped quantum wells are: $m_e^* = 0.067m_0$, $m_{hh}^* = 0.52m_0$, $m_{lh}^* = 0.087m_0$, $\epsilon_r = 12.5$ and $10^{12} \leq p_{2D} \leq 10^{14}\,\mathrm{cm}^{-2}$.

In Fig. 1 the potential profile of the $pnpDD$ quantum wells are depicted for three interwell distances, remaining fixed the impurity density in the δ-doped layers, $n_{2D} = 1 \times 10^{12}\,\mathrm{cm}^{-2}$ and $p_{2D} = 1 \times 10^{13}\,\mathrm{cm}^{-2}$. From this figure we can see that the width of the confining region increase as the potential barriers are moved away from the n-type δ-doped layer. This fact is reflected in the number of trapped states and the effective confinement of them, see Fig. 2.

In Fig. 3 the relative mobility is shown as a function of the interwell distance of the n- and p-type δ-doped wells. The impurity density in the n- and p-type δ-doped layers is the same as in the preceding figures, Figs. 1 and 2, for the upper curve and $p_{2D} = 2 \times 10^{12}\,\mathrm{cm}^{-2}$ for the bottom curve. The relative mobility presents a very interesting and quite different behavior as a function of the interwell distance as compared to the DDD case [7, 8]. Firstly, the relative mobility has its maximum value for the shortest interwell distance considered (100 Å), this is a direct consequence of the interaction between the electron cloud and the impurity planes, that in this kind of systems is linear, so the carrier mobility increases as the impurity planes and the electron cloud are closer to

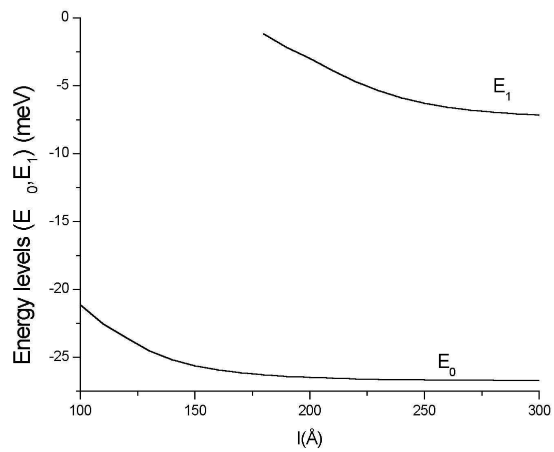

Figure 2: Electron energy levels versus the distance between the n-type δ-doped well and the p-type δ-doped wells with $n_{2D} = 1 \times 10^{12}\,\mathrm{cm}^{-2}$ and $p_{2D} = 1 \times 10^{13}\,\mathrm{cm}^{-2}$.

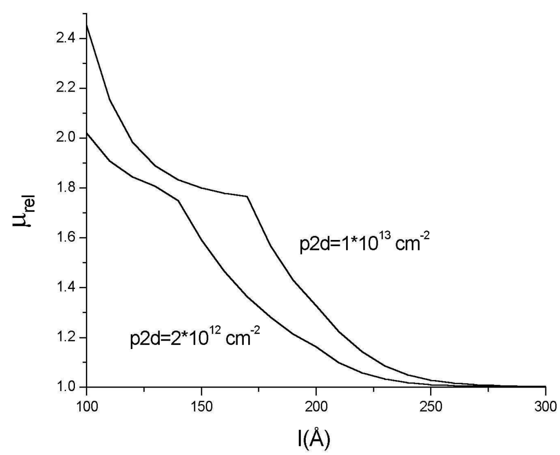

Figure 3: Relative mobility versus the distance between the n- and the p-type δ-doped wells for $n_{2D} = 2 \times 10^{12}\,\mathrm{cm}^{-2}$ and $p_{2D} = 1 \times 10^{13}\,\mathrm{cm}^{-2}$ for the upper curve ($p_{2D} = 2 \times 10^{12}\,\mathrm{cm}^{-2}$ for the bottom curve).

each other. The minimum distance that we have consider between the n- and p-type wells is 100 Å in order to avoid possible compensation effects, since the electron and hole Bohr radius has a value of the order of 100 Å in GaAs. The mobility for the particular impurity densities consider here is around 2.5 (upper curve) and 2.0 (bottom curve) times grater than in the *SDD* case. Secondly, the relative mobility diminishes as the p-type barrier are moving away from the n-type δ-doped quantum well until it reaches the unity. Far way from the n-type δ-doped quantum well the p-type barriers don't modify the electronic structure and the ratio of the mobilities is 1. Thirdly, considering a low p-type impurity density the potential barrier height diminishes, as a result the electrons can penetrate deeper into the potential barriers and consequently the relative mobility diminishes.

In conclusion, we have study the electronic structure and the relative mobility in *pnpDD* quantum wells. It is shown that the relative mobility in these structures is improved substantially with respect to *SDD* and *DDD* ones. So, the *pnpDD* quantum wells can be of interest for possible technological applications in high speed and high power electronic devices.

REFERENCES

1. Zheng, X., T. K. Carns, K. L. Wang, and B. Wu, "Electron mobility enhancement from coupled wells in delta-doped GaAs," *Appl. Phys. Lett.*, Vol. 62, No. 5, 504–506, 1993.
2. Gurtovoi, V. L., V. V. Valyaev, S. Y. Shapoval, and A. N. Pustovit, "Electron transport

properties of double delta-doped GaAs structures grown by low-pressure metalorganic chemical vapor deposition," *Appl. Phys. Lett.*, Vol. 72, No. 10, 1202–1204, 1998.

3. Schubert, E. F. and K. Ploog, "The δ-doped field-effect transistor," *Jpn. J. Appl. Phys.*, Vol. 24, No. 8, 1985.
4. Nakagawa, K., A. A. van Gorkum, and Y. Shiraki, "Atomic layer doped field-effect transistor fabricated using Si molecular beam epitaxy," *Appl. Phys. Lett.*, Vol. 54, No. 19, 1869–1871, 1989.
5. Gaggero-Sager, L. M. and R. Perez-Alvarez, "A simple model for delta-doped filed-effect transistor electronic states," *J. Appl. Phys.*, Vol. 78, No. 7, 4566–4569, 1995.
6. Martinez-Orozco, J. C., L. M. Gaggero-Sager, and S. J. Vlaev, "A simple model for the differential capacitance profile in atomic layer doped field effect transistor (ALD-FET) in GaAs," *Mater. Sci. Eng. B*, Vol. 84, No. 3, 155–158, 2001.
7. Rodriguez-Vargas, I., L. M. Gaggero-Sager, and V. R. Velasco, "Thomas-Fermi-Dirac theory of the hole gas of a double p-type δ-doped GaAs quantum wells," *Surf. Sci.*, Vol. 537, No. 1–3, 75–83, 2003.
8. Rodriguez-Vargas, I. and L. M. Gaggero-Sager, "Subband and transport calculations in double n-type δ-doped quantum wells in Si," *J. Appl. Phys.*, Vol. 99, No. 3, 033702–033707, 2003.
9. Gaggero-Sager, L. M., "Exchange and correlation via functional of Thomas-Fermi in delta-doped quantum wells," *Modelling Simul. Mater. Sci. Eng.*, Vol. 9, No. 1, 1–5, 2001.
10. Gaggero-Sager, L. M., M. E. Mora-Ramos, and D. A. Contreras-Solorio, "Thomas-Fermi approximation in p-type δ-doped quantum wells of GaAs and Si," *Phys. Rev. B*, Vol. 57, No. 11, 6286–6289, 1998.

Dynamic Behaviors of PbS Irradiated by Laser Pulse

Jinjing Feng[1], **Jixiang Yan**[1], **and Shouhuan Zhou**[2]
[1]Department of Optoelectronic Engineering, Beijing Institute of Technology, China
[2]NCRIEO (North-China Research Institute of Electric Optics), China

Abstract— PbS detector is known as an important infrared (IR) detector which is widely used. The study of laser irradiation on PbS is important in military and commercial area. When the PbS sample is irradiated by laser pulse, the temperature rises in the sample. As the power density of the laser pulse increases, transient phase transformation may occur. In this paper, we will simulate the temperature field in PbS, and discuss the dynamic behaviors of PbS irradiated by laser pulse.

1. INTRODUCTION

In recent years, the study of laser irradiation on semiconductor has attracted growing attention. It is suggested that the temperature rises when the sample is irradiated by laser beam. When the power density increases to sufficient quantity, various permanent effects may occur in the semiconductor, such as melting, vaporization, removal of material from the sample surface.

PbS detector which is known as a kind of infrared (IR) detector was first used in world war II. It causes more and more attention then, and is widely used in military and commercial area. PbS detector works in the wave band of 1–3 µm.

In this paper, we will discuss the dynamic behavior in PbS sample which is irradiated by laser pulse, by simulating the temperature field.

2. HEAT CONDUCTION EQUATION

It is indicated in previous research work that the intermediate mechanisms of energy transformation from laser to sample heating can be neglected, if

1. The diffusion length of free carriers before recombination is shorter than the light penetration depth or the heat diffusion length during pulse duration.
2. Free carrier absorption is negligible compared with lattice (band-to-band)-absorption.
3. The lifetime of free carriers is shorter than pulse duration.

The heat conduction equation is still valid here.

We presume,

1. The properties of the materials don't change in this course.
2. There is no energy loss caused by surface rediation and convection.

The transient temperature distribution can be determined by solving the heat conduction equation,

$$\frac{dT}{dt} = \frac{K}{\rho c_p}\nabla^2 T + \frac{Q}{\rho c_p} \tag{1}$$

T is the transient temperature of the material, ρ is the density of the material, K is the thermal conductivity, c_p is the specific heat, Q is the interior heat source.

The diffusion length in the material is

$$L_T = \sqrt{2k\tau_L} \tag{2}$$

k is the thermal diffusivity, τ_L is the duration of laser pulse. In our experiment, the duration of the laser pulse is very short ($\tau_L = 30\,\mathrm{ns}$), $k = 0.077\,\mathrm{cm}^2\cdot\ \mathrm{s}^{-1}$ for PbS. The diffusion length $L_T = 6.79 \times 10^{-5}\,\mathrm{cm}$. It is much smaller than the radius of the laser beam. In consequence, the heat conduction course can be simplified to one-dimension heat conduction course.

$$\frac{dT}{dt} = \frac{K}{\rho c_p}\frac{d^2T}{dx^2} + \frac{Q}{\rho c_p} \tag{3}$$

In one-dimension condition, Q is defined as

$$Q = (1 - R)I_0 e^{-x/\delta}/\delta \tag{4}$$

R is the reflectivity of the material, I_0 is the power density of the laser beam, δ is the heat diffusion depth.

The boundary conditions of the one-dimension heat conduction equation is

$$-K\frac{\partial T}{\partial t}|_{x=0} = \alpha(T - T_0) \tag{5}$$

$$T(x,t)|_{x=\infty} = const. \tag{6}$$

$$T(x,t)|_{t=0} = const. \tag{7}$$

T_0 is the initial temperature. It is room temperature here. $T_0 = 293K$. And the constant in Equations (6) and (7) correspond to 293 K.

We suppose the absorption coefficient is very large, the Equation (3) can be approximate to

$$T(x,t) = \frac{2(1-R)I_0}{K} \cdot \sqrt{Dt} \cdot ierfc\left(\frac{x}{2\sqrt{Dt}}\right) \tag{8}$$

The surface temperature can be approximate to

$$T(0,t) \approx \frac{2(1-R)I_0}{K} \cdot \sqrt{\frac{Dt}{\pi}} = 2(1-R)I_0\left(\frac{t}{K\rho c_p \pi}\right)^{\frac{1}{2}} \tag{9}$$

Thus the time when melting occurs can be determined by

$$t_m = \frac{\pi K \rho c_p T_m^2}{4(1-R)^2 I_0^2} \tag{10}$$

3. NUMERICAL SOLUTION

The calculation and experiment are carried out on PbS sample. The physical parameters of PbS are shown in Table 1. We presume the duration of the laser beam is 30 ns (FWHM), the wavelength is 1.06 µm, the power density is $I = 1.14 \times 10^8\,\mathrm{w \cdot cm^{-2}}$. The calculated results of the transient temperature field in the sample of PbS is shown in Fig. 1.

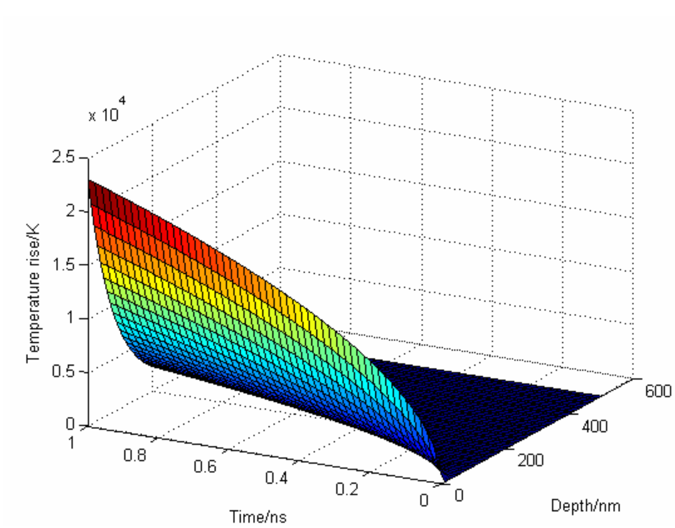

Figure 1: The transient temperature field in the sample of PbS at the power density of $1.14 \times 10^8\,\mathrm{w \cdot cm^{-2}}$.

Table 1: The physical parameters of PbS.

Density ρ	Thermal conductivity K	Specific heat c_p	Reflectivity R	Melting temperature T_m
$7.6\,\mathrm{g{\cdot}cm^{-3}}$	$0.03\,\mathrm{W{\cdot}cm^{-1}{\cdot}K^{-1}}$	$0.0511\,\mathrm{J{\cdot}\ g^{-1}{\cdot}\ K^{-1}}$	0.31	1387 k at 1 at m

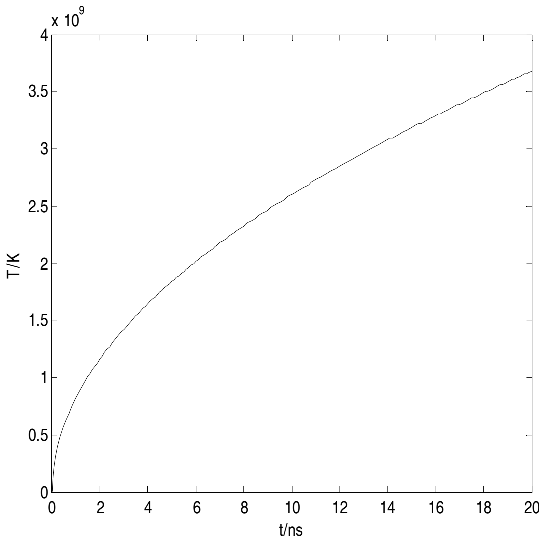

Figure 2: The temperature of the front surface at the power density of $1.14 \times 10^8\,\mathrm{w \cdot cm^{-2}}$.

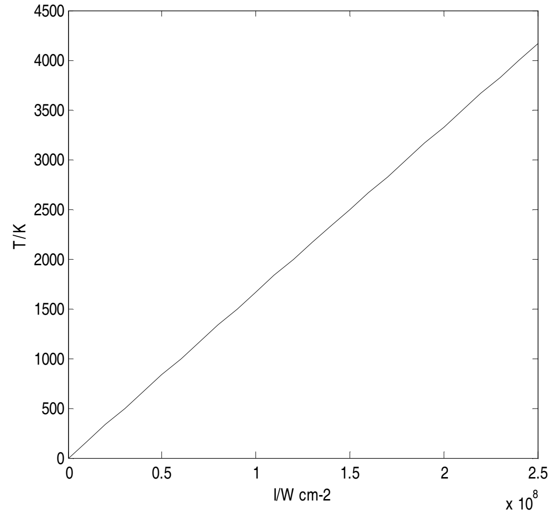

Figure 3: The surface temperature vs power density.

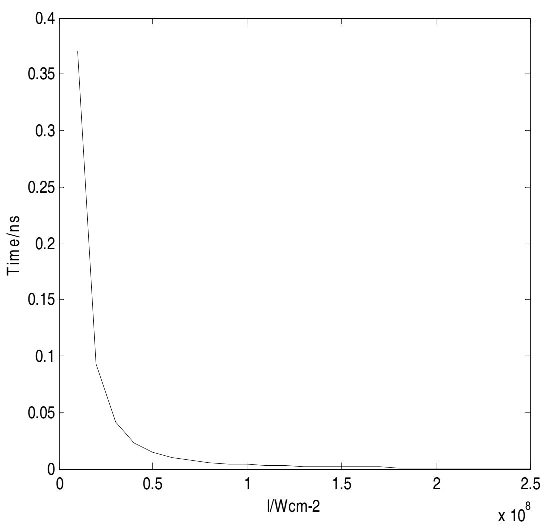

Figure 4: Time when melting occurs vs power density.

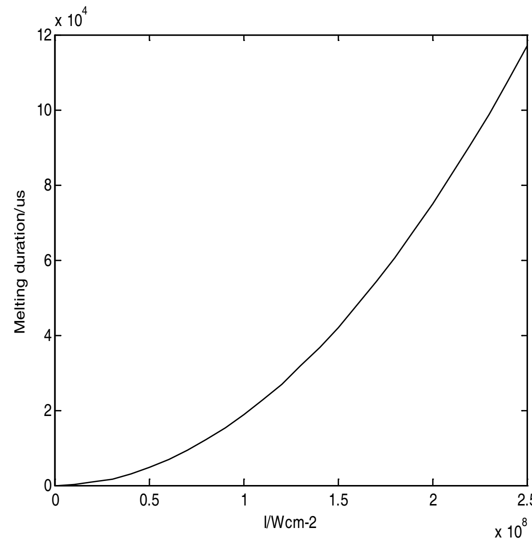

Figure 5: The melting duration vs power density.

4. CONCLUSION

In this paper the transient temperature field in detector material of PbS is simulated. The melting behavior in the sample is also analyzed by numerical calculation. The result is proved by experiments on PbS sample. It is reasonable to believe the thermal model used in this paper is appropriate and the result is correct.

ACKNOWLEDGMENT

The research work is supported by National Nature Science Foundation of China (60378002). We are grateful to Feng Longling for the research instruction, and Zhang Huihui for the assistance.

REFERENCES

1. Khaibullin, I. B., E. I. Shtyrkov, M. M. Zaripov, M. F. Galijautdinov, and R. M. Bajazikov, "Laser annealing of implanted lyers," *VINITIN*, 2061–74, 1974.
2. Wang, J. C, R. F. Wood, and P. P. Pronko, "Theoretical analysis of thermal and mass transport in ion-implanted laser-annealed silicon," *Appl. Phys. Letts.*, Vol. 33, No. 5, 455–458, 1978.
3. Jiang, Z., T. Liang, and Q. Lu, "Heat effect calculations of PC type hgCdTe detectors when irradiated by laser," *Applied Laser*, Vol. 15, No. 4, 155–157, 1995.
4. Yang, S. and W. Tao, *Thermal Conduction*, High Education Press, Beijing, 1998.
5. Ding, L., *Numerical Calculation Method*, Beijing Institute of Technology Press, Beijing, 1997.

Dynamic Behavior of a Mono-coil Linear Actuator

A. K. Aguillar, J. P. A. Bastos, N. Sadowski, and N. J. Batistela
Grupo de Concepção e Análise de Dispositivos Eletromagnéticos — GRUCAD, Brazil

Abstract— This paper presents a brief explanation of a mono-coil actuator and its advantages. A simulation of the dynamic behavior is shown and the methodology using parametrization based on the FEM (Finite Elements Method) is presented. The actuator modeling is based on the coupling between mechanical and electric circuit equations. We compared two groups of data with different supplying voltages. The computed data and the experimental results are also presented and show good agreement with each other.

1. INTRODUCTION

Magnetic actuators are used in several applications. The device under study is connected to a circuit breaker. It imposes a force on a mechanical apparatus in order to open an electric circuit. Many works are related to magnetic actuators having two coils. Here we will propose an investigation of a mono-coil actuator.

The main difference between these two types of devices is the fact that for double coil actuators, the movement in each direction is commanded by one of the coils, while for mono-coil devices both movements are realized by the same coil. Using a single coil, the movement orientation depends on the direction of the applied current and the position of the mobile part.

The major advantage of a mono-coil actuator is the reduction of the total number of structure parts by eliminating one extra coil and the reduction of the weight, complexity as well as its costs.

This work is the basis for a project designing to be used by a company interested on developing an entire line of actuators. Therefore, the direct use of FEM is not convenient since it is time consuming and difficult to be handled by their engineers team. Then, we are putting together a simplified modeling that can be easily employed and will act as a part of whole project computational system. Taking into account this aspect, the model here presented is not intended to provide a very high degree of accuracy but rather a fast approach to achieve the dimensioning of the actuator.

Due to its particularities, the dynamic behavior analysis is relevant for its design. Basically, it consists on determining the time response of some quantities such as the current across the coil, the displacement of the mobile part and the necessary time to perform the movement.

To obtain the time response of these factors it is necessary to solve simultaneously the magnetic field, the electric circuit and the mechanical motion equations. The equation system is solved by a coupled model. There are different ways to solve such a system as seen in [1].

The model used in this work is a parameterized coupled model, where the electromagnetic quantities are previously calculated. Then the corresponding results are used in connection with the electric circuit and the mechanical motion equations, which are solved simultaneously.

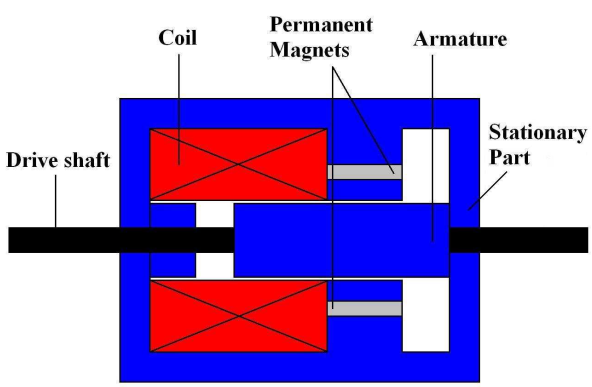

Figure 1: General structure of the permanent magnetic.

The Figure 1 below shows the proposed actuator where there are the stationary part, the two permanent magnets, the coil and a drive shaft. The magnetic circuit is composed by a massive (without lamination) ferromagnetic material, the rare earth permanent magnets (Nd-Fe-Bo, neodymium-iron-boron) and a non ferromagnetic drive shaft.

The operating principle of this actuator was explained in [2]. In this paper we present, firstly, the methodology to obtain the necessary parameters and then we describe the equation system used for the time response. Finally, the comparison between experimental and computed data is performed.

2. PARAMETRIZATION

Before solving the equation system, the actuator parameters must be calculated. As it will be shown shortly, the equations to be solved are dependent on three functions: $F_{mag}(x,i)$, $L(x,i)$, $\frac{dL}{dt}(x,i)$, where F_{mag} is the magnetic force, L is the inductance, x the displacement and i the current.

The first and the second functions are obtained by varying both the displacement and current using a FEM analysis. The derivation of $L(x,i)$ is easily obtained by time discretization. In the numerical procedure, the functions are linearly interpolated in order to acquire the necessary values related to the displacement and current with good accuracy.

The FEM analysis is realized with the software EFCAD [3] developed by GRUCAD – UFSC.

3. ELECTRIC CIRCUIT AND MECHANICAL MOTION EQUATIONS

The actuator electric circuit is shown in Figure 2, where L is the coil inductance, R is the coil resistance and U is the DC supply voltage.

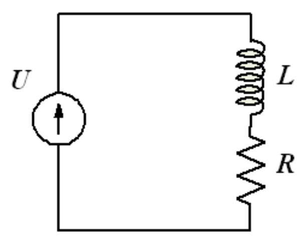

Figure 2: Supplying circuit of the actuator.

The equation system to be solved is the following [4]:

$$U = Ri + \frac{d\Psi}{dt} \quad (1)$$

$$m\frac{d^2x}{dt^2} = F_{mag} - F_c \quad (2)$$

where : $i = SJ$, $\Psi = N\Phi$,
Ψ represents the total flux linkage, m is the mass of the moving part, F_{mag} is the magnetic force, F_c is the total counter force, S is the cross-sectional area of an exciting coil, J is the external current density, N is the number of coil turns and Φ is the magnetic flux.

Due to the relation $\Psi = Li$ and introducing the velocity v as an unknown, the equation (1) becomes

$$U = Ri + L\frac{di}{dt} + i\frac{dL}{dx}v \quad (3)$$

and the final set of equations to be solved becomes:

$$\frac{di}{dt} = \frac{1}{L}\left(U - Ri - i\frac{dL}{dt}v\right) \quad (4)$$

$$\frac{dx}{dt} = v \quad (5)$$

$$\frac{dv}{dt} = \frac{1}{m}\left(F_{mag} - F_c\right) \quad (6)$$

where, as mentioned, the quantities $F_{mag}(x,i)$, $L(x,i)$ and $\frac{dL}{dt}(x,i)$ were previously determined.

The system of equations (4)–(6) is solved by using a classical 4-range Runge-Kutta method, which furnishes the following results. On the drawings below, comparisons for two different supply voltages ($U = 60\,\mathrm{V}$ and $U = 70\,\mathrm{V}$) were performed.

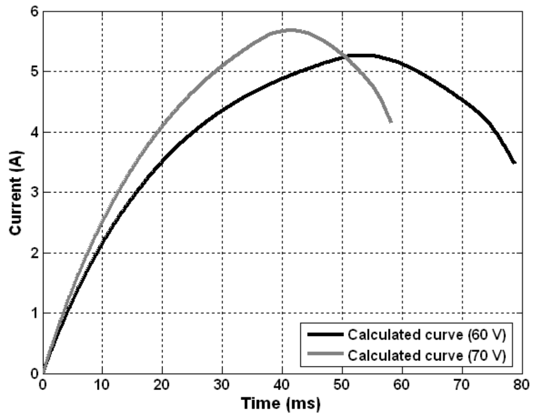

Figure 3: Current in the coil during the movement of the armature.

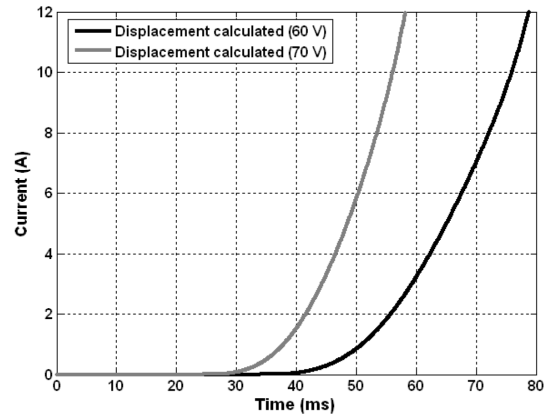

Figure 4: Displacement of the armature.

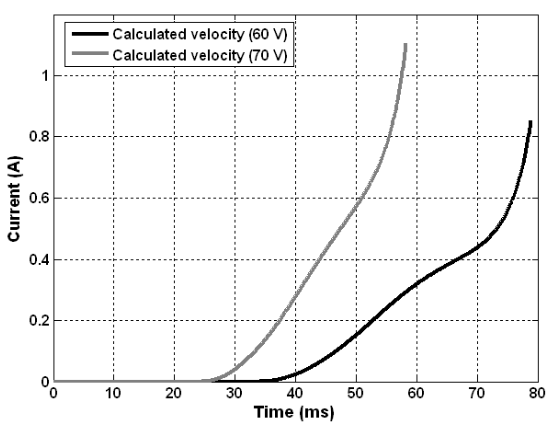

Figure 5: Velocity of the armature.

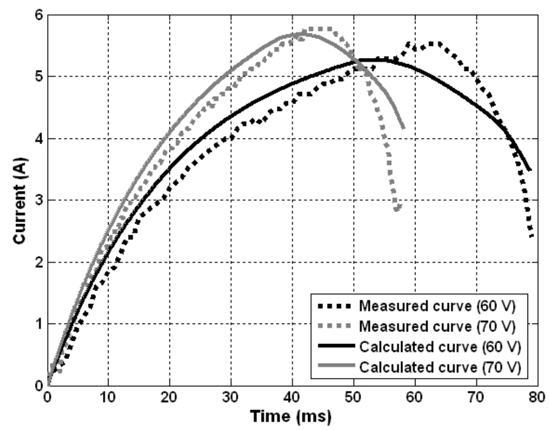

Figure 6: Comparison between experimental and computed data, after correction.

4. COMPARISON BETWEEN EXPERIMENTAL DATA AND COMPUTED DATA

In order to compare the numerical simulation with experimental data a prototype was developed in our laboratory. The actuator is supplied with DC voltage and the current behavior can be observed by an oscilloscope. The experimental data are stored in a personal computer and compared with the simulation results.

As the prototype is built with massive conductive material, eddy currents are present. It has a strong influence on the performance of the actuator and therefore the computed results differ from the experimental data. Therefore, it is necessary to modify the computed data by applying a correction factor on the parameters of the dynamic simulation. Doing so, the new computed results and the experimental data are shown in Figure 6 for the same two voltages, 60 V and 70 V. We see there is a good agreement between the results calculated from analytical model and measured from the experiment. With the correction factor, the modeling furnishes results with reasonable accuracy.

5. CONCLUSION

This paper presents a method for calculating the dynamic behavior of a mono-coil actuator by using a coupling of mechanical and electric equations. The numerical analysis of the mono-coil actuator is realized and a comparison between experimental and calculated data is performed. Because of eddy currents in the magnetic circuit it was necessary to calibrate the computed data. Doing it, simulation curves and experimental data presented good agreement.

The present article concerns the movement of the armature towards the direction corresponding to the opening of the circuit breaker, which is the most critical. The opposite movement has a different approach and it will be the subject of future works.

REFERENCES

1. Ren, Z. and A. Razek, "Modeling of dynamical behaviors of electro-magneto-mechanical coupled systems," *IEE conference, Second International Conference on Computation in Electromagnetic*, Nottingham, 12–14 April 1994.
2. Aguillar, A. K., J. P. A. Bastos, and N. Sadowski, "Introdução ao estudo de um atuador linear biestável mono-bobina," 7° CBMag — Congresso Brasileiro de Eletromagnetismo.
3. EFCAD — Electromagnetic Fields Computer Aided Design, Software, GRUCAD — UFSC, http://www.grucad.ufsc.br, 2006.
4. Xin, L., G. Huijun, and C. Zhiyuan, "Magnetic field calculation and dynamic behavior analyses of the permanent magnetic actuator," *IEEE 19th Int. Symp. on Discharges and Electrical Insulation in Vacuum.*

Time Variant Thresholds — Automatic Adjustment When Filtering Signals in MR Tomography

E. Gescheidtova[1], **R. Kubasek**[1], **Z. Smekal**[1], **and K. Bartusek**[2]

[1]Faculty of Electrical Engineering and Communication, Brno University of Technology, Czech Republic
[2]Institute of Scientific Instruments, Academy of Sciences of the Czech Republic, Czech Republic

Abstract— Removing noise from an FID signal (a signal detected in MR measurement) is of fundamental significance in the analysis of results of NMR spectroscopy and tomography. Optimum solution can be seen in removing noise by means of a digital filter bank that uses half-band mirror frequency filters of the type of low-pass and high-pass filters. A filtering method using digital filters and the approach of automatic threshold adjustment is described in the paper.

1. INTRODUCTION

The MR imaging techniques of tomography and spectroscopy are exploited in many applications. For the MR instruments to function properly it is necessary to maintain high quality of homogeneity of the fundamental magnetic field.

The MR phenomenon can be detected as an electrical signal that will induce in a measuring coil a rotating magnetic moment of the nuclei being measured. This signal is referred to as free induction decay (FID). Since the frequency of an FID signal is identical with the natural frequency of nuclei, the kind of nuclei measured can be established on the basis of signal intensity and the number of nuclei. In the case of commonly used MR spectroscopes and tomographs the natural frequency of nuclei and thus also the fundamental frequency of an FID signal is of the order of tens to hundreds of MHz. But the signal spectral band is relatively small with respect to the fundamental frequency, of the order of tens to thousands of Hz. The signal is therefore commonly transformed into the fundamental band, i.e., zero natural frequency [1, 2]. Since the spectrum of FID signal is not symmetrical around the fundamental frequency, the FID signal after being transformed into the fundamental band is a complex signal. Because of technical considerations the MR phenomenon is in practice called forth not by changing a fundamental magnetic field but by short-term superposition of another magnetic field. This further magnetic field is of rotational nature, which is achieved by excitation using a coil through which electric current is flowing and has a harmonic waveform of suitable amplitude modulated, so-called high-frequency excitation impulse. The frequency of the impulse (and thus also of field rotation) is chosen to be close to the natural frequency of the rotation of nuclei.

2. NOISE IN MR SIGNAL

When defining the area being measured in localized spectroscopy and tomography, the gradient field is excited by very short impulses of sufficient magnitude. This gives rise to a fast changing magnetic field, which induces eddy currents in the conducting material near the gradient coils. These currents then cause retrospectively unfavorable deformation of the total magnetic field. The effect of eddy currents acts against the fast temporal changes in the magnetic field. The basic idea of a method that compensates this effect consists in replacing the missing leading edge of the field waveform by an overshoot of excitation current. To have the best possible compensation it is necessary to find an optimum shape of excitation impulse. Basically, this consists in obtaining the spectrometer response impulse, inverting it and using this inversion to filter the excitation impulse. The term pre-emphasis compensation method is based on the fact that the compensation filter is in the nature of a differentiating element (high-pass filter).

Measuring the magnetic field gradient is converted to measuring the magnetic field induction in two symmetrically placed thin layers of the specimen being measured. A change in the magnetic field induction results in the phase (as well as amplitude) modulation of the FID signal. Instantaneous frequency of the FID signal is directly proportional to the magnetic field induction in the two regions defined. The frequency of an FID signal measured from the moment of the trailing edge of gradient excitation is in the nature of an exponentially descending function (it copies the drop in magnetic field induction) [3, 4].

In order to establish the optimum parameters of pre-emphasis filter it is necessary to know the exact time course of the induction of a gradient magnetic field induced by a certain exactly defined excitation pulse. Several measuring methods have been developed. All of them establish the instantaneous magnitude of magnetic field induction from the instantaneous frequency of the FID signal being measured. A limiting factor of these methods is, above all, the signal-to-noise ratio (SNR), which deteriorates with time and the information sought gets usually lost in noise 10 ms or more after the arrival of the high-frequency excitation impulse. This situation is in Fig. 1.

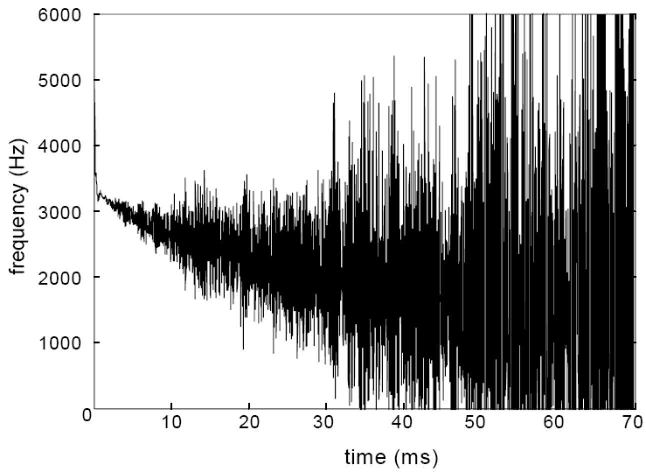

Figure 1: Noise appearing in a signal that defines the course of instantaneous frequency.

Instantaneous frequency is the differentiation of instantaneous phase with respect to time. The method of numerical differentiation of the Newton interpolation polynomial is used. Fig. 2 is the

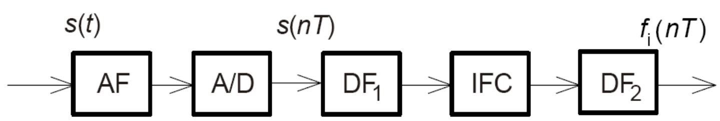

Figure 2: Block diagram of establishing instantaneous frequency of FID signal.

flow chart of establishing the instantaneous frequency course of FID signal. An analog signal $s(t)$ is first filtered by antialiasing low-pass filter AF. A/D conversion at the sampling frequency $f_s = 1/T$ is then performed using the A/D block. The digital signal is filtered again by low-pass filter DF_1. The calculation of instantaneous frequency is realized by the IFC block. In the end, this signal is again filtered by low-pass filter DF_2 [5].

As mentioned above, noise greatly affects the calculation accuracy of numerical differentiation. While the error in phase calculation can be small even for a noisy signal, differentiating the phase will increase this error considerably since in the frequency domain it acts as a high-pass filter, which accentuates the high-frequency components. The basic requirement thus is to suppress noise in the FID signal as much as possible before calculating its instantaneous phase.

3. NOISE SUPPRESSION METHOD

The basic idea of noise suppression consists in removing noise frequency components, which carry minimum information about the phase of FID signal but draw much energy. In practice, some distortion of useful signal is admissible if it is balanced by a sufficient increase in the SNR. If real-time processing is not a condition and post-acquisition processing is thus allowed, several noise suppression methods are available for application. In the beginning, methods of classical digital filtering were used but they did not bring the anticipated results [5]. Therefore an adaptive digital filtering method has been developed and tested [6]. Seen as most promising can be digital filtering by means of filter banks on the wavelet transform basis.

3.1. Filtering with the Aid of Digital Filter Banks

When making use of a digital filter bank, the principle of two-stage sub-band digital filtering is used [7, 8], The block diagram of this type of processing and the principle of processing the signal in blocks WF_1 (Wavelet Filter 1) and WF_2 can be seen in greater detail in Fig. 3.

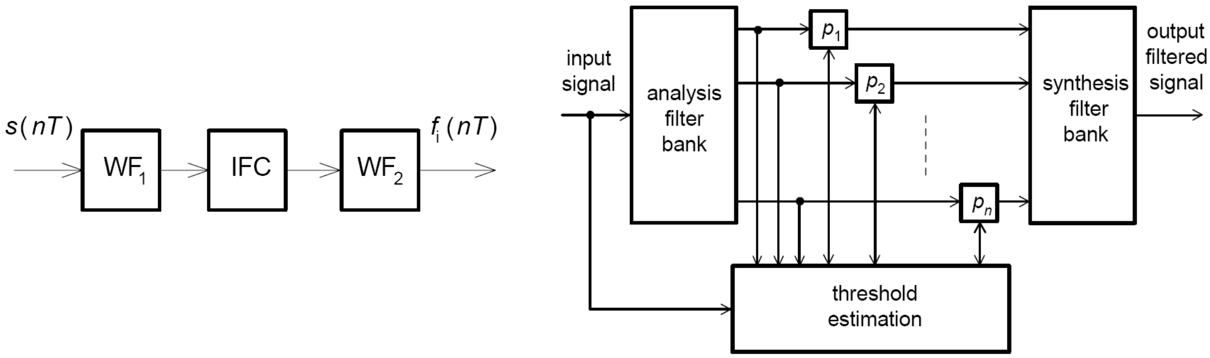

Figure 3: Block diagram of two-stage digital filtering using digital filter banks.

The two processing stages contain a bank of analysing digital filters, which will divides the FID signal and the instantaneous frequency signal into frequency sub-bands, and a bank of synthesizing digital filters, which signal into subsequent to thresholding and noise removal will again synthesize the resultant signal. The banks are made up of several pairs of mirror frequency filters of the type of low-pass and high-pass filters. Since both the FID signal and the instantaneous frequency filter have a roughly exponential distribution of power spectrum density, both the analysing filter bank and the synthesizing filter bank are of octave spectrum division.

Noise thresholding in individual frequency sub-bands follows after the analysing filter bank. In both the WF_1 and WF_2 blocks the magnitudes of thresholds p_i are calculated by means of block threshold estimation on the basis of calculating the standard deviation at the end of the measured section of both the FID signal and the instantaneous frequency signal. In the former case, soft thresholding is utilized. In the latter case the noise in block WF_2 is of non-stationary nature and the values of thresholds p_i are time-dependent. The magnitude of standard noise deviation increases with time and therefore it is necessary to use different types of thresholding.

3.2. Automatic Adjustment of Time-variant Thresholds

In automahreshold adjustment we start from the block diagram in Fig. 4.

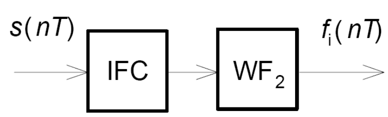

Figure 4: Block diagram of filtering an instantaneous-frequency signal.

Noise filtering is only applied in the instantaneous frequency region in the WF_2 block. The time-variant thresholds p_i are adjusted automatically, in dependence on the magnitude of sub-band signal noise. Calculating the instantaneous frequency in block IFC will completely alter the properties of the noise contained in the useful signal. The question is in what way the noise in the instantaneous frequency signal changed. By analysing the operation of calculating instantaneous frequency from the FID signal it is possible to obtain the noise parameters of instantaneous-frequency signal necessary for automatic threshold adjustment. The instantaneous phase of FID signal will be calculated using

$$\varphi = \arctan\left(\frac{\mathrm{IM[FID]}}{\mathrm{Re[FID]}}\right) \tag{1}$$

When the real and the imaginary parts of signal change by Δ, the calculated phase will change by

$$\Delta\varphi = \arctan\left(\frac{\mathrm{IM[FID]}+\Delta}{\mathrm{Re[FID]}-\Delta}\right) - \arctan\left(\frac{\mathrm{IM[FID]}-\Delta}{\mathrm{Re[FID]}+\Delta}\right) \tag{2}$$

It is exactly $\Delta\varphi$ that represents the noise contained in the instantaneous frequency signal of FID signal. The magnitude of the change Δ in the real and the imaginary parts of the signal is directly linked with the magnitude of standard noise deviation, $\delta \approx \Delta$. Since the standard noise deviation of FID signal is constant, $\Delta\varphi$ changes in dependence on the magnitude of the FID signal and is thus non-linearly dependent also on SNR.

The instantaneous frequency signal is obtained via differentiating the instantaneous phase. In our case, we calculate the derivative from two points only, in order to be able to follow the fast frequency changes in FID signal which occur at its beginning.

A signal containing higher frequency components is amplified together with noise more than low-frequency signals are. For these reasons it is necessary to set the threshold magnitude of higher sub-band signals larger than in the lower bands. Fig. 5 gives the other sub-band signal together with its automatically adjusted threshold. This sub-band signal contains, in the first place, noise; only in the beginning is there also useful signal, thanks to the step change in the instantaneous frequency signal. The useful signal remains preserved since its value is higher than the threshold while the noise is removed since its level is below the threshold. The threshold then proceeds as a continuous function without step changes, which eliminates possible transition events. In spite of this, filter banks of lower orders (5–10) need to be used.

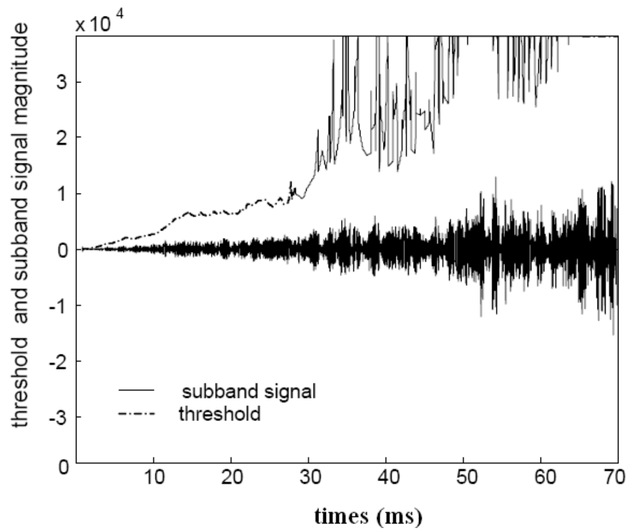

Figure 5: Second sub-band signal (solid) and its threshold (dash-dotted).

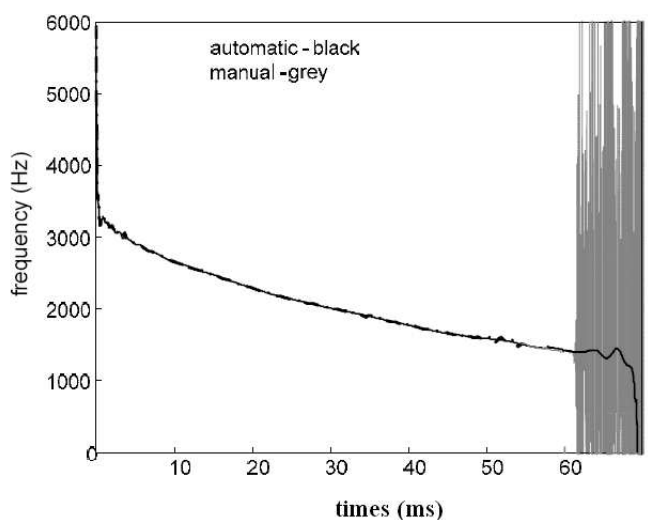

Figure 6: Instantaneous frequency of FID signal processed by dual wavelet filtering.

Figure 6 gives the instantaneous frequency signal for filtering with manually adjusted thresholds and with automatically adjusted thresholds. The two curves are of almost identical shape; they only differ at the end of filtering. This is because due to its very low SNR ($\ll 1$) the signal can no longer be measured. For automatically adjusted thresholds the transition event is larger because the maximum possible threshold is calculated in connection with the zero magnitude of FID signal, and thus the signal is step-changed.

4. CONCLUSION

Removing noise from FID signals is of fundamental significance in analysing the results of MR spectroscopy and tomography. Optimum methods were sought for removing noise from a signal that describes the values of instantaneous frequency of FID signals during an MR experiment. The method of filtering MR by digital filter banks and using the wavelet transform yields very good results. Unlike filtering methods, which make use of current digital FIR filters and adaptive filtering as described in the introduction, it extends considerably the time for which MR signal with sufficiently high SNR can be detected. Automatic threshold adjustment does away with prolonged operations of adjusting the thresholds manually.

ACKNOWLEDGMENT

The paper was prepared within the framework of B208130603 project of the Grant Agency of the Academy of Sciences of the Czech Republic and with the support of the research plan MSM 21630513.

REFERENCES

1. Vlaardingerbroek, M., *Magnetic Resonance Imaging*, Springer-Verlag, 2000.
2. Mansfield, P. and B. Chapman, "Active magnetic screening of gradient coils in NMR imaging," *Journal of Magnetic Resonance*, No. 66, 573–576, 1986.
3. Bartusek, K. and V. Puczok, "The MULTIFID method for measurement of magnetic field gradients," *Meas. Sci. Technol.*, No. 4, 357, 1993.
4. Bartusek, K. and B. Jílek, "Measurement of the gradient magnetic field for NMR tomography," *Proceedings of the 1st Nottingham Symposium on Magnetic Resonance in Medicine*, Nottingham, 1994.
5. Bartusek, K. and E. Gescheidtova, "Instantaneous frequency of spin echo method for gradient magnetic field measurement in MR systems," *Journal of Electrical Engineering*, Vol. 53, 49–52, 2002.
6. Bartusek, K. and E. Gescheidtova, "Adaptive digital filter for gradient magnetic field measurement in MR tomography," *Proceedings of the IEEE International Conference APCCAS'*, 79–82, 2002.
7. Vich, R. and Z. Smekal, *Digital Filters*, Academia, Praha, 2000.
8. Fliege, N., *Multirate Digital Signal Processing*, John Wiley & Sons, Chichester, 1996.

A Slotted Coaxial Antenna as an Alternative to Wire Dipole Antennas

M. B. Perotoni[1] **and S. E. Barbin**[2]

[1]Institut fuer Theorie Elektromagnetischer Felder, Germany
[2]Departamento de Engenharia de Telecomunicações e Controle
Escola Politécnica da Universidade de São Paulo, Brazil

Abstract— Miniaturization of antennas is nowadays a very important issue as they must fit into modern electronic systems with small dimensions. As a matter of fact, the use of CMOS technology in the RF and microwave ranges presents a great challenge to the traditional antenna designer, in reducing the radiant element in the same proportion as the rest of the circuit. The rapid advances achieved in the field of MEMS technology also enable the fabrication of very small circuits and systems. Since antenna dimensions are in general ruled by the resonant frequency and not by technological parameters, as for circuits, its design imposes severe constraints, when the dimensions are to be kept small. Here a slotted coaxial antenna is presented as an alternative to small radiant element antennas. The ISM band (2.45 GHz) was chosen for the operational frequency, since it is a range in which normally wire dipoles are employed, in devices such as WiFi network cards and related equipments. Some advantages in comparison to dipole antennas are also discussed.

1. INTRODUCTION

Common solutions for achieving small radiant elements have been intensively investigated. Some of them involve the use of fractal geometries [1], slots in planar patches [2], meander lines or loops [3] or loading with high permittivity substrates [4]. However, some solutions present drawbacks, such as low-gain or high complexity and/or fabrication costs. Here a solution is presented based on a slotted coaxial cable. Its construction and feeding method are kept as simple as possible, in order to make it a reasonable alternative to wire dipole antennas.

2. SLOTTED COAXIAL ANTENNA

Periodic slotted coaxial cables are usually employed as a mean for establishing communication among fixed and mobile units inside tunnels and mines [5]. The modeling of these antennas is usually described by means of Floquet Modes field expansion, in order to account for the periodicity. Low loss operation is usually desirable, so that long distances can be covered with the slotted coaxial antenna. Some alternatives for low-loss operation are the multiangle-multislot configuration [6] and the vertical periodic slots configuration [7].

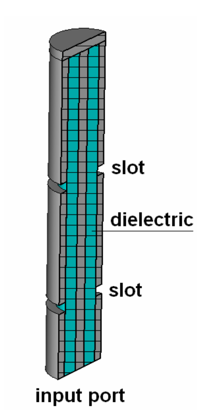

(a)

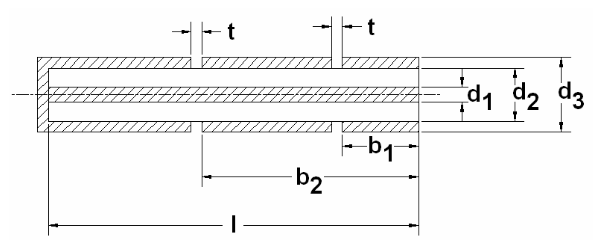

(b)

Figure 1: (a) Basic scheme of the slotted coaxial antenna; (b) dimensions definition.

The antenna hereby analyzed uses only two slots, as illustrated in Fig. 1. The coaxial dimensions were chosen to match the ones of commercial coaxial cables (dimensions d1, d2 and d3) and the dielectric material has a permittivity of 2.33. The feeding is made with a conventional coaxial connector (unbalanced), which compares very favorably to dipole antennas, where the need of balanced-feed demands the use of baluns.

The presence of two slots instead of one eases the matching process by the introduction of another degree of freedom. Simulated field distributions showed that the slot closer to the input port is the one responsible for the radiation. The matching and tuning process involves the cable length l (which is about half wavelength long) adjustment and subsequent changes of the slots positions b_1 and b_2. Fine tuning can be implemented by changing the lengths t of the slots.

Simulations have also shown that the slots should be cut only in the outer metallic shell, as illustrated in Fig. 1. The cases for the cut going into the dielectric have shown inferior performance, in terms of both return loss and gain.

Two designs are presented for the slotted coaxial antenna: with and without ground plane (as for wire monopoles). Both structures were optimized for the resonant frequency of 2.45 GHz.

2.1. Slotted Coaxial Antenna without Ground Plane

The dimensions, after numerical optimization using the Finite Integration technique [8], for the antenna without ground plane are presented in Table 1.

Table 1: Dimensions for the slotted coaxial antenna without ground plane [cm].

d_1	d_2	d_3	B_1	B_2	l	T
0.28	1	1.4	1.44	4.1	7	0.2

2.2. Slotted Coaxial Antenna with Ground Plane

For the antenna with ground plane, the dimensions, after numerical optimization, are presented on Table 2. The goals were to provide a wide bandwidth as well as with a small dimension antenna.

Table 2: Dimensions for the slotted coaxial antenna with ground plane [cm].

d_1	d_2	d_3	b_1	b_2	l	T
0.28	1	1.4	0.9	1.7	2	0.2

It is interesting to notice that the antenna length (2 cm) is about only $\lambda/6$, for a wave at 2.45 GHz. A standard monopole antenna would have a length of about $\lambda/4$ at the same frequency. This means that the slotted coaxial antenna is 50% smaller than the monopole.

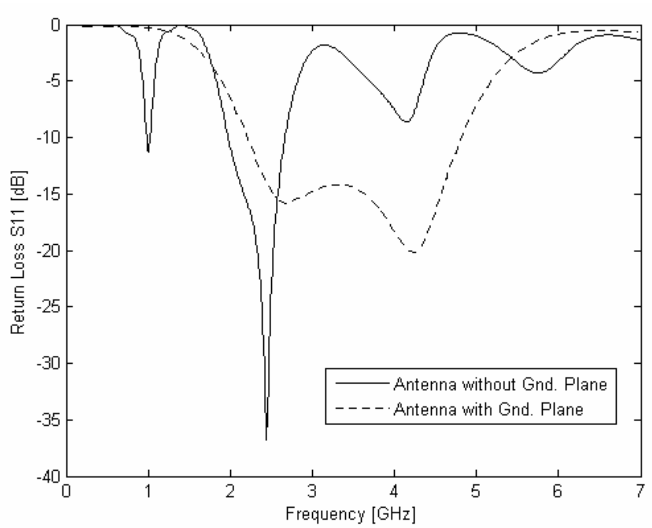

Figure 2: Simulated return loss for both designs.

The return loss for both design, is presented in Fig. 2. The slotted coaxial antenna without ground plane shows a 680 MHz bandwidth, considering a 10 dB limit. The antenna with ground plane exhibits a bandwidth of 2.58 GHz (relative bandwidth of 73%).

The gain curves for both cases, with and without ground planes are presented in Fig. 3. For the frequency of 2.45 GHz, the gain for the antenna without ground plane was 2.66 dB, while for the case with ground plane it was 5.1 dB. Fig. 4 depicts the far field pattern for the two designs. It can be seen that the antenna with the ground plane presents a more constant gain profile over the whole band, in comparison with the other design.

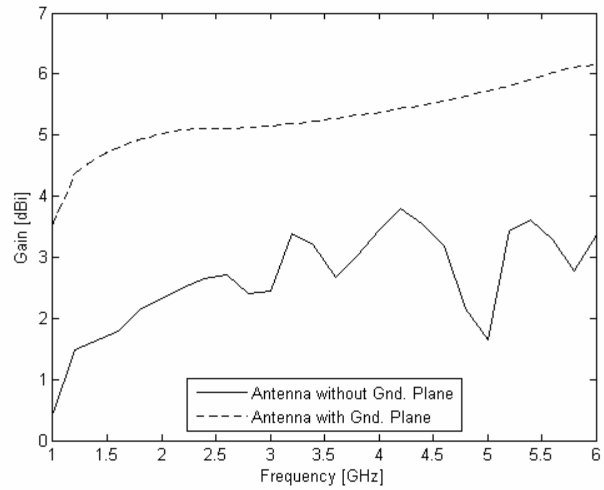

Figure 3: Simulated gain for the two antennas.

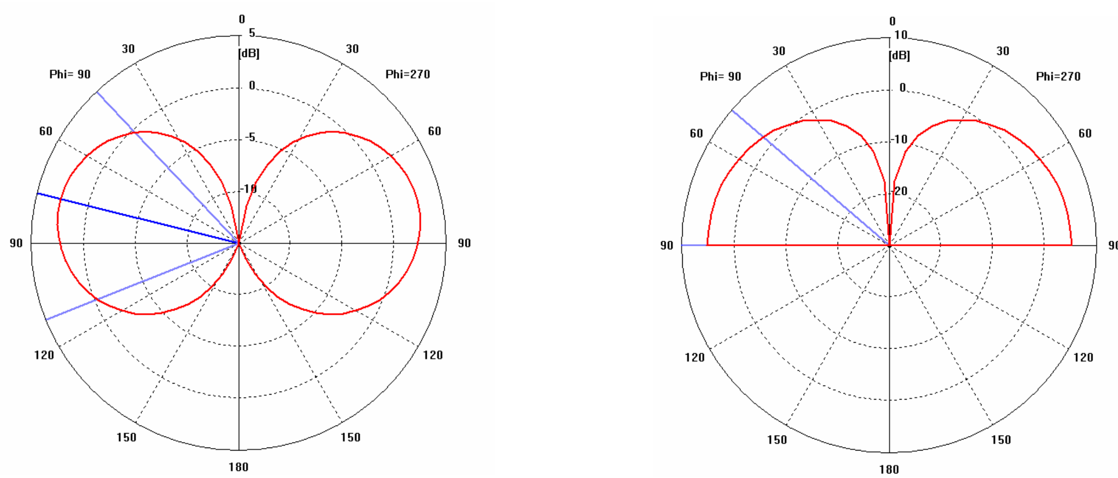

(a) (b)

Figure 4: Far field pattern for the antenna without (a) and with ground plane (b).

3. CONCLUSION

A miniaturized antenna based on a slotted coaxial cable was presented. The antenna has very attractive characteristics, such as broad bandwidth and easy implementation. The model without ground plane has the benefit of unbalanced feeding, without the need of baluns. The antenna with ground plane was optimized so that the overall dimensions were kept as small as possible, and its computed return loss showed a bandwidth of 73%, with moderate gain over the band.

REFERENCES

1. Nessel, J. A., A. J. Zaman, and F. A. Miranda, "A miniaturized antenna for surface-to-surface and surface-to-orbiter applications," *Microwave and Optical Technology Letters*, Vol. 48, No. 5, 859–862, May 2006.
2. Ju, J. M., G. T. Jeong, J. H. Yoon, S. W. Ko, and K. S. Kwak, "Design of a multiple U-shaped slot microstrip patch antenna for 5-GHz band WLANs," *Microwave and Optical Technology Letters*, Vol. 43, No. 6, 486–488, Dec. 2004.

3. Kim, Y. D. and H. L. Lee, "Design of compact triple-band meander chip antenna using LTCC technology for mobile handsets," *Microwave and Optical Technology Letters*, Vol. 48, No. 1, 160–162, Jan. 2006.
4. Wong, K. L., *Planar Antennas for Wireless Communications*, Wiley, New York, 2003.
5. Ahn, C. H., D. W. Yi, and W. S. Park, "Design of a radiated-mode multislot leaky coaxial-cable," *Microwave and Optical Technology Letters*, Vol. 45, Issue 4, 338–342, May 2005.
6. Kim, S. T., G. H. Yun, and H. K. Park, "Numerical analysis of the propagation characteristics of multiangle multislot coaxial cable using moment method," *IEEE Transactions on Microwave Theory and Techniques*, Vol. 46, 1998.
7. Wang, J. H. and K. K. Mei, "Theory and analysis of leaky coaxial cables with periodic slots," *IEEE Transactions on Antennas and Propagation*, Vol. 49, No. 12, 1723–1732, Dec. 2001.
8. CST GmbH, Darmstadt, Germany, www.cst.com.

Study of Certain Subband-based Adaptive Modulation Schemes in an OFDM System

L. J. Shi[1], L. Rong[2], R. F. Lin[1], and Y. Du[1]

[1]The Electromagnetics Academy at Zhejiang University, Zhejiang University, Hangzhou 310058, China
[2] Shanghai Research Center for Wireless Communications, Shanghai 200050, China

Abstract— In applying adaptive schemes to an OFDM system to adaptively adjust the transmission format based on channel state information, a practical scheme would group the subcarriers into similar-quality subbands to reduce the associated modem mode-signaling requirements. One way to determine the modulation mode for a specific subband is based on the average signal-to-noise ratio (SNR) of the subband. To find the optimal switching levels, knowledge of the probability density function of this average SNR is required. Another popular way to determine the modulation mode is based on the SNR of the worst subcarrier of the suband, which may represent an overconservative choice of order statistic. This approach can be extended to deploying other statistic as well, for example, the second or the third worst statistic. Analysis of the above approaches is the focus of this study, and performances of these schemes are compared through numerical simulations.

For an OFDM system in wireless communication, due to multipath fading, subcarriers experience signal-to-noise ratio (SNR) degradation to varying degree. Adaptive modulation schemes are effective to mitigate such detrimental effect, where in principle the transmitted power and bit rate of each subcarrier are allowed to change dynamically according to channel variations. Yet such a full treatment implies high complexity in modem hardware and high signalling overhead over the feedback channel from the receiver to the transmitter, a scheme that may not be plausible in high-speed wireless data applications. Such concern leads to some suboptimal schemes. Grunheid et al. [1] and Keller and Hanzo [2] proposed to group the subcarriers into similar-quality subbands with single constellation being used for the subcarriers within a subband. Dardari [4] proposed an ordered subcarrier selection algorithm where among the available N subcarriers only the K subcarriers ($K \leq N$) with the highest SNRs are used, to which uniform bit and power level allocation are applied.

For a mode-switching-assisted adaptive modulation scheme, the bit-error-rate (BER) and throughput performances are determined by the set of switching levels. Chung and Goldsmith [4] and Choi and Hanzo [5] analyzed for single carrier system the constant power variate rate adaptive modulation scheme. The optimal switching levels that maximize the average bits-per-symbol (BPS) throuput for a target average BER are found to depend on the channel quality statistics. In extending this technique to multicarrier system where subband based adaptive modulation scheme is adopted, Keller and Hanzo [2] proposed to use the subcarrier experiencing the worst SNR. This approach may appear somehow conservative, which motivates us to analyze the problem using other order statistic of the subcarrier SNRs, such as the second or the third order worst statistic. Another plausible approach is to use the average SNR of all the subcarriers within a subband, where the optimal switching levels can be determined by using the probability density function (pdf) of the average SNR in conjunction with Lagrangian optimization technique. These approaches form the body of the current study.

In the order statistic approach, the subcarriers are usually assumed to be independently and identically distributed (i.i.d) Rayleigh fading channels for mathematical convenience [3], although they are in general correlated. Consider a subband containing P subcarriers, where the pdf of the SNR γ of each subcarrier is

$$f_\gamma(\gamma) = \frac{1}{\overline{\gamma}} e^{-\frac{\gamma}{\overline{\gamma}}} \tag{1}$$

with $\overline{\gamma}$ being the mean SNR of each subcarrier. The pdf of the nth worst order statistic of the subcarrier SNRs is expressed as

$$f_n(\gamma_n) = \frac{P!(1 - e^{-\frac{\gamma_n}{\overline{\gamma}}})^{n-1} e^{-\frac{\gamma_n}{\overline{\gamma}}(P-n+1)}}{\overline{\gamma}\,(n-1)!\,(P-n)!}. \tag{2}$$

Specifically, the pdfs of the worst, second worst and third worst order statistics are respectively

$$f_n(\gamma_n) = \frac{P!(1-e^{-\frac{\gamma_n}{\overline{\gamma}}})^{n-1}e^{-\frac{\gamma_n}{\overline{\gamma}}(P-n+1)}}{\overline{\gamma}\,(n-1)!\,(P-n)!} \tag{3}$$

$$f_2(\gamma_2) = \frac{P\,(P-1)}{\overline{\gamma}}\left(e^{-\frac{\gamma_2}{\overline{\gamma}}(P-1)} - e^{-\frac{\gamma_2}{\overline{\gamma}}P}\right) \tag{4}$$

and

$$f_3(\gamma_3) = \frac{P\,(P-1)\,(P-2)}{2\overline{\gamma}}\left(e^{-\frac{\gamma_3}{\overline{\gamma}}(P-2)} - 2e^{-\frac{\gamma_3}{\overline{\gamma}}(P-1)} + e^{-\frac{\gamma_3}{\overline{\gamma}}P}\right) \tag{5}$$

The optimal switching levels can be thus obtained by making use of the above pdf in conjunction with Lagrangian optimization technique [5].

In the average SNR approach, where the average SNR $\gamma_a = \frac{1}{P}\sum_{m=1}^{P}\gamma_m$, if SNRs of the subcarriers are still assumed to be i.i.d random variables, then the pdf of γ_a can be expressed as

$$f_a(\gamma_a) = \left(\frac{P}{\overline{\gamma}}\right)^P \frac{(\gamma_a)^{P-1}}{P!} e^{-\frac{P\gamma_a}{\overline{\gamma}}}. \tag{6}$$

However, a more rigorous expression for γ_a where the correlations between subcarriers are accounted for is derived by Du [6] as

$$f_a(\gamma_a) = \frac{1}{2}\sum_{k=1}^{P}\left[\alpha^{2P-2}\exp\left(-\frac{\gamma_a}{2\alpha}\right)\prod_{r=1,r\neq k}^{P}(\alpha-\alpha_r)^{-1}\right]_{\alpha=\alpha_k} \tag{7}$$

where $\alpha_k = \lambda_k / P\sigma_n^2$, σ_n^2 is the variance of the AWGN noise, λ_k are the eigenvalues of the covariance matrix of subcarriers.

To study the performance of these two proposed approach, we simulate a MC-SS system where the parameters are given in Table 1. The modulate modes are NO-Transmission, BPSK, QPSK, 16QAM, and 64QAM. The target average BER is 10^{-4}. The channel under consideration is the BRAN-A channel, which has 11 Rayleigh fading paths. Yet the 20 MHz sampling rate of the system cannot completely distinguish these paths, leading to a combination of these paths to six distinguishable paths. Channel estimation is assumed to be ideal. For each BER and throughput data point, 50000 channel realizations are used.

Table 1: MC-SS system parameters.

Carrier Frequency	5.2 GHz	Number of Rayleigh Fading Paths	11
Mobile Speed	3 km/h	Number of Pilots	9
Doppler Frequency Shift	14.444 Hz	Sampling Frequency	20 MHz
Bandwidth per Subcarrier	156.25 kHz	maximum delay	0.243 us
Size of the FFT	128	Protecting Interval	5
Number of Subcarriers per OFDM Symbol	128	Period of Data Interval	6.40 ms
Number of Available Subcarriers per OFDM Symbol	96	Spreading Factor	8

For order statistic based adaptive modulation scheme, Fig. 1 shows the BER performance, where there are six neighboring subcarriers in each subband, resulting in a total of 16 subbands. It is expected that the worse the subcarrier SNR statistic is used, the more conservative thus the better the BER performance. Fig. 1 shows that it indeed is the case. Yet the BER curves also demonstrate distinct feature quite different from that of the single carrier case: the target average BER is achieved for the latter case but not for the former one. The reason for such difference highlights the fact that the BER performance of a multicarrier system is collectively determined by subcarriers (here all subcarriers within a subband), so the BER constraint condition imposed on an individual subcarrier may not be fulfilled collectively.

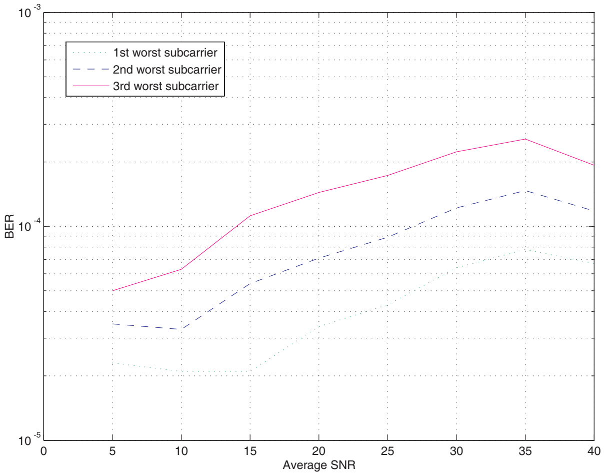

Figure 1: BER performance for order statistic based adaptive modulation system.

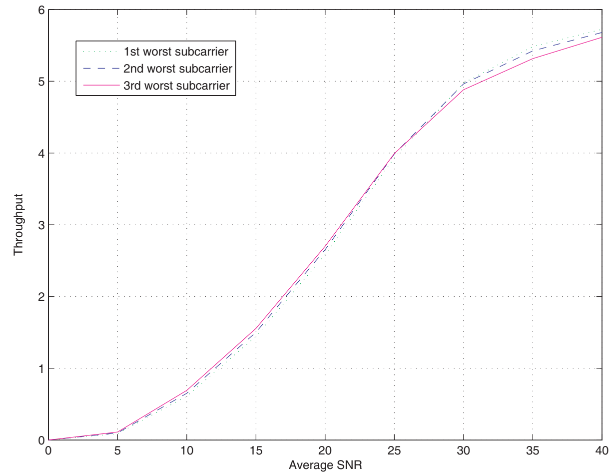

Figure 2: Throughput performance for order statistic based adaptive modulation system.

Figure 2 shows the corresponding throughput performance. In the case where the average SNR is not too high, as one may expect, the worse the subcarrier SNR statistic is used, the more conservative thus the worst the throughput performance. When the average SNR is considerably high, the relative throughput performance reverses the trend due to the appreciably high BER for the adaptive modulation schemes using order statistic other than the worst. However, the differences in throughput due to different choice of order statistic are not appreciable across the range of the average SNR.

For average subband SNR based adaptive modulation scheme, Fig. 3 shows the BER performance, where there are also six neighboring subcarriers in each subband. It shows that the BER performance associated with the true statistics of the average subband SNR is actually inferior to that of assuming i.i.d subcarriers, as welll as that of simply using AWGN switching levels. This calls into question that the latter two schemes may be more conservative. To verify this we examine the relative throughput performances (Fig. 4) and find that it indeed is the case.

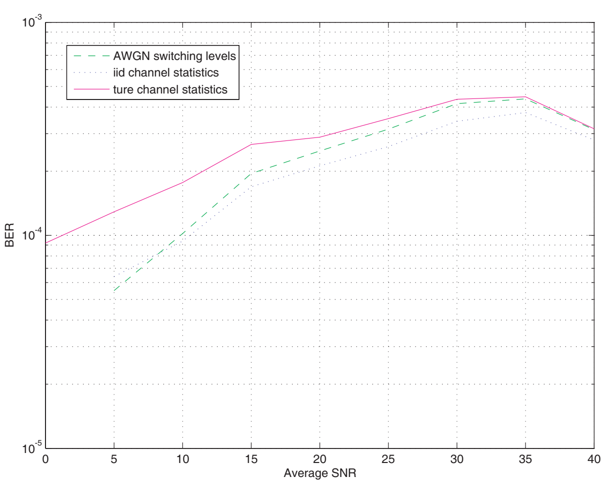

Figure 3: BER performance for average subband SNR based adaptive modulation system.

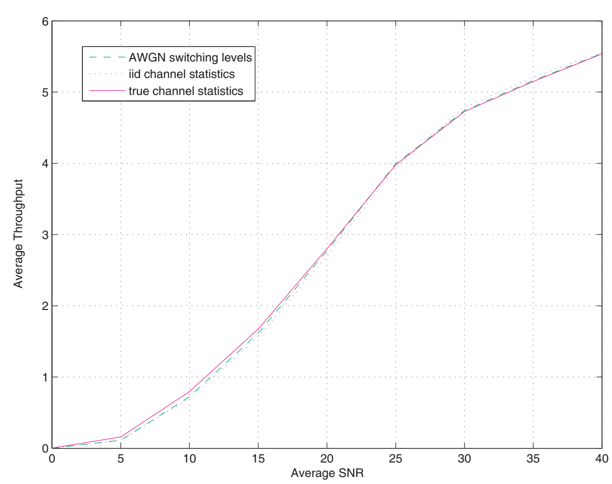

Figure 4: Throughput performance for average subband SNR based adaptive modulation system.

REFERENCES

1. Grunheid, R., E. Bolinth, and H. Rohling, "A blockwise loading algorithm for the adaptive modulation technique in OFDM systems," *Proc. IEEE Vehicular Technology Conf.*, Vol. 2, 948–951, 2001.
2. Keller, T. and L. Hanzo, "Adaptive modulation techniques for duplex OFDM transmission," *IEEE Trans. Veh. Tech.*, Vol. 49, 1893–1906, 2000.

3. Dardari, D., "Ordered subcarrier selection algorithm for OFDM-based-high-speed WLANs," *IEEE Trans. Wireless Commun.*, Vol. 3, 1452–1458, 2004.
4. Chung, S. T and A. J. Goldsmith, "Degrees of freedom in adaptive modulation: a unified view," *IEEE Transactions on Communications*, Vol. 49, 1561–1571, 2001.
5. Choi, B. and L. Hanzo, "Optimum mode-switching-assisted constant-power single- and multicarrier adaptive modulation," *IEEE Transactions on Vehicular Technology*, Vol. 52, 536–560, 2003.
6. Du, Y., "On the probability density function of the average SNR of a subband in an OFDM system," submitted to *IEEE Trans. Info. Theory.*

Study of the Optimal Switching Levels of Adaptive Modulation for a Two-user System under Constant Power Condition

Y. M. Fang[1], **L. Rong**[2], **R. F. Lin**[1], **and Y. Du**[1]

[1]The Electromagnetics Academy at Zhejiang University, Zhejiang University, Hangzhou 310058, China
[2]Shanghai Research Center for Wireless Communications, Shanghai 200050, China

Abstract— In this paper we analyze the problem of optimizing the switching levels of adaptive modulation for a two-user system under constant power condition, in order to maximize the overall system throughput for a target average bit-error-rate (BER) for each user. Since the optimal switching levels depend on the probability density of the signal-to-interference-noise ratio (SINR), expression for this probability density is derived and the optimal switch levels are obtained through a Lagrange optimization technique. This approach can be readily extended to multiple-user case. It is shown by simulation that the proposed jointly optimizing method achieves the average BER target for each user while an individually optimizing method fails. The effects of these two methods and of the interference coefficients on the average system throughput are also analyzed.

Wireless communication channels typically exhibit channel quality fluctuations, and to mitigate their detrimental effects a number of approaches have been proposed in the literature. Methods based on adaptive modulation according to the near-instantaneous channel quality information have gained popularity. For Rayleigh fading channel, Chung and Goldsmith [1] showed that variable power variable-rate schemes are optimal, but they also found that the extra throughput achieved by the additional variable power assisted adaptation over the constant power variable rate schemes is marginal for most types of fading channels.

Constant power variable rate adaptive scheme is also analyzed by Choi and Hanzo [2], where the target average BER forms the constraint condition. They established the relationship among the optimal mode switching levels, and found that although such relationship holds regardless of the underlying channel scenarios, the switching levels do depend on the statistics of the channel quality.

The above studies were focused on single user scenario. Yet in wireless communication, a user typically suffers from the interference of other users, which in the GSM system may be due to multipath channel conditions, and in the CDMA system may stem from the loss of orthogonality among the spread sequences. Several approaches have been proposed based on power control and base station selection [3, 4], with little consideration for adaptive modulation. In [5] Qiu and Chawla approached the multiuser problem by using power control and adaptive modulation. They showed that adaptive modulation without power control scheme outperforms SINR-balance power control scheme in terms of overall throughput, a finding that indicates the significance of constant power adaptive modulation for multiuser system. In their approach, the switching levels were obtained by using the method due to Webb and Steele, and a parametric approximation for throughput for all modulation modes was also adopted.

In this paper we propose a constant-power adaptive modulation scheme for downlink transmission in a multiuser system. It is based on a Lagrangian optimization technique. We consider two-user case here to highlight the concept. Extension to multiuser case can be readily carried out.

The downlink transmission model is shown in Fig. 1, which is similar to the one used in [6]. The received signals are for user 1

$$r_1 = \sqrt{s_1 h_1} d_1 + \sqrt{\beta s_2 h_2} d_2 + n_1 \tag{1}$$

and for user 2

$$r_2 = \sqrt{s_2 h_2} d_2 + \sqrt{\alpha s_1 h_1} d_1 + n_2 \tag{2}$$

where for user $k s_k$ are transmit power, h_k are the channel coecicients, d_k are transmitted symbols, and α and β are the interference coefficients from user 2 to user 1 and from user 1 to user 2, respectively. The received sigal-to-interference-noise ratios are for user 1

$$\gamma = \frac{s_1 h_1}{\beta s_2 h_2 + \sigma_{n_1}^2} \tag{3}$$

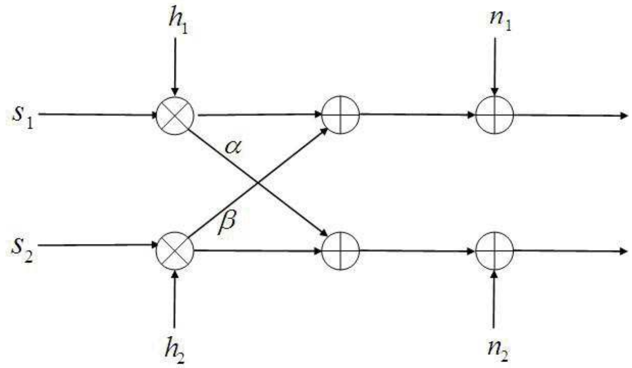

Figure 1: Channel model for two-user system.

and for user 2

$$\varsigma = \frac{s_2 h_2}{\alpha s_1 h_1 + \sigma_{n_2}^2} \tag{4}$$

To comply by the practical system, here we consider the case where the modulation modes for each user are no-transmission, BPSK, QPSK, 16-QAM, and 64-QAM. Other cases corresponding to alternative set of modulation modes can be analyzed similarly. Let the associated switching levels be $\{\gamma_0, \gamma_1, \gamma_2, \gamma_3\}$ for user 1 and $\{\varsigma_0, \varsigma_1, \varsigma_2, \varsigma_3\}$ for user 2. The overall throughput for the 2-user system is

$$B_{total} = \sum_{i=0}^{3} b_i \int_{\gamma_i}^{\gamma_{i+1}} f_\gamma(u)du + \sum_{k=0}^{3} b_k \int_{\varsigma_k}^{\varsigma_{k+1}} f_\varsigma(v)dv, \tag{5}$$

where $f_\gamma(u)$ and $f_\varsigma(v)$ are the probability densities of user 1 and 2 respectively, b_k is the BPS throughput under modulation mode k. For user 1, the average BER is

$$\overline{BER_1} = \frac{\sum\limits_{i=0}^{3} b_i \int_{\gamma_i}^{\gamma_{i+1}} BER_i(u) f_\gamma(u)du}{\sum\limits_{i=0}^{3} b_i \int_{\gamma_i}^{\gamma_{i+1}} f_\gamma(u)du}, \tag{6}$$

where the probability density $f_\gamma(u)$ is

$$f_\gamma(u) = \frac{1}{4\sigma_1^2\sigma_2^2 s_1} e^{-\frac{\sigma_{n_1}^2 u}{2\sigma_1^2 s_1}} \left[\frac{4\sigma_1^2\sigma_2^2\sigma_{n_1}^2 s_1}{2\sigma_2^2\beta s_2 u + 2\sigma_1^2 s_1} + \frac{(4\sigma_1^2\sigma_2^2 s_1)^2 \beta s_2}{(2\sigma_2^2\beta s_2 u + 2\sigma_1^2 s_1)^2} \right]. \tag{7}$$

The average BER and the probability density $f_\varsigma(v)$ for user 2 can be expressed similarly.

The objective here is to optimize the overall throughput while maintaining the average BER of each user at the specified level $\overline{BER_1}$ and $\overline{BER_2}$ respectively. It is an optimization problem with constraints, whose Langrange equation is

$$\begin{aligned} & J(\gamma_0, \gamma_1, \ldots, \gamma_{N-1}, \varsigma_0, \varsigma_1, \ldots, \varsigma_{K-1}) \\ = & \sum_{i=0}^{N-1} b_i \int_{\gamma_i}^{\gamma_{i+1}} f_\gamma(u)du + \sum_{k=0}^{K-1} b_k \int_{\varsigma_k}^{\varsigma_{k+1}} f_\varsigma(v)dv + \lambda_{11} \left[\sum_{i=0}^{N-1} b_i \int_{\gamma_i}^{\gamma_{i+1}} \left(BER_i(u) - \overline{BER_1} \right) f_\gamma(u)du \right] \\ & + \lambda_{12} \left[\sum_{k=0}^{K-1} b_k \int_{\varsigma_k}^{\varsigma_{k+1}} \left(BER_k(v) - \overline{BER_2} \right) f_\varsigma(v)dv \right] \end{aligned} \tag{8}$$

where λ_{11} and λ_{12} are the Langrange parameters. Taking derivatives with respect to γ_j and ς_j and forcing them to be zero give rise to the following equations

$$\frac{1}{b_i - b_{i-1}} \left(b_i BER_i(\gamma_i) - b_{i-1} BER_{i-1}(\gamma_i) \right) = \overline{BER_1} - \frac{1}{\lambda_{11}} \tag{9}$$

and

$$\frac{1}{b_k - b_{k-1}} \left(b_k BER_k(\varsigma_k) - b_{k-1} BER_{k-1}(\varsigma_k) \right) = \overline{BER_2} - \frac{1}{\lambda_{12}} \tag{10}$$

It is seen that (9) and (10) are decoupled equations. The procedure for solving each of them is well documented in [2]. The key results from that study are the following: 1) the optimal values of γ_j depend on that of the rst switch level γ_0; 2) The optimal γ_0^* depends on the probability density $f_\gamma(u)$. Similar results apply to ς_j. Determination of γ_0^* is through solving the constraint equation

$$\sum_{i=0}^{3} b_i \int_{\gamma_i}^{\gamma_{i+1}} BER_i(u) f_\gamma(u) du - \overline{BER_1} \sum_{i=0}^{3} b_i \int_{\gamma_i}^{\gamma_{i+1}} f_\gamma(u) du = 0 \tag{11}$$

which is a highly nonlinear equation which requires a numerical routine in general.

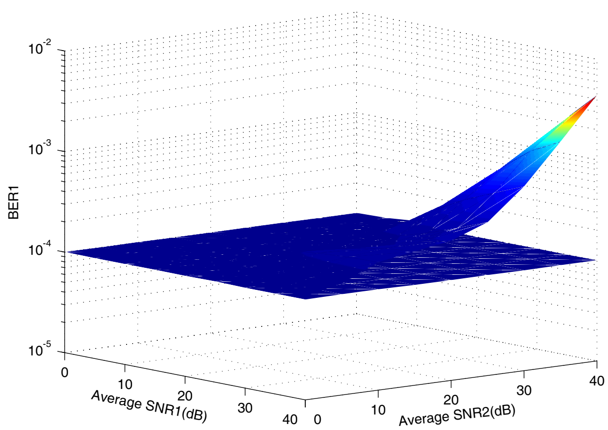

Figure 2: Comparison of BER performance between individually and jointly optimizing methods.

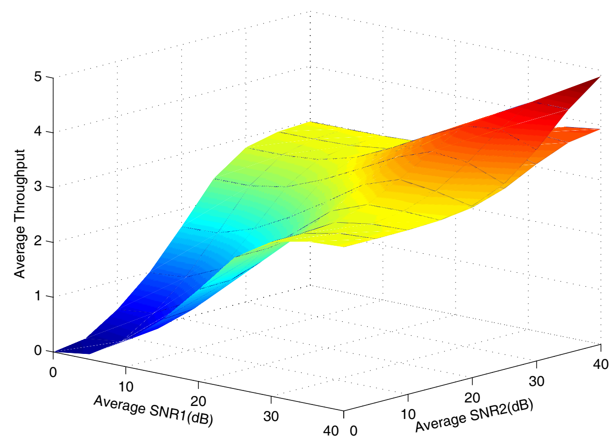

Figure 3: Comparison of average system throughput performance between individually and jointly optimizing methods.

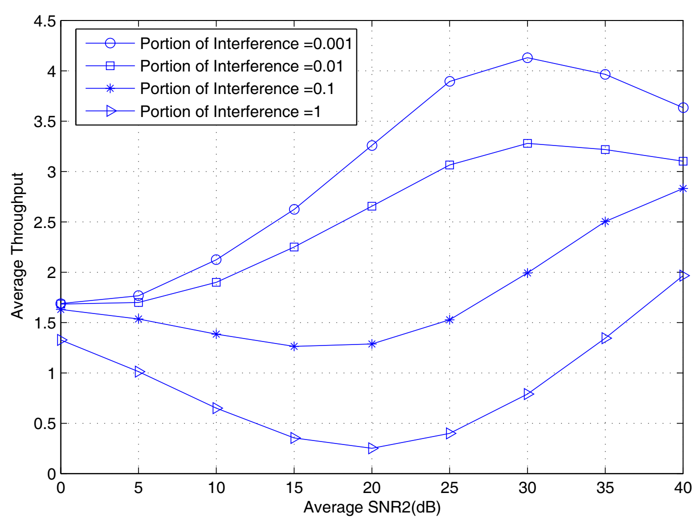

Figure 4: The impact of interference coecients on system throughput using joint optimization.

In the following we present several numerical simulation cases to illustrate the effects of several parameters on the system BER and throughput performance. Fig. 2 compares the BER performances of joint optimization and separate optimization. The interference coefficients are $\alpha = \beta = 0.01$. The target average BERs for both users are 10^{-4}, and the noise variances are -20 dBm. It is seen that the BER under joint optimization attains the target average BER, while the BER under separate optimization is larger than the target average BER, with a rapidly increasing tendency as the SNR of each user increases. This is because higher SNR for one user also means higher interference to the other user, which will present a problem when separate optimization is used. Fig. 3 compares the average throughput performances of joint optimization and separate optimization. The average throughput of separate optimization is slightly better than that of joint optimization, but from above we know that the average BER of separate optimization does not fulfill the BER requirements. Fig. 4 illustrates the effect of interference coefficients on the average throughput using joint optimization. The interference coefficients are symmetric ($\alpha = \beta$, ranging from 0.001 to 1. The average SNR for user 1 is 20 dB, while that of user 2 ranges from 0 to 40 dB. The average throughput shows a convex behavior for $\alpha = 0.1$ and 1, and a concave behavior for $\alpha = 0.01$ and 0.001. This is expected since for high values of interference coefficient, when the SNR of user 2 begins to increase from 0 dB, loss of throughput of user 1 due to high interference outweighs gain of throughput of user 2, and this trend continues until the SNR of user 2 approaches 20 dB, after which, the gain of throughput of user 2 outweighs loss of throughput of user 1. The same analysis applies to small values of interference coefficient.

REFERENCES

1. Chung, S. T. and A. J. Goldsmith, "Degrees of freedom in adaptive modulation: a unified view," *IEEE Transactions on Communications*, Vol. 49, 1561–1571, 2001.
2. Choi, B. and L. Hanzo, "Optimum mode-switching-assisted constant-power single- and multicarrier adaptive modulation," *IEEE Transactions on Vehicular Technology*, Vol. 52, 536–560, 2003.
3. Yates, R. D., "A framework for uplink power control in cellular radio systems," *IEEE Journal on Select Areas in Communications*, Vol. 13, 1341–1348, 1995.
4. Yates, R. D. and C. Y. Huang, "Integrated power control and base station assignment," *IEEE Transactions on Vehicular Technology*, Vol. 44, 638–644, 1995.

Backbone Network Logical Design for Connecting between Sub-networks with WDM System

Amornrat Mahaprom and Noppin Anantrasirichai
ReCCIT, Faculty of Engineering, King Mongkut's Institute of Technology Ladkrabang
Ladkrabang, Bangkok, 10520, Thailand

Abstract— This paper studies the methodology of WDM Networks logical design, by using TOT (Telephone Organization of Thailand) backbone network for connecting between sub-networks. Bellman-Ford's algorithm is used for computing and simulation for optimal logical design of WDM network. There are three main parameters consider in this paper. Including minimum cost, shortest-path routing and re-computing of minimum cost to find out final shortest path. Furthermore, we have compared the result from logical computation with physical topology. Existing backbone optical network and traffic require of TOT are used as raw data for this study.

1. INTRODUCTION

Design of WDM Backbone Network for connecting between Sub-networks is important. Not only considering about traffic of sub-networks all around Thailand but also the operating cost and losses in fiber optic also. Backbone network logical design is chosen for study how to make an optimal and efficiency routing in carrying increasing amounts of commercial traffic. Reliability and steady performances have become critical factors when designing and managing those networks. Large network today offer Service Level Agreements (SLAs) covering delay, port availability and losses across their network which must be maintained even if the network experiences congestion or failure. This provides strong incentives for designing conditions, i.e., fluctuating traffic patterns and intensities or topological changes caused by link and node failures [4].

In this paper, our focus is on logical design of TOT Backbone Network by considering three main parameters, Minimum Cost, Shortest-Path Routing and Re-computing of Minimum Cost in case of major category of failures, specifically "link failures" to find out optimal routing.

2. BELLMAN-FORD ALGORITH

Bellman-Ford Algorithm makes each node periodically broadcast its routing tables to all its neighbors. This algorithm have to maintain the distance tables (which is a one-dimension array — "a vector"), which tell the distances and shortest path to sending packets to each node in the network. The information in the distance table is always updated by exchanging information with the neighboring nodes. The number of data in the table equals to that of all nodes in networks (excluded itself). Each data contains the path for sending packets to each destination in the network and distance/ or time to transmit on that path (we call this as "cost"). The measurements in this algorithm are the number of hops, latency, the number of outgoing packets, etc.

In Fig. 1 if we would like to find the shortest-path between Node 2 to Node 6, from Node 2 with Node 1, 4 and 5 are neighbors and we can expect that the shortest link cost form Node 1, 4 and 5 to Node 6 are 3, 3 and 2 consequently. If we route through Node 1, the total cost is $3 + 3$ which is equal 6, on the other hand if we route through Node 4, the total cost is $1 + 3$ which is equal 4

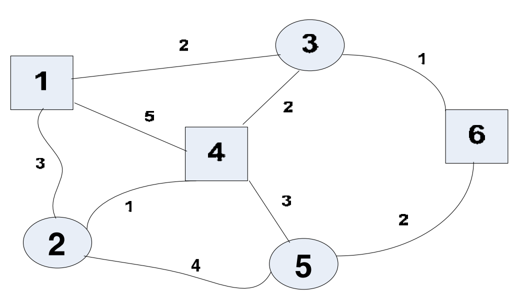

Figure 1: Sample network with link cost.

and if we route through Node 5, the total cost is $4+2$ which is equal 6. Thus the shortest-path between Node 2 to Node 6 is routed through Node 4.

The starting assumption for distance-vector routing is each node knows the cost of the link of each of its directly connected neighbors. Next, every node sends a configured message to its directly connected neighbors containing its own distance table. Now, every node can learn and update its distance table with cost and next hops for all nodes network. Repeat exchanging until no more information between the neighbors.

Consider a node 2 to the destination node 6, the minimum cost can be found form

$$\begin{aligned} D_2 &= \min\{C_{21}+D_1,\, C_{24}+D_4,\, C_{25}+D_5\} \\ &= \min\{3+3,\, 1+3,\, 4+2\} \\ &= \min\{6,\, 4,\, 6\} \\ &= 4 \end{aligned} \tag{1}$$

where C_{ij} is link cost between node i to node j, for example $C_{13}=C_{31}=2$ and $C_{ii}=0$. So the minimum cost from node 2 to node 6 is equal 4. Thus, we can calculate the other routing as follow: From node 1 to node 6

$$D_1 = \min\{C_{12}+D_2,\, C_{13}+D_3,\, C_{14}+D_4\} \tag{2}$$

while form node 4 to node 6

$$D_1 = \min\{C_{41}+D_1,\, C_{42}+D_2,\, C_{45}+D_5\} \tag{3}$$

Ford, the distance to destination, we can consider Bellman-Ford Algorithm as follow:

1. Initial state

$$D_i = \infty \quad \text{where} \quad i \neq d \tag{4}$$

$$D_d = 0 \tag{5}$$

2. Update state (to find out the shortest-path to destination via neighbors) where $i \neq d$

$$D_i = \min\{C_{ij} D_j\} \quad \text{for} \quad j \neq i \tag{6}$$

This equation suggests that the form of neighbor-to-neighbor communication that will take place in the DV algorithm — each node must know the cost of each of its neighbors' minimum-cost path to each destination. Hence, whenever a node computes a new minimum cost to some destination, it must inform its neighbors of this new minimum cost.

$$D_{ij} = 0 \tag{7}$$

$$D_{ij} = \min(C_{ik}+D_{kj}) \tag{8}$$

D_{ij} is the minimum cost from node i to destination node j. When update state node i will distribute vector $\{D_{i1},\, D_{i2},\, D_{i3},\, \ldots\}$ to its neighbors.

3. LINK COST CALCULATION

In this paper, we calculate the link cost from 3 factors: the number of wavelength in each physical link (λ), Total losses (L), and Distance (d) between nodes. The formula can be represented as

$$\text{Link Cost} = \mathrm{A}+\mathrm{B}+\mathrm{C} \tag{9}$$

where

$$\begin{aligned} \mathrm{A} &= (1/\lambda) * \mathrm{w1} \\ \mathrm{B} &= \mathrm{L} * \mathrm{w2} \\ \mathrm{C} &= \mathrm{d} * \mathrm{w3} \end{aligned}$$

The total losses are from Fiber loss (0.2525 dB/km), Connection losses (0.5 dB/1 connection point) and Margin (4 dB/section) where weight setting are $w1+w2+w3=1$ and $w1=0.5$, $w2=0.3$, $w3=0.2$.

From Equation (9) we will get backbone network with link cost as in Fig. 2.

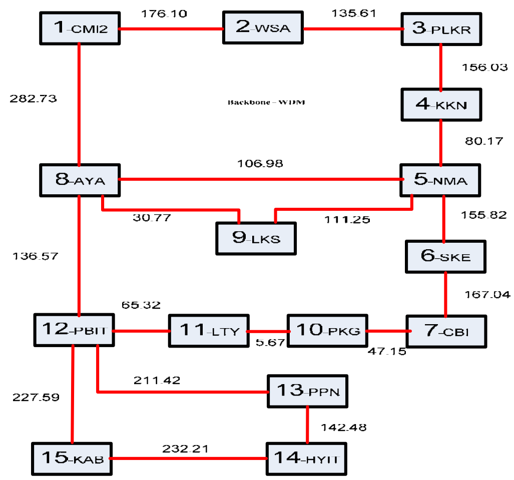

Figure 2: TOT backbone network with link cost.

4. MINIMUM COST CALCULATION

For all node i, the assign value are (n, D_i) where n is the shortest next hop and D_i is the minimum cost from node i to node j as the Equation (6). In case of none specific destination we have to assign n equal -1 for the first time calculation. The starting assumption for distance-vector routing is each node knows the cost of the link of each of its directly connected neighbors. Next, every node sends a configured message to its directly connected neighbors containing its own distance table. Now, every node can learn and update its distance table with cost and next hops for all nodes network. Repeat exchanging until no more information between the neighbors.

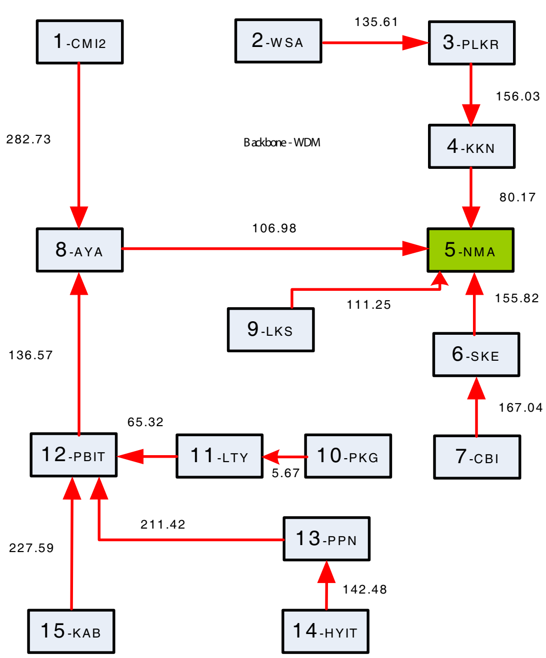

Figure 3: The shortest-path routing to destination Node 5.

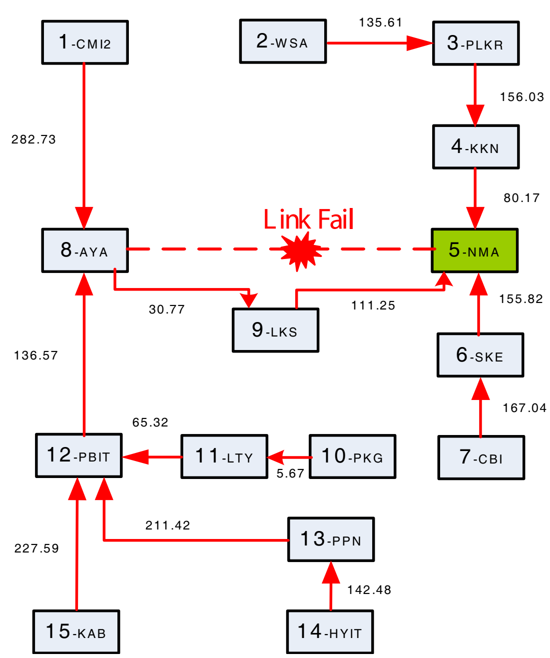

Figure 4: The new shortest-path routing to destination Node 5 with link failure.

5. SHORTEST-PATH ROUTING

From Section 4, after exchanging cost until no more information between the neighbors, we will get shortest-path routing. In this paper we consider the condition from Equations (7) and (8) and use Matlab to calculate Minimum Cost and Shortest-path.

Figure 3 shows the example of calculate result to route a path connection between destination node 5 to other nodes with the shortest-path and minimum cost.

6. MINIMUM COST RE-COMPUTATION

It is beneficial to discuss the concept of critical links and our approach for finding them. Our goal is to compute a routing solution that protects the network performance against the failure of links that impact the network most on failure. In case of physical link failure, we have to re-routing path to the other route. We can follow up the process of Section 5 by generate the link cost of failure to zero and re-start calculate shortest-path and update its distance table with cost and next hops for all nodes network.

Figure 4 shows the new shortest-path routing to destination Node 5 when the link failure occur between node 8 and node 5.

7. NUMERICAL RESULTS

In this section, we present the curves to compare the results of Physical Cost and Logical Link Cost and between Logical and Physical Hop count. The parameters of node to node, we have chosen node 5 and node 14 as destination nodes. Fig. 5 shows the comparison between Physical and Logical link cost of node i to node 5 and node 14 and Logical and Physical hop count. The same hop count on both techniques shows that the algorithm will provide the optimize path that match to the real network. Fig. 6 shows the Cost of distance and hop count in link failure between node 11 and node 12. Fig. 7 shows the Cost of distance and hop count in link failure between node 5 and node 8.

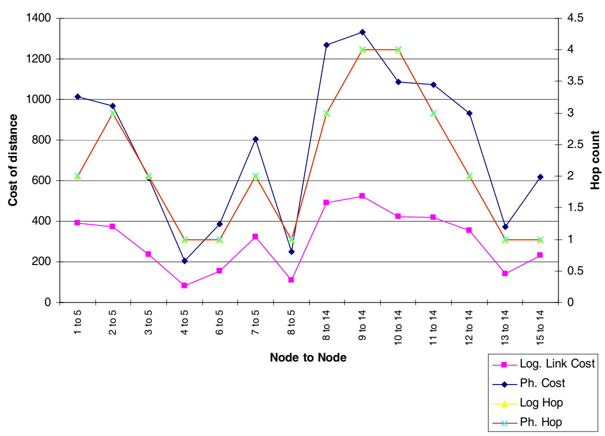

Figure 5: The comparison between Physical and Logical Cost Distance and Hop count.

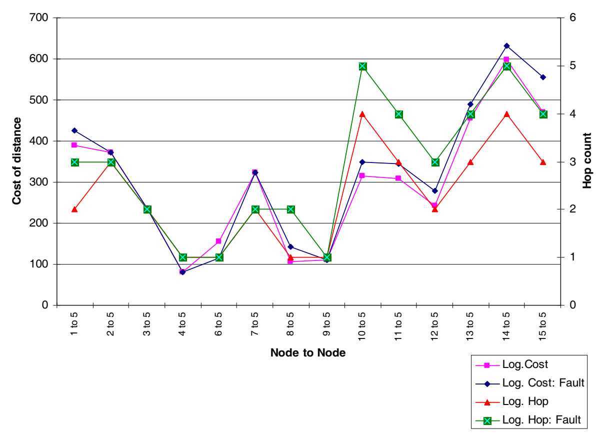

Figure 6: The new shortest-path routing to destination Node 5 with link failure.

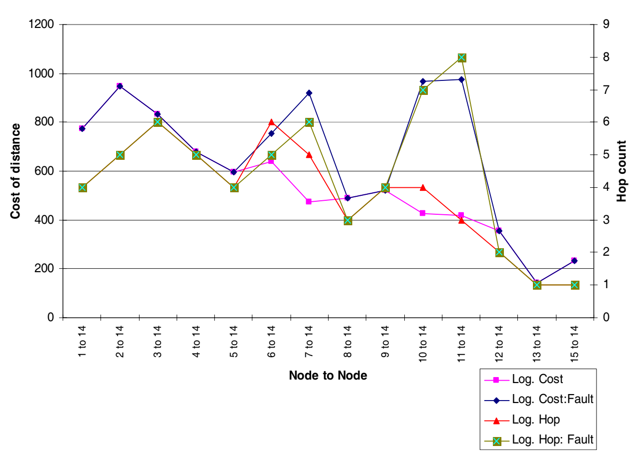

Figure 7: The new shortest-path routing to destination Node 11 with link failure.

8. CONCLUSIONS

Shortest-path routing is introduced into design logical network for connecting between Sub-networks. Bellman-Ford's Algorithm is used for computing and simulation for optimal logical design of WDM network. Three main parameters consider in this paper including Minimum Cost, Shortest-Path Routing and Recomputing of Minimum Cost to find out final shortest path. Furthermore, we have compared the result from logical computation with physical topology.

REFERENCES

1. Leon-Garcia, A. and I. Widjaja, *Communication Networks: Shortest-Path Routing*, Mc-Grawhill, 552–530, 2004.
2. Gumaste, A. and T. Antony, *DWDM Network Design and Engineering Solution: The Graph Coloring Approach to Wavelength Assignment Problem*, Cisco Press, 194–197, 2002.
3. Tanenbaum, A. S., *Computer Networks*, Pearson Education, 294–302.
4. Sridharan, A., R. Guerin, and C. Diot, "Achieving near-optimal traffic engineering solutions for current OSPF/IS-IS networks," *Proceeding of INFOCOM'2003*, April 2003.

Laser Speckle Imaging of a Finger by Scattered Light Optics

A. Kuramoto, **A. Hori**, and **I. Fujieda**

Ritsumeikan University, Japan

Abstract— We have demonstrated Laser speckle imaging of a finger with an optical configuration based on scattered light detection. Laser light enters a light-guide from its edge and propagates inside. A finger in contact with the light-guide scatters the light and the leaking light is imaged by a camera placed nearby. The speckle image fluctuates with time because the light scattered by the blood flowing inside the finger generates interference patterns varying with time. When the level of the blood flow is decreased by occlusion, the temporal randomness of the speckle image subsides.

1. INTRODUCTION

As we grow older, our health conditions gradually deteriorate. Some diseases are related to narrowing blood vessels and limiting oxygen-rich blood cells can cause tissue and cell death. Monitoring signals related to a blood flow is a first step toward delaying such unwanted aging effects. Conventional optical technologies for acquiring health-related signals in a non-invasive manner include accelerated plethysmography [1] and laser Doppler perfusion imaging [2]. Imaging systems consisting of a light source and a CCD camera have been also used for visualizing hemoglobin distributions in a foot [3] and a wrist [4]. We are investigating an optical fingerprint sensing technology, which might give us information about the blood flow in a finger-tip in a short period of time [5, 6]. If some signal extracted from a finger-tip were correlated to the conditions of a blood flow or the stiffness of a blood vessel, health-monitoring and data-logging would be quick and easy.

Laser speckle imaging is an interesting possibility that has been applied for visualizing cerebral blood flow [7] as well as the blood flow in human retina [8]. We might be able to adopt this technique to acquire an image that reflects the blood vessel conditions in a finger-tip as schematically illustrated in Fig. 1. When a finger is illuminated by a coherent light from a Laser, interference of the reflected light generates a speckle pattern. Due to the blood flow in the finger, the speckle image will fluctuate with time.

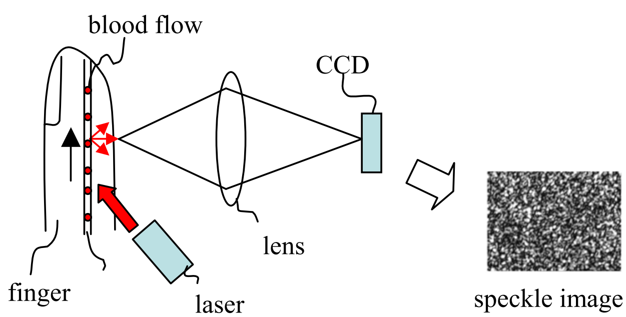

Figure 1: Laser Speckle Imaging.

However, a direct observation of a reflected light by a finger does not give a high-contrast image of a fingerprint. For this matter, we have studied a somewhat indirect optical configuration in an attempt to improve the valley-ridge contrast. This is based on scattered light detection [9]. In this paper, we report that Laser speckle imaging is actually possible with this sensor configuration based on scattered light detection and that its variation with time is related to a blood flow.

2. SPECKLE IMAGING

Figure 2 illustrates our sensor configuration and the three fingers that we have tried to image. The first finger is a genuine living finger. The second finger is an artificial finger made of urethane resin [10] and its photograph is shown in Fig. 2(d). We hold the artificial finger with our fingers and pressed it against the light-guide in Fig. 2(b). In Fig. 2(c), we put a weight on top of the artificial finger to apply pressure so that the finger deformation becomes similar to those of other cases. The wavelength of the Laser diode is 780 nm. The specifications of the camera used here are as follows: 640×480 pixels, 30 frames/sec, 8-bit gray, and 1 msec exposure time.

The raw images corresponding to the three situations in Fig. 2 are shown in Fig. 3. Because these are still images, the difference is not clear. Next, we monitored the value of a certain pixel in the video images acquired at this frame rate (30 fps). The results are compared in Fig. 4. The real finger shows a large variation with time and so does the artificial finger pressed by the real fingers. However, the variation is much smaller in case of (c) where the pressure applied to the artificial finger is by a weight. We suspect that the variation in case of (b) is caused by the vibration of the real fingers. Therefore, it is not clear whether the variation observed in the real finger is caused by

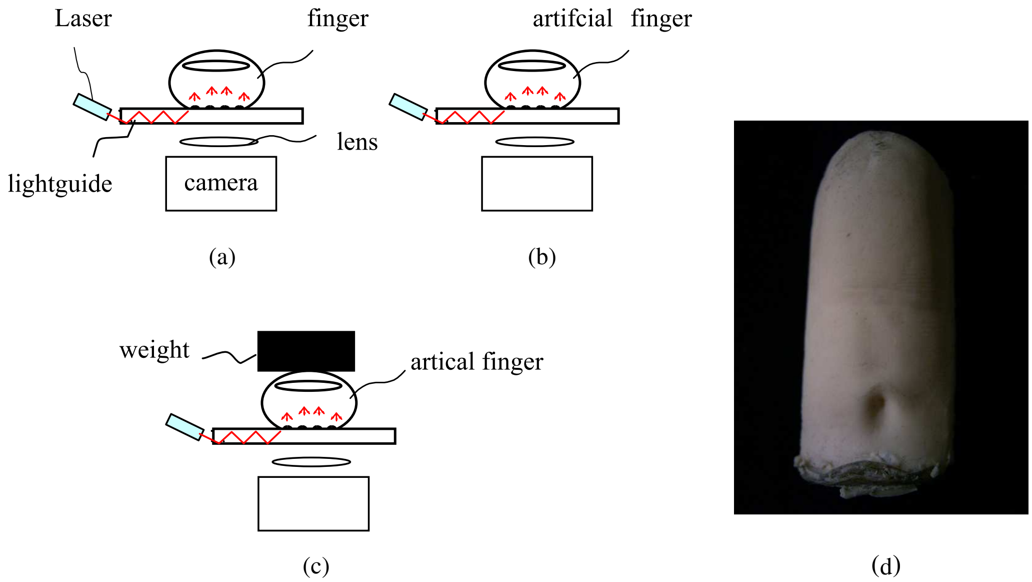

Figure 2: Experiment with three fingers.

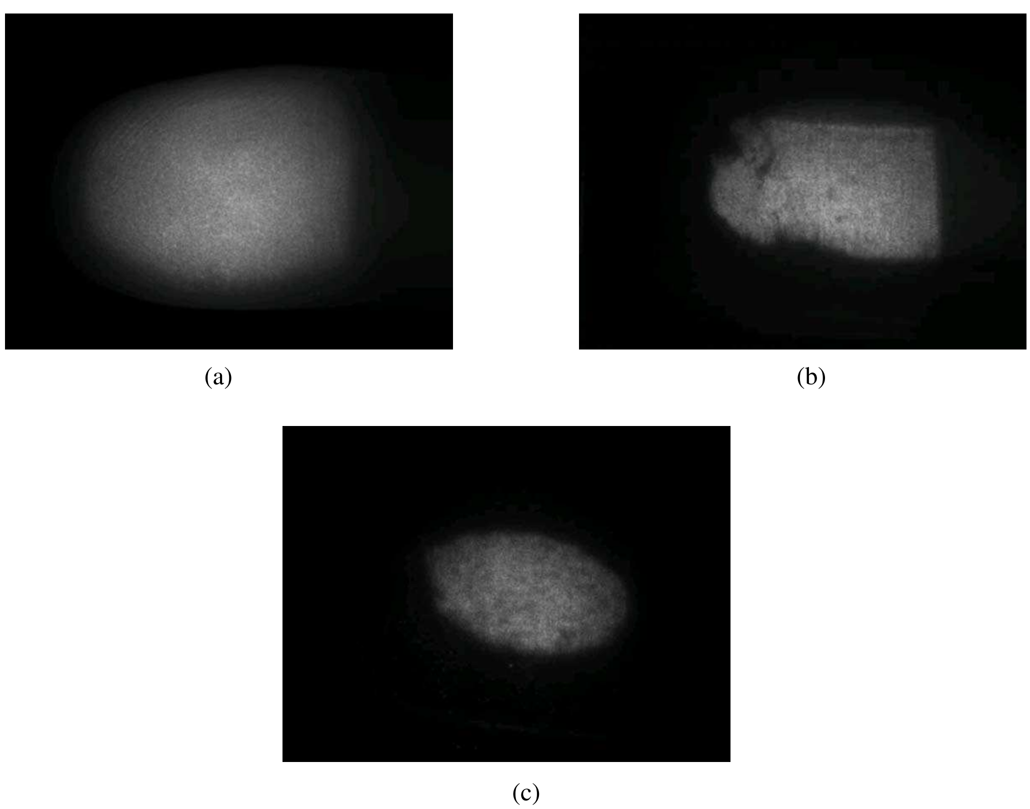

Figure 3: Speckle images obtained with the three fingers in Fig. 2.

the blood flow or by the vibration introduced unintentionally by the finger-pressing action.

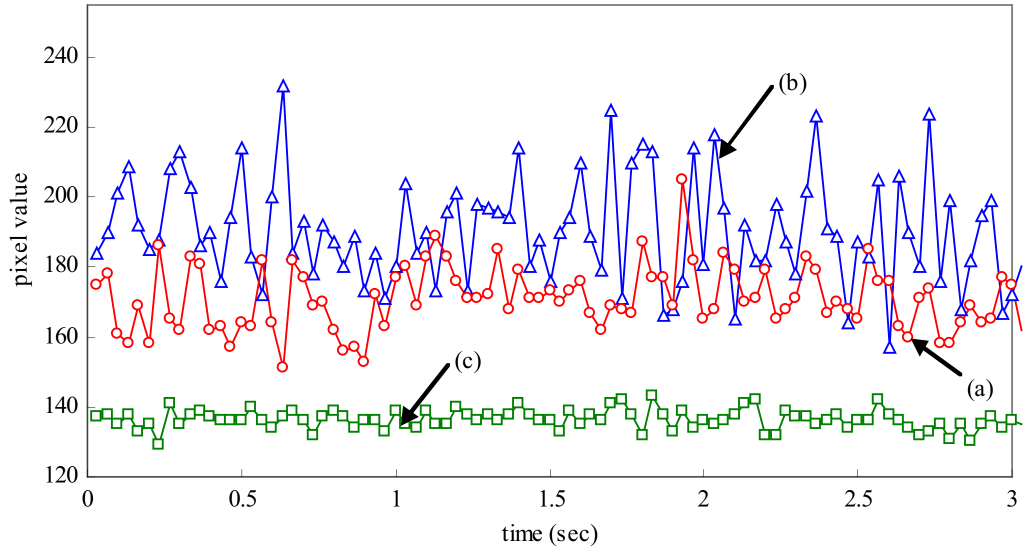

Figure 4: Time variation of a pixel value for the three cases in Fig. 3.

3. OCCULUSION AND RELEASE

For clarifying the origin of the pixel variation with time in Fig. 3(a), we decreased the level of a blood flow in a finger by putting a rubber band as shown in Fig. 5. The sequence of the image acquisition was as follows. First, we recorded 32 images in a series at 30 fps when we pressed the normal living finger against the light-guide. We put the rubber band and a minute later we recorded another 32 images. We repeated this image acquisition every two minutes. Nine minutes later, we removed the rubber band continued repeating the acquisition sequence.

Figure 5: Rubber band around a finger.

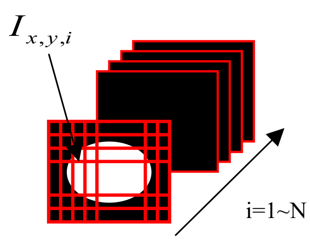

$$SBR_{x,y} = \left(\frac{\frac{1}{N}\sum_{i=1}^{N} I_{x,y,i}}{\frac{1}{N}\sum_{i=1}^{N}\left| I_{x,y,i} - \frac{1}{N}\sum_{i=1}^{N} I_{x,y,i} \right|} \right)^2$$

Figure 6: Definition of the "SBR" value.

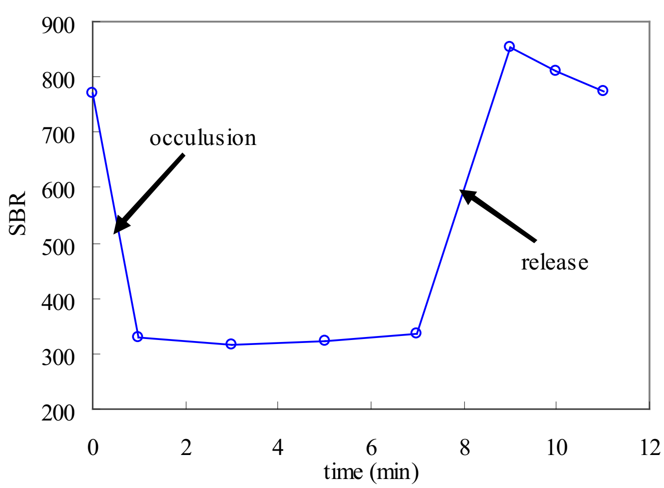

Figure 7: The variation of the SBR value in the finger occlusion and release experiment.

For quantifying the level of pixel value variation, we derived the "SBR" value used in Ref. [7]. Here, we deal with N images and let $I_{x,y,i}$ be the pixel value at a position (x, y) in the ith image. The SBR value is calculated for each pixel according to the definition reproduced in Fig. 6. The result is shown in Fig. 7. The rubber band reduces the level of blood flow in the finger and the SBR value decreases accordingly. When the rubber band was removed, the blood flow returned to its normal level and so does the SBR value. Therefore, we conclude that our scattered light optics can detect the speckle change due to the variation in the blood flow level in a finger.

4. CONCLUSION

We are investigating a fingerprint sensor that might give us a signal related to a blood flow. With an optical configuration based on scattered light detection, we have observed Laser speckle images of a finger. When we suppress the level of the blood flow by placing a rubber band, the temporal randomness of the speckle image subsides. When the rubber band is removed, the randomness returns to its normal level. Therefore, we believe that the speckle variation is related to the level of the blood flow in the finger.

REFERENCES

1. Sano, Y., Y. Kataoka, and T. Ikuyama, "Evaluation of peripheral circulation with accelerated plethysmography and its practical application," *J. Science of Labor*, Vol. 68, 17–25, 1988 (in Japanese).
2. Serov, A. and T. Lasser, "High-speed laser Doppler perfusion imaging using an integrating CMOS image sensor," *Optics Express*, Vol. 13, No. 17, 6416–6428, 2005.
3. Konishi, I., Y. Ito, N. Sakauchi, M. Kobayashi, and Y. Tsunazawa, "A new optical imager for hemoglobin distribution in human skin," *Optical Review*, Vol. 10, No. 6, 592–595, 2003.
4. Ozawa, T., Y. Ikeda, T. Saitou, and S. Numada, "Non invasive measurement for hemoglobin concentration using reflective near infrared spectroscopic imaging method," *Japan Soc. ME&BE*, N2-0201, Dogo, Matsuyama, Japan, Nov. 2004 (in Japanese).
5. Fujieda, I., E. Matsuyama, and M. Kurita, "Signatures of live fingers extracted from a series of fingerprint images," *Proceedings of SPIE*, Vol. 5677, 177–185, San Jose, CA, U.S.A., January 2005.
6. Fujieda, I., A. Hori, and K. Tai, "Image subtraction analysis for finger color variation," this conference.
7. Andrew, J., K. Dunn, H. Bolay, M. A. Moskowitz, and David A, "Dynamic imaging of cerebral blood flow using laser speckle," *Cerebral Blood Flow and Metabolism*, Vol. 21, 195–201, 2001.
8. Konishi, N., Y. Tokimoto, K. Hohra, and H. Fujii, "New laser speckle flowgraphy system using CCD camera," *Optical Review*, Vol. 9, No. 4, 163–169, 2002.
9. Fujieda, I. and Hiroshi Haga, "Fingerprint input based on scattered light detection," *Applied Optics*, Vol. 36, No. 35, 9152–9156, 1997.
10. Tai, K., M. Kurita, and I. Fujieda, "Life recognition based on color variations in fingerprint images of live and artificial fingers," *Proc. of SPIE*, Vol. 6075, 6075Z, 2006.

Electrokinetic Mixing Using Electrical Conductivity Gradients and Electric Field Intensity Perturbations

Win-Jet Luo[1], **Kuo-Ching Chang**[2], **Kao-Feng Yarn**[2]
Shou-Ping Hsu[1], **I-Ting Hsieh**[2], **and Jian-Cheng Chen**[2]

[1]Department of Refrigeration and Air Conditioning
Chin-Yi University of Technology, Taichung, Taiwan, China
[2]Department of Electronic Engineering, Far East University, Hsin-Shih, Tainan 744, Taiwan, China

Abstract— Electrokinetic instabilities occur under high electric fields in the presence of electrical conductivity gradients. Such instabilities are a key factor limiting the robust performance of complex electrokinetic bio-analytical systems, but can also be exploited for rapid mixing and flow control for microscale devices. This paper investigates the microfluidic instability phenomenon in a T-junction micro-channel. In the system, aqueous electrolytes of 3.5:1 conductivity ratio were electrokinetically driven into a common mixing channel by a steady electric field. Fluctuating unstable waves were observed with nominal threshold electric field intensity, and then propagate downstream. Electric field intensity perturbations are applied at one inlet of micro-channels which are perpendicular to the mixing channel, and the electric field perturbations are in the direction of the conductivity gradient. These specific perturbations can stir the microfluidic instability, and antedate the onset of instability. Through the instability phenomena by electric field perturbations, the mixing efficiency can be further promoted even in a initial stable state.

1. INTRODUCTION

Over the past fifteen years, integrated electrokinetic Microsystems have been developed with a variety of functionalities including sample pretreatment, mixing and separation. These systems are a primary component of so called micro total analysis systems with aim to integrate multiple chemical analysis functions onto microfabricated chip system. As system-level designs increase in complexity, robust control of electrokinetic processes with heterogeneous samples becomes critical. One important regime is on-chip biochemical assays with high conductivity gradients, which might occur intentionally as in sample stacking processes, or unavoidably as in multi-dimensional assays. Such conductivity gradients may lead to instability under high electric field as shown in this paper. Electrokinetic instability can be treated as a specialized form of electrohydrodynamic instability which is coupled with electroosmotic flow. Taylor [1] and Saville [2] developed Ohmic model to describe the instability of the electrohydrodynamic flows where interfacial electrokinetic effects are not considered. In this model, liquids are described as having both polarizability and free charge, and the internal electric field generated by accumulated charges can be on the order of the externally imposed field. The model often uses a formulation for conservation of net charge and conductivity as scalar quantities. Hoburg and Melcher [3] performed a stability analysis for an electric field parallel to a liquid Cliquid interface (perpendicular to the conductivity gradient) and flow initially at rest. Their analysis, which neglects molecular diffusion, showed the interface is stable for all electric fields when the liquid-liquid interface is assumed to be infinitely sharp, and is unstable for all applied electric fields when the interface is modeled with a finite width. Baygents and Baldessari [4] performed an analysis including the diffusion of conductivity showing that the flow is unstable when the applied electric field is above a critical value. Lin et al., [5] considered a long, rectangular-cross-section channel, and assumed a conductivity gradient is orthogonal to the main flow direction, and an electric field is applied in the streamwise direction. It is found that such a system exhibits a critical electric field above which the flow is highly unstable, resulting in fluctuating velocities and rapid stirring. Oddy and Santiago [6] studied a four-species electrokinetic instability model, and considered a high aspect ratio flow geometry, a base state where the conductivity gradient is orthogonal to the applied electric field. They presented the experimental image data which show good qualitative agreement with their numerical simulation results for a conductivity ratio of 1.05. Chen et al., [7] studied the electrokinetic flow instabilities using a microfluidic T-junction. They performed a linear stability analysis on a physical model and applied Briggs-Bers criteria to select physically unstable modes and determine the nature of instability. From scaling analysis and numerical results, they showed that the instability is governing by two key controlling parametersratio of dynamic to dissipative forces which governs the onset of instability, and ratio of electroviscous to electroosmotic velocities which governs the convective versus absolute nature of instability.

In this paper, we investigate the microfluidic instability phenomenon in a single sample T-junction micro-channel injection system. In the system, aqueous electrolytes conductivity ratio were electrokinetically driven into a common mixing channel by a steady electric field. Convectively unstable waves were observed only when the applied electric field intensity is above a nominal threshold. The unstable flow has the character of fluctuating velocities and rapid stirring which are beneficial to enhance the species mixing efficiency in the various microchannel geometries. However, the threshold of the electric field intensity limits the practicability of electrokinetic instability application for the microfluidics mixing. In order to practically apply EKI to the sample mixing, antedating the onset of the instability becomes more important. In this paper, Electric field intensity perturbations which are perpendicular to the mixing channel are applied at one inlet of the micro-channels injection systems, and the electric field perturbations are in the direction of the conductivity gradient. We perform numerical simulations on a physical model to investigate the effects of the electric field perturbations on the flow electrokinetic instability.

2. FORMULA

The conductivity distribution and electric field are governed by the electrolytic Ohmic model, and the fluid motion is governed by the incompressible Navier-Stokes equations,

$$\frac{\partial\sigma}{\partial t}+(v\cdot\nabla)\sigma = D_{\mathit{eff}}\nabla^2\sigma, \tag{1}$$

$$\nabla\cdot(\sigma\nabla\phi) = 0, \tag{2}$$

$$\nabla\cdot v = 0, \tag{3}$$

$$\rho\frac{\partial v}{\partial t}+\rho(v\cdot\nabla)v = -\nabla p+\mu\nabla^2 v+\varepsilon\left(\nabla^2\phi\right)\nabla\phi, \tag{4}$$

where ρ is mass density, p is pressure and μ is the dynamic viscosity of the working liquid. The electric field is assumed to be quasi-static and is related to electric potential ϕ by $E=-\nabla\phi$. Note that the electric body force term in the momentum equation couples the electric and flow fields.

In this paper, we assume the physics of the electric double layer influences the instability dynamics only in that the double layer determines an electroosmotic velocity very close to the microchannel wall. This assumption is supported by the fact that the electric double layers of interest here have a characteristic Debye length (λ_D) which is less than 10 nm, and is much smaller than the characteristic channel dimensions. The boundary conditions are therefore,

$$\begin{aligned} n\cdot\nabla\sigma &= 0\\ n\cdot\nabla\phi &= 0\\ v &= -\varepsilon\zeta\nabla\phi/\mu, \end{aligned}$$

where n denotes wall-normal direction, and ζ is the zeta potential of the electrical double layer. Boundary conditions are consequences of non-penetrating walls. The electroosmotic velocity at the wall is a function of local concentration and electric field, and is given by the Smoluchowski equation. In our thin-double-layer electrolyte system, the plane at which the electroosmotic velocity condition is posed can support both a non-zero velocity and a shear stress; this plane is only a few Debye lengths away from the wall and can be assumed to be collocated with the physical walls. Zeta potential is related to ionic concentration, which is proportional to ionic conductivity for dilute solutions under the electro-neutrality condition. The following correlation is assumed $\zeta/\zeta_r = (\sigma/\sigma_r)^{-n}$, where n is an empirical constant, and ζ_r is a reference zeta potential at the reference conductivity of σ_r. In the study, n is choose to be zero.

3. RESULS AND DISCUSSION

As shown in Figure 1(a), this study considers a T-type two-dimensional micro-channel with a uniform width and height of 60 μm. Two electrodes are installed at two inlets of the micro-channel, and the outlet connects to ground. The solutions with low and high conductivities are driven into the micro-channel from the bottom inlet and the top inlet respectively. The conductivity ratio of the two streams from two inlets is 3.5 in this study. Figure 1(b) shows the voltage scheme used in the study. A relatively low voltage corresponding to electric field intensity of 357 V/cm

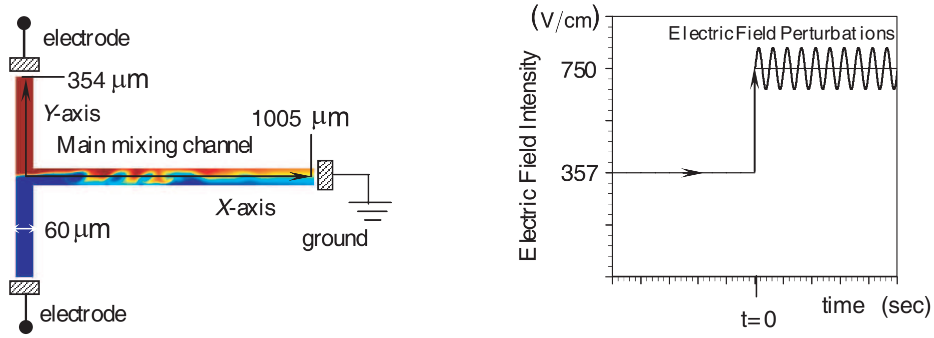

(a) (b)

Figure 1: (a) The geometry and setup of the t-junction micro-channel, (b) the voltage scheme used in the study.

was applied to establish the interface between the two streams initially. At time $t = 0$ sec, a DC voltage corresponding to electric field intensity of 750 V/cm higher than the critical voltage was applied to produce instability waves. In Figure 2, the successive images in each column show the temporal evolution of electric conductivity under a constant DC electric field intensity. In this color scheme, blue corresponds to the low conductivity stream, and the red to the high conductivity stream. For an electric field intensity of 750 V/cm, the interface is only slightly perturbed and only slight fluctuations are apparent in the images at 0.03 sec. At 0.05 sec to 0.07 sec, the interface exhibits a rapidly growing wave pattern with spatial wavelengths and amplitudes. At 0.11 sec, low conductivity regions extended into the high conductivity region of the flow in a series of finger-like structures align with the concentration minima in the initial wave. At 0.14 sec, the interface and fingering structures break down into a more complex pattern with concentration fluctuations occupying the full width of the channel. The transverse and fluctuating velocities associated with this unstable motion result in rapid mixing of the two streams. From the case in Figure 2, we can see that the electrokinetic instability can be stirred when the value of the applied electric field intensity is above a threshold of electric field intensity. In this case, the critical value of the threshold electric field intensity is 550 V/cm. For another case, a sinusoidal electric field with amplitude of 20 V and frequency of 20 Hz is added to the previous DC electric field (750 V/cm) installed at the top inlet of the T-type micro-channel, and the DC electric field (750 V/cm) still installed at bottom inlet. The distributions of the applied perturbed electric filed varying with time installed at top inlet are also shown in Figure 1(b). The evolutions of the electric conductivity under the influence of the sinusoidal electric field perturbations are illustrated in Figure 3. The conductivity ratio of two inlet streams is also 3.5 in this case. In comparison to the case in Figure 2, three weak waves are generated at the interface of the two streams in the junction of the T-type micro-channel and rapidly grow wave pattern at $t = 0.03$ sec. From $t = 0.03$ sec to $t = 0.07$ sec, due to the electric field perturbations from the top inlet, the wave patterns twist and break down into a more complex pattern propagating downstream with the electroosmotic velocity. At $t = 0.11$ sec, several weak fluctuations being generated at the interface in the upstream of the mixing channel gradually grow in size and amplify the occupying scope, and then result in another stage of chaotic state as shown in Figure 3. In comparison with the cases in Figure 2 and Figure 3, we can see almost 0.11 sec is required to reach complex instability state in the case of Figure 2, and in the case of Figure 3, only 0.07 sec is required to get the chaotic instability state. Therefore, electric field intensity perturbations applied at the inlet of the micro-channel can stir the micro-fluidic in the micro-channel into chaotic instability. Figure 4 shows the distributions of the conductivity mixing efficiency along the X-axis direction at $t = 0.1$ sec. The solid line denotes the case with a constant electric field intensity (357 V/cm) under the nominal threshold electric field intensity. The dotted line denotes the case with a constant electric field (357 V/cm) above the nominal threshold electric field intensity. The solid line with square symbols denotes the case with sinusoidal electric field perturbations. From the figure we can see the instability state of the micro-flow can enhance the mixing efficiency. Otherwise, the electric field perturbations not only antedate the onset of the instability but can stir the micro-fluidic into chaotic instability. Hence, the conductivity mixing efficiency is further promoted.

When constant electric fields applied at the two inlets of the micro-channel are less than the threshold electric field intensity, the interface between the two streams from the inlets is very clear and the flow becomes a stratified form. Through the diffusion of the conductivity concentration, the

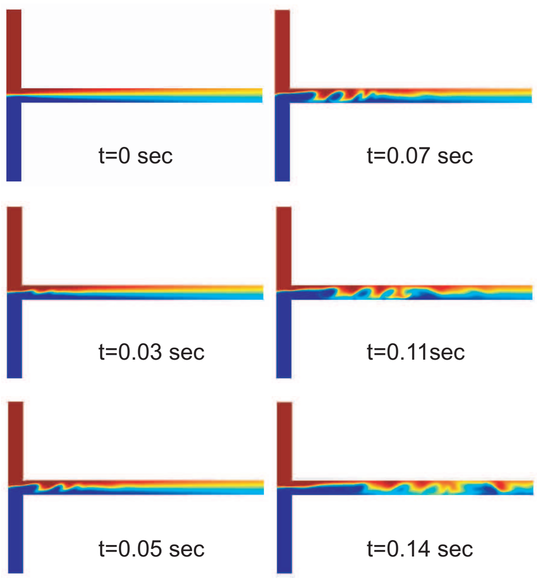

Figure 2: Temporal evolution of electric conductivity under a constant DC electric field intensity of 750 V/cm.

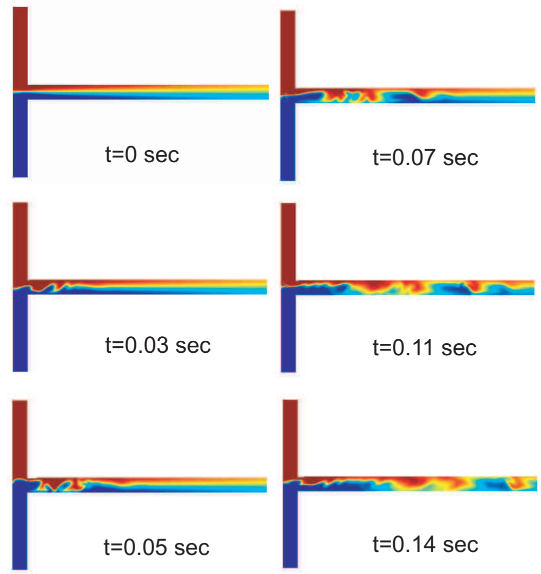

Figure 3: Temporal evolution of electric conductivity under a constant DC electric field intensity of 750 V/cm with electric field perturbations.

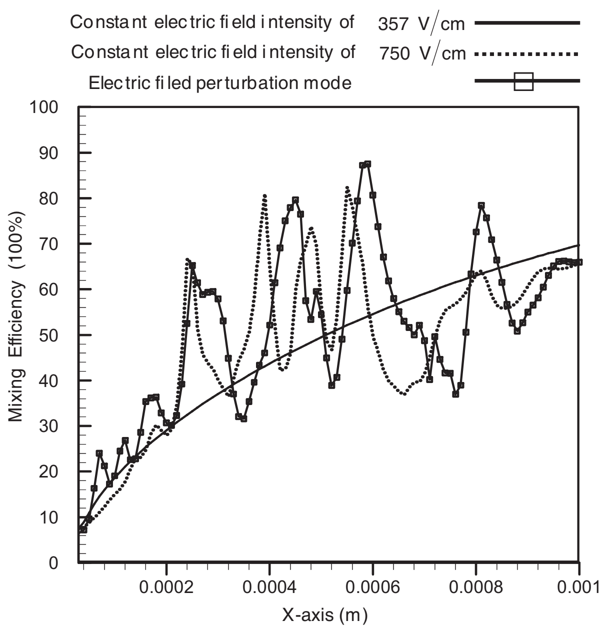

Figure 4: Distributions of the conductivity mixing efficiency along the X-axis direction at $t = 0.1$ sec.

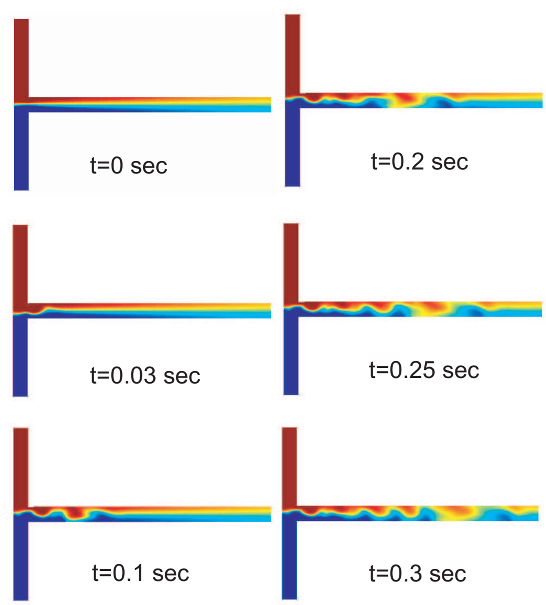

Figure 5: Temporal evolution of electric conductivity under a constant DC electric field intensity of 357 V/cm with electric field perturbations.

bandwidth of the interface gradually expands along the axial direction. From the case in Figure 3, electric field intensity perturbations added to the original DC electric filed above the threshold value at the inlet of the micro-channel can stir the flow into instability. However, when the applied DC electric field intensity is under the threshold value, the flow in the micro-channel is in a stable state. In the same way, a sinusoidal electric field perturbation is added to the DC electric field at inlets of the micro-channel, can the stable flow in the micro-channel be stirred to become unstable? Figure 5 demonstrates the flow evolutions in the micro-channel under the influence of a sinusoidal electric field with amplitude, 20 V, and frequency, 20 Hz, added to a constant electric field, (357 V/cm), at the top inlet of the micro-channel while the same constant electric field is applied to another inlet. Due to the electric field perturbation from the top inlet, the conductivity interface in the

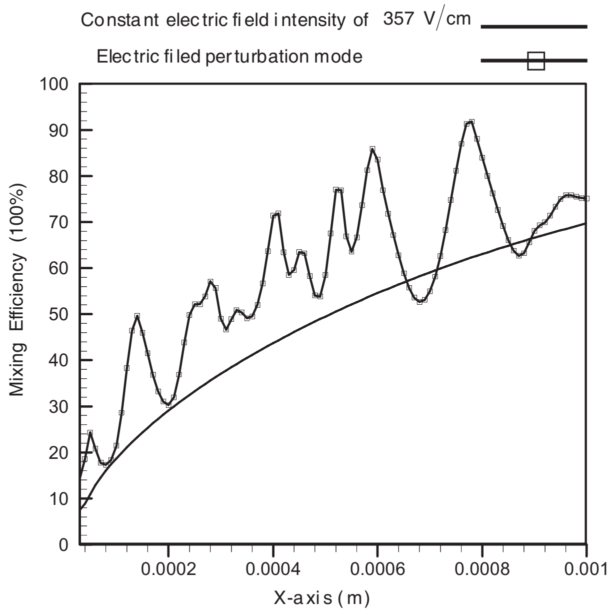

Figure 6: Distributions of the conductivity mixing efficiency along X-axis direction at $t = 0.3$ sec.

junction of the T-type micro-channel reciprocates periodically between the walls of the main mixing channel. With the interface reciprocation in the junction of the micro-channels, weak waves are continuously generated at the interface in the upstream of the mixing channel after $t = 0.02$ sec. The waves gradually grow in size and propagate downstream with the electroosmotic velocity of the bulk flow, and then occupy the full width of the channel. Figure 6 shows the distributions of the conductivity mixing efficiency along X-axis direction at $t = 0.3$ sec. The solid line denotes the case with a constant electric field intensity (357 V/cm) under the nominal threshold electric field intensity. The solid line with square symbols denotes the case with sinusoidal electric field perturbations. From the figure, we can the electric field perturbations can also stir the stable flow into instability and enhance the mixing efficiency even the applied electric field is under the threshold value.

4. CONCLUSIONS

Electrokinetic instabilities occur under high electric fields in the presence of electrical conductivity gradients. Such instabilities are a key factor limiting the robust performance of complex electrokinetic bio-analytical systems, but can also be exploited for rapid mixing and flow control for microscale devices.

This paper investigates the microfluidic instability phenomenon in a single sample T-junction micro-channel injection system, In the system, aqueous electrolytes of 3.5:1 conductivity ratio were electrokinetically driven into a common mixing channel by a steady electric field. Fluctuating unstable waves were observed with nominal threshold electric field intensity, and then propagate downstream. Electric field intensity perturbations are applied at one inlet of the micro-channel which are perpendicular to the mixing channel, and the electric field perturbations are in the direction of conductivity gradient. These specific perturbations can stir the microfluidic instability, and antedate the oneset of instability. Through the instability phenomena by electric field perturbations, the mixing efficiency can be further promoted even in a initial stable state.

ACKNOWLEDGMENT

The current authors gratefully acknowledge the financial support provided to this study by the National Science Council under Grant No. NSC 95-2212-E-269-026.

REFERENCES

1. Melcher, J. R. and G. I. Taylor, *Annu. Rev. Fluid Mech.*, Vol. 1, 111, 1969.
2. Saville, D. A., *Annu. Rev. Fluid Mech.*, Vol. 29, 27, 1997.
3. Hoburg, J. F. and J. R. Melcher, *Phys. Fluids*, Vol. 20, 903, 1976.

4. Baygents, J. C. and F. Baldessari, *Phys. Fluids*, Vol. 10, 301, 1998.
5. Lin, H., B. D. Storey, M. H. Oddy, C.-H. Chen, and J. G. Santiago, *Phys. Fluids*, Vol. 16, 1922, 2004.
6. Oddy, M. H., J. C. Mikkelsen, and J. G. Santiago, *Analyt. Chem.*, Vol. 73, 5822, 2001.
7. Chen, C.-H., H. Lin, S. K. Lele, and J. G. Santiago, *J. Fluids Mech.*, Vol. 524, 263, 2005.

Numerical Analysis of Curved Surface Perforated Periodically with Apertures

Yulian Liu, Qiang Zhang, Mingchun Hu, and Tie Gao

Nanjing Research Institute of Electronic Technology
National Key Laboratory of Antenna & Microwave Technology, China

Abstract— In this paper, numerical analysis of curved surface perforated periodically with aperture finite curved FSS is present. For validation the results of finite flat FSS of patch elements are given with good agreement with the published data. The finite aperture-type FSS with different curvatures is analyzed by using MoM and FMM. The details of the field along the aperture are given. It has shown that the curvature leads to resonant frequency shift compared with the response of infinite plane FSS with apertures.

1. INTRODUCTION

Frequency Selective Surfaces (FSSs) with periodically metallic patch elements or aperture elements have been widely and extensively studied in the past decades. For infinite FSS, there are many numerical methods of plane FSS such as modal matching technique [1, 2], spectral-iteration [3], method of lines [4] and so on. In recent years, a few works have been done in the analysis of finite FSS. For example, the spectral-Galerkin method [5] was used to compute the current and far field of finite FSS illuminated by plane-wave. By using hybrid volume-surface integral method, the scattering of finite curved FSS was found [6]. Ray tracing method [7] is introduced to calculate the transmission efficiency of curved FSS radome.

Although a lot of paper have covered the analysis of infinite FSS and a few have been devoted to the finite FSS, the paper regarding with the curved effects on the band-pass FSS radome has not yet been published. The difficulty lay mainly in the structure consisting of not only the conducting plate but also dielectric substrate. In this paper, the numerical analysis is present. The MoM and FMM (Fast Multipole Method) are used to attack this problem. The surface current is found. The electric field along the aperture is given. Based on the simulation results, the resonant frequency shift is observed. Since in practical projects, band-pass radome with FSS is generally curved, the study of curved and finite FSS with apertures is very useful in the radome design.

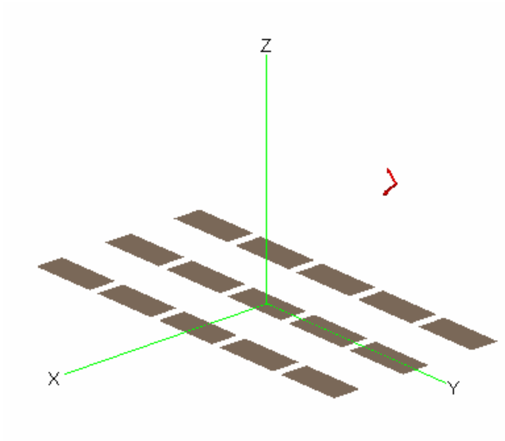

Figure 1: 5 by 3 plane patch-type FSS.

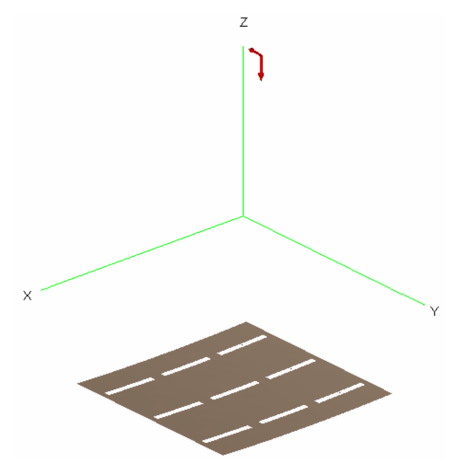

Figure 2: 3 by 3 curved aperture-type FSS.

2. PLANE FSS WITH PATCH ELEMENTS

For validation, referring to paper [5], the electric field of finite plane FSS of patch elements are computed. Consider 5 by 3 patches FSS, placed in XOY plane (shown in Figure 1), width of patch is 6 mm, length is 14 mm, and both spacing along X and Y direction is 16 mm. The excitation is assumed as a plane wave transferred in the direction of $\theta = 45°$, $\varphi = 1°$. The polarization of the plane wave is TM mode. The amplitude is 1 V/m. The calculated far field is illustrated in Figure 3 and the agreement with data [5] is quite well.

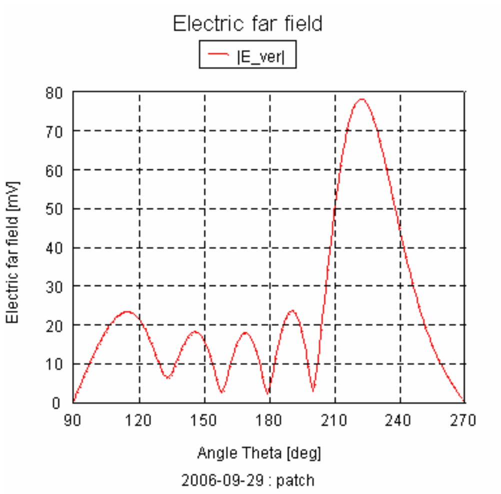

Figure 3: Far field of finite patches at 10 GHz.

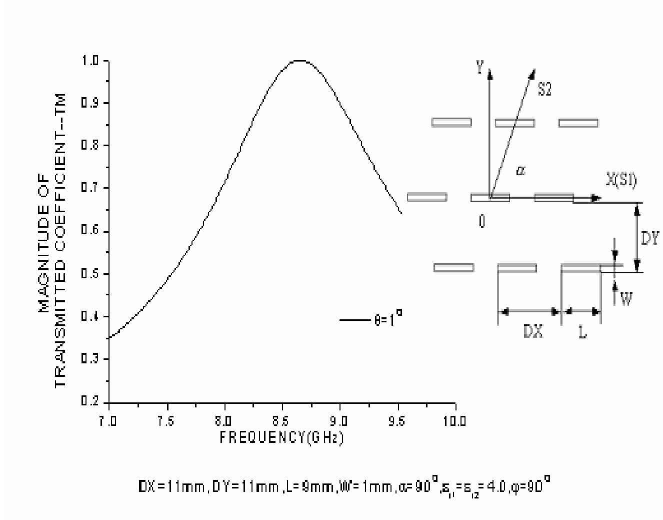

Figure 4: Infinite plane FSS with apertures.

3. INFINITE PLANE FSS WITH APERTURES

By using modal matching technique and MoM, an infinite plane FSS with apertures covered by a dielectric substrate and a superstratum is computed. It is assumed that the width of aperture is 1 mm and length is 9 mm. Both spacing in the x and y direction is 11 mm. The parameters of dielectric layer are $\varepsilon_{r1} = \varepsilon_{r2} = 4.0$, $t_1 = t_2 = 1$ mm. As discussed in [2], the entire domain basis function is chosen as follows:

$$\bar{h}_q = \hat{y} \sin\left(\frac{q\pi}{L}\left(x + \frac{L}{2}\right)\right) P_x(0, L)\, P_y(0, w) \tag{1}$$

where $P_x(0, L) = \begin{cases} 1 & |x| \le \frac{L}{2} \\ 0 & \text{else} \end{cases}$, $P_y(0, w) = \begin{cases} 1 & |y| \le \frac{w}{2} \\ 0 & \text{else} \end{cases}$.

Transmitted TE-mode coefficients of the infinite plane FSS are shown in Figure 4. It is obvious that the resonant frequency is about 8.6 GHz.

4. SINGLE-CURVED FSS WITH APERTURES

Consider a finite single-curved FSS (shown in Figure 2) with 3 by 3 apertures, and with both a dielectric substrate and a superstratum where the parameters are $\varepsilon_{r1} = \varepsilon_{r2} = 4.0$, $t_1 = t_2 = 1$ mm. The conducting surface is part of the cylinder rotated along the Y. the radius of the cylinder is R. the aperture is perforated along the arc of the cylinder. The spacing of the apertures in the Y and arc direction is uniform taken to be 11 mm. The width of aperture is 1 mm and length is 9 mm.

The excitation is assumed as a plane wave transferred in the direction of $\theta = 1°$, $\varphi = 90°$. The polarization of the plane wave is TM mode. The amplitude is 1 V/m. The frequency is taken as 7 GHz, 7.4 GHz, 7.74 GHz, 8.6 GHz, 9.4 GHz, it is found that the Maxim Electric Field in the center aperture varies significantly as the frequency changes shown as Table 1. The peak amplitude of the field at the center aperture is occurred at 7.74 GHz.

Table 1: Maxim electric field in the center aperture.

Frequency (GHz)	7.0	7.4	7.74	8.6	9.4
Electric field (V/m)	3.7	7.0	34.9	4.9	4.7

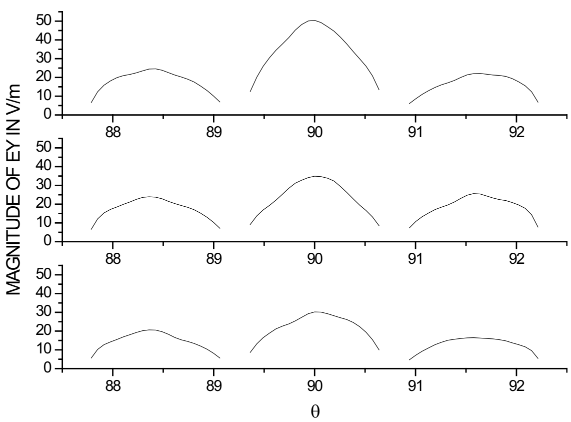

Figure 5: Magnitude of Ey in each aperture when R is 0.4 m, frequency is 7.74 GHz.

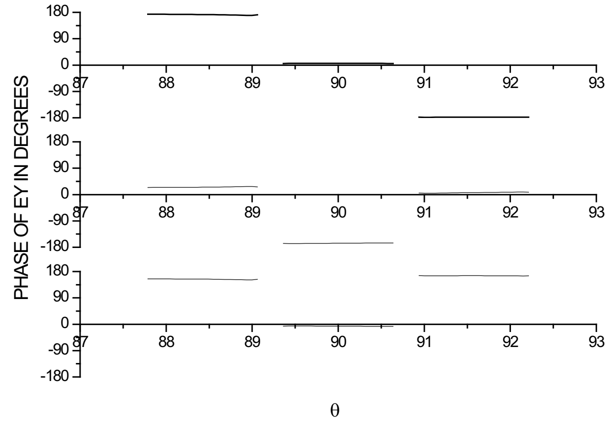

Figure 6: Phase of Ey in each aperture when R is 0.4 m, frequency is 7.74 GHz.

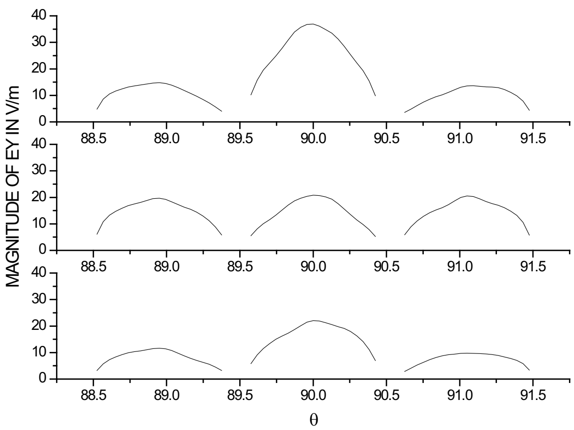

Figure 7: Magnitude of Ey in each aperture when R is 0.6 m, frequency is 7.74 GHz.

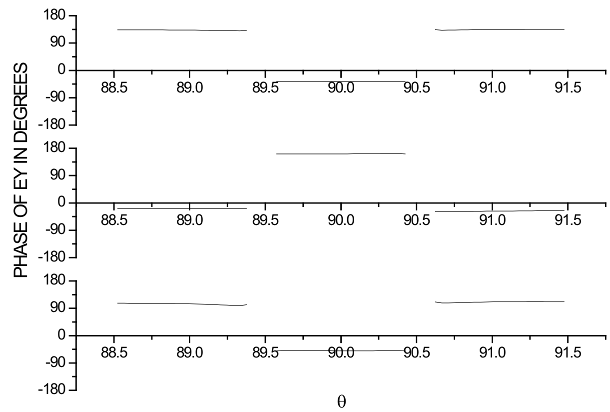

Figure 8: Phase of Ey in each aperture when R is 0.6 m, frequency is 7.74 GHz.

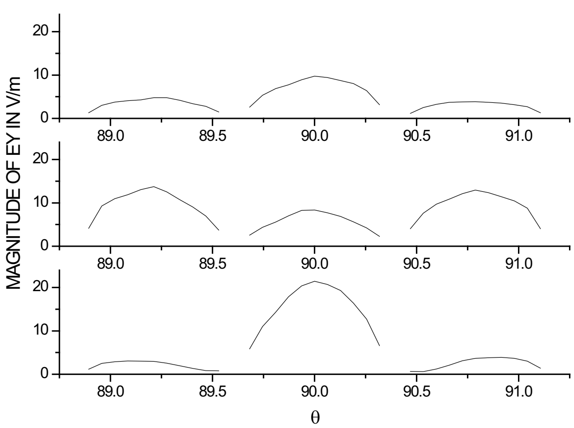

Figure 9: Magnitude of Ey in each aperture when R is 0.8 m, frequency is 7.74 GHz.

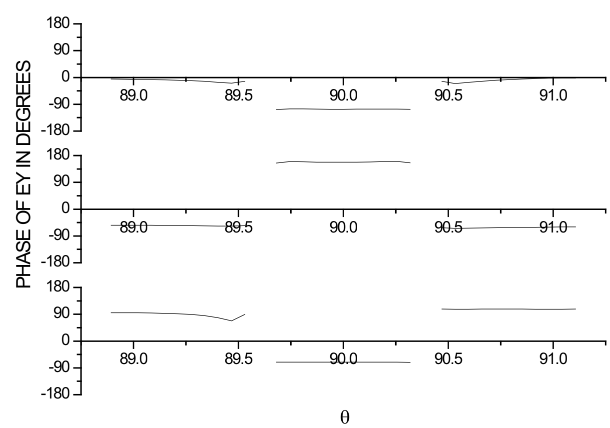

Figure 10: Phase of Ey in each aperture when R is 0.8 m, frequency is 7.74 GHz.

The distributions of the field in the resonant frequnency are shown as Figure 5 though to Figure 10.

REFERENCES

1. Chen, C. C., "Transmission through a conducting screen perforated periodically with aperture," *IEEE Trans.*, Vol. MTT-18, 627–632, 1970.

2. Mittra, R., C. H. Chan, and T. Cwik, "Techniques for analyzing frequency selective surfaces-A review," *Proceedings of the IEEE*, Vol. 76, No. 12, 1593–1615, Dec. 1988.
3. Taso, C. H., "A spectral-iteration approach for analyzing scattering from frequency selective surfaces," *IEEE Trans.*, Vol. AP-30, 303–308, 1982.
4. Worm, S. B. and R. Pregla, "Hybrid-Mode analysis of arbitrarily shaped planar microwave structures by the method of lines," *IEEE Trans.*, Vol. MTT-32, 191–196, 1984.
5. Koleck, T., H. Diez, and J. C. Bolomey, "Techniques for analyzing finite frequency selective surfaces," *10th International Conference on Antennas and Propagation*, No. 436, Conference Publication, IEE, 14–17 April 1997.
6. Yu, C. and C.-C. Lu, "Analysis of finite and curved frequency-selective surfaces using the hybrid volume-surface integral equation approach," *Microwave and Optical Technology Letters*, Vol. 45, No. 2, 107–112, 2005.
7. Phillips, B., et al., "Ray tracing analysis of the transmission performance of curved FSS," *IEE Proc. Microw. Antennas Propag.*, Vol. 142, No. 3, 193–200, 1995.

Unit Cell Models for Composite Right/Left-handed Transmission Lines (CRLH-TL) Metamaterials

Wanzhao Cui and Wei Ma

National Key Laboratory of Space Microwave Technology
Xi'an Institute of Space Radio Technology, Xi'an 710100, China

Abstract— Based on the homogeneous composite right/left-handed transmissions lines (CRLH-TL) equivalent circuit model, an unit cell model for CRLH-TL metamaterials having left-handedness (LH), right-handedness (RH) and stop-bandedness at different frequencies presented. The CRLH TL unit model is a meta-structured TL composed of a series capacitance and a shunt inductance as well as a series inductance and a shunt capacitance. The series capacitance and the shunt inductance provide the LH nature at lower frequencies, whereas the series inductance and the shunt capacitance provide the RH nature at higher frequencies and possible exhibiting stop-banded properties of supporting an infinite-wavelength wave at a finite and nonzero frequency, an unique characteristic of CRLH-TL. We can obtain $|S_{21}| = 1$ at a desired center frequency and also make a desired phase shift over a unit cell possible. The unit cell model for CRLH-TL is analyzed using S-parameter formulations resulting in some useful closed-form expressions for design purposes. Finally, the relationships between the frequencies f and ε, μ, the index of refraction n, β are analyzed, respectively. These results provide some useful references in significantly facilitating the design of CRLH-TL for a given specification.

In 1968, lossless propagation of an electromagnetic wave in the materials with negative permittivity (ε) and negative permeability (μ) was first investigated by V. G. Veselago [1], and was experimentally verified in 2001 based on split-ring resonators(SSR) and rods [2]. These materials were named "Left-Handed Metamaterials" (LHMs) because the vectors E, H, and $\boldsymbol{k}$ form a left-handed triplet. Many researchers have studied the characteristics and applications of SRR-based LHMs. However, since SRRs are lossy and narrow-banded, they are often difficult to implement for microwave applications [3, 4]. Several researchers soon realized that a transmission line (TL) approach towards LHMs was possible. By modeling a composite right/left-handed (CRLH) metamaterial as an equivalent TL unit model, TL theory can be used to analyze and design CRLH metamaterials for practical applications. Moreover, TL approach for LHM based on periodically loading a host microstrip transmission line with series capacitors and shunt inductors has been considered simultaneously [5].

The unit cell models for these left-handed transmission lines have been suggested in varied forms [6–8]. In this paper, an unit cell model for composite right/left-handed transmissions lines metamaterials having left-handedness (LH), right-handedness (RH) and stop-bandedness is presented on the basis of the homogeneous CRLH-TL equivalent circuit model. The CRLH TL unit model is a meta-structured TL composed of a series capacitance and a shunt inductance as well as a series inductance and a shunt capacitance. The series capacitance and the shunt inductance provide the LH nature at lower frequencies, whereas the series inductance and the shunt capacitance provide the RH nature at higher frequencies and possible exhibiting stopbanded properties of supporting an infinite-wavelength wave at a finite and nonzero frequency, an unique characteristic of CRLH-TL. We can obtain $|S_{21}| = 1$ at a specified passband center frequency and also make a desired phase shift from $-150°$ to $150°$ over a unit cell possible at a specified frequency. The unit cell model for CRLH-TL is analyzed using S-parameter formulations resulting in some useful closed-form expressions for design purposes. Finally, the relationships between the frequencies f and ε, μ, the index of refraction n, β are analyzed, respectively. These results provide some useful references in significantly facilitating the design of CRLH-TL for a given specification.

1. UNIT CELL MODELS FOR CRLH-TL

Figure 1 shows the asymmetric CRLH-TL unit cell model. The total electrical length of the transmission line for CRLH is k_d. The characteristic impedance of the CRLH-TL is Z_0. The LH comes from the combination of the lumped series capacitor C_L and the shunt inductor L_L, whereas the RH comes from the combination of the series inductor L_R and the shunt capacitor C_R.

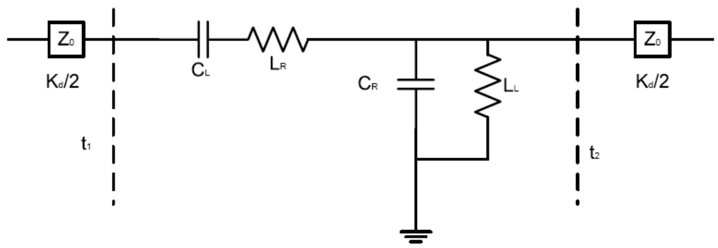

Figure 1: The CRLH-TL unit cell model.

The input impedance Z_{in} at the reference plane t_1 is given by

$$Z_{in} = \frac{1}{j\omega C_L} + j\omega L_R + Z_0 // \frac{1}{j\omega C_R} // j\omega L_L = \frac{1}{j\omega C_L} + j\omega L_R + \frac{j\omega Z_0 L_L}{Z_0 - \omega^2 L_L C_R Z_0 + j\omega L_L} \tag{1}$$

The characteristic impedance of a CRLH-TL unit cell model is given by

$$Z_0 = \sqrt{\frac{\omega L_R - \frac{1}{\omega C_L}}{\omega C_R - \frac{1}{\omega L_L}}} \tag{2}$$

The TL relations can be related to the constitutive parameters of a CRLH material, and since the propagation constant of a material is $\beta = \omega\sqrt{\mu\varepsilon}$, the following relation can be set up:

$$\omega^2 \mu\varepsilon = \left(\omega C_R - \frac{1}{\omega L_L}\right)\left(\omega L_R - \frac{1}{\omega C_L}\right) \tag{3}$$

The TL's characteristic impedance can be related to the material's intrinsic impedance $\eta = \sqrt{\mu/\varepsilon}$ by [9]

$$Z_0 = \eta \tag{4}$$

which with Eq. (3) relates the permeability and permittivity of a material to the impedance and admittance of the CRLH-TL unit cell model

$$\mu = L_R - \frac{1}{\omega^2 C_L} \tag{5}$$

$$\varepsilon = C_R - \frac{1}{\omega^2 L_L} \tag{6}$$

The input reflection coefficient

$$S_{11} = \frac{A + B/Z_0 - CZ_0 - 1}{A + B/Z_0 + CZ_0 + 1} \tag{7}$$

The transmission coefficient

$$S_{21} = S_{12} = \frac{2}{A + B/Z_0 + CZ_0 + 1}, \tag{8}$$

and the output reflection coefficient

$$S_{22} = \frac{-A + B/Z_0 - CZ_0 + 1}{A + B/Z_0 + CZ_0 + 1} \tag{9}$$

where

$$\begin{aligned} A &= 1 + \frac{L_R}{L_L} - \frac{1}{\omega^2 L_L C_L} - \omega^2 L_R C_R + \frac{C_R}{C_L} \\ B &= j\omega L_R + \frac{1}{j\omega C_L} \\ C &= j\omega C_R + \frac{1}{j\omega L_L} \end{aligned}$$

If $\omega > \omega_{\Gamma 1} = \max\left(\frac{1}{\sqrt{L_L C_R}}, \frac{1}{\sqrt{L_R C_L}}\right)$, the phase constant

$$\beta = \sqrt{\left(\omega L_R - \frac{1}{\omega C_L}\right)\left(\omega C_R - \frac{1}{\omega L_L}\right)} > 0 \tag{10}$$

which provides the RH nature, and the index of refraction $n = c\beta/\omega > 0$.

If $\omega < \omega_{\Gamma 2} = \min\left(\frac{1}{\sqrt{L_L C_R}}, \frac{1}{\sqrt{L_R C_L}}\right)$, the phase constant

$$\beta = -\sqrt{\left(\omega L_R - \frac{1}{\omega C_L}\right)\left(\omega C_R - \frac{1}{\omega L_L}\right)} < 0 \tag{11}$$

which provides the RH nature, and index of refraction $n = c\beta/\omega < 0$.

If $\max\left(\frac{1}{\sqrt{L_L C_R}}, \frac{1}{\sqrt{L_R C_L}}\right) > \omega > \min\left(\frac{1}{\sqrt{L_L C_R}}, \frac{1}{\sqrt{L_R C_L}}\right)$, the phase constant

$$\alpha = \sqrt{-\left(\omega L_R - \frac{1}{\omega C_L}\right)\left(\omega C_R - \frac{1}{\omega L_L}\right)} \tag{12}$$

$$\beta = 0 \tag{13}$$

and a stop-band occurs, which is an unique characteristic of the CRLH TL.

2. RESULTS

The relationships between the frequencies f and ε, μ, the index of refraction n, β are shown in Fig. 2 for the proposed model with $L_R = 100\,\text{pH}$, $C_R = 100\,\text{pF}$, $L_L = 20\,\text{pH}$, $C_L = 30\,\text{pH}$ and $k_d = 0$, respectively.

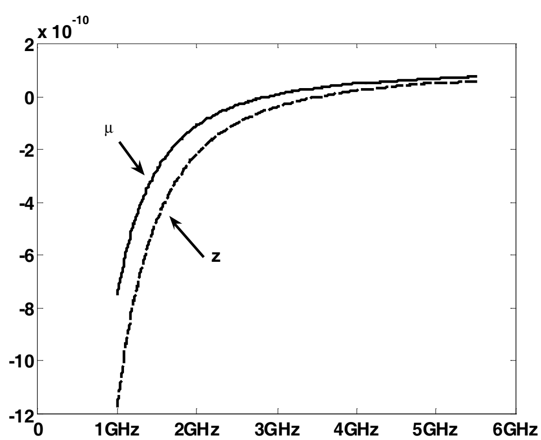

(a)

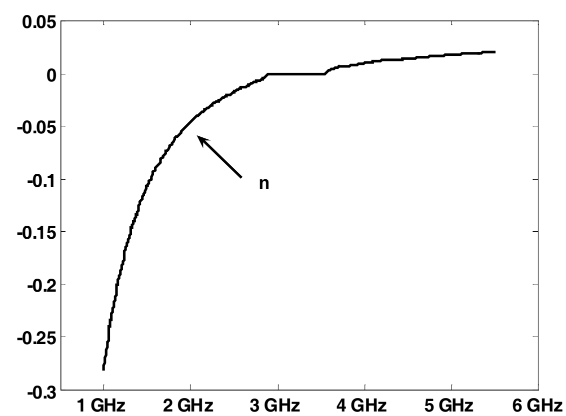

(b)

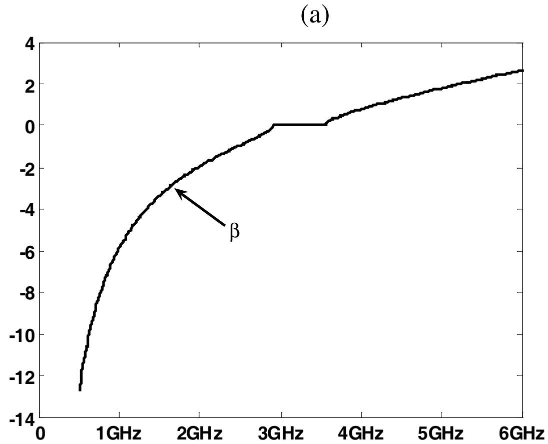

(c)

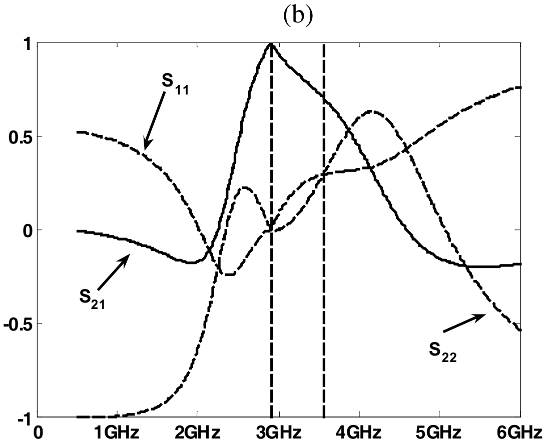

(d)

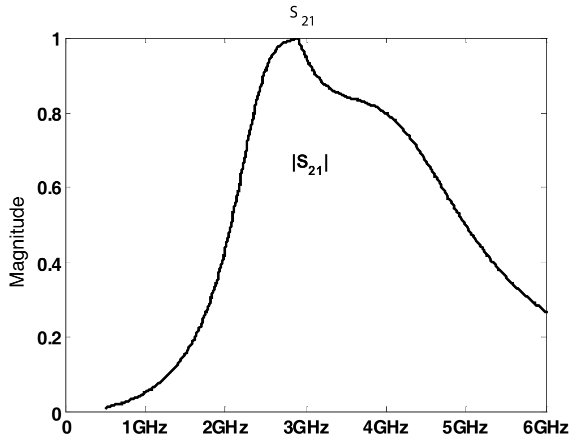

(e)

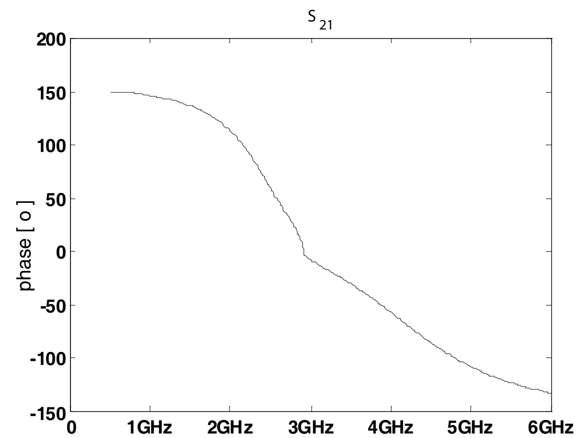

(f)

3. CONCLUSION

An unit cell model for composite right/left-handed transmissions lines metamaterials having left-handedness, right-handedness and stop-bandedness at different frequencies presented based on the homogeneous CRLH-TL equivalent circuit model. The asymmetrical unit cell models for CRLH-TL have been analyzed using S-parameter formulations resulting in some useful closed-form expressions for design purposes. The relationships between the frequencies f and ε, μ, the index of refraction n, β are analyzed, respectively.The simple and essential expressions provided here facilitate the design of CRLH-TL.

REFERENCES

1. Veselago, V. G., "The electrodynamics of substances with simultaneously negative values of ε and μ," *Sov. Phys.-Usp.*, Vol. 10, No. 4, 509–514, Jan.–Feb. 1968.
2. Shelby, R. A., D. R. Smith, and S. Schultz, "Experimental verification of a negative index of refraction," *Science*, Vol. 292, No. 5514, 77–79, 2001.
3. Lai, A., C. Caloz, and T. Itoh, "Composite Right/Left-handed transmission line metamaterials," *IEEE Microwave Magazine*, 34–50, 2004.
4. Caloz, C. and T. Itoh, *Electromagnetic Metamaterials, Transmission Line Theory and Microwave Applications*, Wiley, New York, 2005.
5. Iyer, A. K. and G. V. Eleftheriades, "Negative refractive index metamaterials supporting 2-D waves," *IEEE MTT-S Dig.*, Vol. 2, 1067–1070, 2002.
6. Caloz, C., A. Sanada, and T. Itoh, "A novel composite right-/left-handed coupled-line directional coupler with arbitrary coupling level and broad bandwidth," *IEEE Trans. Microwave Theory Tech.*, Vol. 52, No. 3, 980–992, March 2004.
7. Islam, R. and G. V. Eleftheriades, "A planar metamaterial co-directional coupler that couples power backwards," *IEEE MTT-S Digs.*, Vol. 3, 321–324, 2003.
8. Kim, H.-M. and B. Lee, "Unit cell models for Right/Left-handed Transmission Lines (RLH-TL)," *APMC*, 1–4, 2005.
9. Pozar, D. M., *Microwave Engineering*, John wiley & Sons, New York, 2005.

An Improved Design of Feed-forward Power Amplifier

Hongbo Ma and Quanyuan Feng

Institute of Microelectronics, Southwest Jiaotong University, ChengDu, 610031, China

Abstract— Amplifier's nonlinear phenomenon is the significant factor that affects the performance of radio & microwave communication system. In this paper, the principle of feed-forward technology and various improved solutions are introduced. Meanwhile, aiming at their shortages of classic feed-forward and OCFF topology, a new high linearization solution is proposed for the large power output, which reduces difficulty of the error amplifier design and input power. The results show it can improve the power efficiency remarkably without adding the complexity of the system, which is of practical value for improving the communication quality.

With the development of large capacity 3 G mobile communication, owing to adding channels, branching the bandwidth and employing higher frequency modulation method, the higher linearization for the power amplifier is especially important for communications system. The linearization matter has been one of the key issues of the new generation mobile communication system [1]. In radio & microwave communications system, nonlinear character of power amplifier is the most resource to result in the system's nonlinear. Therefore, it is meaningful for the communication development to analyze the nonlinear character and to study on the simple, feasible Linearization method of the power amplifier.

At present, the linearization technologies for RF & microwave power amplifier are classified into four kinds: power back-off, feedback, predistortion and feed-forward, which are different in system architecture and advantages. Especially the double loop feed-forward topology, which is applied widely in many productions owing to its high performance, better linearization, wider available bandwidth. For the present, many papers focus on the parameter optimization and controlling the phase and amplitude, meanwhile, there are some papers researching on improving the performance of passive element. But few people pay attention to improve the system solution [6].

In this paper, the classic feed-forward technology and various improved solutions are introduced, at the same time, aiming at the shortage of the classic feed-forward and OCFF technology, a new improved measurement for large power output is presented, the results show it can improve the power efficiency remarkably and reduce difficulty of the assist amplifier design without adding the complexity of the system.

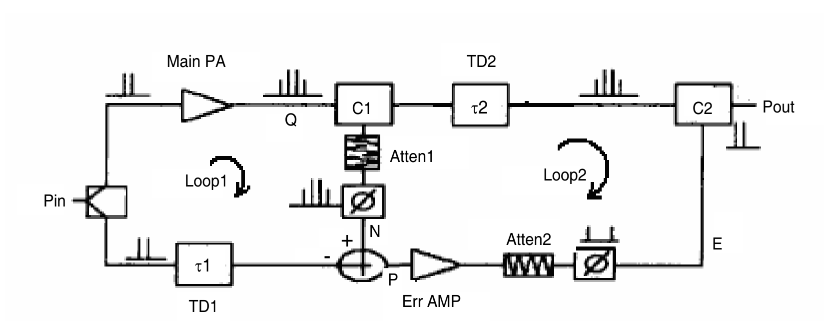

Figure 1: The principle diagram of a traditional feed-forward topology [1, 2].

According to the feed-forward theory, it is key issue for the performance of feed-forward power amplifier reasonably to control the signal amplitude and phase accurately. Fig. 1 illustrates the traditional implement method of the feed-forward topology. Its main function is to control counterbalance frequency spectrum regeneration of output signal of power amplifier by balancing the distortion signal of the two loops. The other is the over-compensation feed forward method, which is shown as Fig. 2. The idea of the predistortion method is employed in OCFF method. The predistortion amplifier is used to get the error signal by the mean of feed-forward method, and then it enters into the main PA and cancelled the error signal from the main PA. The higher efficiency and lower cost relative to the traditional feed-forward is OCFF's advantages. Fig. 3 shows the simulation result of the traditional FF PA and the OCFF PA in the two tones harmonic

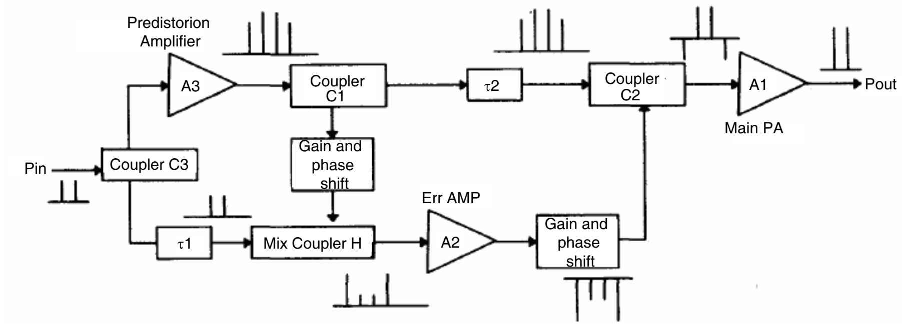

Figure 2: The over-compensation feed-forward & OCFF [5].

balance simulation method, which argues that the latter is at least higher 9 dB than the former in the third order inter-modulation distortion [5].

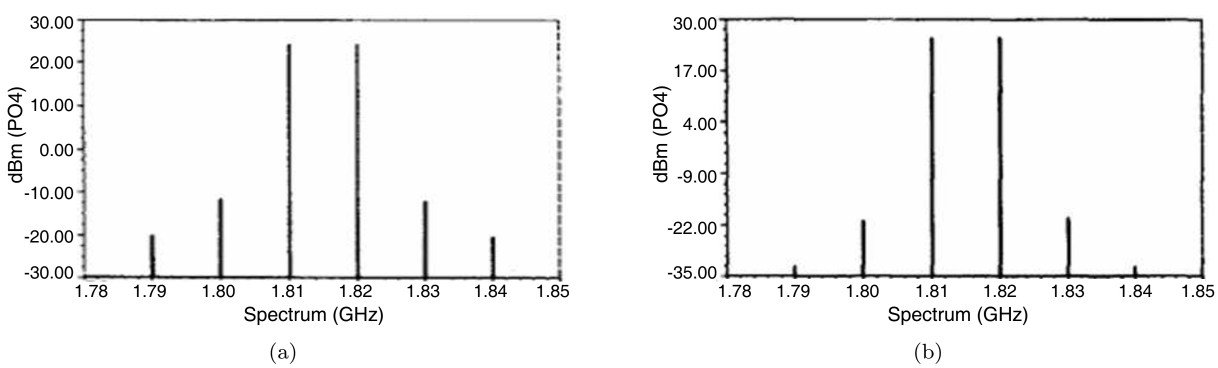

Figure 3: (a) The traditional FF PA's output power spectrum, (b) the OCFF PA's output power spectrum[5].

Describe as paper [5], the traditional FF method has some shortages as follows: (1) error amplifier in error cancellation loop increases the difficulty, complexity and cost of the system, (2) the circuit size is larger because of the microstrip line and coaxial cable as delay line, (3) low efficiency is the chief problem. Efficiency is particular critical for power amplifier as the large power device, (4) sacrificing the gain of main PA and error amplifier, and difficult to design error amplifier, (5) unsuitable for the large power output requirement. Simultaneously the design of predistortion amplifier is the bottleneck for the implement of OCFF topology. Therefore an improved feed-forward power amplifier is proposed to solving these problems in this paper.

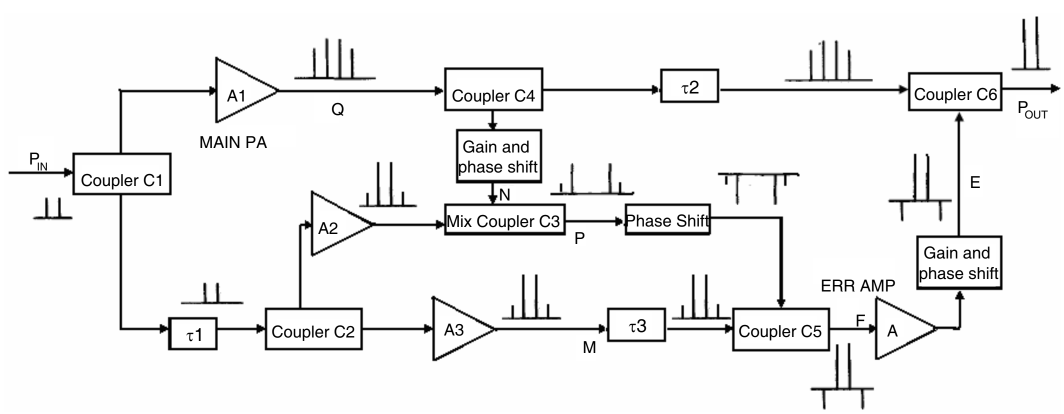

Figure 4: The diagram of a improved feed-forward topology.

Figure 4 illustrates the principle diagram of an improved feed-forward topology, in which the spectrum in every point is marked. The idea of the power back-off is employed in the improved feed-forward topology, PA2 and PA3 is the common power amplifier similar to the power amplifier of the power back-off method. But it is not same that PA2 and PA3 needn't be design as the large power PA.

A PA generates an output voltage waveform that can be viewed as the sum of a linear replica of the input signal and an error signal. As shown in Fig. 4, the input power P_{IN} is divided in the three roads, which enters the PA marked for $A1$, $A2$ and $A3$ respectively.

Assume their voltages are V_{IN1}, V_{IN2} and V_{IN3}, and V_Q stands for the output of the main PA, which is scaled by $1/A$ through the Attenuator, then generate V_N, where A is the gain of Attenuator.

In the ideal case, i. e., the PA2 and PA3 operate in the linear region (PA2 and PA3 are absolute linear). We note that $V_Q = A_{V1}V_{IN1} + V_{D1}$, where V_{D1} represents the distortion content, then we have

$$V_N = V_{IN1} * \frac{A_{V1}}{A} + \frac{V_{D1}}{A}, \tag{1}$$

Yielding (if adjusting the A according to PA2 reasonably).

$$\begin{aligned} &V_P = V_{D1}/A \\ &V_M = A_{V3}V_{IN3} \\ &V_F = A_{V3}V_{IN3} + V_{D1}/A \\ &V_E = A_{VE} * A_{V3} * V_{IN3} + V_{D1} \end{aligned} \tag{2}$$

where V_{D1} in point F and E is 180° phase difference compared to V_{D1} in point N.

$$\text{Hence} \qquad V_{\text{OUT}} = A_{V1}V_{IN1} + A_{VE} * A_{V3} * V_{IN3}. \tag{3}$$

In practice, the two amplifiers marked for $A2$ and $A3$ are not absolute linear, let V_D represents their distortion contents, and we find that

$$\begin{aligned} V_P &= \frac{V_{D1}}{A} + V_D \\ V_M &= A_{V3}V_{IN3} + V_D \\ V_F &= A_{V3}V_{IN3} + V_{D1}/A \\ V_{\text{OUT}} &= A_{V1}V_{IN1} + V_{VE} * A_{V3} * V_{IN3} \end{aligned} \tag{4}$$

Likewise, the amplified useful signal is gotten in the output port.

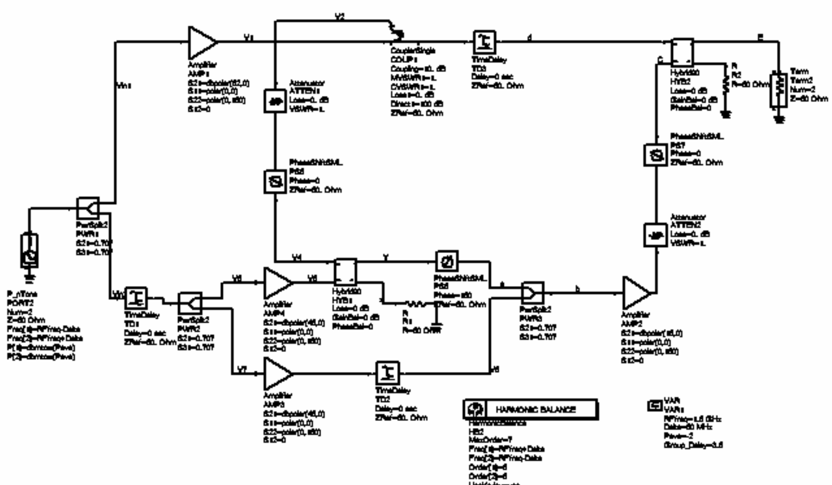

Figure 5: The simulation scheme of a improved feed-forward topology.

By the above analysis, this improvement topology has many advantages as follows: (1) reducing the gain of attenuator, system size, the dependence on delay line and cost.because less passive are employed, (the delay line $\tau1$ can be deleted) due to adding the PA2, (2) reducing the difficulty of error amplifier design, and increasing the utilization of error amplifier because of amplifying the used signal, (3) increasing the linearity of PA2 and PA3 on process of improving main PA's linearity,

(4) higher power utilization. The output power is the sum of the three linear power amplifiers, (5) reducing the difficulty of system implement without adding the system complexity. Hence this improvement solution is more suitable for the requirement of higher linear and higher output power compared to the various feed-forward solutions.

Figure 5 is the simulation circuit of the improvement feed-forward topology based on the ADS software, which is simulated for the 3 G application by the two tone harmonic balance method of $f_1 = 1750\,\mathrm{MHz}$ and $f_2 = 1850\,\mathrm{MHz}$. The main PA parameters are set according to the first edition of microwave products handbook 2001. To get $P\mathrm{out} \geq 47\,\mathrm{dBm}$, the Pin is set as $-2\,\mathrm{dBm}$. In the simulation, to control the phase difference exactly, the directional coupler is employed to replace the coupler $C4$, respectively, Hybird 90° for $C6$ and $C3$ because of controlling the phase accurately.

The $A2$ and $A3$ are set as the idea power amplifier in our simulation, which argues feasibility of the topology, but as shown as the above analysis, it is useful for the nonlinear amplifier. Figure 6(b) shows the out spectrum without the feed-forward linearization method in the condition that the $-2\,\mathrm{dBm}$ power is employed in the main PA input port. Fig. 6(c) displays the output spectrum of the improvement feed-forward power amplifier. 29 dBm cross distortion contents is cancelled from Fig. 6.

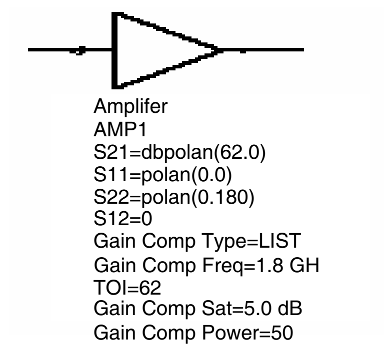

(a)

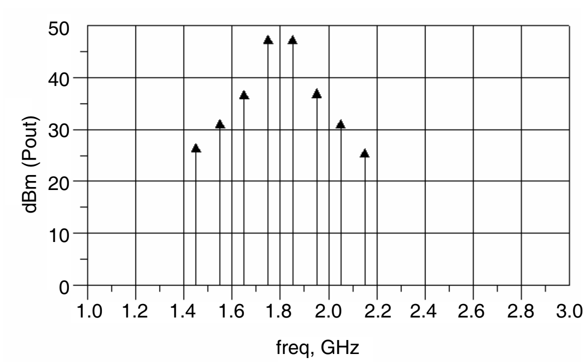

(b)

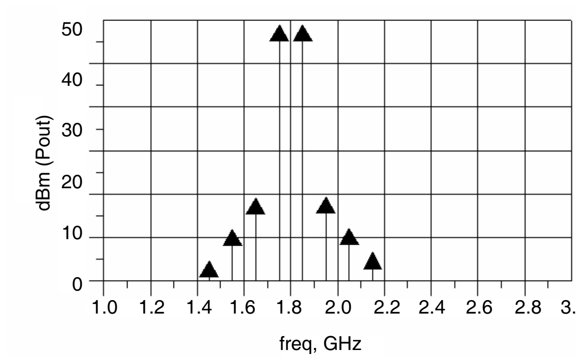

(c)

Figure 6: (a) The Main PA parameters, (b) the output spectrum without the feed-forward linearization method, (c) the output spectrum of the improvement feed-forward method in the paper.

We know the input Main PA power is only is the one part of the total input power, i. e., they only amplify the one part of the total input power in the traditional FF and OCFF power amplifier. But, the improved feed-forward power amplifier amplifies the total input power; hence the lager output power can be gotten in the output port when the $A2$ and $A3$ parameters is set well, which is of higher power utilization.

However, the disadvantage of this method similar to the above traditional FF and OCFF method is as follows: (1) this system can also not monitor and modify the effect of temperature's varying and device's ageing, (2) the system need to be adjusted when input signal condition vary owing to the PA's irregularity of frequency response and nonlinear operation, which reduce the utility of feed-forward linearization topology. At present, the self-adaptive controlling technology is employed to solve the above problem [5]. Many papers have been published about the traditional FF method employing self-adaptive controlling technology; hence the improvement FF method adding the self-adaptive controlling technology will be researched in the future.

The author wishes to thank three teachers. Firstly the Professor Feng quanyuan, Institute of Microelectronics, Southwest Jiaotong University, for his support and encouragement, secondly, the Professor Chen kangsheng, Zhe Jiang University, for his some advices, at last, Doctor Huangfu jiangtao, Zhe Jiang University, for his explanation for some problems.

This work was supported by Postgraduate Foundation for Creation on traffic & transport engineering of Southwest Jiaotong University, and by National Science Foundation of P. R. China, Grant No. 60371017 and the Leader of Academic & Technology of Sichuan province.

REFERENCES

1. Roy, M. K, "Distortion cancellation performance of miniature delay filters for feed-forward linear power amplifiers," *IEEE Transactions on Ultrasonics, Ferroelectrics and Frequency Control*, Vol. 49, Issue 11, 1592–1595, Nov. 2002.
2. Shcherbelis, Y., D. S. G. Chambers, and D. C. McLernon, "Microwave feed-forward low noise amplifier design for cellular base station," *Electronics Letters*, Vol. 37, Issue 6, 359–361, 15 Mar., 2001.
3. Han, Y. K. G., V. Postoyalko, and J. R. Richardson, "Design and characterization of a microwave feed-forward amplifier with improved wide-band distortion cancellation," *IEEE Transactions on Microwave Theory and Techniques*, Vol. 49, Issue 1, 200–203, Jan. 2001.
4. Boulejfen, N., A. Harguem, and F. A. Ghannouchi, "New closed-form expressions for the prediction of multitone intermodulation distortion in fifth-order nonlinear RF circuits/systems[J]," *IEEE Trans on Microwave Theory and Tech.*, Vol. 52, No. 1, 121–132, 2004.
5. Zhang, Y., H. Zhang, X. Xiao, and J. Xu, "Research on the linearization technique of feed-forward power amplifier," *Telemetry & Telecontrol*, Vol. 26, No. 1, 58–61, 1 Jan., 2005.
6. Ogawa, T., T. Iwasaki, H. Maruyama, K. Horiguchi, M. Nakayama, Y. Ikeda, and H. Kurebayashi, "High efficiency feed-forward amplifier using RF predistortion linearizer and the modified Doherty amplifier," *2004 IEEE MTT-S International Microwave Symposium Digest*, Vol. 2, 537–540, 6–11 June, 2004.

Design of a Low Power, High Performance BICMOS Current-limiting Circuit for DC-DC Converter Application

Hongbo Ma and Quanyuan Feng

Institute of Microelectronics, Southwest Jiaotong University, ChengDu 610031, China

Abstract— A low power, high performance current-limiting circuit implemented in 0.6 um BICMOS process, which has been successfully applied to the chip of high efficiency, wide input voltage range DC-DC boost switch power management chip, is presented. The circuit as the core sub-block of the chip consists of current-limiting comparator, soft starting and slop compensation. The dynamic bias and slop compensation technology in current-limiting comparator is adopted to improve the performance and to reduce power consume. In this paper, the deign methodology and process of the circuit is analyzed in detail. The simulation and test results based HSPICE show: under the power supply of 3.3 V, the circuit has the gain of 117 dB and low quiescent current of 15 UA.

With the rapid development of the integrated circuit technology, the requirement of low power consumption, small volume, low cost for portable and powered equipment such as MP3, PDA and digital camera can be satisfied impossibly, meanwhile, the new functions belonging to the "energy hunger and thirst" type are increasing with day, so it is key issue in this field how to integrate these new functions in smaller volume and to prolong the service time of battery-operated equipments. At present, the switch-mode DC-DC converters have been widely used in power supply systems and are becoming a common building block in modern VLSI systems, which are taking place of LDO and will be the best solution because of its high efficiency. Therefore, it is meaningful and better market prospect to research the power management IC of high efficiency, low power.

Figure 1 illustrates a simplified boost dc-dc converter's functional block diagram. Its main function is to convert input dc voltage to higher output dc voltage with minimum power loss. The converter is composed of a power stage and feedback control circuits. V_S is a battery voltage, which supplies input dc voltage, and is the boosted output dc voltage. The inductor L, diode D1, and capacitor C are off-chip components. Resistors R1 and R2 sense the output voltage and generate the scaled output voltage to the error amplifier. RLOAD is the load of the dc-dc converter.

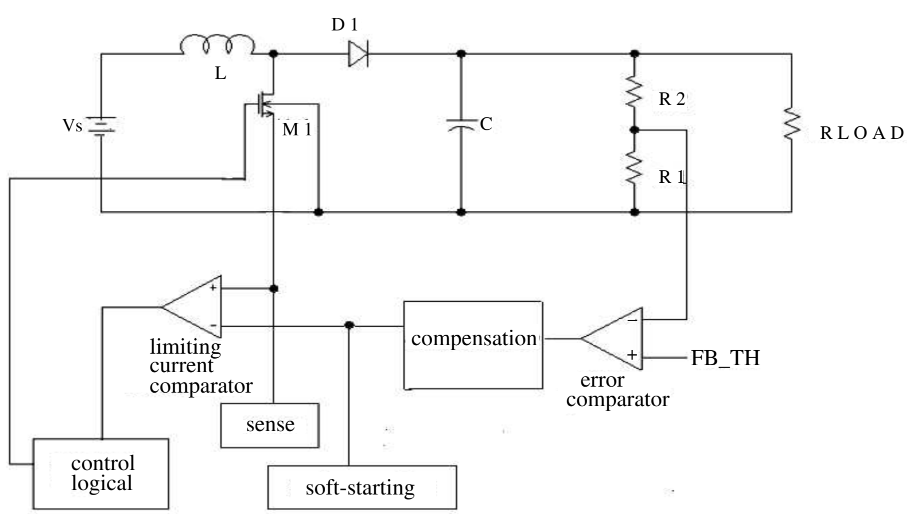

Figure 1: Boost dc-dc converter's functional block diagram.

From Figure 1, it is found that the performance of current-limiting circuit makes great effect on the total performance of the switch-mode DC-DC converters, such as power consumption, efficiency, temperature characteristics and so on. In this paper, a 0.6 um low power, high performance BICMOS current-limiting Circuit is designed, which is applied to a high efficiency boost type switch mode DC-DC chip as shown as Figure 1. The chip has been widely applied in portable and powered equipment such as MP3, PDA and digital camera and reflection from market is beyond our expectation.

Classic Current-limiting Comparator: Usually, it is hoped that the requirement of high-speed, high-gain and high dynamic range to comparator is implemented in condition of lower supply voltage and minimum power consumption, Figure 2 displays various comparators employed in DC-DC converter. In Figure 2(a), the folded cascode configuration is used to input stage, which is characteristic of better frequency response and PSRR, but larger power consumption and low-gain are its deadly shortcoming. The classic two-stage comparator is shown as Figure 2(b), whose gain is higher, but PSRR and speed is lower. Figure 2(c) shows the cascade configuration of one telescopic configuration and many differential structure employing resister load, which is high-gain at cost of the area and power consumption, and difficult to design the matching between many stages. Likewise, there are some other types, but those are cascade of folded cascode, telescopic, differential structure employing resister load or current mirror and single transistor configuration.

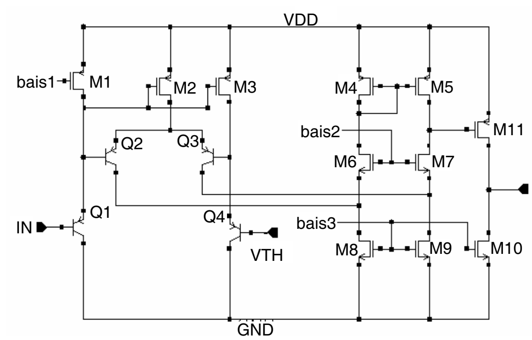

(a) Two-stage comparator with Folded input.

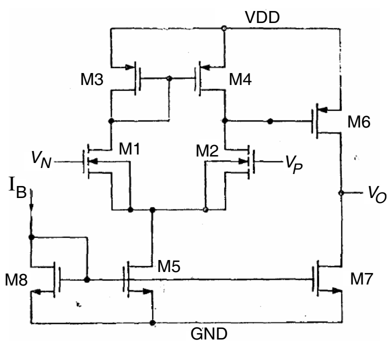

(b) Two-stage comparator.

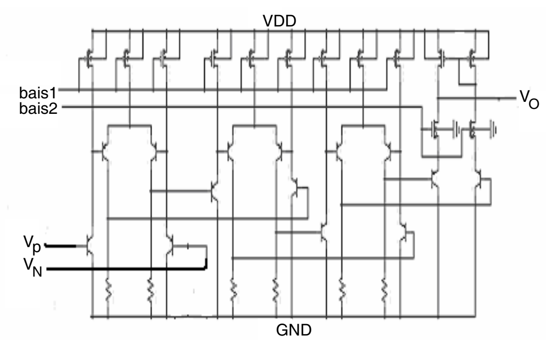

(c) Many-stages cascaded comparator.

Figure 2: The various conventional current comparators.

According to our experience, the above circuit's gain does not exceed 100 dB, and that out swing of circuit (c) is reduced. Therefore, to improve DC-DC converter's efficiency and reduce the power consumption, some improvements and optimizations are done in this paper.

Design of Low Power, High Performance Current-limiting Circuit: Based on current mode PWM controlling method, the current-limiting circuit includes current-limiting comparator, soft-start and slop compensation circuit. Concretely, the current sensing circuit is arranged in high-performance comparator, meanwhile, the comparing threshold is provide by soft-start and slop compensation time-dividedly, i.e., when system is enabled, the soft-start provides the increasing threshold, then taken by slop compensation's out when the starting function is completed, which reduces surge current and improves the system stability, insure the system stability, make the inductor current not vary with the duty ratio, and decrease the error between peak and average value, also contain the inferior harmonic wave oscillation and ring inductor current.

Deign of Current-limiting Comparator: As shown as Figure 3, CS is the sampling input port, R4, C1, R6 constitutes the sampling network, and Vbais is the bias voltage, which is provided by OUT1 of the soft-starting circuit. SOFT_OUT and SLOP_OUT is the comparing threshold, which provides the comparing threshold time-dividedly, OUT is the output port, in order to improve the drive ability and compatible to the digital circuit, an inverter composed of M18, M19 is added before OUT signal.

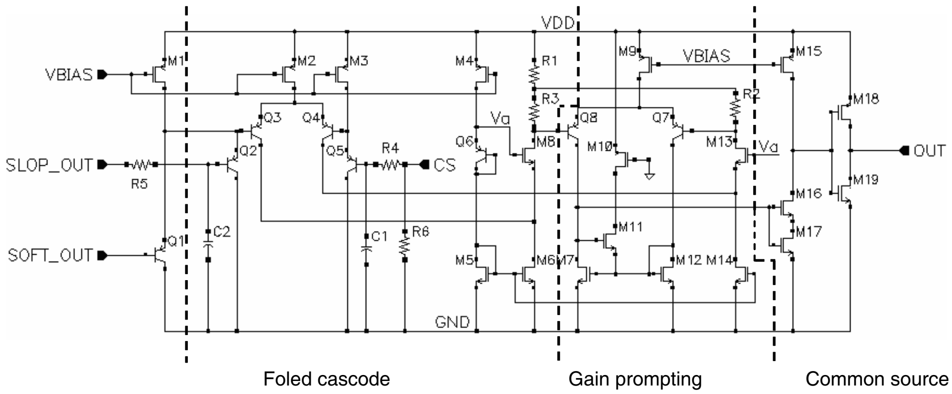

Figure 3: The current-comparator schematic in the paper.

(1) The high performance design of comparator

Comparing the valuable frameworks, the three stages is chosen in the circuit configuration: in the first stage, the folded-cascode is adopted employing resistor load and Darlington difference transistors, which is characteristics of wide common-mode input rang to enlarge the coverage of the comparator. The difference with the load of current mirror constitute the second stage to raise the gain of comparator, respectively, the output stage is implemented in the common source with current source load. The M16 and M17 is cascaded as a transistor (owing to the $L_{\max}$, and $W_{\max}$ of 0.6 um technology). All the MOS transistors is operated in the saturation region, respectively, all the BJT transistors are operated in the linear region.

Obviously, the CMR of the circuit is decided by the first stage, i. e.,

$$V_{CM(\min)} = V_{OVM6}(\text{sat}) + |V_{BCQ3}|(\text{linear}) - |V_{BEQ2}|(\text{linear}) \tag{1}$$

$$V_{CM(\max)} = V_{DD} - V_{OVM2}(\text{sat}) + |V_{BEQ2}|(\text{linear}) - |V_{BEQ3}|(\text{linear}) \tag{2}$$

The total gain about 120 dB is gotten by multiplying the three gains.

$$A_{V1} = G_{m1}R_{\text{out1}} = g_m^c * \{R_o//[(g_{mM8} + g_{mbM8})r_{oM8}r_{0M6}]\} \tag{3}$$

R_o represents the load

$$g_m^c = \frac{g_m}{1 + \left(\dfrac{r_{\pi1}}{(\beta_0 + 1)r_{\pi2}}\right)} \tag{4}$$

$$g_m = \frac{\partial I_c}{\partial V_{be}} = \frac{I_c}{V_T} \tag{5}$$

$$A_{v2} = g_{m7}R_oA_{V3} = G_mR_{out3} = G_mr_{0M15} \tag{6}$$

where G_m represents the equivalent transconductance of M16 and M17 in series.

Specially, the branch the M10, M11 provides the gate voltage for M7, M12 to decrease the real voltage of high level, which improves the propagation delay time, but the power consumption is added.

(2) Condensations on power consumption

When the system works normally:

$$I_{\text{total}} = I_{M1} + I_{M2} + I_{M3} + I_{M4} + I_{M6} + I_{M14} + I_{M9} + I_{M15} \tag{7}$$

Assume the current of M1 in the saturation region $I = \frac{1}{2}U_PC_{ox}\left(\frac{15u}{7.2u}\right)(V_{DD} - V_{\text{bais}} - V_{th})^2$, according to the parameters, we know $I_{\text{total}} = 65I$.

It can be known from above formula that the quiescent current is too large. To decrease the current, the dynamic bias is adopted.

Provided that a square wave voltage (V1 is the best bias voltage and V2 is more than V1, T is the period) is used to provide the bias voltage,

In a period, the total power consumption of comparator:

$$P_{\text{total}} = V_{DD} \cdot \frac{1}{2} U_P C_{ox} \left(\frac{15u}{7.2u}\right) \left[(V_{DD} - V_1 - V_{th})^2 \frac{T}{2} + (V_{DD} - V_2 - V_{th})^2 \frac{T}{2}\right] \tag{8}$$

However, on the condition of the fixed offset voltage:

$$P_{\text{total}} = V_{DD} \cdot \frac{1}{2} U_P C_{ox} \left(\frac{15u}{7.2u}\right) [(V_{DD} - V_1 - V_{th})^2 T \tag{9}$$

$$\because V2 > V1, \therefore P_{dynamic} < P_{fixed}.$$

Design of this dynamic VBIAS circuit is arranged in soft-starting circuits.

Soft-stating and slop compensation circuit

This soft-starting circuit has the two functions as shown as Figure 4: (1) it is employed to provide the increasing threshold gradually for the comparator when system is enabled, which improve the reliability and efficiency of system due to suppressing the surge current and solve the re-starting problem, (2) it is used to provide the dynamic bias for the comparator at normal operation to reduce the quiescent power.

Figure 5 shows the simplified slop compensation schematic, which is designed for providing the threshold after the soft-start function, is completed. At present, the current mode has more advantages than the voltage mode, but it also exists some disadvantages, for example, the system's instability when the duty exceeds the 50%, the inferior harmonic vibration, poor interference rejection capability and so on.

To improve these shortages, the slop compensation is employed in paper. Slop compensation voltage usually is designed in PWM comparator threshold or current feed-back voltage. In this paper, the slop compensation is implemented in PWM comparator threshold port. The slop amplitude and slope can be adjusted by C3, R4 and current value for charging and discharging to improve the compensation performance.

The current-limiting comparator and other sub-blocks of the current-limiting circuit are simulated by HSPICE. The result is shown as Figure 6.

The simulation results are gotten by coopering from all the sub-blocks. From the (a) and (b), the gain can attain 100 dB, the highest of 121 dB and the worst of 90 dB, the propagation delay time, CMRR and CMR is also higher than the same application comparator, even though the propagation delay time includes the delay time of relevant signals. In the Figure (c), the quiescent current of comparator varies periodically with bias voltage as our analysis, respectively Figure (d)

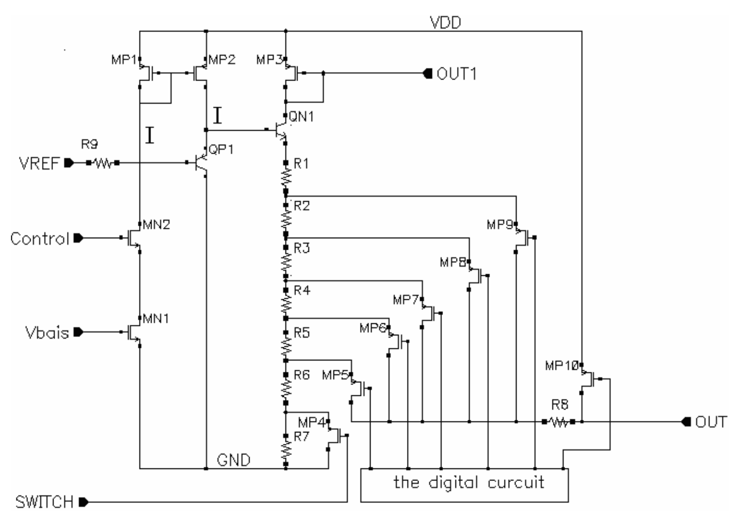

Figure 4: The soft-starting schematic in the paper.

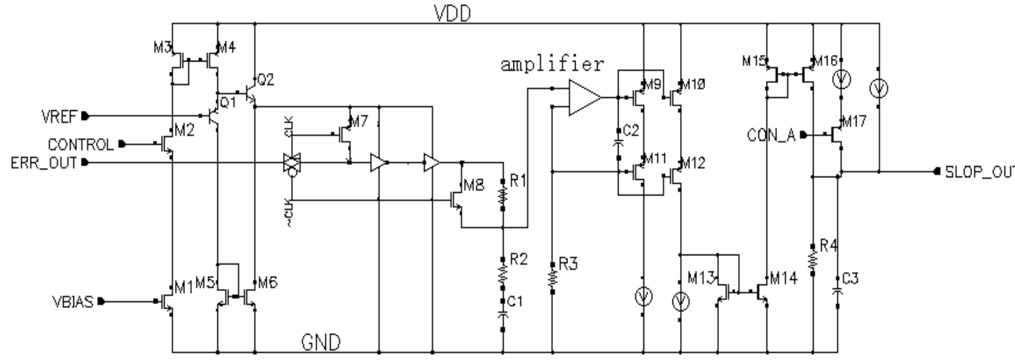

Figure 5: The simplified slop compensation schematic.

illustrates the time sequence of relevant signals with the comparator, whose real work behavior, real value and their relationship is shown as Figure 6(d). To reduce the simulation timethe absolution time of every signals is reduced in rata. The instability of SOFT_OUT and VBAIS is resulted in by the reference voltage not established at this moment.

A 0.6 um BICMOS current-limiting circuit is successfully designed with the dynamic offset and slop compensation for DC-DC converter application. The simulation and test results show that this circuit is characteristic of low power consumption, high performance, which satisfies fully the requirements of the new generation DC-DC products. Moreover, it has been applied to a DC-DC switch mode power management IC, which provides a solution to design portable and powered equipments such as MP3, PDA and digital camera for low power, small volume, and multi-function.

Among the many people who have been greatly helpful during my work, my advisor, Professor Feng quayuan is first one to whom I would like to express my most sincere appreciation, for the most source of support on my research. I would also like to thank my colleagues, for their help in my design. This work was supported by Postgraduate Foundation for Creation on traffic & transport engineering of Southwest Jiaotong University, and by National Science Foundation of P. R. China,

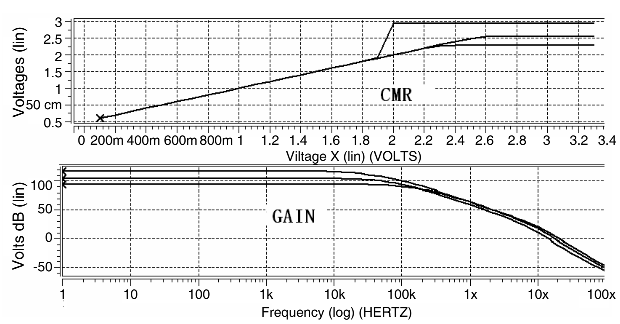

(a)

CMR data table unit:V

TEMP / CMR	-40℃	25℃	85℃
max	1.9	2.23	2.5
min	0.1	0.1	0.1

propagation delay time data table unit: s

TEMP	-40℃	25℃	85℃
TPLH	0.53e-006	0.38e-6	0.605e-006
TPHL	0.96e-006	0.92e-6	1.1e-006

gain data table unit:dB

temp	vdd / model	0.6um lib GAIN
85℃	2.7	101
	3.3	104
	5.5	111
25℃	2.7	115
	3.3	117
	5.5	121
-40℃	2.7	90.9
	3.3	93.7
	5.5	106

CMRR data table unit: dB

Temp	vdd / model	0.6um lib CMRR
85℃	2.7V	-88.8
	3.3V	-130
	5.5V	-111
25℃	2.7V	-89.7
	3.3V	-113
	5.5V	-108
-40℃	2.7V	-101
	3.3V	-97.5
	5.5V	-97

(b)

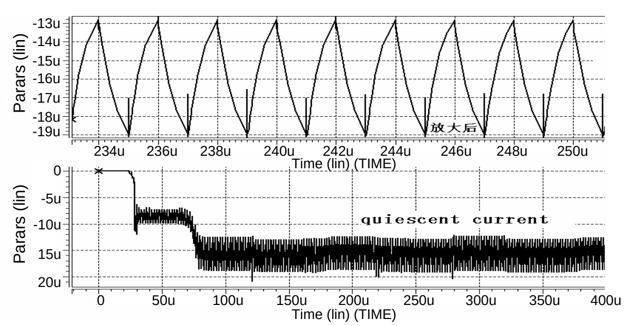

(c)

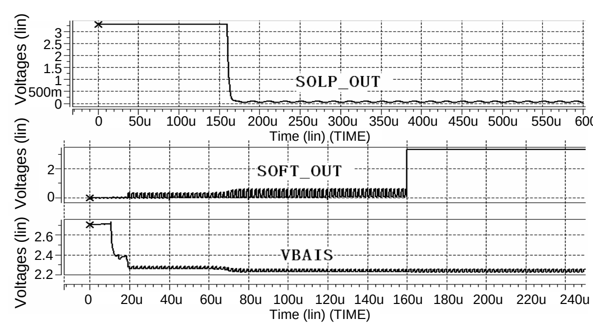

(d)

Figure 6: (a) the CMR and gain of comparator, (b) the data table of comparator, (c) Quiescent Current of comparator, (d) the sketch map of all the signals.

Grant No. 60371017 and the Leader of Academic & Technology of Sichuan province.

REFERENCES

1. Ridley, R. B., "A new continuous-time mode for current-mode control," *IEEE Transaction on Power Electronics*, April 1991.
2. Kazimierczuk, M. K. and LaVern A. Starman, "Dynamic performance of PWM DC-DC boost converter with input voltage feedforward control," *IEEE Transactions on Circuits and Syestems-I: Fundamental Theory and Applications*, Vol. 46, No. 12, 1473–1481, December 1999.
3. Lee, C. F. and P. K. T. Mok, "A monolithic current-mode CMOS DC-DC converter with on-chip current-sensing technique," *IEEE J. Solid-state Circuits*, Vol. 39, No. 1, 3–14, Jan. 2004.
4. Roh, J. "High-performance error amplifier for fast transient DC-DC converters," *IEEE Transactions On Circruits and System-II: Express Briefs*, Vol. 52, No. 9, September 2005.
5. Vorperian, V., "Simplified analysis of PWM converters using model of PWM switch," *IEEE Transactions on Aerospace and Electronic Systems*, Vol. 26, No. 3, 490–496, May 1990.

Analysis of Composite Right/Left-handed Coplanar Waveguide Zeroth-order Resonators with Application to a Band-pass Filter

C. Li, K. Y. Liu, and F. Li
Institute of Electronics, Chinese Academy of Science, Beijing, China

Abstract— Design and performance of a coplanar waveguide (CPW) bandpass filter (BPF) using Composite Right/Left-handed (CRLH) Zeroth-order Resonators have been studied. The Bloch analysis is applied based on the S parameters to derive the characteristics of the eigenmodes (Bloch modes), from which the right/left-handed frequency band and the zeroth-order resonant frequency are clearly determined. Then, the susceptance slope parameter of the resonator is extracted and the admittance (J-) inverters are introduced to synthesize a capacitively coupled CPW BPF. The measured results show that the size of the filter is greatly reduced (more than 60%) when compared to a conventional structure.

1. INTRODUCTION

Left-handed materials (LHMs) are characterized by simultaneously negative permittivity and permeability. It was first investigated theoretically by Veselago [1]. The experimental realization of LHM with resonance structures was demonstrated by Smith et al., [2]. Since then, LHM has gained significant interest and started to be integrated into novel microwave and optical applications. The resonance structures, however, suffer from large losses in the microwave regime and narrow working bandwidth. To overcome these problems, the transmission-line (TL) approach was later proposed to realize LHMs [3, 4]. LH-TL is the dual structure of the conventional RH-TL in which the inductance and capacitance are interchanged. All practical LH structures include parasitic RH effects, and are therefore composite right/left-handed (CRLH) in reality [5, 6]. Since CRLH can be realized by planar circuits, it can be conveniently implemented in microwave circuits and antennas [7]. A novel resonator composed of microstrip lines and lumped elements with zero degree of phase shift has been proposed by UCLA group and named as the zeroth-order resonator [8].

In this study, a CRLH CPW zeroth-order resonator is designed to synthesize BPFs with compact size. The unit cell of the CRLH CPW is fabricated by embedding a series interdigital capacitor and two shunt stub inductors between two sections of CPWs. Based on the results of Bloch analysis, the left and right handed frequency bands are clearly identified and the zeroth-order resonant frequency is easily found. Then, the resonance properties of zeroth-order resonator is specified by the susceptance slope parameters and used to synthesize a novel CPW BPF. The experimental results show that the BPF works at center frequency $f_0 = 5.8\,\text{GHz}$ with 11% bandwidth. The effective length of the BPF is 11.6 mm which has more than 60% size reduction as compared to the conventional capacitively coupled half-wavelength CPW BPF.

2. ANALYSIS OF THE ZEROTH-ORDER RESONATOR

Figure 1 shows the layout of the CRLH CPW unit cell. It's fabricated on a substrate with a dielectric constant of 10.2 and thickness of 0.635 mm. The unit cell consists of two sections of CPWs embedded with a series interdigital capacitor and two shunt stub inductors. The dimensions are as follows: $l = 4.1\,\text{mm}$, $l_1 = 0.75\,\text{mm}$, $l_2 = 0.65\,\text{mm}$, $l_3 = 0.65\,\text{mm}$, $l_4 = 2\,\text{mm}$, $W_1 = 0.1\,\text{mm}$, $W = 1.4\,\text{mm}$. The line width of the CPWs is chosen for the characteristic impedance of 50 Ohm.

Since the CRLH CPW TLs are formed by the periodical network of the unit cells, Bloch-Floquet theorem can be used to derive the eigen modes directly from the S parameters of the unit cell. Two important factors related to the eigen modes are the Bloch impedance Z_B and the wave number β. Generally, they are both complex values. Then, the unit cell with length l can be modeled equivalently as a segment of uniform TL with characteristic impedance Z_B and phase shift $\phi = \beta l$. The LH and RH frequency bands can be identified by the sign of the product $\mathrm{Re}(\beta)\mathrm{Re}(Z_B)$. In the frequency band where $\mathrm{Re}(\beta)\mathrm{Re}(Z_B) < 0$, the eigen modes are backward waves and the frequency bands are LH bands. In contrast, the RH band is characterized by $\mathrm{Re}(\beta)\mathrm{Re}(Z_B) > 0$.

For the unit cell structure illustrated in Fig. 1, the phase shift and the Bloch impedance are calculated and shown in Fig. 2. It's seen that the LH frequency band exists from 3 to 4.7 GHz and the RH frequency band exists from 5.8 to 9 GHz. In the frequency band from 4.7 to 5.8 GHz, the wave number β is pure imaginary and a band gap exists. At the upper edge of the band gap

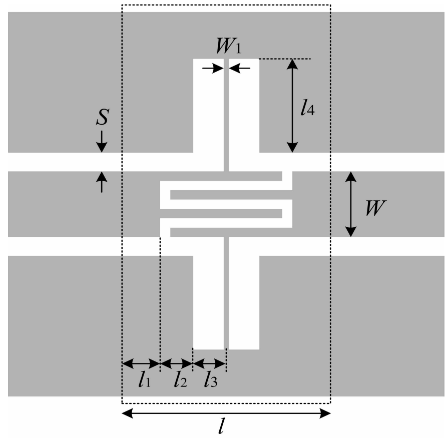

Figure 1: The layout of the CRLH CPW unit cell.

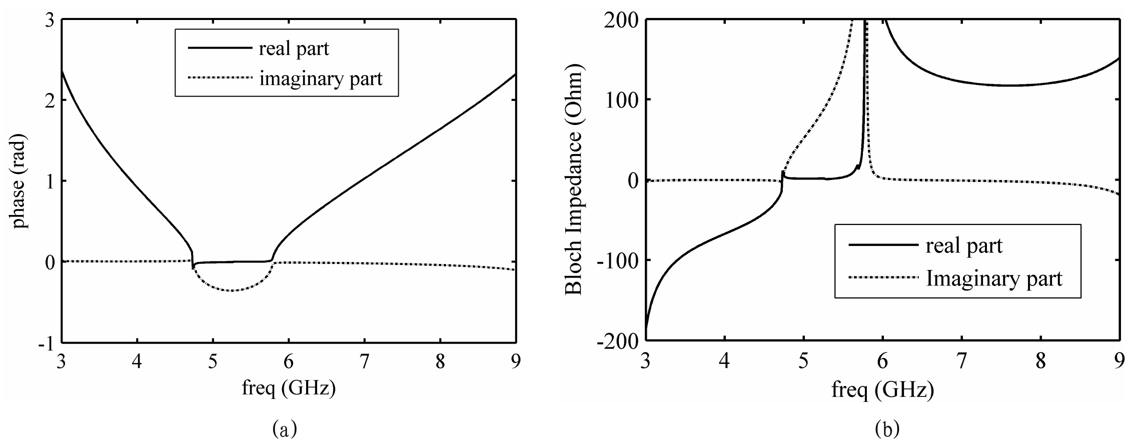

Figure 2: The results of Bloch analysis for CRLH CPW. (a) phase shift (b) Bloch impedance.

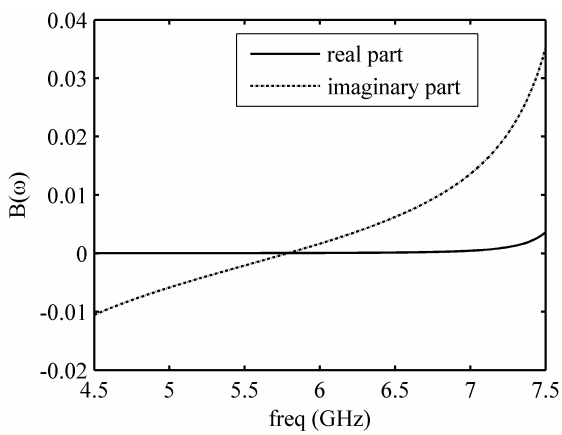

Figure 3: The susceptance of the zeroth-order resonator.

$f_0 = 5.8\,\text{GHz}$, the phase shift ϕ is zero and the zeroth-order resonance occurs. Since the Bloch impedance is very large at f_0, the unit cell terminated in open circuit has infinite input impedance (zero input admittance) and exhibits a parallel type of resonance. The resonance properties of such a resonator can be conveniently specified by evaluating the susceptance slope parameter, which is widely used in the design of bandpass filters. By calculating the input admittance of the resonator by full wave simulation, the susceptance $B(f)$ is obtained and shown in Fig. 3. The susceptance slope parameter b can be calculated by deriving the susceptance,

$$b = \frac{f_0}{2}\left.\frac{dB(f)}{df}\right|_{f=f_0} \tag{1}$$

It's calculated to be 0.0219 Siemens.

3. DESIGN OF CPW BPF

A third-order Chebyshev response CPW BPF is designed to illustrate the synthesis procedure using the resonators as proposed in Fig. 1. The passband ripple is 0.3 dB, the center frequency is 5.8 GHz, and fractional bandwidth 11.9%. The elements values of its low-pass filter prototype are select as $g_0 = g_4 = 1$, $g_1 = g_3 = 1.371$, $g_2 = 1.138$. As shown in Fig. 4, the BPF is designed using the traditional admittance (J-) inverter transformation and synthesis procedure. The admittance (J-) inverters are realized by embedding series gap capacitors between negative lengths of uniform CPWs. Note that the negative lengths can be simply subtracted from the adjacent lines in the zeroth-order resonators.

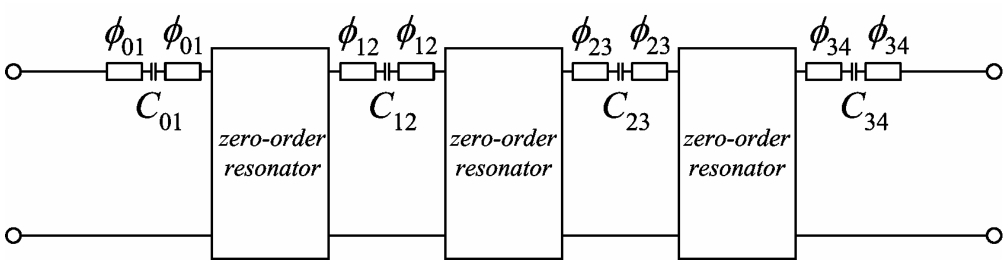

Figure 4: Schemetic diagram of a series capacitively coupled bandpass filter.

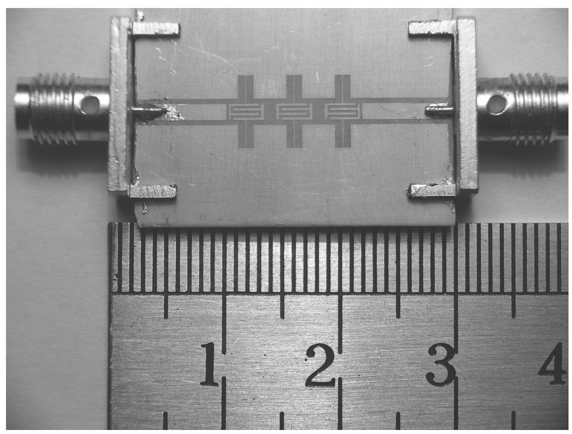

Figure 5: The photograph of the CPW BPF.

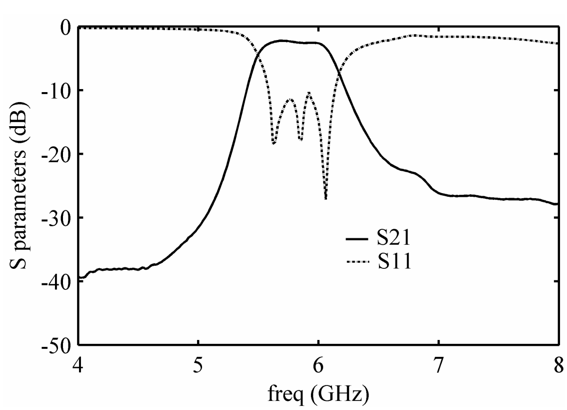

Figure 6: The measured performance of the CPW BPF.

Figure 5 shows the photograph of the BPF and its measured S-parameters are reported in Fig. 6. It's seen that the measured 3-dB fractional bandwidth is 11% centered at 5.8 GHz. The total length of the filter is 11.6 mm. At the frequency 5.8 GHz, the length of a conventional half-wavelength CPW resonator with the same substrate is more than 10 mm. This means the length of a third-order filter with these conventional resonators is more than 30 mm. Hence the size of the filter proposed in this paper is greatly reduced (more than 60%) as compared to a conventional structure.

4. CONCLUSION

Design and performance of a CPW BPF using CRLH Zeroth-order Resonators have been studied. The zeroth-order resonant frequency of the CRLH unit cell is determined from the results of Bloch analysis. The susceptance slope parameter is extracted to effectively describe the resonance properties of the resonator. By introducing series gap capacitors as admittance inverters, a third-order CPW BPF is designed, fabricated, and measured. It's shown that the size of the filter is greatly reduced (more than 60%) as compared to a conventional structure working in the same frequency band.

ACKNOWLEDGMENT

This work was supported by the National Natural Science Foundation of China under Grant No. (60501018, 60271027), and the National Basic Research Program of China under Grant No. 2004CB719800.

REFERENCES

1. Veselago, V. G., "The electrodynamics of substances with simultaneously negative values of ε and μ," *Sov. Phys.-Usp.*, Vol. 10, No. 4, 509–514, 1968.
2. Shelby, R. A., D. R. Smith, and S. Schultz, "Experimental verification of a negative index of refraction," *Science*, Vol. 292, 77–79, 2001.
3. Eleftheriades, G. V., A. K. Iyer, and P. C. Kremer, "Planar negative refractive index media using periodically L-C loaded transmission lines," *IEEE. Trans. Microw. Theory Tech.*, Vol. 50, 2702–2712, 2002.
4. Caloz, C. and T. Itoh, "Application of the transmission line theory of left-handed (LH) materials to the realization of a microstrip LH transmission line," *IEEE AP-S Int. Symp. Dig.*, Vol. 2, 412–415, 2002.
5. Caloz, C. and T. Itoh, "Novel microwave devices and structures based on the transmission line approach of meta-materials," *IEEE-MTT int. Symp. Dig.*, 195–198, 2003.
6. Sanada, A., C. Caloz, and T. Itoh, "Characteristics of the composite right/left-handed transmission lines," *IEEE Microw. Wireless Compon. Lett.*, Vol. 14, No. 2, 68–70, 2004.
7. Grbic, A. and G. V. Eleftheriades, "Experimental verification of backward wave radiation from a negative refractive index material," *J. Appl. Phys.*, Vol. 92, No. 10, 5930–5935, 2002.
8. Sanada, A., C. Caloz, and T. Itoh, "Novel zeroth-order resonance in composite right/left-handed transmission line resonator," *Proc. Asia-Pacific Microwave Conf.*, 1588–1591, 2003.

A New Type of Microstrip Coupler with Complementary Split-Ring Resonator (CSRR)

K. Y. Liu, C. Li, and F. Li
Institute of Electronics, Chinese Academy of Science, China

Abstract— A new type of microstrip Coupler with Complementary Split-Ring Resonator (CSRR) is proposed. The characteristic impedance of the even mode can be enhanced by etching CSRR structure in the grounded plane of a conventional microstrip double-line coupler. This results in a higher degree of coupling. Based on the analysis of the odd and even modes, a new type of microstrip coupler was designed. The results of simulation and measurement show that the new coupler achieves a high degree of coupling (3 dB coupling) over a wide frequency band (38.1% relative bandwidth).

1. INTRODUCTION

A well-known problem of the conventional microstrip parallel-coupled couplers is their difficulty to achieve tight backward coupling because of the excessive small lines-gap required [1]. Alternative components include non-coupler-line couplers such as the branch-line or rat-race, however, these couplers are inherently narrowband (no more than 15% bandwidth) circuit. The Lange coupler [2] is a solution widely used in the MMIC industry for broadband 3-dB coupling, but it has the disadvantage of requiring bonding wires. In the past few years, there has been a great interest in the emerging field of meta-materials and more specially left-handed (LH) structures. Couplers based on LH transmission lines (TL) was proposed by some authors [3, 4]. This couplers, which composed of one or two LH-TL constituted of series interdigital capacitors and shunt shorted-stub inductors, can provide arbitrary loose/tight coupling levels. But designing this coupler is too complicated.

Very recently, Complementary Split-Ring Resonator (CSRR), which is the negative image of Split-Ring Resonators (SRR) [5] (see Fig. 1), have been reported by some authors [6]. It has been demonstrated that CSRR etched in the ground plane or in the conductor strip of planar transmission media (microstrip or CPW) provide a negative effective permittivity to the structure. CSRR has been successfully applied to the narrow band filters and diplexer with compact dimensions [7, 8].

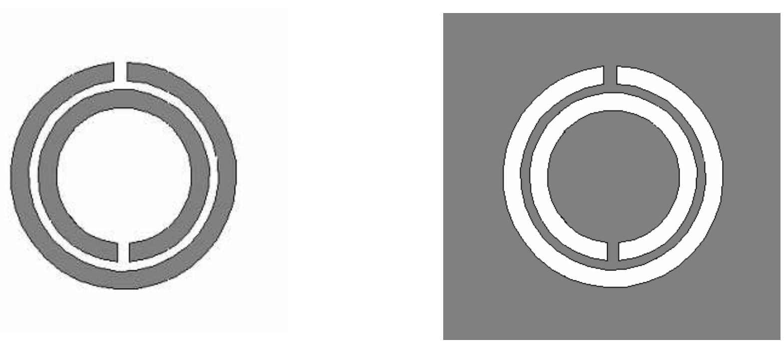

(a) (b)

Figure 1: (a) Topology of the SRR, (b) Topology of CSRR (Metal regions are depicted in gray).

In this paper, a novel coupled-line backward coupler based on CSRR is presented. The characteristic impedance of the even mode can be enhanced by etching CSRR structure in the grounded plane of a conventional microstrip double-line coupler. This results in a higher degree of coupling. The results of simulation and measurement show that the new coupler achieves a high degree of coupling (3 dB coupling) over a wide frequency band (38.1% relative bandwidth).

2. ODD AND EVEN MODES ANALYSIS

The electric fluxline of coupling microstrip of odd mode and even mode are showed in Fig. 2. In odd mode, the E-field is asymmetric and continuous even in the presence of CSRR slot. Signal does not slow down just as the one without CSRR. In even mode, the E-field is discontinuous along the middle line of coupler. The CSRR act as open circuit for the even mode.

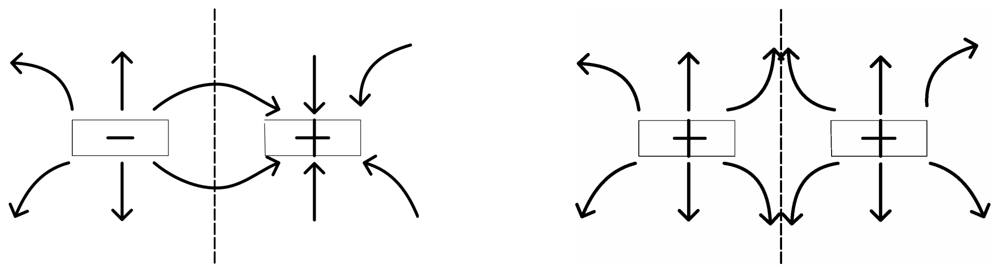

(a) (b)

Figure 2: Electric fluxline of coupling microstrip. (a) odd mode, (b) even mode.

The odd and even modes S-parameters of the coupler of Fig. 3 were computed by full-wave simulation, and are showed in Fig. 4. Table 1 shows the odd and even characteristic impedances

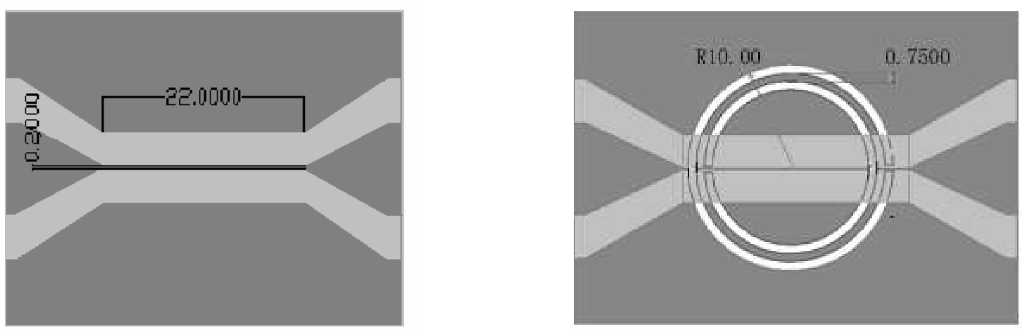

(a) (b)

Figure 3: (a) Structure of conventional directional coupler, (b) Structure of CSRR-based directional coupler.

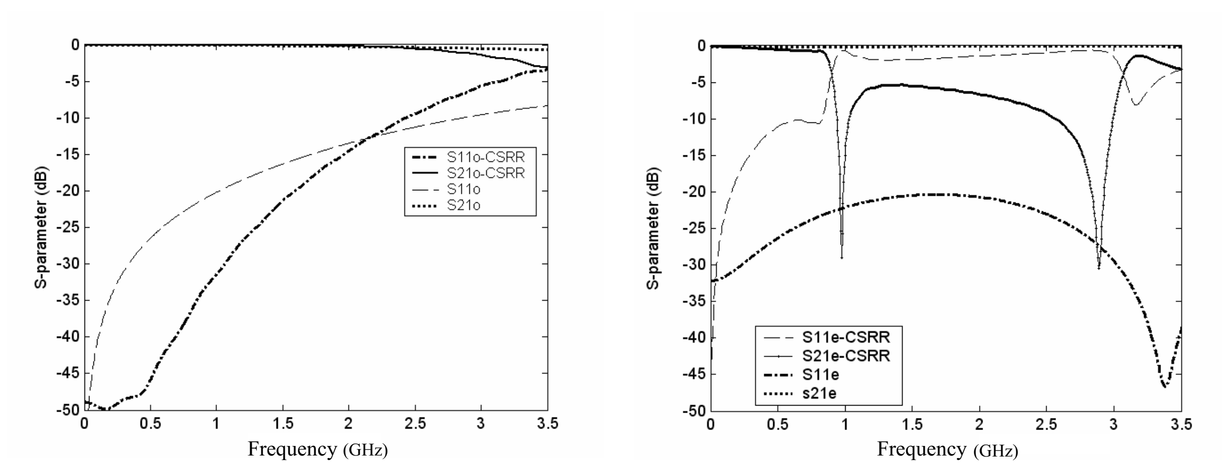

(a) (b)

Figure 4: Magnitude of the S-parameters for the two structures showed in Fig. 3 obtained by simulation. (a) odd mode, (b) even mode.

at the frequency of 2.1 GHz computed from the odd and even S-parameters, using the general formula

$$Z_{ci} = Z_0\sqrt{(\Pi_i - 1)\,/\,(\Pi_i + 1)}, \qquad (i = e, o) \tag{1}$$

with

$$\Pi_i = \left(S_{21i}^2 - S_{11i}^2 - 1\right)/\left(2S_{11i}\right).$$

Table 1: Odd and even impedance for the two structures showed in Fig. 3 at the central frequency (2.1 GHz).

	Z_{co}	Z_{ce}
Conventional coupler	38.7 Ω	69.6 Ω
CSRR coupler	38.2 Ω	240 Ω

It is demonstrated that the characteristic impedance of the even mode can be enhanced by CSRR structure. This results in a higher degree of coupling.

3. DESIGN OF CSRR-BASED 3 DB DIRECTIONAL COUPLER

The structure of CSRR-based directional coupler is showed in Fig. 5. The parameter of substrate is $\varepsilon_r = 2.65$, $h = 1.5$ mm. The characteristic impedance at the ports is set to $Z_0 = 50\,\Omega$. The results obtained by full-wave simulation and measurement are showed in Fig. 6. The performances of the 3-dB coupler are the following: 3.7 ± 0.5 dB backward coupling, return loss smaller than -18 dB and isolation better than 25 dB over the 1.7 to 2.5 GHz range (38.1% fractional bandwidth).

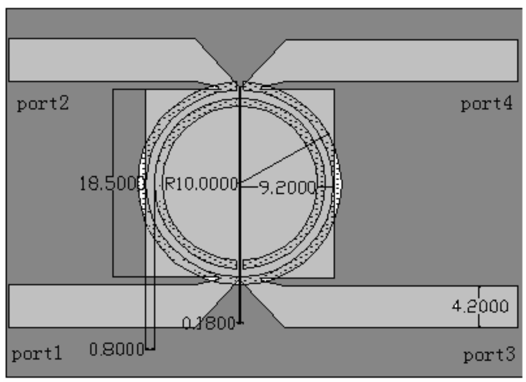

Figure 5: Structure of CSRR-based directional coupler.

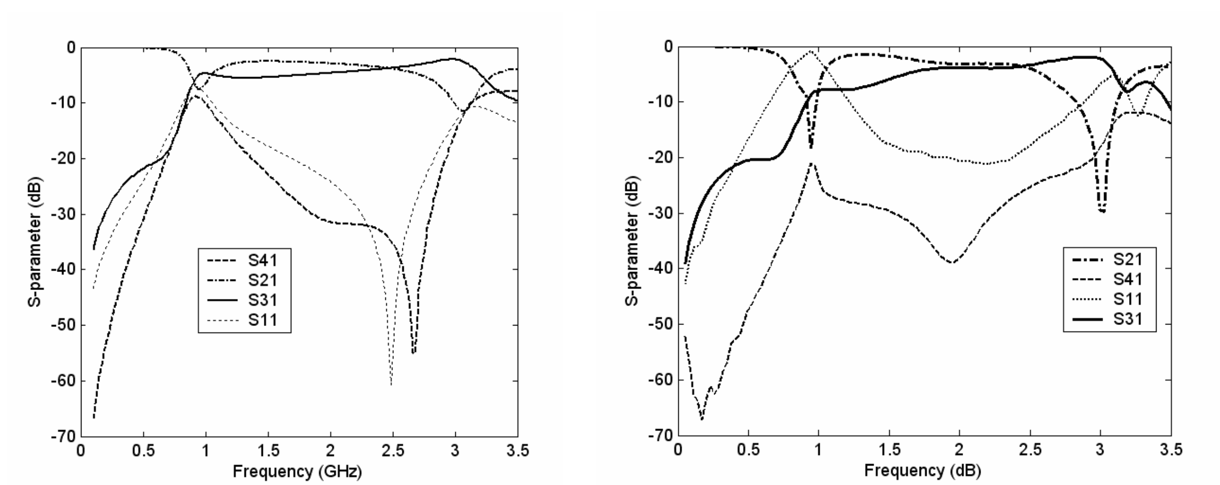

(a) (b)

Figure 6: (a) Magnitude of the S-parameters for the coupler of Fig. 4 obtained bysimulation (Ansoft-Design) (b) Magnitude of the S-parameters for the coupler of Fig. 4 obtained by measurement.

ACKNOWLEDGMENT

This work was supported by the National Natural Science Foundation of China under Grant No. (60501018, 60271027), and the National Basic Research Program of China under Grant No. 2004CB719800.

REFERENCES

1. Mongia, R., I. Bahl, and P. Bhartia, *RF and Microwave Coupler-line Circuits*, Artech House, Norwood, MA, 1999.
2. Lange, J., "Interdigital stipline quadrature hybrid," *IEEE Trans. Microwave Theory and Tech.*, Vol. MTT-26, 1150–1151, 1969.
3. Caloz, C. and T. Itoh, "A novel mixed conventional microstrip and composite right/left-handed backward-wave directional coupler with broadband and tight coupling characteristics," *IEEE Micro. Wireless Comp. Lett.*, Vol. 14, No. 1, 31–33, 2004.
4. Caloz, C., A. Sanada, and T. Itoh, "A novel composite right/left-handed coupled-line directional coupler with arbitrary coupling level and broad bandwidth," *IEEE Trans. Microw. Theory and Tech.*, Vol. 52, 980–992, 2004.
5. Pendry, J. B., A. J. Holden, D. J. Robbins, and W. J. Stewart, "Magnetism from conductors and enhanced nonlinear phenomena," *IEEE Trans. Microw. Theory Tech.*, Vol. 47, No. 11, 2075–2084, 1999.
6. Falcone, F., T. Lopetegi, J. D. Baena, R. Marques, F. Martin, and M. Sorolla, "Effective negative-ε stop-band microstrip lines based on complementary split ring resonators," *IEEE Microw. Wireless Compon. Lett.*, Vol. 14, No. 6, 280–282, 2004.
7. Bonache, J., I. Gil, J. Garcia-Garcia, et al., "Novel Microstrip Bandpass filters based on Complementary Split-Ring resonators," *IEEE Trans. Microw. Theory Tech.*, Vol. 54, No. 1, 265–271, 2006.
8. Bonache, J., I. Gil, J. Garcia-Garcia, et al., "Complementary split ring resonators for microstrip diplexer design," *ELECTRONICS LETTERS*, Vol. 41, No. 14, 2005.

Equations for the Interaction between Deformation and Electromagnetic Field

Jianhua Xiao

Henan Polytechnic University, Jiaozuo 454000, Henan, China

Abstract— The Minskowski form of electromagnetic field equations for constant moving non-deformable medium are extended to the electromagnetic field equations for deformable medium with arbitrary moving speed. Firstly, after introducing the mechanics equations for finite deformation, the electromagnetic-dependent deformation are established in non-relativity range. Then, by putting these equations into the electromagnetic field equations for moving medium, the deformation-electromagnetic field equations are established. Finally, through combining these equations with the mechanical deformation equations, the complete dynamic equations for the interaction between deformation and electromagnetic field are obtained. The results can be used to solve three typical engineering problems: (1) calculating the medium dynamic deformation for the known electromagnetic field in the laboratory reference frame; (2) calculating the electromagnetic field in the laboratory reference for the known moving velocity and deformation of media; (3) calculating the interaction between the deformable moving medium and the electromagnetic field when both of deformation and electromagnetic field are un-known.

1. INTRODUCTION

Along with the wide application of electromagnetic media in space-air devices, the vibration of media becomes a problem not only in the sense that it causes signal transmission noise problem but also in the sense that the serious interaction between the moving media deformation and the electromagnetic field may damage the functions of the devices. So, the electromagnetic field in moving deformable media still is a problem which has essential importance for theoretic research. Based on theoretical consideration, moving deformable media problem has been addressed already by many researchers [1]. Differencing from the available research, this research seeks a resolution which is suitable for engineering calculation while maintaining the theoretic strictness.

From engineering consideration, there are three typical problems: (1) calculating the media deformation in laboratory reference for the known electromagnetic field in laboratory reference frame; (2) calculating the electromagnetic field in laboratory reference for the known moving velocity and deformation of media; (3) calculating the interaction between the deformable moving media and the electromagnetic field when both of deformation and electromagnetic field are un-known.

For moving media, the electromagnetic field cannot be obtained from classical Maxwell equations directly. For the non-relativity case, for the non-deformable constant-speed moving media, the Minkowski transformation establishes the relation between the electromagnetic field in the laboratory reference and the electromagnetic field in co-moving reference. In principle, the interaction between moving media and the electromagnetic field can be established on such a base. However, once the media is deformable, the related problems must be re-examined [2].

For the deformation caused by electromagnetic field, the method proposed by G. H. Livens [3] is that firstly calculating the body force produced by the electromagnetic and then put the force into the mechanics equation of deformation to calculate the deformation. Under this sense, the view-point of this method is focused on the electromagnetic-dependent deformation. The reaction of deformation to electromagnetic field is ignored by this method. Hence, it is an approximation.

To overcome the shortage of this method, D. J. Kortoweg and H. von. Holmholtz [4] suggest the parameters of constitutive equations in electromagnetic fields are deformation-dependent. Then, the effects of deformation on electromagnetic field are calculated. Under this sense, the view-point of this method is focused on the deformation-dependent electromagnetic field. The reaction of electromagnetic field to deformation is ignored by this method. Therefore, it is also an approximation. Although both methods are difficult to calculating the interaction between media and electromagnetic field, they are good for engineering calculation when the deformation is very small. For large deformation or large rotation case, the interaction is strong. To get a suitable calculation method, R. A. Toupin [5] introduces the mechanics of finite deformation to retreat the related interaction problem. However, his treatment is too complicated in mathematics which is a shortage for engineering calculation.

As in practical engineering problems, when the medium is static in laboratory reference, the related electromagnetic field and deformation is well known or can be well examined. The essential question is that once the medium is applied in space-air devices what behavior can be inferred from ground observations. Therefore, this research takes the advantage of this fact to develop the related equations for the interaction between moving deformable medium and electromagnetic field. Such a formulation is expected to be easy for engineering calculation. The fast development of computation technology may make this kind of calculation very prospective.

2. EQUATIONS FOR ELECTROMAGNETIC-DEPENDENT DEFORMATION FIELD

For the purpose of this paper, the deformation is viewed as a point-set transformation. That is to say the deformation is described by a commoving dragging coordinator system. Under this selection, the configuration of static medium without deformation is taken as initial reference configuration.

Under above two definitions, the material element of medium is identified by its Lagranian coordinator $(x^1,\ x^2,\ x^3)$. For simplicity, the standard rectangular coordinator system is defined on the initial configuration. By this definition, the deformation gradient is defined on Lagranian coordinator. The deformation is described by the changes of gauge vectors that are measured in laboratory standard rectangular system. As the electromagnetic reference field is defined on the initial configuration, the field is also identified by the Lagranian coordinators. Therefore, the material invariant principle is maintained [6, 7].

For large deformation, the current gauge vectors $\vec{g}_i$ and the initial gauge vectors $\vec{g}_i^0$ are related by the deformation gradient tensor F_j^i:

$$\vec{g}_i = F_i^j \vec{g}_j^0 \tag{1}$$

where,

$$F_i^j = \frac{\partial U^j}{\partial x^i} + \delta_i^j \tag{2}$$

Here, U^j is the displacement field measured in laboratory standard rectangular coordinator system, δ_i^j is Kronecker delta. For details please refer [2].

The stress tensor is defined with the help of material constant tensor C_{jk}^{il} as:

$$\sigma_j^i = C_{jk}^{il}\left(F_l^k - \delta_l^k\right) \tag{3}$$

Note that the stress may be not symmetric. Generally speaking, the symmetry requirement is not true for large deformation as the medium may appear intrinsic local rotation. The related research shows that, when there is no body force, the motion Equations [2, 8] are:

$$\begin{aligned} &\frac{\partial \sigma_l^i}{\partial x^l} = \frac{\partial}{\partial t}\left(\rho \frac{\partial U^i}{\partial t}\right) \\ &\frac{\partial \sigma_j^i}{\partial x^i} = \frac{\partial}{\partial t}\left(\rho \frac{\partial U^i}{\partial t} F_j^i\right) \\ &e_{ijk} F_l^j \sigma_k^l = 0 \end{aligned} \tag{4}$$

Where, e_{ijk} is a skew tensor; ρ is mass density. They form the basic equations for the mechanical deformation. The first equation is identical with traditional form; the other two are related with angular momentum conservation. Especially, when the deformation is very small that $F_j^i \approx \delta_j^i$, the Equation (4) returns to the classical symmetric stress case where only the first one equation is needed. Its difference from the deformation mechanics equation given in paper [1] is in that here only the angular momentum related with deformation is included into the motion equations. Chen's research shows that Euler rotation is included in the transformation F_j^i as in fact for small rotation $F_j^i = S_j^i + R_j^i$ where the symmetric tensor S_j^i represents stretching and the orthogonal rotation tensor R_j^i represents the local relative rotation. Therefore, the second equation, in fact, should be called Euler equation.

For the media with electromagnetic field, the Maxwell-Lorentz body force f^i should be introduced:

$$f^i = \sigma E^i + e_{jk}^i J^l B^k \tag{5}$$

where, $e^i_{jk} \equiv e_{ijk}$ as the laboratory coordinator system is rectangular system; σ, E^i, B^i, J^i are current charge density and field measured in the laboratory coordinator system. The equation shows that Maxwell-Lorentz body force has the same position as inertia force. In this case, the Equation (4) becomes:

$$\begin{aligned}
&\frac{\partial \sigma^i_j}{\partial x^l} = f^i + \frac{\partial}{\partial t}\left(\rho \frac{\partial U^i}{\partial t}\right) \\
&\frac{\partial \sigma^i_j}{\partial x^i} = f^i F^i_j + \frac{\partial}{\partial t}\left(\rho \frac{\partial U^i}{\partial t} F^i_j\right) \\
&e_{ijk} F^j_l \sigma^l_k = 0
\end{aligned} \tag{6}$$

They form the equations for electromagnetic-dependent deformation field.

3. EQUATIONS FOR DEFORMATION-DEPENDENT ELECTROMAGNETIC FIELD

As the mechanic field and electromagnetic field are identified with Lagranian coordinators for meeting the requirement of material indifference principle, the related surface integration and closed-line integration should be taken on the invariant material. To this target, the Gauss-Faraday equation, Faraday equation, Gauss-Coulomb equation, and Ampere-Maxwell equation be expressed as:

$$\begin{aligned}
&\oint_S \left(B^i \vec{g}^0_j\right) \cdot \left(\mathrm{d}a_j \vec{g}^j\right) = 0 \\
&\oint_C \left(E^i \vec{g}^0_i\right) \cdot \left(\mathrm{d}x^j \vec{g}_j\right) = -\frac{\partial}{\partial t}\int_S \left(B^i \vec{g}^0_i\right) \cdot \left(\mathrm{d}a_j \vec{g}^j\right) \\
&\oint_S \left(D^i \vec{g}^0_i\right) \cdot \left(\mathrm{d}a_j \vec{g}^j\right) = \int_V \sigma \sqrt{g}\mathrm{d}v \\
&\oint_C \left(H^i \vec{g}^0_i\right) \cdot \left(\mathrm{d}x^j \vec{g}_j\right) = \frac{\partial}{\partial t}\int_S \left(D^i \vec{g}^0_i\right) \cdot \left(\mathrm{d}a_j \vec{g}^j\right) + \int_S \left(J^i \vec{g}^0_i\right) \cdot \left(\mathrm{d}a_j \vec{g}^j\right)
\end{aligned} \tag{7}$$

where, $\vec{g}^j$ is determined by equation $\vec{g}_i = g_{ij}\vec{g}^j$; $g_{ij} = F^l_i F^l_j$; $\mathrm{d}a_i = e_{ijk}\mathrm{d}x^j \mathrm{d}x^k$; $\mathrm{d}v = \mathrm{d}x^1\mathrm{d}x^2\mathrm{d}x^3$; $g = \det|g_{ij}|$. It is easy to verify that [2, 8]:

$$\vec{g}^{0i} = F^i_j \vec{g}^j, \ \vec{g}^i = G^i_j \vec{g}^{0j} \tag{8}$$

$$\frac{\partial \vec{g} i}{\partial t} = V^l \frac{\partial F^i_l}{\partial t}\vec{g}_i \tag{9}$$

where, $G^i_l F^l_j = \delta^i_j$; $V^i = \dfrac{\partial U^i}{\partial t}$ is the inertia velocity of material element.

Therefore, the Equations (7) can be converted into differential equations:

$$\begin{aligned}
\frac{\partial\left(B^i G^j_i\right)}{\partial x^j} &= 0 \\
e_{ijk}\frac{\partial\left(E^l F^j_l\right)}{\partial x^k} &= -F^i_l \frac{\partial B^l}{\partial t} - e_{ijk} B^j V^l \frac{\partial F^k_l}{\partial t} \\
\frac{\partial\left(D^i G^j_i\right)}{\partial x^j} &= \sigma\sqrt{g} \\
e_{ijk}\frac{\partial\left(H^l F^j_l\right)}{\partial x^k} &= F^i_l \frac{\partial D^l}{\partial t} + e_{ijk} D^l V^j \frac{\partial F^k_l}{\partial t} + J^l F^i_l
\end{aligned} \tag{10}$$

These equations modify the Maxwell-Minkowski electrodynamics equations [1], where only the inertia velocity effects are concluded while the deformation effects are, in essential sense, ignored.

The charge conservation gives out:

$$\frac{\partial J^i}{\partial x^i} + \frac{\partial \sigma}{\partial t} + \frac{\partial}{\partial x^i}\left(\sigma \frac{\partial U^i}{\partial t}\right) = 0 \tag{11}$$

The Equations (10) and (11) form the equations for deformation-dependent electromagnetic field.

4. FINAL RESULT: EQUATIONS FOR THE INTERACTION BETWEEN DEFORMATION AND ELECTROMAGNETIC FIELD

Combining the equations for electromagnetic-dependent deformation field and the equations for deformation-dependent electromagnetic field, the equations for the interaction between deformation and electromagnetic field are established.

The results can be used to solve three typical engineering problems: (1) calculating the media dynamic deformation for the known electromagnetic field in laboratory reference frame; (2) calculating the electromagnetic field in laboratory reference for the known moving velocity and deformation of media; (3) calculating the interaction between the deformable moving media and the electromagnetic field when both of deformation and electromagnetic field are un-known.

REFERENCES

1. Pao, Y.-H., *Electromagnetic Force in Deformable Continuum*, Science Press, Beijing, 1996. (Its original version is in the *Modern Mechanics*, Vol. 4, 1995)
2. Chen, Z., *Rational Mechanics (Proc. Modern Chinese Science, Mechanics Sires)*, Chongqin Press, Chongqin, 2000. (Original version: *Rational Mechanics*, China University of Mining & Technology Press, Xizuo, 1987)
3. Landau, L. D. and E. M. Lifshitz, *Electrodynamics of Continuum Media*, Mass: Addison-Wesley, 1960.
4. Penfield Jr., P. and H. A. Haus, *Electrodynamics of Moving Media*, Mass: M.I.T. Press, 1967.
5. Toupin, R. A., "Elastic dielectric," *J. R. Mech.* & *Anal.*, Vol. 5, 849–916, 1956.
6. Lodge, A. S., *Body Tensor Fields in Continuum Mechanics*, Academic Press, New York, 1974.
7. Erickson, J. L. and R. S. Rivlin, "Large elastic deformations of homogeneous anisotropic materials," *J. R. Mech. Anal.*, Vol. 3, 281–301, 1954.
8. Xiao, J., *Evolution of Continuum from Elastic Deformation to Flow*, E-print, arXiv: physics/0511170, 1–25, 2005.

A Novel Analysis for Circular-groove Guide

Yinqin Cheng
Northwest University for Nationalities, China

Abstract— Using method of moment, the circular-groove guide has been studied. The characteristic equation of circular-groove guide has been gotten with this method. The transmission characteristics of the dominant mode have been obtained and discussed.

1. INTRODUCTION

The method of moment (MOM) [1] is one of the classical numerical computation methods for electromagnetic field. It has been widely applied to analyze the electromagnetic radiation and scattering. As one of the millimeter waves transmission lines, the transmission characteristic of circular-groove guide has been studied in previous papers [2–4]. In this paper, it's the first time that eigenvalue equation of the circular-groove guide is obtained by using the method of moment and its cut-off characteristic is gotten and discussed.

2. THEORY ANALYSIS

The cross section of open circular-groove guide and its geometrical dimensions are shown in Fig. 1. Whole guide can be divided into three parts, central groove region I and two parallel plane regions II. According to the geometrical shape, rectangular coordinates in regions II and cylindrical coordinates in region I are adopted. They are of the same z direction. Suppose electromagnetic wave transmits along the z direction, the transverse wave function $\psi_i(x, y)$ satisfies two-dimensional Helmholtz equation in the cross section of groove guide as follows:

$$\nabla_{\mathrm{T}}^2 \psi_i(x, y) + k_{\mathrm{c}}^2 \psi_i(x, y) = 0 \quad (i = 1, 2). \tag{1}$$

where ∇_{T}^2 is transverse Laplacian operator. Wave function $\psi_i(x, y)$ is E_Z for TM modes or H_Z for TE modes. $k_{\mathrm{c}}^2 = k^2 - \beta^2$, here k_{c} is called longitude cut-off wavenumber of waveguide, k is wavenumber in the free space and β is phase-shift constant. Where $i = 1$ and $i = 2$ represents central groove region I and parallel plane regions II respectively.

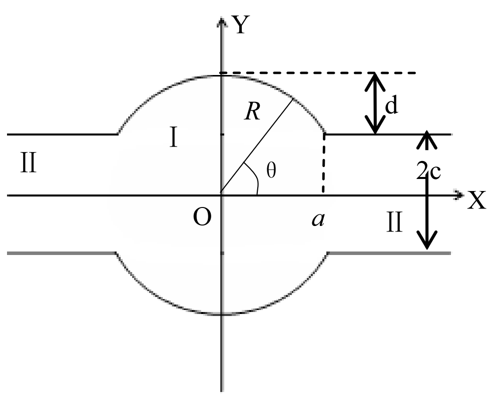

Figure 1: The cross-section of circular-groove guide.

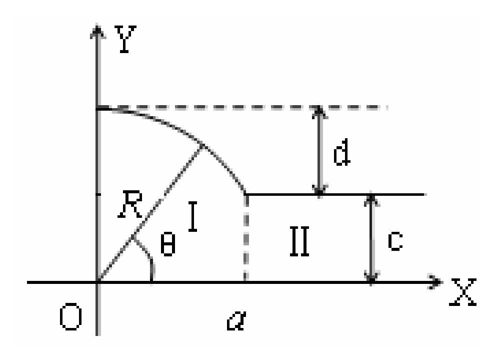

Figure 2: 1/4 analytic model of circular-groove guide.

On the boundary of the cross-section of the waveguide, Equation (1) satisfies Dirichlet boundary condition for the TM modes or the Neumann boundary condition for the TE modes as follows:

$$\begin{cases} \psi = 0 \\ \dfrac{\partial \psi}{\partial n} = 0 \end{cases} \tag{2}$$

Considering symmetry of electromagnetic field structures and simplifying calculation complexity, 1/4 analytic model shown in Fig. 2 is adopted in this paper. According to the electromagnetic structures, for the main mode TE_{11}, planes at $x = 0$ and $y = 0$ can be respectively regarded as electric wall and magnetic wall.

Let $L = -\nabla_{\mathrm{T}}^2 = -\frac{\partial^2}{\partial x^2} - \frac{\partial^2}{\partial y^2}$, $\xi = k_{\mathrm{c}}^2$, Equation (1) can be written as:

$$L\psi_i = \xi\psi_i \tag{3}$$

The above problem is just the eigenvalue problem of the MOM. Base functions $\{f_n(x, y)\}$, $\{g_n(x, y)\}$ and corresponding weight functions $w_m(x, y)$, $v_m(x, y)$ are chosen in region I and regions II respectively. And then the transverse wave function $\psi_i(x, y)$ can be expanded as follows:

$$\psi_1(x, y) = \sum_{n=1}^{N} a_n f_n(x, y) \tag{4}$$

$$\psi_2(x, y) = \sum_{n=1}^{N} b_n g_n(x, y) \tag{5}$$

According to Galerkin method described in the MOM, the matrix eigenvalue equation of circle-groove for region I and regions II can be obtained, i.e.,

$$[\mathrm{L}_{mn}][\mathrm{a}_n] = \xi[\mathrm{M}_{mn}][\mathrm{a}_n] \tag{6}$$

$$[\mathrm{P}_{mn}][\mathrm{b}_n] = \xi[\mathrm{Q}_{mn}][\mathrm{b}_n]. \tag{7}$$

where,

$$[\mathrm{L}_{mn}] = \begin{bmatrix} < w_1, Lf_1 > & < w_1, Lf_2 > & \dots & < w_1, Lf_n > \\ < w_2, Lf_1 > & < w_2, Lf_2 > & \dots & < w_2, Lf_n > \\ \dots\dots\dots & \dots\dots\dots & \dots\dots\dots & \dots\dots \end{bmatrix},$$

$$[\mathrm{M}_{mn}] = \begin{bmatrix} < w_1, f_1 > & < w_1, f_2 > & \dots & < w_1, f_n > \\ < w_2, f_1 > & < w_2, f_2 > & \dots & < w_2, f_n > \\ \dots\dots\dots & \dots\dots\dots & \dots\dots\dots & \dots\dots \end{bmatrix}$$

$$[\mathrm{P}_{mn}] = \begin{bmatrix} < v_1, Lg_1 > & < v_1, Lg_2 > & \dots & < v_1, Lg_n > \\ < v_2, Lg_1 > & < v_2, Lg_2 > & \dots & < v_2, Lg_n > \\ \dots\dots\dots & \dots\dots\dots & \dots\dots\dots & \dots\dots \end{bmatrix},$$

$$[\mathrm{Q}_{mn}] = \begin{bmatrix} < v_1, g_1 > & < v_1, g_2 > & \dots & < v_1, g_n > \\ < v_2, g_1 > & < v_2, g_2 > & \dots & < v_2, g_n > \\ \dots\dots\dots & \dots\dots\dots & \dots\dots\dots & \dots\dots \end{bmatrix}$$

$$[\mathrm{a}_n] = [a_1\, a_2\, \dots\, a_n]^{\mathrm{t}}$$

$$[\mathrm{b}_n] = [b_1\, b_2\, \dots\, b_n]^{\mathrm{t}}.$$

According to the matching condition of two regions on the plane $x = a$, i.e.,

$$\begin{cases} \psi_1 = \psi_2 \text{ for } |\mathrm{y}| \le c \\ \dfrac{\partial\psi_1}{\partial x} = \dfrac{\partial\psi_2}{\partial x} \text{ for } |\mathrm{y}| \le c \end{cases} \tag{8}$$

following equation can be got.

$$\sum_{n=1}^{N} a_n f_n(a, y_i) = \sum_{n=1}^{N} b_n g_n(a, y_i) \tag{9}$$

Here,

$$y_i = \frac{ic}{N+1} \in [0, c],\ i = 1, 2, \dots, N.$$

The matrix equation corresponding to (9) is

$$[\mathrm{C}_{mn}][\mathrm{a}_n] = [\mathrm{D}_{mn}][\mathrm{b}_n]. \tag{10}$$

where,

$$[\mathrm{C}_{mn}] = \begin{bmatrix} f_1(a,y_1) & f_2(a,y_1) & \dots & f_N(a,y_1) \\ f_1(a,y_2) & f_2(a,y_2) & \dots & f_N(a,y_2) \\ \dots & \dots & \dots & \dots \\ f_1(a,y_N) & f_2(a,y_N) & \dots & f_N(a,y_N) \end{bmatrix},$$

$$[\mathrm{D}_{mn}] = \begin{bmatrix} g_1(a,y_1) & g_2(a,y_1) & \dots & g_N(a,y_1) \\ g_1(a,y_2) & g_2(a,y_2) & \dots & g_N(a,y_2) \\ \dots & \dots & \dots & \dots \\ g_1(a,y_N) & g_2(a,y_N) & \dots & g_N(a,y_N) \end{bmatrix}$$

Based on (10), relationship of $[\mathrm{b}_n]$ and $[\mathrm{a}_n]$ can be obtained, i.e.,

$$[\mathrm{b}_n] = [\mathrm{D}_{mn}]^{-1}[\mathrm{C}_{mn}][\mathrm{a}_n] = \mathrm{K}_{mn}[\mathrm{a}_n]$$

Plus (6) and (7), the following equation can be obtained

$$[\mathrm{A}_{mn}][\mathrm{a}_n] = \xi[\mathrm{B}_{mn}][\mathrm{a}_n] \tag{11}$$

where,

$$[\mathrm{A}_{mn}] = [\mathrm{L}_{mn}] + [\mathrm{P}_{mn}]\mathrm{K}_{mn}, \quad [\mathrm{B}_{mn}] = [\mathrm{M}_{mn}] + [\mathrm{Q}_{mn}]\mathrm{K}_{mn}$$

Equation (11) is exactly eigenvalue equation of the circular-groove guide. So the cut-off wavenumber k_c can be got by solving it's eigenvalue $\xi = k_c^2$. After the characteristic vectors $[\mathrm{a}_n]$ and $[\mathrm{b}_n]$, namely expansion coefficients $\{a_n\}$ and $\{b_n\}$, are solved from the above equations, the wave function $\psi_i(x,y)$, i.e., the approximate solutions of electromagnetic field in the groove region and parallel plane regions, will be determined.

3. NUMERICAL RESULTS AND DISCUSSIONS

Power function is used as the base function in central groove region I and exponential function, which attenuates along x direction, is used as the base function in parallel plane regions II. They satisfy the electromagnetic boundary condition. Based on the above theory analysis, the cut-off characteristic curves for main mode TE_{11} of circular-groove guide can be gotten and shown in Fig. 3–Fig. 5.

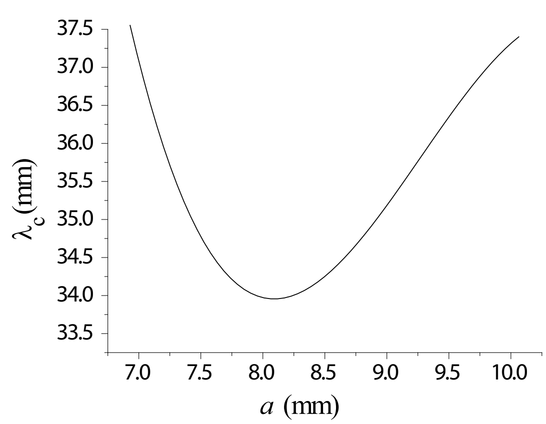

Figure 3: The cut-off characteristic of circular-groove guide with a.

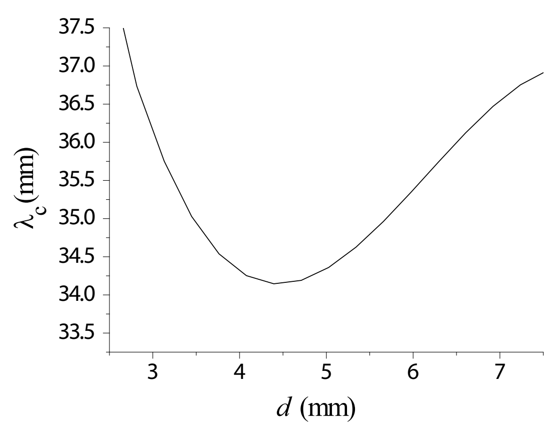

Figure 4: The cut-off characteristic of circular-groove guide with d.

It can be seen from Fig. 3–Fig. 5 that cut-off property of circular-groove guide is better than that of circular guide.

Moreover, the varying tendency of cut-off wavelength of circular-groove guide with groove width a, groove depth d and plane width c is nonlinear. This is in agreement with before.

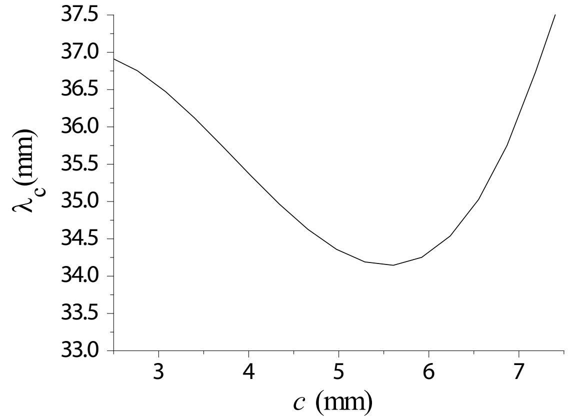

Figure 5: The cut-off characteristic of circular-groove guide with c.

4. CONCLUSION

Using the method of moment, the eigenvalue equation of circular-groove guide is obtained. And the transmission characteristics of the main mode is gotten and discussed. The numerical results concluded in this paper are in agreement with before. So the efficiency of this method is verified. To make the analysis simple, 1/4 analytical model is adopted. The obtained results are of important application values in analyzing and computing the groove guides performances in practical engineering problems.

REFERENCES

1. Harrington, R. F., translated by Wang Erjie, *Field Computation by Moment Methods*, 144–191, National Defence Industry Press, Beijing, 1981.
2. Yang, H., J. Ma, and Z. Lu, "The characteristic eauation and solution of circular-groove guide," *International Journal of Infrared and Millimeter Waves*, Vol. 12, No. 5, 535–541, 1991.
3. Xu, Z., H. Yang, and Z. Lu, "The novel boundary integral equation method for solving arbitrary cross-section waveguides," *International Journal of Infrared and Millimeter Waves*, Vol. 16, No. 7, 1239–1247, 1995.
4. Yan, H. and H. Yang, "A new circular groove guide analysis," *International Journal of Infrared and Millimeter Waves*, Vol. 20, No. 1, 149–154, 1999.

Approximate ML Detection Based on MMSE for MIMO Systems

Fan Wang[1], **Yong Xiong**[2], **and Xiumei Yang**[2]

[1]The Electromagnetics Academy at Zhejiang University, Zhejiang University, China
[2]Shanghai Research Center for Wireless Communications, China

Abstract— We derive two types of approximate maximum likelihood (ML) detection based on minimum mean squared error (MMSE), MMSE-CML (conditional ML) detection and MMSE-CLML (conditional local ML) detection, for MIMO communication system. A simple reliability judge rule to judge the estimate of the transmit symbols is also given. For the proposed MMSE-CML detection, received signals are first sent into MMSE detector to do linear equalization, then the estimate of transmit signals is judged in reliability judge module; If the estimate is judged to be reliable, we take the estimate as the final result; if not, the received signals are then sent into conditional ML (CML) detector to get the final result; Unlike conventional ML detector, the CML detector performs a tree search till the estimate satisfies the reliability judge rule or an entire tree search has been done. For the proposed MMSE-CLML detection, we use CLML search instead of CML search in MMSE-CML, which searches in the neighborhood of the output provided by the MMSE detector. Simulation results show that the MMSE-CML detector achieves near the same performance as optimal CML detector at reduced complexity, and MMSE-CLML detector achieves suboptimal performance at remarkably reduced complexity.

1. INTRODUCTION

Multiple input multiple output (MIMO) systems have attracted much attention because of high spectrum efficiency [1, 2]. Many different detection techniques are developed to get the diversity gain introduced by MIMO techniques. The ML detector is able to provide optimal performance, but has a disadvantage of extremely high computational complexity.

Linear detectors for BLAST systems are ZF detector and minimum mean square error (MMSE) detector, which are low in complexity and poor in performance. Ordered successive interference cancellation (OSIC) detector, proposed in [3–5], which detects the transmit symbols one by one according to the post-detection SNR and does successive interference cancellation, can achieve better performance at relatively high complexity. However, there is still a big performance gap between these detectors and ML detector.

Various advanced techniques have been studied to approach the performance of the ML detector, such as sphere decoding (SD) [6], m-algorithm [7] and probabilistic data association (PDA) [8]. These techniques can approach the ML performance with higher complexity than linear detectors.

There are some works on combining linear detectors and ML detector [9, 10], to achieve a tradeoff between the BER performance and computational complexity. In their works, a local ML (LML) search is performed in the neighborhood of the output of zero-forcing (ZF)/MMSE detector. In this contribution we develop a novel reliability judge rule (RJR) to judge whether the output of MMSE detector and the symbol vector of the tree search are true or not. With this RJR, we can estimate part of transmit symbols using MMSE detection or conditional ML search instead of ML detection with negligible performance loss, resulting in a reduced complexity. We also propose a MMSE-CLML method using a CLML search instead of ML search, which possesses the advantage of having further reduced complexity with some performance loss to the ML detector.

The rest of the paper is organized as follows. In Section 2, we give the system model. The reliability judge rule (RJR) is presented in Section 3. Two types of MMSE-based approximate ML detectors are proposed in Section 4. In Section 5 we present some simulation results, and finally conclude the paper in Section 6.

2. SYSTEM MODEL

Consider a MIMO system with N_t transmit antennas and N_r receive antennas ($N_r \geq N_t$). The transmit vector can be denoted as $\mathbf{s} = [s_1, \cdots, s_{N_t}]^T$, where the superscript T stands for the transpose, s_i is the complex signal transmitted by antenna i, with a modulation type as BPSK, QPSK, 16QAM, etc., and the constellation of modulation type is denoted by $\boldsymbol{\Delta}$ with a size of M_c. And $\mathbf{y} = [y_1, \cdots, y_{N_r}]^T$ denotes the received vector, $\mathbf{y} = [y_1, \cdots, y_{N_r}]^T$, where y_i is the received signal of antenna i. We have:

$$\mathbf{y} = \mathbf{H}\mathbf{s} + \mathbf{n} \tag{1}$$

where $\mathbf{H}$ is the channel matrix of dimension $N_r \times N_t$ with the element h_{ij} representing the channel between transmit antenna j and receive antenna i, and $\mathbf{n}$ is a $N_r \times 1$ noise vector with each entry is a complex Gaussian noise with zero mean and a variance of σ^2.

3. RELIABILITY JUDGE RULE (RJR)

The aim of using RJR is to judge whether the estimate of transmit symbols is reliable or not.

Denoting the estimate of transmit symbols r as $\tilde{\mathbf{s}}$, we consider the following value:

$$\alpha = \left\|\mathbf{y} - \mathbf{H}\tilde{\mathbf{s}}\right\|^2 / \sigma^2 \tag{2}$$

If $\tilde{\mathbf{s}}$ is the right estimate of transmit symbols, then α has a chi square distribution with N_r degrees of freedom and N_r mean. The PDF of α is given by:

$$f_{\chi^2(N_r)}(x) = \begin{cases} \dfrac{1}{2^{\frac{N_r}{2}}\Gamma\left(N_r/2\right)} e^{-\frac{x}{2}} x^{\frac{N_r}{2}-1}, & x > 0 \\ 0, & x \le 0 \end{cases} \tag{3}$$

If $\tilde{\mathbf{s}}$ is the wrong estimate of transmit symbols, then α has a noncentral chi square distribution with N_r degrees of freedom, noncentral parameter of γ, and $N_t + \gamma$ mean, where

$$\gamma = \left\|\mathbf{H}(\tilde{\mathbf{s}} - \mathbf{s})\right\|^2 / \sigma^2 \tag{4}$$

And the PDF of $\alpha$is given by:

$$f_{\chi^2(N_r,\gamma)}(x) = \begin{cases} \sum\limits_{k=0}^{\infty} \dfrac{\left(\frac{\gamma}{2}\right)^k}{k!\Gamma\left(\frac{N_r}{2}+k\right)} \dfrac{x^{\frac{N_r}{2}+k-1}}{2^{\frac{N_r}{2}+k}} e^{-\frac{\gamma+x}{2}}, & x > 0 \\ 0, & x \le 0 \end{cases} \tag{5}$$

Now we can present an ideal RJR, which can be denoted as

$$f_{\chi^2(N_t)}(\alpha) > \max(f_{\chi^2(N_r,\gamma)}(\alpha)) \tag{6}$$

If the probability density of chi square distribution is higher than that of all noncentral chi square distributions, we judge that the estimated symbols are reliable; If not, we judge that the detector should do further detection to get the final result.

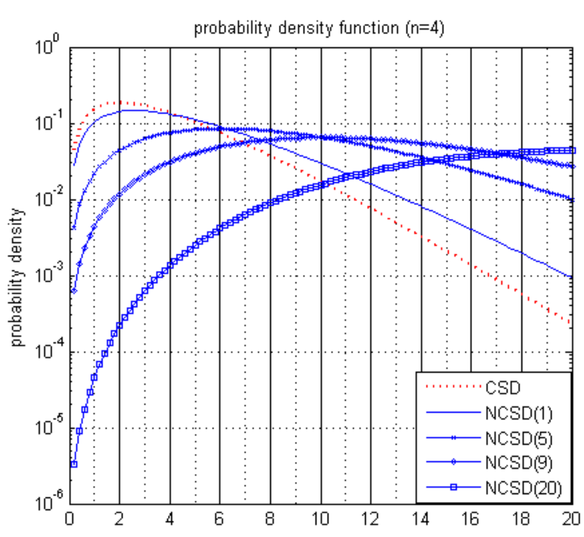

Figure 1: PDF of chi square distribution and noncentral chi square distribution with $N_r = 4$ degrees of freedom.

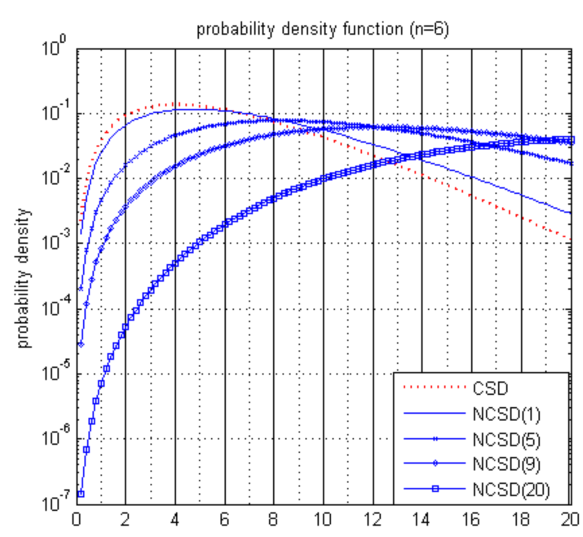

Figure 2: PDF of chi square distribution and noncentral chi square distribution with $N_r = 6$ degrees of freedom.

Figure 1 and Fig. 2 are the PDF curves of chi square distribution (CSD) and noncentral chi square distributions (NCSD) with different γ. Denote the abscissa of intersection point of $f_{\chi^2(N_r)}(x)$ and $f_{\chi^2(N_r,\gamma)}(x)$ as $\bar{x}(N_r,\gamma)$, we have:

$$\begin{cases} f_{\chi^2(N_r)}(x) \geq f_{\chi^2(N_r,\gamma)}(x) & 0 < x \leq \bar{x}(N_r,\gamma) \\ f_{\chi^2(N_r)}(x) < f_{\chi^2(N_r,\gamma)}(x) & x > \bar{x}(N_r,\gamma) \end{cases} \tag{7}$$

And if N_r is fixed, we have

$$\bar{x}(N_r,\gamma_1) > \bar{x}(N_r,\gamma_2) \quad \text{if } \gamma_1 > \gamma_2 \tag{8}$$

Combining (4), (6), (7), (8), we can get the ideal RJR as:

$$\alpha < \bar{x}(N_r, \min(\gamma)) \tag{9}$$

Now we can conclude ideal RJR as

1) Compute all the values of γ using (4), and get $\min(\gamma)$.
2) Compute $\bar{x}(N_r,\min(\gamma))$ subject to $f_{\chi^2(N_r)}(x) = f_{\chi^2(N_r,\min(\gamma))}(x)$
3) Compute α using (2). If $\alpha < \bar{x}(N_r,\min(\gamma))$, output the estimate of transmit symbols as the final result; if not, do further detection to get the final result.

As we can see, the progress of computing $\min(\gamma)$ is very complex. To get all the values of γ needs to consider all possible transmit symbols, with the same complexity as ML decoding. When the channel is slow fading, the ideal RJR is feasible because we only need to compute $\min(\gamma)$ for several consecutive symbol periods. But when the channel is fast fading, the ideal RJR is complexity prohibitive.

From Fig. 1 and Fig. 2, we can find that

$$\forall_\gamma > 0, \quad N_r \leq \bar{x}\left(N_r,\gamma\right) \tag{10}$$

Combing (2), (9), (10), we can get a simplified RJR as follows.

$$\|\mathbf{y} - \mathbf{H}\tilde{\mathbf{s}}\|^2 / \sigma^2 < N_r \tag{11}$$

Since σ^2 is known at the receiver, we can rewrite the simplified RJR as follows.

$$\|\mathbf{y} - \mathbf{H}\tilde{\mathbf{s}}\|^2 < N_r\sigma^2 \tag{12}$$

As we can see, the computation cost of simplified RJR will be very low.

4. MMSE-CML AND MMSE-CLML

4.1. MMSE-ML

An MMSE-based conditional ML detector with reliability judge rule (RJR) is proposed for MIMO BLAST systems. The structure of MMSE-CML detector is illustrated in Fig. 3. The decoding procedure of MMSE-CML can be divided into 3 steps:

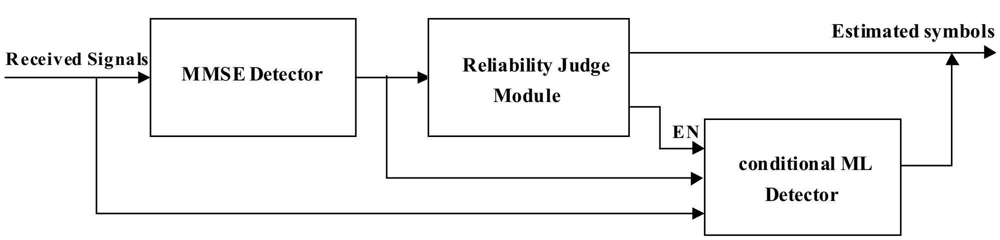

Figure 3: Structure of MMSE-CML detector.

Step 1. Get the estimate of transmit symbols in MMSE detector. Put received signals into MMSE detector. The MMSE detector gets the estimate of transmit symbols using MMSE rule and hard decisions as follows:

$$\begin{aligned}\tilde{\mathbf{x}}_{MMSE} &= (\mathbf{H}^H\mathbf{H} + \sigma^2\mathbf{I}_{N_t})^{-1}\mathbf{H}^H\mathbf{y} \\ \tilde{\mathbf{x}} &= Q(\tilde{\mathbf{x}}_{MMSE})\end{aligned} \tag{13}$$

where $Q(.)$ stands for hard decision operation.

Step 2. Judge the estimate reliable or not. Judge $\tilde{\mathbf{x}}$ in reliability judge module using (12). If (12) is satisfied, output the estimate as the final result; if not, go step 3.

Step 3. Do a conditional ML search. For a possible transmit symbol vector $\mathbf{x}_i \in \mathbf{X}$, where $\mathbf{X}$ is the set of all possible transmit symbol vector, calculate the squared distance d_i from the received vector $\mathbf{y}$ as follows

$$d_i = \|\mathbf{y} - \mathbf{H}\mathbf{x}_i\|^2 \tag{14}$$

if (12) is satisfied, that is, $d_i < N_r\sigma^2$, output $\mathbf{x}_i$ as the final result; else if the entire tree has been searched, choose the lowest squared distance and output the corresponding $\mathbf{x}$ as the final result; else, continue the tree search.

4.2. MMSE-LML

Although the MMSE-ML detector can achieve near the ML performance, which will be further proved later by the simulation results, it has a drawback of still possibly doing an exhaustive tree search. In order to further reduce the computational complexity, we consider the LML technique based on MMSE detection, which is characterized by a fixed complexity, and enables performance-complexity tradeoffs between the MMSE and ML detector [10].

Our MMSE-CLML detector is similar to MMSE-CML detector, with a difference in **Step 3**. Here we do a conditional local ML search by exploring only the neighborhood of the MMSE detector's output $\tilde{\mathbf{x}}$, which is a subset of $\mathbf{X}$.

We define the neighborhood of $\tilde{\mathbf{x}}$ as the set

$$\mathbf{X}_{near}(\tilde{\mathbf{x}}, P) = \{\mathbf{x} \in \mathbf{X} | d_H(\mathbf{x}, \tilde{\mathbf{x}}) \le P\} \tag{15}$$

where $d_H(\mathbf{x}, \tilde{\mathbf{x}})$ denotes the hamming distance between $\mathbf{x}$ and $\tilde{\mathbf{x}}$, and P is a integer from 0 to $N_t \log_2 M$.

As we can easily find, if we set P to $N_t \log_2 M$, CLML detector does a conditional ML search using RJR, which is similar to the MMSE-CML method; and if we set P to a lower value, CLML detector does a conditional local tree search, which will further reduce the complexity.

5. SIMULATION RESULTS

In this section, we compare the BER performance of the MMSE-CML detector, MMSE-CLML detector and ML detector. We further compare the computation complexity of these detectors.

In our simulations, we set $N_t = N_r = 4$ and consider a QPSK modulation, no channel coding and ergodic Rayleigh fading channels. And we suppose the channel condition is perfectly known at the receiver.

Figure 4 shows the performances of MMSE detector, MMSE-CML detector, MMSE-CLML detector with $P = 1, 2, 4$, and ML detector. We can see that MMSE-CML detector achieves near the same performance as ML detector. The MMSE-CLML detector approaches the ML performance when P increases. In this case, The MMSE-CLML detector with $P = 4$ approaches the ML performance in the low SNR region. When BER $= 10^{-2}$, the MMSE-CLML ($P = 2$) detector provides about 6 dB gain with respect to the MMSE detector, and about 1 dB loss to the MMSE-CLML ($P = 4$) detector.

Figure 5 presents the percentage of running the CML detector in MMSE-CML detector at different SNR levels. We can find that we can use MMSE detector, instead of ML detector, to get reliable estimate of transmit symbols at a percent of about or larger than 50%.

Figure 6 gives the average number of symbol vectors visited by various detectors. As we know, the computation cost of MMSE is much lower than ML detector. So we use the average number of symbol vectors visited to compare the computation complexity of various detectors. Since the complexity of MMSE-CML detector is about half or lower to ML detector, we think the MMSE-CML is more efficient than ML detector. We also find that the MMSE-CLML detectors with

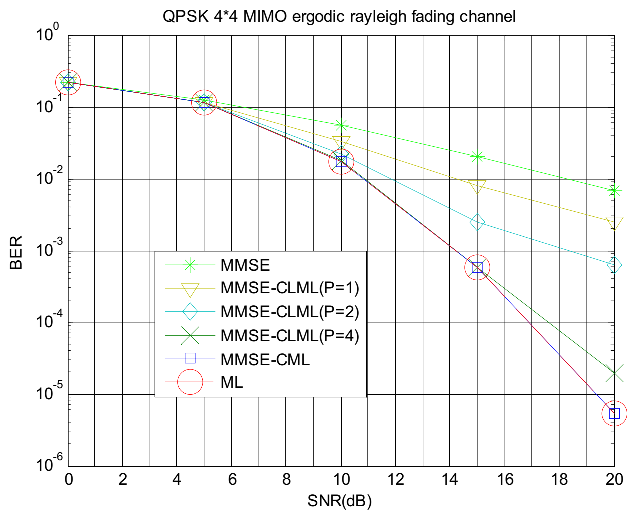

Figure 4: BER performance of various detectors.

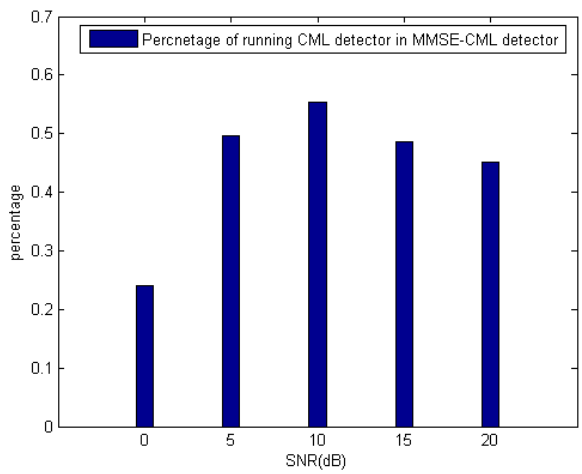

Figure 5: Percentage of running the CML detector in MMSE-CML detector.

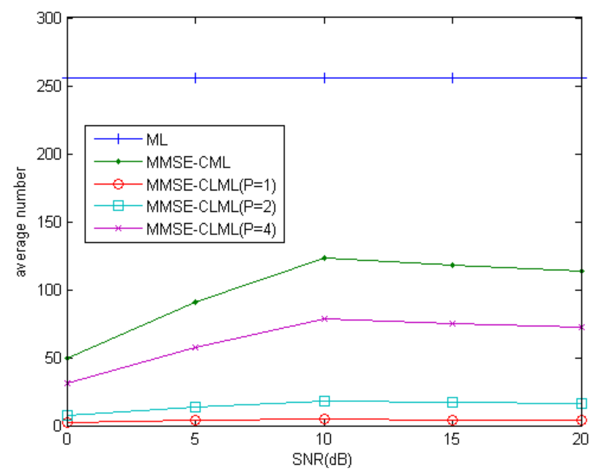

Figure 6: Average number of symbol vectors visited.

$P = 1, 2, 4$ work at lower complexity. Considering that the MMSE-CLML ($P = 4$) detector can approach the ML performance with about only 25% complexity of ML detector in low SNR region, we think our MMSE-CLML detector is more efficient in this case.

6. CONCLUSIONS

We have proposed two MMSE-based approximate ML detection schemes for MIMO BLAST systems together with a simplified reliability judge rule. We have shown that using the simple RJR we can estimate part of transmit symbols using MMSE method instead of ML method, with negligible performance loss, which effectively reduces the computation complexity. In the MMSE-CML detection, we do a conditional ML search when the output of MMSE detection is judged to be not reliable, which is replaced by a conditional local ML search in the MMSE-CLML detection. Simulation results demonstrate that the MMSE-CML detector can achieve near the same performance as ML detector at reduced complexity, and MMSE-CLML detector is more efficient in low SNR region at further reduced complexity.

ACKNOWLEDGMENT

This work was supported in part by National Hi-Tech Research and Development Program of China (National 863 Program) under Grant 2004AA4123310.

REFERENCES

1. Telatar, I. E., "Capacity of multi-antenna gaussian channels," *European Transactions on Telecommunications*, Vol. 10, No. 6, 585–595, Nov./Dec. 1999.
2. Foschini, J. and M.J. Gans, "On limits of wireless communications in a fading environment when using multiple antennas," *Wireless Personal Communications*, Vol. 6, 311–335, 1998.
3. Wolniansky, P. W., G. J. Foschini, G. D. Golden, et al., "V-BLAST: An architecture for realizing very high data rates over the rich-scattering wireless channel," *International Symposium on Signals, Systems, and Electronics, ISSSE 98[C]*, 295–300, 1998.
4. Li, X. and X. Cao, "Low complexity signal detection algorithm for MIMO-OFDM systems," *Electronics Letters*, Vol. 41, Issue 2, 83–85, Jan. 2005.
5. Wubben, D., R. Bohnke, J. Rinas, V. Kuhn, and K. D. Kammeyer, "Efficient algorithm for decoding layered sapce-time cods," *Electronics Letters*, Vol. 37, Issue 22, 1348–1350, Oct. 2001.
6. Viterbo, E. and J. Boutros, "A universal lattice code decoder for fading channels," *IEEE Trans. Inform. Theory*, Vol. 45, 1639–1642, July 1999.
7. Kim, K. J., Y. Jiang, R. A. Iltis, et al., "A QRD-M/Kalman filter-based detection and channel estimation algorithm for MIMO-OFDM systems," *IEEE Transactions on Wireless Communications*, Vol. 4, Issue 2, 710–721, Mar. 2005.
8. Luo, J., K. R. Pattipati, P. K. Willett, and F. Hasegawa, "Near-optimal multiuser detection in synchronous CDMA using probabilistic dataassociation," *IEEE Commun. Lett.*, Vol. 5, 361–363, Sep. 2001.
9. Pammer, V., Y. Delignon, W. Sawaya, and D. Boulinguez, "A low complexity suboptimal MIMO receiver: the combined ZF-MLD algorithm," *PIMRC 2003*, Vol. 3, 7–10, 2271–2275, Sep. 2003.
10. Rugini, L, P. Banelli, and G. B. Giannakis, "MMSE-based local ML detection of linearly precoded OFDM signals," *2004 IEEE International Conference on Communications*, Vol. 6, 20–24, 3270–327, Jun. 2004.

Realization of Impedance Boundary in Terms of a Slab of Wave-guiding Medium

I. V. Lindell and A. H. Sihvola
Helsinki University of Technology, Finland

Abstract— Introducing a class of metamaterial, labeled as wave-guiding anisotropic media, it shown that given impedance boundary conditions can be exactly realized by a slab of such a material when backed by a PEC plane. An analytic relation is derived between the surface admittance dyadic of the boundary and the parameters of the material slab and verified with non-trivial special cases of the theory.

The impedance boundary condition (IBC) defines a linear relation between the time-harmonic electric and magnetic field components tangential to the boundary surface. Denoting by $\overline{\overline{\mathsf{Y}}}_s$ the surface-admittance dyadic and by $\mathbf{n}$ the outer normal, the reation can be expressed as

$$\mathbf{n} \times \mathbf{H} = \overline{\overline{\mathsf{Y}}}_s \cdot \mathbf{E}.$$

The admittance dyadic is two-dimensional satisfying $\mathbf{n} \cdot \overline{\overline{\mathsf{Y}}}_s = \overline{\overline{\mathsf{Y}}}_s \cdot \mathbf{n} = 0$.

The IBC is required to make the solution of an electromagnetic boundary-value problem unique. Physically, IBCs are generally approximate when they replace real interface conditions at a surface separating two regions. Mathematically IBCs make the problem easier to handle in restricting the region of solution to one side of the surface, only.

The basic form of the IBC with scalar surface impedance was introduced by Shchukin and Leontovich in the 1940's [1]. Its use in solving electromagnetic problems is, however, limited when applied to physical interface problems. Basically, to be exact, Shchukin-Leontovich IBC requires that the field be constant along the boundary. For a planar boundary this is satisfied for a normally incident plane wave, while for oblique incidence the IBC introduces some error. During the last couple of decades, modifications to the basic IBC have been made by treating the surface impedance as an operator. Taking care of the lowest-order derivatives of the field along the boundary surface, numerical procedures based on the generalized IBC have been generated.

In contrast to the view that IBC's are approximative in nature one can point out that there exist problems where the IBC is exact. Of course it is known that a PEC obstacle can be exactly represented by the surface impedance $Z_s = 0$ and the PMC obstacle by the surface admittance $Y_s = 0$. Also, certain tuned corrugated structures can be represented by an impedance dyadic with zero and infinite components along two orthogonal directions on the surface, as the soft-and-hard surface. Actually these correspond to physical realizations for some special cases of the impedance surface. An idea on how to construct a realization for the general surface admittance dyadic $\overline{\overline{\mathsf{Y}}}_s$ was obtained when a realization for another special case, the perfect electromagnetic (PEMC) boundary, was recently found [2, 3]. The realization was based on a certain metamaterial, labeled as gyrotropic wave-guiding medium.

In the present case the wave-guiding medium is defined more generally as an anisotropic medium with permittivity and permeability dyadics consisting of components normal and transverse to the guiding z axis,

$$\overline{\overline{\epsilon}} = \epsilon_o \left(\overline{\overline{\epsilon}}_t + \epsilon_z \mathbf{u}_z \mathbf{u}_z \right), \qquad \overline{\overline{\mu}} = \mu_o \left(\overline{\overline{\mu}}_t + \mu_z \mathbf{u}_z \mathbf{u}_z \right).$$

The dimensionless dyadics $\overline{\overline{\epsilon}}_t$ and $\overline{\overline{\mu}}_t$ are two-dimensional, $\mathbf{u}_z \cdot \overline{\overline{\epsilon}}_t = \overline{\overline{\epsilon}}_t \cdot \mathbf{u}_z = 0$, $\mathbf{u}_z \cdot \overline{\overline{\mu}}_t = \overline{\overline{\mu}}_t \cdot \mathbf{u}_z = 0$ and assumed to possess two-dimensional inverses. The axial parameters are assumed to grow without limit, $\epsilon_z \to \infty$, $\mu_z \to \infty$.

Considering a field of the form

$$\mathbf{E}(\mathbf{r}) = \mathbf{E} f(\boldsymbol{\rho}) e^{-j\beta z}, \qquad \mathbf{H}(\mathbf{r}) = \mathbf{H} f(\boldsymbol{\rho}) e^{-j\beta z}$$

where $\mathbf{E}$ and $\mathbf{H}$ are the amplitude vectors and $f(\boldsymbol{\rho})$ is a function of the transverse position vector $\boldsymbol{\rho} = \mathbf{u}_x x + \mathbf{u}_y y$, one can show that the propagation factor β of the field is independent of its transverse distribution $f(\boldsymbol{\rho})$. Also, the axial field components vanish,

$$\mathbf{u}_z \cdot \mathbf{E} \to 0, \qquad \mathbf{u}_z \cdot \mathbf{H} \to 0,$$

whence the field is TEM with respect to the axial direction $\mathbf{u}_z$. There is no restriction to the transverse function $f(\boldsymbol{\rho})$ by the Maxwell equations. Since the field propagates along the z coordinate in the medium like a wave in parallel waveguides with no interaction between them, the medium is called the wave-guiding medium.

In the paper it is shown how a slab of wave-guiding material can be represented exactly as an impedance boundary. Conversely, the medium parameters and dimensions of the slab can be determined for realizing a given surface admittance $\overline{\overline{\mathrm{Y}}}_s$. The analysis is checked by simple nontrivial examples.

REFERENCES

1. Pelosi, G. and P. Y. Ufimtsev, "The impedance-boundary condition," *IEEE Ant. Propag. Mag.*, Vol. 38, No. 1, 31–35, February 1996.
2. Lindell, I. V. and A. H. Sihvola, "Perfect electromagnetic conductor," *J. Electromag. Waves Appl.*, Vol. 19, No. 7, 861–869, 2005.
3. Lindell, I. V. and A. H. Sihvola, "Realization of the PEMC boundary," *IEEE Trans. Antennas Propag.*, Vol. 53, No. 9, 3012–3018, September 2005.

Size Reduction of SRRs for Metamaterial and Left Handed Media Design

J. García-García, **F. Aznar**, **M. Gil**, **J. Bonache**, **and F. Martín**

GEMMA/CIMITEC, Dpto. de Ingenieria Electrònica de la Universidad Autònoma de Barcelona
Edifici Q, Campus de Bellaterra, Cerdanyola del Vallès, 08193, Barcelona, Spain

Abstract— New sub wavelength resonant particles are proposed. The resonant frequency of the particles is reduced by increasing the length of the resonators and increasing the coupling between resonators. Since this frequency reduction is equivalent to an area reduction, the structure can be used to achieve high compactness levels in Left Handed (LH) based circuits. As illustrative example an LH cell is implemented by using this new resonator.

1. INTRODUCTION

The metamaterial field has been object of a great interest in the last years. Since the publication of the first left handed synthesized metamaterial in 2000 [1], there have been hundreds of publications related with these artificial media. Many of the fabricated metamaterials are based on sub-wavelength resonators, such as the split rings resonator (SRR). This particle becomes also of great interest to the design of reduced size planar passive components due to the fact that these structures can be understood as a clever way to implement compact LC resonators. Thus, several microwave components have been designed and fabricated based on SRRs, where both left handedness and conventional (right handed) propagation have been used [2–5].

In this work, a variation of the SRR structure is proposed in which, by using vias and metallic strips, the sub-wavelength property of the SRRs is enhanced. Due to this miniaturization enhancement, we call this new particle Ultra Compact Split Rings Resonator (UCSRR). In section II, the structure is presented and its main properties and possibilities of size reduction as compared to SRRs are discussed. This latter point is illustrated through experiments. In section III, the possibility to implement LH cells by using the proposed UCSRR is discussed. As it has been shown in other works by the authors [3], these LH cells can be used to implement standard filters with high performance and small dimensions. Here similar LH cells are implemented by using UCSRR and SRR with open windows in the ground plane. Similar behaviour, namely left handedness, is demonstrated in both cases. Finally, in section IV, the conclusions of the work are exposed.

2. STRUCTURE AND PROPERTIES OF THE UCSRR RESONANT PARTICLES

As it is well known, the SRR was initially designed with the aim to be a small size resonator as compared with the signal wavelength at the resonant frequency [6]; in other words, it is a sub-wavelength resonator. To achieve this goal, a high coupling between the two rings forming the structure is required. This way, the individual resonances of either ring forming the SRR split-off, with the result of two new resonant frequencies for the SRR: one below and another above the pair of resonances corresponding to either isolated ring. The lower frequency can be driven to small values provided there is a strong coupling between the inner and outer ring. Thus, it is at the first resonance where the particle can be made electrically small [7].

Figure 1 shows how the coupling between the inner and outer rings is able to reduce a percentage of roughly 20% the resonant frequency of the isolated outer ring. To obtain these frequency responses, we have carried out simulations of the individual rings and the SRR by exciting them by means of a microstrip configuration (*Agilent ADS2005A-Momentum* has been used).

With the aim to further reduce the first resonant frequency of the structure, vias and strips in the bottom side of the substrate are added to the resonator design. The resulting structure is shown in the inset of Figure 2. This addition will reduce the resonant frequency of the structure in two different ways. First of all, by incrementing the length of the two individual resonators, a reduction of the inner and outer single rings resonances is achieved. On the other hand, due to the position of the vias and the metallic strips in the second metallic layer, the coupling between the resulting inner and outer resonators is incremented.

The structure shown in Figure 2 has the same dimensions than the SRR shown in Figure 1 however, as can be appreciated, comparing Figure 1 and Figure 2, the resonant frequency of the proposed structure is 50% lower than the SRR resonant frequency. For this reason we will call the structure Ultra Compact Split Ring Resonator (UCSRR).

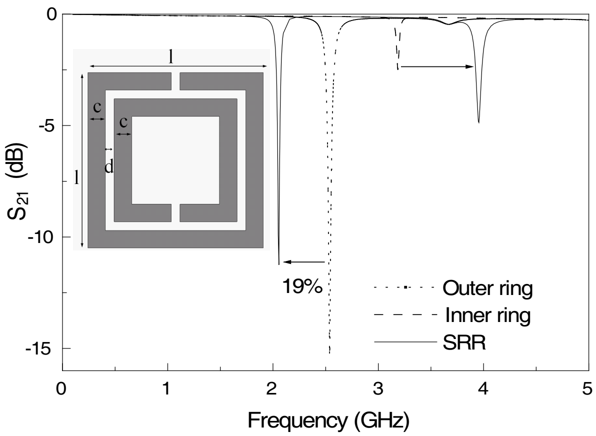

Figure 1: SRR inner and outer rings first resonance. The inset contains a scheme of the SRR. The showed simulated s-parameters results correspond to a UC-SRR with $l = 8\,\mathrm{mm}$, $c = 0.8\,\mathrm{mm}$, $d = 0.4\,\mathrm{mm}$, $h = 1.27\,\mathrm{mm}$ in a $\varepsilon_r = 10.2$ Rogers RO3010 substrate. Simulation performed using ADS 2005A-Momentum simulator.

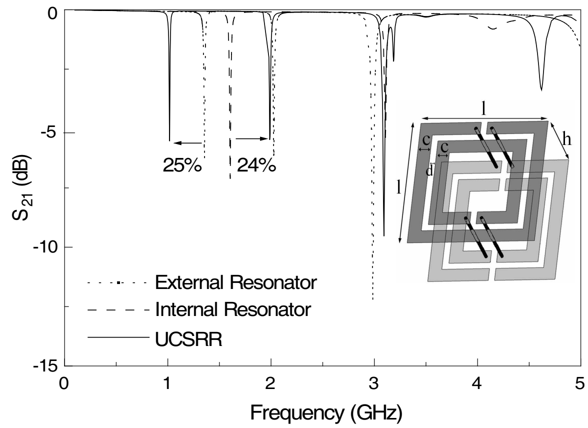

Figure 2: Simulated S_{21} parameters of the inner, outer and UCSRR resonators. In the inset, a scheme of the UCSRR is shown. The simulated results correspond to a UCSRR with $l = 8\,\mathrm{mm}$, $c = 0.8\,\mathrm{mm}$, $d = 0.4\,\mathrm{mm}$, $h = 1.27\,\mathrm{mm}$ in a $\varepsilon_r = 10.2$ *Rogers RO3010* substrate. Simulations are performed using ADS 2005A-Momentum simulator.

In Figure 3(b), it can be appreciated the S-parameters measured for SRR and UCSRR structures of similar dimensions (shown in Figure 3(a)), fabricated on a *Rogers RO3010* substrate.

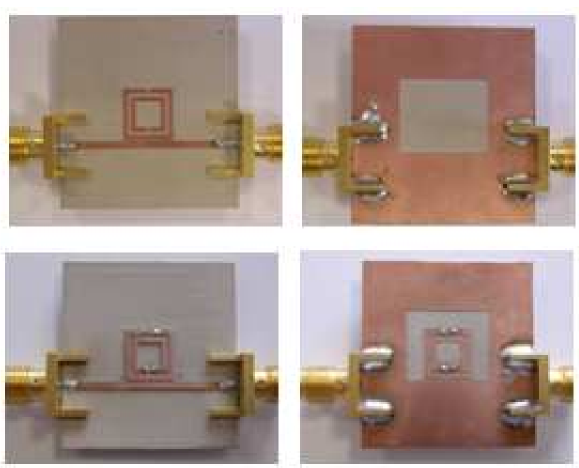

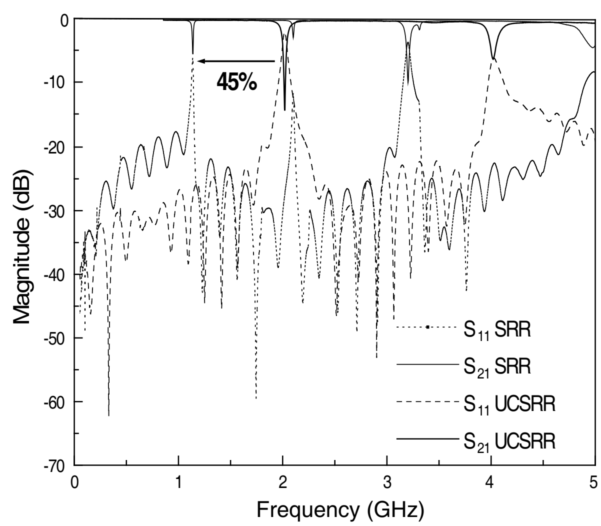

Figure 3: (a) Pictures of the top and bottom sides of the implemented structures using Rogers RO3010 substrate with $\varepsilon_r = 10.2$ and $h = 1.27\,\mathrm{mm}$, (b) Measured responses of the SRR and UCSRR structures.

The structures measured in Figure 3 correspond to those simulated in Figure 1 and Figure 2. However, the frequency reduction is lower in the measurements ($\sim 45\%$ instead of the 50% simulated result). The differences can be explained as due to the tolerances in the fabrication process. Nevertheless a good agreement between simulated and experimental results is found.

3. LEFT HANDED CELL IMPLEMENTED BY MEANS OF UCSRR

Although the resonances measured in the UCSRR are slightly weaker than those observed in the SRR, these particles are suitable to implement LH structures. To demonstrate this affirmation a basic cell similar to the proposed in [3] has been implemented. The only difference between the basic cells proposed here is that a window in the ground plane (area depicted in grey in the Figure 4(a) and Figure 4(b)) below the resonant particles is added.

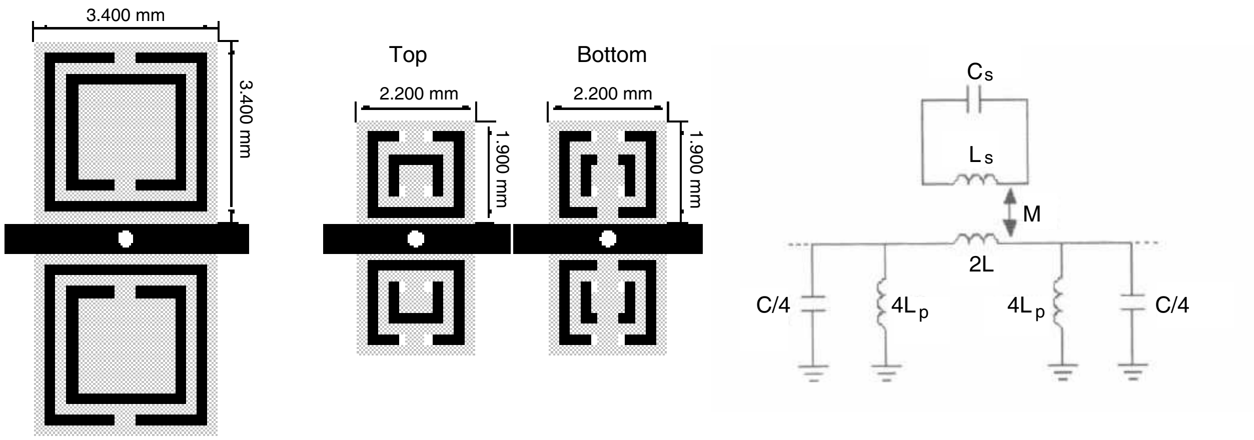

(a) (b) (c)

Figure 4: LHM basic cells operating at the same frequency (a) using SRR, (b) using UCSRR (top and bottom view of the cell), in both cases the grey zone delimits the open window in the ground plane, the black colour are metallic strips and the vias into the structures are in white colour, (c) Equivalent circuit model of both structures.

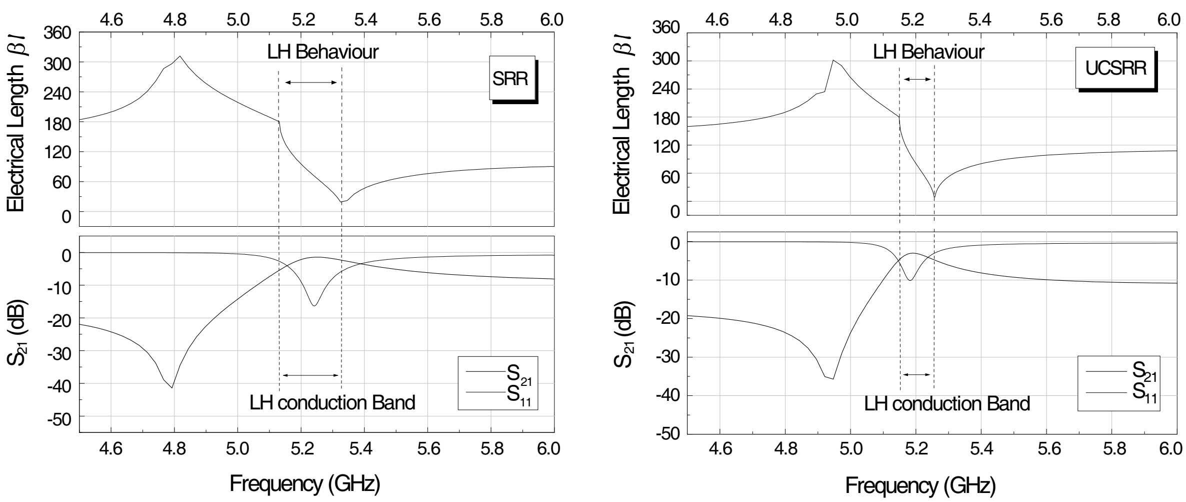

Figure 5: Simulated S-parameters of the basic cells using SRR (a) and SRR (b) resonators using Rogers RO3010 substrate with $\varepsilon_r = 10.2$ and $h = 1.27$ mm. Simulation performed using ADS 2005A-Momentum simulator.

The layout of the LHM basic cells operating at the same frequency are depicted in Figure 4(a) and Figure 4(b). The equivalent circuit model of the cell is the same than that discussed in [3] and it is shown in Figure 4(c). The open window in the ground plane underneath the SRRs modifies the values of C_S and L_S but does not modify the circuit model shown in Figure 4(c). The LH behaviour of a structure implemented using this basic cell is described in detail in the work [3]. In the case of the basic cell with the UCSRR the same circuit model (with appropriates values for C_S and L_S) can be used.

To verify the LH nature of these basic cells it is needed to evaluate the dispersion diagram where the frequency is depicted as a function of the electrical length $\beta \cdot l$. This electrical length, in those regions where the attenuation constant α is zero and hence the complex propagation constant is $\gamma = j\beta$, can be evaluated from the expression:

$$\cos(\beta \cdot l) = \frac{\cos(\phi_T)}{T} \tag{1}$$

where ϕ_T is the phase of the S_{21} and T is the magnitude of the S_{21} parameter. In Figure 5 are plotted the S-parameters of the two basic cells for LHM and the corresponding $\beta \cdot l$. As can be appreciated the slope of the $\beta \cdot l$ plot indicate LH behaviour in the bandpass for both structures i. e., a different sign between the group and phase velocities. It must be mentioned that the only regions where $\beta \cdot l$ is representative are those corresponding to the left handed behaviour, since it is in that regions the attenuation constant is roughly null.

4. CONCLUSION

A new sub-wavelength resonant particle based on the SRR is proposed. In the new proposed particle, the characteristics which produce the sub-wavelength character in the SRR resonator are intensified achieving a 50% reduction in the resonant frequency with similar dimensions. The proposed particle is suitable to implement LH media with high level of miniaturization. Work is in progress to extend these ideas to reduce the dimensions of other resonant particles.

ACKNOWLEDGMENT

This work has been supported by MEC by project contracts TEC2004-04249-C02-01. Thanks to the European Commission for the support given to the GEMMA Group through the NoE META-MORPHOSE. Thanks also to the Generalitat de Catalunya (CIDEM) for funding the *Centro de Investigacion en Metamateriales para La Innovacion en Tecnologias Electronica y de Comunicaciones* (CIMITEC).

REFERENCES

1. Smith, D. R., W. J. Padilla, D. C. Vier, S. C. Nemat-Nasser, and S. Schultz, "Composite medium with simultaneously negative permeability and permittivity," *Phys. Rev. Lett.*, Vol. 84, 4184–4187, May 2000.
2. Bonache, J., I. Gil, J. Garcia-Garcia, and F. Martin, "Novel microstrip bandpass filters based on complementary split-ring resonators," *IEEE Transactions on Microwave Theory and Techniques*, Vol. 54, Issue 1, 265–271, Jan. 2006.
3. Gil, I., J. Bonache, J. Garcia-Garcia, F. Falcone, and F. Martin, "Metamaterials in microstrip technology for filter applications," *2005 IEEE Antennas and Propagation Society International Symposium*, Vol. 1A, 668–671, 3–8 July, 2005.
4. Bonache, J., F. Martín, F. Falcone, J. D. Baena, T. Lopetegi, J. García-García, M. A. G. Laso, I. Gil, A. Marcotegui, R. Marqués, and M. Sorolla, "Application of complementary split rings resonators to the design of compact narrow band pass structures in microstrip technology," *Microwave and Optical Technology Letters*, Vol. 46, Issue 5, 508–512, July 2005.
5. Bonache, J., F. Martín, I. Gil, J. García-García, R. Marqués, and M. Sorolla, "Microstrip bandpass filters with wide bandwidth and compact dimensions," *Microwave and Optical Technology Letters*, Vol. 46, No. 4, 343–346, August 2005.
6. Pendry, J. B., A. J. Holden, D. J. Robbins, and W. J. Stewart, "Magnetism from conductors and enhanced nonlinear phenomena," *IEEE Transactions Microwave Theory Tech.*, Vol. 47, No. 11, 2075–2084, Nov. 1999.
7. García-García, J., F. Martín, J. D. Baena, R. Marqués, and L. Jelinek, "On the resonances and polarizabilities of split rings resonators," *Journal of Applied Physics*, Vol. 98, No. 033103, August 2005.

S-shaped Patch Antenna Fed by Dual Offset Electromagnetically Coupled for 5–6 GHz High Speed Network

Fitri Yuli Zulkifli, **Faisal Narpati**, **and Eko Tjipto Rahardjo**

Antenna propagation and Microwave Research Group (AMRG)
Center for Information and Communication Engineering Research (CICER)
Department of Electrical Engineering, University of Indonesia
Kampus Baru UI Depok, West Java, 16424, Indonesia

Abstract— Novel Design of S-shaped microstrip patch antenna fed by dual offset electromagnetically coupled to generate wideband operation in the 5–6 GHz frequency range is presented. It is demonstrated that by adding two slots opposite to each other to a rectangular patch and using dual offset electromagnetically coupled, wideband operation can be satisfactorily achieved. In advance, the two slots in the rectangular patch can reduce the area of the patch to 19.62%. Importantly, this antenna design is thin and small to be accommodated in a PCMCIA card of standard 5 mm thickness.

1. INTRODUCTION

Microstrip patch antennas are widely used in wireless communications due to their inherent advantages of low profile, less weight, low cost, and ease of integration with microstrip circuits. However, the main disadvantage of microstrip antennas is the small bandwidth. Many methods have been proposed in the literature [1, 2] to improve the bandwidth, and two of these are the use of a thick substrate and the cutting slots. Improvement of broader bandwidth becomes an important need for many applications such as for high speed networks.

Recently, high-speed wireless computer networks have attracted the attention of researchers, especially in the 5–6 GHz band (e. g. IEEE 802.11a). Such networks have the ability to provide high-speed connectivity (>50 Mb/s) between notebook computers, PCs, personal organizers and other wireless digital appliances. Although current 5 GHz wireless computer network systems operate in the 5.15–5.35 GHz band, future systems may make use of the 5.725–5.825 GHz band in addition to the 5.15–5.35 GHz band, for even faster data rates.

Many novel antenna designs have been proposed to suit the standard for high-speed wireless computer networks. Some approaches resulted in the probe-fed U-slot patch antenna [2], the E-shape patch antenna [3], and its improved version [4]. Reference [4] had also been designed to operate in the frequency 5–6 GHz, but this antenna uses coaxial feedline and inserts foam material between the patch and the ground plane.

In this paper, we propose a more simple design, a new S-shaped patch antenna (SSPA) design, which can cover all the sub band of wireless computer network systems, in the frequency range of 5–6 GHz. This antenna has wide bandwidth, in addition to being thin and small to be accommodated in a PCMCIA card of standard 5 mm thickness.

2. ANTENNA CONFIGURATION

The design of proposed S-shaped antenna is depicted in Figure 1. Substrate properties used for patch are TACONIC TLY 5 with substrate thickness of 1.6 mm, loss tangent factor of 0.0009 and dielectric constant of 2.2. Two slots with rectangular shape are embedded on the patch in opposite position, which form the S-shape of the patch. The two slots in the rectangular patch can reduce the area of the patch. This means the space required for antenna fabrication is less than the conventional rectangular patch antenna dedicated for wideband operation usage at a fixed operating frequency. By adding the two slots, the area of the rectangular patch can be reduced to 19.62%, which is from conventional rectangular patch area of 358.4 mm^2 to 288.08 mm^2 for the rectangular patch with two slots.

The parameters that characterize the antenna are the patch length and width (Lp, Wp), the width of slot (Ws), the length of slot (Ls) and the distance between two slots (Ps).Those three slot parameters are important in controlling the achievable bandwidth. The symmetrical S-shaped patch antenna has two resonant frequencies: a higher frequency and a lower frequency. Since the target bandwidth of the antenna is approximately 5–6 GHz, the two resonant frequencies are selected to be around 5.25 and 5.75 GHz. These are approximately the centre frequencies of the lower and upper bands of the IEEE 802.11a standard.

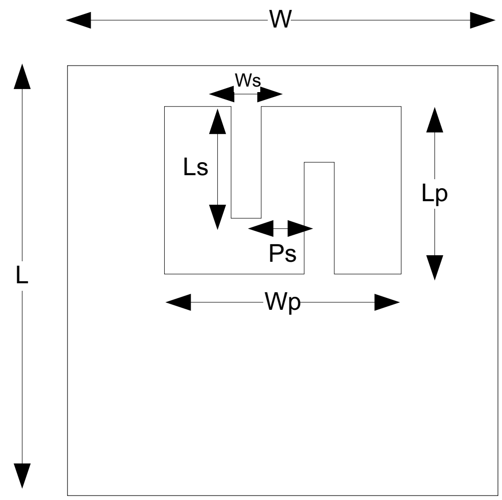

Figure 1: S-shaped microstrip antenna with W=L=40 mm, Wp= 22.2 mm, Lp= 15.6 mm, Ws= 2.8 mm, Ls= 10.4 mm, Ps= 4.2 mm.

The patch is fed electromagnetically coupled with microstrip line with 5 mm in width. To achieve matching condition, dual offset feed line matching technique is used. In this configuration as shown in Figure 2, the impedance delivered to each feed line at the aperture is nominally 100 Ω. The feed lines ($Zo = 100\,\Omega$) are joined by a reactive power combiner. Subsequently, a SSPA suitable for WLAN PCMCIA card was designed. The area of the ground plane was reduced to $40{\times}40\,\mathrm{mm}^2$ with total substrate height of 3.2 mm.

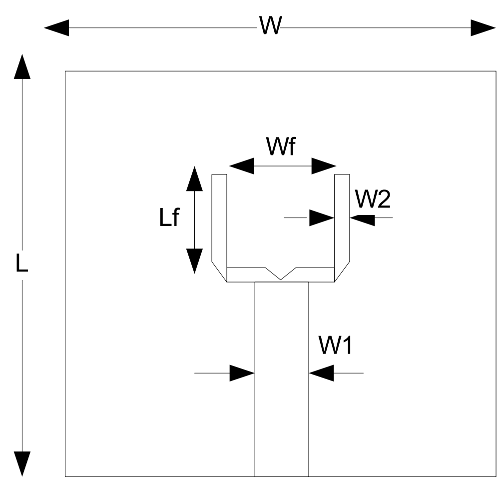

Figure 2: Configuration of dual offset feedline with W1= 5 mm, W2= 1.4 mm, Lf= 8.4 mm, Wf= 10.6 mm.

3. RESULTS AND DISCUSSION

3.1. Simulation Result

Adding S-slots in the radiator element has made significant effect on the result. The slot plays an important role to control the wide-band behavior of the S-shaped patch antenna.

Simulation result of the antenna is shown in Figure 3. The figure shows that the return loss of the antenna has its minimum return loss at 5750 MHz (−31,824 dB). Bandwidth of return loss is 951.3 MHz from the frequency of 4961.4 MHz to 5912.7 MHz.

3.2. Experiment Result

Several antennas based on the design have been fabricated to test the consistency of the design. The antennas are also been measured in anechoic chamber. As we can see in the measurement result of

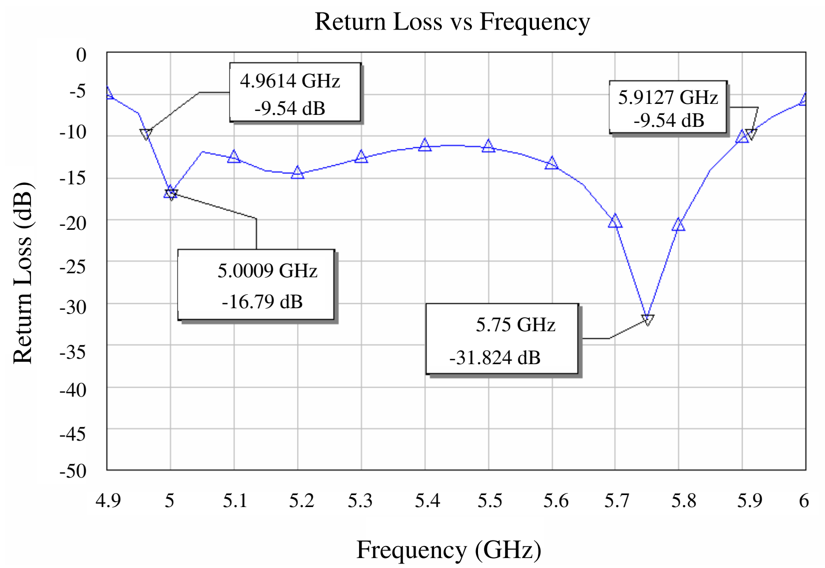

Figure 3: Simulated Return loss of Proposed Antenna.

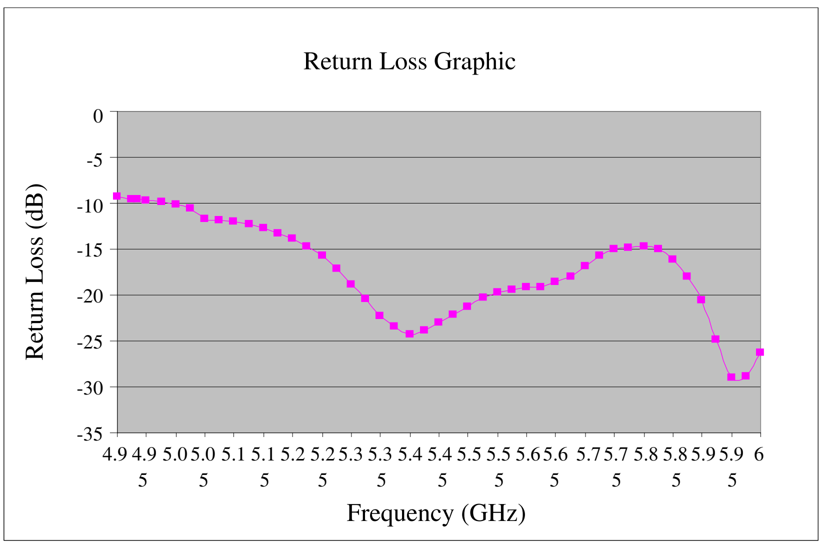

Figure 4: Measured Return Loss of Proposed antenna.

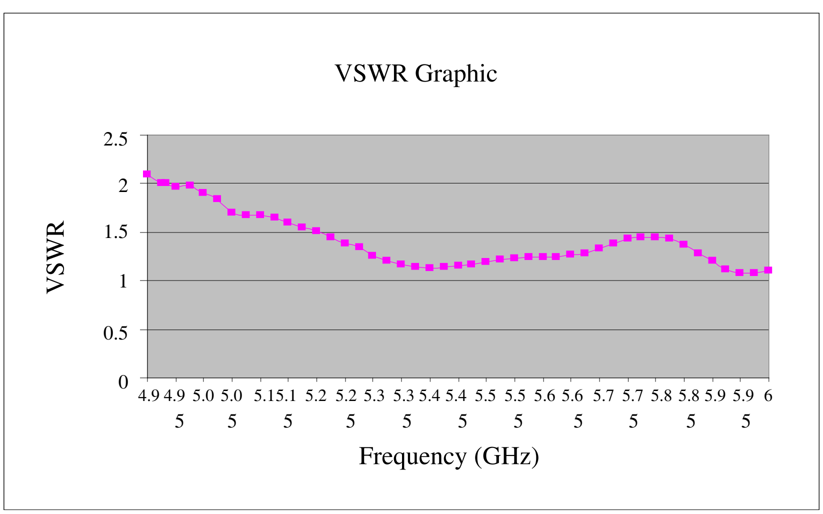

Figure 5: Measured VSWR of Proposed antenna.

return loss in Figures 4 and 5, the impedance bandwidth (VSWR 2:1) achieved from the frequency 4933.3 MHz to above 6000 MHz. The precise upper frequency could not be measured because of the limitation of the measurement equipment. The Minimum VSWR is 1,072 at 5962 MHz. Those results have passed the two IEEE 802.11a WLAN bands (5.15–5.35 GHz and 5.725–5.825 GHz).

Figure 6 shows the measurement result of proposed antenna of E and H plane radiation pattern at 5.415 GHz. The result shows the pattern at 5.912 GHz is similar. Although the gain and pattern parameters are not specified in the IEEE 802.11a standard, broad low-gain patterns such as the pattern in Figure 6 are desirable for WLAN systems.

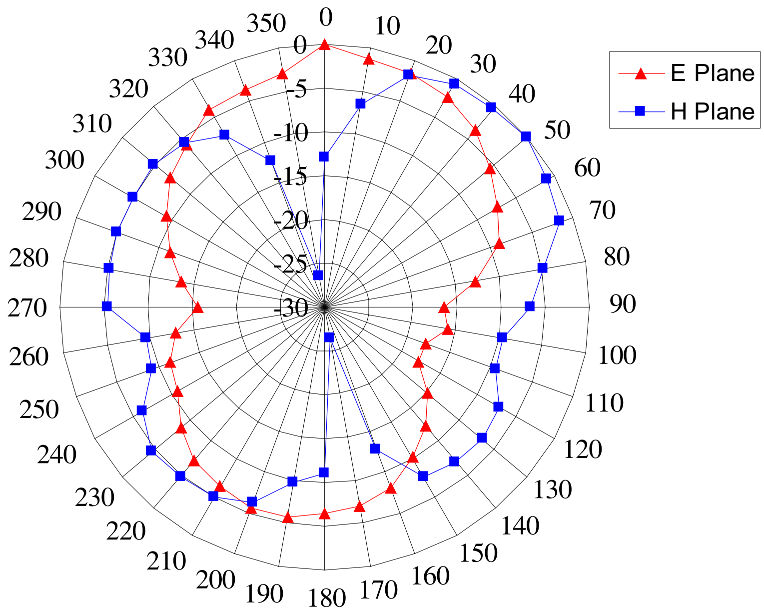

Figure 6: Measured Radiation Pattern of Proposed antenna at 5.415 GHz.

4. CONCLUSION

Our results demonstrate that it is possible to design an S-shaped patch antennas that has wide bandwidth to cover all the sub bands of the IEEE 802.11a high-speed WLAN standard. At the same time, this antenna are thin to be contained inside a PCMCIA card of standard 5-mm thickness. The antenna impedance bandwidth and resonant frequency can be adjusted by reconfiguring the three slot parameters.

REFERENCES

1. Sanad, M., “Double C-patch antennas having different aperture shapes,” *Proc. IEEE AP-S Symp.*, 2116–2119, Newport Beach, CA, June 1995.
2. Lee, K. F., K. M. Luk, K. F. Tong, S. M. Shum, T. Huynh, and R. Q., “Experimental and simulation studies of the coaxially fed U-slot,” *Proc. Inst. Elec. Eng.*, pt. H, Vol. 144, 354–358, Oct. 1997.
3. Yang, F., X.-X. Zhang, X. Ye, and Y. Rahmat-Samii, “Wide-band E-shaped patch antennas for wireless communications,” *IEEE Trans. Antennas and Propagat.*, Vol. 49, No. 7, 1091–1100, July 2001.
4. Ge, Y., K. P. Esselle, and T. S. Bird, “E-Shaped patch sntennas for high-speed wireless networks,” *IEEE Trans. Antennas and Propagat.*, Vol. 52, No. 12, 3213–3219, December 2004.

Realization of Generalized Soft-and-hard Boundary

I. Hanninen, I. V. Lindell, and A. H. Sihvola
Electromagnetics Laboratory, Helsinki University of Technology, Finland

Abstract— The classical soft-and-hard surface boundary conditions have previously been generalized to the form $\mathbf{a} \cdot \mathbf{E} = 0$ and $\mathbf{b} \cdot \mathbf{H} = 0$ where $\mathbf{a}$ and $\mathbf{b}$ are two complex vectors tangential to the boundary. A realization for such a boundary is studied in terms of a slab of special wave-guiding anisotropic material. It is shown that analytic expressions can be found for the material parameters and thickness of the slab as functions of the complex vectors $\mathbf{a}$ and $\mathbf{b}$.

1. INTRODUCTION

Soft-and-hard surface (SHS) is defined by symmetric boundary conditions for the electric and magnetic fields which are of the form [1, 2]

$$\mathbf{v} \cdot \mathbf{E} = 0, \quad \mathbf{v} \cdot \mathbf{H} = 0, \tag{1}$$

where $\mathbf{v}$ denotes a real unit vector tangential to the boundary surface, i.e., it satisfies $\mathbf{n} \cdot \mathbf{v} = 0$ when the unit vector normal to the boundary is denoted by $\mathbf{n}$. Originally, SHS was defined as a useful model approximating boundary structures with tuned metallic corrugations introduced in 1944 [3–5], which have found early applications in antenna design [6]. We can also define a more general class of anisotropic ideal boundaries [7], which have the condition

$$\mathbf{a} \cdot \mathbf{E} = 0, \quad \mathbf{a}^* \cdot \mathbf{H} = 0, \tag{2}$$

where $\mathbf{a}$ is a tangential complex unit vector satisfying $\mathbf{n} \cdot \mathbf{a} = 0$ and $\mathbf{a} \cdot \mathbf{a}^* = 1$. Because (2) generalizes the SHS condition (1), it appears natural to introduce the even more general condition

$$\mathbf{a} \cdot \mathbf{E} = 0, \quad \mathbf{b} \cdot \mathbf{H} = 0, \tag{3}$$

in terms of two complex vectors $\mathbf{a}, \mathbf{b}$ satisfying $\mathbf{n} \cdot \mathbf{a} = \mathbf{n} \cdot \mathbf{b} = 0$ and

$$\mathbf{a} \cdot \mathbf{b} = 1. \tag{4}$$

The class of media defined by (3) was labeled as generalized soft-and-hard surfaces (GSHS) in [8]. The GSHS boundary can be tailored to change any given polarization of an incident plane wave to any other given polarization for the reflected field by choosing the vectors $\mathbf{a}$ and $\mathbf{b}$ properly, as demonstrated in [7]. This and any other possible application in mind gives motivation for finding a realization of the GSHS boundary.

2. BOUNDARY ADMITTANCE

Impedance-boundary condition is a mathematical restriction to ensure unique solutions for differential equations in a region terminated by the boundary. For electromagnetic fields it takes on the form of a linear relation between the electric and magnetic field components tangential to the boundary surface. Let us consider the form

$$\mathbf{n} \times \mathbf{H} = \overline{\overline{\mathsf{Y}}}_s \cdot \mathbf{E}, \tag{5}$$

in terms of a two-dimensional surface admittance dyadic $\overline{\overline{\mathsf{Y}}}_s$ satisfying

$$\mathbf{n} \cdot \overline{\overline{\mathsf{Y}}}_s = \overline{\overline{\mathsf{Y}}}_s \cdot \mathbf{n} = 0. \tag{6}$$

To approach the GSHS boundary, let us consider the following form of a normalized surface admittance dyadic:

$$j\eta_o \overline{\overline{\mathsf{Y}}}_s = \frac{A}{\delta}\mathbf{ba} + B\delta\mathbf{ab}^{\times}_{\times}\mathbf{nn}, \tag{7}$$

where $A \neq 0$ and $B \neq 0$ are two scalar admittance parameters and δ is a dimensionless scalar parameter. The normalizing factor $j\eta_o = j\sqrt{\mu_o/\epsilon_o}$ taken for convenience anticipates imaginary components for $\overline{\overline{\mathsf{Y}}}_s$ when the boundary is lossless. In the limit $\delta \to 0$, the admittance dyadic (7) will correspond to the GSHS boundary with conditions (3) valid for any nonzero values of A and B.

3. REALIZATION OF GSHS

In [9] a structure involving a layer of gyrotropic anisotropic material was introduced to realize a special impedance surface called the perfect electromagnetic conductor (PEMC). The material was generalized in [10] for the realization of the general impedance surface and the same structure will be considered here. Let us assume a slab of anisotropic medium of thickness d which is terminated by a PEC plane. The anistropic medium is defined by permittivity and permeability dyadics of the form

$$\overline{\overline{\epsilon}} = \epsilon_o(\overline{\overline{\epsilon}}_t + \epsilon_n \mathbf{nn}), \quad \overline{\overline{\mu}} = \mu_o(\overline{\overline{\mu}}_t + \mu_n \mathbf{nn}), \tag{8}$$

with $\epsilon_n \to \infty, \mu_n \to \infty$. In the medium (8) the wave is split in two eigenwaves propagating along the normal direction with propagation factors β_1, β_2 depending on the medium dyadics as [10]

$$\beta_{1,2}^2 = \frac{k_o^2}{2}\left(\overline{\overline{\epsilon}}_t {}^\times_\times \overline{\overline{\mu}}_t^T : \mathbf{nn} \pm \sqrt{(\overline{\overline{\epsilon}}_t {}^\times_\times \overline{\overline{\mu}}_t^T : \mathbf{nn})^2 - 4\Delta(\overline{\overline{\epsilon}}_t)\Delta(\overline{\overline{\mu}}_t)}\right), \tag{9}$$

where Δ denotes determinant of a two-dimensional dyadic, which can be computed in terms of dyadic algebra as [12, 13]

$$\Delta(\overline{\overline{\epsilon}}_t) = \frac{1}{2}\overline{\overline{\epsilon}}_t {}^\times_\times \overline{\overline{\epsilon}}_t : \mathbf{nn}, \quad \Delta(\overline{\overline{\mu}}_t) = \frac{1}{2}\overline{\overline{\mu}}_t {}^\times_\times \overline{\overline{\mu}}_t : \mathbf{nn}, \tag{10}$$

and

$$\overline{\overline{\epsilon}}_t {}^\times_\times \overline{\overline{\mu}}_t^T : \mathbf{nn} = \Delta(\overline{\overline{\epsilon}}_t + \overline{\overline{\mu}}_t^T) - \Delta(\overline{\overline{\epsilon}}_t) - \Delta(\overline{\overline{\mu}}_t). \tag{11}$$

A relation between the transverse permittivity and permeability dyadics, the thickness of the slab and the surface admittance dyadic at the interface of the slab was derived in [10]. The resulting analytic expression has the form

$$\overline{\overline{\mathsf{Y}}}_s = \frac{\beta_1 \cot \beta_1 d - \beta_2 \cot \beta_2 d}{j k_o \eta_o (\beta_1^2 - \beta_2^2)} k_o^2 \overline{\overline{\epsilon}}_t + \frac{\beta_2 \beta_1^2 \cot \beta_2 d - \beta_1 \beta_2^2 \cot \beta_1 d}{j k_o \eta_o (\beta_1^2 - \beta_2^2)} (\overline{\overline{\mu}}_t^{-1} {}^\times_\times \mathbf{nn}) \tag{12}$$

when assuming $\beta_1^2 \neq \beta_2^2$. The question is how to determine the medium dyadics $\overline{\overline{\epsilon}}_t, \overline{\overline{\mu}}_t$ and the thickness d of the slab to obtain the GSHS admittance (7) in the limit $\delta \to 0$. This can be done by using a limiting process, where we first assume that the thickness of the slab is depends on the parameter δ, so that originally the thickness is d' and approaches d as

$$d' = d(1 + \delta) \to d \tag{13}$$

when $\delta \to 0$. By substituting this into (12) and taking the limit $\delta \to 0$, we are able to solve the thickness of the slab d,

$$\beta_1 d = \pi, \quad \beta_2 d = \pi/2. \tag{14}$$

Finally, we are able to find the expressions for the medium dyadics in the form

$$\overline{\overline{\epsilon}}_t = \frac{1}{k_o d}\left(\pi^2 A \mathbf{ba} - B \mathbf{ab} {}^\times_\times \mathbf{nn}\right) \tag{15}$$

and

$$\overline{\overline{\mu}}_t = \frac{1}{k_o d}\left(-\frac{\pi^2}{4}\frac{1}{B}\mathbf{ab} + \frac{1}{A}\mathbf{ba} {}^\times_\times \mathbf{nn}\right). \tag{16}$$

The expressions (15) and (16) can be considered as forming the solution for the realization problem. Because the GSHS boundary conditions are obtained for any values of the scalars A and B, their choice depends on the realizability of the medium dyadics $\overline{\overline{\epsilon}}_t$ and $\overline{\overline{\mu}}$.

4. CONCLUSION

A realization for the GSHS boundary in terms of a slab of special wave-guiding anisotropic material has been studied, and analytic expressions for the material parameters and thickness of the slab have been derived in terms of the vectors **a**, **b**, using a limiting process. With these analytic expressions, it is in theory possible to construct any GSHS boundary defined by (4).

REFERENCES

1. Kildal, P. S., "Definition of artificially soft and hard surfaces for electromagnetic waves," *Electronics Letters*, Vol. 24, No. 3, 168–170, 1988.
2. Kildal, P. S., "Artificially soft and hard surfaces in electromagnetics," *IEEE Trans. Antennas Propagat.*, Vol. 38, 1537–1544, Oct. 1990.
3. Cutler, C. C., "Electromagnetic waves guided by corrugated surfaces," *Bell Telephone Labs. Report*, MM-44-160-218, Oct. 1944.
4. Cutler, C. C., "Genesis of the corrugated electromagnetic surface," *IEEE Int. Antennas Propagat. Symp. Dig.*, Vol. 32, 1456–1459, June 1994.
5. Elliott, R. S., "On the theory of corrugated plane surfaces," *I.R.E. Trans. Antennas Propagat.*, 71–81, Apr. 1954.
6. Rumsey, V. H., "Horn antennas with uniform power patterns around their axes," *IEEE Trans. Antennas Propagat.*, Vol. 14, 656–658, Sept. 1966.
7. Lindell, I. V., "The ideal boundary and generalized soft-and-hard surface," *Proc. IEE Microw. Antennas Propagat.*, Vol. 147, 495–499, Dec. 2000.
8. Lindell, I. V., "Generalized soft-and-hard surface," *IEEE Trans. Antennas Propagat.*, Vol. 50, No. 7, 926–929, July 2002.
9. Lindell, I. V. and A. H. Sihvola, "Realization of the PEMC boundary," *IEEE Trans. Antennas Propagat.*, Vol. 53, No. 9, 3012–3018, Sep. 2005.
10. Lindell, I. V. and A. H. Sihvola, "Realization of impedance boundary," submitted to *IEEE Trans. Antennas Propagat.*.
11. Viitanen, A. J., S. A. Tretyakov, and I. V. Lindell, "On the realization of the generalized soft-and-hard surface," *Radio Science*, Vol. 35, No. 6, 1257–1264, 2000.
12. Gibbs, J. W. and E. B. Wilson, *Vector Analysis*, Dover, New York, 1960.
13. Lindell, I. V., *Methods for Electromagnetic Field Analysis*, 2nd Ed., University Press, Oxford, 1995.

UPML Absorbing Boundary Condition for Truncating the Boundary of DNG Metamaterials

K. S. Zheng[1], W. Y. Tam[1], and D. B. Ge[2]

[1]Department of Electronic and Information Engineering
The Hong Kong Polytechnic University, Kowloon, Hong Kong, China
[2]Department of Physics, Xidian University, Shaanxi 710071, China

Abstract— The conventional perfectly matched layer (PML) absorbing boundary condition is shown to be unstable when it is extended to truncate the boundary of the double negative (DNG) medium. It is a consequence of the reverse directions of the Poynting and phase-velocity vectors of plane waves propagating in such material. In this paper, a modified uniaxial PML (UPML) which is stable for the DNG medium is derived. The auxiliary differential equation technique is introduced to derive the discrete field-update equations of DNG-UPML. Numerical results demonstrate the effectiveness and stability of the new UPML for the DNG medium.

1. INTRODUCTION

The plane-wave propagation in a material whose permittivity and permeability are assumed to be simultaneously negative is theoretically investigated by Veselago [1]. Recently, several papers have exposed the usefulness of double negative (DNG) medium with negative permittivity and permeability [2–5]. However, in order to further study unusual electromagnetic phenomena in DNG medium, full-wave numerical simulations have become more and more important. The FDTD method is a good choice for these electromagnetic problems. The absorbing boundary condition in FDTD is required to truncate the computation domain without reflection in the simulation of DNG medium properties and applications. An absorbing boundary condition for DNG medium has been proposed [6, 7]. Since first introduced by Berenger in 1994 [8], the perfectly matched layer (PML) has become the most popular and efficient absorbing boundary condition. Unfortunately, standard versions of PML are inherently unstable when it is extended to truncate the boundary of DNG medium without any modification [9, 10]. Recently, a nearly PML, named by NIMPML absorbing boundary condition, is discussed, and 50-cell layers for NIMPML is used to truncate the DNG medium [10]. Later, a modified PML absorbing boundary condition based on the complex-coordinate stretching variables has been proposed for PSTD method [11]. In this paper, a modified uniaxial PML (UPML) which is stable for the DNG medium is presented. It is worth noting that only 10-cell layers for UPML is used and provides a clearly reduced error to truncate the DNG medium.

Firstly, we adopt the UPML medium for truncating the DNG medium. Then, by using the auxiliary differential equation technique, the efficient DNG-UPML is implemented in the FDTD method. Finally, the relative error of DNG-UPML in the one-dimensional case is calculated. Numerical example was used to demonstrate the stability of the proposed DNG-UPML absorbing boundary condition.

2. NUMERICAL METHOD

2.1. Maxwell's Equations in the DNG Medium

The time-harmonic Maxwell's curl equations to be solved are

$$j\omega\varepsilon \boldsymbol{E} = \nabla \times \boldsymbol{H} \tag{1}$$

$$j\omega\mu \boldsymbol{H} = \nabla \times \boldsymbol{E} \tag{2}$$

By replacing the derivatives with their central finite difference counterparts, the FDTD formulations of Eq. (1) and Eq. (2) can be obtained easily. For a lossy DNG material, negative permittivity and permeability are realized using the Drude medium model as follows:

$$\varepsilon(\omega) = \varepsilon_0\varepsilon_r(\omega) = \varepsilon_0\left(1 + \frac{\omega_{pe}^2}{\omega(j\Gamma_e - \omega)}\right) \tag{3}$$

$$\mu(\omega) = \mu_0\mu_r(\omega) = \mu_0\left(1 + \frac{\omega_{pm}^2}{\omega(j\Gamma_m - \omega)}\right) \tag{4}$$

2.2. UPML for the DNG Meidum

For a matched condition, the permittivity and permeability in the UPML can be written as $\varepsilon(\omega) = \varepsilon_0\varepsilon_r(\omega)\bar{\bar{s}}$ and $\mu(\omega) = \mu_0\mu_r(\omega)\bar{\bar{s}}$, where $\bar{\bar{s}}$ is the diagonal tensor defined by

$$\bar{\bar{s}} = \begin{bmatrix} s_y s_z s_x^{-1} & 0 & 0 \\ 0 & s_x s_z s_y^{-1} & 0 \\ 0 & 0 & s_x s_y s_z^{-1} \end{bmatrix} \tag{5}$$

In order to truncate the DNG medium, a good choice for s in Eq. (5) is

$$s = 1 + \frac{\sigma}{j\omega\varepsilon_0\sqrt{\mu_r\varepsilon_r}} = 1 + \frac{\sigma}{j\omega\varepsilon_0\left(1 + \frac{\omega_p^2}{\omega(j\Gamma-\omega)}\right)} \tag{6}$$

where $\omega_{pe} = \omega_{pm} = \omega_p$ and $\Gamma_m = \Gamma_e = \Gamma$.

From Eqs. (1)–(6), the Ampere's law in a matched DNG-UPML can be expressed as

$$\begin{bmatrix} \dfrac{\partial H_z}{\partial y} - \dfrac{\partial H_y}{\partial z} \\ \dfrac{\partial H_x}{\partial z} - \dfrac{\partial H_z}{\partial x} \\ \dfrac{\partial H_y}{\partial x} - \dfrac{\partial H_x}{\partial y} \end{bmatrix} = j\omega\varepsilon_0\varepsilon_r(\omega) \begin{bmatrix} \dfrac{s_y s_z}{s_x} & 0 & 0 \\ 0 & \dfrac{s_x s_z}{s_y} & 0 \\ 0 & 0 & \dfrac{s_x s_y}{s_z} \end{bmatrix} \begin{bmatrix} E_x \\ E_y \\ E_z \end{bmatrix} \tag{7}$$

where the assumed tensor coefficients in x, y, and z directions for the DNG medium are

$$s_x = \kappa_x + \frac{\sigma_x}{j\omega\varepsilon_0\sqrt{\mu_r\varepsilon_r}}; \quad s_y = \kappa_y + \frac{\sigma_y}{j\omega\varepsilon_0\sqrt{\mu_r\varepsilon_r}}; \quad s_z = \kappa_z + \frac{\sigma_z}{j\omega\varepsilon_0\sqrt{\mu_r\varepsilon_r}} \tag{8}$$

In order to derive the discrete field-update equations for Eq. (7), we adopt auxiliary differential equation FDTD techniques that permit direct time integration of the full-vector Maxwell's equations [12]. Now, substituting Eq. (8) into Eq. (7), the system of equations in Eq. (7) can be transformed into time domain and be discretized on the standard Yee lattice. This yields time-stepping expressions for E_x, E_y, and E_z. For example, the E_x updating equation is given by

$$\begin{aligned} E_x^{n+1} = & \frac{1}{\frac{b_1}{2\Delta t} + \frac{b_2}{\Delta t^2} + \frac{b_3}{4}} \left[\left(\frac{2b_2}{\Delta t^2} - \frac{b_3}{2} \right) E_x^n + \left(\frac{b_1}{2\Delta t} - \frac{b_2}{\Delta t^2} - \frac{b_3}{4} \right) E_x^{n-1} \right. \\ & \left. + \left(\frac{a_1}{2\Delta t} + \frac{a_2}{\Delta t^2} + \frac{a_3}{4} \right) R_x^{n+1} + \left(\frac{a_3}{2} - \frac{2a_2}{\Delta t^2} \right) R_x^n + \left(\frac{a_2}{\Delta t^2} - \frac{a_1}{2\Delta t} - \frac{a_3}{4} \right) R_x^{n-1} \right] \end{aligned} \tag{9}$$

where the parameters are

$$\begin{aligned} a_1 &= \sigma_x + \kappa_x\Gamma; \quad a_2 = \kappa_x; \quad a_3 = \sigma_x\Gamma + \kappa_x\omega_p^2 \\ b_1 &= \sigma_y + \kappa_y\Gamma; \quad b_2 = \kappa_y; \quad b_3 = \sigma_y\Gamma + \kappa_y\omega_p^2 \end{aligned} \tag{10}$$

The auxiliary field variable R_x can be updated using

$$R_x^{n+1} = \left(\frac{2\varepsilon_0\kappa_z - \varepsilon_0\sigma_z\Delta t - \beta_d\Delta t}{2\varepsilon_0\kappa_z + \varepsilon_0\sigma_z\Delta t + \beta_d\Delta t} \right) R_x^n + \frac{2\Delta t}{2\varepsilon_0\kappa_z + \varepsilon_0\sigma_z\Delta t + \beta_d\Delta t} \left[(\nabla \times \boldsymbol{H})|_x^n - \frac{1}{2}(k_d + 1)J_x^n \right] \tag{11}$$

where the expression of $(\nabla \times \boldsymbol{H})|_x^n$ denotes the x-directed curl of magnetic field quantity calculated at the time point $t_n = n\Delta t$. The updating equation of the variable J_x can be written as

$$J_x^{n+1} = k_d J_x^n + \beta_d (R_x^{n+1} + R_x^n) \tag{12}$$

where the parameters k_d and β_d are defined as

$$k_d = \frac{2 - \Gamma\,\Delta t}{2 + \Gamma\,\Delta t}; \quad \beta_d = \frac{\varepsilon_0\omega_p^2\kappa_z\Delta t}{2 + \Gamma\,\Delta t}(R_x^{n+1} + R_x^n) \tag{13}$$

Similar expressions can be derived for the remaining two E-field components in the lossy DNG-UPML. Overall, updating the components of $\boldsymbol{E}$ in the DNG-UPML requires three steps. Firstly, obtaining the new values of the components of $\boldsymbol{J}$ according to Eq. (12), and secondly, using these new $\boldsymbol{J}$ components to obtain the new values of the components of $\boldsymbol{R}$ according to Eq. (11), and thirdly, using these new $\boldsymbol{R}$ components to obtain the new values of the $\boldsymbol{E}$ components according to Eq. (9).

A similar three-step procedure can be derived to update the components of $\boldsymbol{H}$ in the DNG-UPML using the same approach.

3. NUMERICAL RESULTS

In this section, numerical results are presented in one-dimensional cases. The relative error of DNG-UPML absorbing boundary condition is also discussed.

The time function of line electric-current source is given by the multiple cycle m-n-m pulse [13]. It is a sinusoidal signal that has a smooth windowed turn-on for m cycles, constant amplitude for n cycles, and then a smooth windowed turn-off for m cycles. Hence, it has an adjustable bandwidth centered at the frequency f_0, as shown in Figure 1.

Firstly, we show the performance of the DNG-UPML. The 1-D structure under study is shown in Figure 2. The total space of the computational domain is filled with the DNG medium, where the parameters in Eq. (3) and (4) are as follows: $\Gamma_e = \Gamma_m = \Gamma = 0$, and $\omega_{pe} = \omega_{pm} = \omega_p = 2.665 \times 10^{11}$ rad/s. The UPML ABC is used to truncate the boundary of DNG medium. An x-directed electric line current source is located at the center of a 4000-cell one dimensional FDTD grid. The center frequency f_0 of the current source is 30 GHz, and its time function is the 5-10-5 pulse. In particular, the values of $\mathrm{Re}(\varepsilon_r)$ and $\mathrm{Re}(\mu_r)$ at the center frequency f_0 are approximately -1.0.

The FDTD grid has $\Delta z = 0.01$ cm and a time-step of 0.5 times the Courant limit. The E-field is probed at point A, as shown in Figure 2. Point A is one cell from the right-side PML boundary. Time-stepping runs over 22,000 iterations, well past the steady-state response. 10-cell UPML ABCs are used with polynomial-scaled σ [14] with $m = 3$, $\sigma_{\max} = \sigma_{\mathrm{opt}}$, and $\kappa_{\max} = 1$, yielding the properties of UPML.

The reference solution $E_{\mathrm{ref}}|_k^n$ at grid location k and time-step n is obtained using 40,000-cell grid. An identical current source is centered within this grid, and the field-observation point A is at the same position relative to the source as in the test grid. The reference grid is sufficiently large such that there are no reflections from its outer boundaries during the time-stepping span of interest. This allows a relative error to be defined as

$$\mathrm{R}_{\mathrm{error}}|_k^n = 20 \log_{10} \left(\left| E|_k^n - E_{\mathrm{ref}}|_k^n \right| / \left| E_{\mathrm{ref\,max}}|_k \right| \right) \tag{14}$$

where $E_{\mathrm{ref\,max}}|_k$ is the maximum amplitude of the reference field at the location k, as observed during the time-stepping span of interest.

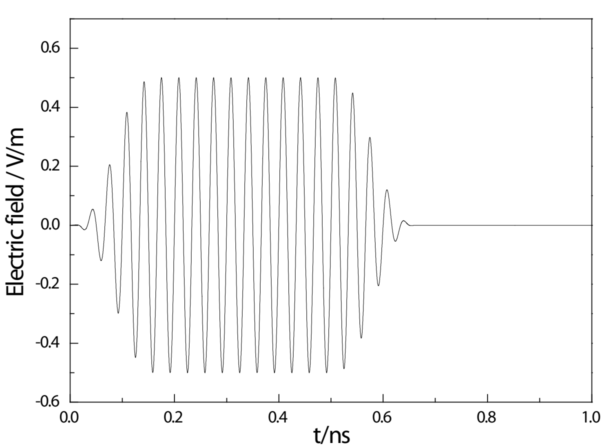

Figure 1: Waveform of the electric current source in time domain.

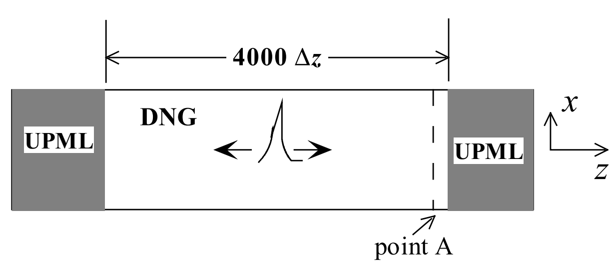

Figure 2: Sketch of the numerical simulation.

Figure 3 shows the DNG-UPML simulation is stable enough to compute a solution for at least 100,000 time steps. Figure 4 depicts the relative error at point A over 22,000 time-steps of the FDTD run for 10-cell PMLs. From Figure 4, we see that the DNG-UPML provides a clearly reduced error. The maximum relative error is below 80 dB. This accuracy is good enough to simulate lots of the numerical simulation of the electromagnetic problems in DNG medium.

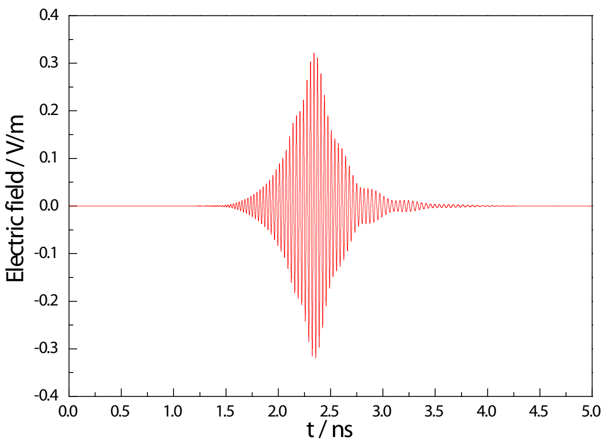

Figure 3: Stable time-domain field for DNG-UPML.

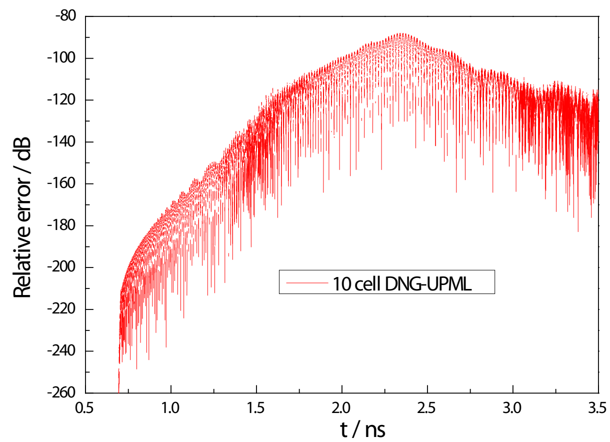

Figure 4: Relative error at point A for 10-cell PMLs.

4. CONCLUSION

In this paper, a new DNG-UPML absorbing boundary condition has been derived in order to overcome the instability of standard PML for truncating the boundary of the DNG medium. Using the auxiliary differential equation approach, the efficient formulations of the DNG-UPML are presented. Numerical FDTD simulations are provided. Numerical results have demonstrated the accuracy and stability of the DNG-UPML absorbing boundary condition.

ACKNOWLEDGMENT

This work described in this paper was supported in part by the Research Grants Council of the Hong Kong Administrative Region, China, under Grant PolyU 5262/05E.

REFERENCES

1. Veselago, V. G., "The electrodynamics of substances with simultaneously negative values of ε and μ," *Sov. Phys. Usp.*, Vol. 10, No. 4, 509–514, 1968.
2. Shelby, R. A., D. R. Smith, S. C. Nemat-Nasser, and S. Schultz, "Microwave transmission though a two-dimensional, isotropic, left-handed metamaterial," *Appl. Phys. Lett.*, Vol. 78, 489–491, 2001.
3. Shelby, R. A., D. R. Smith, and S. Schultz, "Experimental verification of a negative index of refraction," *Science*, Vol. 292, 77–79, 2001.
4. Smith, D. R. and N. Kroll, "Negative refractive index in left-handed materials," *Phys. Rev. Lett.*, Vol. 85, 2933–2936, 2000.
5. Pendry, J. B., "Negative refraction makes a perfect lens," *Physical Review Letter*, Vol. 85, 3966–3969, 2000.
6. Wittwer, D. C. and R. W. Ziolkowski, "Two time-derivative Lorentz material (2TDLM) formulation of a Maxwellian absorbing layer matched to a lossy media," *IEEE Trans. Antennas Propag.*, Vol. 48, No. 2, 192–199, 2000.
7. Wittwer, D. C. and R. W. Ziolkowski, "Maxwellian material based absorbing boundary conditions fro lossy media in 3D," *IEEE Trans. Antennas Propag.*, Vol. 48, 200–213, 2000.
8. Berenger, J. P., "A perfectly matched layer for the absorbing EM waves," *J. Computat. Phys.*, Vol. 114, 185–200, 1994.
9. Dong, X. T., X. S. Rao, Y. B. Gan, B. Guo, and W. Y. Yin, "Perfectly matched layer-absorbing boundary condition for left-handed materials," *IEEE Microwave Wireless Compon. Lett.*, Vol. 14, 301–303, 2004.
10. Cummer, S. A., "Perfectly matched layer behavior in negative refractive index materials," *IEEE Antennas Wireless Propagat. Lett.*, Vol. 3, 172–175, 2004.

11. Shi, Y., Y. Li, and C. H. Liang, "Perfectly matched layer absorbing boundary condition for truncating the boundary of the left-handed medium," *Microwave Opt. Technol. Lett.*, Vol. 48, No. 1, 57–62, 2006.
12. Taflove, A. and S. C. Hagness, *Computational Electrodynamics: The Finite-difference Time-domain Method*, Third Ed., Artech House, Norwood, MA, 2005.
13. Ziolkowski, R. W. and A. D. Kipple, "Causality and double-negative metamaterials," *Physical Review E*, Vol. 68, 026615, 2003.
14. Gedney, S. D., "An anisotropic perfectly matched layer absorbing media for the truncation of FDTD lattices," *IEEE Trans. Antennas Propagat.*, Vol. 44, 1630–1639, 1996.

A Fast Volume-surface Integral Equation Solver for Scattering Properties of NIMs

Y. N. Li, H. Y. Yao, and L. W. Li
Department of Electrical and Computer Engineering, National University of Singapore, Singapore

Abstract— This paper presents a fast hybrid volume-surface integral equation approach for the computation of electromagnetic scattering from composed negative index media (NIM) such as split-ring-resonators (SRR) with wires. The volume electric field integral equation (EFIE) is applied to the dielectric region of this NIM, and the surface electric field integral equation is applied on the conducting surface. The method of moments (MoM) is used to discretize the integral equation into a matrix solution and adaptive integral method (AIM) is employed to reduce the memory requirement and CPU time for the matrix solution. The present approach is sufficiently versatile in handling scattering problems of composed NIMs, due to the combination of surface and volume electric field integral equations. Numerical results of calculating radar cross section (RCS) of such a NIM slab are finally presented to demonstrate the accuracy and efficiency of this technique.

NIM, which is also known as left-handed material (LHM) [1], presents dielectric constants (permeability and permittivity) simultaneously negative. Typical NIMs, such as SRR [2], are composed of dielectric body and conducting patches. Base on this feature, to investigate the scattering problem of such NIMs, we can employ volume EFIE to the dielectric region and surface EFIE on the conducting surface [3]. Previous researchers often use MoM [4] to discretize the integral equations. And AIM [5, 6, 3] has already been proved to be an efficient solver in reduce the memory requirement for storage and to speed up the matrix-vector multiplication in the iterative solver.

For an SRR structure, in the dielectric region V, by taking the scattered field from both the surface current and volume current into consideration, the total electric field becomes:

$$E(r) = E^{inc}(r) + E_V^{sca}(r) + E_S^{sca}(r) \tag{1}$$

Since the tangential components of total electric field vanishes on conducting surface, we get:

$$\hat{n} \times E^{inc}(r) = -\hat{n} \times E_V^{sca}(r) - \hat{n} \times E_S^{sca}(r) \tag{2}$$

Equations (1) and (2) are known as the EFIE as the formulations involve only electric field. EFIE is suitable for open conducting surface. Inside the dielectric region V and on the surface of conducting body S, the incident wave induces volume current J_V and surface current J_S. The induced volume and surface currents will generate scattered EM field as following:

$$E_\Omega^{sca}(r) = \ -jk_0\eta_0 A_\Omega(r) - \nabla\Phi_\Omega(r), \quad \Omega = S \text{ or } V \tag{3}$$

where the magnetic vector potential is defined as:

$$A_\Omega(r) = \ \int_\Omega J_\Omega(r, r')g(r, r')dr', \quad \Omega = S \text{ or } V \tag{4}$$

and the electric scalar potential is defined as:

$$\Phi_\Omega(r) = \ -\frac{\eta_0}{jk_0}\int_\Omega \nabla' \cdot J_\Omega(r, r')g(r, r'dr'), \quad \Omega = S \text{ or } V \tag{5}$$

where $g(r, r') = \frac{e^{-jk_0|r-r'|}}{4\pi|r-r'|}$, $\eta_0 = \sqrt{\frac{\mu_0}{\varepsilon_0}}$, and k_0 denotes the wavenumber of background medium (free space).

The volume of dielectric material and surface of conducting body are meshed into tetrahedral elements and triangular patches, respectively. These elements are used because of their flexibility to model arbitrarily shaped 3-D object. The volume and surface current are expanded using different vector basis functions. For surface elements, it is convenient to use the planar triangular basis functions or Rao-Wilton-Glisson (RWG) basis functions [7] to expand the equivalent surface electric current. For volume elements, similarly, we can apply Schaubert-Wilton-Glisson (SWG) basis functions [8] to expand the equivalent volume electric current.

$$J_S = \sum_{n=1}^{N_S} I_n^S f_n^S \tag{6}$$

$$J_V = j\omega \sum_{n=1}^{N_V} \frac{\tilde{\varepsilon}(r) - \varepsilon_0}{\tilde{\varepsilon}(r)} I_n^V f_n^V = j\omega \sum_{n=1}^{N_V} \kappa(r) I_n^V f_n^V \tag{7}$$

where $\kappa(r) = \frac{\tilde{\varepsilon}(r)-\varepsilon_0}{\tilde{\varepsilon}(r)}$ is the contrast ratio and $\tilde{\varepsilon}(r)$ is the permeability of a tetrahedron element.

After substituting above equations into EFIE, we applying the Galerkin's testing procedure. Then the integral equations are converted into a linear equation system written as:

$$\begin{bmatrix} \bar{Z}^{VV} & \bar{Z}^{VS} \\ \bar{Z}^{SV} & \bar{Z}^{SS} \end{bmatrix} \begin{bmatrix} I^V \\ I^S \end{bmatrix} = \begin{bmatrix} E^V \\ E^S \end{bmatrix} \tag{8}$$

where the vectors I^V and I^S represent the coefficients of volume current and surface current respectively. The excitation vector can be computed using

$$E_m^V = \int_{V_m} f_m^V \cdot E^{inc}(r')dr' \tag{9}$$

$$E_m^S = \int_{S_m} f_m^S \cdot E^{inc}(r')dr' \tag{10}$$

Then, we apply AIM and decompose $\bar{Z}$:

$$\bar{Z}I = \bar{Z}^{near}I + \bar{Z}^{far}I \tag{11}$$

where $\bar{Z}^{near}$ is a sparse matrix that contains only the nearby elements within a threshold distance and can be compute with iteration method. $\bar{Z}^{far}$ represents the far-zone interaction of the elements. We apply FFT to $\bar{Z}^{far}I$ in order to make a good approximation in the far-zone:

$$\bar{Z}^{far}I = \bar{\Lambda}\Im^{-1}\left\{\Im\{\bar{g}\} \cdot \Im\{\bar{\Lambda}^T I\}\right\} \tag{12}$$

where $\Im\{\bullet\}$ and $\Im^{-1}\{\bullet\}$ stand for FFT and inverse FFT respectively. The Matrix $\bar{g}$ is Toeplitz. $\bar{\Lambda}$ represents the basis transformation matrix of the elements.

A direct solver of MoM requires $O(N^3)$ operations to solve the equation while an iterative solver requires $O(N^2)$ operations in each iteration. Both solvers require $O(N^2)$ memory to store the matrix elements. However, the computational complexity for AIM is $O(N1.5logN)$ and $O(NlogN)$ for surface and volume scatterers, respectively.

Numerical Result

First, we work with one row of SRR structure (3 inclusions placed side by side along y-). The geometry and dimensions of this kind of inclusions are shown in Figure 1. The width of all metal

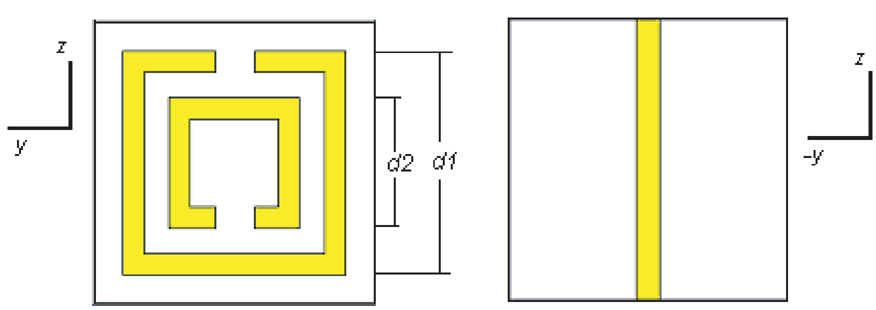

Figure 1: Geometry of a single inclusion-SRR and Wire (d1=2.63 mm, d2=1.53 mm).

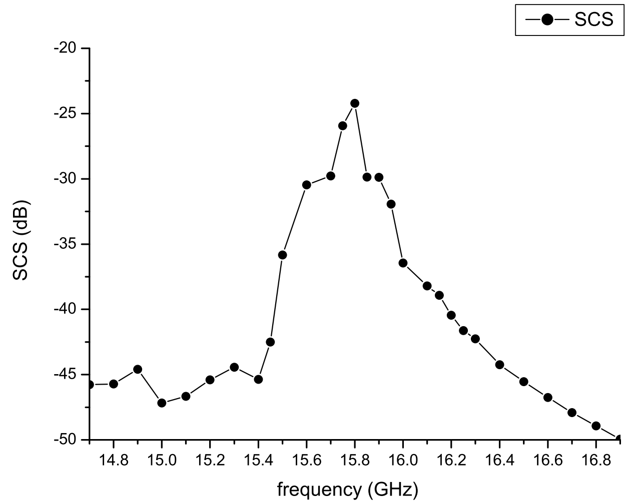

Figure 2: SCS versus frequency for a row of inclusions (3 SRRs) at $\theta = \phi = 90°$.

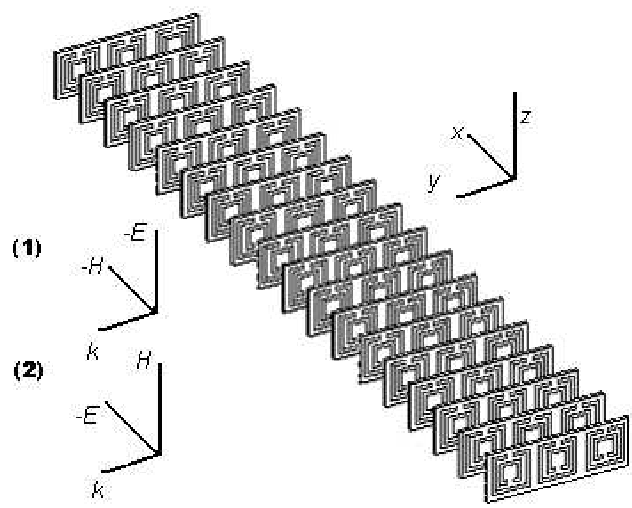

Figure 3: Structure of the slab composed by SRRs and wires with two different incidents.

strips is 0.25 mm, the thickness of dielectric is 0.254 mm and the length of each square is 3.3 mm. The relative permittivity of dielectric is set to be $\varepsilon = 1$.

We examine the scattering cross section (SCS) [9] of this row of 3 elements and plot it verses frequency in Figure 2. It can be seen that the resonant frequency is approximately 15.80 GHz.

Next, at this resonant frequency, we analyze the propagation characteristics of electromagnetic wave in a NIM sample placed in the free space. It's a NIM slab composed of many rows of inclusions shown in Figure 1. The 3-D view of this slab is depicted in Figure 3. The space distances of the inclusions denoted, respectively, by d_x, d_y and d_z in the x-, y- and z-directions, are all 3.3 mm. There are totally 54 SRR elements which are arranged into 18 rows along x- and 3 columns along y-. In order to show that our AIM algorithm is suitable for this structure, we illuminate the slab with two different plane waves coming from $-y$ direction as shown in Figure 3, and then we check the RCS of this SRR slab in each case. Actually, SRR requires the electric field E^{inc} in parallel with the plane of the ring (yOz plane) to get maximum magnetic resonant. In other words, the rings are not supposed to be on the $H - k$ plane [10]. So if E^{inc} is perpendicular with the plane of rings (case (2) in Figure 3), the RCS must be very small and the whole structure becomes no more than an ordinary scatterer which does not acquire negative refractive index. Figure 4 and Figure 5 show values of E_z and RCS when the illuminators are of case (1) and case (2), respectively.

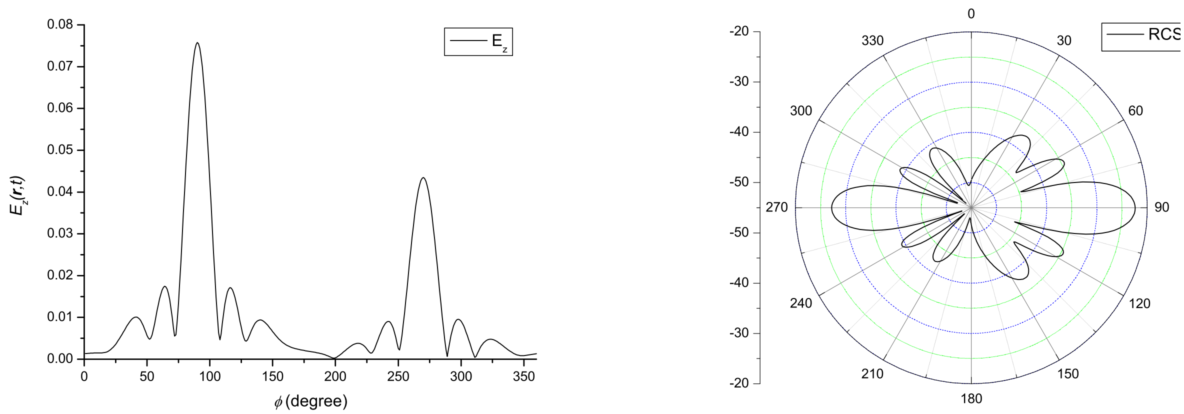

Figure 4: $Ez(\mathbf{r}, t)$ and RCS of the slab of case (1) in Figure 3 at 15.8 GHz.

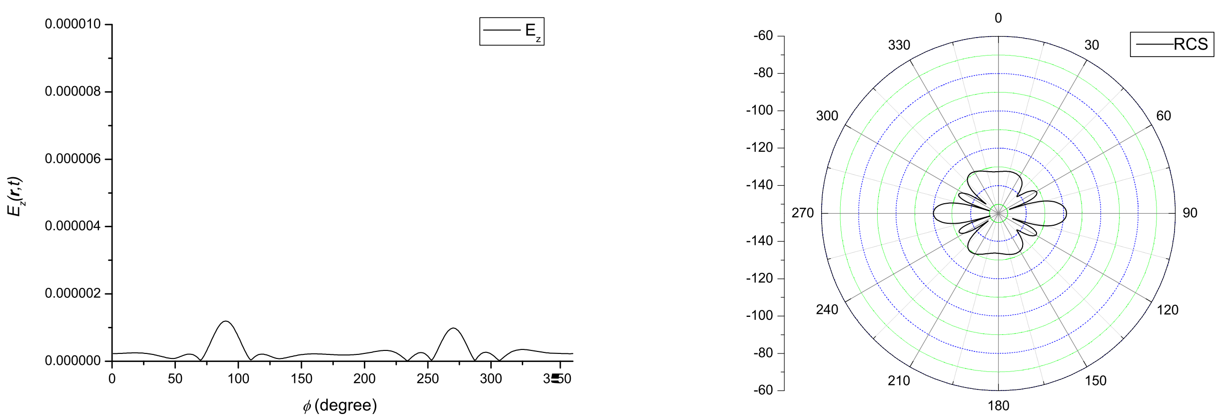

Figure 5: $Ez(\mathbf{r}, t)$ and RCS of the slab of case (2) in Figure 3 at 15.8 GHz.

Conclusions

The structures of SRR with wires behave as a magnetic conductor in the vicinity of resonant frequency. By applying the fast solver AIM, the CPU time per iteration as well as memory requirement is greatly reduced. SRR structures are often electrically small and have a large number of unknowns, so AIM is especially suitable to analyze such kind of NIMs. We first use a few inclusions to find the resonant frequency, then at the vicinity of this frequency, an SRR slab is tested when the illuminator are two different plane waves. When the E is in parallel with the ring, most power can be scattered which satisfies the property of NIM. However, when E is perpendicular with the ring, there is neither magnetic resonance nor negative refractive index.

REFERENCES

1. Veselago, V. G., "The Electrodynamics of substances with simultaneously negative values of ε and μ," *Sov. Phy. Usp*, Vol. 10, No. 4, 509–514, 1968.
2. Smith, D. B., D. C. Vier, and S. Schultz, "Direct calculation of permeability and permittivity for a left-handed metamaterial," *Phys. Rev.*, Vol. 85, No. 14, 2933–2936, 2000.
3. Ewe, W. B., L. W. Li, and M. S. Leong, "Fast solution of mixed dielectric/conducting scattering problem using volume-surface adaptive integral method," *IEEE Trans. Antennas Propagat.*, Vol. 52, No. 11, 3071–3077, 2004.
4. Harington, R. F., *Field Computation by Moment Method*, Macmillan Company, New York, 1968.
5. Bleszybski, E., M. Bleszynski, and T. Jaroszewicz, "A fast integral-equation solver for electromagnetic scattering problems," in *Antennas and Propagation Society International Symposium*, AP-S. Digest, Vol. 1, Issue, 20–24, 416–419, 1994.

6. Ling, F., C. F. Wang, and J. M. Jin, "An efficient algorithm for analyzing large-scale microstrip structures using adaptive integral method combined with discrete complex-image method," *IEEE Trans. Microwave Theory Tech.*, Vol. 48, No. 5, 832–839, 2000.
7. Rao, S. M., D. R. Wilton, and A. W. Glisson, "Electromagnetic scattering by surfaces of arbitrary shape," *IEEE Trans. Antennas Propagat.*, Vol. 30, No. 11, 409–418, 1982.
8. Schaubert, D. H., D. R. Wilton, and A. W. Glisson, "A tetrahedral modeling method for electromagnetic scattering by arbitrarily shaped inhomogeneous dielectric bodies," *IEEE Trans. Antennas Propagat.*, Vol. 32, No. 1, 77–85, 1984.
9. Yao, H. Y., W. Xu, and L. W. Li, "Propagation property analysis of metameterial Conductive SRRs and wires using the MGS-based algorithm," *IEEE Trans. Antennas Propagat.*, Vol. 53, No. 4, 1469–1476, 2005.
10. Katsarakis, N., T. Koschny, and M. Kafesaki "Electric coupling to the magnetic resonance of split ring resonators," *Applied Phys. Lett.*, Vol. 84, No. 15, 2943–2945, 2004.

Novel Sequential Monte Carlo Method to Bearing Only Tracking

Hongquan Qu and Shaohong Li

School of Electronics and Information Engineering, Beihang University
Beijing 100083, China

Abstract— Extended Kalman Filter (EKF) and Unscented Kalman Filter (UKF) are often used in target tracking, but the required Posterior Density Function (PDF) is still approximated by a Gaussian, which may be a gross distortion of the true underlying structure and lead to filter divergence when performing EKF or UKF. Because the uncertainty of process model in bearing only tracking is small compared with the uncertainty of the measurements, resample introduces the problem of loss of diversity among the particles with Particle Filter. This may lead to undesired clustering of the samples and eventually inaccurate results. The SMCEKF and SMCUKF algorithms given in this paper ensure the independency of particles by introducing parallel independent EKFs and UKFs for the bearing only tracking problem. The resample technique, which was suggested in the particle filter as a method to reduce the degeneracy problem, is given up. The required density of the state vector is represented as a set of random samples, which is updated and propagated recursively on their own estimate. The performance of the filters is greatly superior to the standard EKF and UKF. Analysis and simulation results of the bearing only tracking problem have proved validity of the algorithms.

1. INTRODUCTION

The EKF is the most popular approach to target tracking, but it sometimes can degrade estimator performance and exhibits unstable behavior. The bootstrap filtering, which was applied to perform nonlinear non-Gaussian filtering, was known variously as Sequential Monte Carlo (SMC) filter, particle filter. The key ideal is to represent the required PDF by a set of random samples with associated weights and to compute estimates based on these samples and weights [5]. The Unscented Transformation (UT) was developed as a method to propagate mean and covariance information through nonlinear transformation [10]. These two methods were deeply researched and extensively applied.

Sampling/important resampling (SIR) was generalization of Bootstrap, and was also called classical or basic particle filter. The Extended Kalman Particle Filter (EKPF) and Unscented Particle Filter (UPF) was obtained from choice of proposal distributions [1, 2, 7–9], Regularized PF (RPF) is based on sample from continuous PPDF [1, 2], Rao-Blackwellised (RBPF) was presented for dimensinality reduction and reducing the number of required particles [3, 4]. Other SMC methods include Auxiliary Sample Important Resample (ASIR) and Markov Chain Monte Carlo (MCMC) particle filter, etc [2, 9]. For the system, where the uncertainty of process model is high compared with the uncertainty of the measurements, particle filter in general can accounts for the reasonable performance only using basic SIR algorithms, relatively a few particles. For first example in literature [5] only 500 samples was used, it was decided by basic principle of the particle filter [1, 2]. For second example in literature [5] (Bearing-only target tracking), where the uncertainty of process model was small compared with the uncertainty of the measurements, the number of particles was increased to 5000, and roughning and prior edit modification have been implemented for combating the consequent reduction in the number of truly distinct samples values. Its computational cost was relatively high, and literature [2, 3] and [6] used 5000, 8000, 20000 particles, respectively.

Based survey of principle and connection of PF and its variants, it was pointed out that the theoretical foundations of the SMC methods might remain unclear and that the modification was possible [1]. For the system, where the uncertainty of process model is small compared with the uncertainty of the measurements, resample of PF and its variants introduce the problem of loss of diversity among the particles [1, 2].

In order to improve the performance of the situation, a novel SMC approach, where EKF or UKF is introduced in order to propagate and update the particles, is proposed in this paper. The algorithm, called SMCEKF or SMCUKF, consists of an independent EK or UK filter group, one of which is initianlized by random samples according to prior PDF. PPDF is approximated by the independent propagated particles, so the algorithm overcomes the loss of the diversity of the particles. Analysis and simulation results have proved validity of the algorithms.

2. ALGORITHM OF SMCEKF AND SMCUKF

The EKF is probably the most widely used estimation algorithm for nonlinear systems, but EKF have unacceptable performance and sometimes exhibits unstable behavior characteristics for bearing-only target tracking problem because poor initial state prior knowledge and approximating PDF by linearization. UKF approximates state PDF using the true nonlinear system model or measurement model. The state distribution is still represented by a Gaussian density, but it is specified with a set of deterministically chosen sample points. The sample points completely capture the true mean and covariance of the Gausssian random vector. When propagated through any non-linear system, the sample points capture the posterior mean and covariance accurately to the second order or higher. Linearization only uses the first-order terms. Problem of passive track, especially bearing-only target tracking from single moving platform, is representative problem where the uncertainty of process model is small compared with the uncertainty of the measurements.

In order to improve its performance, SMCEKF and SMCUKF algorithms are given in this paper, and they belong to random sample methods and combine SMC, EKF and UKF to increase power of representing PDF by samples.

First of all, bearing-only target tracking from single moving platform is stated simply.

2.1. Bearing-only Target Tracking from Single Moving Platform

For a single moving platform collecting angular measurements, target state becomes observable only if the observer "outmanoevres" the target (i. e., observer motion is one derivative higher than that of the target) and a component of this motion must be perpendicular to the LOS [6]. Specifically, a constant, nonzero velocity observer can estimate the position of a stationary target and an accelerating observer can estimate the position and velocity of a constant velocity target. Because the problem was discussed in many literatures, system state equation and measurement equation are directly below given:

$$X_{Tk} = f\left(X_{Tk-1},\, w_k\right) = FX_{Tk-1} + \Gamma w_k \tag{1}$$

$$z_k = h\left(X_{Tk},\, v_k\right) = \tan^{-1}\left(\left(y_{T_k} - y_{Ok}\right)/\left(x_{Tk} - x_{Ok}\right)\right) + v_k \tag{2}$$

Target motion state is $X_{Tk}{=}\left(x_T,\, y_T,\, \dot{x}_T,\, \dot{y}_T\right)_k^T$ and observer motion state is $X_{Ok}{=}\left(x_O,\, y_O,\, \dot{x}_O,\, \dot{y}_O\right)_k^T$, then

$$F = \begin{bmatrix} 1 & 0 & T & 0 \\ 0 & 1 & 0 & T \\ 0 & 0 & 1 & 0 \\ 0 & 0 & 0 & 1 \end{bmatrix}, \quad \Gamma = \begin{bmatrix} T^2/2 & 0 \\ T & 0 \\ 0 & T^2/2 \\ 0 & T \end{bmatrix}$$

The system noise is a zero mean Gaussian white noise process with covariance Q: $E\left[w_k w_j^T\right]{=}Q\delta_{jk}$, $Q = qI_2$ and I_2 is 2×2 identify matrix. The measurement noise v_k is a zero mean Gaussian white noise with covariance r: $E\left[v_k v_j\right] = r\delta_{kj}$.

Task of the problem is estimation of target track $\{X_{T0},\, X_{T1},\, \ldots,\, X_{Tn}\}$ is obtained according to observer trajectory $\{X_{O0},\, X_{O1},\, \ldots,\, X_{On}\}$, measurement sequence $\{z_0,\, z_1,\, \ldots,\, z_n\}$, q, r and Equations (1) and (2). Various forms of algorithms have been proposed and they mainly fall into two categories: batch processing and recursive type. The algorithm of this paper belongs to the later. EKF and UKF obtained directly target trajectory $\{X_{T0},\, X_{T1},\, \ldots,\, X_{Tn}\}$, SMC algorithms perform approximation of the PPDF, and then compute estimation of trajectory based on these samples and weights.

The EKF and UKF are repeated here for the completeness.

2.2. EKF and UKF Method

2.2.1. EKF

Considering a linear and time-invariant state equation and a non-linear measurement equation, EKF is given [6]

$$\begin{cases} \hat{X}_{Tk+1|k} = F\hat{X}_{Tk|k}, & P_{k+1|k} = FP_{k|k}F' + \Gamma Q\Gamma' \\ \hat{X}_{Tk+1|k+1} = \hat{X}_{Tk+1|k} + G_{k+1}\left[z_{k+1} - h\left(\hat{X}_{Tk+1|k}\right)\right], & P_{k+1|k+1} = \left[I - G_{k+1}\hat{H}_{k+1}\right]P_{k+1|k} \\ G_{k+1} = P_{k+1|k}\hat{H}'_{k+1} \times \left[\hat{H}_{k+1}P_{k+1|k}\hat{H}'_{k+1} + r\right]^{-1} & \end{cases} \tag{3}$$

2.2.2. UKF

UKF is to propagate mean and covariance information through UT method, a set of points (sigma points) are chosen according to specific method, the nonlinear function is applied to each point, in turn, to yield a cloud of transformed points. The statistics of the transformed points can then be calculated to form an estimate of nonlinearly transformed mean and covariance. If measurement equation is $Z = h(X)$, dimension of state X is n_X, its mean and covariance are $\bar{X}$ and P_X. The most general formulation augments the state vector with the process and noise terms to give an *augmented* $n_a = n_X + n_w + n_v$-dimensional vector, n_X, n_w, n_v are dimension of state, process noise and measurement noise, respectively.

$$X_a = [X \quad w \quad v]' \tag{4}$$

State equation is $\bar{X}_a = f_a(X_a)$, and measurement equation is $z = h_a(X_a)$. Mean and covariance of the augmented state is,

$$\bar{X}_a = \left[\bar{X} \quad 0_{n_w \times 1} \quad 0_{n_v \times 1}\right]', \quad P_{X_a} = \begin{bmatrix} P_X & 0 & 0 \\ 0 & Q & 0 \\ 0 & 0 & r \end{bmatrix} \tag{5}$$

General UKF algorithm is as fellow [9]:

① The set of sigma point is created by applying a sigma selection algorithm according to [9].

$$\hat{X}_{ai} = f_a(X_{ai}), \, i = 0, 1, \ldots, 2n_a \tag{6}$$

②

$$\bar{X}_a = \sum_{i=0}^{2n_a} W_i^{(m)} \hat{X}_{ai} \tag{7}$$

③

$$\hat{P}_{X_a} = \sum_{i=0}^{2n_a} W_i^{(c)} \left(\hat{X}_{ai} - \bar{X}_a\right)\left(\hat{X}_{ai} - \bar{X}_a\right)' \tag{8}$$

④

$$\hat{z}_i = h\left(\hat{X}_{ai}\right), \quad \bar{z} = \sum_{i=0}^{2n_a} W_i^{(m)} \hat{z}_i, \quad i = 0, 1, \ldots, 2n_a \tag{9}$$

⑤

$$\hat{S} = \sum_{i=0}^{2n_a} W_i^{(c)} (\hat{z}_i - \bar{z})(\hat{z}_i - \bar{z}), \tag{10}$$

⑥

$$\hat{P}_{Xz} = \sum_{i=0}^{2n_a} W_i^{(c)} \left(\hat{X}_{ai} - \bar{X}_a\right)(\hat{z}_i - \bar{z})' \tag{11}$$

⑦

$$\hat{X}_a = \bar{X}_a + W(z - \bar{z}), \quad W = \hat{P}_{Xz}\hat{S}^{-1}, \quad P_{X_a} = \hat{P}_{X_a} - W\hat{S}W^{-1} \tag{12}$$

2.3. SMCEKF and SMCUKF

In the Bayesian approach to dynamic state estimation one attempt to construct the PPDF of the state, based on all available information, including the sequence of received measurements. PDF of state is represented by a set of random samples and corresponding weight, and then mean and covariance are approximated. SMC filter in this paper consists of independent EK, UK filters, which are initialized by a set of random samples.

If $\left\{X^{(i)}, \, i = 1, \ldots, N\right\}$ is a set of support points, PDF, mean and covariance of the states are [2]:

$$p(X) \approx \sum_{i=1}^{N} \delta\left(X^{(i)}\right) W^{(i)}, \quad \sum_{i=1}^{N} W^{(i)} = 1 \tag{13}$$

The expected value of a function $h(X)$ of the random states X is

$$E[h(X)] \approx \sum_{i=1}^{N} h\left(X^{(i)}\right) W^{(i)} \tag{14}$$

Let $\left\{X^{(i)}, W^{(i)}\right\}$ denote a random measure that characterizes the joint posterior $p\left(X_k|Z_k\right)$. Using (14) with $h(X) = X$ and $h(X) = \left(X - \bar{X}\right)^2$ yields mean and covariance of random states, respectively. SMC is to compute $\left\{X^{(i)}, W^{(i)}\right\}$ of approximating PPDF recursively.

The measurement sequence is $\{Z_0, Z_1, \ldots, Z_n\}$, the sequence of all target states up to time k is $\{X_0, X_1, \ldots, X_n\}$, and the following notations will be used $p\left(X_k\right) = p\left(X_k|Z_k, \ldots, Z_0\right)$. SMC filter is a technique for implementing a recursive Bayesian filter [1, 2]:

$$\begin{aligned} p\left(X_k\right) &= \frac{p\left(Z_k|X_k, Z_{k-1}, \ldots, Z_0\right) P\left(X_k|Z_{k-1}, \ldots, Z_0\right)}{p\left(Z_k|Z_{k-1}, \ldots, Z_0\right)} \\ &= \frac{p\left(Z_k|X_k, Z_{k-1}, \ldots, Z_0\right) p\left(X_k|X_{k-1}, Z_{k-1}, \ldots, Z_0\right)}{p\left(Z_k|Z_{k-1}, \ldots, Z_0\right)} p\left(X_{k-1}\right) \\ &\propto p\left(Z_k|X_k\right) p\left(X_k|X_{k-1}\right) p\left(X_{k-1}\right) \end{aligned}$$

X_k is calculated form (1) with X_{k-1}, w_k in PF. Because uncertainty of the process model is small relatively, speed of moving particles to the regions of high likelihood is very slow, then resample introduces the loss of diversity among the particles, so it may lead to undesired clustering of the samples and eventually inaccurate results.

To overcome the problem, EK and UK is introduced to compute X_k instead of resampling. It prevents samples from particle degeneracy and collapse simultaneously. Particles move to regions of high likelihood (except for divergence), so performance of approximating PDF and algorithms are improved. Because EKF and UKF are introduced, it is obtained that

$$p\left(X_k\right) \propto p\left(Z_k|X_k\right) p\left(X_{k-1}\right) \tag{15}$$

$W_k^{(i)}$ in Eq. (13) can calculated as follow:

$$W_k^{(i)} \propto p\left(Z_k|X_k\right) W_{k-1}^{(i)} = \frac{p\left(Z_x|X_k\right) W_{k-1}^{(i)}}{\sum\limits_{i=1}^{N} p\left(Z_k|X_k\right) W_{k-1}^{(i)}} \tag{16}$$

Initial random samples of state PDF are given according to prior and Z_0:

$$X_0^{(i)} \sim N\left(X_0, P_0\right), \;\; i = 1, \ldots, N$$

Notation "$\sim$" indicates sample from a random distribution. $\left\{X_0^{(i)}, W_{k-1}^{(i)}\right\}$ and $p\left(Z_k|X_k^{(i)}\right)$ are calculated recursively by N independent EK or UK filters with $\left\{X_0^{(i)}, W_0^{(i)}\right\}$ and $W_k^{(i)}$ obtained form (16), the above is SMCEKF and SMCUKF methods.

Taken bearing-only tracking for example, the SMCEKF and SMCUKF are given as fellow:

① Get N samples from distribution $p\left(X_0^{(i)}|Z_0\right)$, $\left\{X_0^{(1)}, X_0^{(2)}, X_0^{(N)}\right\}$, $W_0^{(i)} = 1/N$, $i = 1, \ldots, N$

For bearing-only tracking, initial distribution is given in Section 3;

② For MCEKF, compute $\left\{X_1^{(i)}, P_{1|0}^{(i)}\right\}$ according to Eq. (3). For MCUKF, compute $\left\{X_1^{(i)}, S^{(i)}\right\}$ according to Eqs. (6)–(12);

③ For MCEKF,

$$p\left(z_1|X_1^{(i)}\right) = \frac{1}{\sqrt{2\pi} P_{1|0}^{(i)}} \exp\left[-\frac{1}{2}\left(\frac{z_1 - F X_1^{(i)}}{P_{1|0}^{(i)}}\right)^2\right] \tag{17}$$

For MCUKF,

$$p\left(z_1|X_1^{(i)}\right) = \frac{1}{\sqrt{2\pi}\hat{S}} \exp\left[-\frac{1}{2}\left(\frac{z_1 - FX_1^{(i)}}{\hat{S}}\right)^2\right] \tag{18}$$

④ Calculate $W_1^{(i)}$ with Eq. (16);
⑤ Calculate $\hat{X}_1$, $\hat{P}_1$ with Eq. (14);
⑥ Repeat ② to ⑤.

3. SIMULATION RESULTS

A single observer-target encounter is considered shown in Fig. 1. This observer platform flies in a circle of radius 4.25 km and at speed of 0.25 km/s. The target is flying with a CV motion and at speed (−0.2 km/s, −0.2 km/s) in the 100 s.

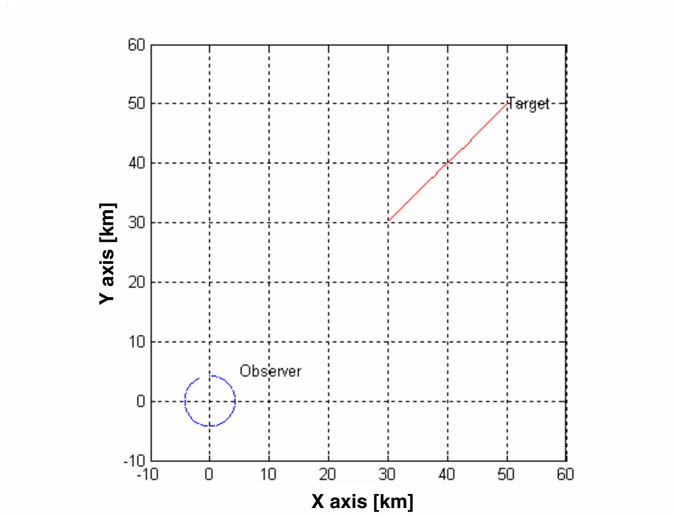

Figure 1: True target track geometry in the plane.

Small amount of process noise was used in the generation of trajectory with $q = 0.01$. The error standard deviation of angular measurement is $\sigma = 0.5°$. The performance of the filters is compared based on the standard deviation of errors in target position and velocity along the x- and y-axis. The error curves are estimated by averaging over 500 Monte-Carlo runs, and the number of random samples of initial state is 10. The sampling interval of observer is 1 s, and PDF of initial states is $N(X_{T0}, P_0)$, and $X_{T0} = [x_{T0}\ y_{T0}\ \dot{x}_{T0}\ \dot{y}_{T0}]'$. X_{T0} is taken as

$$x_{T0} = x_{O0} + r_0 \cos z_0, \quad y_{T0} = y_{O0} + r_0 \sin z_0, \quad \dot{x}_{T0} = 0, \quad \dot{y}_{T0} = 0 \tag{19}$$

$r_0 = (r_{\max} + r_{\min})/2 = (100 + 0)/2 = 50$ km. $r_{\max}$ and $r_{\min}$ can be taken as the maximum and the minimum range of sensor. For a CV model, we let [12]:

$$P_0 = \begin{bmatrix} \sigma_x^2 & \sigma_{xy}^2 & 0 & 0 \\ \sigma_{xy}^2 & \sigma_y^2 & 0 & 0 \\ 0 & 0 & \sigma_v^2 & 0 \\ 0 & 0 & 0 & \sigma_v^2 \end{bmatrix} \tag{20}$$

with

$$\begin{cases} \sigma_x^2 = r_0^2\sigma^2 \cos^2 z_0 + \sigma_r^2 \sin^2 z_0 \\ \sigma_y^2 = r_0^2\sigma^2 \sin^2 z_0 + \sigma_r^2 \cos^2 z_0 \\ \sigma_{xy}^2 = \left(\sigma_r^2 - r_0^2\sigma^2\right) \sin z_0 \cos z_0 \end{cases} \tag{21}$$

Covariance P_0, defined by Eq. (20), is calculated with $\sigma_r = 35$ km, $\sigma_v = 0.2$ km/s. For MCEKF and MCUKF, we get 10 samples: $X_{T0}^{(i)} \sim N(X_{T0}, P_0)$. Error performance curve is shown in Fig. 2

without considering the divergent runs. The number of divergent runs is 45 for EKF, and it is zero for other algorithms. Divergence is declared when the positional error $\sqrt{(\hat{x}-x)^2+(\hat{y}-y)^2}$ is greater than 50 km. Computational loads of various algorithms are shown in Table 1.

Table 1: Computational load of the four tracking algorithms.

Method	EKF	UKF	SMCEKF	SMCUKF
Times	0.029	0.366	0.35	3.659

Performance of SMCUKF and SMCEKF are superior to EKF and UKF. The difference between SMCEKF and SMCUKF is small, however, the time used in the SMCEKF is much less than the SMCUKF, and it is very close to UKF. Therefore SMCEKF is a more efficient approach. For comparison, a reference Cramer Rao limited bound [6] is gived in Fig. 1.

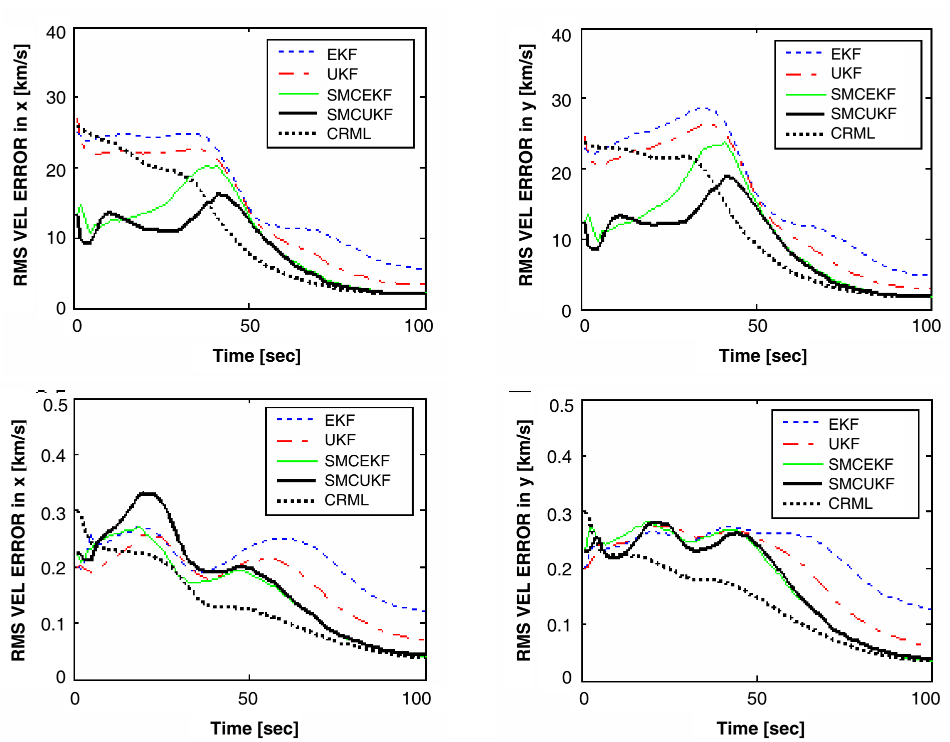

Figure 2: Error performance comparisons.

The number of samples is a compromise between performance and computational load. If expected performance is better, then the number of particles is increased. Otherwise, little samples are used. If one of the filters have been divergence, weight is go zero, cancel the filter to decrease the computational load.

4. CONCLUSION

The SMCEKF and SMCUKF algorithms are proposed to improve the performance of a class of non-linear systems. The algorithms introduce parallel independent EKFs and UKFs. The independence and efficiency of each filter are guaranteed and the errors of initial value and linearization could be decreased. Analysis and simulation results for the bearing only tracking problem have proved the validity of SMCEKF and SMCUKF algorithms. The results also show that the performance of SMCEKF and SMCUKF is greatly superior to the standard EKF and UKF.

REFERENCES

1. Heine, K., *A Survey Of Sequential Monte Carlo Methods*, 53–83, Tampare University of Technology, Departmant of Science and Engineering, 2005.

2. Ristic, B., S. Arulampalam, and N. Gordon, *Beyond the Kalman Filter-particle Filter for Tracking Applications*, 32–55, Artech House, 2004.
3. Nordlund, P.-J. and F. Gustafsson, "Sequential Monte Carlo filtering techniques applied to integrated navigation system," *Proceedings of the American Control Conference*, 4375–4380, Arlington, 2001.
4. Nordlund, P.-J., "Recursive state estimation of nonlinear systems with application to integrated navigation," *Technical Report LITH-ISY-R-2321*, 42–52, Department of Electronic Engineering, Linkoping University, SE-58183 Linkoping, Sweden, 2000.
5. Gordon, N. J., D. J. Salmond, and A. F. M. Smith, "Novel approach to nonlinear/non-Gaussian Bayesian state estimation," *IEE Proceedings-F*, Vol. 140, No. 2, 107–113, 1993.
6. Ristic, B. and M. S. Arulampalam, "Tracking a manoeuvring target using angle-only measurements: algorithms and performance," *Signal Processing*, 1223–1238, 2003.
7. Arulampalam, M. S., S. Maskell, N. Gordon, and T. Clapp, "A tutorial on particle filters for online nonlinear/non-Gaussian Bayessian tracking," *IEEE Transactions on Signal Processing*, 174–188, 2002.
8. Crisan, D. and A. Doucet, "A survey of convergence result on particle filtering methods for practitioners," *IEEE Transactions on Signal Processing*, 736–746, 2002.
9. Van der Merwe, R., A. Doucet, and N. de Freitas, "The unscented particle filter," *Technical Report CUED/F-INFENG/TR 380*, 7–10, Cambridge University Engineering Department, 2000.
10. Julier, S. J. and J. K. Uhlmann, "Unscented filtering and nonlinear estimation," *Proceedings of the IEEE*, 401–422, 2004.
11. Nardon, S. C., A. G. Lindgren, and K. F. Gong, "Fundamental properties and performance of conventional bearing-only target motion analysis," *Transactions on Automatic Control*, 775–787, 1984.
12. Blackman, S. and R. Popoli, *Design and analysis of Modern Tracking Systems*, 178–181, Artech House, 1999.

Applications of Pseudo-polar FFT in Synthetic Aperture Radiometer Imaging

Cheng Zhang[1,2], **Ji Wu**[1], **and Weiying Sun**[1],

[1]Center for Space Science and Applied Research, CAS, Beijing, China
[2]Graduate University of Chinese Academy of Sciences, Beijing, China

Abstract— In this study we analyzed the potential use of Pseudo-Polar FFT algorithm for image reconstruction of synthetic aperture radiometer, and developed an effective method to improve the image reconstruction accuracy and computational efficiency simultaneously. The advantage of the new algorithm is that it takes pseudo-polar grid instead of Cartesian grid to perform the inverse Fourier transform, and it involves only 1-D interpolation, which leading to a more fast and accurate performance. As a critical stage, the interpolation algorithms that perform the changing from polar grid to pseudo-polar grid are present. At last, the superiority of the new algorithm is validated by numerical simulation. It is believed that the new approach may have wide-spread application in science and practice for synthetic aperture radiometer system.

1. INTRODUCTION

The Synthetic aperture radiometer is an interferometric technology that introduced from radio astronomy in the late 1980s [1]. With the main benefits of simpler mechanical structure and high spatial resolution it is getting increasingly attractive. Recently, the NASA's ESTAR [2] and ESA's MIRAS [3] have been demonstrated successfully, and a C-band and X-band synthetic aperture radiometer also have been developed in china [4, 5]. Further more some institutes proposed and investigated the use of aperture synthesis techniques in millimeter wave for reconnaissance and surveillance applications [6]. All the activities set up an indication that the synthetic aperture radiometer will be dominant in the passive microwave remote sensing in the future.

The antenna array plays an important role in imaging. The antenna configurations, such as 'T', 'U' or 'Y' shapes and so on [7], are all have redundant baselines inevitably and lead to an enormous hardware expense. Then in order to further reduce the system complexity, a new rotate configuration that can achieve sufficient samples by rotating a simple non-redundant antenna array is proposed [8, 9], which is deemed to be the most practicable way. As the sampling data is distributed in circles, the conventional Cartesian FFT method could not be used directly. A general way is to interpolate the polar grid data to Cartesian grid. However, because of the large difference between them and the low accuracy of general 2-D interpolation methods, it would introduce large errors. It is noted that the idea of CLEAN method that broadly used in radio astronomy [10] and the Moor-Penrose inversion that used by ESTAR system [2] are not suitable for this case, because the former is based on the iterative algorithm suited for point sources image but not plane sources, and the later need complicated pre-calibrate work of hardware and has high computational complexity in 2-D situation.

In this paper we introduce the pseudo-polar FFT algorithm [11, 12] to the image reconstruction. We choose pseudo-polar grid as the halfway point instead of Cartesian grid. We interpolate the polar data to pseudo-polar grid firstly and perform the Pseudo-Polar Fourier transform at last to produce the image. As the pseudo-polar grid is more closed to polar gird and only 1D interpolation is needed, and the transform can also done by 1-D FFT with complexity of $O\{N2\log N\}$, the proposed new algorithm is more accurate and high-speed.

2. PSEUDO-POLAR FFT ALGORITHM

The Pseudo-Polar Fourier transform is based on a definition of a polar like grid constituted by concentric squares, shown as Fig. 1. The pseudo-polar grid points can be separated into two groups, basically vertical (BV) subsets, shown as hollow points in the figure, and basically horizontal (BH) subsets, shown as solid points. When the points are defined in frequency domain of $\xi \in [-\pi, \pi]^2$, their coordinates are given by

$$BH = \{\xi_y = \pi l/N, \xi_x = \xi_y \cdot 2m/N | -N/2 \leq m < N/2, -N \leq l < N\} \tag{1a}$$
$$BV = \{\xi_x = \pi l/N, \xi_y = \xi_x \cdot 2m/N | -N/2 \leq m < N/2, -N \leq l < N\} \tag{1b}$$

The Fourier transform of the BH and the BV points are completely parallel. Our description will refer to the BH points only. With the given Cartesian data $f[k_1,k_2]$, and plugging Eq. (1a) as the frequency coordinates into the Fourier transform equation, we obtain

$$\begin{aligned} F(\xi_{p,q}) = F[m,l] &= \sum_{k_1=0}^{N-1}\sum_{k_2=0}^{N-1} f[k_1,k_2]\cdot\exp\left(\frac{2\pi k_1 lm}{N^2}+\frac{\pi k_2 l}{N}\right) \\ &= \sum_{k_1=0}^{N-1}\exp\left(-i\frac{2\pi k_1 lm}{N^2}\right)\sum_{k_2=0}^{N-1} f[k_1,k_2]\cdot\exp\left(-i\frac{\pi k_2 l}{N}\right) \end{aligned} \tag{2}$$

Assuming $f[k_1,k_2]$is zero padded to $N\times 2N$, the inner summation part of Eq. (2) will be calculated as 1-D FFT

$$F_1[k_1,l] \equiv \sum_{k_2=0}^{N-1} f[k_1,k_2]\cdot\exp\left(-i\frac{\pi k_2 l}{N}\right) = \sum_{k_2=0}^{2N-1} f_2[k_1,k_2]\cdot\exp\left(-i\frac{2\pi k_2 l}{2N}\right) \tag{3}$$

Then the second summation part of Eq. (2) can be proceed as

$$F[m,l] = \sum_{k_1=0}^{N-1} F_1[k_1,l]\cdot\exp\left(-\frac{2\pi k_1 m}{N}\cdot\frac{l}{N}\right) \tag{4}$$

which is same as regular 1D-FFT with a factor $\alpha = l/N$ in its exponent part. This is known as the Fractional Fourier Transform, and can be computed efficiently with $30N\log N$ operations based on 1D-FFT. Adding to the previous stage complexity and cover both the BH and BV data, the whole forward transform of Pseudo-Polar Fourier transform is need $140N^2\log N$ operations.

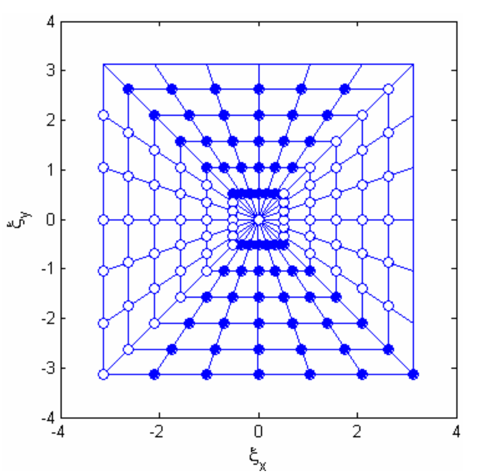

Figure 1: Schematic diagram of the pseudo polar grid ($N = 6$).

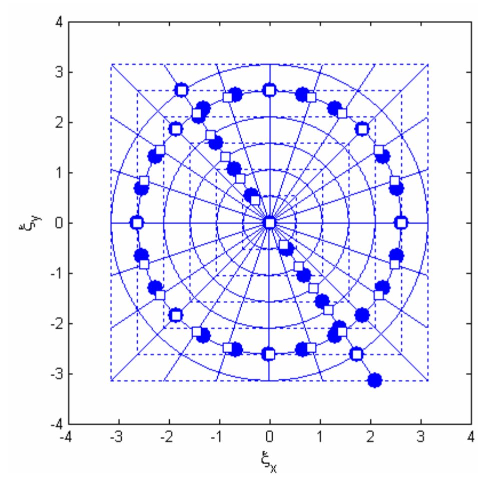

Figure 2: Schematic diagram of the interpolation stages.

The Pseudo-Polar FFT can be inversed by the method of Least-Squares (LS) with Conjugate Gradient (CG) algorithm. The optimization problem can be approached iteratively by

$$f_{k+1} = f_k - D\cdot T_{PP}^H(T_{PP}(f_k) - F) \tag{5}$$

where T_{PP} is the forward transform, D is the matrix that will speed up the convergence to the true solution, T_{PP}^H is the adjoint transform, theoretically same as T_{PP}, referring to BV it can be compute by

$$\tilde{f}[k_1,k_2] = \sum_{l=-N}^{N-1}\exp\left(i\frac{\pi k_2 l}{N}\right)\sum_{m=-N/2}^{N/2-l} F[m,l]\cdot\exp\left(i\cdot\frac{2\pi k_1 lm}{N^2}\right) \tag{6}$$

which could be done in $O\{N^2\log N\}$ operations. It can achieve high accuracy solution with only 2–6 iterations.

3. IMAGE RECONSTRUCTION ALGORITHM BASED ON PSEUDO-POLAR FFT

The fundamental theory of synthetic aperture imaging is based on the Van Cittert-Zernike theory. In summary, the receivers measures the cross correlations between all pairs of antennas to get the so-called visibility function

$$V_{kl}(u_{kl}, v_{kl}) = \frac{1}{\sqrt{\Omega_k \Omega_l}} \iint_{\xi^2+\eta^2\leq 1} \frac{T_B(\xi,\eta)}{\sqrt{1-\xi^2-\eta^2}} \cdot F_{nk}(\xi,\eta) F^*_{nl}(\xi,\eta) \cdot r_{kl}\left(-\frac{u_{kl}\xi + v_{kl}\mu}{f_0}\right) \cdot e^{(-j2\pi(u_{kl}\xi + v_{kl}\mu))} \mathrm{d}\xi \mathrm{d}\mu \tag{7}$$

where: Ω is antenna solid angle, $T_B(\xi,\eta)$ is brightness temperature, $(u_{kl}, v_{kl}) = (x_k - x_l, y_k - y_l)/\lambda$ is normalized antennas spacing that measured in wavelengths, $(\xi,\eta) = (\sin\theta\cos\varphi, \sin\theta\sin\varphi)$ is direction cosines, F_n is normalized antenna voltage pattern, r_{kl} is the so called fringe-wash function, $r_{kl} \approx 1$ for limiting narrow band case. So for an ideal interferometer the visibility function and the brightness temperature can be associated by Fourier transform.

The sampling data measured by the rotate scanning synthetic aperture radiometer is laid in circle polar grid, which could not be inversed through Cartesian IFFT directly. As described in the previous session we use Pseudo-Polar instead of Cartesian to be the interpolated destination grid. The 1-D interpolation involved can be separated into two steps, as shown in Fig. 2, the angular interpolation that rotate the sampling points, and the radial interpolation that square the circles.

The sampling data in a circle and be deemed as a periodic function with a period of 2π, so the angular interpolation problem can be solved by the periodic function sampling theorem, according to which, when given the periodic function x(t) with highest frequency $f_{max} = K/T$, it can be reconstructed exactly from $N \geq 2K+1$ of its uniformly spaced samples. The proof of this theorem is given in [13]. When we assume the visibility function $F(\rho,\theta)$ is angular band limited to K, it could be reconstructed by $2M \geq 2K+1$ sampling points according to

$$F(\rho_n, \theta) = \sum_{l=0}^{2M-1} F\left(\rho_n, \frac{\pi l}{M}\right) \frac{\sin\left[\frac{1}{2}(2M-1)\left(\theta - \frac{\pi l}{M}\right)\right]}{2M \sin\left[\frac{1}{2}\left(\theta - \frac{\pi l}{M}\right)\right]} \tag{8}$$

It's noted that $F(\rho,\theta)$ is not angular band limited in most cases, therefore the interpolation will produce certain artifacts in the reconstructed image. The errors can be controlled by increasing the sampling density.

The radial interpolation implemented after angular interpolation is the last stage to get the pseudo-polar grid. As it is known that the spatial domain corresponds to the sampling frequency is limited to a round disc of unit radius, $F(\rho,\theta)$ is band limit to 2 in ρ direction, and can be reconstructed exactly according to Shannon theory. But the sampling distance in ρ is not uniformly spaced in some case and the sampling length is limited. Then the uniform Sinc interpolation could not be used. However, the band limitation property implies the relatively smoothness of $F(\rho,\theta)$ in radial directions, a perfect interpolation is possible with appropriate samples. We considered the nonuniform Lagrange interpolation algorithm as the radial interpolation, which is defined as

$$F(\rho, \theta_n) = \sum_{i=0}^{n} F(\rho_i, \theta_n) \frac{w(\rho)}{(\rho - \rho_i) w'(\rho_i)} \tag{9}$$

where $w(\rho) = (\rho - \rho_0) \dots (\rho - \rho_n)$. Empirical studies indicated it has a good performance for radial interpolation.

4. RESULTS

We apply this new algorithm in an assumed imager system with 8-elements antenna array. There are 28 nearly even baselines altogether [14], shown as Fig. 3. In order to ensure no errors in the forward process of the simulation, we choose the Shepp-Logan phantom as the initial spatial image. Its frequency values can be calculate exactly. The Mean Square Errors (MSE) of the angular interpolations in each baseline is shown in Fig. 4, and the relative error of radial interpolation for the ray of 90° is shown in Fig. 5. We can see that the worst case error is lower than 10^{-4} for angular interpolation and 10^{-3} for radial interpolation. The best case error is about 10^{-17} for angular interpolation and 10^{-14} for radial interpolation. They are all in the acceptable field.

The next stage is taking Pseudo-Polar IFFT to obtain the final image. The result is shown as Fig. 6(b). Other Cartesian FFT based methods are also applied, such as the Delannay triangulation

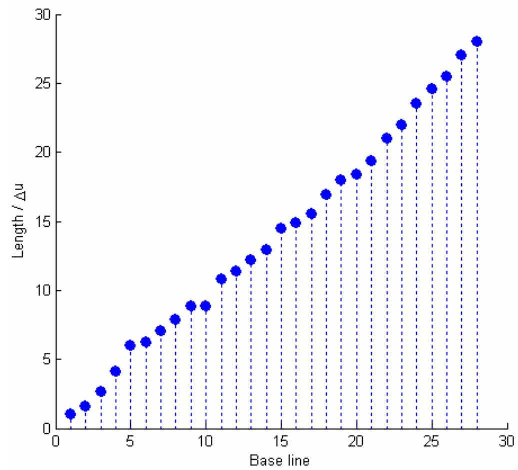

Figure 3: Baselines of 8 antenna array.

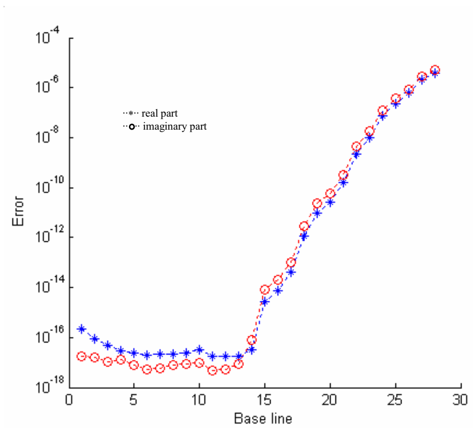

Figure 4: Errors of angular interpolation.

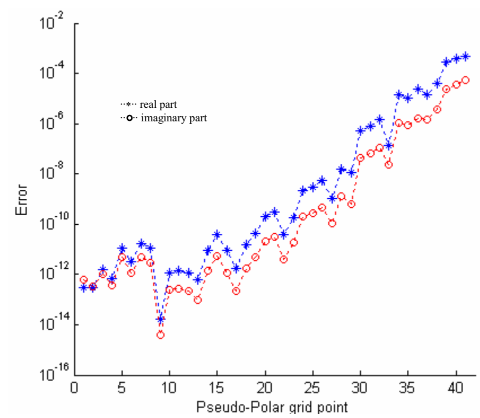

Figure 5: Errors of radial interpolation.

based linear interpolation and the Biharmonic Spline interpolation. The results are shown as Fig. 6(c) and Fig. 6(d). Table 1 exhibits the parameters of MSE, correlation coefficient (as a token of similarity) and running time of each method.

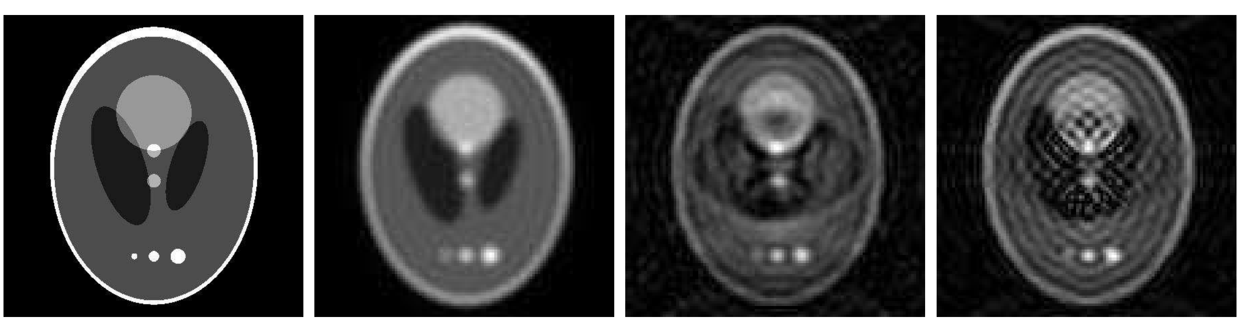

(a) (b) (c) (d)

Figure 6: The initial image (a) and the reconstruction results by the new algorithm (b), Linear (c), and B-spline (d).

The simulations show that the linear method has the worst image quality. The B-spline method needs a long running time. The new method is not only has the best image quality but also the fast running speed.

Table 1: Comparison between the used methods.

Methods	Error(MSE)	Similarity	Running time
Method of this paper	0.1890	0.8530	3.6400 s
Linear	0.2569	0.8026	0.2970 s
B-spline	0.2169	0.8315	29.6410 s

5. CONCLUSIONS

In this article we developed a fast and accurate method for the rotate scanning synthetic aperture radiometer imaging. Since the frequency domain is sampled in polar coordinates, we interpolated the sampling data to pseudo polar grid by 1-D interpolation algorithm and applied Pseudo-Polar IFFT algorithm to produce the image. The performance of the new algorithm was demonstrated with a simulated 2-D scene for a given imager system. Both from the theoretical and empirical view points, the new approach is not only efficient with complexity of $O\{N^2 \log N\}$, but also more accurate than the known state-of-the-art methods based on Cartesian FFT. Furthermore, the interpolation stages were analyzed which plays the key role in the image reconstruction. Future work might consider various methods for improvements.

ACKNOWLEDGMENT

This work was supported by NSFC, project No. 40574070.

REFERENCES

1. Ruf, C. S., C. T. Swift, A. B. Tanner, and D. M. Le Vine, "Interferometric synthetic aperture microwave radiometry for the remote sensing of the earth," *IEEE Trans. G. R. S*, Vol. 26, No. 9, 597–611, 1988.
2. Le Vine, D. M., et al., "ESTAE: A synthetic aperturer microwave radiometer for remote sensing applications," *Proceedings of the IEEE*, Vol. 82, No. 12, 1787–1801, 1994.
3. Martin-Neira, M., Y. Menard, J. M. Goutoule, and U. Kraft, "MIRAS: a two-dimensional aperture synthesis radiometer," *Proc. IEEE IGARSS*, Vol. 3, 1323–1325, 1994.
4. Wu, J., H. Liu, et al., "Research activity on synthetic aperture radiometry in CSSAR/CAS," *Progress In Electromagnetics Research Symposium*, 1–5, Huangzhou, China, August 2005.
5. Liu, H., J. Wu, et al., "The CAS airborne x-band synthetic aperture radiometer: system configuration and experimental results," *Proc. IEEE IGARSS*, Vol. 3, 2230–2233, 2004.
6. Markus, P., S. Helmut, and D. Stephan, "High resolution passive millimeter-wave imaging technologies for reconnaissance and surveillance," *Proceedings of SPIE*, Vol. 5077, 77–87, 2003.
7. Kraft, U. R., "Dornier satellite syst and gmbh, munich, two-dimensional aperture synthesis radiometers in a low earth orbit mission and instrument analysis," *Proc. IEEE IGARSS*, Vol. 2, 866–868, 1996.
8. Wu, J., H. Liu, et al., "The rotate mother & son satellite system for passive microwave imaging," China Patent, App. No. 200510123633.2, Pub. No. CN1782734, 2005.
9. Jirousek, M., M. Peichl, et al., "A multi-frequency microwave aperture synthesis radiometer for high resolution imaging," *Proc. IEEE IGARSS*, Vol. 3, 2222–2225, 2004.
10. Schwarz, J. J., "Mathematical statistical description of the iterative beam removing technique (method CLEAN)," *Astronomy and Astrophysics*, Vol. 65, 345–356, 1978.
11. Averbuch, A., R. Coifman, D. L. Donoho, and M. Israeli, "Fast slant stack: a notion of radon transform for data in a cartesian grid which is rapidly computible, algebraically exact, geometrically faithful and invertible," Technical Report, Statistics Department, Stanford University, 2003.
12. Keller, Y., A. Averbuch, and M. Israeli, "A pseudopolar FFT technique for translation, rotation and scale-invariant image registration," *IEEE Trans. Image Process*, Vol. 14, No. 1, 12–22, 2005.
13. Stark, H. and M. Wengrovitz, "Comments and corrections on the use of polar sampling theorems in CT," *IEEE Trans on Acoust., Speech, Signal Processing*, Vol. 31, No. 5, 1329–1331, 1983.

14. Sun, W. Y., B. Y. He, and J. Wu, "Optimization of fourier plane coverage of antenna arrays for SPORT," *Proc. PIERS*, Vol. 1, No. 5, 533–53, 2005.

Backscattering Border Effects for Forests at C-band

L. Villard and P. Borderies

ONERA, France

Abstract— A coherent model for simulating interaction of electromagnetic waves with forests has been developed. It allows the retrieval of interferometric and fully polarimetric data. Forests considered, including finite size ones, are generated from a description following ground truth. This model is used here to simulate the impact of border effects in the monostatic case with high resolution.

1. INTRODUCTION

Radar remote sensing of forests turns out to be of great importance for environmental issues and military ones. To predict and analyze the performances, direct discrete models has been proposed (see [1–5] for example) to account for the wave interaction addressing SAR configurations. Most of these models assume that overflown areas are horizontally statistically homogeneous and of infinite extent. However, borders are often present in SAR images. Logically, their role is enhanced when the imaged landscape is composed of parcels of relatively small extent, and also when the SAR resolution is important. In these cases, simulation of SAR data require correct account of the presence of these boundaries.

In the first part of the paper it is described how the electromagnetic model takes into account these effects. Section 3 illustrates and analyses the results obtained in C-band, stating from previous simulations matched to ERS data [7].

2. MODEL PRESENTATION

2.1. Scene Description

The zone we intend imaging is rectangular, of size Lx^*Ly, with a resolution of dx^*dy (see Fig. 1). This zone may include one rectangular parcel of forest, of size l^*h, tilted with respect to Ox by an angle α. The forest area is generated using a classical multi layer description, which might fit incoherent, monostatic models like for example [1] or [4] or coherent models like [2, 3, 5]. Each pixel in each layer is randomly filled with the more appropriate elements, following statistics representative of in-situ measurements data in terms of sizes, composition, orientations and concentrations of typical discrete constituents. These constituents are represented by canonical elements: flat homogeneous ellipsoïds for leaves and finite homogeneous cylinders for branches or trunks. Forest soil is characterized by its root mean square height and a two dimensional exponential correlation function. Outside the forest parcel, we assume here a bare soil following the same characterization but with distinct parameters.

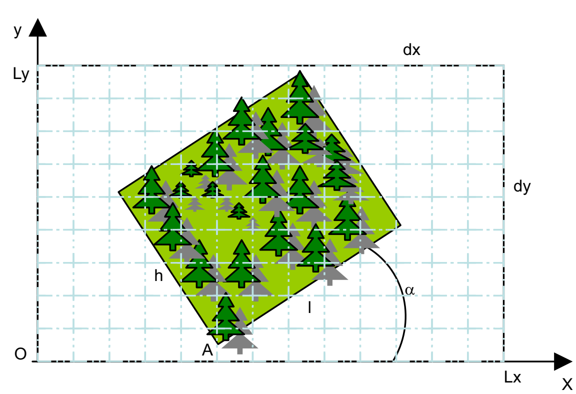

Figure 1: Scene geometry.

2.2. Electromagnetic Computation

Originality of the model lies in its ability of encompassing finite size forests whatever the radar resolution which imply boundary and 3D migration effects. To perform the media electromagnetic response we use Born extended approximation, like in [2, 3] and [5] for example. Contributions of all the scatters present in the scene are coherently summed for all polarizations combinations: this approach is fully polarimetric and phase preserving so it allows full polarimetric, interferometric and POLINSAR simulations. For each scatter we can then distinguish several mechanisms:

Volume contribution: Each element is envisioned as a discrete scatter which scattering matrix is analytically known: see [8] for ellipsoïds, [9, 10] for finite size cylinders. Influence of the surrounding scatters are accounted for with Foldy-Lax approximation through the use of an effective propagation constant (attenuation) derived from the forward scattering theorem [7]. Geometrical computations are performed to compute all intersection points if any between emitter-scatter ray and all vertical and horizontal boundaries of the layers. This process is repeated for the scatter-receiver ray. Then complex transmittivity matrices [4] factor between emitter and scatter and between scatter and receiver are computed taking into account all eventual path lengths in each layer.

Soil contribution: We use Integral Equation Method [13]. To account for speckle effects and fit with observed data, we spread the backscattering coefficient on the pixel surface with sub-sampling it and attributing to it a random phase, which traduces large scale roughness.

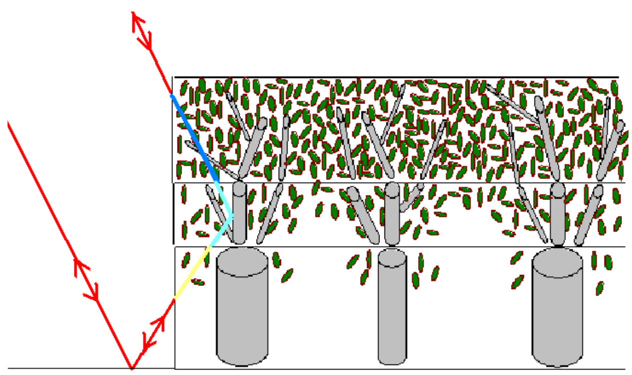

Figure 2: Layer decomposition.

Interaction volume/soil: For each path considered, similar geometrical computations are implemented (see Fig. 2) and subsequent transmissivity matrices derived. For each mechanism, soil specular reflection is accounted for through modified Fresnel coefficients [16, volume 1].

We then can generate two kind of outputs. Traditional ones consists in the complex summation of all the contributions for all the scattereres belonging to a given cell (idx, jdy). In this case border effects emphasize image contrasts [14], reinforcement ahead and shadowing effects at the back, as we can see in Fig. 3. Nevertheless, in high resolution case with low incidence and finite areas, we can't neglect migration effects so that we need range gated data (equivalent to raw data with a perfect azimuth compression). Each mechanism related to a given scattering element is further located in its corresponding range gate, keeping the azimuth location of the scattering element, before the complex summation of scattering events included in a cell (range, azimuth).

Validation of previous versions of this code have been performed first with comparing with experimental data obtained with ERS on the Fontainebleau forest at C band [5] for the radiometry and with checking expected symmetries in the amplitudes and phases of polarimetric interferometric observables on a canonical random volume over ground case. The present code, with forests of infinite horizontal extent (border effects inhibited), reproduces the previous monostatic results. When matched to parcels, we will see in Section 3 that it retrieves these ERS data.

3. C-BAND RESULTS

We present here radar simulation results to investigate the response of a forest of arbitrarily reduced size based on the ground truth [7] extracted from Fontainebleau area. We choose a surface of 50*45 meters square which is sufficient to fully represent the border effect for the height of 14.5 m at 23 degrees incidence angle (Fig. 8) without introducing unnecessary computations. The parcel is located (see Fig. 3) at coordinates (25, 45, 0) and the radar at (50, 330.103, 785.103). We also

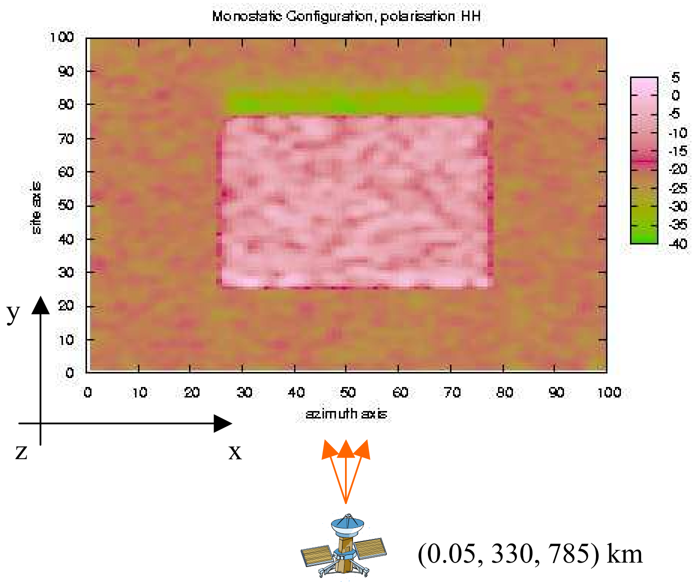

Figure 3: Radar and parcel configuration.

consider two different periods during the year: March and September. For each period we show the VV range gated image and the evolution of the VV backscattered coefficient along the site axis, after taking the average over the azimuth one.

The main differences between the seasons concern the humidity which affects dielectric constants and also the leaves presence or not. We also consider in the two cases a similar soil outside the forest. Humidity rate decrease from 53% in March to 47% in September for vegetation and from 36% to 17% for the soil which fit to the respective dielectric values: (13.48, −6,979), (10.92, −5.967) and (18.12, −2.84), (8.23, −1.04).

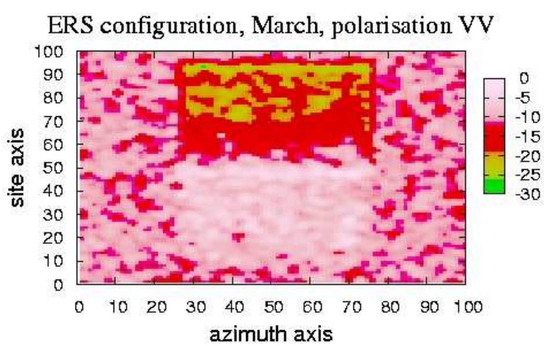

Figure 4: March image.

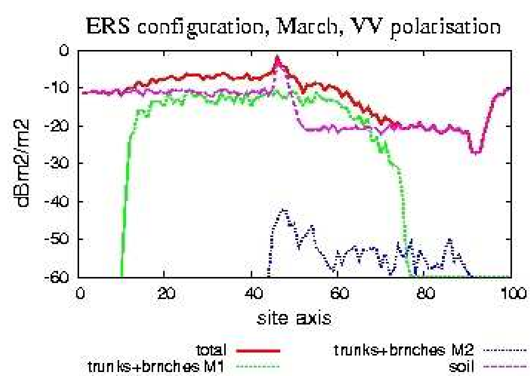

Figure 5: March profile.

In Figs. 4 and 5 we can see the energy level for each radar echo and for each electromagnetic mechanism, which evolution can be easily explained by means of geometrical considerations as shown in Fig. 6. First we have the soil only (before zone one), then gradually the high layer contributions to the bottom one. We haven't got a linear increment because of the fact that scatterers are more and more extinguished by the depth penetration. At 45 m, we can clearly recognize the beginning of the forest with the double bounce contribution, which imply an significant peak to the total contribution as the trunks ahead of the plot aren't extinguish as those in the core, that's a typical border effect. The soil contribution also present a peak because the soil inside is rougher and wetter than outside. Its linear decrement gives directly a idea of the media extinction. The third zone (between 51 meters to 56) is also interesting because it will give the same result as

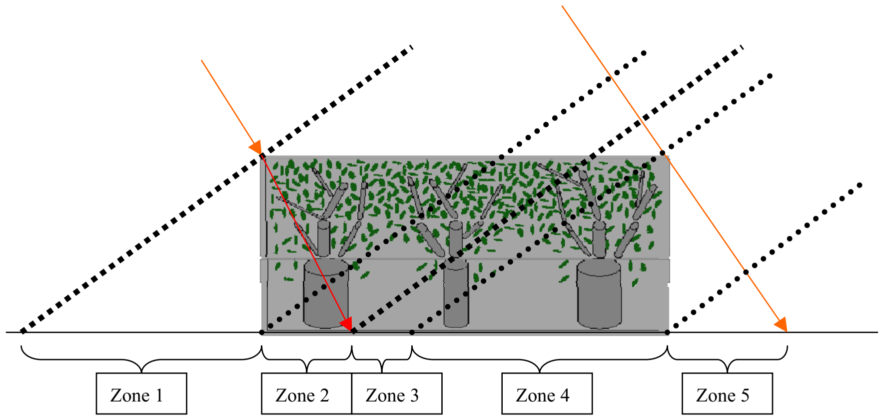

Figure 6: Geometry of range gating.

in the infinite forest case. Indeed we retrieve an energy level around $-8.5\,\mathrm{dbm}^2/\mathrm{m}^2$ given by ERS campaigns. In zone 4, the backscattering decrease gradually as radar cells contains less volume content. In zone 5 (90–96 m) we have only the soil part but lower than the bare soil due to the shadowing effect.

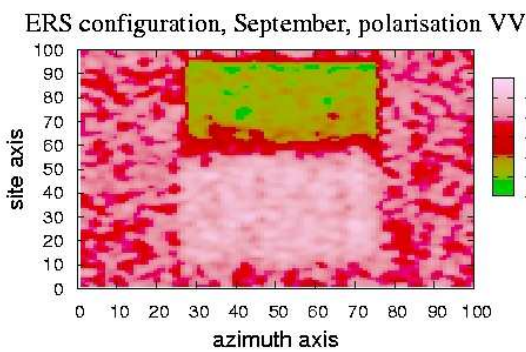

Figure 7: September image.

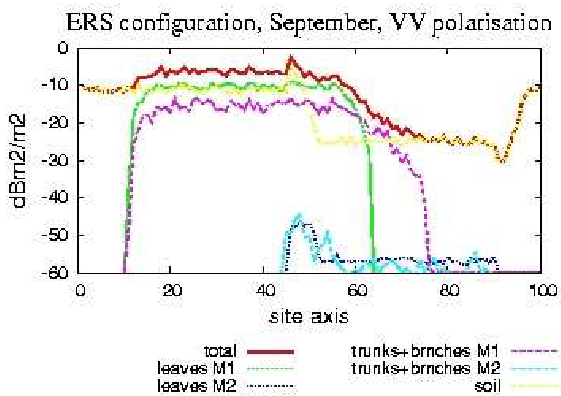

Figure 8: September profile.

In the second simulation, we can observe the same trends except the fact that the leaves presence is of great importance in the total level. In Fig. 8, $M1$ means the volume contribution and $M2$ the double bounce. It is interesting to see that extinction is about 5 db higher and that the leave volume is the major contribution.

4. CONCLUSION

The coherent, polarimetric scattering code for forests of finite extent presented here has shown its ability to reproduce the complex border effects arising with high resolution imaging SAR due the vertical stratification of the forests. The results (total field) presented here have shown to be coincident with reported experimental ones in the part of the parcel where border effects are absent, thereby validating the simulations, but possibly significantly higher or lower in the border zone. The border influence on the partial contributions is much more significant, in their extent and in the variation of their amplitude. Future prospects include the analysis of these effects as a function of the radar parameters, including the bistatic case.

REFERENCES

1. Ulaby, F. T. and K. Sarabandi, "Michigan microwave canopy scattering model," *Int. J. Remote Sens.*, Vol. 11, No. 7, 1223–1253, 1990.
2. Sarabandi, K., "Δk-radar equivalent of interferometric SAR's: A theoretical study for determi-

nation of vegetation height," *IEEE Trans. Geosc. Remote. Sensing*, Vol. 35, 1267–1276, Sept. 1997.

3. Marliani, F., S. Paloscia, P. Pampaloni, and J. A. Kong "Simulating coherent backscattering from crops during the growing cycle," *IEEE Transactions on Geoscience and Remote Sensing*, Vol. 40, No. 1, January 2002.
4. Ruiz, C., P. Borderies, I. Chênerie, E. Mougin, and C. Proisy, "Modeling of electromagnetic waves interaction with forest canopies," *CEOS Workshop*, Toulouse, October 1999.
5. Ruiz, C. and P. Borderies, "Sensitivity analysis for forest interferometric, polarimetric observables estimation," *Proceeding of Polinsar2005*, Frascatti, Italy, January 2005.
6. Tsang, L., J. A. Kong, and R. Shin, *Theory of Microwave Remote Sensing*, Wiley Interscience, 1985.
7. Proisy, C. and E. Mougin, "Temporal variations of interferometric coherence over a deciduous forest," *Proc. Committee on Earth Observation Satellites Workshop*, Toulouse, France, October 1999.
8. Karam, M. A. and A. K. Fung, "Leaf-shape effects in electromagnetic wave scattering from vegetation," *IEEE Transactions on Geoscience and Remote Sensing*, Vol. 27, No. 6, 687–697, 1989.
9. Karam, M. A. and A. K. Fung, "Electromagnetic scattering from a layer of finite randomly oriented, circular cylinders over a rough interface with application to vegetation," *Int. J. Rem. Sens.*, Vol. 9, No. 6, 1109–1134, 1988.
10. Tsang, L., J. A. Kong, and R. Shin, *Theory of Microwave Remote Sensing*, Vol. 3, Wiley Interscience, 19...
11. Ulaby, F. T. and M. A. El-Rayes, "Microwave dielectric spectrum of vegetation — II: Dual-dispersion model," *IEEE Transactions on Geoscience and Remote Sensing*, Vol. GE, 550–557, 1987.
12. Fung, A. K., *Microwave Scattering and Emission Models and Their Applications*, Artech House, 1994.
13. Koudogbo, F., P. Combes, and H.-J. Mametsa, "Numerical and experimental validations of IEM for bistatic scattering from natural and manmade rough surfaces."
14. Villard, L., P. Borderies, and J. B. Laforest, "Bistatic synthetic aperture radar simulation for forests including border effects," *ICR Conference Proceedings*, Shanghai, China, 17–20 Oct., 2006.

Effects of Fresnel Corrections in the Scattered Field of General Ellipsoids

J. Y. Koay, H. T. Ewe, and H. T. Chuah

Multimedia University, Malaysia

Abstract— The study of the scattered field of non-spherical scatterers is becoming an important field, especially in the remote sensing of vegetation. In this study, the scattered field of general ellipsoidal scatterers is formulated based on the generalized Rayleigh-Gans approximation, in which at least one of the dimensions of the ellipsoid is comparably smaller than the wavelength. The scattered field is formulated for the case in which far field approximations are used, as well as for the case in which the Fresnel zone effects are included. Results show that when the Fresnel corrections are considered, the calculated backscattering cross section gives a better match with measurement data compared to when far field approximations are used.

The generalized Rayleigh-Gans approximation has been widely used in the calculation of scattered fields of non-spherical scatterers such as circular disks, needles and cylinders [1]. In such calculations however, far field approximations are usually used. The importance of including the Fresnel zone effects in the calculation of the scattered fields in a medium with closely spaced scatterers has been studied for the cases of circular disks and needles [2, 3], as well as for cylinders [3].

In this study, the effects of Fresnel corrections in the scattered field of general ellipsoids will be analyzed. The scattered field of the general ellipsoid is formulated based on the generalized Rayleigh-Gans approximation [4], where the scattered field is given by [5]:

$$\hat{p}_{sl} \cdot \bar{E}_{sl}(\bar{r}) = \frac{k^2(\varepsilon_r - 1)}{4\pi} \int\limits_{V''} \frac{\exp(-jk|\bar{r} - \bar{r}''|)}{|\bar{r} - \bar{r}''|} \left(\hat{p}_{sl} \cdot \bar{E}_{\text{int}}\right) d\bar{r}'' \tag{1}$$

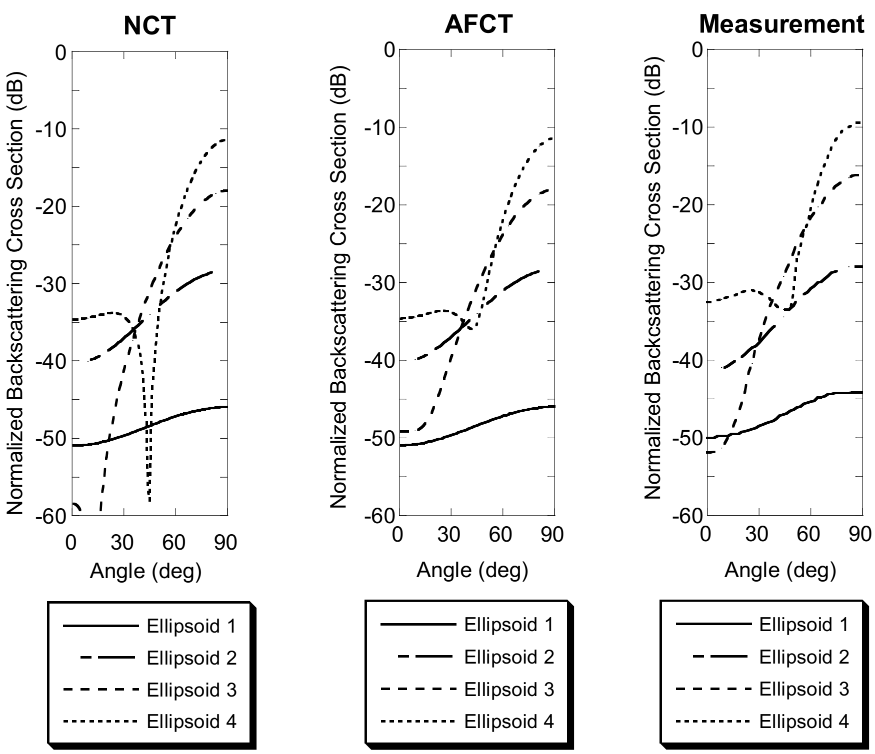

Figure 1: Comparisons between calculated values with and without Fresnel corrections and measured values of the normalized backscattering cross section for four prolate spheroids illuminated by a circularly polarized wave over various incident angles.

where $\bar{E}_{\text{int}}$ is the internal field of the scatterer, $\hat{p}_{sl}$ the scattered polarization unit vector in the local frame and V'' refers to the volume of the scatterer. $\bar{r}$ is the local frame location vector at the observation point. The vector $\bar{r}''$ is the local frame location vector for the volume element in the scatterer. The term $|\bar{r}-\bar{r}''|$ can be approximated by [2,3]:

$$\left|\bar{r}-\bar{r}''\right| \approx r - \hat{s}'' \cdot \bar{r}'' + \frac{r''^2}{2r}\left[1-\left(\hat{s}''\cdot\hat{r}''\right)^2\right] \tag{2}$$

where $\hat{s}'' = \dfrac{\bar{r}}{r}$, and $\hat{r}'' = \dfrac{\bar{r}''}{r''}$.

In far field approximations, only the first two terms of (2) are considered. To include the Fresnel zone effects, all the terms in (2) are used instead.

Comparisons between results for the normalized backscattering cross section of prolate spheroids calculated using far field approximations (NCT) and with the Fresnel zone effects (AFCT) are shown in Figure 1, together with results obtained through measurements in [6]. It is observed that the backscattering cross section calculated with Fresnel corrections are generally in good agreement with the measured values, and perform better when compared to the theoretical results employing far field approximations.

REFERENCES

1. Karam, M. A., A. K. Fung, and Y. M. M. Antar, "Electromagnetic wave scattering from some vegetation samples," *IEEE Transactions on Geoscience and Remote Sensing*, Vol. 26, No. 6, 799–807, 1988.
2. Fung, A. K., M. F. Chen, and K. K. Lee, "Fresnel field application applied to scattering from a vegetation layer," *Remote Sensing of Environment*, Vol. 23, 35–50, 1987.
3. Ewe, H. T. and H. T. Chuah, "A study of fresnel scattered field for non-spherical discrete scatterers," *Progress In Electromagnetics Research*, PIER 25, 189–222, 2000.
4. Schiffer, R. and K. O. Thielheim, "Light scattering by dielectric needles and disks," *Journal of Applied Physics*, Vol. 50, No. 4, 2476–2483, 1979.
5. Fung, A. K., *Microwave Scattering and Emission Models and Their Applications*, Artech House, Norwood, Massachusetts, 1994.
6. Allan, L. E. and G. C. McCormick, "Measurements of the backscatter matrix of dielectric bodies," *IEEE Transactions on Antennas and Propagation*, Vol. 28, No. 2, 166–169, 1980.

Toolbox for Calculation of Optical Forces and Torques

T. A. Nieminen, V. L. Y. Loke, G. Knöner, and A. M. Brańczyk
The University of Queensland, Australia

Abstract— We describe a toolbox, implemented in Matlab, for the computational modelling of optical forces and torques.

The optical forces and torques that are used for optical trapping, micromanipulation, and binding are essentially the result of scattering by the trapped particle altering the momentum or angular momentum flux if the incident laser beam. Thus, computational modelling of such forces consists of solving the electromagnetic scattering problem, and finding the changes in these fluxes.

At first glance, the problem appears quite straightforward. In a typical optical tweezers application, one has a single particle — usually a homogeneous isotropic sphere — that is not too large compared to the wavelength interacting with the trapping beam. Given that scattering by a sphere is one of the few cases where an analytical solution is available — the Lorenz-Mie solution [1, 2] — it is somewhat surprising that so much of the work done on modelling optical tweezers has made use of approximate methods such as geometric optics or Rayleigh scattering, neither of which are valid for particles of the size usually trapped.

However, this apparent simplicity conceals two major difficulties. Firstly, optical tweezers makes use of a highly focussed laser beam, while most treatments of the theory of scattering, and available computer codes, assume plane wave illumination. Indeed, the work of Lorenz and Mie made this same assumption.

Secondly, since the incident field is *not* a plane wave, the scattering by the particle depends on it's position within the beam. This leads to the need for repeated calculations. For example, to find the equilibrium position of a particle in an optical tweezers trap can require dozens of calculations, which determining the force as a function of position can require thousands of calculations, even if we only do so in a single plane. This appears to explain the lack of widespread application of general methods of solution of electromagnetic scattering such as the finite-difference time-domain method (FDTD) and finite element methods, although both have been applied to the problem of modelling optical tweezers [3–5]. The requirement for efficiency greatly reduces the utility of such general methods.

However, the extension of the Lorenz–Mie theory to arbitrary illumination is known — usually called generalised Lorenz-Mie theory (GLMT) — and has been used to model optical tweezers, including some thorough theoretical treatments [6–11]. The chief weakness of GLMT is its restriction to homogeneous isotropic spheres. A limited range of other shapes, such as spheroids, can also be treated in a similar manner [12, 13].

Unfortunately, none of these efforts appear to have resulted in publically available codes for the modelling of optical tweezers, optical micromanipulation, or optical binding. While there are many descriptions of the algorithms etc. available in the literature, the mathematical intricacy of the theory makes implementation in computer code challenging for the newcomer. Given this significant barrier to entry, and the value that reliable and accurate computational modelling can add to research we feel that it is important to make suitable tools for the modelling of optical trapping and micromanipulation freely available. Our project is described at url: http://www.physics.uq.edu.au/people/nieminen/software.html, where our code — implemented in Matlab — is available.

Our code makes use of the T-matrix description of scattering [14–16], which can be thought of as the further extension of the GLMT to arbitrary particles. As we have rotated and aligned non-spherical particles for some years, this has been necessary for the modelling of our own experiments. Furthermore, we also include the ability to model trapping by arbitrary laser beam modes, including Laguerre-Gauss modes which carry orbital angular momentum about the beam axis and can be used to rotate trapped particles.

Below, we describe our methods for the modelling of optical tweezers, typical use of our code, and our plans for future work to further improve our toolbox.

1. MODELLING OPTICAL TWEEZERS WITH THE T-MATRIX METHOD

The T-matrix method in wave scattering is essentially a Hilbert space description of the scattering properties of the scatterer. This involves writing the relationship between the wave incident upon a scatterer, expanded in terms of a discrete sufficiently complete basis set of functions $\psi_n^{(\mathrm{inc})}$, where n is mode index labelling the functions, each of which is a solution of the Helmholtz equation,

$$U_{\mathrm{inc}} = \sum_n^{\infty} a_n \psi_n^{(\mathrm{inc})}, \tag{1}$$

where a_n are the expansion coefficients for the incident wave, and the scattered wave, also expanded in terms of a basis set $\psi_k^{(\mathrm{scat})}$,

$$U_{\mathrm{scat}} = \sum_k^{\infty} p_k \psi_k^{(\mathrm{scat})}, \tag{2}$$

where p_k are the expansion coefficients for the scattered wave, is written as a simple matrix equation

$$p_k = \sum_n^{\infty} T_{kn} a_n \tag{3}$$

or, in more concise notation,

$$\mathbf{P} = \mathbf{T}\mathbf{A} \tag{4}$$

where T_{kn} are the elements of the T-matrix. Since here we are interested in electromagnetic scattering, the functions making up the basis must be divergence-free solutions of the vector Helmholtz equation.

Since the basis functions are discrete, this method lends itself well to representation of the fields on a digital computer, provided that the geometry of the problem permits expansion of the waves as discrete series in terms of the chosen basis, that the response of the scatterer to the incident wave is linear, and that the expansion series for the waves can be truncated at a finite number of terms. For a finite scatterer, if we make use of spherical coordinates, the convergence of the series is well-behaved and known [17].

The T-matrix depends only on the properties of the particle — its composition, size, shape, and orientation — and the wavelength, and is otherwise independent of the incident field. This means that for any particular particle, the T-matrix only needs to be calculated once, and can then be used for repeated calculations. This is the key point that makes this a highly attractive method for modelling optical trapping and micromanipulation, providing a significant advantage over many other methods of calculating scattering where the entire calculation needs to be repeated.

2. INCIDENT AND SCATTERED WAVE EXPANSIONS

The natural choice of coordinate system for optical tweezers is spherical coordinates centered on the trapped particle. Thus, the incoming and outgoing fields can be expanded in terms of incoming and outgoing vector spherical wavefunctions (VSWFs):

$$\mathbf{E}_{\mathrm{in}} = \sum_{n=1}^{\infty} \sum_{m=-n}^{n} a_{nm} \mathbf{M}_{nm}^{(2)}(k\mathbf{r}) + b_{nm} \mathbf{N}_{nm}^{(2)}(k\mathbf{r}), \tag{5}$$

$$\mathbf{E}_{\mathrm{out}} = \sum_{n=1}^{\infty} \sum_{m=-n}^{n} p_{nm} \mathbf{M}_{nm}^{(1)}(k\mathbf{r}) + q_{nm} \mathbf{N}_{nm}^{(1)}(k\mathbf{r}). \tag{6}$$

where the VSWFs are

$$\begin{aligned} \mathbf{M}_{nm}^{(1,2)}(k\mathbf{r}) &= N_n h_n^{(1,2)}(kr) \mathbf{C}_{nm}(\theta,\phi) \qquad (7) \\ \mathbf{N}_{nm}^{(1,2)}(k\mathbf{r}) &= \frac{h_n^{(1,2)}(kr)}{krN_n} \mathbf{P}_{nm}(\theta,\phi) + N_n \left(h_{n-1}^{(1,2)}(kr) - \frac{n h_n^{(1,2)}(kr)}{kr} \right) \mathbf{B}_{nm}(\theta,\phi) \end{aligned}$$

where $h_n^{(1,2)}(kr)$ are spherical Hankel functions of the first and second kind, $N_n = [n(n+1)]^{-1/2}$ are normalization constants, and $\mathbf{B}_{nm}(\theta,\phi) = \mathbf{r}\nabla Y_n^m(\theta,\phi)$, $\mathbf{C}_{nm}(\theta,\phi) = \nabla \times (\mathbf{r} Y_n^m(\theta,\phi))$, and

$\mathbf{P}_{nm}(\theta,\phi) = \hat{\mathbf{r}}Y_n^m(\theta,\phi)$ are the vector spherical harmonics [14–16, 18], and $Y_n^m(\theta,\phi)$ are normalized scalar spherical harmonics. The usual polar spherical coordinates are used, where θ is the co-latitude measured from the $+z$ axis, and ϕ is the azimuth, measured from the $+x$ axis towards the $+y$ axis.

$\mathbf{M}_{nm}^{(1)}$ and $\mathbf{N}_{nm}^{(1)}$ are outward-propagating TE and TM multipole fields, while $\mathbf{M}_{nm}^{(2)}$ and $\mathbf{N}_{nm}^{(2)}$ are the corresponding inward-propagating multipole fields. Since these wavefunctions are purely incoming and purely outgoing, each has a singularity at the origin. Since fields that are free of singularities are of interest, it is useful to define the singularity-free regular vector spherical wavefunctions:

$$\mathbf{RgM}_{nm}(k\mathrm{r}) = \frac{1}{2}[\mathbf{M}_{nm}^{(1)}(k\mathrm{r}) + \mathbf{M}_{nm}^{(2)}(k\mathrm{r})], \tag{8}$$

$$\mathbf{RgN}_{nm}(k\mathrm{r}) = \frac{1}{2}[\mathbf{N}_{nm}^{(1)}(k\mathrm{r}) + \mathbf{N}_{nm}^{(2)}(k\mathrm{r})]. \tag{9}$$

Although it is usual to expand the incident field in terms of the regular VSWFs, and the scattered field in terms of outgoing VSWFs, this results in both the incident and scattered waves carrying momentum and angular momentum away from the system. Since we are primarily interested in the transport of momentum and angular momentum by the fields (and energy, too, if the particle is absorbing), we separate the total field into purely incoming and outgoing portions in order to calculate these. The user of the code can choose whether the incident-scattered or incoming-outgoing representation is used otherwise.

We use an over-determined point-matching scheme [18], providing stable and robust numerical performance and convergence.

Finally, one needs to be able to calculate the force and torque for the same particle in the same trapping beam, but at different positions or orientations. The transformations of the VSWFs under rotation of the coordinate system or translation of the origin of the coordinate system are known [17, 19–21]. It is sufficient to find the VSWF expansion of the incident beam for a single origin and orientation, and then use translations and rotations to find the new VSWF expansions about other points [18, 22]. Since the transformation matrices for rotation and translations along the z-axis are sparse, while the transformation matrices for arbitrary translations are full, the most efficient way to carry out an arbitrary translation is by a combination of rotation and axial translation. The transformation matrices for both rotations and axial translations can be efficiently computed using recursive methods [19–21].

3. OPTICAL FORCE AND TORQUE

The force and torque exerted on a particle by the beam can be found by integration of the Maxwell stress tensor over a surface surrounding the particle. Fortunately, in the T-matrix method, the bulk of this integral can be performed analytically, exploiting the orthogonality properties of the VSWFs. In this way, the calculation can be reduced to sums of products of the expansion coefficients of the fields.

It is sufficient to give the formulae for the z-components of the fields, as given, for example, by Crichton and Marston [23]. We use the same formulae to calculate the x and y components of the optical force and torque, using 90° rotations of the coordinate system [21]. It is also possible to directly calculate the x and y components using similar, but more complicated, formulae [24].

The axial trapping efficiency Q is

$$\begin{aligned} Q = \frac{2}{P}\sum_{n=1}^{\infty}\sum_{m=-n}^{n} & \frac{m}{n(n+1)}\mathrm{Re}(a_{nm}^{\star}b_{nm} - p_{nm}^{\star}q_{nm}) \\ & -\frac{1}{n+1}\left[\frac{n(n+2)(n-m+1)(n+m+1)}{(2n+1)(2n+3)}\right]^{\frac{1}{2}} \\ & \times\mathrm{Re}(a_{nm}a_{n+1,m}^{\star} + b_{nm}b_{n+1,m}^{\star} - p_{nm}p_{n+1,m}^{\star} - q_{nm}q_{n+1,m}^{\star}) \end{aligned} \tag{10}$$

in units of $n\hbar k$ per photon, where n is the refractive index of the medium in which the trapped particles are suspended. This can be converted to SI units by multiplying by nP/c, where P is the beam power and c is the speed of light in free space.

The *torque efficiency*, or normalized torque, about the z-axis acting on a scatterer is

$$\tau_z = \sum_{n=1}^{\infty} \sum_{m=-n}^{n} m(|a_{nm}|^2 + |b_{nm}|^2 - |p_{nm}|^2 - |q_{nm}|^2)/P \tag{11}$$

in units of $\hbar$ per photon, where

$$P = \sum_{n=1}^{\infty} \sum_{m=-n}^{n} |a_{nm}|^2 + |b_{nm}|^2 \tag{12}$$

is proportional to the incident power (omitting a unit conversion factor which will depend on whether SI, Gaussian, or other units are used). This torque includes contributions from both spin and orbital components, which can both be calculate by similar formulae [23]. Again, one can convert these values to SI units by multiplying by P/ω, where ω is the optical frequency.

4. TYPICAL USE OF THE TOOLBOX

The toolbox largely consists of the following components:

- routines to calculate the T-matrix,
- routines to calculate the multipole expansion coefficients of the incident beam (ie a_{nm} and b_{nm}),
- routines to obtain (from the preceding) the expansion coefficients for an arbitrary choice of origin and orientation of the axes,
- routines to calculate the optical force and torque, and
- routines to automate common tasks, such as finding the equilibrium position of a trapped particle, spring constants, and force maps, and release-and-track for a particle.

Typically, for a given trap and particle, routines 1 and 2 only need to be executed once. Routines 3 and 4 will usually be run repeatedly, in many cases called from routines 5 rather than directly by the user.

The speed of calculation depends on the size of the beam, the size of the particle, and the distance of the particle from the focal point of the beam. Even for a wide beam and a large distance, the force and torque at a particular position can typically be calculated in much less than one second.

Agreement with precision experimental measurements suggests that errors of less than 1% are expected.

5. FUTURE DEVELOPMENT

We are actively engaged in work to extend the range of particles for which we can model trapping. This currently included birefringent particles and particles of arbitrary geometry. Routines to calculate the T-matrices for such particles will be included in the main code when available.

We also expect feedback from the optical trapping and micromanipulation community to help us add useful routines and features.

REFERENCES

1. Lorenz, L., "Lysbevægelsen i og uden for en af plane lysbølger belyst kugle," *Videnskabernes Selskabs Skrifter*, Vol. 6, 2–62, 1890.
2. Mie, G., "Beiträge zur optik trüber medien, speziell kolloidaler metallösungen," *Ann. Phys.*, Vol. 25, No. 3, 377–445, 1908.
3. White, D. A., "Vector finite element modeling of optical tweezers," *Comp. Phys. Commun.*, Vol. 128,558–564, 2000.
4. White, D. A., "Numerical modeling of optical gradient traps using the vector finite element method," *J. Comp. Phys.*, Vol. 159, 13–37, 2000.
5. Collett, W. L., C. A. Ventrice, and S. M. Mahajan, "Electromagnetic wave technique to determine radiation torque on micromachines driven by light," *Appl. Phys. Lett.*, Vol. 82, 2730–2732, 2003.
6. Ren, K. F., G. Gréhan, and G. Gouesbet, "Prediction of reverse radiation pressure by generalized Lorenz-Mie theory," *Appl. Opt.*, Vol. 35, 2702–2710, 1996.

7. Wohland, T., A. Rosin, and E. H. K. Stelzer, "Theoretical determination of the influence of the polarization on forces exerted by optical tweezers," *Optik*, Vol. 102, 181–190, 1996.
8. Maia Neto, P. A. and H. M. Nussenzweig, "Theory of optical tweezers," *Europhys. Lett.*, Vol. 50, 702–708, 2000.
9. Mazolli, A., P. A. Maia Neto, and H. M. Nussenzveig, "Theory of trapping forces in optical tweezers," *Proc. R. Soc. London A*, Vol. 459, 3021–3041, 2003.
10. Lock, J. A., "Calculation of the radiation trapping force for laser tweezers by use of generalized Lorenz-Mie theory. I. Localized model description of an on-axis tightly focused laser beam with spherical aberration," *Appl. Opt.*, Vol. 43, 2532–2544, 2004.
11. Lock, J. A., "Calculation of the radiation trapping force for laser tweezers by use of generalized Lorenz–Mie theory. II. On-axis trapping force," *Appl. Opt.*, Vol. 43, 2545–2554, 2004.
12. Han, Y. and Z. Wu, "Scattering of a spheroidal particle illuminated by a Gaussian beam," *Appl. Opt.*, Vol. 40, 2501–2509, 2001.
13. Han, Y., G. Gréhan, and G. Gouesbet, "Generalized Lorenz-Mie theory for a spheroidal particle with off-axis Gaussian-beam illumination," *Appl. Opt.*, Vol. 42, 6621–6629, 2003.
14. Waterman, P. C., "Symmetry, unitarity, and geometry in electromagnetic scattering," *Phys. Rev. D*, Vol. 3, 825–839, 1971.
15. Mishchenko, M. I., "Light scattering by randomly oriented axially symmetric particles," *J. Opt. Soc. Am. A*, Vol. 8, 871–882, 1991.
16. Nieminen, T. A., H. Rubinsztein-Dunlop, and N. R. Heckenberg, "Calculation of the T-matrix: general considerations and application of the point-matching method," *J. Quant. Spect. Radiative Transfer*, Vol. 79–80, 1019–1029, 2003.
17. Brock, B. C., "Using vector spherical harmonics to compute antenna mutual impedance from measured or computed fields," Sandia report SAND2000-2217-Revised, Sandia National Laboratories, Albuquerque, New Mexico, USA, 2001.
18. Nieminen, T. A., H. Rubinsztein-Dunlop, and N. R. Heckenberg, "Multipole expansion of strongly focussed laser beams," *J. Quant. Spect. Radiative Transfer*, Vol. 79–80, 1005–1017, 2003.
19. Videen, G., "Light scattering from a sphere near a plane interface," *Light Scattering from Microstructures*, F. Moreno and F. González, eds., *Lecture Notes in Physics*, Vol. 534, Ch. 5, 81–96, Springer-Verlag, Berlin, 2000.
20. Gumerov, N. A. and R. Duraiswami, "Recursions for the computation of multipole translation and rotation coefficients for the 3-D Helmholtz equation," *SIAM J. Scientific Computing*, Vol. 25, No. 4, 1344–1381, 2003.
21. Choi, C. H., J. Ivanic, M. S. Gordon, and K. Ruedenberg, "Rapid and stable determination of rotation matrices between spherical harmonics by direct recursion," *J. Chem. Phys.*, Vol. 111, 8825–8831, 1999.
22. Doicu, A. and T. Wriedt, "Computation of the beam-shape coefficients in the generalized Lorenz-Mie theory by using the translational addition theorem for spherical vector wave functions," *Appl. Opt.*, Vol. 36, 2971–2978, 1997.
23. Crichton, J. H. and P. L. Marston, "The measurable distinction between the spin and orbital angular momenta of electromagnetic radiation," *Elec. J. Diff. Eq.*, Vol. Conf. 04, 37–50, 2000.
24. Farsund, Ø. and B. U. Felderhof, "Force, torque, and absorbed energy for a body of arbitrary shape and constitution in an electromagnetic radiation field," *Physica A*, Vol. 227, 108–130, 1996.

Generation of Magnetic Fields: Various Multipolar Seed Fields

D. K. Callebaut[1] and H. Kikuchi[2]

[1]Physics Department, CGB University of Antwerp
Antwerp B-2020, Belgium
[2]Institute for Environmental Electromagnetics
Tokyo B-2020, Japan

Abstract— The exact solution for the kinematic dynamo in spherical coordinates (r, ϑ, φ) is given by Callebaut [1] when the azimuthal velocity is supposed to be a given, but arbitrary, function of r and ϑ only. Using a bipolar seed field yielded a qualitative agreement with the sunspot butterfly diagram and the polar faculae butterfly diagram. Next we have investigated the case that a quadrupolar seed field resides in the Sun (Callebaut and Khater, 2006) as some observations reveal a quadrupolar and even an octupolar contribution to some surface and interplanetary phenomena. A combination of a bipolar, a quadrupolar and an octupolar field may yield a fairer agreement with observations. However, the ratio of the various components is still a problem: determination from the solar surface or from interplanetary space gives approximate values. The separation between the sunspot region and the polar faculae, although both are generated by the same mechanism, is manifest: the region where the radial variation of the angular frequency of the rotation vanishes. One serious drawback: as for other models the agreement near the poles is poor, although it was improved much in comparison with a bipolar field alone by realizing that the coefficients of bipolar and quadrupolar field have opposite signs.

1. INTRODUCTION

When a conducting fluid or a plasma in motion is pervaded by a magnetic field an interaction between the motion and the field takes place and energy may be exchanged. The field may be increased or decreased by the dynamo action while it looses energy by resistive dissipation. In turn the motion is influenced by the Lorentz force. The applications range from laboratory experiments and industrial use (generation of electricity by dynamos in cars or power plants, pollution problems) to astrophysics. The latter application involves the Sun, stars, galaxies and planets (in particular the Earth). Here we are essentially interested in the solar application, in particular the generation of the butterfly diagrams of the sunspots and of the polar faculae. However, the application has not to be limited to the Sun, in particular as an exact and easy analytical solution is given for the equation of evolution for the magnetic field in the ideal magnetohydrodynamic (MHD) approximation. The basic equations concerned with the magnetic field $\mathbf{H}$ are the equation of evolution for the field together with the conservation of magnetic flux:

$$\partial_t \mathbf{H} = rot(\mathbf{v} \times \mathbf{H}) - rot\eta rot\mathbf{H} + rot\alpha\mathbf{H}, \tag{1}$$

$$div\mathbf{H} = 0, \tag{2}$$

where $\mathbf{v}$ is the velocity and $\eta = 1/\mu\sigma$ is the resistivity with σ the conductivity and μ the magnetic permeability taken to be constant (SI units).

In general the electromagnetic equations above have to be supplemented by the whole set of (hydrodynamic) equations linked to them through the velocity on the one hand and through the Lorentz force on the other hand. However, in the case of the so-called kinematic dynamo it is assumed that $\mathbf{v}$ is given. This simplification restricts the set of equations to (1) and (2). Moreover, we consider ideal MHD, i. e., $\eta = 0$, and we neglect the α term as well for a first approximation.

2. SOLUTION

Suppose that the velocity is purely azimuthal and depends only on r and ϑ:

$$v_\varphi = r\omega(r, \vartheta) \sin \vartheta, \tag{3}$$

where $\omega(r, \vartheta)$ is the angular frequency and (r, ϑ, φ) are spherical coordinates. The general solution of Equations (1) and (2) for $\alpha = \eta = 0$ which gives single-valued magnetic field components, is then, Callebaut [1],

$$H_r = \frac{-\partial_\vartheta \Phi}{r^2 \sin\vartheta} + P_r(r, \vartheta, \omega t - \varphi), \tag{4}$$

$$H_\vartheta = \frac{\partial_r \Phi}{r \sin\vartheta} + P_\vartheta(r, \vartheta, \omega t - \varphi), \tag{5}$$

$$H_\varphi = \frac{-t\partial(\omega, \Phi)}{r\partial(r, \vartheta)} + P_\varphi(r, \vartheta, \omega t - \varphi), \tag{6}$$

where the Jacobian is introduced. P_r, P_ϑ and P_φ are purely periodic functions of $\omega t - \varphi$ and contain r and ϑ in addition. They are completely arbitrary, except that they still have to satisfy Equation (2), and, of course, may not have singularities. As we are looking for long-term field amplification and not in the waxing and waning of the field in a timespan of one solar rotation we do not consider them any further here although they may be relevant in other situations.

The stream function Φ is an arbitrary function of r and ϑ only. We note that, upon dropping the periodic terms, H_r and H_ϑ are independent of time while H_φ depends linearly on time. Hence there is no violation of the theorem of Cowling which states that no stationary rotationally symmetric dynamo can exist. The linear growth with time is a consequence of the fact that the (differential) rotation is stationary.

3. CHOICE OF THE SEED FIELD

Equations (4)–(6) give the exact solution of the equation of evolution in ideal MHD. Given the value of $\mathbf{H}$ at any particular time we can write down immediately the magnetic field at all times. For the desired field amplification in the Sun we have thus to find a seed magnetic field. As we are not concerned at the moment with the periodic terms in Equations (4)–(6), the choice is already somewhat limited: a seed field independent of φ and in which the H_r and H_ϑ components are linked by the flux conservation, Equation (2). This limits the freedom to one component dependent on r and ϑ only. Moreover, the following localizations are possible for the seed field (broadly speaking): the radiative core, the convective zone and the tachocline, separation and link between the previous ones. As this was discussed by Callebaut and Khater (2006) and as it does not matter to convey the ideas we omit this here.

3.1. Choice of Bipolar Field

Any magnetic field located in the central part of the Sun may be approximated by a multipolar field. The Earth and several planets have to a good approximation a dipolar field and thus it is indicated to start with a dipolar field as a first trial. Moreover, as the Sun has a fairly symmetrical behavior when averaging over several cycles, we take the axis along the axis of rotation. Hence we consider the following bipolar field as seed field:

$$H_{br} = \frac{H_b \cos\vartheta}{r^3}, \quad H_{b\vartheta} = \frac{H_b \sin\vartheta}{2r^3}, \tag{7}$$

where H_b is a constant and where the index b is used to distinguish from the quadrupolar field with index q in next subsection. The field may be situated at the tachocline or any place in the convective zone. The third component $H_{b\varphi}$ may have any initial value independent of φ; it will further take its appropriate value according to the solution of the evolution equation given above. As we are mainly interested in the growth of the field we omit the time independent part of $H_{b\varphi}$. From Equations (4) and (5) we deduce

$$\Phi = \frac{-H_b \sin^2\vartheta}{2r}, \quad \partial_r \Phi = \frac{H_b \sin^2\vartheta}{2r^2}, \quad \partial_\vartheta \Phi = \frac{-H_b \sin\vartheta \cos\vartheta}{r}. \tag{8}$$

3.2. Choice of Quadrupolar and Octupolar Fields

The bipolar field is certainly a good start. However, the tachocline is situated around $0.7R$ and at this (not quite large) distance from the solar center the influence of higher order polarities will not be negligible. Hence, as a second example, we consider the following quadrupolar field as seed field:

$$H_{qr} = \frac{H_q \cos\vartheta}{r^4}, \quad H_{q\vartheta} = \frac{H_q \sin\vartheta}{r^4}, \tag{9}$$

while the time independent part of $H_{q\varphi}$ is omitted. H_q is again a constant. When a combination of a bipolar and a quadrupolar one is used the ratio rH_b/H_q will be relevant. We attempted to estimate this value from the observations in Makarov, Tlatov, Callebaut et al., (2001), but this did not yet work out. From the 'bashful ballerina' observations by Hiltula and Mursula [6] we estimate very roughly that the ratio of the amplitudes of quadrupolar to bipolar field at the solar surface will be about 1/4. However, the orientation is opposite, which makes the agreement with observations somewhat better than when parallel as considered previously (Callebaut and Khater, 2006). In agreement with Equations (4) and (5) we have for the corresponding stream function Ψ:

$$\Psi = \frac{-H_q \sin^2\vartheta}{2r^2}, \quad \partial_r\Psi = \frac{H_q \sin^2\vartheta}{r^3}, \quad \partial_\vartheta\Psi = \frac{-H_q \sin\vartheta\cos\vartheta}{r^2}. \tag{10}$$

The difference with the bipolar field is not strong: the power of r in the denominator is a unit more in all expressions here and a factor 2 occurs in some terms; thus it is mainly the r-dependence which will be investigated by comparison with the bipolar case. It is possible to investigate the ϑ-dependence by using $\cos^n\vartheta\sin^m\vartheta$ with $n = 0, 1, 2, 3, \ldots$ and $m = 2, 3, \ldots$ in he numerator of Φ and Ψ.

Similar expressions and considerations apply for the octupolar field. However, as its coefficient is estimated to be much smaller (about $H_b/20$) its influence will be much less, although at the tachocline ($r = 0.7\,R$) this may be increased by a factor 6 in view of the r^{-5} in the denominator of H_φ for the octupolar field.

4. AMPLIFICATION

Combining Equations (6), (9) and (10) we obtain for the quadrupolar field (using the same expression for $\omega(r,\vartheta)$ as for the bipolar case:

$$\begin{aligned} H_\varphi \;=\; & \frac{5.77 H_p t \sin\vartheta\cos\vartheta}{r^4(R-r_0)\cos^2\vartheta_0}\big[r(\cos^2\vartheta_0 - \cos^2\vartheta)(1 + 0.87\cos^2\vartheta) \\ & + 2(r - r_0)\sin^2\vartheta(1 - 0.87\cos^2\vartheta_0 + 1.74\cos^2\vartheta)\big]. \end{aligned} \tag{11}$$

A similar expression is obtained for the octupolar field. Those formulas are very similar to the one for a bipolar field: e.g., for the quadrupolar case r^{-4} appears as a factor instead of r^{-3} and a factor 2 in the second part of the formula. The extension to fields with more involved ϑ-dependence is a way to have more variation in the amplification and may be required for the fine tuning of the theory to match better the observations. Proceeding with $r_0 = 0.7R$ (and $r_0 = 0.5R$ too, to see the influence) and $\cos\vartheta_0 = 0.6$ we obtain for H_φ and for X, the amplification factor per year, results similar to those obtained for the bipolar field.

1. Again we have very small growth in the region around latitude 37° or $\vartheta = 53°$. Here $\cos\vartheta = \cos\vartheta_0$ and $\partial_r\omega = 0$. Again for the latitudes in the vicinity of 37° there may be some growth of the field in one sense near $r = r_0$, while the growth is in the opposite sense near the solar surface $r = R$, resulting in a small total growth. This latitude band marks the separation between the equatorial region with sunspots and the polar region with polar faculae as $\partial_r\omega$ reverses sign.
2. Again there is no growth at the equator and at the poles. Again H_φ has opposite signs in both hemispheres. This suggests again that applying a time dependent seed field with period of about 22 years may be very suitable to explain the magnetic cycle (22 years) and not only the cycle of 11 years. However, as pointed out by Callebaut [1], it is not a simple matter to explain the origin of such a time variation of the seed field. The so-called meridional motion may explain this partially but some internal oscillation near the tachocline is presumably active.
3. Near the poles the growth rate is much too large in comparison from what we may expect from the obserations of polar faculae. This misfit occurs for the bipolar field too and in most numerical models. However, the bipolar and qudrupolar contributions may cancel one another partially: see item 5.
4. An amplification of one order of magnitude is easily possible in some latitude bands. However, the growth rates are somewhat smaller than with a bipolar field. The general result matches qualitatively the sunspot butterfly diagram and the polar faculae butterfly diagram.

5. Using a combination of a bipolar and a quadripolar field may improve further the results by using appropriately chosen coefficients for both fields. This is a snag as we do not have a good estimate of the relative ratios. However, from the observations of Makarov and Callebaut (2006), Makarov, Callebaut and Tlatov [9], Makarov, Makarova and Callebaut (2006) it is possible to derive such an estimate, at least approximately. Similarly one may add an octopolar field with appropriate small coefficient, again in agreement with the observations of Makarov and coworkers. In fact a serious improvement in comparison with Callebaut and Khater (2006) comes from the insight (Hiltula and Mursula, [6]) that the coefficient of the quadrupolar field has the opposite sign of the bipolar one. The ratio of those coefficients is estimated roughly to be one quarter, with a minus sign. Thus the unusually large growth rates near the poles (a drawback which occurs in numerical models too) is moderated. This influence is the more strong the nearer the locus of the amplification is to the solar center. This points to the tachocline as the mayor place of amplification of the field.
6. Similar remarks are valid for the octupolar field which yield a further correction, although smaller.

5. CONCLUSION

Growth rates of more than an order of magnitude during one solar cycle are easily possible in certain latitude bands when using a quadrupolar seed field. We obtained, without using yet the α-effect, a qualitative correspondence for two of the main features of the solar activity depending on the latitude: the sunspot and polar faculae activities are explained by the same mechanism, but with some latitude gap between them due to the reverse of sign of $\partial_r\omega$ near latitude 37°. Making the bold (and still difficult to explain) hypothesis that the seed field oscillates with a period of 22 years would even allow to explain the magnetic cycle of 22 years period. Moreover, it turned out that the poleward migration of the circulation is not essential for the generation of the magnetic field. However, it may play a role in the (partial) recycling of the seed field.

The use of a quadrupolar magnetic field as a seed field for the field generation in the solar dynamo seems plausible as an additional effect to the use of a bipolar field, in particular by correcting for the much too large amplifications near the poles. Adding a weak octupolar seed field improves the results further. The appropriate ratios of bipolar, quadrupolar and octupolar seed field may be chosen in order to give a best fit and/or estimated from certain observations on the solar surface and from the interplanetary space (cf. the bashful ballerina of Hiltula and Mursula, [6]). Yet, the determination of the coefficients of the various multipolar fields is still a difficulty. The use of a more involved dependence on the latitude than just $\sin^2\vartheta$ for Φ and the corresponding multipolar fields is a further problem and a further extension. The main feature, the separation of the equatorial region with sunspots from the polar region with polar faculae, is mainly due to the fact that $\partial_r\omega$ reverses sign at a certain latitude (previously 37°, but expected to be evolve toward the equator with each cycle) and not to the choice of the seed field.

REFERENCES

1. Callebaut, D. K., "Exact solution for MHD evolution equation," *A. P. J.*, submitted, 2006.
2. Callebaut, D. K. and A. H. Khater, "Generation of sunspot and polar faculae butterflies using bipolar and quadripolar seed fields," *IAUS*, Vol. 233, Cairo, Egypt, March 31–April 4, 2006.
3. Callebaut, D. K. and A. H. Khater, "Generation of solar magnetic fields: contribution of octupolar seed field," *Progress in Electromagnetics Reseach Symposium (PIERS 2006)*, Abstracts, 47, Tokyo, Japan, August 2–5, 2006.
4. Callebaut, D. K. and V. I. Makarov, "Latitude-time distribution of 3 types of magnetic field activity in the global cycle," *Solar Phys.*, Vol. 141, 381–390, 1992.
5. Callebaut, D. K. and V. I. Makarov, "Generation of sunspots and polar faculae from a kinematic dynamo," *Proc. Solar Phys. Meeting*, Vol. SPM-11, in press, Louvain, Belgium, 11–16 Sept., 2005.
6. Hiltula, T. and K. Mursula, *Geoph. Res. Letters*, Vol. 33, L03105, 2006.
7. Makarov, V. I., A. G. Tlatov, and D. K. Callebaut, "Increase of the magnetic flux from polar zones of the Sun in the last 120 years," *Solar Phys.*, Vol. 206, No. 2, 383–399, 2002.
8. Makarov, V. I. and D. K. Callebaut, *Solar Phys.*, submitted.
9. Makarov, V. I., D. K. Callebaut, and A. G. Tlatov, *Solar Phys.*, Vol. 170, 373–388, 1997.
10. Makarov, V. I. and V. V. Makarova, *Solar Phys.*, Vol. 163, 267–289, 1996.

11. Makarov, V. I. and V. V. Makarova, *Proc. 9th Eur. Meeting on Solar Phys.*, 121–124, (ESA SP-448), A. Wilson (ed.), 1999.
12. Makarov, V. I., V. V. Makarova, and D. K. Callebaut, *Solar Phys.*, submitted.
13. Makarov, V. I., V. V. Makarova, and K. R. Sivaraman, *Solar Phys.*, Vol. 119, 45, 1989.
14. Makarov, V. I., A. G. Tlatov, D. K. Callebaut, V. N. Obridko, and B. D. Shelting, *Solar Phys.*, Vol. 206, No. 2, 383–399, 2002.
15. Makarov, V. I., A. G. Tlatov, and D. K. Callebaut, *Solar Phys.*, Vol. 224, No. 2, 49–56, 2004.

Numerical Model of Inductive Flowmeter

P. Fiala, **T. Jirku**, **and I. Behunek**

Department of Theoretical and Experimental Electrical Engineering, Brno University of Technology
Kolejni 2906/4, Brno 612 00, Czech Republic

Abstract— This article deals with physical and chemical processes during measurement with an inductive flowmeter. A theoretical model and an example of numerical solution are presented here. We prepared numerical models based on the combined finite element method (FEM) and the finite volume method (FVM) of one of the three variants and computed the output voltage of the flowmeter electrodes. The model joins the magnetic, the electric and the current fields, the flow field and a chemical nonlinear ion model. The results were obtained by means of the FEM/FVM as a main application in ANSYS software.

1. INTRODUCTION

The full electro-hydro-dynamical (EHD) model of an inductive flowmeter is a coupled problem. There are coupled electric, magnetic, fluid flow fields and electric circuit and chemical (ions) models, Fig. 1. This model was solved with combined finite element methods (FEM) and finite volume methods (FVM). Results from the numerical model and the experiments were compared and the numerical equality was very good.

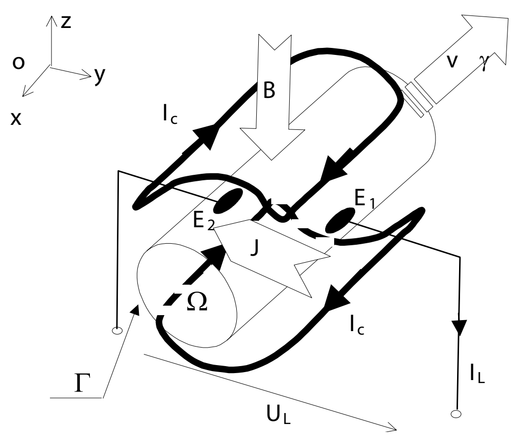

Figure 1: Principle of the induction flowmeter.

2. NUMERICAL MODEL

According to the research report [1], the electromagnetic part of the flowmeter is derived from reduced Maxwell equations

$$rot\,\boldsymbol{H} = 0, \tag{1}$$
$$div\,\boldsymbol{B} = 0, \tag{2}$$

where $\boldsymbol{H}$ is the vector of magnetic field intensity, $\boldsymbol{B}$ is the vector of magnetic field induction, $\boldsymbol{J}$ is the vector of current density.

$$rot\ \boldsymbol{E} = 0, \tag{3}$$
$$div\ \boldsymbol{J} = 0, \tag{4}$$

where $\boldsymbol{E}$ is the vector of electric field intensity. Material properties are represented by the equation

$$\boldsymbol{B} = \boldsymbol{H}\mu_0 \tag{5}$$
$$\boldsymbol{J} = \boldsymbol{E}\gamma, \tag{6}$$

where μ_0 is the permeability of vacuum, γ is the specific conductance of measured liquid. Vector functions of the electric and the magnetic field are expressed by means of scalar electric ϕ_e and magnetic potentials ϕ_m

$$\boldsymbol{E} = -\mathrm{grad}\phi_\mathrm{e}, \tag{7}$$

$$\boldsymbol{H} = -\mathrm{grad}\phi_\mathrm{m}. \tag{8}$$

Final current density from (4) $\boldsymbol{J}$ is influenced by velocity $\boldsymbol{v}$ of the flowing ion solution and outer magnetic field

$$\boldsymbol{J} = \gamma(\boldsymbol{E} + \boldsymbol{v} \times \boldsymbol{B}). \tag{9}$$

If electrodes E_1 and E_2 have different electrical potentials (Fig. 2), then the current density $\boldsymbol{J}$ is created in the Ω area according to (9) and current I_L flows in the ion solution

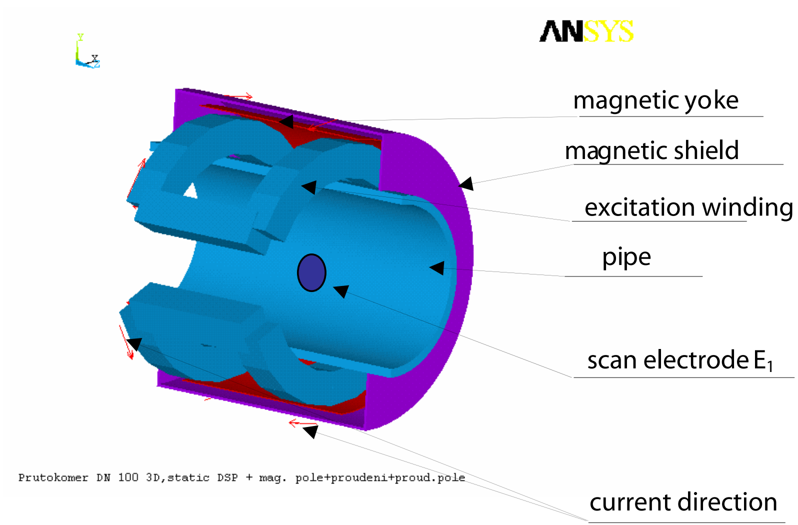

Figure 2: Geometric model of flowmeter body.

$$I_L = \iint\limits_{S_e} \boldsymbol{J} \cdot d\boldsymbol{S} = \iint\limits_{S_e} \gamma(\boldsymbol{E} + v \times \mathbf{B}) \cdot d\boldsymbol{S}. \tag{10}$$

where S_e is a directed area of electrodes E_1 and E_2 into space Ω. In Equation (10) there is the electric field intensity E for ion solution

$$|\mathbf{E}| << |\boldsymbol{v} \times \mathbf{B}| \tag{11}$$

therefore we ignore the influence of the electric field intensity. The specific force f which affects the moving charge q

$$\boldsymbol{f} = \boldsymbol{J} \times \mathbf{B}, \tag{12}$$

and the force in whole Ω area is

$$\boldsymbol{F} = \iiint\limits_{\Omega} \boldsymbol{J} \times \boldsymbol{B} dV. \tag{13}$$

We obtain the voltage between the flowmeter electrodes E_1, E_2 from

$$U_L = \int_{E_1}^{E_2} \boldsymbol{E} \cdot d\ell, \tag{14}$$

where the electric field intensity is derived from force $\boldsymbol{F}$ which affects a charge q. Current density $\boldsymbol{J}(\boldsymbol{v})$ depends on the immediate ion velocity between E_1 and E_2. After modification, the voltage on the flowmeter electrodes is

$$U_L = \iiint\limits_{\Omega} \left(\frac{\boldsymbol{J}(\boldsymbol{v})}{I_L} \times \boldsymbol{B} \right) \cdot (\boldsymbol{v}_{io} + \boldsymbol{v})\, dV. \tag{15}$$

The model of fluid velocity distribution is derived for incompressible fluid as

$$div\boldsymbol{v} = 0, \tag{16}$$

for a stabile state of flow holds

$$div\rho\boldsymbol{v} = 0, \tag{17}$$

from the energy conservation law where ρ is specific density. We assume the turbulent flow

$$rot\boldsymbol{v} = 2\boldsymbol{\omega}, \tag{18}$$

where $\boldsymbol{\omega}$ is the angular velocity of fluid. If we use Stokes theorem, Helmoholtz theorem for moving particle and continuity equation we can formulate from the equilibrium of forces the Navier-Stokes equation for the fluid element

$$\frac{\partial \boldsymbol{v}}{\partial t} + \boldsymbol{v} \cdot \mathrm{grad}\boldsymbol{v} = \boldsymbol{A} - \frac{1}{\rho}\mathrm{grad}p + \upsilon \cdot \Delta\boldsymbol{v}, \tag{19}$$

where $\boldsymbol{A}$ is the external acceleration and $\boldsymbol{\upsilon}$ the kinematic viscosity. In Equation (19) we can substitute pressure losses

$$\begin{aligned} \mathrm{grad}\ p = \quad & -\left(K_x \rho v_x |\boldsymbol{v}| + \frac{f_r}{D_h} \rho v_x |\boldsymbol{v}| + C_x \mu_p v_x \right) \boldsymbol{u}_x \\ & -\left(K_y \rho v_y |\boldsymbol{v}| + \frac{f_r}{D_h} \rho v_y |\boldsymbol{v}| + C_y \mu_p v_y \right) \boldsymbol{u}_y \\ & -\left(K_z \rho v_z |\boldsymbol{v}| + \frac{f_r}{D_h} \rho v_z |\boldsymbol{v}| + C_z \mu_p v_x \right) \boldsymbol{u}_z \end{aligned} \tag{20}$$

where $\boldsymbol{K}$ are the suppressed pressure losses, f the resistance coefficient, D_h the hydraulic diameter, C the air permeability of system, μ the dynamic viscosity, and $\boldsymbol{u}$ the unit vector of the Cartesian coordinate system. The resistance coefficient is obtained from the Boussinesq theorem

$$f_r = aR_e^{-b}, \tag{21}$$

where a, b are coefficients from [1]. The next step was the derivation of the FEM and FVM models [1]. The final term for the output voltage on the flowmeter electrodes which was evaluated is

$$\begin{aligned} U_L \cong & \left(\frac{1}{|ik^+| + \dfrac{1}{|ik^-|}} \right) \frac{1}{2F_c^2 I_L} \sum_{e=1}^{N_\Omega} \frac{|\boldsymbol{J}_e|}{\Delta V_e^2 \sqrt{\left(|\boldsymbol{v}_{m,e}|^2 + \left(\dfrac{\left|\boldsymbol{v}_{ok,e}^+\right| + \left|\boldsymbol{v}_{ok,e}^-\right|}{2} \right)^2 \right)}} (\boldsymbol{J}_e \times \boldsymbol{B}_e) \\ & \cdot \left(\boldsymbol{J}_e \left(\frac{1}{|ik^+|} + \frac{1}{|ik^-|} \right) + \Delta V_e F_c \boldsymbol{v}_{m,e} \right) \end{aligned} \tag{22}$$

where $\boldsymbol{v}_{ok,e}^+ = \dfrac{\boldsymbol{J}_e}{F_c \Delta V_e ik^+}$, $\boldsymbol{v}_{ok,e}^- = \dfrac{\boldsymbol{J}_e}{F_c \Delta V_e ik^-}$, $ik^+ = \sum\limits_{k=1}^{N_{\mathrm{ion}+}} c_k^+ N_k^{+\mathrm{ion}} = 1.2902 \cdot 10^{-5}\,\mathrm{mol/m^3}$,

$$ik^- = \sum_{k=1}^{N_{\mathrm{ion}-}} c_k^- N_k^{-\mathrm{ion}} = -1.3175 \cdot 10^{-5}\,\mathrm{mol/m^3}, \tag{23}$$

and where F_c is the Faraday constant, $F_c = 96484\,\text{C.mol}^{-1}$, $\boldsymbol{E}_e$ the electric field intensity in direction of ions motion in an element of mesh, c^+ the positive ions concentration, c^- the negative ions concentration, ΔV_e is the element volume, $N_k^{+\text{ion}}$ is the integer multiple of electron charge for a specific positive ion, $N_k^{-\text{ion}}$ is the integer multiple of electron charge for a specific negative ion, q_e^- is the whole charge of negative ions in one element, q_e^+ is the whole charge of positive ions in one element, $N_{\text{ion}+}$ is the number of different positive charge carriers (elements, compounds), $N_{\text{ion}-}$ is the number of different negative charge carriers (elements, compounds). Potable water has, for instance, this composition of ions with volume density m_{io}:

Positive ions	**Negative ions**	
Na … 32,71 mg/dm^3	F … 1,58 mg/dm^3	HCO_3 762,4 mg/dm^3
K … 1,525 mg/dm^3	Cl … 5,350 mg/dm^3	
Mg … 43,81 mg/dm^3	SO_4 … 13,08 mg/dm^3	
Ca … 157,7 mg/dm^3	NO_3 … 0,540 mg/dm^3	

Neutral substances:

CO_2 … 4063 mg/dm^3

H_2O … 1000000 mg/dm^3

3. NUMERICAL MODEL AND EXPERIMENTAL MEASUREMENT

Partial results of an EHD model are shown in Fig. 3. The dependence of output voltage on fluid velocity is shown in Fig. 4. This result is practically identical with experimental measurement on DN-100 ELIS s.r.o Brno.

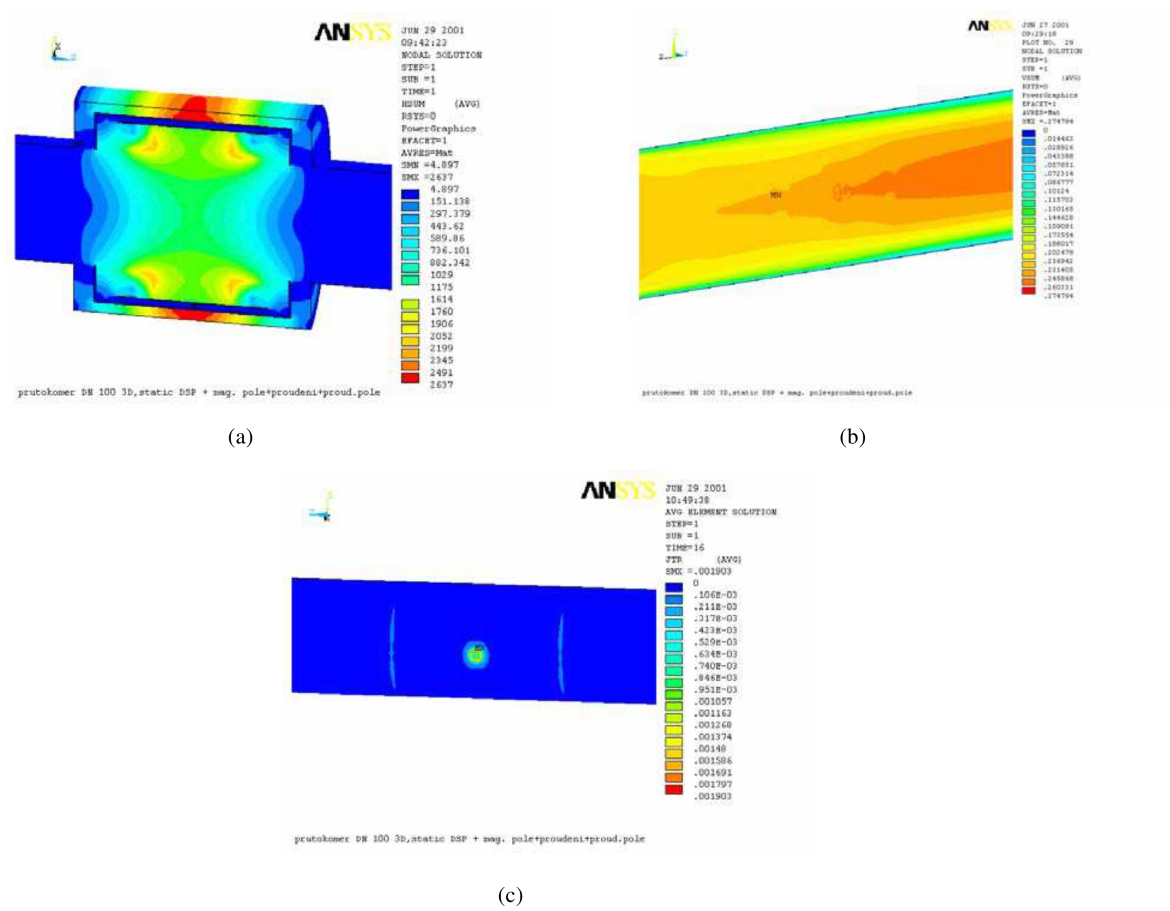

(a) (b) (c)

Figure 3: Distribution of (a) magnetic field intensity H in the flowmeter body, (b) immediate module of velocity in liquid, (c) current density J in the flowmeter body.

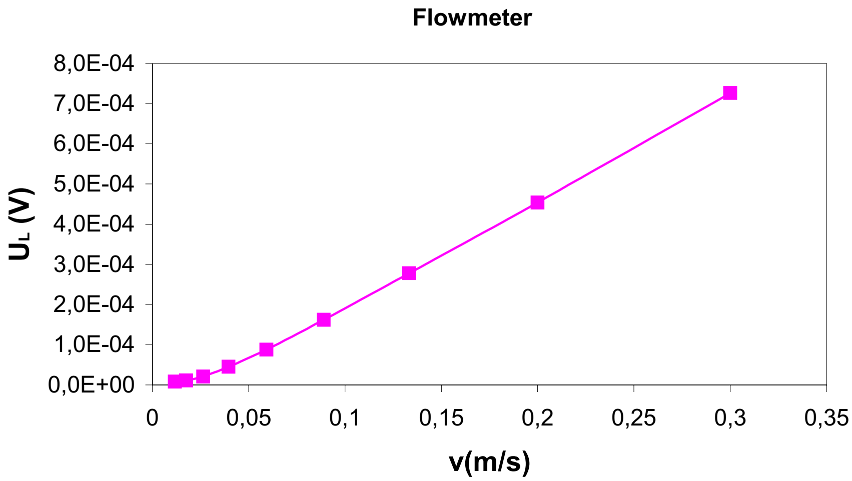

Figure 4: Dependence of voltage U_L on flow velocity v.

ACKNOWLEDGMENT

The research described in the paper was financially supported by the FRVŠ research plan No MSM 0021630513 ELCOM, No. MSM 0021630516 and grant GAAV No. B208130603.

REFERENCES

1. Fala, P., "Model of inductive flowmeter DN-100," Research Report No. 2/01, Laboratory of Modelling and Optimisation of Electromechanical Systems BUT FECT, 1–23, Brno, Czech Republic, 21. 6. 2001.
2. Fleischner, P., *Hydromechanika*, Paperback VUT FS, VUT Brno, ISBN 80-214-0266-1, 1990.
3. Črnoch, S., *Strojně technická příručka*, SNTL Praha, 1968.
4. Moore, J. W., *Fyzikální chemie*, SNTL Praha, 1981.
5. Brdička, R.-D. J., *Základy fyzikální chemie*, Academia Praha 1977.

New Numerical Technique for Non-destructive Testing of the Conductive Materials

T. Bachorec, T. Jirku, and J. Dedkova

Department of Theoretical and Experimental Electrical Engineering, Brno University of Technology
Kolejní 2906/4, Brno 612 00, Czech Republic

Abstract— The image reconstruction is an ill-posed inverse problem of finding such internal impedivity distribution that minimizes certain optimization criteria. The optimization necessitates algorithms that impose regularization and some prior information constraint. The regularization techniques vary in their complexity. This paper proposes new variants of the regularization techniques to be used for the acquirement of more accurate reconstruction results and the possibility of the applying differential evolution algorithms in an optimization process.

1. INTRODUCTION

The image reconstruction problem is a widely investigated problem with many applications in physical and biological sciences. The Electrical impedance tomography (EIT) can be used for reconstruction process. The theoretical background of EIT is given in [1]. The currents are applied through the electrodes attached to the surface of the object and the resulting voltages are measured using the same or additional electrodes. Internal impedivity distribution is recalculated from the measured voltages and currents. It is well known that while the forward problem is well-posed, the inverse problem is highly ill-posed. Various numerical techniques with different advantages have been developed to solve this problem. The aim is to reconstruct, as accurately and fast as possible, the impedivity distribution in two or three dimensional models. Usually, a set of voltage measurements is acquired from the boundaries of the determined volume, whilst it is subjected to a sequence of low-frequency current patterns, which are preferred to direct current ones to avoid polarization effects. Since the frequency of the injected current is sufficiently low, usually in the range of 10–100 kHz, EIT can be treated as a quasi-static problem. So we only consider the conductivity for simplicity. The scalar potential U can be therefore introduced, and so the resulting field is conservative and the continuity equation for the volume current density can be expressed by the potential U

$$\mathrm{div}(\sigma\,\mathrm{grad}U) = 0 \tag{1}$$

Equation (1) together with the modified complete electrode model equations [2] are discretized by the finite element method (FEM) in the usual way. Using FEM we calculate approximate values of electrode voltages for the approximate element conductivity vector σ (NE $\times$ 1), NE is the number of finite elements. Furthermore, we assume the constant approximation of a conductivity distribution σ on the finite element region. The forward EIT calculation yields an estimation of the electric potential field in the interior of the volume under certain Neumann and Dirichlet boundary conditions. The FEM in two or three dimensions is exploited for the forward problem with current sources.

2. SOLUTION OF INVERSE PROBLEM

Image reconstruction of EIT is an inverse problem, which is usually presented as minimizing the suitable objective function $\Psi(\sigma)$ relative to σ: To minimize the objective function $\Psi(\sigma)$ we can use a deterministic approach based on the Least Squares (LS) method. Due to the ill-posed nature of the problem, regularization has to be used. First the standard Tikhonov Regularization method (TRM) described in [3] was used to solve this inverse EIT problem

$$\min_\sigma \Psi(\sigma) = \min_\sigma \left[\frac{1}{2}\sum \|U_M - U_{\mathrm{FEM}}(\sigma)\|^2 + \alpha\|L\sigma\|^2\right]. \tag{2}$$

Here σ is the volume conductivity distribution vector in the object, UM is the vector of measured voltages on the boundary, and $U_{\mathrm{FEM}}(\sigma)$ is the vector of computed peripheral voltages in respect to σ, which can be obtained using FEM, α is a regularization parameter and L is a regularization matrix connecting adjacent elements of the different conductivity values. For the solution of (2) we can apply the Newton-Raphson method and after the linearization we used the iteration procedure. The iterative procedure is likely to be trapped in local minima and so sophisticated regularization must be taken into account to obtain the stable solution. The stability of the TRM algorithm is a bit sensitive to the setting of the starting value of conductivity. The regularization parameter α controls the relative weighting allocated to the prior information. Its optimal choice provides balance between the accuracy and stability of the solution. On the basis of many numerical experiments, it is supposable that we obtain higher accuracy of the reconstruction results for smaller value of the parameter α, but if the value of α is decreasing, the instability of the solution is increasing. In this novel approach, we search the optimal value of α during the iteration procedure using the following algorithm TRMα

set starting variable σ, initialize parameter α
while regularization is stable and reduction of Ψ has been obtained
use to recover optimized value of σ and decrease α
end while

In this way, we can obtain the stable solution with required higher accuracy of the reconstruction results.

Global optimizing evolutionary algorithms, such as genetic algorithms, have been recently applied to the EIT problem [4]. Some results of genetic algorithm research are described in [5]. Compared to the genetic algorithm, the differential evolution algorithm (DEA) is a relatively new heuristic approach to minimizing nonlinear and non-differentiable functions in a real and continuous space. DEA converges faster and with more certainty than many other global optimization methods according to various numerical experiments. It requires only a few control parameters and it is robust and simple in use. The DEA maintains a population of constant size that consists of N real-valued vectors $x_{i,G}$, $i = 1, 2, 3, \ldots, N$, where i indicates the index of population and G is the generation the population belongs to. The initial population of DEA is randomly generated within the feasible range of the parameter. Subsequently, mutation is performed. For each target vector $x_{i,G}$ a mutant vector $v_{i,G+1}$ can be generated

$$v_{i,G+1} = x_{i,G} + \alpha_p \left(x_{\text{best},G} - x_{i,G}\right) + \alpha_p \left(x_{r1,G} - x_{r2,G}\right)$$

where $x_{\text{best},G}$ is the best member of the current population, random indexes r_1, $r_2 \in \{1, 2, 3, \ldots, N\}$ are mutually different integers, at the same time different from running index i. Parameter $\alpha_p \in \langle 0, 2\rangle$ is a real constant which controls the amplification of the differential variations. Crossover is introduced to increase the diversity of the population. New vectors are formed using random generation, permutation and replacement of randomly chosen parts of two different individuals. To decide whether or not the new vector should become a member of generation $G+1$, the new vector is compared with the target vector $x_{i,G}$. The vector with a smaller objective function is retained in minimization. Finally, to guarantee the parameter values located inside their allowed ranges after reproduction, a simple method of replacing the parameter values that violate boundary constraints with random value generated within feasible range is used. The evolution will be determined once the objective function reaches a predetermined value or the evolution comes to the present generations.

3. SIMULATION RESULTS AND COMPARISON

The following examples describe the use of the above mentioned methods for recovering a collection of linear cracks in a homogeneous electrical conductor from boundary measurements of voltages induced by specified current fluxes. To recover conductivity distributions the LS method with a different type of the regularization's way was used. Furthermore, we compare the results obtained by DEA together with the results which were recovered by the TRMα to different values of the regularization parameter α during the reconstruction's process and the initial values of conductivity σ. To evaluate the quality of simulation results, the total error Err of the recovered conductivity distribution σ is defined as

$$Err = \sqrt{\sum_{i=1}^{NE} \left(\sigma(i) - \sigma_{\text{orig}}(i)\right)^2 \Big/ \sum_{i=1}^{NE} \left(\sigma_{\text{orig}}(i)\right)^2} 100\% \tag{3}$$

where σ_{orig} (in S/m) is the actual value, σ is the value recovered by EIT. The above proposed algorithms for 2D model have been written in MATLAB 7.0.4. Both the above described techniques have been applied to 3D model and have been implemented into a new program written in ANSYS. An example of 2D arrangement for a numerical experiment is given in Fig. 1. A circle model is shown with dimensions in cm; the total number of electrodes is 20. We applied a total of 20 different cosine current excitations calculating 19 independent nodal voltages for each excitation.

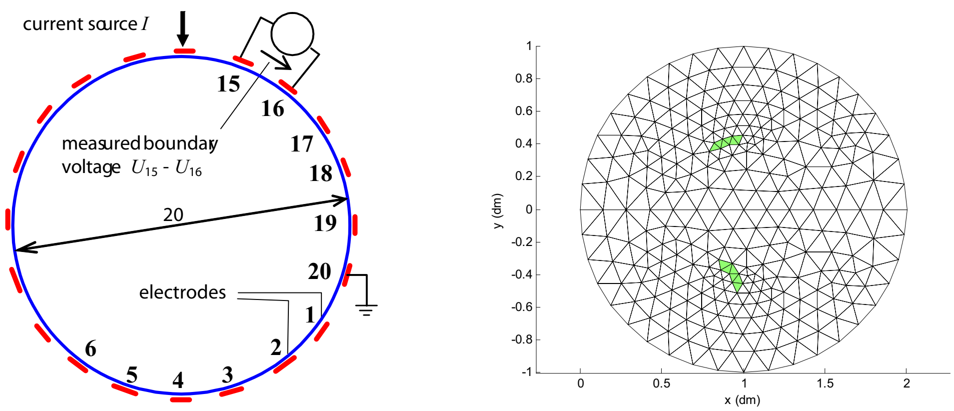

Figure 1: An arrangement for 2D experiments.

In Fig. 1 on the right you can see the FEM mesh, the total number of elements is NE = 500, the number of nodes is NU = 271. We assume a homogeneous object with conductivity 60 MS/m on all elements except for the chosen ones where the values of conductivity are 0 S/m (colored elements in Fig. 1), which can represent some cracks. The recovered conductivity distributions obtained using TRMα (left) and using DEA with number of generations G = 60 are shown in Fig. 2 (right). The starting and final values of parameter α, primal objective function $\Psi(\sigma)$, and total error Err are given in Table 1. We can say that the suitable choice of starting value of parameter α is necessary to assure the stability of the reconstruction process using TRMα.

One 3D example is shown in Fig. 3. There is FEM grid with 570 nodes, 432 elements and 40 electrodes. The radius of the cylinder is 10 cm, its height is 20 cm. We applied a total of 40 different current excitations calculating 39 independent nodal voltages for each excitation. We assume a homogeneous object with conductivity 10 S/m on all elements except for the chosen ones

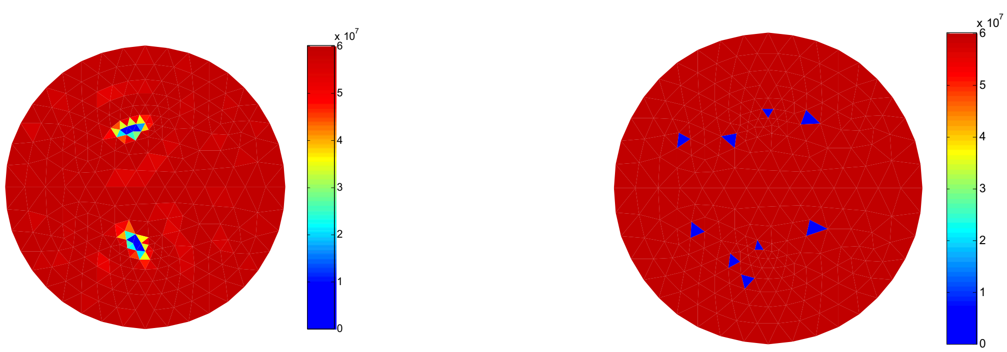

Figure 2: Final conductivity distributions obtained using TRMα and using DEA.

Table 1: Comparison of recovered results for example 2D.

	α, starting	α, final	$\Psi(\sigma)$, starting	$\Psi(\sigma)$, final	Err, starting	Err, final
TRM	$5 \cdot 10^{-40}$	$5 \cdot 10^{-40}$	$5 \cdot 10^{-18}$	$1 \cdot 10^{-18}$	35%	25%
TRMα	$5 \cdot 10^{-40}$	$4 \cdot 10^{-43}$	$5 \cdot 10^{-18}$	$3 \cdot 10^{-19}$	35%	11%
DEA	-	-	$5 \cdot 10^{-14}$	$7 \cdot 10^{-20}$	27%	10%

where the values of conductivity are 0 S/m.

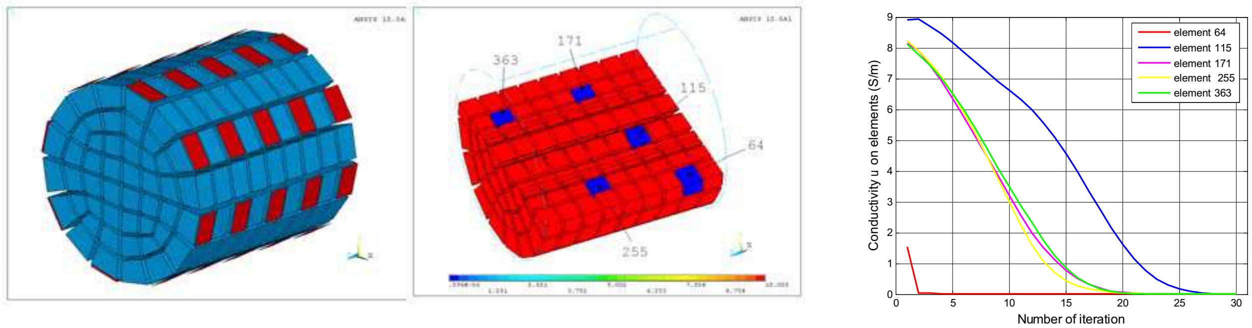

Figure 3: FEM grid with electrodes, five selected elements, conductivity changes on non-homogeneities.

There is also an example of the reconstruction results obtained using TRMα. The starting values of conductivity are 8 S/m on all elements; the starting value of parameter α is $1 \cdot 10^{-10}$ and its final value is $0.3 \cdot 10^{-17}$. The conductivity changes during 30 iterations are shown in Fig. 3 on the right. The final value of the primal objective function $\Psi(\sigma)$ is $5.3 \cdot 10^{-39}$ and the total error Err is 0.01%.

To recover the same conductivity distribution we also used DEA. Experimental results are shown in Fig. 4; here you can see the starting and final values of the conductivity distribution of the best member of 207 generation. The final value of the primal objective function $\Psi(\sigma)$ is $2.8 \cdot 10^{-14}$ and the total error Err is 16%.

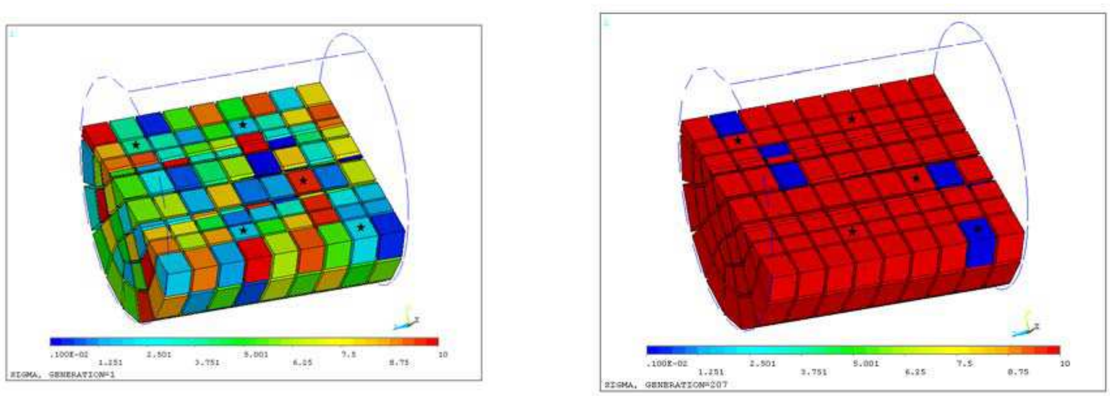

Figure 4: Starting and final values of a conductivity distribution obtained using DEA.

4. CONCLUSIONS

In this paper, a new practical approach to the reconstruction of non-homogeneities using EIT has been presented. Many numerical experiments performed during the above described research have resulted in the conclusion that the applications of the TRMα and DEA reconstruction algorithm have an advantage over the TRM approach. We mostly obtain higher accuracy using the TRMα but there is often an unstable reconstruction process. On the other hand the results obtained using DEA are less accurate but there is always a stable process. All the results stated above as well as many other examples were obtained using a program written in MATLAB for 2D reconstruction and in ANSYS for 3D reconstruction by the authors. It would be very worth to try another new ways of an effective and an absolutely stable reconstruction of the conductivity distribution with the highest accuracy. It can be tested for example an apposite combination of certain heuristic technique with the widely known method Total Variation PDI PM [6], methods based on Genetic Algorithm, Level Set Method [7] etc.

ACKNOWLEDGMENT

The research described in the paper was financially supported by the research program MSM 0021630513.

REFERENCES

1. Cheney, M., D. Isaacson, and J. C. Newell, "Electrical impedance tomography," *SIAM Rev.*, Vol. 41, No. 1, 85–101, 1999.
2. Somersalo, E., M. Cheney, and D. Isaacson, "Existence and uniqueness for electrode models for electric current computed tomography," *SIAM J. Appl. Math.*, Vol. 52, 1023–1040, 1992.
3. Vauhkonen, M., D. Vadász, P. A. Karjalainen, E. Somersalo, and J. P. Kaipio, "Tikhonov regularization and prior information in electrical impedance tomography," *IEEE Trans. Med. Eng.*, Vol. 17, 285–293, 1998.
4. Olmi, R., M. Bini, and S. Priori, "A genetic algorithm approach to image reconstruction in electrical impedance tomography," *IEEE Trans. Evol. Comp.*, Vol. 4, 83–88, 2000.
5. Michalewicz, Z., *Genetic algorithms+Data Structure=Evolution Programs*, 2nd ed., Springer Verlag Berlin, 1994.
6. Borsic, A., "Regularization methods for imaging from electrical measurement," PhD. Thesis, Oxford Brookes University, 2002.
7. Burger, M., "A level set method for inverse problems," *Inverse Problems*, Vol. 17, 1327–1356, 2001.

Perturbation of Singular Chasma Equation

D. K. Callebaut

Physics Department, CGB University of Antwerp, Antwerp B-2020, Belgium

Abstract— An ionizing beam (electrons, ions, atoms, photons) between plane-parallel plates, either parallel or perpendicular to the plates (like in the multipactor effect and hf cavities) may create an accumulating ion charge. The resulting steady state of the chasma ('non-quasi-neutral plasma') has a potential φ satisfying a quasi-singular non-linear integro-differential equation. The investigation of the perturbations reveals problems due to the singular character of the integrand. However, in the case that the beam density (b) and the ion production (P) are constant the potential is given by $\varphi = -kx^2$, where k is the positive root of a cubic equation. Perturbing and linearizing the latter equation yields the change dk for a disturbance db and dP, which may be time dependent provided slow enough that the ions may readapt to the new steady state. Some particular cases are studied.

For more involved cases one should return to the singular equation or it may be better to the original set of partial differential equations, which avoids the singularity problem. However, this makes the investigation much more wide and much more involved.

1. INTRODUCTION

The quasi-neutrality of ionized matter was and still is commonly assumed among plasma physicists as a matter of fact. It is generally believed that a (strong) deviation from quasi-neutrality is only possible in special circumstances as in cases where very good isolation is secured as in electrostatics or else over distances smaller than the Debye length, λ_D, as in plasma sheaths or Debye spheres. Actually, when Tonks and Langmuir [12] advanced the complete plasma-sheath equation in their classical paper they applied it essentially to two cases: the plasma (basically quasi-neutral over volumes larger than λ_D) and its sheath (of thickness λ_D and deviating from quasi-neutrality). Both those domains have been explored by numerous authors. However, that are not the only cases. Some observations and some experiments have displayed strong to extreme deviations from quasi-neutrality over distances much larger than the Debye length in one, two or even three dimensions. In fact already during the fifties non-quasi-neutral plasmas played a very negative, if not killing, role in some linear accelerators and some other microwave devices in which the so-called multipactor effect or secondary resonance electron discharge (SERD) occurred. Callebaut [1] studied this effect in a linear electron accelerator and more specifically in a re-entrant cavity devised on purpose for it. Some hypotheses were used of which the most important one is probably that a steady state regime could be reached before instabilities destroyed or altered it drastically. Callebaut and Knuyt [7] considered separately the problem of determining the density of ions which are generated by ionizing beams; they extended the one dimensional case to two or three dimensions. Non-quasi-neutral plasmas were termed "charged plasmas" or "chasmas" subsequently. The name suggests that chasmas are very similar to plasmas except in a crucial aspect: they are not quasi-neutral over distances of at least several Debye lengths. One can say that plasma sheaths are a subclass of chasmas, but as those have been studied abundantly elsewhere they are not considered here. Similarly for double layers (see e. g., Schrittwieser, [11]). We are considering cases in which the quasi-neutrality is violated over several Debye lengths instead of roughly one Debye length in the case of plasma sheaths.

It should be stressed that chasmas do occur during transitions of configurations and in particular during instabilities. In this connection the study of post-magnetohydrodynamics (post-MHD) is relevant too: in MHD one neglects the displacement current which is precisely related to the variation in time of the space charge. See Callebaut and Khater [5]. This makes a link with the electro-hydrodynamics and electro-magneto-hydrodynamics considered by Kikuchi [8–10].

2. STEADY STATE

We consider a plane-parallel situation (e. g., plane-parallel electrodes) for simplicity. Suppose an ion is created at a place y and reaches the place x, both on the x-axis, perpendicular to the electrodes (no y or z *dependence*). The electrons that are created are quickly swept away by a high frequency field and are neglected here (extensions possible by including the electrons through an integral like the one for the ions). The beam charge density is $b(x)$; it may be positive or negative or zero. The beam may be parallel to the electrodes or perpendicular to them, as in the case of the multipactor effect where they are the secondaries generated at the walls (electrodes) each half period and which are accelerated to the opposite wall. The production of ions is $P(x)$ at the position x; normally it is the product of the beam density, the ionization probability and the density of the neutral particles at the position x. The Poisson equation for the potential φ becomes

$$-\partial_{xx}^2 \epsilon\varphi = b(x) + \int_0^x \frac{P(y)dy}{v(y,x)}. \tag{1}$$

Here ϵ is the permittivity and $v(y,x)$ is the velocity of an ion (mass M, charge e) which is created at y without initial velocity and has arrived at x due to the potential difference. The conservation of energy gives:

$$Mv^2(y,x)/2 = e(\varphi(y) - \varphi(x). \tag{2}$$

Combining both equations yields the following quasi-singular non-linear integro-differential equation:

$$-\epsilon\partial_{xx}^2\varphi = b(x) + \sqrt{M/2e}\int_0^x \frac{P(y)dy}{\sqrt{\varphi(y)-\varphi(x)}} \tag{3}$$

In the (frequent) case that b and P are constant, it turns out that the potential is simply quadratic in x and that the integral in Equation (3) is constant, meaning that the ion density is constant as well. The positive root of the following cubic equation yields the coefficient k of the potential $\varphi = -kx^2$.

$$2\epsilon k^3 - bk - \frac{\pi P}{2}\sqrt{\frac{M}{2e}} = 0. \tag{4}$$

This very particular situation is valid in the 2D and 3D cases for homogeneous beams and ion production too. For the cases when b and/or P are not constant we found a way to make the Equation (1) slightly less complicated (no more singular) by multiplying it by $d\varphi/dx$ and integrating once:

$$-\epsilon\left((\partial_x\varphi)^2 - (\partial_x\varphi)_0^2\right) = 2\int_0^x b(y)\partial_y\varphi dy + 4\sqrt{M/2e}\int_0^x P(y)\sqrt{\varphi(y)-\varphi(x)}dy. \tag{5}$$

The latter allows easily a series development and thus a fair approximation may be obtained. We started recently a more general approach [3] using the full original set of basic equations like in plasma physics instead of the singular integro-differential equation instead of considering the case in which one may reduce this set to one (quasi-singular) equation. This makes the domain vastly more wide and correspondingly more involved.

3. PERTURBATION

3.1. P and b Varying in Time, But Not in Space

Perturbing Equation (3) or Equation (5) and linearizing leads to involved equations with singular kernels. However, for the case that b and P are not dependent on x, but vary in time we may exploit Equation (4) instead. Supposing that the beam is altered (db) and that the ion production is altered (dP) and supposing that the time variation is slow enough so that a new steady state is established, we may perturb Equation (4). Linearizing yields

$$6\epsilon k^2 dk - bdk - kdb - \frac{\pi dP}{2}\sqrt{\frac{M}{2e}} = 0, \tag{6}$$

or

$$dk = \frac{kdb + \frac{\pi dP}{2}\sqrt{\frac{M}{2e}}}{6\epsilon k^2 - b}, \tag{7}$$

In which one substitutes the initial k. We consider 3 particular cases.

3.1.1. Indifferent Steady State: $dk = 0$?

We have $dk = 0$ if

$$k = -\frac{\pi dP}{2db}\sqrt{\frac{M}{2e}}. \tag{8}$$

The production of ions P is usually proportional to the beam density b. Thus dP and db may be expected to be proportional in the same way: $dP/db = P/b$ and equation becomes

$$k = -\frac{\pi P}{2b}\sqrt{\frac{M}{2e}}. \tag{9}$$

If the beam has the same sign as the ions then the right hand side of Equation (9) is negative, while k is chosen to be always positive. However, with an electron beam both sides of Equation (9) are positive and on substitution in Equation (4) we obtain $-2\epsilon((\pi/2)(M/2e)^{1/2}(P/b))^3 = 0$ which is false. Hence, if P and b vary proportionally, then k has to change too: an indifferent stable steady state is not possible. One may prove this directly from Equation (4) too.

3.1.2. Strongly Unstable Case: $dk \to \infty$?

The denominator in Equation (8) vanishes for

$$k^2 = b/6\epsilon. \tag{10}$$

This is possible only if $b > 0$. Then dk would become infinite (in the linearized version). Substituting in Equation (4) yields the following condition between P and b:

$$b^3 = \frac{27\epsilon\pi^2 MP^2}{16e}. \tag{11}$$

(These expressions occur in the exact solution of the cubic Equation (4) too, which then simplifies considerably.)

3.1.3. Photon or Atom Beam: $b = 0$.

Then we have simply from Equation (4)

$$k = \left(\frac{\pi P}{4\epsilon}\sqrt{\frac{M}{2e}}\right)^{1/3}, \tag{12}$$

where the positive root counts only. Equation (12) shows immediately the variation of k with P, without linearizing.

3.2. Cases with b and P Dependent on x.

The previous examples may still give an idea of the behavior, e. g., by using for b and P averages.

When b and P vary in space we have first to determine the steady state by solving Equation (3). Using a series expansion, obtained e. g., from Equation (5), allows to calculate the effect of db and dP on the potential. Linearizing a few terms may be sufficient to see whether an instability may develop.

4. CONCLUSION

We may expect that chasmas in general become fairly easily unstable in view of the strong tendency to quasi-neutrality. This was made clear by Callebaut and Khater [4]. Here we used a different approach, based on the exact solution of the quasi-singular non-linear integro-differential equation describing a class of chasmas (constant beam density and constant ion production). Some special cases were considered. However, we are dealing here with the shift from one steady state to another rather than with instability.

The general case when beam density and ion production vary in space and are perturbed requires the study of an nonlinear singular integro-differential equation or the full set of the basic equations.

REFERENCES

1. Callebaut, D. K., *Physica*, Vol. 29, 784–802, 1963; *Physica*, Vol. 31, 1177–1192, 1965.; *Physica*, Vol. 32, 1151–1158, 1966.
2. Callebaut, D. K., *Second URSI-ICPIG-RIKEN Symposium on Critical Problems of Discharge and Plasma Physics and Electro-Plasmo-Meteorology*, 40–41, Riken (The Institute of Physical and Chemical Research), Wako, Saitama, 351-01, Japan, 1995.
3. Callebaut, D. K., G. K. Karugila, and A. H. Khater, *Proc. PIERS 2005*, 720–723, Hangzhou, China, August 22–26, 2005.
4. Callebaut, D. K. and A. H. Khater, *PIERS2006*, 403–405, Cambridge, USA, March 26–29, 2006.
5. Callebaut, D. K. and A. H. Khater, *PIERS2007*, these Proc., Beijing, China, March 26–30, 2007.
6. Callebaut, D. K. and A. H. Khater, *International Symposium on Unconventional Plasmas (ISUP-97)*, 1–2, (Eds. H. Kikuchi and D. K. Callebaut), Niigata, Japan, 1997; *ISUP-06*, 36–39, Eindhoven, the Netherlands, 2006.
7. Callebaut, D. K. and G. K. Knuyt, *Phys. Lett.*, Vol. 29A, 72, 1969; *Plasma Phys.*, Vol. 20, 511–523, 1978; *Plasma Phys.*, Vol. 20, 524–550, 1978; *Relation between Laboratory and Space Plasmas*, 207–230, (Ed. H. Kikuchi) Reidel Publ. Co. (Dordrecht, The Netherlands), 1981.
8. Kikuchi, H. (ed.), *Relation between Laboratory and Space Plasmas*, Reidel Publ. Co., Dordrecht, The Netherlands, 1981.
9. Kikuchi, H., *Handbook of Atmospheric Electrodynamics*, Vol. 1, 167, H. Volland (ed.), CRC Press, Bonn, 1995.
10. Kikuchi, H., *Electrodynamics in Dusty and Dirty Plasmas (Gravito-Electrodynamics and EHD)*, ASSL, Vol. 258, Kluwer Acad. Press, Dordrecht, 2001.
11. Schrittwieser, R. W. (ed.), *Fourth Symposium on Double Layers and other Nonlinear Potential Structures in Plasmas*, (Innsbruck, Austria), World Scientific, Singapore, 1993.
12. Tonks, L. and Langmuir, I., *Phys. Rev.*, Vol. 34, 876, 1929.

Post-magneto-hydrodynamics

D. K. Callebaut[1] **and A. H. Khater**[2]

[1]Physics Department, CGB, University of Antwerp
Antwerp B-2610, Belgium
[2]Department of Mathematics, Faculty of Science, University of Beni-Suef
Beni Suef, Egypt

Abstract— Magneto-hydrodynamics (MHD) as conceived by Alfvén is based on the evolution equation for the magnetic field. The main applications concern the magnetic fields in flows and dynamo mechanisms. Various extensions have been made. Here we consider the contribution due to the displacement current of Maxwell. This adds a term proportional to $\epsilon\mu = c^{-2}$ and thus is expected to be very small at low frequencies. Using the exact solution of the evolution equation obtained by Callebaut we may calculate precisely the correction and iterate if necessary. Thus we have compared the displacement current with the MHD current. The displacement current may become comparable to and exceed the MHD current at high frequencies and slowly varying structures in space.

It is stressed that the space charge is an independent variable. We introduce a dimensionless quantity as a measure for it.

This post-MHD may be particularly relevant in connection with the 'non-linear Fourier-Callebaut' analysis showing that the accumulation of some small *oscillations* (however, including the non-linear terms) may lead, in narrow strips to very large, even divergent, velocities. In those strips turbulent resistivity may occur which allow the dissipation times to be 4 to 5 orders of magnitude shorter than those of ordinary MHD. This may explain the short explosion times for solar flares, coronal mass ejections (CMEs), etc.

1. INTRODUCTION

Magnetohydrodynamics (MHD) is a combination of fluid motions and electromagnetism. Hence the frequencies are usually in between those of both domains and usually not extremely high, thus allowing Alfvén (Nobel prize 1970) to neglect the displacement current (which Maxwell had rightfully added to the older electromagnetic system in order to obtain consistency). MHD is an excellent approximation for electromagnetic phenomena in conducting fluids. There results one equation of evolution for the magnetic field $\mathbf{H}$, however still linked to the set of (hydro)dynamic equations through the velocity $\mathbf{v}$:

$$\partial_t \mathbf{H} = rot(\mathbf{v} \times \mathbf{H}) - rot\eta rot\mathbf{H}. \tag{1}$$

in which $\eta = 1/\mu\sigma$ is the resistivity ($\mu = 4\pi 10^{-7}$ henry/m or kgm/C^2, the magnetic permeability, taken to be constant; σ is the conductivity; SI units). Various extensions of Equation (1) exist. An important correction is due to the Hall current due to the Lorentz force $\mathbf{j}\times\mathbf{B}$. Another contribution comes from the convection or turbulence: according to the mean field theory this corresponds to $rot\alpha\mathbf{H}$, with α a constant or a function of the variables. Here we want to draw attention to the so-called displacement current which adds a term

$$\epsilon\mu\eta\partial^2_{tt}\mathbf{H}, \tag{2}$$

to the right hand of Equation (1). Here ϵ is the permittivity: $\epsilon = 8.86\,10^{-12}$ farad/m (or (Cs)^2/kgm^3) in vacuum. As $\epsilon\mu = c^{-2}$, with c the speed of light, it is immediately clear that this term is often negligible unless the frequency is very high. However, we shall show that the this is not the only relevant quantity and that the variation in space plays a role too.

The plan of the paper is as follows: in Section 1 we consider the space charge and introduce a dimensionless quantity to represent it. In Section 2 we reproduce briefly the results of Callebaut and Khater [6]. Section 3 gives the results of Callebaut and Karugila [3, 4] and considers the application to flares, CMEs, etc. Section 4 gives the conclusion.

2. SPACE CHARGE

Putting $\eta = 0$, Callebaut [1], Callebaut and Makarov [8]; Callebaut and Khater [6] succeeded in solving the resulting equation exactly in spherical coordinates (r, ϑ, φ), provided $\mathbf{v}$ has only an azimuthal component v_φ which depends only on r and ϑ. (Clearly the aim was to apply it to the generation of magnetic fields in the Sun where the azimuthal component is the dominant one. However, the extension to include the azimuth and the time is possible.) With a straightforward explicit solution one may calculate the other fields from the equations of Maxwell and see how important the correction is. The question arises how good the MHD approximation is and when a post-MHD should be considered. It may be noted that Igor Veselovsky [14, 15] too drew attention, in general terms, to the importance of the space charge, which is neglected in MHD, but represents an extra variable. Callebaut, Karugila and Khater [5] introduced the 'chasma frequency'

$$\omega_{ch}^2 = \frac{|n_+ - n_-|e^2}{\epsilon m_-}, \tag{3}$$

with obvious notations and which is relevant for the steady state and the (in)stability of a chasma or 'non-quasi-neutral plasma'. Using this one may introduce the dimensionless quantity q representing the space charge

$$|q| = \frac{\omega_{ch}^2}{\omega_p^2}, \tag{4}$$

or more simply

$$q = \frac{n_+ - n_-}{n_+ + n_-}. \tag{5}$$

For a plasma we have $n_+ = n_-$ and $q = 0$. For pure electron gas we have $n_+ = 0$ and $q = -1$. For a pure positive ion gas we have $q = 1$. It should be noted that a very small deviation from quasi-neutrality may yield gigantic electric fields. Consider e. g., $1\,\mathrm{m}^3$ of an ionized gas containing $10^{20} - 10^{17}$ electrons and 10^{20} once ionized positive particles. The parameter $q = 5\,10^{-4}$ but the corresponding electric field at 1 m from the center is more than 10^8 Volt/m! One can at once imagine the effect in a fusion device, in the magnetosphere of the Earth and in the Sun. One usually objects that precisely due to this huge electric fields the quasi-neutrality is quickly restored. This is usually true, but when *instabilities* develop (especially fast ones) the unbalanced charges may be quite important.

The example illustrates as well that the use of the ratio of the negative and positive densities $q' = n_-/n_+$ is not very suitable: this ratio is usually extremely close to unity in actual situations. Moreover the use of q is directly linked with the relevant frequencies ω_p and ω_{ch}. A general problem which arises, however, is to estimate the importance of the space charge in a particular situation, i. e., what is small or not? One needs a way of comparison. A possibility may be by comparing the energy (density) associated with the net space charge with the magnetic energy (density). In next section we circumvented the problem by comparing the displacement current with the MHD current.

Actually there occur in and around the Sun (and in fusion devices as well) many phenomena which are not understood, e. g., the occurrence of turbulent resistivity; the very short flash phase of a solar flare (a quarter of an hour, while the resistive characteristic decay time is several years). The characteristic decay time may be reduced due to filamentation. This points to the need to investigate the length and time scales of some parts or subparts of the phenomena which may lead to corrections to MHD. Having an exact solution of Equation (1), albeit for $\eta = 0$, allows to calculate exactly all fields and terms in the relations of Maxwell and thus to calculate the value of the neglected terms and to estimate their relative importance.

An example of the calculation of the space charge was developed by Callebaut and Khater [7]: we shall use it here, at least formally, although it is not yet as general as desired.

3. COMPARISON OF MHD CURRENT WITH DISPLACEMENT CURRENT

The resistivity is supposed to vanish. The solution of Equation (1), which is independent of φ and which is generated by an initially bipolar field $(H_r,\, H_\vartheta,\, 0)$, reads

$$H_r = \frac{H_b \cos\vartheta}{r^3}, \quad H_\vartheta = \frac{H_b \sin\vartheta}{2r^3}, \quad H_\varphi = -\frac{t\partial(\omega, \Phi)}{r\partial(r, \vartheta)}, \quad \Phi = -\frac{H_b \sin^2\vartheta}{2r}, \tag{6}$$

where H_b is a constant, where $\omega(r,\vartheta)$ is the angular frequency (in this case representing the differential rotation of the Sun) and where Φ is the stream function generating H_r, H_ϑ:

We obtained for the electric field $\mathbf{E}$

$$\mathbf{E} = \frac{\mu H_b \omega}{2r^2}(\sin^2\vartheta, -2\sin\vartheta\cos\vartheta, 0), \tag{7}$$

and for the space charge density ρ

$$\rho = div\mathbf{D} = \epsilon\left(\frac{\partial_r(r^2E_r)}{r^2} + \frac{\partial_\vartheta(\sin\vartheta E_\vartheta)}{r\sin\vartheta}\right) = \frac{\epsilon\mu H_b}{2r^3}\left(r\sin^2\vartheta\partial_r\omega - \sin 2\vartheta\partial_\vartheta\omega + 2\omega(\sin^2\vartheta - 2\cos^2\vartheta)\right). \tag{8}$$

The displacement current is

$$\partial_t\mathbf{D} = \epsilon\partial_t\mathbf{E} = \frac{\epsilon\mu H_b\partial_t\omega}{2r^2}(\sin^2\vartheta, -\sin 2\vartheta, 0). \tag{9}$$

As foreseen the charge density and the displacement current are proportional to $\epsilon\mu = c^{-2}$ which is very small indeed. The MHD current density is

$$\mathbf{j} = \left[\frac{tH_b\partial_\vartheta(\sin^2\vartheta(2r\cos\vartheta\partial_r\omega + \sin\vartheta\partial_\vartheta\omega))}{2r^4\sin\vartheta}, \frac{-tH_b sin\vartheta\partial_r(r^{-2}(2r\cos\vartheta\partial_r\omega + \sin\theta\partial_\vartheta\omega))}{2r}, 0\right] \tag{10}$$

The φ-component of the current vanishes here as H_r and H_ϑ form a gradient. Thus the MHD current is zero at $t = 0$, but grows linearly with time. The intial field had no azimuthal component at $t = 0$, which explains the special time interval.

Taking 100 gauss for the field, i. e., $\mu H_b/r^3$ about 0.01 tesla, requires ω of the order of 10^{10} cycles/s to generate a charge density of 10^{-3} coulomb/m^3, which is quite huge as we have seen. However, it is difficult to say what is small and what is large with respect to charge. For the currents we have the possibility to compare the displacement current with the MHD current: we have then to compare $\partial_t\omega/c^2$ with $(t/r)\partial^2_{r\vartheta}\omega$ and $t\partial^2_{rr}\omega$ or similar expressions. Hence, we can say that the displacement current may exceed the MHD current, at least at the start, if the time variation of ω, i. e., of the velocity, is very fast and the space variation is very slow. If we consider the radius of the Sun ($7\ 10^8$ m) and a time variation of 1 cycle/s the displacement current may exceed the MHD current during a few seconds. Considering a phenomenon of 1 km and a time variation of 1 megacycle/s, then the displacement current may exceed the MHD current during the first microseconds. An intermediate case: in a structure like a prominence (the average current density may be a milli-ampere per square meter cross-section; yet, because of the huge volumes involved the total current may be 10^{11} ampere) with 10^4 km as diameter of the flux tube the time variation should be 10^4 cycles for the displacement current to be comparable to the MHD current during some seconds. Hence *rapid motions in configurations which vary slowly in space* may require the post-MHD approach. (It may be noted that these conditions do not easily go together, but in the example below the may go together). We expect this behavior to be of a general nature, although we studied a specific case.

4. APPLYING THE NONLINEAR FOURIER-CALLEBAUT ANALYSIS

Callebaut and Karugila [2–4] developed a nonlinear theory by considering first a single first order perturbation. They calculated (computer algebra) many higher order terms associated with the selected first order term. They showed in some cases analytically and in all cases numerically that the total sum of all the higher order terms can become divergent for a certain value of the amplitude of the first order term. E. g., for a cold infinite plasma the limit of convergence is reached when the first order density amplitude equals e^{-1} (37 per cent) of the equilibrium density. Next they have considered several first order perturbations of moderate amplitude occurring together. Each separately leads to a family of higher order terms which may total a somewhat larger amplitude. The interference terms between the various families may easily be obtained from a combinatorial rule once the family of a single first order term is obtained. All the non-linear terms of all first order perturbations (although each one small in itself) may lead for a certain phase to a very large and even a divergent result. This may be delayed according to the initial amplitudes and the commensurability of the phases. However, a kind of bunching, concentration of the energy in small periodic phase intervals, occurs sooner or later. This gives an instability or rather an explosion, even if all the initial perturbations are *oscillations*. The critical phase and corresponding strip in space is repeated periodically; moreover these strips move in space as the critical phase moves, so that the whole plasma is wiped periodically by the 'divergent strip', causing the instability of the whole plasma and the corresponding dissipation of energy. Indeed, as the velocities in such a strip become very large (infinite), turbulence may develop in it. This turbulence may increase the resistivity by 4 to 5 orders of magnitude. This allows the magnetic energy to be dissipated much faster. Moreover, runaway electrons are created which may explain (at least partially) the high energy electrons and radiation.

Moreover, this may act as a trigger for neighboring configurations which have much more stored energy and thus cause gigantic explosions. In fact a chain reaction may occur: a combination of small oscillations (e. g., sound waves) at the solar surface may thus cause an instability corresponding to a bright point. The (larger) waves generated by several bright points may cause the flashing of a prominence or a solar flare or a CME. This may explain some other sudden outbursts which occur on Earth (interruption of power generators) and in the laboratory as well.

Inducing several moderate perturbations in a quiet plasma (e. g., in a Q-machine) may allow experimental verification of the theoretical convergence limit. Cf. Schrittwieser and Eder [12], Schrittwieser [13]). This convergence limit lowers when the thermal motions of the electrons and/or ions are taken into account.

5. CONCLUSION

In MHD the displacement current and hence the space charge are neglected. We have stressed the importance of the space charge as an independent variable, especially during instabilities. We have investigated a post-MHD approach in a particular situation. We compared the displacement current and the MHD current. The displacement current becomes relevant for high frequencies (often above 1 Mcycle/s) and when the space variation is small. This is particularly true in the beginning of a new phenomenon, e. g., an instability.

Approaching the problem of post-MHD from an other side we have considered small waves which interfere (including their higher order terms) and thus cause 'divergent strips', which are periodic in space and time, thus moving and wiping over the whole plasma and making it unstable. As turbulence is expected to be generated the dissipation times may be shortened by 4 or 5 orders of magnitude, allowing flashes. Moreover, chain reactions may occur: e. g., starting from sound waves, yielding bright points and next prominences and/or flares.

We have put here the post-MHD approach and the nonlinear wave approach more or less side by side. A more involved approach would be a fuller combination of both. Cf. the electro-hydrodynamics and electro-magneto-hydrodynamics of Kikuchi [9–11].

REFERENCES

1. Callebaut, D. K., *A. P. J.*, submitted, 2006.
2. Callebaut, D. K. and G. K. Karugila, *Physica Scripta*, Vol. 68, No. 1, July 7–21, 2003.
3. Callebaut, D. K. and G. K. Karugila, *Sec. Int. Symp. Unconv. Plasmas*, Vol. 23, Eindhoven Univ. of Techn., Eindhoven, the Netherlands (Eds. D. K. Callebaut, G. C. Dijkhuis and H. Kikuchi), Aug. 2006.
4. Callebaut, D. K. and G. K. Karugila, *Canadian J. of Physics*, submitted, 2006.
5. Callebaut, D. K., G. K. Karugila, and A. H. Khater, *Proc. PIERS 2005*, 720, Hangzhou, China, Aug. 2005.
6. Callebaut, D. K. and A. H. Khater, "Solar activity and its magnetic origin," *Proc. IAU Symp.*, Vol. 233, Ed. V. Bothmer and A. A. Hady, Cairo, Egypt, March 2006.
7. Callebaut, D. K. and A. H. Khater, *Proc. ISUP, Sec. Int. Symp. Unconv. Plasmas*, 36, Eindhoven Univ. of Techn., Eindhoven, the Netherlands (Eds. D. K. Callebaut, G. C. Dijkhuis and H.Kikuchi), Aug. 2006.
8. Callebaut, D. K. and V. I. Makarov, *Proc. IX Pulkovo Int. Conf. on Solar Phys.: Solar Activity as a Factor of Cosmic Weather*, 379, Pulkovo Astr. Obs., (A. V. Stepanov, A. A. Solov'ev and V. A. Dergachev), 196140 St. Petersburg, Russia, July 2005.
9. Kikuchi, H. (ed.), *Relation between Laboratory and Space Plasmas*, Reidel Publ. Co., Dordrecht, The Netherlands, 1981.
10. Kikuchi, H., *Handbook of Atmospheric Electrodynamics*, Vol. 1, 167, H. Volland (ed.), CRC Press, Bonn, 1995.

11. Kikuchi, H., *Electrodynamics in Dusty and Dirty Plasmas (Gravito-Electrodynamics and EHD)*, ASSL, Vol. 258, Kluwer Acad. Press, Dordrecht, 2001.
12. Schrittwieser, R. W. and G. Eder, (eds.), *Proc. Sec. Symp. on Plasma Double Layers and Related Topics*, Inst. für Theor. Physik, Univ. of Innsbruck, A-6020 Innsbruck, Auqstria, 1984.
13. Schrittwieser, R. W. (ed.), *Fourth Symp. on Double Layers and other Nonlinear Potential Structures in Plasmas*, (Innsbruck, Austria), World Scientific, Singapore, 1993.
14. Veselovsky, I. S., *Proc. IAU Symp. 233: Solar Activity and its Magnetic Origin*, Ed. V. Bothmer and A. A. Hady, Cairo, Egypt, March 2006.
15. Veselovsky, I. S., *Proc. ISUP, Sec. Int. Symp. Unconv. Plasmas*, 172, Eindhoven Univ. of Techn., Eindhoven, the Netherlands (Eds. D. K. Callebaut, G. C. Dijkhuis and H. Kikuchi), Aug. 2006.

Helicity or Vortex Generation in Hydrodynamic (HD), Magneto-hydrodynamic (MHD), and Electrohydrodynamic (EHD) Regimes

H. Kikuchi
Institute for Environmental Electromagnetics, 3-8-18, Komagome, Toshima-ku, Tokyo 170, Japan

Abstract— Usually the source-origins of helicity or vortex generation have been considered to be thermohydrodynamic in the hydrodynamic (HD) regime and/or magnetohydrodynamic in the magnetohydrodynamic (MHD). Then fluid helicity is defined as $h_{\mathrm{F}} = \boldsymbol{v} \cdot \boldsymbol{\Omega}$ ($\boldsymbol{v}$: fluid velocity, $\boldsymbol{\Omega}$: fluid vorticity, like-wise magnetic helicity is defined as $h_{\mathrm{M}} = \boldsymbol{v} \cdot \boldsymbol{H}$ ($\boldsymbol{H}$: magnetic field). It has been shown, however, by the present author that an electric quadrupole is also capable for helicity or vortex generation and a new electric helicity defined as $h_{\mathrm{E}} = \boldsymbol{v} \cdot \boldsymbol{E}$ ($\boldsymbol{E}$: electric field) has been introduced. Accordingly, we have now three kinds of helicity, namely fluid, magnetic, and electric helicity. In many cases of atmospheric and space electricity phenomena in nature, helicity or vortex generation is involved as typically seen in tornadic thunderstorms. Conventional theory of tornadic thunderstorms, however, space-charge and electric fields have never been considered properly so far, surprisingly in spite of their effects of significance, because of no theorv for such cases, although those effects have been recognized implicitly by field experiments. This paper fills up these demands by newly introducing the concept of '**Electric Helicity**' based on '**Electrohydrodynamics (EHD)** established and developed over the last more than two decades and such a whole theory is applied to **tornadic thunderstorms**.

1. INTRODUCTION

It is now recognized that there are three kinds of helicity, fluid, magnetic, and electric helicity in the regime of hydrodynamics (HD), magnetohydrodynamics (MHD), and electrohydro-dynamics (EHD), respectively. While fluid and magnetic helicity are known, there have never appeared any ideas on an electric version of helicity surprisingly, except the author's report [1]. This does not mean no existence or importance of *electric helicity*, but simply means no attention of scientists to that so far. Analogously, electric helicity concept should be evolved on the basis of EHD for unconventional plasmas including dusty and dirty plasmas and/or aerosols, that has been developed recently.

2. CLOSE RELATIONSHIP AMONG THREE KINDS OF HELICITY AND FIELD MERGING-RECONNECTION

It has been known that an aircraft moving through the air generates two counter-rotating vortices backwards from each wing tip and that merging-reconnection of the two vortices can be seen in the condensation trails occasionally for high flying jet aircraft [2–5]. The pheno- menological and formal similarities between the merging of aircraft vortex trails and the merging of magnetic field lines have recently been discussed, based upon high resolution photographs with smoke injected into the airstream at the wing tip of an airplane [6]. Fig. 1 shows a schematic diagram of the merging-reconnection for fluid vortex lines (a), magnetic (b), and electric field lines (c).that always involve helicity generation.

High resolution photogeaphs of of smoke trails from the wings tips of a high flying jet aircraft reveal that the two counter-rotating vortices generated back-wards merge together down stream of the spacecraft. This trails form into an X-type configuration and then separated into two U-shaped segments [6] as shown in Fig. 1(a).

Similarly Fig. 1(b) shows the merging-reconnection of oppositely directed magnetic field lines forming a separatrix of an X-type, with the neutral point at the center of the X, as seen on the nightside of the earth during substorms and in the region of solar corona during solar flares. When magnetic merging-reconnection occurs, magntic field energy is converted to plasma kinetic energy as the plasma flow across the separatrix that is also a phenomenon of magnetic helicity.

Figure 1(c) shows the merging-reconnection of oppositely directed electric field lines, the X type on the left panel and the O type on the right panel, as discussed in Chaps. 3, 4, 6, and 7 in [1] that involves a manifestation of electric helicity.

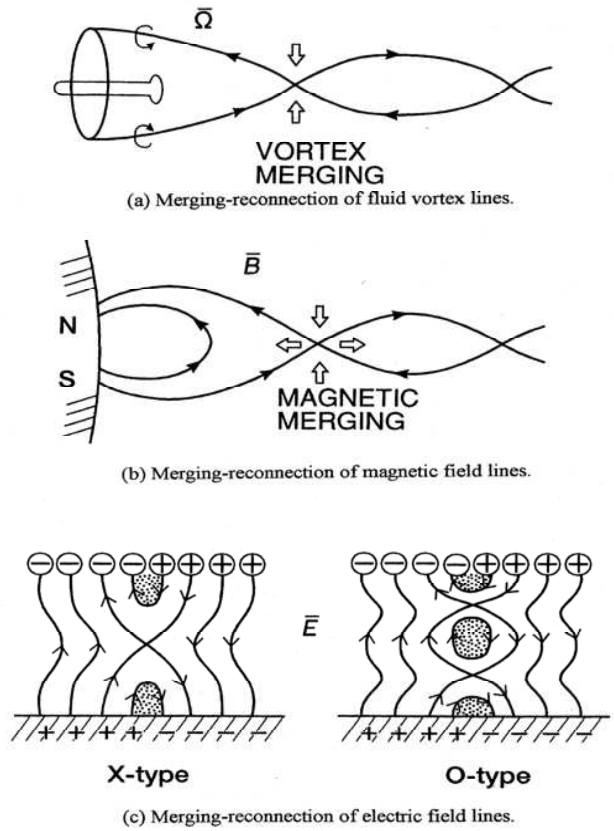

Figure 1: A schematic diagram for the merging-reconnection of fluid vortex lines (a), magnetic field lines (b), and electric field lines (c).

Incorporating a new phenomenon of electric field line merging-reconnection described in [1] into conventional fluid vortex and magnetic field line merging-reconnection, we have now three kinds of mergng-reconnection and helicity that have phenomenological and formal similarities but at the same time essential differences. They are all understood on the basis of the Kelvin-Helmholtz theorem, the source-free frozen-in field concept for high Reynolds and magnetic Reynolds numbers, and the space-charge related frozen-in field concept for high electric Reynolds numbers, and are described by new transport equations for finite Reynolds numbers. However, the electric field transport is largely influenced by electric space charges on the basis of EHD or EMHD in contrast to no space charge in HD or MHD. Magnetic merging concept is based on MHD for a conducting fluid, while electric merging concept is based on EHD or EMHD for a dielectric fluid. This is an essential difference between electric and magnetic merging. Electric field merging-reconnection is most easily triggered by the presence of space charges, typically in dusty and dirty plasmas, causing *space-charge related merging-reconnection*. This type of new reconnection must be understood on the basis of a more basic frozen-in concept, simply derived from the equation of continuity or conservation law for the total current. In fact, electric merging-reconnection could be a significant cause of electric discharges in the atmosphere and in cosmos, and may play important roles in a variety of cosmic and atmospheric phenomena in dusty and dirty plasmas.

3. CONVENTIONAL FLUID AND MAGNETIC HELICITY

Usually the source-origins of helicity or vortex generation have been considered to be thermohydrodynamic in the hydrodynamic (HD) regime and/or magnetohydrodynamic in the magnetohydrodynamic (MHD) and both are so familiar to geoastro and plasma physicists. Then fluid helicity is defined as $h_{\mathrm{F}} = \boldsymbol{v} \cdot \boldsymbol{\Omega}$ ($\boldsymbol{v}$: fluid velocity, $\boldsymbol{\Omega}$: fluid vorticity, like-wise magnetic helicity is defined as $h_{\mathrm{M}} = \boldsymbol{v} \cdot \boldsymbol{H}$ ($\boldsymbol{H}$: magnetic field) as already seen Figs. 1(a) and (b) where $h_{\mathrm{F}} = \boldsymbol{v} \cdot \boldsymbol{\Omega} \neq 0$ and $h_{\mathrm{M}} = \boldsymbol{v} \cdot \boldsymbol{H} \neq 0$.

4. NEW ELECTRIC HELICITY, FLUID VORTEX MERGING AND ELECTRIC RECONNECTION

In contrast to conventional fluid and magnetic helicity, it has been shown by the present author that an electric quadrupole is also capable for helicity generation and a new electric helicity defined as $h_E = \boldsymbol{v} \cdot \boldsymbol{E}$ ($\boldsymbol{E}$: electric field) has been introduced and developed on the basis of a new '**Electrohydrodynamics (EHD)**' established and developed over the last more than two decades. Accordingly, the concept of **Electric Helicity** is closely related to **electric cusp-mirror and reconnection model** and plays most significant roles in atmospheric and space electricity phenomena such as tornadic thunderstorms.

Suppose a dipole or space-charge double layer above a conducting plane or ground, as shown on the left panel of Fig. 2. Then we have an electric cusp or electric field reversal (electrically neutral line or sheet) between opposite space charges where any perturbation leads to electric merging-reconnection, X-type or O-type as shown on the middle or right panel, respectively, as described in Chaps. 4∼6 of [1].

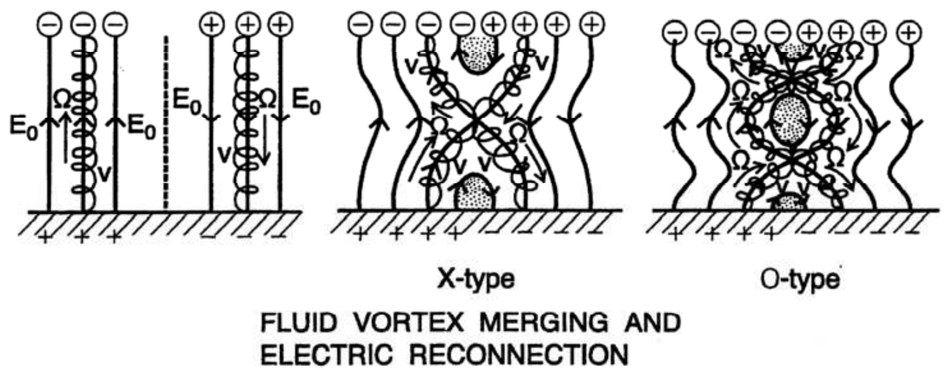

Figure 2: Some possible configurations for coexistence of aligned space charges with an electric cusp and fluid vortex lines: fluid vortex merging and electric reconnection.

Analogously, fluid vortex merging is a phenomenon in which vortex lines in one direction tend to connect other adjacent vortex lines in the opposite direction. In other words, cyclonic and anti-cyclonic helical flows tend to connect each other, leading to vortex breakdown or merging.

When both the fluid and electric Reynolds numbers are high enough in the EHD regime, for instance in the presence of helical turbulence and a DC electric field on the background, both the fluid vorticity and electric field satisfy the Kelvin-Helmholtz equation, as discussed in Chap. 7 of [1] and as illustratd on the left panel of Fig. 2. Then, the following relations hold:

$$h_F = \boldsymbol{v} \cdot \boldsymbol{\Omega} \neq 0, \tag{1}$$

$$h_F = \boldsymbol{v} \cdot \boldsymbol{E} \neq 0, \tag{2}$$

$$\boldsymbol{\Omega} \times \boldsymbol{E} = 0, \qquad (\boldsymbol{E} = \boldsymbol{E}_0), \tag{3}$$

where h_F and h_E stand for fluid and electric helicity respectively. Actually, the electric field due to a space-charge double layer above a ground produces an electric cusp, and makes the background turbulence helical, the Reynolds and electric Reynolds numbers high, and electric and vortex lines frozen to the fluid at least for an initial stage of the evolution of vortices.

However, any perturbation exerted on a cusp region, for instance an invasion of dust particles into a cusp region, can cause local singularities and a local decrease in both the fluid line reconnection could occur most likely in that region, indicating a coalescence of fluid vortex and electric Reynolds numbers, leading to a local breakdown of the frozen-in field concept for both fluid vorticity and electric field. Consequently, both vortex line merging and electric field breaking point and electric reconnection point, X-type or O-type, as illustrated on the middle or right panel of Fig. 2.

5. APPLICATION OF EHD THEORY WITH ELECTRIC HELICITY AND RECONNECTION TOGETHER WITH A CONVENTIONAL HD THEORY TO TORNADIC THUNDERSTORMS

In the previous sections, a description of an electrified or charged fluid vortices in the EHD regime, termed as *EHD vortices*, has been presented with their basic features as an extension of conventional uncharged or non-ionized vortices in the HD regime. These EHD vortices are necessarily thought to be relevant to tornadic thunderstorms, cyclones, hurricanes, typhoons, whirlwinds, and sand or dust storms. In this secion, we consider *tornadic thunderstorms* as a typical example of EHD vortices.

In many cases, tornadoes are thought to be composed of uncharged and charged components different from each other in terms of velocity, vorticity, helicity, and appearance (shape and luminosity). Their usual visible dark portion may correspond to uncharged tornadoes, while luminous or bright part may involve charged tornadoes, accompanying lightning discharge with return strokes. Usually, visible tornadoes have been considered to be ascending hot streams of thermo-hydrodynamic origin. As already stressed, however, quadrupole-like cloud-charge configurations with their images onto ground can be a source-origin of helicity and vortex generation in large-scale even if ascending fluids are uncharged as well as small-scale helical turbulence, implying the possibility of additional large-scale vortex generation. Profound better description of tornadic thunderstorms can be now drawn by a new 'electrohydrodynamics (EHD)' with novel physical concepts of 'electric reconnection' and 'critical velocity', introducing '**Electric Helicity and Vortex-Generation**'. Actually, artificial mapping of charge distributions and electric field lines onto existing fluid vortex lines sketched for Minneapolis, Minesota tornado provides a reasonable self-consistent overall picture of the EHD model with particular reference to tornadic destructtion by dust cluster injection into vortex breakdown or electric cusp (X-type and/or O-type) points.as in Chap. 9 (Fig. 9.3) of [1].

6. CONCLUSION

A new concept of '**Electric Helicity**' has been introduced based on '**EHD with Electric Cusp-Mirror and Reconnection Model**' in addition to conventional concepts of 'Fluid Helicity' in the HD regime and of 'Magnetic Helicity' in the MHD regime. While these three kinds of helicity play remarkable roles in atmospheric and cosmic environments, their relative importance for terrestrial atmospheric phenomena such as thunderstorms are summarized as follows:

1. So far conventional theory has mainly been limited to fluid and/or magnetic helicity. For example, tornadoes have been based mainly on (T)HD and partly on MHD, since they have been considered to be as ascending hot air streams of (T)HD origin and magnetic field generation due to return stroke currents has been drawn by MHD;
2. In many cases, however, tornadoes involve or accompany lightnings, and for these cases, no theory has been seriously attempted as yet, though observations have been fairly accumulated. It has been shown in this paper for the first time that electric helicity plays most significant roles in tornadic thunderstorms that now can be described by a new EHD with novel physical concepts of 'electric reconnection' and critical velocity' as well as modern concepts of 'self-organization' and 'chaos'.
3. In particular, tornadic thunderstorms are involved by close couplings between vortex merging and electric reconnection and magnetic field effects are only secondary.
4. Utilizing 'dust-related electric reconnection' by injection of DUST clusters into electric cusps (X- and/or O-type) a new method of tornado destruction is newly proposed.

REFERENCES

1. Kikuchi, H., *Electrohydrodynamics in Dusty and Dirty Plasmas*, Kluwer Academic Publishers, Dordrecht/The Netherlands, 2001.
2. Smith, T. B. and K. M. Beesmer, "Contrail studies of jet aircraft," *ASTIA AD*, Vol. 217, 188, Meteorology Research Inc., Pasadena, CA, 1959.
3. Crow, S. C., "Stability theory for a pair of trailing vortices," Amer. Inst. of Aeronautics and Astronautics, Vol. 8, 2172–2179, 1970.
4. Pumir, A. and E. D. Siggia, "Vortex dynamics and existence of solutions to the Navier-Stokes equations," *Phys. Fluids*, Vol. 30, 1606–1626, 1987.

The 3D GL EM-Flow-Heat-Stress Coupled Modeling

G. Xie, **J. H. Li**, **L. Xie**, **F. Xie**, **and J. Li**

GL Geophysical Laboratory, USA

Abstract— In the steel and metal continuous caster the EM stirring installation plays important role. We have proposed the 3D and 2.5D AGILD electromagnetic stirring (EMS) modeling in PIERS 2005 in Hangzhou and PIERS 2006 in Cambridge. The AGILD EMS modeling can be used to accurately calculate the EM field in the EM stirring. The electromagnetic field in the stirring generates the Lorenz force. The voluminal distributed Lorenz force drives the steel and metal liquid rotationally to move under high temperature. Therefore, it is necessary to consider EM, flow, heat, stress coupled effective action in the EM stirring caster. In this paper, we propose a 3D Global and Local GL EM, flow, heat and stress coupled modeling. The inhomogeneous EM, flow, heat, and mechanical parameter domain is divided into a set of several small sub domains. The parameters in the sub domain are isotropic or anisotropic piecewise constant. The initial Global EM, flow, temperature, and displacement field are updated successively by the local scattering field in each sub domain. When all sub domains are scanned, the GL coupled EM, flow, temperature, and displacement field are obtained. In the method, there is no boundary reflection error. There is no big matrix needs to be solved. The coordinate singularity in $\rho = 0$ is removed. The simulations show that our 3D GL EM, flow, heat and stress coupled modeling (EMFHS) is fast, accurate, consistent and stable. The GL EMFHS coupled modeling has wide application in the EM stirring in the cast, atmosphere, environment, geophysics, earth sciences and space sciences and engineering.

1. INTRODUCTION

The EM stirring installation plays important role in the steel and metal continuous caster. In PIERS 2005 in Hangzhou we proposed the 3D AGILD EMS stirring modeling [1]. The 2.5D AGILD EMS modeling in the cylindrical coordinate system was published in PIERS 2006 in Cambridge [2]. The GILD EMS modeling can be used to accurately calculate the EM field in the EM stirring caster. In this paper, we propose a 3D Global and Local GL EM, Flow, Heat, and Stress coupled modeling. The EM field in the stirring generates the Lorenz force. The volume distributed Lorenz force drives the steel and metal liquid rotationally to move under high temperature. Then the strain and stress occur in the solidification process. Therefore, it is necessary to consider EM, flow, heat, stress coupled effective action in the EM stirring caster. In this paper, we propose a 3D Global and Local GL EM, flow, heat and stress coupled GL EMFHS modeling [3]. The GL EMFHS coupled modeling can consistent couple EM, flow, temperature, and stress field in the EM stirring processes. The modeling can exactly calculate EM, flow, temperature, and displacement coupled field in the stirring in te caster. The GL EMFHS coupled modeling has wide application in the EM stirring in the caster, atmosphere, environment, geophysics, earth sciences and space sciences and engineering.

Meir et al. [4] described Finite Element Method (FEM) for flow velocity in molten metals during electromagnetic stirring. Moffatt studied the fluid flow induced by a rotating magnetic field in the paper [5] in 1965. In these investigations the artificial boundary condition for the magnetic field is difficult. Some researcher used current, in stead of magnetic field, to avoid artificial boundary condition for the magnetic field. The complete EM, flow, heat, and stress coupled modeling is lack in the previous study. Our EMFHS is the complete EM, flow, heat, and stress coupled modeling.

The GL EMFHS coupled modeling is different from the previous methods in [4, 5]. The inhomogeneous EM, flow, heat, and mechanical parameter domain are divided into several small sub domains. The parameters in the sub domain are isotropic or anisotropic piecewise constant. The initial Global EM, flow, temperature, and displacement field are updated successively by the local scattering field in each sub domain. When all sub domains are scanned, the GL coupled EM, flow, heat, and stress field are obtained. In the GL EMFH method, there is no artificial boundary and error boundary reflection. There is no big matrix needs to be solved. The coordinate singularity in the $\rho = 0$ is removed. The GL EMFHS coupled modeling is accurate, fast, consistent, and stable. The GL EMFHS coupled modeling has advantages over FEM and Finite Difference method (FD).

The plan of this paper is as follows. The introduction is described in Section 1. The EM, incompressible viscous flow, thermal heat and stress coupled model is described in Section 2. In Section 3, we propose the GL EMFHS coupled modeling. The advantages of the GL EMFHS coupled modeling are described in Section 4. The simulation and applications are described in Section 5. In Section 6, we conclude the paper.

2. THE EM, FLOW, HEAT, AND STRESS COUPLED MODEL

2.1. The Electromagnetic Model

We consider electromagnetic field in the EM stirring caster. The stirring is similarly designed by asynchronism electromotor stator. The Maxwell equation governs the EM field in the stirring. The rotational fluid steel and metal flow generates the induction electric field which couples EM and flow field as follows,

$$\begin{aligned} \nabla \times E &= -i\omega\mu H, \\ \nabla \times H &= (\sigma + i\omega\varepsilon)E + (\sigma + i\omega\varepsilon)\mu V \times H + J, \end{aligned} \tag{1}$$

where E is the electric field, H is the magnetic field, V is the flow velocity, J is the electric current, σ is the electric conductivity, ε is the dielectric, μ is the magnetic permeability, and ω is the angle frequency.

2.2. The Incompressible Viscous Flow Model

The incompressible viscous steady flow is governed by the Navier Stocks flow equation

$$-\eta\Delta V + \rho(V \cdot \nabla)V + \nabla p = J \times \mu H - \beta\rho T g, \tag{2}$$

where V is the flow velocity vector, p the hydrodynamic pressure, H is the magnetic field, T is the temperature, ρ is the density which depends on the temperature, η is the viscosity, β is thermal expansion coefficient. g is the gravity acceleration, μ is the magnetic permeability.

2.3. The Thermal Heat Model

In the EM stirring caster, the magnetic permeability is μ_0 because the temperature is higher than Curie point. The thermal heat should be coupled into the steel and metal flow motion as follows

$$\Delta T - q(V \cdot \nabla)T = h(E, H, V) \tag{3}$$

where T is the temperature, $q = \rho/\kappa$, ρ is the density, κ is the thermal conductivity, V is the flow velocity victor, h is the heat source which is nonlinear function of the electric field E, magnetic field H, and flow velocity V.

2.4. The Boundary Condition

The magnetic field H, flow velocity field V, and temperature T are coupled by the Equations (1), (2), and (3) nonlinearly. The magnetic field H and temperature T are of the far field radiation at the infinite. The boundary condition of the velocity, $V = V_0$, on the cylindrical tube wall.

2.5. The Displacement and Stress Model

The solidification displacement and stress model is governed by the following elastic-plastic flow thermal magnetic joint equation,

$$\begin{aligned} &\frac{\partial \sigma_{s,ij}}{\partial x_j} + \omega_s^2 \rho_s u_s = f_i(B, p, T), \\ &\sigma_{s,ij} = D\left(\lambda_s, \mu_s\right) \varepsilon_s\left(u_s\right), \end{aligned} \tag{4}$$

and the corresponding boundary condition or radiation boundary conditions, where $\sigma_{s,ij}$ is solidification stress tensor which symbol is different from the electric conductivity, u_s is the displacement which symbol is different from the vortex $u = \nabla \times V$, ω_s is displacement field frequency which is very low and different from the EM field frequency ω, ρ_s is the density which is different from the resistivity, λ_s, μ_s are the Lame constants, μ_s is different from the magnetic permeability. ε_s is the strain field which is different from the dielectric parameter, the right hand of the (4), $f_i(B, pT)$, depends on the magnetic flux B, pressure p, and temperature T.

3. GL EMFHS COUPLED MODELING

The novel Global and Local field modeling and inversion is proposed in [3], we propose GL EMFHS COUPLED MODELING in this section

3.1. Iteration for Solving the Coupled Nonlinear Equations

We use the following iteration to solve the EM, Navier Stocks flow, heat, and mechanical coupled nonlinear Equations (1)–(4).

$$\nabla \times \frac{1}{(\sigma + i\omega\varepsilon)} \nabla \times H^{(n)} + \left(\nabla \times \mu V^{(n-1)} \times H^{(n)}\right) = Q_M, \tag{5}$$

$$-\eta \Delta V^{(n)} + \rho \left(V^{(n-1)} \cdot \nabla\right) V^{(n)} + \nabla p = J^{(n)} \times \mu H^{(n)} - \beta \rho T^{(n-1)} g, \tag{6}$$

$$\Delta T^{(n)} - q \left(V^{(n)} \cdot \nabla\right) T^{(n)} = h \left(E^{(n)}, H^{(n)}, V^{(n)}\right). \tag{7}$$

We solve the linearization Equations (5), (6), and (7) in order to form the nth circle of the iteration. Then we solve the following elastic-plastic flow thermal magnetic joint Equation (4) to find the solidification displacement, strain and stress,

$$\begin{aligned} &\frac{\partial \sigma_{s,ij}^{(n)}}{\partial x_j} + \omega_s^2 \rho_s u_s^{(n)} = f_i \left(B^{(n)}, p^{(n)}, T^{(n)}\right), \\ &\sigma_{s,ij}^{(n)} = D\left(\lambda_s, \mu_s\right) \varepsilon_s \left(u^{(n)}\right). \end{aligned} \tag{8}$$

3.2. Division of the Domain

The inhomogeneous EM, flow, thermal, and mechanical parameter domain Ω is divided into a set of the several sub domains $\{\Omega_k\}$, $k = 1, 2, \ldots N$. such that $\Omega = \bigcup_{k=1}^{N} \Omega_k$. The division is mesh or meshless.

3.3. GL Modeling for Solving the Magnetic Field Linearization Equation (5)

3.3.1.

In each Ω_k, $k = 1, 2, \ldots N$, we solve the adjoint Green's magnetic field differential integral equation of the Equation (4). By the dual curl procession, the adjoint Green's magnetic field differential integral equations are reduced into 3×3 matrix equations. By solving the 3×3 matrix equations, the 3×3 magnetic Green's function tensor $G_k^{M,(n)}(r', r)$ is calculated.

3.3.2.

The global magnetic field is updated by the following local scattering magnetic field differential integral equation

$$\begin{aligned} H_k^{(n)}(r) \;=\; & H_{k-1}^{(n)}(r) + \int\limits_{\Omega_k} \left(\frac{1}{(\sigma + i\omega\varepsilon)_{k-1}} - \frac{1}{(\sigma + i\omega\varepsilon)_k}\right) \nabla \times G_k^{M,(n)}(r', r) \left(\nabla \times H_{k-1}^{(n)}(r')\right) dr' \\ & + \int\limits_{\Omega_k} \left(\nabla \times \left(G_k^{M,(n)}(r', r)\right) \times \mu \left(V_{k-1}^{(n)} - V_k^{(n)}\right)\right) H_{k-1}^{(n)}(r')\, dr'. \end{aligned} \tag{9}$$

The $H^{(n)}(r) = H_N^{(n)}(r)$ is the GL magnetic field solution of the Equation (5).

3.4. GL Modeling for Solving the Flow Field Linearization Equation (6)

Let $u = \nabla \times V$, the Navier Stocks flow Equation (6) is reduced to

$$\Delta u^{(n)} - \kappa \left(V^{(n-1)} \cdot \nabla\right) u^{(n)} = M(E^{(n)}, H^{(n)}, T^{(n)}), \tag{10}$$

where $\kappa = \rho/\eta$,

3.4.1.

In each Ω_k, $k = 1, 2, \ldots N$, we solve the adjoint Green's flow field differential integral equation of the Navier Stocks Equation (10). By the dual gradient procession, the adjoint Green's flow field differential integral equations are reduced into 3×3 matrix equations. By solving the 3×3 matrix equations, the 3×3 magnetic Green's function tensor $G_k^{F,(n)}(r', r)$ is calculated.

3.4.2.

The Global flow field is updated by the following local scattering flow field differential integral equation

$$u_k^{(n)}(r) = u_{k-1}^{(n)}(r) + \int\limits_{\Omega} \nabla \cdot \left(\left(\kappa_k V_k^{(n-1)}\left(r'\right) - \kappa_{k-1} V_{k-1}^{(n)}\left(r'\right) \right) G_k^{F,(n)}\left(r', r\right) \right) u_{k-1}^{(n)}\left(r'\right) dr', \tag{11}$$

The $u^{(n)}(r) = u_N^{(n)}(r)$ is the GL flow field solution of the Equation (10). $V^{(n)} = \frac{1}{4\pi} \int\limits_{\Omega} \frac{\nabla \times u^{(n)}(r')}{|r'-r|} dr'$ is the GL Navier Stocks flow velocity solution of the Equation (6),

The pressure $p^{(n)} = \frac{1}{4\pi} \int\limits_{\Omega} \frac{\nabla \cdot \left(\rho\left(V^{(n)} \cdot \nabla\right) V^{(n)}\right) + \nabla \cdot \left(J^{(n)} \times \mu H^{(n)} - \beta \rho T^{(n-1)} g\right)}{|r'-r|} dr'$ is obtained.

3.5. GL Modeling for Solving The Thermal Temperature Field Linearization Equation (7)

3.5.1.

In each Ω_k, $k = 1, 2, \ldots N$, we solve the adjoint Green's thermal field differential integral equation of the heat Equation (7). By the dual gradient procession, the adjoint Green's temperature field differential integral equations are reduced into 3×3 matrix equations. By solving the 3×3 matrix equations, the 3×3 temperature Green's function tensor $G_k^{H,(n)}\left(r', r\right)$ is calculated.

3.5.2.

The Global temperature field is updated by the following local scattering temperature field differential integral equation

$$T_k^{(n)}(r) = T_{k-1}^{(n)}(r) + \int\limits_{\Omega} \nabla \cdot \left(\left(q_k V_k^{(n)}\left(r'\right) - q_{k-1} V_{k-1}^{(n)}\left(r'\right) \right) G_k^{H,(n)}\left(r', r\right) \right) T_{k-1}^{(n)}\left(r'\right) dr'. \tag{12}$$

The $T^{(n)}(r) = T_N^{(n)}(r)$ is the GL temperature field solution of the Equation (7).

3.6. GL Modeling for Solving The Elastic-plastic Flow Thermal Magnetic Linearization Equation (8)

3.6.1.

In each Ω_k, $k = 1, 2, \ldots N$, we solve the adjoint Green's flow field differential integral equation of the mechanical elastic Equation (8). By the dual gradient procession, the adjoint Green's displacement field differential integral equations are reduced into 3×3 matrix equations. By solving the 3×3 matrix equations, the 3×3 magnetic Green's function tensor $G_k^{D,(n)}\left(r', r\right)$ is calculated.

3.6.2.

The Global displacement field is updated by the following local scattering displacement and strain field differential integral equation

$$\vec{u}_{s,k}^{(n)}(r) = \vec{u}_{s,k-1}^{(n)}(r) - \int\limits_{\Omega_k} \vec{\varepsilon}^{T} \left(\vec{G}_k^{D(n)}\left(r', r\right) \right) D\left(\lambda_{s,k} - \lambda_{s,k-1}, \mu_{s,k} - \mu_{s,k-1}\right) \vec{\varepsilon}\left(\vec{u}_{s,k-1}^{(n)}\left(r'\right) \right) dr', \tag{13}$$

The $\vec{u}_s^{(n)}(r) = \vec{u}_{s,N}^{(n)}(r)$ is the GL displacement field solution of the Equation (8), $\sigma_{s,ij}^{(n)} = D\left(\lambda_s, \mu_s\right) \varepsilon_s \left(u_{s,N}^{(n)}\right)$ is the solidification stress tensor.

4. THE ADVANTAGES OF THE GL EMFHS COUPLED MODELING

The GL method has advantages for resolving the historical difficulties in FEM and FD and Born methods [3]. We describe the advantages of the GL EMFHS modeling in this section.

4.1. There Is No Matrix Equation in the GL EMFHS Modeling

Our GL EMFHS coupled modeling has advantages to overcome the difficulties of the FEM and FD methods. Because of using the FEM and implicit FD method, the EM, flow, thermal heat, and stress modeling are discretized into the big matrix equations. The cost to solve the coupled big matrix equations is very high. In the GL EMFHS coupled modeling, there is only 3×3 matrix equations need to be solved to obtain adjoint Green's function. There is no big matrix equation to be solved in the GL EMFHS coupled modeling that greatly reduces the computational cost.

4.2. There Is No Artificial Boundary and No Absorption Condition in the GL EMFHS Modeling

The absorption condition on the artificial boundary is necessary for FEM or implicit FD modeling. The error reflections from the numerical absorption condition on the artificial boundary degrade the accuracy of the FEM and FD modeling. To avoid of using the complex artificial boundary condition, paper [4] used the electric current instead of the magnetic field that caused very heavier cost to solve big full matrix equation. The temperature boundary condition on the wall is an approximation in [4]. The approximation thermal boundary condition is removed in the GL EMFHS coupled modeling, therefore the GL EMFHS modeling increases the accuracy of coupled EM, flow, temperature, displacement and stress field.

4.3. There Is No Coordinate Singularity in the GL EMFHS Modeling

There are $1/\rho$ and $1/\rho^2$ coordinate singularity at the pole point $\rho = 0$ in the cylindrical coordinate EM, flow, heat, and displacement equations. The coordinate singularity appears in the FEM and FD discretization equations of the EM, flow, heat, and Lame displacement equations that is a difficulty. Because there is no coordinate singularity in the analytic Green's function, the GL EMFHS overcomes the coordinate singularity difficulty.

4.4. GL EMFHS Parallel Modeling

The big matrix equation, complicated and inaccurate absorption boundary condition, and coordinate singularity discretization are difficulties and obstacles to parallelize FEM and FD modeling. The GL EMFHS has no big matrix equation, no artificial absorption condition, and no coordinate singularity that greatly reduce the computational cost, complexity, and increase the accurate, moreover, GL EMFHS is self parallel algorithm.

5. GL EMFHS MODELING SIMULATIONS AND APPLICATIONS

5.1. The GL EMFHS Coupled Modeling Simulation in the EM Stirring in the Steel Caster

Our GL EMFHS coupled modeling has been used to calculate the EM field, flow velocity, pressure, temperature, displacement, strain, and stress field for some EM stirring. The outer radius of the stirring is 500 mm, the internal radius is 350 mm, and it is divided into 6 sectors. The electric current has inverse direction for any adjoining two sectors. The thick of the copper tube is 3.5 mm. The conductivity, σ_{steel}, of the carbon steel is 749617 S/M, the conductivity, σ_{copper}, of the copper tube is 3.16628779×10^7, the conductivity, σ_{stirring}, of the stirring is 369417 S/M. The steel liquid is in inside of the copper tube. The stirring surrounds the copper tube and is outside of the tube. The length of the stirring is 250 mm. The density of the steel, ρ_{steel}, is $2:38\ \times 10^3\,\text{kg m}^{-3}$. The viscosity, η, of the steel fluid is $1.8 \times 10^{-3}\,\text{kg m}^{-1}\ \text{s}^{-1}$. The thermal conductivity of the steel, κ_{steel}, is 28 Btu/(hr.Ft.F). The Young's modulus of the steel is $200 \times 10^9\,\text{N/M}^2$. The frequency is 4 Hz. The input electric current density intensity is $1\,\text{A/mm}^2$. The GL EMFHS coupled modeling

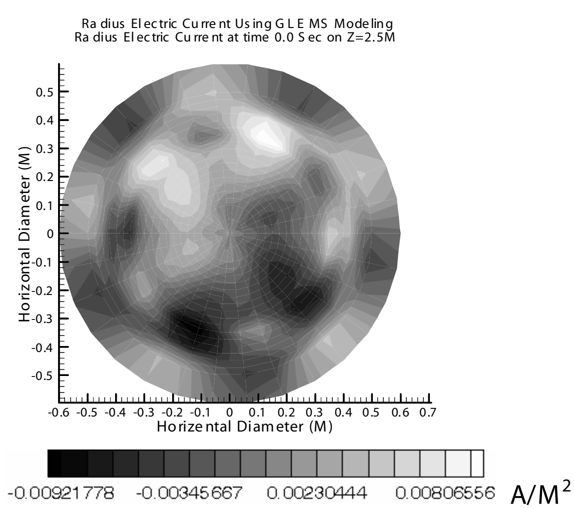

Figure 1: Radius electric current at 0 sec. using GL EMFHS modeling.

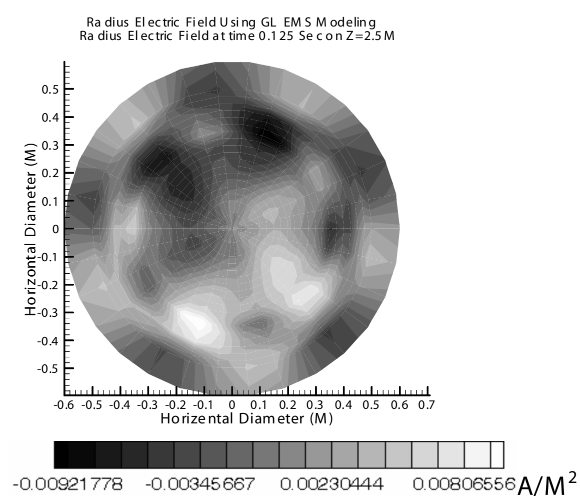

Figure 2: Radius electric current at 0.125 sec. using GL EMFHS modeling.

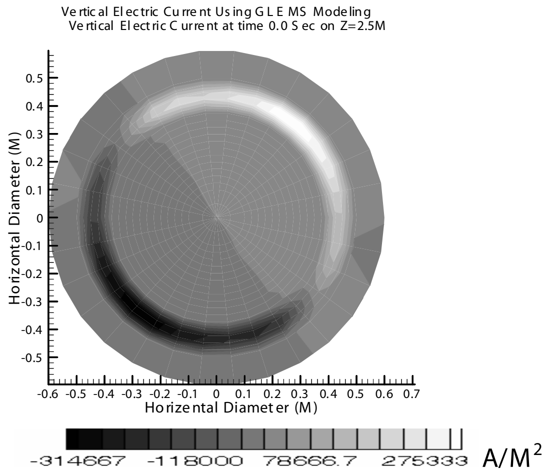

Figure 3: Vertical electric current at 0 sec. using GL EMFHS modeling.

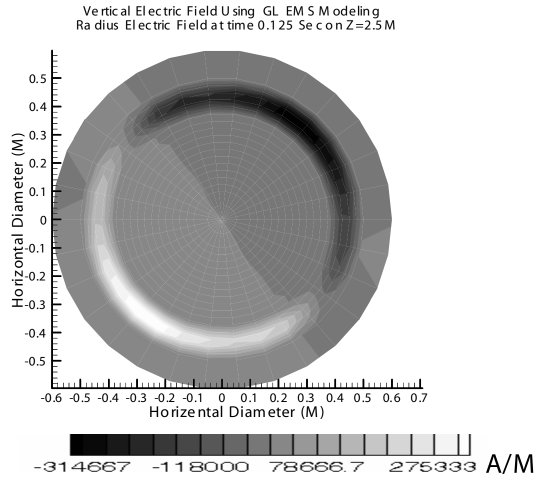

Figure 4: Vertical electric current at 0.125 sec. using GL EMFHS modeling.

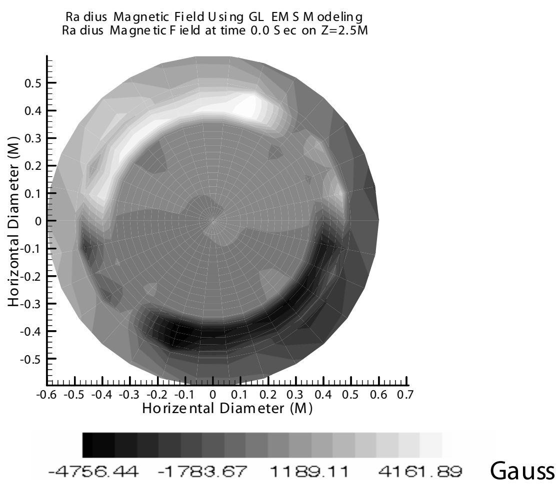

Figure 5: Radius magnetic flux at 0.sec. using GL EMFHS modeling.

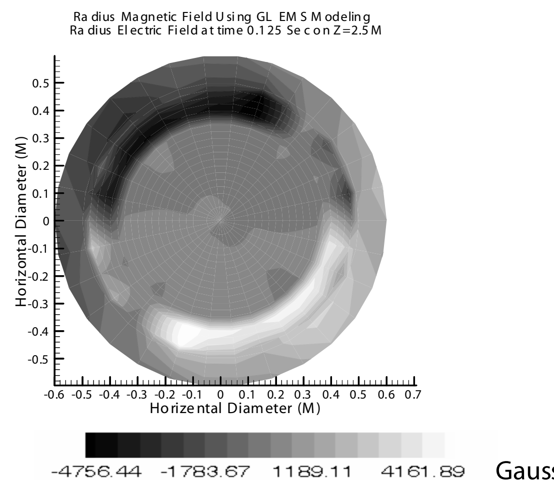

Figure 6: Radius magnetic flux at 0.125 sec. using GL EMFHS modeling.

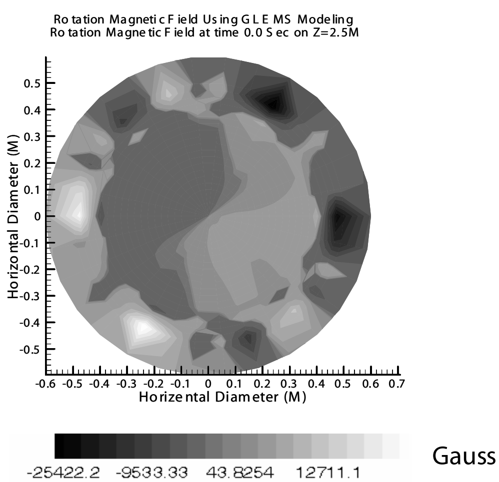

Figure 7: Rotation magnetic flux at 0.0 sec. using GL EMFHS modeling.

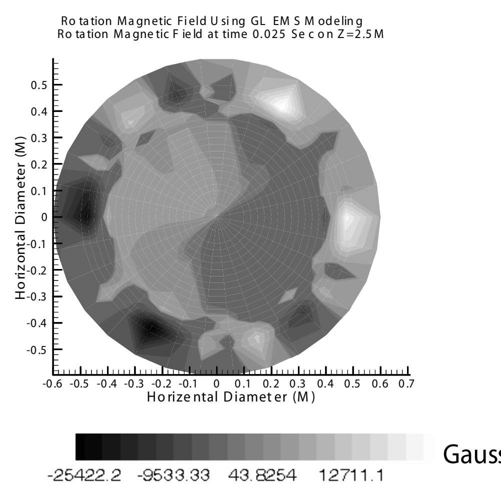

Figure 8: Rotation magnetic flux at 0.125 sec. using GL EMFHS modeling.

calculates EM, flow velocity, temperature, displacement, strain, and stress field. Due to the page limitation, we present the electric current density and the magnetic flux density distribution on the horizontal section at $Z = 0,25\,\mathrm{M}$ in the Figures 1–8. Before installation of the stirring without steel flow, the factor did measure the magnetic flux intensity. By using digit magnetic GAUSS meter, the measurement value of the magnetic flux intensity at the center of the stirring is 1300 Gauss. By using our GL EMFHS coupled modeling simulation, the evaluated magnetic flux intensity is 1308 Gauss at the center of the stirring. The simulation results of the stirring in steel caster and in uninstallation show that the GL EMFHS modeling is accurate, fast, consistent, and stable. To compare the EM field in Figures 1–8 with the EM field in the corresponding figures in paper [2], The GL EMFHS modeling accurately calculates the coupled effect in the EM field in Figures 1–8.

5.2. The Application of the GL EMFHS Coupled Modeling In The Earth Science

There is magnetic field, rock and metal flow with high temperature, and ground stress in the internal of Earth. The GL EMFHS Coupled Modeling in the sphere coordinate can accurately and quickly calculate the EM, rock flow velocity, temperature, displacement, and stress field distribution in the internal of the Earth. The GL EMFHS Coupled Modeling is very useful for Earth science, geological structure, geophysical and oil exploration, and Earthquake sciences and engineering.

5.3. The Application of the GL EMFHS Coupled Modeling in the Space Science and Engineering

The GL EMFHS Coupled Modeling has important applications for the space science and engineering and atmosphere sciences.

6. CONCLUSIONS

The GL EMFHS coupled modeling is proposed and validated in this paper. The simulations show that the GL EMFHS coupled modeling is accurate, stable, and fast. The adjoint differential integral Equations (9), (11), (12), and (13) are new equation. The GL EMFHS coupled modeling has wide application in the EM stirring in the caster, atmosphere, environment, geophysics, earth sciences and space sciences and engineering.

REFERENCES

1. Xie, G., J. Li, J. H. Li, and F. Xie, "New AGILD EMS electromagnetic field modeling," *Progress in Electromagnetics Research Symposium 2005*, 168–172, Hangzhou, China, August 22–26, 2005.
2. Xie, G., J. H. Li, J. Li, and F. Xie, "3D and 2.5D AGILD EMS stirring modeling in the cylindrical coordinate system," *Proc. of PIERS*, 505–509, Cambridge, 2006.
3. Xie, G., F. Xie, L. Xie, and J. Li, "New GL method and its advantages for resolving historical difficulties," *Progress in Electromagnetics Research*, Vol. PIER 63, 141–152, 2006.
4. Meir, A. J. and P. G. Schmidt, "Analysis and finite element simulation of MHD flows, with an application to liquid metal processing," *Fluid Flow Phenomena in Metals Processing, Proceedings, 1999 TMS Annual Meeting*, 561–569, Pennsylvania, 1999.
5. Mffatt, H. K., "On fluid flow induced by a rotating magnetic field," *Journal of Fluid Mechanics,* Vol. 22, 521–528.

Reconstructing Properties of Subsurface from Ground-penetrating Radar Data

Hui Zhou[1,3], **Dongling Qiu**[2], **and Takashi Takenaka**[3]

[1]College of Marine Geoscience, Ocean University of China, Qingdao 266003, China
[2]College of Chemistry and Chemical Engineering, Ocean University of China, Qingdao 266003, China
[3]Department of Electrical and Electronic Engineering, Nagasaki University, Nagasaki 852-8521, Japan

Abstract— This paper discusses the reconstruction of permittivity, permeability and conductivity from ground-penetrating radar (GPR) data by using a time-domain reconstruction technique. The objective functional is defined as the integration over time of some power of weighted residual between observed and calculated data. The power of the objective functional is any number larger than 1. The gradients of the functional to the unknown parameters are derived. A synthetic reconstruction example from multi-offset noise-free and noisy data is illustrated by using L_2, $L_{1.6}$ and $L_{1.2}$ norm of objective functional. A reconstruction example from experimental common-offset data is also demonstrated. In this example L_2 and $L_{1.2}$ norms are used. Both synthetic and experimental reconstructed results show that the reconstructed results by using low-order norms are better than those by using the conventional Euclidean norm.

1. INTRODUCTION

Surface ground-penetrating radar (GPR) has been applied to various fields and solved many detection requirements [1–5]. As one kind of interpretation methods, the techniques to reveal quantitative properties of subsurface from GPR data have been investigated by many researches [5–16]. Among these methods, the inverse scattering reconstruction techniques in the time- and frequency-domain have been proposed [9–16].

We have discussed a forward-backward time-stepping (FBTS) method to reconstruct electrical property profiles of objects using the time-domain microwave data [15, 16]. The gradients of the cost functional with respect to unknown parameters can be expressed explicitly by introducing an adjoint field. The norm used in the objective functional is Euclidean.

Generally, the reconstructed result may be degraded when the data are contaminated by noise. However, the result may be improved by using low-order norms [17]. In this paper we define the objective functional as the integration over time of some power of weighted residual between observed and calculated data. The power of the objective functional is any number larger than 1. The gradients of the functional with respect to unknown parameters are derived.

To demonstrate the effect of the norms to reconstruction results a synthetic and an experimental reconstruction example for nonmagnetic media are conducted. For the synthetic example the nonconductive subsurface is reconstructed from multi-offset noise-free and noisy data. L_2, $L_{1.6}$ and $L_{1.2}$ norms are used in this example. For the experimental example, the reconstruction is conducted from common-offset data by using L_2 and $L_{1.2}$ norms. The data are acquired by a network analyzer based radar system. The transmitting and receiving antennas are 2.7-cm long dipoles. Before the reconstruction the data are transformed into two-dimensional (2-D).

2. RECONSTRUCTION METHOD

Maxwell's equations for TM mode in a 2-D nondispersive medium are expressed as $L\mathbf{v}=\mathbf{j}$, where $\mathbf{v} = (E_y\,\eta H_x\,\eta H_z)^t$, $\mathbf{j} = (\eta J_y\,0\,0)^t$, and $L \equiv \bar{\mathbf{A}}\frac{\partial}{\partial x} + \bar{\mathbf{B}}\frac{\partial}{\partial z} - \bar{\mathbf{F}}\frac{\partial}{\partial(ct)} - \bar{\mathbf{G}}$, $\bar{\mathbf{A}}$, $\bar{\mathbf{B}}$ are 3 by 3 constant matrixes, $\bar{\mathbf{F}}$, $\bar{\mathbf{G}}$ are 3 by 3 matrixes of relative permittivity and permeability, or conductivity. c is the speed of light, t is time. Superscript t means transpose.

Suppose that in a homogeneous background there is an inhomogeneous object. A transmitter at $\mathbf{r}^t_m (m = 1, 2, \cdots, M)$ illuminates the object by a current pulse $J_y(t)$ in the y-direction. For each illumination the y-component of time-domain electric field data are collected by receivers at $\mathbf{r}^r_n (n = 1, 2, \cdots, N)$. The distributions of the electrical parameters $\mathbf{p} = (\varepsilon_r\,\mu_r\,\eta\sigma)^t$ are reconstructed from the received data by minimizing a L_l norm objective functional

$$Q(\mathbf{p}) = \int_0^{cT} \sum_{m=1}^{M} \sum_{n=1}^{N} K_m(\mathbf{r}^r_n, t) \left|\nu_{1m}(\mathbf{p}; t) - \tilde{E}_{ym}(\mathbf{r}^r_n, t)\right|^l d(ct), \tag{1}$$

where $l > 1$ is the power, $\tilde{E}_{ym}(\mathbf{r}_n^r, t)$ is observed electric field, $\nu_{1m}(\mathbf{p}; \mathbf{r}_n^r, t)$ is the calculated field for guessed parameters $\mathbf{p}$, $K_m(\mathbf{r}_n^r, t)$ is a weighting function with a value of 0 at $t = T$, T is the duration of observed data. η is the impedance of vacuum, ε_r, μ_r are relative permittivity and permeability of the medium, σ is conductivity.

The gradients g_ε, g_μ, $g_{\eta\sigma}$ of $Q(\mathbf{p})$ with respect to ε_r, μ_r, and $\eta\sigma$ are expressed explicitly as

$$g_\varepsilon = d_1 = l\int_0^{cT}\sum_{m=1}^{M} w_m^1(\mathbf{p}; \mathbf{r}, t)\frac{\partial\nu_{1m}(\mathbf{p}; \mathbf{r}, t)}{\partial(ct)}d(ct), \tag{2}$$

$$g_\mu = d_2 = l\int_0^{cT}\sum_{m=1}^{M}\sum_{i=2}^{3} w_m^i(\mathbf{p}; \mathbf{r}, t)\frac{\partial\nu_{im}(\mathbf{p}; \mathbf{r}, t)}{\partial(ct)}d(ct), \tag{3}$$

$$g_{\eta\sigma} = d_3 = l\int_0^{cT}\sum_{m=1}^{M} w_m^1(\mathbf{p}; \mathbf{r}, t)\nu_{1m}(\mathbf{p}; \mathbf{r}, t)d(ct), \tag{4}$$

where $w_m^i(\mathbf{p}; \mathbf{r}, t) = \sum_{n=1}^{N} w_m^i(\mathbf{p}; \mathbf{r}, t)$, $\mathbf{w}_{mn}(\mathbf{p}; \mathbf{r}, t)$ satisfies

$L^*\mathbf{w}_{mn} = \mathbf{i}_y K_m(\mathbf{r}_n^r, t)\left|\nu_m(\mathbf{p}; \mathbf{r}_n^r, t) - \tilde{E}_{ym}(\mathbf{r}_n^r, t)\right|^{l-1} sign\left[\nu_m(\mathbf{p}; \mathbf{r}_n^r, t) - \tilde{E}_{ym}(\mathbf{r}_n^r, t)\right]\delta(\mathbf{r}-\mathbf{r}_n^r)$, and $\mathbf{w}_{mn}(\mathbf{p}; \mathbf{r}, T) = \mathbf{0}$, $\mathbf{i}_y$ is the unit vector of the y-direction, $\delta(\mathbf{r} - \mathbf{r}_n^r)$ is the Dirac function, L^* is the adjoint operator of L, $sign$ is the sign function.

The optimization of (1) can be achieved by conjugate gradient method. In each iteration the modification step sizes α_i $(i = 1, 2, 3)$ of the parameters can be determined by minimizing

$$Q(\mathbf{p}+\delta\mathbf{p}) = Q(\mathbf{p}+\sum_{i=1}^{3}\alpha_i\mathbf{e}_i) = \int_0^{cT}\sum_{m=1}^{M}\sum_{n=1}^{N} K_m(\mathbf{r}_n^r, t)\left|\nu_{1m}(\mathbf{p}+\sum_{i=1}^{3}\alpha_i\mathbf{e}_i; \mathbf{r}_n^r, t) - \tilde{E}_{ym}(\mathbf{r}_n^r, t)\right|^l d(ct), \tag{5}$$

where $\mathbf{e}_i = (0\ \cdots\ 0\ \mathbf{d}_i\ 0\ \cdots\ 0)^t$, $\mathbf{d}_i = (d_{i1}\ d_{i1}\ \cdots\ d_{iK})^t$, K is the number of points in the reconstruction region. $\nu_{1m}(\mathbf{p} + \sum^3 \alpha_i\mathbf{e}_i; \mathbf{r}_n^r, t)$ can be expressed as (6) by using the Taylor's expansion

$$\begin{aligned}\nu_{1m}(\mathbf{p} + \sum_{i=1}^{3}\alpha_i\mathbf{e}_i; \mathbf{r}_n^r, t) &\approx \nu_{1m}(\mathbf{p}; \mathbf{r}_n^r, t) + \delta\nu_{1m}(\mathbf{p}, \sum_{i=1}^{3}\alpha_i\mathbf{e}_i; \mathbf{r}_n^r, t)\\ &= \nu_{1m}(\mathbf{p}; \mathbf{r}_n^r, t) + \sum_{i=1}^{3}\alpha_i\delta\nu_{1m}(\mathbf{p}, \mathbf{e}_i; \mathbf{r}_n^r, t).\end{aligned} \tag{6}$$

By substituting (6) into (5), finding the derivatives of (5) to α_i $(i = 1, 2, 3)$, and setting the derivatives to zero, we can get a nonlinear system of α_i

$$\begin{aligned}&l\int_0^{cT}\sum_{m=1}^{M}\sum_{n=1}^{N} K_m(\mathbf{r}_n^r, t)|\nu_{1m}(\mathbf{p}; \mathbf{r}_n^r, t) + \sum_{i=1}^{3}\alpha_i\delta\nu_{1m}(\mathbf{p}, \mathbf{e}_i; \mathbf{r}_n^r, t) - \tilde{E}_{ym}(\mathbf{r}_n^r, t)|^{l-1}\\ &\quad\times sign\left[\nu_{1m}(\mathbf{p}; \mathbf{r}_n^r, t) + \sum_{i=1}^{3}\alpha_i\delta\nu_{1m}(\mathbf{p}, \mathbf{e}_i; \mathbf{r}_n^r, t) - \tilde{E}_{ym}(\mathbf{r}_n^r, t)\right]\delta\nu_{1m}(\mathbf{p}, \mathbf{e}_j; \mathbf{r}_n^r, t)d(ct) = 0,\ (j=1, 2, 3).\end{aligned} \tag{7}$$

Eq. (7) can be solved by numerical methods.

3. SYNTHETIC RECONSTRUCTION RESULTS

By using 2-D finite-difference time-domain (FDTD) simulation method with perfectly matched layer (PML) absorbing boundary conditions to obtain "observed" data. As shown in Figure 1, in a homogeneous nonconductive nonmagnetic background medium there are two low permittivity and nonconductive objects. The permittivity of the background and the objects are 6 and 4 respectively. The depths of the top of the objects are 26 cm and 36 cm, and the heights are 15 cm. Each transmitter has 10 receivers, the smallest and largest offset is 2.4 cm and 24 cm, and the interval of receiver is 2.4 cm. The transmitter and receivers are 1.2 cm above the surface. The number

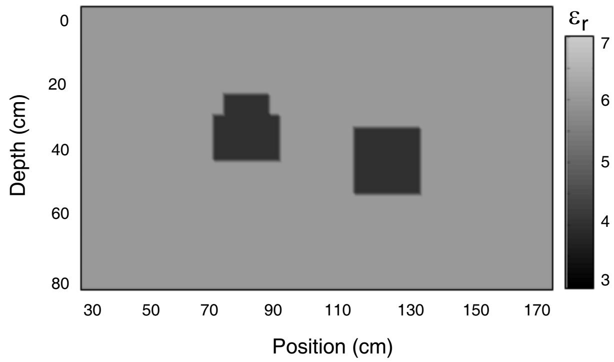

Figure 1: The actual distribution of relative dielectric constant in the reconstruction region.

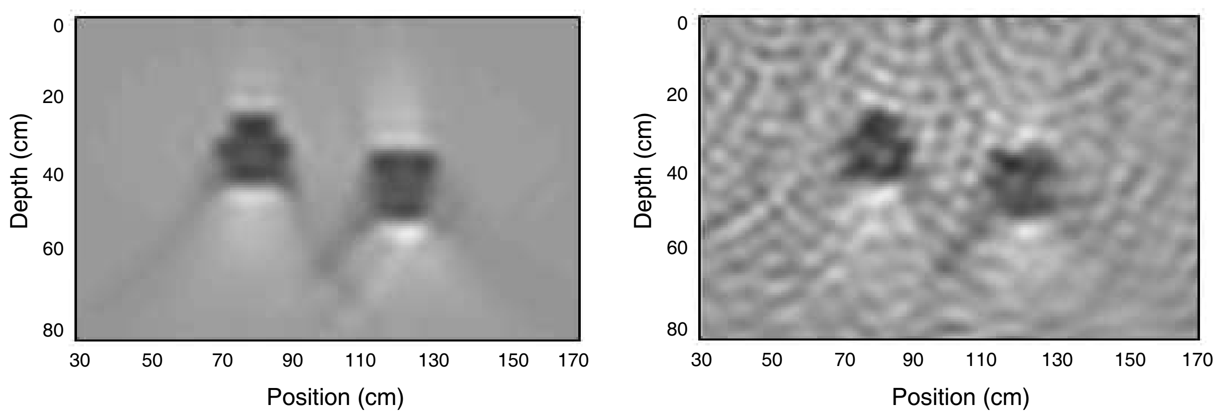

(a) (b)

Figure 2: The reconstructed distribution of relative dielectric constant after 70 iterations from noise-free (a) and noisy data (b) L_2 norm objective function is used.

of transmitting positions is 18, and the interval of transmitter is 10.8 cm. The first transmitting position is at 0 cm. The reconstruction region is from 24 cm to 184.8 cm in lateral direction and from 0 cm to 81.6 cm in vertical direction. In the reconstruction and simulation the grid size in two directions is 1.2 cm.

Figure 2 shows the reconstructed distribution of relative dielectric constant after 70 iterations from noise-free and noisy data. The power of the objective functional is 2. The signal-to-noise ratio (SNR) is 25 dB. SNR is defined as 10 times the logarithm of the ratio of the total energy of signal to that of filtered random noise. The bandwidth of signal is 0–0.8 GHz, and that of the filtered noise is 0–2 GHz. Figure 2(a) depicts that two objects are reconstructed correctly, in size and position. However, the shape is not reconstructed perfectly, and the reconstructed value of relative permittivity is litter bit greater than the actual value. Figure 2(b) shows that the influence of the noise is severe, and that it deforms the shapes of the objects. However, the objects at their actual positions can be detected from the image.

Figure 3 shows the reconstructed distribution of relative dielectric constant after 70 iterations from the noisy data. The power the objective function is 1.6 and 1.2 respectively. Figure 3 illustrates that the influence of the noise is evidently weakened compared with Figure 2(b). The shape of the objects can be easily recognized. The difference between Figure 3(a) and (b) is small.

4. EXPERIMENTAL RECONSTRUCTION RESULTS

In laboratory common-offset data are acquired by a network analyzer based radar system. Two 2.7-cm long dipoles are used as transmitter and receiver. The resonant frequency of the antenna is about 4.5 GHz. The data are recorded between 0.5–9.0 GHz with 1800 frequency points.

In a foam box with a length of 50 cm, width of 40 cm, and height of 25 cm dry sand is filled. In the sand two long nonconductive strips of foam with 1.5 cm by 1.5 cm square section are buried at depths of 5 cm and 3.5 cm, the gap of the strip is 6.5 cm. The offset between antennas is 5.2 cm. The direction of dipoles is along that of the strips. The number of measurement positions is 36,

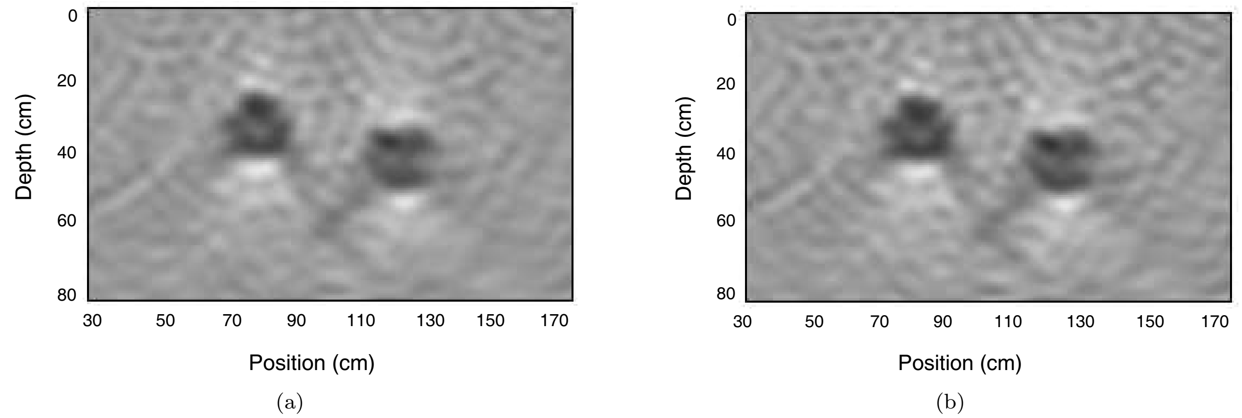

Figure 3: The reconstructed distribution of relative dielectric constant after 70 iterations from noisy data. $L_{1.6}$ (a) and $L_{1.2}$ (b) norm objective function is used.

and the interval of measurement is 6.5 mm. The dipoles are 3.9 mm above the surface. The first and last measurement point is at 4 cm and 26.5 cm in lateral direction.

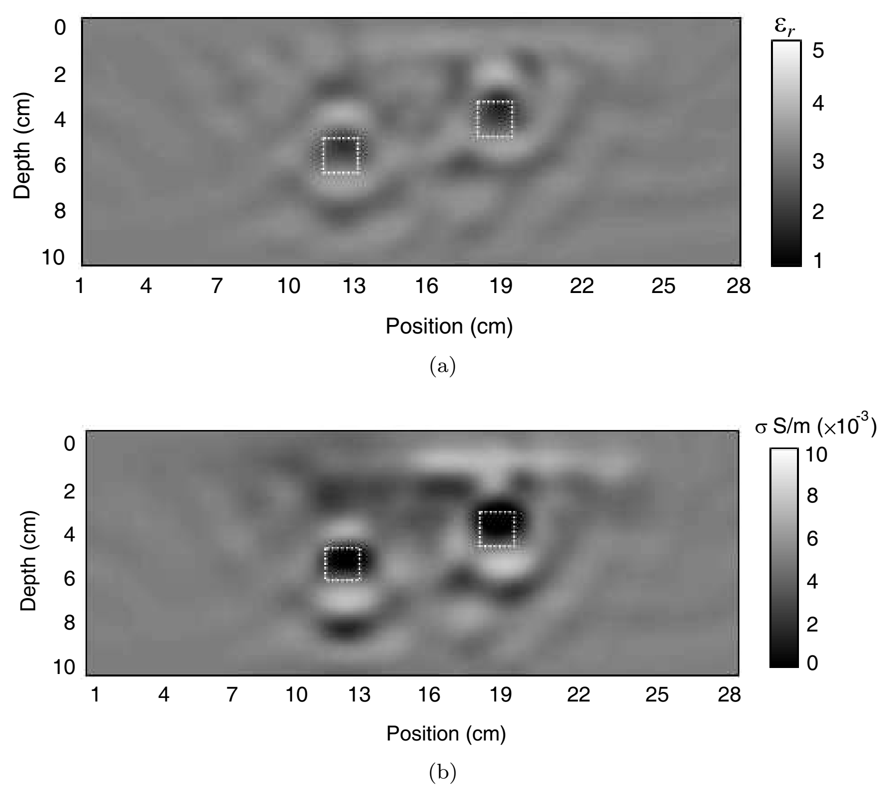

Figure 4: The distribution of reconstructed relative dielectric (a) and conductivity (b) from experimental data after 75 iterations. L_2 norm objective function is used.

In reconstruction, the cell size is 1.3 mm by 1.3 mm. Figure 4 is the results of relative permittivity and conductivity after 75 iterations by using L_2 norm. The initial guesses of them are 3 and 0.005 m/s. The white dashed squares indicate the actual positions of the strips. There are two low permittivity and conductivity zones, and their sizes are close to the actual ones. Figure 5 is the reconstructed results by using $L_{1.2}$ norm objective functional. By comparing Figures 4 and 5 we learn that Figure 5 is better than Figure 4. For example, at the sallow and the deep part of Figure 5(b) is improved greatly, and the reconstructed value of permittivity of the strips are closer to the true value 1, and the position indicated by the reconstructed conductivity is more accurate.

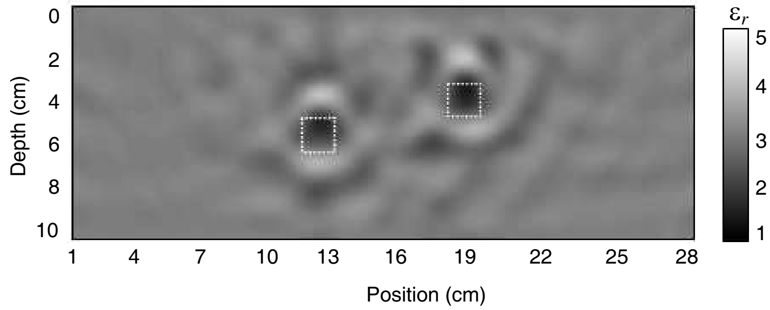

(a)

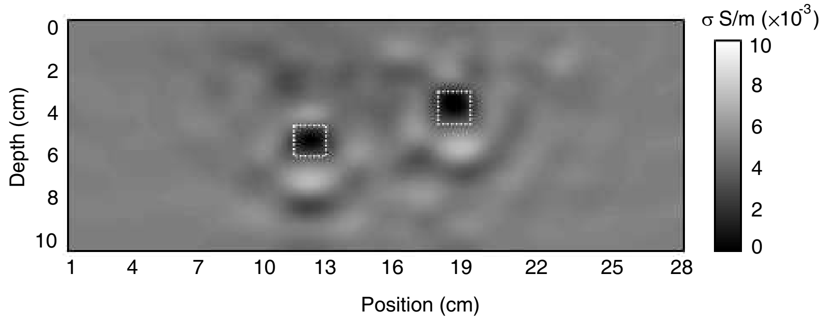

(b)

Figure 5: The distribution of reconstructed relative dielectric (a) and conductivity (b) from experimental data after 70 iterations. $L_{1.2}$ norm is used.

5. CONCLUSIONS

Two-dimensional FBTS reconstruction method, in which the power of the objective functional is any number greater than 1, is discussed. A synthetic reconstruction example for nonconductive and nonmagnetic media is conducted. From the reconstructed results of this example it is clear that the influence of noise can be greatly suppressed by using low-order norms. As a result the reconstructed images are more reliable. An experimental example for nonmagnetic media is illustrated too. In data collection and preprocessing, some sources of error, such as, measurement error, positioning error, data transform error, may degrade the quality of reconstruction results. The reconstruction results indicate clearly that the reconstructed results can be improved evidently by using a low-order norm of objective functional.

ACKNOWLEDGMENT

This work was supported in part by the National Natural Science Foundation of China under Grant-in-Aid 40574053.

REFERENCES

1. Davis, J. L. and A. P. Annan, "Ground-penetrating radar for high-resolution mapping of soil and rock stratigraphy," *Geophysical Prospecting*, Vol. 37, 531–551, 1989.
2. Beres, M. Jr. and F. P. Haeni, "Application of ground penetrating radar methods in hydrogeologic studies," *Ground Water*, Vol. 29, 375–386, 1991.
3. Liner, C. L. and J. L. Liner, "Application of GPR to a site investigation involving shallow faults," *Leading Edge*, Vol. 16, 1649–1651, 1997.
4. Lehmann, F. and A. G. Green, "Topographic migration of georadar data: Implication for acquisition and processing," *Geophysics*, Vol. 65, 836–848, 2000.
5. Zhou, H., M. Sato, and H. Liu, "Migration velocity analysis and prestack migration of common-transmitter ground-penetrating radar data," *IEEE Transactions on Geoscience and Remote Sensing*, Vol. 43, No. 1, 86–91, 2005.
6. Morrow, I. L. and P. V. Genderen, "Effective imaging of buried dielectric objects," *IEEE Transactions on Geoscience and Remote Sensing*, Vol. 40, No. 4, 943–949, 2002.

7. Xu, X., E. L. Miller, C. M. Rappaport, et al. "Statistical method to detect subsurface objects using array GPR data," *IEEE Transactions on Geoscience and Remote Sensing*, Vol. 40, No. 4, 963–976, 2002.
8. Greaves, R. J., D. P. Lesmes, J. M. Lee, et al. "Velocity variations and water content estimated from multi-offset, ground-penetrating radar," *Geophysics*, Vol. 61, 683–695, 1996.
9. Lázaro-Mancilla, O. and E. Gómez-Treviño, "Ground penetrating radar inversion in 1-D: an approach for the estimation of electrical conductivity, dielectric permittivity and magnetic permeability," *Journal of Applied Geophysics*, Vol. 43, 199–213, 2000.
10. Hansen, T. B. and P. M. Johansen, "Inversion scheme for ground penetrating radar that takes into account the planar air-soil interface," *IEEE Transactions on Geoscience and Remote Sensing*, Vol. 38, No. 1, 496–506, 2000.
11. Gentili, G. G. and U. Spagnolini, "Electromagnetic inversion in monostatic GPR: TEM horn calibration and application," *IEEE Transactions on Geoscience and Remote Sensing*, Vol. 38, No. 4, 1936–1946, 2000.
12. Meincke, P., "Linear GPR inversion for lossy soil and a planar air-soil interface," *IEEE Transactions on Geoscience and Remote Sensing*, Vol. 39, No. 12, 2713–2721, 2001.
13. Cui, T. and W. C. Chew, "Diffraction tomographic algorithm for the detection of three-dimensional objects buried in a lossy half-space," *IEEE Transactions on Antenna and Propagation*, Vol. 50, No. 1, 42–49, 2002.
14. Leone, G., et al. "Analysis of the distorted Born approximation for subsurface reconstruction: truncation and uncertainties effects," *IEEE Transactions on Geoscience and Remote Sensing*, Vol. 41, No. 1, 66–74, 2003.
15. Qiu, D. L., H. Zhou, T. Takenaka, and T. Tanaka, "Source group method to speed up the reconstruction of objects from radar data by using the FBTS method," *Microwave and Optical Technology Letters*, Vol. 48, No. 1, 67–71, 2006.
16. Takenaka, T., H. Zhou, and T. Tanaka, "Inverse scattering for a three-dimensional object in the time domain," *Journal of Optical Society of America A*, Vol. 20, No. 10, 1867–1874, 2003.
17. Menke, W., *Geophysical Data Analysis: Discrete Inverse Theory*, Revised Edition, Academic Press, San Diego, 1989.

Study on Transmission Characteristic of Split-ring Resonator Defected Ground Structure

Bian Wu, **Bin Li**, **Tao Su**, **and Chang-Hong Liang**

National Key Laboratory of Antennas and Microwave Technology
Xidian University, Xi'an, 710071, China

Abstract— A square split-ring resonator (SRR) defected ground structure (DGS) is studied in this paper. This DGS structure has a flat low-pass characteristic and a sharp band-gap property compared to the conventional dumbbell DGS. A detailed analysis of the relationship between the transmission characteristic and the split-ring dimension is made. In order to enhance the out-band suppression, an improved SRR DGS cell with open stubs loaded on the conductor line is then presented and fabricated.

1. INTRODUCTION

In 1999, defected ground structure was firstly proposed by Park et al. based on the idea of photonic band-gap (PBG) structure, and had found its application in the design of planar circuits and low-pass filters [1–3]. Defected ground structure is realized by etching a defective pattern in the ground plane, which disturbs the shield current distribution in the ground plane. This disturbance can change the characteristics of a transmission line such as equivalent capacitance and inductance to obtain the slow-wave effect and band-stop property.

Split-ring resonators (SRRs) have been successfully applied to the fabrication of left-handed metamaterial (LHM) and the design of planar circuits. Pendry et al. have demonstrated that an array of SRRs exhibits negative permeability near its resonant frequency [4]. Gay-Balmaz et al. study experimentally and numerically the electromagnetic resonances in individual and coupled split-ring resonators [5]. Markos et al. have investigated the dependence of the resonance frequency of the periodic array of SRRs on the ring thickness, inner diameter, radial and azimuthal gap, as well as on the electrical permittivity of the board and the embedding medium [6]. Bonache et al. have found the application of complementary circular split-ring resonators to the design of compact narrow band-pass structures in microstrip technology [7].

In this paper, a square split-ring resonator DGS and its equivalent circuit are investigated. The dependence of the transmission characteristic on the dimension of the split ring is then analyzed. At last, the authors propose an improved SRR DGS cell to improve the out-band suppression.

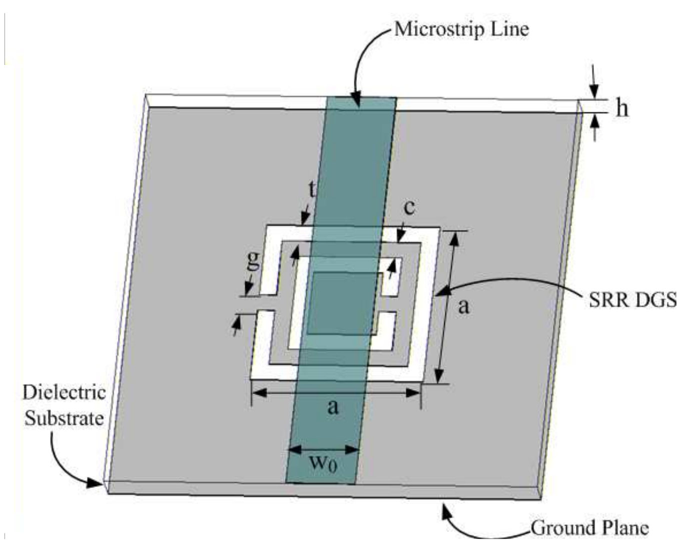

Figure 1: SRR DGS cell model.

2. STRUCTURE OF THE SRR DGS CELL

The SRR DGS is obtained by etching two concentric split-ring defective pattern which have different size and inverse split direction in the ground plane, as shown in Fig. 1. The permittivity of the microstrip line is $\varepsilon_r = 2.65$, the height of the dielectric board is $h = 1.5\,\text{mm}$, and width of the conductor line is 4.1 mm. Due to the discontinuity of impedance in defective region, an electromagnetic resonance is obtained and thus a band-gap is formed.

Compared with the conventional dumbbell DGS, SRR DGS has a flat low-pass property and a narrow band-gap due to the introducing of a transmission zero of elliptic function, as shown in Fig. 2. As a result, this structure can be used to low-pass filter design and harmonic suppression. However, this structure has the disadvantages such as narrow bandwidth of band-gap and insufficient suppression in high frequency range that need to be improved when implemented to practical engineering.

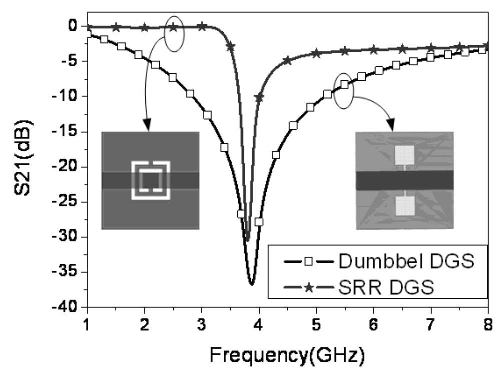

Figure 2: Comparison of band-gap property between SRR DGS and dumbbell DGS.

3. ANALYSIS OF THE TRANSMISSION ZERO FOR THE SRR DGS CELL

50-ohm transmission line is equivalent to right-hand transmission line (RHTL) which is composed of two serial inductors and a shunt capacitor, and the split-ring resonator forms a parallel resonant circuit. Therefore, etching split-ring defective pattern in the ground plane will add a parallel resonant circuit to the equivalent RHTL, but will have a little affection on the value of the elements $L2$ and $C2$. The final equivalent circuit is shown in Fig. 3.

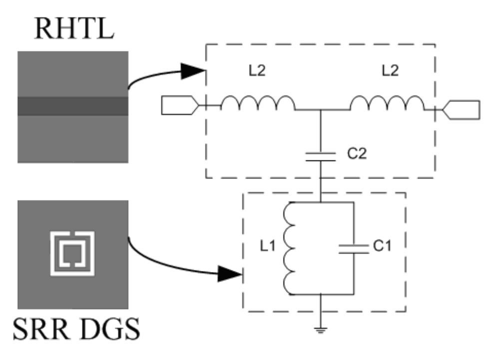

Figure 3: Equivalent circuit of SRR DGS cell model.

The transmission zero location for the SRR DGS cell is determined by the resonant frequency of the shunt circuit, that means it is codetermined by L_1, C_1 and C_2.

The impedance of the parallel LC circuit is given by

$$Z_1 = \frac{1}{j\omega C_1 + \frac{1}{j\omega L_1}} = j\frac{\omega L_1}{1 - \omega^2 L_1 C_1} \tag{1}$$

While the impedance of the single capacitor C_2 is

$$Z_2 = \frac{1}{j\omega C_2} = -j\frac{1}{\omega C_2} \tag{2}$$

The transmission zero is obtained when

$$Z_1 + Z_2 = 0 \tag{3}$$

Then we have the resonant frequency as

$$f_S = \frac{1}{2\pi\sqrt{L_1\,(C_1 + C_2)}} \tag{4}$$

4. TRANSMISSION CHARACTERISTICS OF THE SRR DGS CELL

Generally speaking, there is a corresponding relationship between the dimension of the square SRR DGS cell and the element parameters of the equivalent circuit. The authors investigate the dependence of the transmission characteristic on side-length, split-gap and ring-gap of the square SRR DGS by EM simulator Ansoft HFSS software v9. The line-width is chosen to be the characteristic impedance of 50-ohm microstrip line, ring-width is kept constant to 1 mm, and the substrate with 1.5 mm thickness and a dielectric constant of 2.65 is used for all simulations. Three SRR DGS unit circuits without any period are simulated with the different dimension, there is only one parameter varying for each case.

In case one, both the split-gap and the ring-gap are 1 mm. As the side-length of SRR DGS is increased, the effective inductance L_1 increases, which gives rise to a lower cutoff frequency.

Then in case two, the side-length is kept constant to 8 mm and ring-gap is 1 mm, while the split-gap g varies. The simulation results are shown in Fig. 4(b). As the split-gap increases, the effective capacitance C_1 decreases so that the transmission zero location moves up to higher frequency.

Finally in case three, the ring-gap c is increased while the side-length and split-gap are fixed, as shown in Fig. 4(c). The ring-gap also affects the effective capacitance C_1, which leads to an increasing cut-off frequency.

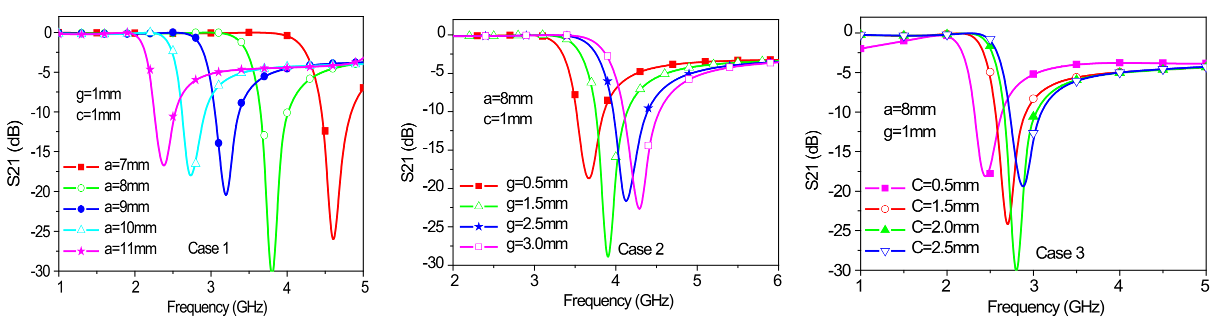

(a) (b) (c)

Figure 4: Variation of transmission curve with (a) side-length a, (b) split-gap g, (c) ring-gap c.

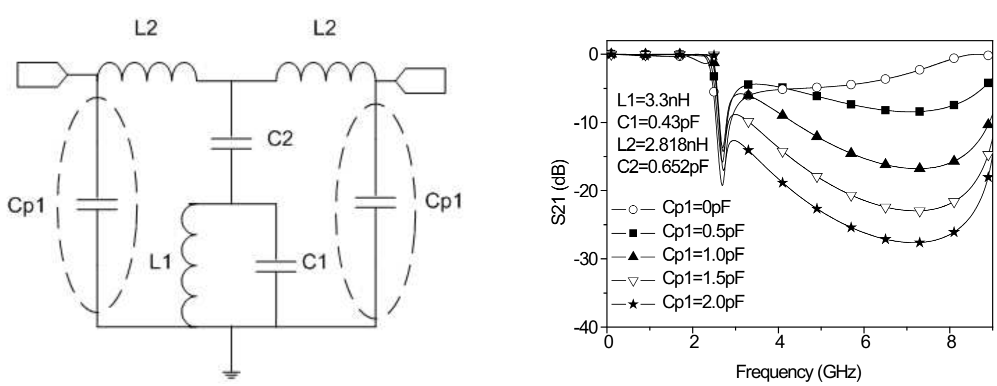

(a) (b)

Figure 5: (a) Topology of the equivalent circuit with parallel capacitors. (b) Variation of the transmission curves with different parallel capacitances.

5. IMPROVED SRR DGS CELL AND MEASUREMENT

If two parallel capacitances are symmetrically added at both sides of the equivalent-circuit, the out-band suppression in the high frequency region will be improved when the capacitance increases within an appropriate range, as shown in Fig. 5. The parallel capacitance in a microstrip line can be realized by loading the open stubs on the conductor line. Fig. 6 shows the photographs of the improved SRR DGS cell. The square SRR DGS cell has a side-length of a=10 mm, a split-gap of g=1 mm and a ring-gap of c=1 mm, and the open-stubs placed on the conductor line have a width of w=3 mm and length of L=8 mm.

The simulation and measured S-parameters as depicted in Fig. 7 shows good agreement. The cut-off frequency and transmission zero location have been found to be f_c =2.5 GHz and f_S=2.7 GHz, respectively. Measured pass-band loss is below 0.5 dB, a sharp slop is obtained at band edge. The out-band suppression within a wide frequency range from 2.7 GHz to 7 GHz is obviously enhanced, which can be used as the unit of the lowpass filters.

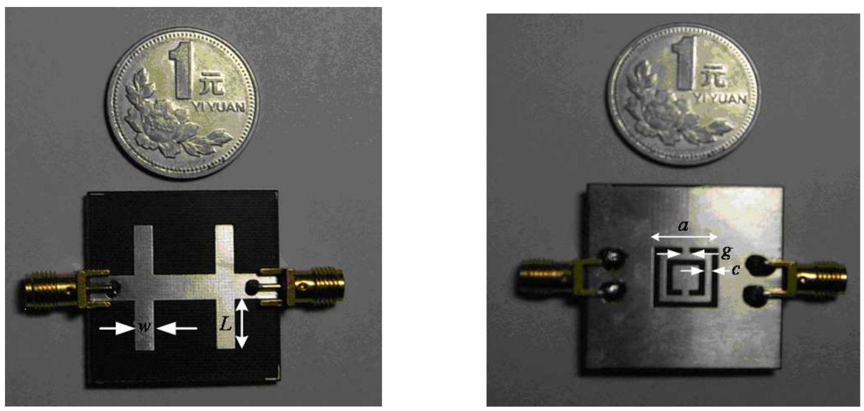

(a) (b)

Figure 6: Photographs of the fabricated improved SRR DGS cell. (a) Top view, (b) Bottom view.

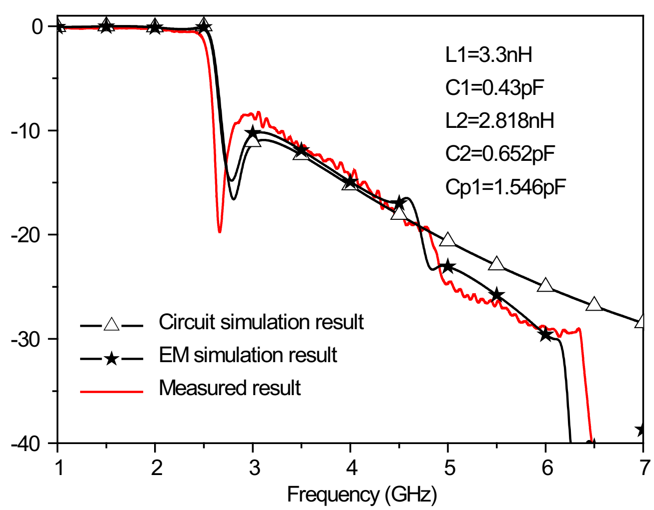

Figure 7: Simulation and measured results of the improved SRR DGS cell.

6. CONCLUSION

A square split-ring resonator DGS and its transmission property are analyzed in this paper. The transmission characteristic mainly depends on the dimension of the split ring. It has been demonstrated that, either an increase in the side-length of the the split-ring or a decrease in the width of split-gap and ring-gap will lead to a decrease in the cut-off frequency of the SRR DGS cell. By loading open stubs on the conductor line which operate as parallel capacitances, the out-band suppression is obviously improved.

ACKNOWLEDGMENT

This work is supported by the National Natural Science Foundation of China under project no. 60501023.

REFERENCES

1. Yablonovitch, E., T. J. Gmitter, and K. M. Leung, "Photonic band structure: The face centered cubic case employing nonspherical atoms," *Physical Review Letters*, Vol. 67, No. 17, 2295–2298, 1991.
2. Park, J. I., C. S. Kim, J. Kim, et al., "Modeling of a photonic bandgap and its application for the low-pass filter design," *Asia Pacific Microwave Conference*, Singapore, 1999.
3. Kim, C. S., J. I. Park, A. Dal, et al., "A novel 1-D periodic defected ground structure for planar circuits," *IEEE Microwave Guided Wave Lett.*, Vol. 10, No. 4, 131–133, 2000.
4. Pendry, J. B., A. J. Holden, D. J. Robbins, et al., "Magnetism from conductors and enhanced nonlinear phenomena," *IEEE Trans. Microwave Theory Tech.*, Vol. 47, No. 11, 2075–2084, 1999.
5. Gay-Balmaz, P. and O. J. F. Martin, "Electromagnetic resonances in individual and coupled split-ring resonators," *Journal of Applied Physics*, Vol. 92, No. 5, 2929–2936, 2002.
6. Markos, P. and C. M. Soukoulis, "Numerical studies of left-handed materials and arrays of split ring resonators," *Physical Review E.*, Vol. 65, 036622-1–036622-8, 2002.
7. Bonache, J., F. Martin, F. Falcone, et al., "Application of complementary split-ring resonators to the design of compact narrow band-pass structures in microstrip technology," *Microwave and Optical Technology Letters*, Vol. 46, No. 5, 508–512, 2005.

3D GL EM and Quantum Mechanical Coupled Modeling for the Nanometer Materials

Ganquan Xie, **Jianhua Li**, **Feng Xie**, **and Lee Xie**

GL Geophysical Laboratory, USA

Abstract— In this paper, we develop a 3D GL EM and quantum mechanical coupled modeling (GLEMQUAN) for studying nanometer materials. We accumulate the EM field energy, quantum energy, and interaction energy into Lagrangian energy in the nanometer material. The variation equation of the Lagrangian energy is the EM and quantum field coupled equations. We propose the GL modeling to solve the EM and quantum field coupled equations. The nanometer material is divided into set of sub-lattices. In the each lattice, the Global EM field and quantum wave function field are successively modified by the local scattering EM and quantum field. When the whole lattice domain is scanned, the GL EM and quantum field solution is obtained. In the GLEMQUAN modeling, there is no big matrix needs to be solved. Also there are no artificial boundary and no error reflection and error dispersion. The synthetic simulations show the GLEMQUAN modeling algorithm is fast, accurate, and very agile. The GLEMQUAN modeling can be used to study optical materials, photosensitivity, photosynthesis, metallography and nanometer materials science and engineering.

1. INTRODUCTION

The nanometer materials have important applications in science and engineering. Their mechanical and electromagnetic (EM) properties are active research projects. In this paper, we develop a 3D GLEMQUAN for studying nanometer materials. We use the quantum field to model the micro inhomogeneous variance property of the nanometer materials. The EM field energy, quantum material field energy, and interaction energy are accounted into the total Langrangian. By taking the Euler variation of the Langrangian, we can obtain the EM field and quantum material field coupled equations. By using the GL modeling method [1, 2], we propose the GLEMQUAN method to solve the EM and quantum coupled field equations. The nanometer material is divided into set of lattices. In each lattice, the Global EM field and quantum wave function field are successively modified by the local scattering EM and quantum field. When the whole lattice domain is scanned, the GL EM and quantum field solution is obtained.

The Lagrangian energy method is the important tool to build theory for EM, mechanical, thermal, and flow etc. The Finite Element method (FEM) is a direct numerical Lagrangian energy method. However, the big matrix and artificial boundary condition are cumbersome burden and cost of the FEM and FD method. In particular, in micro Lagrangian model, there is no general constitute law for variable nanometer materials. The Langrangian energy density is nonstandard and depends variable material experiment and measurement. Therefore, the micro FEM Langrangian energy algorithm and software are often needed to be changed for the different type nanometer materials, it is very inconvenience and cumbersome. In the GLEMQUAN Modeling, there is no big matrix needs to be solved. Also there are no artificial boundary and no error reflection and dispersion. In particular, the GLEMQUAN is very agile to discrete the nonstandard and changeful Lagrangian density for the different type optical materials and nanometer materials. Many simulations show that the GLEMQUAN and GL EMFHS [3] coupled modeling have advantages to overcome the difficulties in FEM Lagrangian modeling.

There are research works to study Lagrangian modeling for optical materials [4]. However, paper [4] only study one dimension case. The 3D Lagrangian modeling for the optical and nanometer materials is lacking. We developed the Macro to Macro, Macro to Micro, and Micro to Micro 3D GLEMQUAN and GLEMHFS coupled modeling.

The GLEMQUAN and GLEMFHS [3] modeling have wide applications in studying optical materials, Bragg grating, photosensitivity, photosynthesis, nanometer materials, metallography, powder metallurgy and metal cast science and engineering.

We arrange the description of the paper as follows. The introduction has been described in Section 1. The Lagragian EM and quantum energy principle for the nanometer materials is described in Section 2. The variation Euler-Lagrangian equation is described in Section 3. In Section 4, we describe GL EM and nanometer quantum field coupled modeling. The simulation and advantages of the GLEMQUAN modeling is described in Section 5. In Section 6, we conclude this paper.

2. LAGRANGIAN OF THE EM FIELD AND QUANTUM FIELD

We consider interaction phenomena that the high frequency EM field, for example X ray, propagates through the nanometer material. The EM field energy, nanometer quantum field energy, and interaction energy are accounted in the Lagragian which is integral of the Lagrangian density.

2.1. The Lagrangian Density

The Lagrangian density of the EM field and quantum field energy is as follows.

$$l_T = l_{EM} + l_{QUAN} + l_{INT}, \tag{1}$$

where l_T is total Lagrangian energy density, l_{EM} is the EM field energy density, l_{QUAN} is the quantum field density, and l_{INT} is the interaction energy due to the interaction between the EM field and quantum nanometer materials,

$$\begin{aligned} l_{EM} &= \frac{1}{2}\varepsilon_0(\boldsymbol{E}\cdot\boldsymbol{E} - c^2\mu_0^2\boldsymbol{H}\cdot\boldsymbol{H}), \\ l_{QUAN} &= \frac{1}{2}i\hbar\left(\Psi^*\frac{\partial\Psi}{\partial t} - \Psi\frac{\partial\Psi^*}{\partial t}\right) - \Psi^*\boldsymbol{H}_Q\Psi, \\ l_{INT} &= \boldsymbol{E}\cdot\boldsymbol{P}. \end{aligned} \tag{2}$$

2.2. Langrangian Energy

The Langrangian energy of the EM field and quantum field is as follows

$$L(\boldsymbol{E},\boldsymbol{H},\Psi,t) = \int_\Omega l_T\left(r'\right)dr'. \tag{3}$$

3. VARIATION EULER-LAGRANGIAN EQUATION

3.1. Langrangian Function

The Langrangian function is as follows

$$\boldsymbol{S}(\boldsymbol{E},\boldsymbol{H},\Psi) = \int_0^\infty \boldsymbol{L}(\boldsymbol{E},\boldsymbol{H},\Psi;t)\,dt. \tag{4}$$

3.2. Euler-Lagrangian Variation

The Eulr-Lagrangian variation equation is the following equation,

$$\delta\boldsymbol{S}(\boldsymbol{E},\boldsymbol{H},\Psi) = 0. \tag{5}$$

3.3. EM Field And Quantum Field Coupled Equation

To take variation of the Lagrangian function in (5), we obtain the EM field and quantum field coupled equation.

$$\begin{aligned} \nabla\times\boldsymbol{E} &= -\mu\frac{\partial\boldsymbol{H}}{\partial t}. \\ \nabla\times\boldsymbol{H} &= \varepsilon\frac{\partial\boldsymbol{E}}{\partial t} + \boldsymbol{J}, \end{aligned} \tag{6}$$

where

$$\boldsymbol{J} = -\frac{i\hbar}{2m}A\left(\Psi^*\nabla\Psi - \Psi\nabla\Psi^*\right) + \sigma(\Psi)\boldsymbol{E}, \tag{7}$$

σ is the electric quantum conductivity, and quantum wave function Ψ satisfies the Schrödinger equation with nanometer quantum Hamiltonian $\boldsymbol{H}_Q$

$$i\hbar\frac{\partial\Psi}{\partial t} = \boldsymbol{H}_Q\Psi, \tag{8}$$

where $\boldsymbol{H}_Q$ is depended on the property of the specific nanometer material and EM filed.

4. GL EM AND NANOMETER QUANTUM FIELD COUPLED MODELING

4.1. The EM and Quantum Field Nonlinear Coupled Equation

The EM field Equation (6), current representation (7) and quantum field Equation (8) couple into EM field and quantum field coupled nonlinear equation. For the nanometer material, we need add the following Macro-Micro constitute nonlinear relation equation,

$$\begin{aligned} \sigma &= \sigma(e, \Psi), \\ \varepsilon &= \varepsilon(e, \Psi), \\ \mu &= \mu(e, \Psi). \end{aligned} \tag{9}$$

4.2. Iteration for Solving the Coupled Nonlinear EM and Quantum Field Coupled Equations

We use the following iteration to solve the EM and quantum field coupled equations

$$\begin{aligned} \nabla \times \boldsymbol{E}^{(n)} &= -i\omega\mu\left(e^{(n-1)}, \Psi^{(n-1)}\right)\boldsymbol{H}^{(n)}, \\ \nabla \times \boldsymbol{H}^{(n)} &= i\omega\varepsilon\left(e^{(n-1)}, \Psi^{(n-1)}\right)\boldsymbol{E}^{(n)} + \boldsymbol{J}\left(e^{(n-1)}, \Psi^{(n-1)}\right), \end{aligned} \tag{10}$$

$$e^{(n)}\Psi^{(n)} = \boldsymbol{H}_Q\left(\boldsymbol{E}^{(n)}, \boldsymbol{H}^{(n)}\right)\Psi^{(n)}. \tag{11}$$

We solve the linearization Equations (10) and (11) in order to form the nth circle of the iteration.

4.3. Division of the Domain

The inhomogeneous domain Ω is divided into a set of the several lattice domains $\{\Omega_k\}$, $k = 1, 2, \ldots, N$, such that $\Omega = \bigcup_{k=1}^{N} \Omega_k$. The division is mesh or meshless super lattice.

4.4. GL Modeling for Solving the EM Field Linearization Equation (10)

4.4.1.

In each lattice Ω_k, $k = 1, 2, \ldots, N$, we solve the adjoint EM Green's tensor integral equation of the Equation (10). By the dual curl process, the adjoint Green's EM field integral equations are reduced into 6×6 matrix equations. By solving the 6×6 matrix equations, the Green's tensor EM field $\boldsymbol{E}_k^{J(n)}$, … and $\boldsymbol{H}_k^{M(n)}$ are obtained.

4.4.2.

The global EM field is updated by the following local scattering EM field integral equation

$$\begin{bmatrix} \boldsymbol{E}(r) \\ \boldsymbol{H}(r) \end{bmatrix}_k^{(n)} = \begin{bmatrix} \boldsymbol{E}(r) \\ \boldsymbol{H}(r) \end{bmatrix}_{k-1}^{(n)} + \int_{\Omega_k} \begin{bmatrix} \boldsymbol{E}_k^{J(n)}(r', r) & \boldsymbol{H}_k^{J(n)}(r', r) \\ \boldsymbol{E}_k^{M(n)}(r', r) & \boldsymbol{H}_k^{M(n)}(r', r) \end{bmatrix} \left[\boldsymbol{D}\left(e^{(n-1)}, \Psi^{(n-1)}\right)\right] \begin{bmatrix} \boldsymbol{E}(r') \\ \boldsymbol{E}(r') \end{bmatrix}_{k-1}^{(n)} dr', \tag{12}$$

$k = 1, 2, \ldots, N$, successively. The $[\boldsymbol{E}_N^{(n)}(r), \boldsymbol{H}_N^{(n)}(r)]$ is the GL solution of the 3D GL EM modeling for solving the EM field linearization Equation (10).

4.5. GL Modeling For Solving The Schrödinger Field Linearization Equation (11)

4.5.1.

In each lattice Ω_k, $k = 1, 2, \ldots, N$, we solve the adjoint quantum Green's wave function integral equation of the Schrödinger Equation (11). By the dual process, the adjoint Green's quantum wave field integral equations are reduced into algebra equation. By solving the algebra equations, the quantum Green's function tensor $\boldsymbol{G}_k^{\pm q,(n)}(r', r)$ is obtained.

4.5.2.

The Global quantum wave field is updated by the following local scattering quantum wave field integral equation

$$\Psi_k^{(n)}(r) = \Psi_{k-1}^{(n)}(r) - \frac{2m}{\hbar^2}\int_{\Omega_k} \left(V\left(\boldsymbol{E}_k^{(n)}, \boldsymbol{H}_k^{(n)}\right) - V\left(\boldsymbol{E}_{k-1}^{(n)}, \boldsymbol{H}_{k-1}^{(n)}\right)\right)\boldsymbol{G}_k^{+q,(n)}\left(r', r\right)\Psi_{k-1}^{(n)}\left(r'\right)dr', \tag{13}$$

$k = 1, 2, \ldots N$, successively. The $\Psi_N^{(n)}(r)$ is the GL quantum field solution of the 3D GL quantum field modeling.

5. THE SIMULATION AND ADVANTAGES OF THE GLEMQUAN MODELING

5.1. Simulation

The 20 nm×20 nm×20 nm Bragg optical sensor material is embedded into the metal bulk cheap with 5 μm×5 μm×5 μm. The X ray propagate through the composite material. The optical material is divided into 1024 lattices. The outside gasket metal bulk is divided into 1024 domains. The initial quantum field is Ψ_0, which satisfies Schrödinger equation with Hamiltonian $\boldsymbol{H}_0$. We use the GLEMQUAN modeling to calculate the EM field and quantum wave field function. The Hy in the transverse section $Y = 5\,\mathrm{nm}$ and on surface of the bulk is shown in Figure 1, Hy is shown in the left graphic, scattering field SHy is shown in the right graphic. A quanta wave package is obviously shown in rectangle frame in rear of the scattering wave. The quanta wave package is an EM-quantum coupled effect which is match to the X ray observation. The GLEMQUAN quanta wave package is shown in the Figure 2, it is different from the rear part of macro EM field in which the scattering wave vanished to zero from peak. From the GLEMQUAN EM field and quantum wave field, the quantum fiber strain is calculated. The deformation of the nanometer material crystal due to the quantum fiber strain is shown in the Figure 3. The electric microscope image of the deformation of the nanometer material is shown in Figure 4. The similarity between images in Figure 3 and Figure 4 shows that the GLEMQUAN modeling can obtain high resolution image of the nanometer fiber deformation. The simulations show that the GLEMQUAN modeling is fast and accurate.

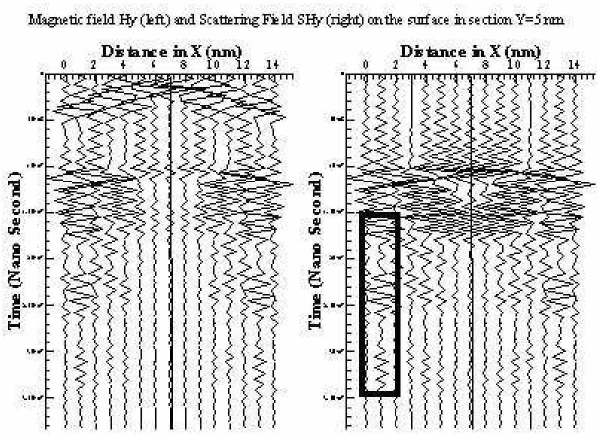

Figure 1: Hy in the transverse section $Y = 5\,\mathrm{nm}$ and on surface, Hy is in the left, scattering field SHy is in the right. A quanta is shown in rectangle frame.

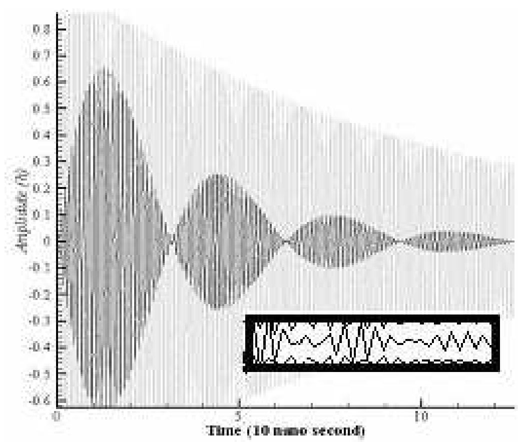

Figure 2: GLEMQUAN quanta in the rear of the scattering magnetic field Hy which is shown in black rectangle frame in Figure 1.

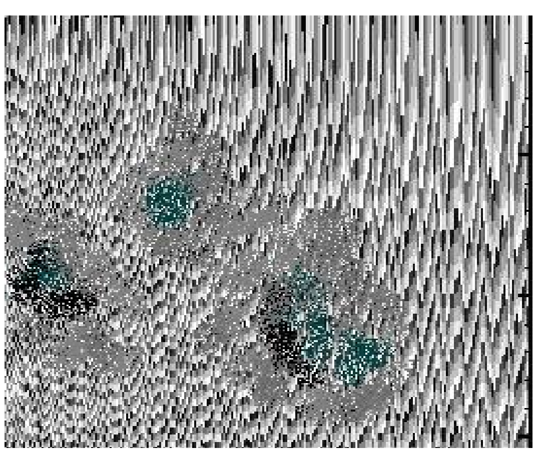

Figure 3: The deformation of the nanometer material crystal due to the quantum fiber strain.

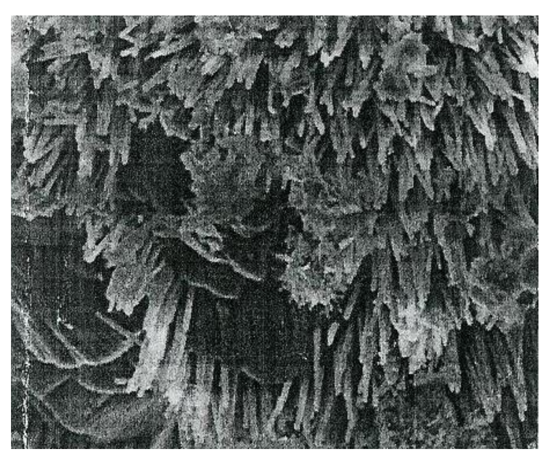

Figure 4: The scan electric microscope SEM image of the deformation of the nanometer material crystal.

5.2. Advantages

The Langrangian principle is very important for sciences. The Langrangian method can be used to model macro and micro mechanics, flow, EM, thermal, and quantum mechanics etc. scientific model. The equivalent between Schrödinger quantum equation and Heisenberg quantum mechanics can be proved by Langrangian principle. The advantage of the Langrangian method is that all macro and micro energy can be written in the Langrangian together. Langrangian method is easy to construct nonstandard modeling. However, its inconvenience is that for each material or process, the Langrangian should be rewritten. The FEM method needs to build and solve big matrix and needs artificial boundary, such that it is very difficult and cumbersome for changeful Langrangian. The GL modeling and inversion method can overcome these difficulties. In the GLEMQUAN modeling, there is no big matrix needs to be solved. There are no artificial boundary and no error reflection and no error dispersion. In particular, the GLEMQUAN is very agile to discrete the nonstandard and changeful Lagrangian density for the different type optical materials and nanometer materials. Using GL method and Langragin principle, we develop GLEMQUAN and GLEMFHS modeling and inversion for macro field to macro material, macro field to micro material, and micro field to micro material[1–3, 5, 6]. The GLEMQUAN and GLEMFHS modeling and inversion is shelf parallelization algorithm.

6. CONCLUSION

The GLEMQUAN EM field and quantum field coupled modeling is proposed and validated in this paper. Many simulations show that the GLEMQUAN and GL EMFHS [3] coupled modelings have advantages to overcome the difficulties in FEM Lagrangian modeling. The GL GLEMQUAN coupled modeling has wide application in optical materials, photosensitivity, photosynthesis, metallography, powder metallurgy, atmosphere chemistry, environment chemistry, nanometer materials sciences and engineering. The patent right of the GLEMQUAN modeling in this paper belongs to the authors of this paper.

REFERENCES

1. Xie, G., F. Xie, L. Xie, and J. Li, "GL method and its advantages for resolving historical difficulties," *Progress In Electromagnetics Research*, PIER 63, 141–152, 2006.
2. Xie, G., J. Li, L. Xie, and F. Xie, "A metro carlo EM inversion," *Journal of Electromagnetic Waves and Applications*, Vol. 20, No. 14, 1991–2000, 2006.
3. Xie, G., J. Li, L. Xie, F. Xie, and J. Li, "The 3D GL EM-Flow-Heat-Stress coupled modeling," *Progress In Electromagnetics Research Symposium 2007*, Beijing, China.
4. Hillery, M. and P. Drummond, "Noise-free scattering of the quantized electromagnetic field from a dispersive linear dielectric," *Physical Review*, Vol. 64, 013815.
5. Lin, C. C., G. Xie, J. Li, and B. J. Lin, "Deformation analysis for materials using GILD mechnical modeling," *The Chinese Journal of Mechanics — Series A*, Vol. 19, No. 1, 73–81.
6. Xie, G., C. C. Lin, and J. H. Li, "GILD EM modeling in nanometer material using magnetic field integral equation," *J. Mathmatica Applicata*, Vol. 16, No. 2, 149–156, 2003.

Radiated EMI Recognition and Identification from PCB Configuration Using Neural Network

P. Sujintanarat[1], **P. Dangkham**[1], **S. Chaichana**[1], **K. Aunchaleevarapan**[2], **and P. Teekaput**[1]

[1]Faculty of Engineering, Chulalongkorn University, Bangkok, Thailand
[2]Electrical and Electronic Products Testing Center, NECTEC, NSTDA, KMITL Bangkok, Thailand

Abstract— In this paper the application of neural network (NN) in EMI radiated measurement is proposed to recognize and identify the basic PCB configuration. The emission of electromagnetic (EMI) noise form printed circuit board (PCB) is studied. The different kinds of PCB shape are used for produce electromagnetic field. The fields are measured using near-field probe with termination load and computation using finite element method (FEM). After measurement by near-field probe and simulation by FEM then, is a thinning process. The images acquired from thinning process will be analyzed to calculate number of junction point, end point, cross point, ratio of black and white, position of end point, vertical line and horizontal line, respectively then pass to NN. The trained NN can identify emission pattern successfully.

1. INTRODUCTION

This paper presents the radiated EMI recognition and identification for PCB configuration measured by near-filed scanner and simulated by Finite Element Method (FEM). Applying by used electromagnetic field radiated from PCB that has many difference shapes to generate electromagnetic field. Then used the neural network to identify the kind of PCB shape. The learning process is achieved by using FEM of the radiated field from difference shapes of PCB.

2. PCB CONFIGURATION

In this paper, six kinds of basic PCBs shape are used to produce radiated EMI. PCB configurations (Fig. 1) included. Strip line(a), radius-shape(b), L-shape(c), H-shape(d), X-shape(e), 7-shape(f) are prepared and used in this research. The trace of the PCB is adjusted to match a 50 Ω resistance at the end of the terminal. Ferrite clamps minimize the influence of the signal cable entering the test-site ensuring that the signal is greater than 20 dB, which is below the emissions measured from the test PCB. The ferrite clamps are included in the test boards.

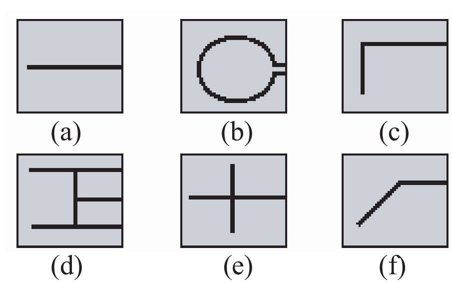

Figure 1: Shown PCB configurations.

3. FINITE ELEMENT METHOD (FEM)

This paper used Finite Element Method (FEM) based on Maxwell's equation including the eddy current and displacement current terms [1]. Finite conductivity, arbitrary configuration and arbitrary dielectric constant may be considered. In this analysis of emission from PCB, the required input data is only physical data, such as conductivity, configuration, dielectric constant, permeability, etc., and no equivalent circuit or characteristic impedance values are required as input data. The analysis based on Maxwell's equations. For electrolysis and computation of resistances of grounding plates we have

$$E = -grad(V) \tag{1}$$

$$J = \sigma E \tag{2}$$

$$divJ = q \tag{3}$$

So

$$-\,div(\sigma * grad(V)) = q \tag{4}$$

where E is the electric field, V is the electric potential, σ is the conductivity and q is the current source.

For discussing the design for PCB trace on ground structures including frame ground. The method of FEM for calculating E-field on PCB by separating a PCB area become a very small elements (Fig. 2(1)). The flux density of strip line PCB is shown in Fig. 2(2), the maximum of flux density appeared at the center of the strip line, then there decrease, continuously when the distance between the strip line and measured point in y-direction increase. Then, the flux density increase again at the edge of the PCB. This phenomenon occurred because the coupling mechanism of the ground plane to the strip line PCB. Fig. 2(3) shown that the flux density of the radius shape is highest amplitude at the edge of the PCB trace and it induce into inside of the loop. In case of L-shape, H-shape and 7-shape of PCB, the flux density appeared at the trace and induced into the inner side of the shape, the highest amplitude occurred at the each corner of the trace (Fig. 2(4), Fig. 2(5) and Fig. 2(7)). Fig. 2(6) shown the flux density of the X-shape PCB, the maximum E-field appeared at he cross point of the trace.

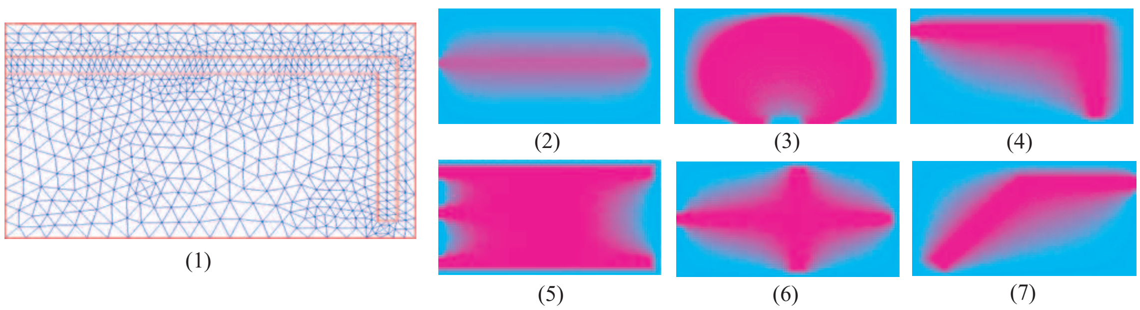

Figure 2: Simulated by Finite Element Method (FEM).

4. NEAR-FIELD SCANNER MEASUREMENT

The near-field measurements are performed in a shielded room with the approximate dimensions $3 \times 5 \times 2\,\text{m}^3$. The kinds of experimental equipment are an EMI receiver, pulse generator, dipole antenna, ferrite clamps and a 24 dB pre-amplifier. The measurement is carried out using a Quasi-

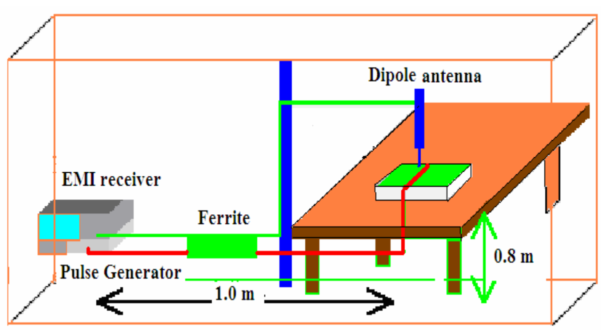

Figure 3: The near-field measurement configuration.

Peak detector with a 100 kHz resolution bandwidth. A generator producing a 30 MHz square-wave with a 50 ns rise time, 5 V peak-to-peak amplitude, 0.5 duty cycle, and a 50 Ω input resistance constitutes the digital source. The magnetic near-field measurement setup is illustrated in Fig. 3. The probe or loop antenna is positioned by a computer controller [2]. The data are acquired at intervals of 1 cm in the X-direction and Y-direction, respectively.

The E-field of 30 MHz frequency of the input signal are measured and plotted in 3D method are depicted in Fig. 4. The measured results also takes into account the averaging effect of the electric field over the PCB trace. The measured results are good in agreement to the FEM calculated results.

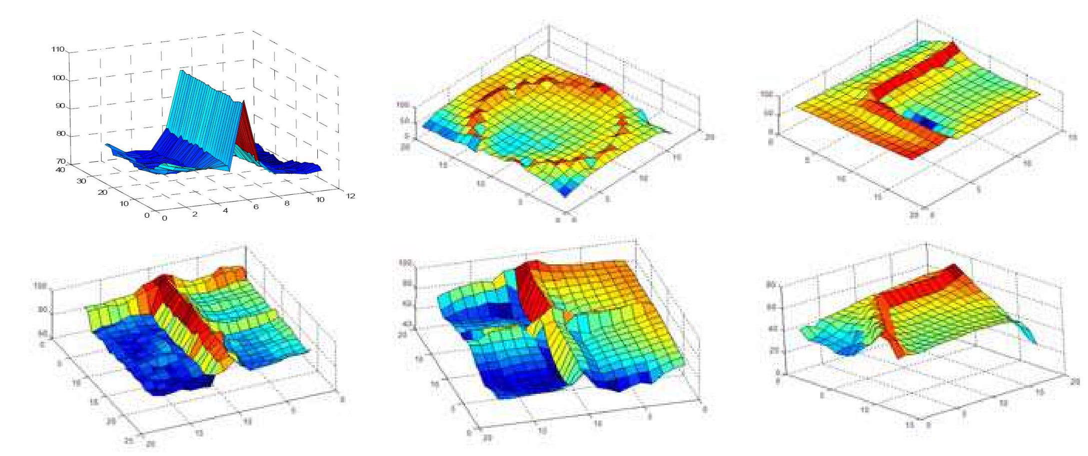

Figure 4: The measured results.

5. THINNING PROCESS

The thinning of set A by a structuring element B, denote $A \otimes B$

$$A * B = (A - B1) \cap (A^{c} - B2) \tag{5}$$

where $B2 = W - B1$, W is the local background, A is an image, B is sequence element and x is don't care

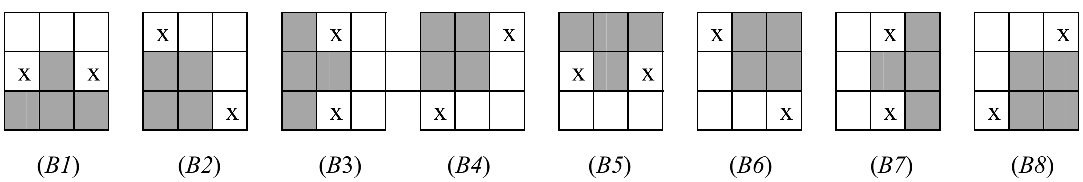

Figure 5: Sequence of element used for thinning.

$$A \otimes B = A - (A * B) = A \cap (A * B)^{c} \tag{6}$$

$$\{B\} = \{B1,\, B2,\, B3,\, \ldots,\, B8\} \tag{7}$$

$$A \otimes \{B\} = ((\ldots((A \otimes B1) \otimes B2) \ldots) \otimes B8) \tag{8}$$

The process is to thin by one pass with $B1$, then thin the result with one pass of $B2$, and so on, until A is thinned with one pass of $B8$. The entire process is repeated until no further changes occur. The results of thinning from simulation by FEM and measuring by near field scanner shown in Fig. 6 and Fig. 7, respectively [4].

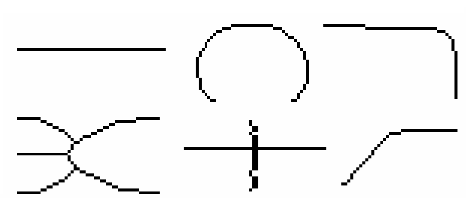

Figure 6: Thinning from simulation.

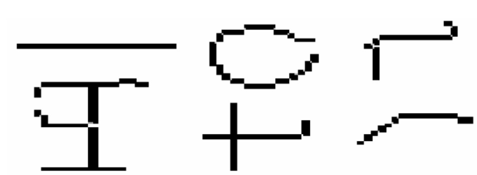

Figure 7: Thinning from measurement.

6. THE NEURAL NETWORK

The recognition method used in this research is using features of PCB (number of junction point, end point, cross point, ratio of black and white, position of end point, vertical line and horizontal line) for classify PCB. The two layer feed-forward backpropagation network is created. The first

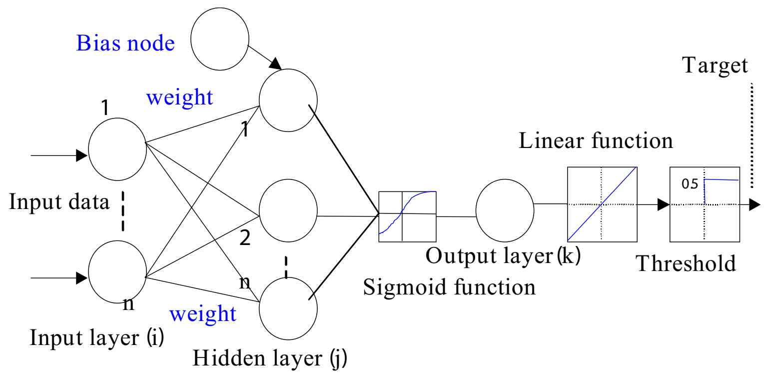

Figure 8: The Neural Network architecture.

layer has 100 log sigmoid neurons, the second layer has 6 purelin neurons, log sigmoid is a transfer functions calculate a layers output from its network input and return value between 0 and 1.

The Neural Network consists an input (i layer), a hidden (j layer) and an output (k layer) is adapted to implement the proposed application. The capability and accuracy in the estimation depends on the number of input, hidden, output node, etc.

The backpropagation network can be thought of as a converter having many inputs and outputs. The learning process begins with feeding the input data into the NN input layer and assigning the NN target for the output layer. The network converts the input data according to connection weights. The calculated output in each hidden node is converted to the output layer using the sigmoid function. The summation of each sigmoid function in the hidden layer is the calculated output node. The calculated result from the output layer is converted to the output data and used for comparing with the NN target using the linear function. From this point, the sum-square error is obtained and used for stopping the learning process. The backpropagation processes begin when the sum-square error is greater than the maximum error. The output data in the output node is back propagated to the hidden layer and the input layer, respectively. During propagation, connection weights are adjusted until the network sum-square error is less then maximum error. When the learning process is finished, the weights are obtained and the NN architecture is defined. The trained NN is ready to identify or predict outputs related to the input data.

Table 1: The training data sets of the NN for learning process.

PCB Conf.	Input data for NN							NN Target					
	Junction point	End point	Cross point	Ratio	Position of end point	Vertical Line	Horizontal Line	T_1	T_2	T_3	T_4	T_5	T_6
E	3	5	0	0.0941	0	0	0	1	0	0	0	0	0
I	0	2	0	0.4712	0	0	0	0	1	0	0	0	0
L	0	2	0	0.0525	4	5	5	0	0	1	0	0	0
O	0	2	0	0.0695	0	0	0	0	0	0	1	0	0
X	0	4	1	0.0542	0	0	0	0	0	0	0	1	0
7	0	2	0	0.0500	4	5	0	0	0	0	0	0	1

7. RESULTS AND CONCLUSIONS

The aims of this paper are recognize and identify the PCB configurations from emission spectrum. After measurement by near-field scanner (30 MHz) and FEM is thinning process then pass to neural network. (Fig. 9). Two layer backpropagation neural network is created and trained by used data from Table 1, the six bits digital output is considered. When the training process is finished the unknown source of radiated emission are fed to the NN input layer for identify PCB configurations. The NN successfully to identify emission pattern from PCB.

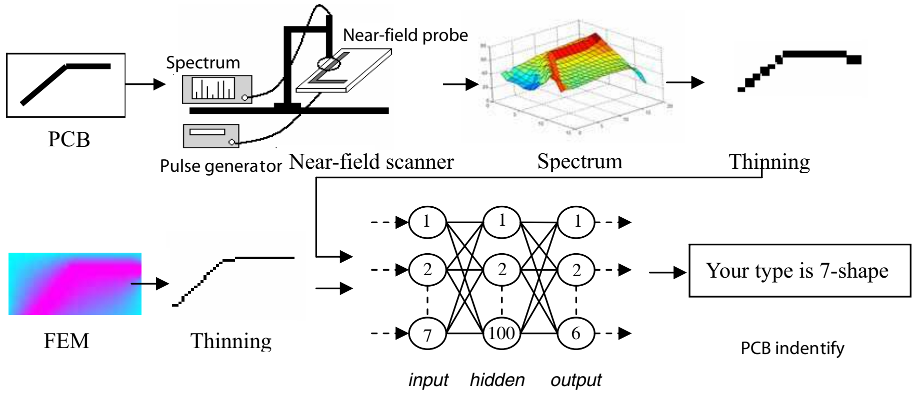

Figure 9: Step of process.

ACKNOWLEDGMENT

This work was supported by National Science and Technology Development Agency (NSTDA) and Thailand Graduate Institute of Science and Technology(TGIST), Thailand.

REFERENCES

1. Roczniak, A., E. M. Petriu, and G. I. Costache, "3D electromagnetic field modeling base on near-field measurements," *IEEE Instrumentation and Measurement Technology Conf.*, Brussels, Belgium, 890–896, June 1996.
2. Laurin, J. J., Z. Ouardhiri, and J. Colinas, "Near-field imageing of radiated emission source on printed-circuit boards," *IEEE International Symposium on Electromagnetic Compatibility*, 368–373, 2001.
3. Aunchaleevarapan, K., K. Paitoonwatanakij, W. Khan-Ngern, and S. Nitta, "Novel method for predicting PCB configurations for near-field and far-field radiated EMI using a neural network," *IEICE Transactions on Communication*, Vol. E86-B, No. 4, 1364–1376, April 2003.
4. Gonzalez, C. R. and E. R. Woods, *Digital Image Processing*, Prentice Hall, New Jersey, 2001.

Recognition and Identification of Radiated EMI for Shielding Aperture using Neural Network

P. Dangkham[1], **P. Sujintanarat**[1], **S. Chaichana**[1], **K. Aunchaleevarapan**[2], **and P. Teekaput**[1]

[1]Faculty of Engineering, Chulalongkorn University, Bangkok, Thailand
[2]Electrical and Electronic Products Testing Center, NECTEC, NSTDA, KMITL, Bangkok, Thailand

Abstract— This paper presents the method to recognize and identify the different type of enclosure with apertures from electromagnetic emission. The square wave generator is fed into the structure-like antenna in the enclosure box. Then the radiated emission from the different type of aperture are measured. The thirteen highest amplitude of the radiated emission are fed into an Artificial Neural Network input for recognition. The target of the neural network are set in four bits in the digital format. When the training process is finished the neural network are used for identify the kind of the aperture. The trained neural network are very successfully in identification all kinds of enclosure with apertures.

1. INTRODUCTION

The shielding enclosure has already been studied many times. It is frequently used to reduce the emission or to improve the immunity of the electronic equipment. In the PC-case, the integrity of shielding enclosures is compromised by slots and apertures for heat dissipation, CD-ROMs, I/O cable penetration or other possibilities. These apertures can radiate the electromagnetic field and emission spectrums are different. While a major problem of a PC-case is a electromagnetic compatibility (EMC) rules. There are many papers present the method for mitigate the radiation from intended apertures [1–3]. Proper design of airflow aperture is critical in minimizing electromagnetic interference (EMI) for PC-case. There are several ways in which they can be applied in order to minimize the error between the expected and predicted spectra of the radiated field such as the Method of Moment (MoM) and the Finite Element Method (FEM). However, they are computationally intensive and suitable only for basis structure and all of them are very expensive.

In this paper, the Neural Network (NN) is used to recognize and identify the effects of apertures shape. For all cases, a metallic container with the dimensions of $20 \times 40 \times 45\,\text{cm}^3$ and a fixed rectangular open area of $18\,\text{cm}^2$ on one wall. There are 9 rectangular apertures for test in shielded room. The results have been taken to training neural network process for using in identification emission spectrums. The aim is to develop a procedure that can be carried out with inexpensive test facilities. The measurement shall be used to give an indication if a product can pass the costly standard EMI test.

2. ENCLOSURE WITH APERTURES CONFIGURATION

For rectangular apertures, we use 9 cases which have the same area of $18\,\text{cm}^2$ are shown in Fig. 1. There are one aperture (1×18, 2×9 and 3×6) and array of apertures (2×1, 1×6, 1×9 and 3×1) for make the difference. In array of apertures, they have been separated into small apertures and aligned to different position. All cases are the one open wall of box which was made from aluminum.

3. NEURAL NETWORK

A neural network (NN) can be considered as a matrix function that provides an approximate model of a system. The approximation model of this function is define a priori, and depends on the type of application (identification, classification, pattern recognition, etc.) [4, 5].

A three-layer NN, (shown in Fig. 2), which consists of an input (the i layer), a hidden (the j layer), and an output (the k layer), is adapted to implement the proposed application. The capability and accuracy in the estimation depends on the number of input nodes, hidden nodes, and output nodes, etc..

The backpropagation network can be thought of as a converter having many inputs and outputs. The learning process begins with feeding the input data into the NN input layer, and assigning the NN target for the output layer. Then, the initial connection weights and bias nodes at the hidden layer and the output layer are set randomly. The maximum error, the learning rate, and

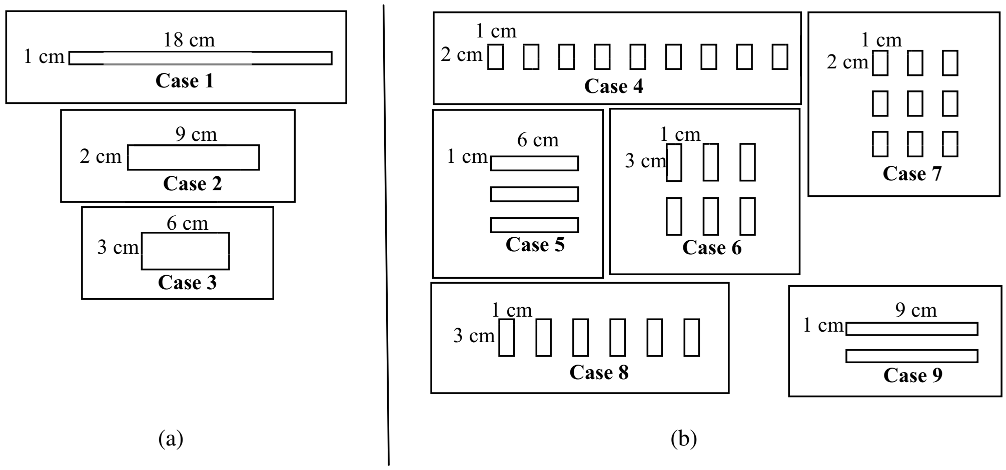

Figure 1: Difference of aperture dimension, (a) One aperture, (b) Array of apertures.

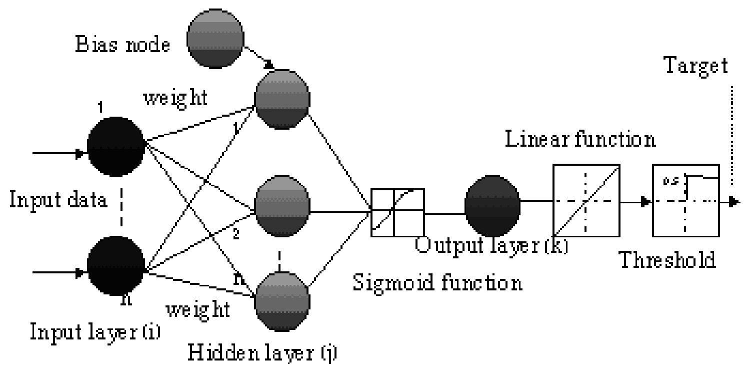

Figure 2: The NN Architecture.

the momentum are set for the NN, respectively. The network converts the input data according to connection weights. The calculated output in each hidden node is converted to the output layer using the Sigmoid function. The summation of each sigmoid function in the hidden layer is the calculated output node. The calculated result from the output layer is converted to the output data and used for comparing with the NN target using the linear activation function and the threshold function, respectively. From this point, the sum-square error is obtained and used for stopping the learning process.

The backpropagation process begins when the sum-square error is greater than the maximum error. The output data in the output node is back propagated to the hidden layer and the input layer, respectively. During propagation, connection weights are adjusted until the network sum-square error is less than the maximum error. When the learning process is finished, the weights are obtained and the NN architecture is defined. The trained NN is ready to identify or predict outputs related to the input data.

4. MEASUREMENTS AND RESULTS

The measurements are measured from 30 MHz up to 1 GHz. The box is placed on an 80 cm high non-metallic table. The radiated field is collected by an antenna located at a 3 m distance from the box , at height of 1 m inside the semi anechoic chamber. The measurement for horizontal polarization E-fields are measured by using a bi-conical antenna. A generator produces a 30 MHz square-wave with a 50 ns rise time, 5 V peak-to-peak amplitude, 0.5 duty cycles, and a 50 input resistance constitutes the digital source. We set the dipole antenna in the box for electromagnetic source. The measurement configuration is shown in Fig. 3.

The measured results for one aperture are shown in Fig. 4(a) for case 1. The peak radiated emission of another kinds of aperture are plotted and show in Fig. 4(b). The radiated spectra of different aperture are similar together, but different in amplitude. From the Fig. 4(b), the peak emission of case 5 are highest compare to case 1 and case 5, because the size of aperture match with

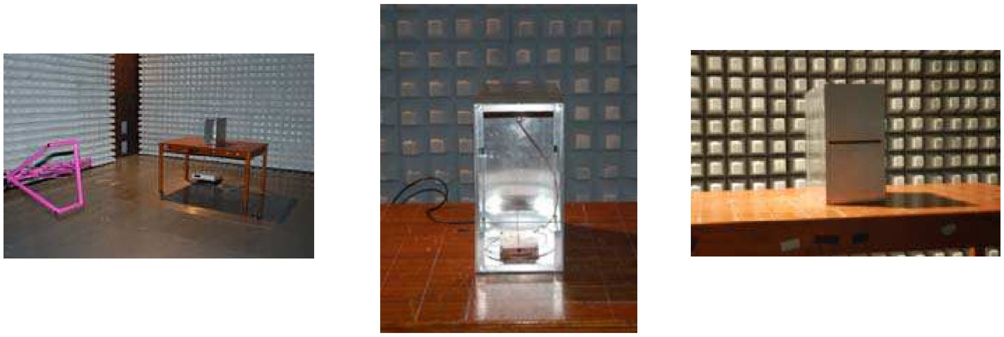

(a) (b) (c)

Figure 3: The measurement configuration, (a) Set up the measurement, (b) Using dipole antenna for EM Source, (c) Enclosure with aperture.

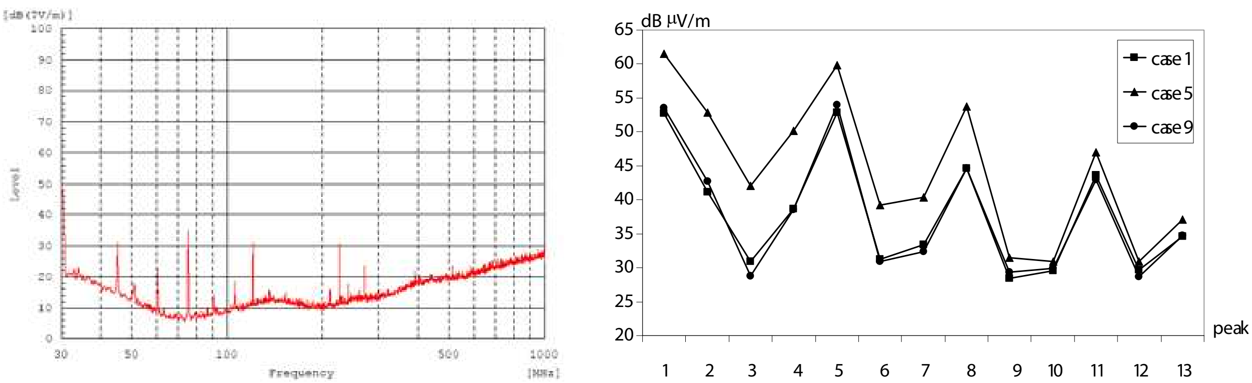

(a) (b)

Figure 4: The emission spectrums, (a) Radiated spectrum of case 1, (b) 13 highest peaks of radiated emission spectra of case 1, 5 and 9.

the antenna length. At 50 MHz frequency, the amplitude of radiated emission is lowest because of resonance of the enclosure box. The measured results from enclosure with aperture in case 1 and case 9 are a few different because of there are located in horizontal polarization and the length of the aperture are not match to the wavelength. The 13 highest peaks of radiated emission spectra are selected for fed into the NN training process.

The obtained amplitudes in each frequencies referring to emission spectrums of the aperture are fed into the input layer of NN. The target of NN consists of different aperture's dimension are set in the binary digital format("0", "1") in four bit. Fig. 5 shows the NN training process.

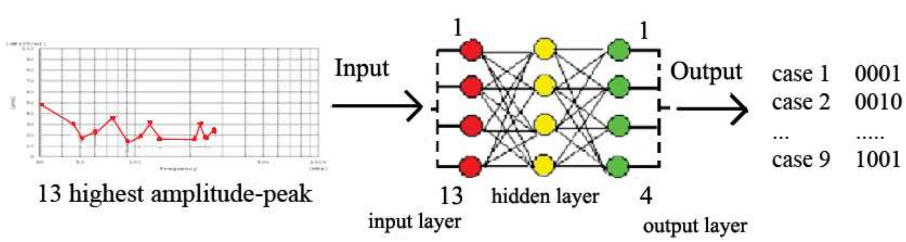

Figure 5: The NN training process.

The three layers of NN, which consist of 13 input nodes, 100 hidden nodes and 4 output nodes, are applied. The maximum error and the learning rate are provided as 0.00001 and 0.05, respectively. The training data sets of the NN for learning process are shown in Table 1.

Table1: The training data sets of the NN for learning process

Aperture Conf.	Input data for NN (dB μV/m)													NN Target			
	30.00 MHz	45.15 MHz	50.90 MHz	60.30 MHz	75.45 MHz	90.60 MHz	105.44 MHz	120.90 MHz	135.74 MHz	210.89 MHz	225.73 MHz	240.88 MHz	270.85 MHz	T_1	T_2	T_3	T_4
Case 1	52.70	41.20	30.90	38.70	52.90	31.20	33.40	44.60	28.40	29.60	43.60	29.70	34.60	0	0	0	1
Case 2	53.70	41.20	33.10	39.40	53.70	33.00	34.00	48.20	30.20	32.00	46.10	32.40	37.30	0	0	1	0
Case 3	54.90	43.10	31.60	40.10	54.10	31.90	33.40	47.00	30.10	28.90	38.00	30.30	33.90	0	0	1	1
Case 4	53.60	41.90	30.20	38.40	53.70	31.00	32.20	43.60	27.90	28.90	43.10	29.40	34.90	0	1	0	0
Case 5	61.50	52.80	42.00	50.20	59.80	39.20	40.40	53.70	31.50	30.90	47.00	30.90	37.10	0	1	0	1
Case 6	61.10	51.30	42.40	48.70	58.90	36.80	38.40	49.80	29.20	30.90	46.90	31.70	36.40	0	1	1	0
Case 7	54.8	42.20	34.60	40.00	54.60	33.00	35.10	50.80	30.80	31.70	43.70	33.10	37.10	0	1	1	1
Case 8	61.60	53.20	40.00	50.10	60.50	38.40	39.10	48.90	29.10	31.90	49.10	31.50	39.00	1	0	0	0
Case 9	53.50	42.70	28.80	38.60	54.00	30.90	32.40	44.60	29.30	29.90	43.00	28.70	34.70	1	0	0	1

5. CONCLUSIONS

In the design process of PC-case, airflow apertures are critical in minimizing electromagnetic interference (EMI). The enclosures of different dimension apertures are studied. We concentrate on the method to identify emission spectrum. The neural network is applied to identify various enclosures of apertures which produce electromagnetic fields. In this process, the peak amplitudes of some frequencies are selected to feed into the input layer of NN. We found the neural network with (13 input nodes, 100 hidden nodes, 4 output nodes) can identify emission spectrums from different apertures. This is especially useful in giving an indication if a product can pass the costly standard EMI test.

ACKNOWLEDGMENT

Electrical and Electronic Products Testing Center (PTEC) is gratefully acknowledged.

REFERENCES

1. Golestani-Rad, L. and J. Rashed-Mohassel, "The effects of apertures' shape and configuration on the shielding effectiveness of metallic enclosures," *Microwave Conference Proceedings, 2005. APMC 2005. Asia-Pacific Conference Proceedings*, Vol. 5, 4–7 Dec., 2005.
2. Belokour, I., J. LoVetri, and S. Kashyap, "Shielding effectiveness estimation of enclosures with apertures," *Electromagnetic Compatibility IEEE International Symposium*, Vol. 2, 2000.
3. Gu, C. and S. Li, "Shielding effectiveness of an enclosure with apertures," *IEEE International Symposium on Microwave, Antenna, Propagation and EMC Technologies for Wireless Communications Proceedings*, 2005.
4. Aunchaleevarapan, K., K. Paitoonwatanakij, W. Khan-Ngern, and S. Nitta, "Novel method for predicting PCB configurations for near-field and far-field radiated EMI using a neural network," *IEICE Transactions on Communication*, Vol. E86-B, No. 4, 1364–1376, April, 2003.
5. Antonini, G. and S. Cristina, "Performance analysis of electromagnetic shields using neural networks," *Proc. 13th Int. Zurich Symp. and Tech. Exhibition on EMC*, Feb. 16–18, 1999.

High Sensitivity Electro-optic Magnetic Field Probe

W. K. Kuo and J. Y. Kuo

Institute of Electro-optical and Material Science, Formosa University
64 Wenhua Rd., Huwei, Yunlin 63208, Taiwan, China

Abstract— This paper presents a new electro-optic magnetic field probe using the Fabry-Perot effect to enhance the sensitivity. The sensing head is made of a plate $LiNbO_3$ crystal with high reflection coating on its up and bottom side. The experiment shows that the sensitivity can be improved by an order of magnitude (20 dB).

1. INTRODUCTION

External electro-optic (EO) probing technique has been a very useful tool for the characterization of high-speed devices and circuits [1]. It has many advantages, such as broadband, non-contact, and less invasiveness. The physical basis of EO probing technique is the linear electro-optic effect or called Pockels effect, which is that presence of an electric field on an electric-optic crystal can cause a change of the refractive indices of the crystal. This change can alter the polarization state of an optical probing beam that propagates through the crystal. Recently, the EO probing technique is extended to obtain the mapping of electric-field strength close to metal structure of a device [2]. Such new field-mapping capability has many derivative applications, such as in the characterization of MEMS antennas and antenna arrays, the verification of electromagnetic compatibility (EMC), and the failure diagnosis of microelectronic integrated circuits. By combing a loop antenna, the EO probing technique can further to apply to magnetic field sensing [3]. This kind of EO magnetic field probe, without metallic cables or balun, can perform magnetic field measurement with little disturbance on the surrounding field. The detected magnetic field signal is transmitted by optic fibers, instead of metallic cables. The optic fibers don't pick any electrical noise as the metallic cables do. These advantages enable the EO magnetic field probe to be an ideal tool to perform high-frequency measurement of magnetic near field with better accuracy than the traditional approach using metallic cables. However, the EO coefficients of an EO crystal are only the order of 10E-12 (pico). Therefore, the sensitivity is an important issue for the EO magnetic field probing system. In this paper, we present a new EO magnetic field probe using the Fabry-Perot effect to enhance the sensitivity. The Fabry-Perot effect had been proposed to enhance the sensitivity the EO probing system [4]. To enhance the magnetic field sensitivity, we combine an EO crystal with the Fabry-Perot and a loop antenna to form an EO magnetic field probe.

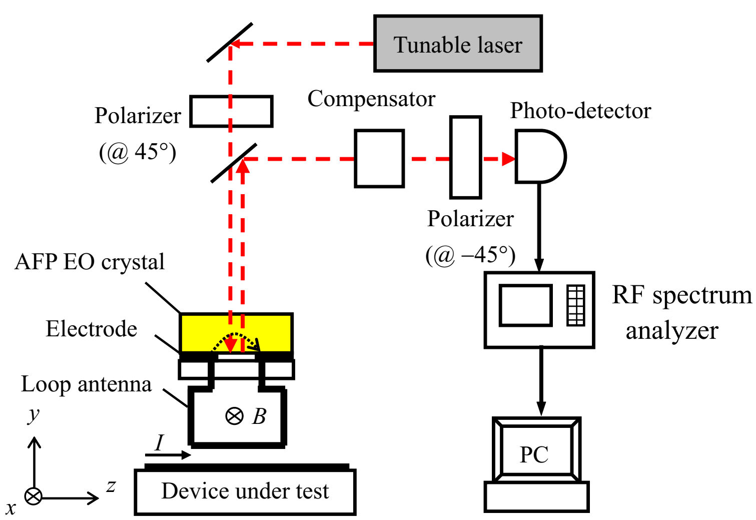

Figure 1: Experiment set-up of the high sensitivity electro-optic magnetic field probe system.

2. THE FABRY-PEROT EO MAGNETIC FIELD PROBE SYSTEM

The new Fabry-Perot magnetic field probe system is shown in Fig. 1. The probe was an Asymmetric Fabry-Perot (AFP) EO crystal equipped with a loop antenna which was the size of 0.5 mm×0.5 mm. The EO crystal is a y-cut $LiNbO_3$ and its top and bottom surfaces have high reflection coating of reflection coefficients of R_1 and R_2, respectively. When the probing beam is propagating through the crystal along the y-axis and reflecting from the bottom surface, the multiple reflections inside the crystal cavity must be taken into account. If the $R_1 < 1$ and $R_2 \cong 1$, this AFP cavity is the so-call Gires-Tournois etalon. Neglecting the absorption of crystal, the total reflection coefficient of AFP EO crystal cavity is [5]

$$R = \frac{-\sqrt{R_1} + \exp(-i2\phi)}{1 - \sqrt{R_1}\exp(-i2\phi)} \tag{1}$$

where ϕ is the phase difference between the beam reflecting from the top surface and the beam propagating through the crystal then reflecting from the bottom surface. It can be expressed as

$$\phi = \frac{2\pi\eta L}{\lambda} \tag{2}$$

where η is the index of reflection of the EO crystal and dependent on the beam polarization direction, L is thickness of the EO crystal plate, and λ is the laser light wavelength in vacuum. Assume that the wavelength λ is tuned to make the phase ϕ to be close to $n\pi$ (n is an integer). Let $\phi = n\pi + \Delta\phi$, the phase shift Φ of the reflection coefficient in Eq. (1) is given by

$$\Phi = -2\tan^{-1}\left(\frac{1+\sqrt{R_1}}{1-\sqrt{R_1}}\tan\phi\right) \approx -\frac{1+\sqrt{R_1}}{1-\sqrt{R_1}} \cdot 2\Delta\phi = -K \cdot 2\Delta\phi \tag{3}$$

It can be seen that the original phase shift $2\Delta\phi$ is enhanced by a factor of $K = (1+\sqrt{R_1})/(1-\sqrt{R_1})$. In the EO probing system, the phase retardation of the probing beam is used to determine the electric-field applied on the crystal. As shown in Fig. 1, when there is a current I in the $+z$ direction, there is a magnetic field B in the x direction. According to Faraday's law, when the antenna is placed in area with a time-varying magnetic field, the induced electric-field appears between the electrodes under the AFP EO crystal. The induced electric-field is along the z-direction and applied on the EO crystal. When the incident laser beam is linearly polarized at 45° with respect to x-axis, the EO-induced retardation is

$$\Delta\Gamma = 2\pi\frac{L_{\mathit{eff}}}{\lambda}\left(\frac{n_e^3 r_{33} - n_o^3 r_{13}}{2}\right)\frac{V}{d_{\mathit{eff}}} = \pi\frac{V}{V_\pi} \tag{4}$$

where n_o and n_e are the ordinary and extraordinary indices of the refraction of the $LiNbO_3$ crystal. For the incident laser beam propagating along the y-direction, the two eigen-indices of refraction are. L_{eff} is the effective length of region in EO crystal where the electric field applied. d_{eff} is the effective spacing of the two electrodes and $V = E_z d_{\mathit{eff}}$. The half wave-length V_π is given by

$$V_\pi = \frac{\lambda d_{\mathit{eff}}}{L_{\mathit{eff}}(n_e^3 r_{33} - n_o^3 r_{13})} \tag{5}$$

The phase retardation is the phase difference between the x and z components of the input laser beam. According to Eq. (3), the EO-induced retardation will be enhanced by the factor of K as well. By adjusting the optical compensator to make the system be under a proper optical bias condition, the modulation index (M_I) of the output laser beam intensity (I_{out}) on the photo-detector is

$$M_I = \frac{I_{out}}{I_0} = K \cdot \pi\frac{V}{V_\pi} \tag{6}$$

where I_0 is the average output laser beam intensity. Therefore, if we tune the laser wavelength to make the AFP cavity length to be multiple of the half wavelength, the EO modulation index will be enhanced by a large factor K. For example, if $R_1 = 0.9$, $K = 38$. This will greatly improve the magnetic field measurement sensitivity.

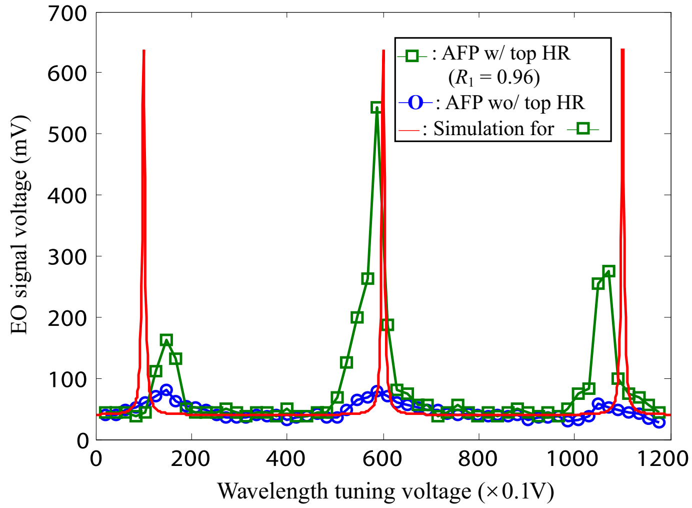

Figure 2: EO signal voltage versus wavelength tuning voltage.

3. EXPERIMENTAL RESULTS

Before performing the magnetic field measurement, we need to tune the laser wavelength of the tunable laser to be with the highest sensitivity for the EO effect. The device under test is a micro-strip line (MSL) and its line width is 3 mm. We applied an AC current to the MSL and the induced electric-field applied on the EO crystal. A tunable laser source with wavelength of 780 nm is the Littrow type laser from Sacher Lasertechnik and its wavelength is tuned by adjusting the driving voltage of the piezo actuator [6]. Two $LiNbO_3$ EO plate samples with different reflection coefficient for the top surface (R_1) were investigated. For the reflection coefficient of the bottom surface (R_2), both two samples are same and equal to 0.098. One had a high reflection coating on the top surface and the reflection coefficient is equal to 0.96 and the other had no coating on the top surface. The size of the loop antenna is 3 mm×3 mm and the gap between two electrodes is 1 mm. Measurement and simulation results are compared and shown in Fig. 2. It can be seen that the signal intensity of the EO crystal with high reflection coating on the top surface is improved by an order of magnitude. In the figure, we notice that there exist some minor discrepancies between measured and simulated results. For example, the peak profile width of the measurement curve is less than that of the simulation curve. The two side peaks are not symmetric and have lower peak value than the main peak in the center. All these discrepancy are due to that the Littrow type laser has an external cavity and change the tilt angle of the grating to tune the wavelength.

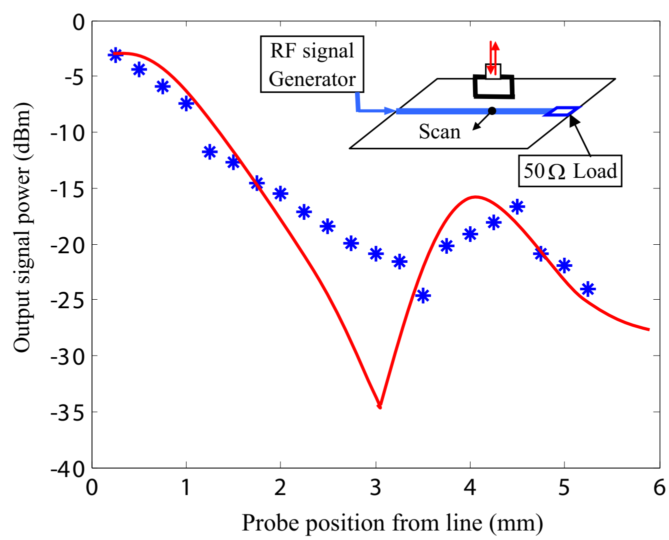

Figure 3: Near-field measurement above the MSL at 1 GHz.

Therefore, when the wavelength is varied, the output beam direction is slight change as well. If we didn't realign the optical path, the laser beam was no longer perpendicular incident into the EO crystal. This deviation may change the reflection condition and weakened the AFP EO effect.

In the second experiment, a RF signal with a frequency of 1 GHz and power of 20 dBm was feed into the MSL. Initially, the loop antenna was placed just above the MSL. Then the MSL was moved by the stage apart from the loop antenna. In other words, the loop antenna was to scan the surface magnetic field of the MSL as shown in Fig. 3. Measured result is also shown in Fig. 3. It can be seen that the measured curve (star) roughly agree with the simulated curve (red). The discrepancy may caused by the difference between the simulation model and the actual measurement situation. Though, this experiment demonstrates that this EO system can be used to sense the surface magnetic field on a testing device with high sensitivity.

4. SUMMARY

In the present paper, we use an AFP EO crystal combing a loop antenna to form a magnetic probe with high sensitivity. The experiment shows that the sensitivity of the AFP EO crystal is almost better than conventional approach by an order of magnitude. We also successfully use this optical probe to perform the magnetic field measurement above an MSL. This optical type probe has not metallic cable as the conventional loop probe and could have better measurement accuracy.

ACKNOWLEDGMENT

The authors would like to acknowledge the financial support from the National Science Council of the Republic of China under grant NSC-94-2212-E-150-025.

REFERENCES

1. Heutmaker, L. M. S. and G. T. Harvey, "Electro-optic sampling of high-speed silicon integrated circuits using a GaAs probe tip," *Appl. Phys. Lett.*, Vol. 59, 146–148, 1991.
2. Yang, K., I. G. David, J.-G. Yook, I. Papapolymerous, L. P. Katechi, and J. F. Whitaker, "Electro-optic mapping and finite-element mideling of the near-field pattern of a microstrip patch antenna," *IEEE Tran. Microwave Theory Tech.*, Vol. 48, 288–294, 2000.
3. Suzuki, E., S. Arakawa, H. Ota, K. I. Arai, and R. Sato, "Optical magnetic field probe working up to 15 GHz using CdTe electrooptic crystals," *IEEE Tran. on EMC*, Vol. 47, No. 2, 344–351, 2005.
4. Quang, D. L., D. Erasme, and B. Huyart, "Fabry-Perot enhanced real-time electro-optic probing of MMICs," *Electrons Letters*, Vol. 29, No. 5, 498–499, 1993.
5. Yeh, P., *Optical Waves in Layered Media*, Wiley, New York, 1988.
6. McNicholl, P. and H. J. Metcalf, "Synchronous cavity mode and feedback wavelength scanning in dye laser oscillators with gratings," *Appl. Opt.*, Vol. 24, No. 17, 2757–2761, 1985.

Microstrip Coupled Line Filters with Spurious Band Suppression

M. C. Velázquez-Ahumada[1], **J. Martel**[2], **and F. Medina**[1]

[1] Department Electronics and Electromagnetism, Physics Faculty, University of Seville, Seville, Spain
[2] Department of Applied Physics II, ETSA, University of Seville, Seville, Spain

Abstract— Passband microstrip coupled line filters are widely used in daily microwave engineering practice. These filters present an undesired pass band at twice the design central frequency of the filter. Two simple methods to suppress this drawback are reported in this communication. The proposed methods, apart from removing the spurious band, provide an extra coupling mechanism that relaxes tolerances of strip width and spacing in those cases where tightly coupled sections are required.

Parallel coupled lines microstrip filters (PCMF) are well known devices in microwave practice. When implemented in their traditional form, i.e., using a single layer substrate in microstrip technology, these filters present two relatively serious drawbacks. First, a spurious pass band appears at $2f_0$ (f_0 is the central frequency of the filter). The second problem comes from the difficulty of fabricating wide band filters because of the weak coupling between the lines in the conventional structure. Strong coupling required by some filter specifications leads to very small values of strip width, w, and strips spacing, s, which can not be sometimes accurately achieved in practice.

In recent years, a number of methods have been proposed to suppress the spurious band in PCMFs [1–8]. In this work we propose a couple of procedures to eliminate the $2f_0$ spurious band which also improve coupling without requiring extremely small line spacing. The first method makes use of a slot in the ground plane below the coupled line sections (see Fig. 1(b)). The slot width can be adjusted so as to get phase velocity compensation [9]. This slot also yields increased coupling. This procedure has been experimentally checked in several filter designs. However, phase compensation has not been possible in some cases involving the use of low permittivity substrates. This problem has been solved by adding a centered floating conductor in the slot region (see Fig. 1(c)). This floating conductor also contributes to increase the coupling level [10].

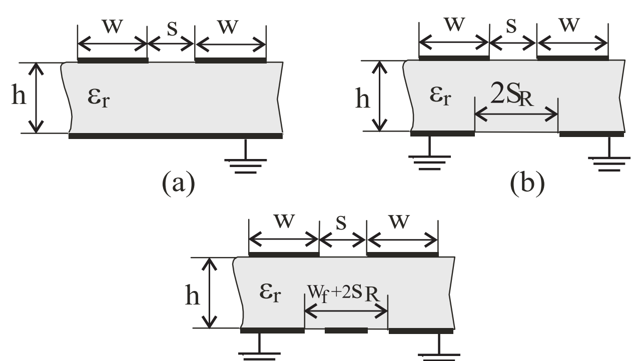

Figure 1: Cross section of the coupled line microstrips used for filter fabrication: (a) conventional structure; (b) coupled strips with slotted ground plane; (c) coupled strips with floating conductor in the ground plane.

Using fast quasi-TEM solvers specially developed for mixed strip-slot structures, an optimization scheme has been developed so as to obtain the initial design of the filter. In case of using the structure in Fig. 1(b), strip widths and slot width are automatically adjusted to get the filter specifications and to cancel the difference between even and odd mode phase velocities. This design is slightly modified using a full-wave simulator in order to completely eliminate the spurious band. As an example, consider the third order filter designs in Table 1 (conventional and slotted plane structures). Note that the separation between the strips are larger in the case of the slotted ground structure (this relax tolerances). The simulation of these filters using a full-wave planar simulator shows that spurious band is meaningfully reduced. However there is still some place for optimization. A slight modification of the slot dimensions along a small region at the ends of the slots allows us to completely suppress the spurious band. In Fig. 2 show the results for the fabricated filter. Note that no spurious band at $2f_0$ appears. An example of design using the structure in Fig. 1(c) is given in Table 2.

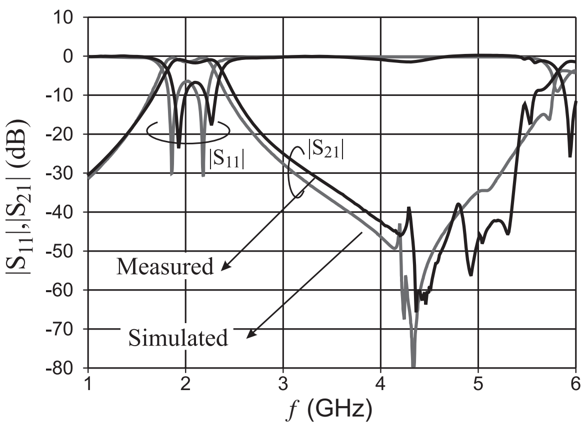

Figure 2: Comparison between simulated and measured results of the final version of filter with slotted ground plane.

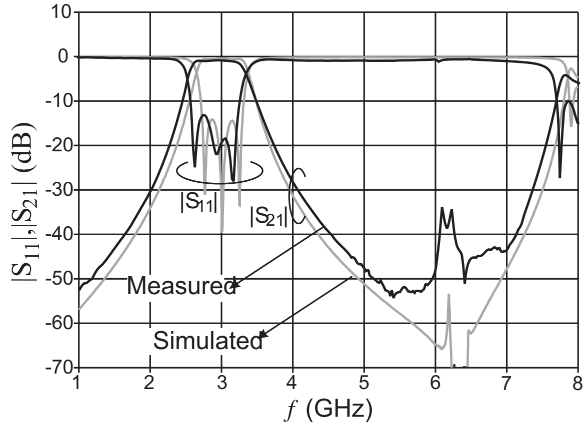

Figure 3: Simulated and measured results for the final version of the filter design in Table 2 (with floating conductor).

Table 1: Dimensions (mm) of conventional and modified coupled line bandpass filter C.

Type of design	Sections 1, 3	Section 2
Conventional	$w = 0.357$, $s = 0.134$, $l = 14.74$ $\epsilon^e_{ef} = 6.86$, $\epsilon^o_{ef} = 5.60$	$w = 0.472$, $s = 0.240$, $l = 14.63$ $\epsilon^e_{ef} = 7.07$, $\epsilon^o_{ef} = 5.69$
Modified	$w = 0.620$, $s = 0.263$, $s_R = 1.59$, $l = 15.93$, $\epsilon^e_{ef} = \epsilon^o_{ef} = 5.54$	$w = 0.865$, $s = 0.551$, $s_R = 2.09$, $l = 15.96$, $\epsilon^e_{ef} = \epsilon^o_{ef} = 5.52$

Table 2: Dimensions (mm) of conventional and modified (with floating ground conductor) coupled line bandpass filter.

Type of design	Sections 1, 4
Conventional	$w = 0.294$, $s = 0.101$, $l = 9.88$ $\epsilon^e_{ef} = 6.74$, $\epsilon^o_{ef} = 5.56$
Modified	$w_f = 0.91$, $w = 0.469$, $s = 0.197$, $s_R = 0.233$, $l = 9.85$, $l_{ex} = 0.4$, $\epsilon^e_{ef} = \epsilon^o_{ef} = 5.59$
Type of design	**Sections 2, 3**
Conventional	$w = 0.484$, $s = 0.261$, $l = 9.74$ $\epsilon^e_{ef} = 7.09$, $\epsilon^o_{ef} = 5.71$
Modified	$w_f = 0.65$, $w = 0.786$, $s = 0.585$, $s_R = 0.602$, $l = 9.20$, $l_{ex} = 0.4$, $\epsilon^e_{ef} = \epsilon^o_{ef} = 5.62$

The authors acknowledge financial support of the Spanish Ministry of Education and Science (project No. TEC2004-03214) and Spanish Junta de Andalucía (project No. TIC-253).

REFERENCES

1. Denis, S., C. Person, S. Toutain, B. Theron, and S. Vigneron, "Parallel coupled microstrip filter with phase difference compensation," *Electronics Letters*, Vol. 31, No. 22, 1927–1928, 1995.
2. Lopetegi, T., M. A. Laso, J. Hernández, M. Bacaicoa, D. Benito, M. J. Garde, M. Sorolla, and M. Guglielmi, "New microstrip wiggly-line filters with spurious passband suppression," *IEEE Trans. on Microwave Theory and Tech.*, Vol. 49, 1593–1598, 2001.

3. Kuo, J. T. and W. Hsu, “Parallel coupled microstrip filters with suppression of harmonic response,” *IEEE Microwave and Wireless Comp. Lett.*, Vol. 12, No. 10, 383–385, 2002.
4. Kim, B., J. W. Lee, and M. Song, “An implementation of harmonic-suppression microstrip filters with periodic grooves,” *IEEE Microwave and Wireless Comp. Lett.*, Vol. 14, No. 9, 413–415, 2004.
5. Garca-Garca, J., F. Martín, F. Falcone, J. Bonache, T. Lopetegi, M. A. G. Laso, M. Sorolla, and R. Marqus, “Spurious passband suppression in microstrip coupled line band pass filters by means of split ring resonators,” *IEEE Microwave and Wireless Comp. Lett.*, Vol. 14, No. 9, 416–418, Sept. 2004.
6. Kuo, J. T., M. Jiang, and H. Chang, “Design of parallel-coupled microstrip filters with suppression of spurious resonances using substrate suspension,” *IEEE Trans. on Microwave Theory and Tech.*, Vol. 52, 83–89, 2004.
7. Kuo, J. T. and M. Jiang, “Enhanced microstrip filter design with an uniform dielectric overlay for suppressing the second harmonic response,” *IEEE Microwave and Wireless Comp. Lett.*, Vol. 14, No. 9, 419–421, 2004.
8. Kuo, J. T., S. Chen, and M. Jiang, “Parallel coupled microstrip filters with over-coupled end-stages for suppression of spurious responses,” *IEEE Microwave and Wireless Comp. Lett.*, Vol. 13, No. 10, 440–442, 2003.
9. Velázquez-Ahumada, M. C., J. Martel, and F. Medina, “Parallel coupled microstrip filters with ground-plane aperture for spurious band suppression and enhanced coupling,” *IEEE Trans. on Microwave Theory and Tech.*, Vol. 52, 1082–1086, 2004.
10. Velázquez-Ahumada, M. C., J. Martel, and F. Medina, “Parallel coupled microstrip filters with floating ground-plane conductor for spurious-band suppression,” *IEEE Trans. on Microwave Theory and Tech.*, Vol. 53, 1823–1828, 2005.

Low-pass Elliptic Filters Using Mixed Microstrip-CPW Technologies

M. C. Velázquez-Ahumada[1], **J. Martel**[2], **and F. Medina**[1]

[1]Department of Electronics and Electromagnetism, Physics Faculty, University of Seville, Seville, Spain
[2]Department of Applied Physics II, ETSA, University of Seville, Seville, Spain

Abstract— Stepped-impedance low-pass elliptic filters are presented in this paper which make use of patterning of both sides of the microstrip substrate. Microstrip and coplanar waveguide components as well as their interactions are used jointly to synthesize the required filter elements. Relatively compact implementations with good electrical performance are obtained in this way.

Conventional stepped-impedance low pass filters (SI-LPF) consist of a cascading of electrically short high and low impedance sections to approximate the corresponding ladder LC lumped circuit prototype [1]. However, this kind of filter inherently presents two problems. One of them is the degradation of the stop band rejection level because of the frequency-distributed behavior of the finite section lines. The second problem comes from the limits imposed by the microstrip technology to achieve very narrow strip widths and, consequently, high impedance section lines.

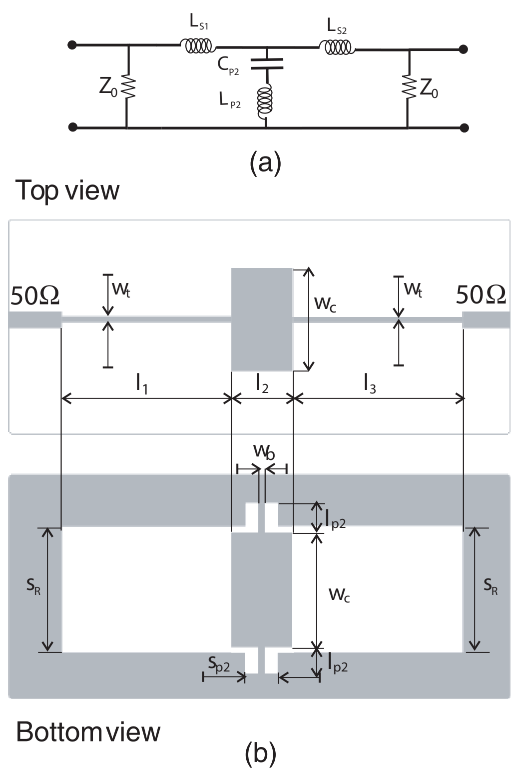

Figure 1: a) Lumped equivalent circuit of a three-pole LPF with a single transmission zero. b) Layout of the SI-LPF proposed in this contribution.

To improve the rejection in the stop band, more sections can be used at expense of higher circuit losses and size. Recently, the use of defected ground structures (DGS) has been reported [2, 3] as an efficient method to attain a good out-of-band response in SI-LPF's. Alternatively, complementary split ring resonators (CSRR) can be etched on the conductor strips of the low impedance sections to suppress spurious band in conventional SI-LPF [4]. Nevertheless, to achieve a more selective and sharper bandpass in LPF's, generalized Chebyshev [5] or elliptic [6, 7] response designs should be implemented.

In this contribution we propose an elliptic LPF implementation that retains the simplicity of the stepped-impedance structure. The method is based on the implementation of the constituent filter elements by combining microstrip and CPW technologies. In Fig. 1 we show a representative

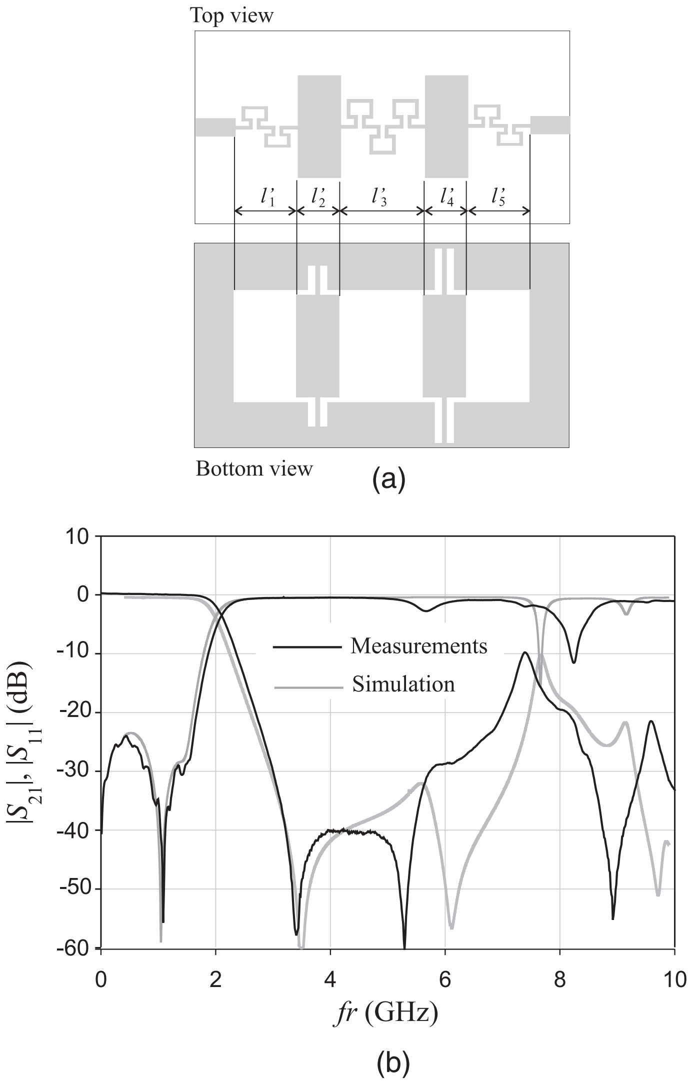

Figure 2: (a) Layout of a miniaturized elliptic SI-LPF with meandered lines. (b) Responses of fabricated filter in (a) obtained from EM simulation (*Ensemble*) and from measurements.

elementary layout of the proposed SI-LPF (a three-pole filter with one transmission zero) and its corresponding lumped equivalent circuit. The series inductors, L_{si}, are implemented as usual with short sections of high characteristic impedance transmission lines (the slot in the ground plane has been included to achieve relatively high values of the characteristic impedance). As a first approximation, low impedance sections are assimilated to parallel plate capacitors to approximate the parallel connected capacitances, C_{pi}. Then, in order to synthesize the transmission poles corresponding to the elliptic design, those capacitors are series connected to the ground plane through high impedance CPW line sections (inductors L_{pi}). Please note that high impedance CPW lines are located at opposite borders of the backside rectangular patch of the capacitors; therefore, they play the additional role of bridges joining the two sides of the ground plane shown in the bottom side of the filter layout. These bridges are essential for a good filter performance because they cancel out undesired ground plane slot modes [8].

The geometrical parameters of the layout are obtained starting from the standard tabulated lumped equivalent circuit components. We make use of the formula for the equivalent circuit of electrically short high characteristic impedance transmission line sections [9] to calculate the length of those sections. The impedance values are obtained from the fast quasi-TEM solver reported in [10]. The lengths of the capacitors are roughly calculated from the trivial expression for the capacitance of an ideal (no edge effects) parallel plate capacitor and finally a tuning adjustment has been applied before obtaining the final design making use of a commercial electromagnetic (EM) simulator. Although the use of slots in the backside of the high impedance sections leads itself to a size reduction with respect to conventional microstrip implementation, we have also used a meander line approach to achieve more compact filters [11]. In this way, the high impedance section lines have been substituted by series open-loops. The geometry of these open-loops has been extracted from EM simulation in such a way that they reproduce the behavior of the original straight line sections.

As an example of the application of the previously described procedure, Fig. 2 shows the layout and the measured and simulated results for a five pole filter of elliptic type. Fairly good agreement can be found between both results, particularly at the low frequency part of the measured spectrum (in and around the pass band). The filter, when compared with conventional Chebyshev SI-LPF implementations, presents meaningfully sharper cut-off, and reduced size (30% reduction for the same cut-off frequency; additional 50% reduction when meandered lines are used).

The authors acknowledge financial support of the Spanish Ministry of Education and Science (project No. TEC2004-03214) and Spanish Junta de Andalucía (project No. TIC-253).

REFERENCES

1. Hong, J. S. and M. J. Lancaster, *Microstrip Filters for RF/Microwave Applications*, New York, Wiley, 2001.
2. Abdel-Rahman, A. D., A. K. Verma, A. Boutejdar, and A. S. Omar, "Control of banstop response of Hi-Lo microtrip low-pass filter using slot in ground plane," *IEEE Trans. on Microwave Theory and Tech.*, Vol. 52, 1008–1013, 2004.
3. Lim, J. S., C. S. Kim, D. Ahn, Y. C. Jeong, and S. Nam, "Design of low-pass filters using defected ground-plane structure," *IEEE Trans. on Microwave Theory and Tech.*, Vol. 53, 2539–2545, 2005.
4. Carcía-Carcía, J., J. Bonache, F. Falcone, J. D. Baena, F. Martìn, I. Gil, T. Lopetegui, M. A. G. Laso, A. Marcotegui, R. Marqués, and M. Sorolla, "Stepped-impedance lowpass filters with spurious passband suppression," *Electronics Letters*, Vol. 40, 881–882, 2004.
5. Alseyab, S. A., "A novel class of generalyzed Chebyshev low-pass prototype for suspended substrate stripline filters," *IEEE Trans. on Microwave Theory and Tech.*, Vol. MTT-30, 1341–1347, 1982.
6. Giannini, F., M. Salerno, and R. Sorrentino, "Design of low-pass elliptic filters by means of cascaded microstrip rectangular elements," *IEEE Trans. on Microwave Theory and Tech.*, Vol. MTT-30, 1348–1353, 1982.
7. Tu, W. and K. Chang, "Compact microstrip low-pass filter with sharp rejection," *IEEE Microw. Wireless Comp. Lett.*, Vol. 15, 404–406, 2005.
8. Velázquez-Ahumada, M. C., J. Martel, and F. Medina, "Parallel coupled microstrip filters with floating ground-plane conductor for spurious-band suppression," *IEEE Trans. on Microwave Theory and Tech.*, Vol. 53, 1823–1828, 2005.
9. Pozar, D. M., *Microwave Engineering*, New York, Wiley, 1990.
10. Martel, J. and F. Medina, "A suitable integral equation for the quasi-TEM analysis of hybrid strip/slot-like structures," *IEEE Trans. on Microwave Theory and Tech.*, Vol. 49, 224–228, 2001.
11. Peddibhotia, H. and R. K. Settagori, "Compact folded line bandstop and low pass filters," *Microwave and Opt. Tech. Letters*, Vol. 42, 44–46, 2004.

An Improved BSIM4 Model for 0.13-μm Gate-length High Linearity CMOS RF Transistors

Chien-Cheng Wei, **Chia-Shih Cheng**, **Shao-Wei Lin**, **Yong-Jhih Chen**
Hsien-Chin Chiu, **and Wu-Shiung Feng**
Department of Electronic Engineering, Chang Gung University
Kwei-Shan, Tao-Yuan, Taiwan, China

Abstract— An improved BSIM4 large-signal model for 0.13-μm gate-length high linearity CMOS RF transistors is presented in this paper. The field-plate technology functions the improvements in linearity and $1/f$ noise of 0.13-μm CMOS devices was in our past investigation. To accurately accomplish the CMOS field-plate device model, an improved BSIM4 model with RLC networks representing the parasitic effects of transmission line and lossy substrate has been adopted for microwave applications up to 40 GHz. Good agreement has been realized between the measured and modeled results in terms of device's DC curves, S-parameters, $1/f$ noise, and power performance.

1. INTRODUCTION

In the recent decade, CMOS devices have been extensively employed in microwave applications because of their low cost and the ability to integrate with digital circuits. High linearity and high power microwave transistors are very important for increasing the dynamic range, and also satisfying the requirements for new-generation communication systems. To improve device's linearity and power performance, a field-plate technology in microwave devices is used to cover the edge of the gate on the drain side to reduce the intensity of electric field [1–3]. According to our experimental results [4], we demonstrated the field-plate technology into the 0.13-μm standard CMOS device and compared DC, RF, noise and power with a conventional one. It indicates that the CMOS field-plate devices exhibit better linearity and $1/f$ noise for microwave circuit designs such as switch, mixer, low noise amplifiers (LNAs), and voltage-controlled oscillators (VCOs).

In the other hand, in order to improve the accuracy of microwave circuit design, an accurate active device model plays an important role for the circuit designers. The BSIM3v3 model can predict the characteristics precisely of deep sub-micron MOSFETs at operation frequencies below one GHz, for digital and analog circuit designs. However it cannot completely describe their behaviors at operation frequencies higher than several GHz, particularly the non-linear behaviors and parasitic effects [5]. To develop a complete MOSFET RF large-signal model for microwave circuit simulation, an extended impedance network representing the lossy substrate induced parasitic effects is added into the standard BSIM4 models. This proposed compact large-signal model can be used for the CMOS field-plate devices under operation frequencies up to 40 GHz with different bias conditions. And this work is the first to demonstrate the field-plate device model in CMOS technology for microwave circuit designs.

2. DEVICE ARCHITECTURE AND CHARACTERIZATION

The basic principle of field-plate is to provide a conducting plane near the junctions and at other locations where high electric fields are existed [2]. The conducting plane smoothes high electric fields, and reduces the high electric-field peaks that result in electric breakdown. Field-plates sufficiently reduce the electric field at the gate edge, enabling high voltages to be applied. However, owing to the scaling down of CMOS technologies, which substantially enables the field-plate to change the intensity of electric field because of the thin dielectric layer between *metal-1* and S/D region. We incorporated field-plate technology into the 0.13-μm standard CMOS device, and compared the DC, RF, noise and power with those of the two NMOS devices with and without field-plate metals (NMOS-FP and NMOS-ST). Figure 1 depicts the device cross-section view. In the 0.13-μm standard process, a 2600-Å-thick metal-1 was deposited on the dielectric layer to form the field-plate metal, and the 0.2-μm-long field-plate metal was offset by 0.07-μm from the drain terminal to suppress the electric field at the gate edge under pinch-off conditions.

The suppression of the electric field by the field-plate in 0.13-μm CMOS devices is associated with interesting phenomena. The field-plate induces depletion region under the drain side because of the suppression of the electric field. The carriers can be kept far from the surface traps, affecting the reduction of the effective drain-to-source current density near the surface. Simultaneously, it achieves the linearity of the device at high input power swing. The reduction of the drain-induced barrier lowering (DIBL) due to the lower electric field, enhancing the leakage current from the surface of the device, is an important issue in reducing the total DC power. Because the leakage current was suppressed by the field-plate, the extra leakage current induced power consumption and surface traps related harmonic phenomenon can both be enhanced.

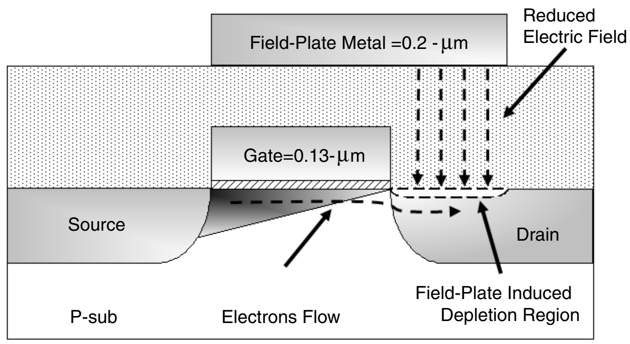

Figure 1: CMOS field-plate device cross-section view, using the *metal-1* as field-plate to cover the gate and the edge of the drain side to suppress the high electric field.

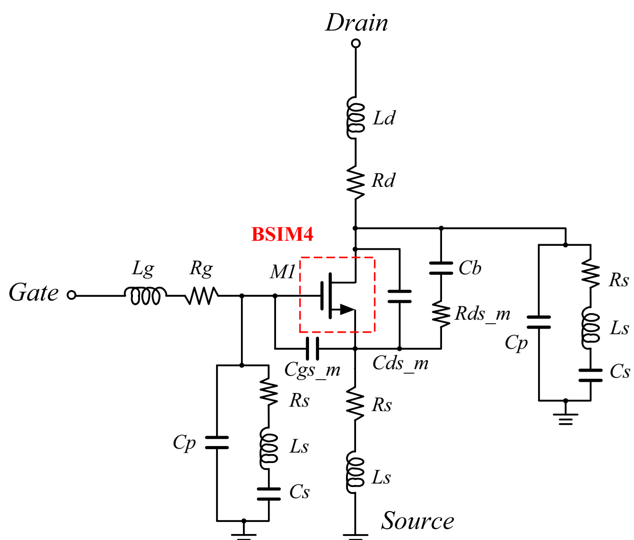

Figure 2: Proposed equivalent small-signal model of the field-plate device.

The measurement results of our previous paper [4] demonstrate that the power ratio between fundamental and IM3 products of NMOS-FP devices is better than that of conventional NMOS-ST devices, being -20.9 dBc for NMOS-ST and -23.7 dBc for NMOS-FP at an input power of -10 dBm, and their output powers of IM3 are -32.4 dBm and -41.8 dBm, respectively. Furthermore, the input third-order intercept points (IIP_3) of both NMOS-ST and NMOS-FP are 2 dBm and 6 dBm, respectively. The experimental results indicate that field-plate technology improves the linearity of the device, by reducing the opportunities for carriers to be combined with the surface traps. As to the $1/f$ noise measurements, the NMOS-FP achieved about one-order lower noise power spectra than NMOS-ST because of the field-plate induced depletion region suppressed the carriers to deeper channel for avoiding the surface traps. As to the high-frequency noise figure measurements for both devices, based on the preliminary measurements, the $NF_{\min}$ are almost identical for both devices. Therefore, using the field-plate technology in CMOS devices enhances the low-frequency noise but not scarifies the high-frequency noise figure. More detailed measurement results and discussions are listed in the [4].

3. IMPROVED BSIM4 MODEL

The field-plate technology in CMOS devices achieve high linearity and lower $1/f$ noise, are well adopted for microwave circuit designs. Especially for switch, mixer, and LNA due to its high linearity, and also suitable for VCO designs owing to the improvement in $1/f$ noise, respectively. To accurately deliver a CMOS field-plate device model therefore becomes an important topic for circuit simulation. The BSIM3v3 model is a standard compact model widely used in deep submicron MOSFETs for general circuit designs below one GHz regime. However, recent works have demonstrated that it is capable up to several GHz by adding some parasitic networks representing the lossy substrate at higher frequencies [5, 6]. But according to the combined effects of ever-shorted channel devices and operation frequencies upper than several tens GHz, further highlights the shortcomings of BSIM3v3 model for microwave applications. However, the BSIM4 model achieves better predictions for the short-channel effects under high supplied voltages, which are related to the output power at microwave frequencies, and also have better descriptions for some RF behaviors by high-frequency correlation parameters. In response to this situation, we propose to adopt the BSIM4 model as the intrinsic core for DC I-V characteristics prediction and add some RLC networks incorporating the transmission line and the parasitic effects for the lossy substrate, to accurately accomplish a CMOS field-plate device model.

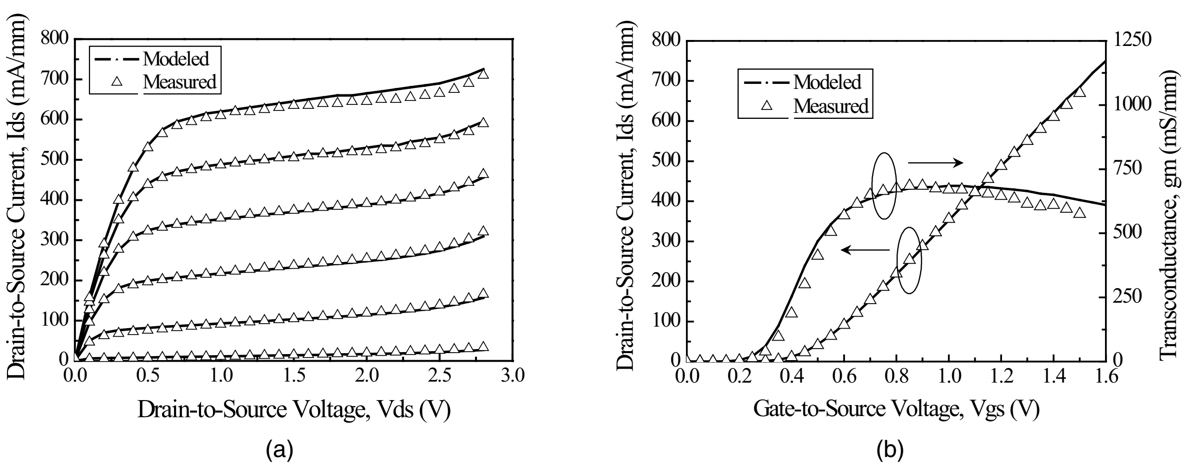

Figure 3: Measured and modeled results of (a) normalized I-V characteristics under V_{ds} from 0 V to 2.8 V, V_{gs} from 0.4 V to 1.4 V with a step of 0.2 V, and (b) normalized I_{ds} and g_m under V_{ds} of 1 V.

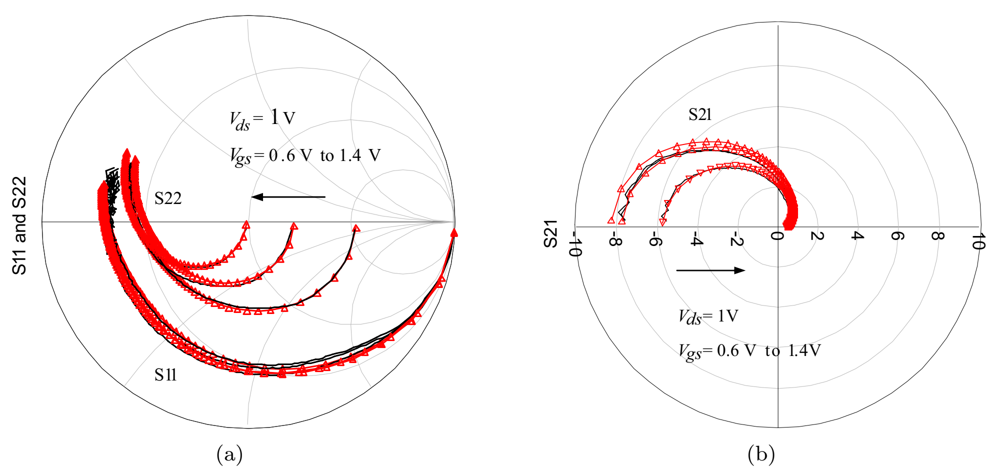

Figure 4: Measured and modeled results of S-parameters under V_{ds} of 1 V, V_{gs} from 0.6 V to 1.4 V with a step of 0.4 V (100 MHz to 40 GHz) (a) S11 and S22, and (b) S21.

The proposed equivalent circuit model of our device is shown in Figure 2. The full circuit contains the intrinsic core M_1, as represented the original BSIM4 model, and the RLC networks at each terminal are the extrinsic parts to represent the high-frequency parasitic effects associated with the practical process and layout. All parameters of BSIM4 model and added passive networks are extracted by fitting the device's I-V and S-parameters measured characteristics under different bias conditions. The modified capacitance C_{gs_m} and C_{ds_m} represent the field-plate induced parasitic capacitance between field-plate metal and gate/drain terminals, which are associated with the device's f_T and f_{MAX}, and the modified R_{ds_m} represents the increased channel resistance owing to the reduction in the DIBL, respectively. The RLC networks incorporating C_p, C_{si}, R_{si} and L_{si} connected from gate/drain to ground are used to simulate the lossy substrate. The parasitic effects at the source terminal are negligible, since the source terminal is directly connected to the bulk, which is grounded during the measurement. The parameters of C_{si}, R_{si} and L_{si} are three key parameters to capture the lossy substrate feature up to 40 GHz. The C_{si} is the primary component for the phase deviation and nonlinear response in lower frequencies, and L_{si} reveals increasing these effects at higher frequencies, respectively. The gate resistance R_g represents the distributed gate resistances, and other resistances R_d and R_s, represent the contact resistance from source and drain terminals, which are related to the diffusion area. Three parameters of L_g, L_d and L_s are the series parasitic inductance in each terminal for metal connections, which are the most important parameters for fitting the S-parameters at high frequencies.

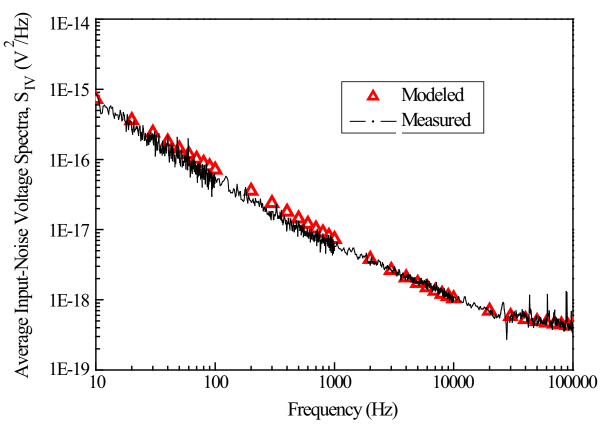

Figure 5: Measured and modeled results of low-frequency noise under V_{ds} of 1 V with biased current of 10 mA (10 Hz to 100 KHz).

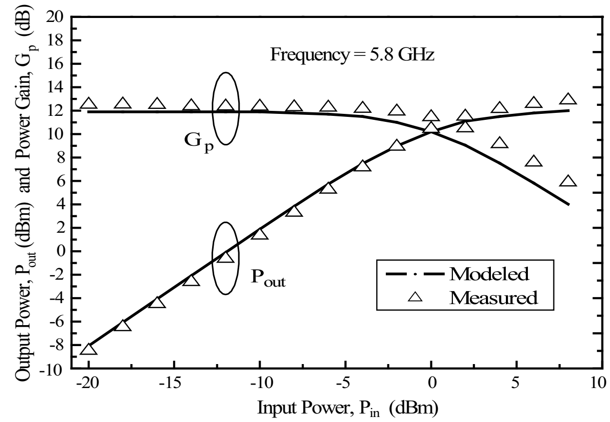

Figure 6: Measured and modeled results for load-pull measurements at 5.8 GHz under V_{ds} of 1 V with biased current of 50 mA.

4. RESULTS AND DISCUSSION

The field-plate devices fabricated by TSMC's (Taiwan Semiconductor Manufacture Company) 0.13-µm CMOS 1P8M standard process were measured and modeled for DC I-V, S-parameters, low-frequency noise and load-pull power characteristics. The intrinsic core of BSIM4 model was transferred and modified through the BSIM3 model provided by the foundry. And the extrinsic parameters of lossy substrate and transmission line were extracted by the extraction methods [5, 6], and optimization was done by using ADS simulator to achieve the best fitting results on the S and Y-parameters for each components. Figure 3(a) shows the DC I-V characteristics of the field-plate device with a gate width of 200-µm. The V_{gs} was from 0.4 V to 1.4 V with a step of 0.2 V, while the V_{ds} was from 0 V to 2.8 V. The predicted results of DC I-V characteristics by BSIM4 model are well matched to the experimental data as shown in this figure. And the most important parts of I-V characteristics are the nonlinearly knee-voltage and near breakdown regions, which are related to the large-signal circuits, especially the key issue for mixer and power amplifier designs. Figure 3(b) plots the transconductance (g_m) of the proposed device, the peak g_m of 130 mS was biased at V_{gs} of 0.8 V, and the extracted f_T and f_{MAX} under peak g_m condition are of 96 GHz and 55 GHz, respectively. Although the increased parasitic-capacitors C_{gs} and C_{ds} due to the field-plate metal lowering the f_T and f_{MAX}, these values are still high enough to apply in microwave applications. Figure 4(a) and (b) show the measured and modeled results of S-parameters up to 40 GHz under biased voltages at V_{ds} of 1 V, and V_{gs} from 0.6 V to 1.4 V with a step of 0.4 V. This figure indicates that the S-parameters during DC to 40 GHz with bias-dependent conditions can be well predicted by the proposed model. If the additional RLC networks are not included in this model, the accuracy of the S-parameter is limited to several GHz. Figure 5 shows the $1/f$ noise characteristics under V_{ds} of 1 V with biased current of 10 mA. These well-predicted results by modified BSIM4 model are very important for the VCO designs, owing to the field-plate substantially improving the $1/f$ noise, which also enhancing the phase noise in the VCO designs. In addition to the device's DC I-V, S-parameters, and low-frequency noise verification, we also conducted the evaluation of large-signal performance. Figure 6 shows the measured and modeled results of load-pull measurements at 5.8 GHz under V_{ds} of 1 V with biased current of 50 mA. The modeled characteristics agree well with the measured data, where the maximum output power of 10 dBm with a linear gain of 12 dB, and the 1 dB compression point of 0 dBm. The results presented in these figures demonstrate a reasonable good agreement between the predictions of our improved BSIM4 model and the measurement of the experimental characterization.

5. CONCLUSIONS

According to the obvious short-channel effects in advanced CMOS technology and much higher operation frequencies in modern radio applications, the BSIM4 model is more suitable for circuit simulations, which has better predictions than BSIM3 model. The 0.13-μm CMOS field-plate devices we have demonstrated in our previous paper achieve the improvements in performance of linearity and $1/f$ noise. To well employ these devices into the microwave circuit design, we have successfully adopted the improved BSIM4 model with RLC networks to verify the DC I-V, RF, noise, and power characteristics. Excellent agreement has been found between measured and modeled results. This accurate model is useful for operation frequencies below 40 GHz to improve the circuit simulation accuracy for microwave applications.

REFERENCES

1. Chini, A., D. Buttari, R. Coffie, L. Shen, S. Heikman, A. Chakraborty, S. Keller, and U. K. Mishra, "Power and linearity characteristics of field-plated recessed-gate AlGaN-GaN HEMTs," *IEEE Trans. Electron Devices*, Vol. 25, No. 5, 229–231, May 2004.
2. Trew, R. J., G. L. Bilbro, and H. Yin, "Microwave AlGaN/GaN HFET," *IEEE Microwave Magazine*, 56–66, March 2005.
3. Chiu, H.-C., Y.-C. Chiang, and C.-S. Wu, "High breakdown voltage $(Al_{0.3}Ga_{0.7})_{0.5}In_{0.5}Ps$/ InGaA quasi-enhancement-mode pHEMT with field-plate technology," *IEEE Trans. Electron Devices*, Vol. 26, No. 10, 701–703, October 2005.
4. Wei, C.-C., H.-C. Chiu, and W.-S. Feng, "High linearity performance of 0.13-μm CMOS devices using field-plate technology," *IEEE Electron Devices Lett.*, Vol. 27, No. 10, 843–845, October 2006.
5. Lai, H.-H., C.-C. Hsiao, C.-W. Kuo, Y.-J. Chan, and T. Sato, "Improved CMOS microwave linearity based on the modified large-signal BSIM model," *IEICE Trans. Electron*, Vol. E87-C, No. 1, Jan. 2004.
6. Guo, J.-C. and Y.-M. Lin, "A new lossy substrate de-embedding method for sub-100-nm RF CMOS noise extraction and modeling," *IEEE Trans. Electron Devices*, Vol. 53, No. 2, 339–347, February 2006.

Enhanced Stop-band Rejection by Symmetric Feeding in 1.8 GHz Cross-coupled Planar HTS Microwave Filters

Hui-Kai Zeng[1,2], Kaung-Hsiung Wu[1], Tseng-Ming Uen[1]
Yi-Shun Gou[1,3] and Jenh-Yih Juang[1,3]

[1]Department of Electrophysics, Chiao-Tung University
1001 Ta Hsueh Road, Hsinchu 30050, Taiwan, China
[2]Department of Electronic Engineering, Chung-Yuan Christian University
200 Chung-Pei Road, Chung-Li 32023, Taiwan, China
[3]Department of Physics, Taiwan Normal University, Taipei, Taiwan, China

Abstract— The superior performance manifested in characteristics of low pass-band insertion loss, high stop-band rejection, and sharp band edge skirt, has led the superconducting microwave filters one of the most attractive candidates for wireless communication applications. In this paper, we report the design and fabrication of the 4-poles cross-coupled planar microwave filters fabricated using YBCO superconducting thin films deposited on both sides of a LAO single crystal substrate by pulsed laser deposition. The resonator geometry allows one to miniaturize the 1.8 GHz filters onto a substrate with dimensions of 1 cm×1 cm. We also demonstrate that by properly choosing the feeding configuration, filters with better selectivity, in particular with an additional pair of deep transmission zeros (poles) outside both sides of pass-band, can be achieved.

1. INTRODUCTION

The fast growth of the wireless communications coupled with its stringent technology demands has led to a revived interest in using the high-temperature superconductor (HTS) filter subsystems for wireless base stations and satellite [1–3]. The low surface resistance inherent to the HTS materials has been the key that offers apparent performance advantages over the conventional materials in microwave circuits. For instance, the test deployment of several superconductive filter subsystems has demonstrated marked improvement in the performance of coverage area and reduced dropped-call rates for wireless communication systems. In practice, the parallel-coupled resonator filters [4] and the hairpin-line resonator filters [5] are the widely used designs for microwave circuits due to the ease of fabrication and compatibility with other processes. However, these filters often have some drawbacks, such as its large dimensions, insufficient depth of stop-band rejection, and fatness of the band edge skirt. Especially, considering the availability of large single crystal substrate as well as the difficulties encountered in obtaining homogeneous HTS film over a large area, there are growing demands in obtaining the compact planar microwave filter structures. One of the commonly used designing was the square open-loop resonator. In that the effective size is reduced to about one-sixth of that of the ordinary half-wavelength resonator with fold-in geometry [6–11]. As an example, Fig. 1 shows the schematics of the 1.8 GHz 4-poles cross-coupled miniaturized hairpin filters used in this study. In addition to featuring the 4 hairpin resonators in a 2×2 configuration on a total area of 1 cm^2, it was also designed to have extra tunable transmission zeros, as will be discussed below.

Besides the overall size reduction, higher selectivity filters are highly required due to the tightness of available frequency bands and the problem of interference coming from out-of-band signals. To this end, the coupling scheme between each resonator is of essential importance. To date, there have been many well-known types of coupling scheme proposed, including the stepped impedance comb-line [12], the hairpin comb-line [13], the parallel or anti-parallel [14], and the cross-coupled planar line structure [6]. The coupling scheme basically determines the signal flow across neighbor resonators. The magnitude of the coupling coefficients between two neighboring resonators is determined by the separation and the relative offset between the resonators. In order to increase the selectivity of the filter, we adopt the cross-coupled scheme to create a pair of transmission zeros near the band edge [6–9]. Since the appearance of the transmission zeros is intimately dependent on the interferences between the signals traveling along the two paths in the present design, the phase coherency between the clockwise and counterclockwise signals and the exact magnitudes of interfering signals might ultimately determine the device's performance [6]. The transmission zeros

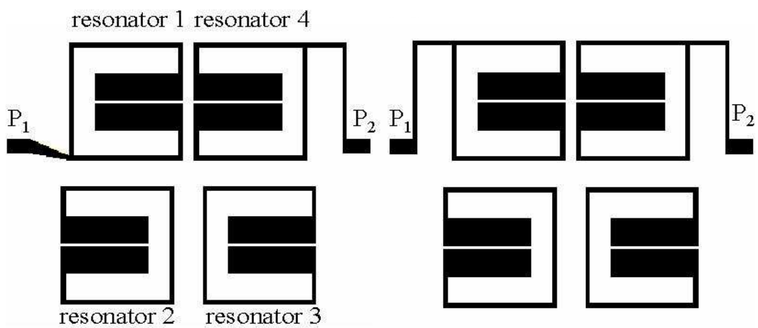

(a) (b)

Figure 1: Layout of the cross-coupled planar microwave filter with (a) symmetric (the input and output tapping positions at resonators 1 and 4) or (b) antisymmetric feed structure used in this study.

can be very helpful in suppressing the band edge signals and, in turn, gives rise to steeper rejection slope forming the skirt.

In practice, the feeding structure is also important. There have been designs of parallel-coupled feed structure [4, 5], end-coupled feed structure [15], or tapped-line feed structure [16, 17]. Among them, the end-coupled feed technique is suitable for the very narrow-band applications because the coupling of this feed structure is very weak. The parallel-coupled technique usually requires two ends of resonator to form feed structure, resulting in drawbacks such as the enlarged dimensions [18]. The tapped-line feed technique directly offers the connection between the first and the last resonators by properly tuning the feed points and the loaded Q_{ext} to achieve the filter design [6, 7]. It has been pointed out that, by controlling the tapping positions of the input and output contacts in a symmetric configuration, an additional pair of transmission zeros can be introduced to increase the rejection in the stop-band [8, 9]. We noted that, although the tapped-line feed technique has been widely used in recent filter design, a successful demonstration with HTS filters remains to be realized.

In this paper, we show that the 4-poles cross-coupled planar filters made of YBCO HTS films not only exhibited marked improvement on the pass-band insertion losses but also showed significant increase in selectivity responses.

2. EXPERIMENTAL

The double-sided $YBa_2Cu_3O_{7-\delta}$ (YBCO) thin film deposited on both sides of a 0.5 mm thick $LaAlO_3$ (LAO) substrate were prepared by pulsed laser deposition [10]. The deposition system consists of a vacuum chamber equipped with a pulsed KrF excimer laser. The YBCO films were deposited from a stoichiometric YBCO target with the substrate temperature being held at 790°C and oxygen pressure kept at 0.3 mbar. The room temperature relative dielectric constant of LAO substrate is about 25 with a loss tangent of $\tan\delta = 6 \times 10^{-5}$ (77 K), which should be adequate for microwave applications. The as-deposited films were all c-axis oriented, with a typical thickness of 300 nm, $Tc = 90$ K. By visual inspection, the films always have some naturally formed twins, presumably originated from the structure change occurring both in film and in LAO substrate. However, we believe such inhomogeneity does not affect the currently interested superconducting properties noticeably. The designed pattern was transferred onto one side of the film by photolithography and wet etch methods, while the other side of superconducting YBCO naturally serves as the ground plane. The sample was put into a gold-coated aluminum housing with SMA connectors placed in a tube and immersed in liquid nitrogen. Four S-parameters were measured at 77 K by a HP8510C microwave vector network analyzer.

3. RESULTS AND DISCUSSION

To demonstrate that the designing guidelines described above are indeed feasible, we carried out simulations of a 4-poles cross-coupled filter, with frequency centered at 1.8 GHz and 3.0% fractional bandwidth by Ansoft Designer software. Fig. 2 shows the simulated coupling coefficients K_{ij} with respect to the distance between resonators i and j. The coupling between each pair of resonators was further controlled to behave primarily magnetic or mixed coupling structures by adjusting the relative orientation of the open gap between neighboring resonators [8]. For instance, the magnetic coupling is obtained when the two open gaps are opposite to each other (resonators 2 and 3). In the current configuration, the magnitude of the coupling coefficients between the two neighboring resonators is determined by the separation and the relative offset between the resonators [6]. The coupling coefficient K_{ij} for each pair of resonators can be calculated as

$$K_{ij} = \frac{f_j^2 - f_i^2}{f_j^2 + f_i^2}, \tag{1}$$

where f_i and f_j are the lower and higher of the two resonant frequencies, respectively. The lumped circuit element values of the coupling coefficient matrix and the loaded Q_{ext} of this prototype filter can be found as

$$K_{ij} = \begin{bmatrix} 0 & 0.0278 & 0 & -0.0077 \\ 0.0278 & 0 & 0.0213 & 0 \\ 0 & 0.0213 & 0 & 0.0278 \\ -0.0077 & 0 & 0.0278 & 0 \end{bmatrix}, \tag{2}$$

and $Q_{ext} = 33.3$.

The cross coupling further gives the input signal two possible paths (clockwise and counterclockwise) to travel between the input and output ports. Depending on the path taken, the magnitude and phase of the corresponding signal can be quite different. For instance, the above results show that the sign of K_{12}, (K_{34}) and K_{23} are positive, while K_{14} is negative and the magnitude of K_{14} being smaller than those of K_{12} and K_{23}. Moreover, each coupling coefficient displays similar behavior with increasing spacing distance (Fig. 2).

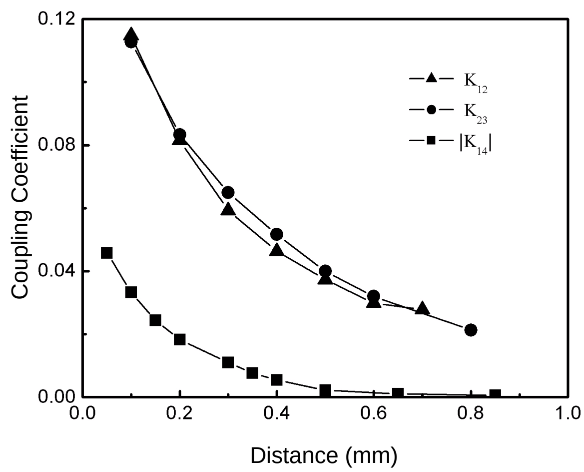

Figure 2: The simulated coupling coefficients K_{ij} with respect to the distancebetween resonators i and j.

The performance of the designed structure was simulated using Ansoft Designer software by assuming the superconductor as a perfect conductor and the parameters of LAO substrate with the structural parameters depicted in the caption of Fig. 1. The simulation results are shown in Figs. 3(a) and (b) with respect to symmetric and anti-symmetric feed structure in Figs. 1(a) and (b), respectively. The anti-symmetric configuration has produced a pair of transmission zeros immediately outside both sides of the pass-band skirt. However, for the symmetric configuration, in addition to the zeros around the vicinity of the pass-band skirt, there are an extra pair of very deep transmission zeros relatively remote from the pass-band. The extra pair of transmission zeros occurred at the frequencies where the corresponding distance from the feed point to both edges is equivalent to quarter-wavelength. These extra transmission zeros can help the rejection of signal and, hence, increase the out-of-band rejection. Note that, this transmission zeros are not expected to appear with anti-symmetric feed structure. The anti-symmetric configuration adopt in the cross-coupled planar structure is to create a pair of transmission zeros near the band edge, which, in turn, will suppress the band edge signals and gives rise to better rejection slope of the skirt. The real device performance for both structures measured at the liquid nitrogen temperature reproduces the simulated results extremely well. As shown in Figs. 3(c) and (d), both transmission (S_{21}) results are very close to the simulated responses with the insertion loss being comparable to the best performance reported for similar devices. For symmetric feeding configuration, the measured central frequency, insertion loss and fractional bandwidth are 1.782 GHz, 0.35 dB and 2.85%, respectively. The return loss is lower than 11 dB in the pass-band, with out-of-band rejection as low as 68 dB. It is noted that there are no apparent ripples and the skirt exhibited slightly asymmetric responses in the pass-band, presumably due to the imperfections caused by the wet-etching processes. Nonetheless, the agreement between the experimental and simulated results is good. In that, the measured center frequency of the filter has shifted by 18 MHz and the fractional bandwidth is reduced by 5.0% as compared to the simulated value. On the other hand, for the anti-symmetric configuration, the center frequency, insertion loss and fractional bandwidth are 1.774 GHz, 0.32 dB and 2.8%, respectively (Fig. 3(d)). In comparison, the central frequency of the filter has shifted by 26 MHz and the measured fractional bandwidth is 6.7% less than the simulation value. We believe that the difference might have arisen from the improvement on the out-of-band rejection due to the introduction of the extra pair of transmission zeros. As it might consequently suppress the dispersion induced interferences.

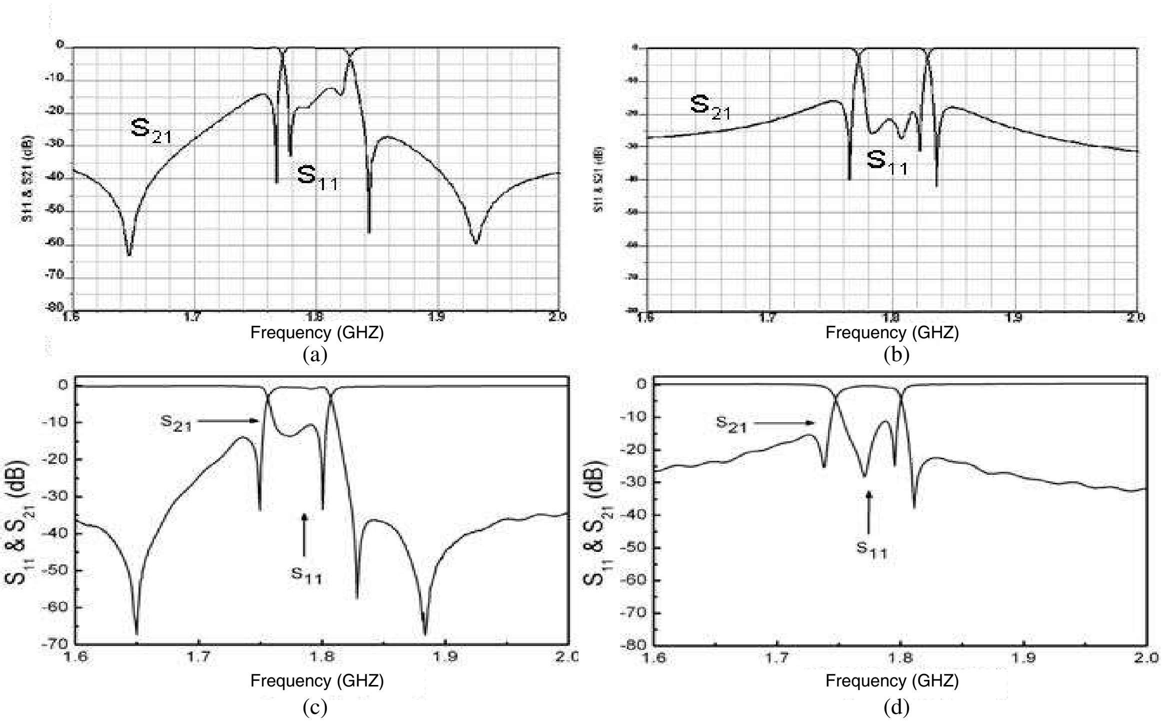

Figure 3: The simulations of S_{21} and S_{11} responses for (a) symmetric and (b) anti-symmetric feed structure filter and the measured results for (c) symmetricand (d) anti-symmetric configuration, respectively.

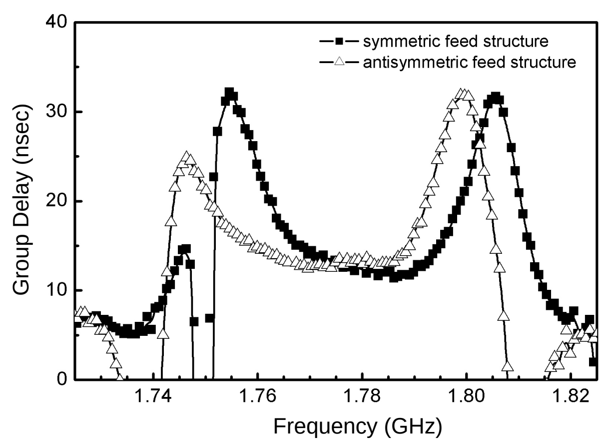

Figure 4: Measured group delay of the HTS filters in the symmetricand anti-symmetric configuration, respectively.

Finally, we show in Fig. 4 the group delay responses of S_{21} displayed in the symmetric and anti-symmetric configurations. The group delay response is a signal distortion performance in the corresponding frequency regime of the circuit. The results show that the symmetric configuration has the time delay of 32.2 ns at 1755 MHz and 31.7 ns at 1806 MHz; while that for the anti-symmetric configuration 24.9 ns at 1746 MHz and 31.8 ns at 1799 MHz, respectively. The spacing between the peaks of group delay is slightly larger than the width of the pass-band because the band edge has the bandwidth margin. The appearance of the both profiles shows very similar behaviors for the typical non-dispersive characteristics of filters made of HTS films.

4. CONCLUSION

We have designed, fabricated, and demonstrated the 4-poles miniaturized cross-coupled planar microwave filter using double-side YBCO HTS thin films. The devices, designed to operate at 1.8 GHz, not only have a size reduction, but also display an insertion loss of 0.3 dB for the frequency responses. In particular, we demonstrated that, by properly arranging the feeding configuration, filters with better selectivity and smaller insertion loss can be realized by introducing a pair of extra transmission zeros at frequencies more remote from the pass-band frequencies.

REFERENCES

1. Hong, J. S. and M. J. Lancaster, *Microstrip Filters for RF/Microwave Applications*, John Wiley & Sons, New York, 2001.
2. Mansour, R. R., "Microwave superconductivity," *IEEE Trans. Microwave Theory Tech.*, Vol. 50, 750–759, March 2002.
3. Simon, R. W., R. B. Hammond, S. J. Berkowitz, and B. A. Willemsem, "Superconducting microwave filter systems for cellular telephone base stations," *Proceedings of the IEEE*, Vol. 92, 1585–1596, Oct. 2004.
4. Cohn, S. B., "Parallel-coupled transmission-line-resonator filters," *IRE Trans. Microwave Theory Tech.*, Vol. MTT-6, 223–231, April 1958.
5. Cristal, E. G. and S. Frankel, "Hairpin-line and hybrid hairpin-line/half-wave parallel-coupled-line filters," *IEEE Trans. Microwave Theory Tech.*, Vol. MTT-20, 719–728, Nov. 1972.
6. Hong, J. S. and M. J. Lancaster, "Couplings of microstrip square open-Loop resonators for cross-coupled planar microwave filters," *IEEE Trans. Microwave Theory Tech.*, Vol. MTT-44, 2099–2109, Dec. 1996.
7. Hong, J. S. and M. J. Lancaster, "Cross-coupled microstrip hairpin-resonator filters," *IEEE Trans. Microwave Theory Tech.*, Vol. MTT-46, 118–122, Jan. 1998.
8. Lee, S. Y. and C. M. Tsai, "New cross-coupled filter design using improved hairpin resonators," *IEEE Trans. Microwave Theory Tech.*, Vol. 48, 2482–2490, December 2000.
9. Tsai, C. M., S. Y. Lee, and C. C. Tsai, "Performance of a planar filter using a 0° feed structure," *IEEE Trans. Microwave Theory Tech.*, Vol. 50, 2362–2367, October 2002.
10. Zeng, H. K., A. Hsiao, W. H. Hsu, S. W. Wu, J. Y. Lin. K. H. Wu, J. Y. Juang, T. M. Uen, Y. S. Gou, and J. T. Kuo "Miniaturized 3 GHz cross-coupled planar microwave filters," *IEEE Trans. Appl. Supercond.*, Vol. 14, 107–111, March 2004.
11. Tsuzuki, G. and S. Ye, "Ultra-selective 22-pole 10-transmission zero superconducting bandpass filter surpasses 50-pole chebyshev filter," *IEEE Trans. Microwave Theory Tech.*, Vol. 50, 2924–2929, Dec. 2002.
12. Ishizaki, T. and T. Uwano, "A stepped impedance comb-line filter fabricated by using ceramic lamination technique," *IEEE MTT-S International Microwave Symposium Digest*, Vol. 2, 617–620, 1994.
13. Matthaei, G. L., N. O. Fenzi, R. J. Forse, and S. M. Rohlfing, "Hairpin-comb filters for HTS and other narrow-band applications," *IEEE Trans. Microwave Theory Tech.*, Vol. MTT-45, 1226–1231, Aug. 1997.
14. Matsuo, M., H. Yabuki, and M. Makimoto, "The design of a half-wavelength resonator BPF with attenuation poles at desired frequencies," *IEEE MTT-S International Microwave Symposium Digest*, Vol. 2, 1181–1184, 2000.
15. Cohn, S. B., "Direct-coupled-resonator filters," *Proceedings of the IRE*, Vol. 45, 187–196, Feb. 1957.
16. Cristal, E. G., "Tapped-line coupled transmission lines with applications to interdigital and combline filters," *IEEE Trans. Microwave Theory Tech.*, Vol. MTT-23, 1007–1012, Dec. 1975.

17. Wong, J. S., "Microstrip tapped-line filter design," *IEEE Trans. Microwave Theory Tech.*, Vol. MTT-27, 44–50, Jan. 1979.
18. Zhang, D., G.-C. Liang, C. F. Shih, Z. H. Lu, and M. E. Johansson, "A 19-pole cellular bandpass filter using 75-mm-diameter high-temperature superconducting thin films," *IEEE Microwave and Guided Wave Letters*, Vol. 5, 405–407, Nov. 1995.

A 10-GHz Low Phase Noise Differential Colpitts CMOS VCO Using Transformer Coupling Technology

Chia-Shih Cheng, **Yi-Tzu Yang**, **Chien-Cheng Wei**, **and Hsien-Chin Chiu**
Department of Electronics Engineering, Chang Gung University, Tao-Yuan, Taiwan, China

Abstract— We demonstrated a 10 GHz low phase noise differential Colpitts Voltage-Controlled Oscillator (VCO) utilizing TSMC 0.18 μm 1P6M CMOS process with transformer coupling technology. The transformer coupling approach not only reduces the phase noise but also improves the power consumption owing to the number of active devices can be reduced. The total power consumption of this VCO is 20 mW and there is only 8 mW power consumption in the oscillator core under lower supply voltages. By adding the buffers to the output terminal, it avoids the influence from the parasitic effects and also achieves a good performance in low phase noise.

1. INTRODUCTION

In recent years, CMOS technology progresses constantly makes it offer superior efficiency, lower cost, higher frequency circuit design, leading to a progressive transceiver and receiver systems of the wireless communication. As to DVB-S (Digital Video Broadcast System) specification, CMOS technology shows the ability to combine it into a single chip [1]. In wireless communication systems, the voltage-controlled oscillator design is a key issue. It consumes most of the area and power in a circuit. In order to get the best phase noise, we must improve power consumption. And with the diminishing of the electron channel, the bearing pressure degree of crystal will reduce. It makes the output signal amplitude be restricted. Then how to design a good phase noise and low power consumption oscillator has been a challenge of the high-frequency circuit designers. In this paper, we demonstrate a CMOS differential Colpitts oscillator by utilizing the transformer coupling technology to improve the phase noise and power consumption owing to active devices can be reduced.

2. OSCILLATOR TOPOLOGY

In the basic oscillator circuits, one of the simplest structures is Colpitts oscillator. It only needs to use an active component **(electric crystal)** and three passive components **(an inductance and two capacities)**. Fig. 1 shows the simplest structure of a Colpitts oscillator, I_{bias} is the current source and V_{bias} is the voltage source [2]. They are both used for tuning the quality-factor (Q) and the working area. After adding the proper passive components, it can make the circuit start to oscillate.

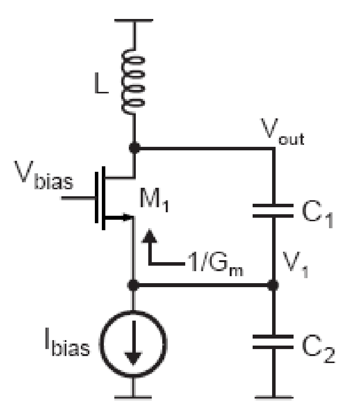

Figure 1: A simplest structure of Colpitts oscillator.

There are two shortcomings by using the Colpitts oscillator. On the one hand, in order to avoid feedback circuit destroying the Q-factor of the passive resonance circuit, the values of the resonance circuit components needs to be relatively great. But in this way, it may be limited to some extent in practical application. On the other hand, resonance circuit only has an active component, so the form of output is single-ended. But it's inconvenient for the users who need double-ended output. Therefore, in order to generate double-ended output signals, we connect two Colpitts oscillator in parallel [2]. While considering the actual operation states, this circuit is similar to the relaxing type oscillator and the mutual use of two pieces of Colpitts circuits. Therefore, the bias current sources can be shared and using a converter to switch. It simplifies the complexity of the original circuit.

The advantage of using a balanced Colpitts oscillator is to get a higher Open-Loop-Gain and make the circuit easier to oscillate than other oscillators by simple oscillatory structures when operating at a high frequency. As to the phase noise, the number of active devices increases because of using a converter (switch). It not only increases the phase noise by active devices itself but also make the converter not an ideal switch due to the non-linear characteristic of the device. These results make the phase noise worse and the output waveform undesirability.

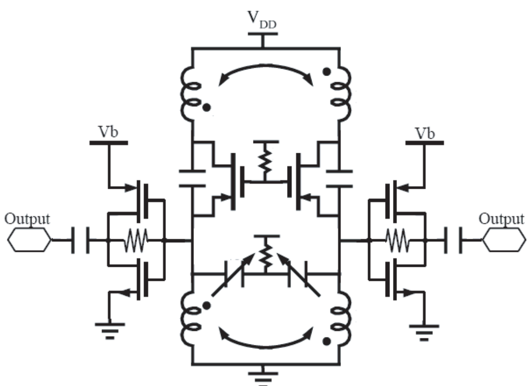

Figure 2: A differential Colpitts CMOS VCO using transformer coupling.

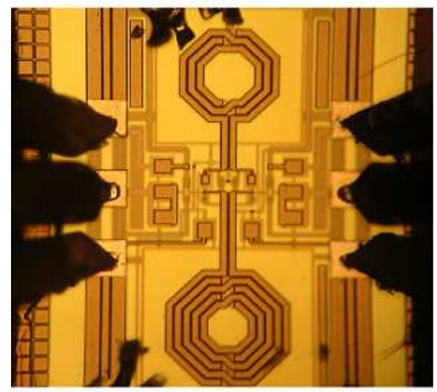

Figure 3: Photograph of the VCO.

In this paper, we utilize transformers replacing by converters in a differential Copitts CMOS VCO. Because of transformers can make the output phase lack of 180 degree and it's also a passive device, so its phase noise is much smaller than active devices. Hence, this approach not only improves the linearity of the circuit but also the phase noise due to the active devices can be reduced. Additionally, the buffers are also added to the output terminal to avoid the influence from the parasitic effects. The schematic of the CMOS VCO utilizing transformer coupling technology is shown in Fig. 2. The chip microphotograph is given in Fig. 3. The total chip size including pads is $1.024 \times 0.570\,\mathrm{mm}^2$. All active devices and center-tapped inductors (tranformer) were provided by TSMC $0.18\,\mu\mathrm{m}$ 1P6M CMOS process.

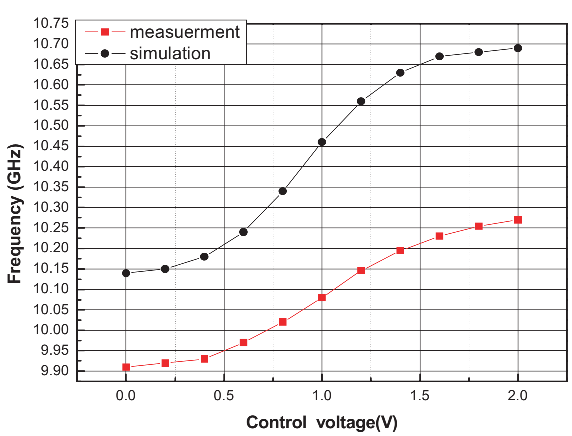

Figure 4: The oscillation frequency versus control voltage.

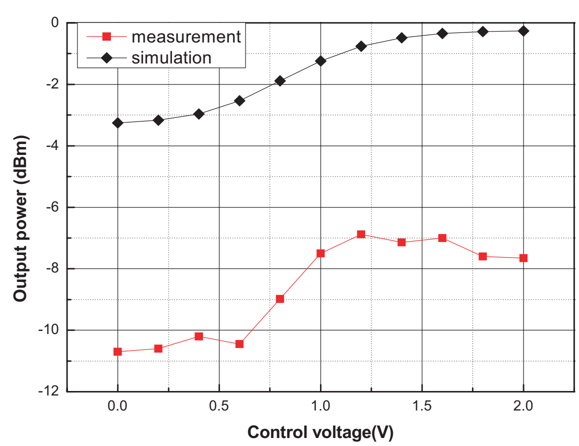

Figure 5: The output power versus control voltage.

3. SIMULATION AND MEASURED RESULTS

The simulated and measured results of oscillation frequencies and output power versus variable voltage are plotted in Fig. 4 and Fig. 5 respectively. The supply voltages of V_{DD} and V_b are 1.6 V and 0.8 V. Under the controlled voltage was biased from 0 V to 2 V, the measured oscillation frequency was ranging from 9.92 GHz to 10.22 GHz and output power was ranging from −10.7 dBm to −7.66 dBm. Additionally, the power consumption of this VCO is 20 mW and there is only 8 mW power consumption in the oscillator core. Fig. 6 shows the measured and simulated results of phase noise versus variable voltage. With a supply voltage of $V_{DD} = 1.6$ V and $V_b = 0.8$ V, the measured phase noise was ranging from −110 dBc/Hz to −115 dBc/Hz under the controlled voltage was biased from 0–2 V.

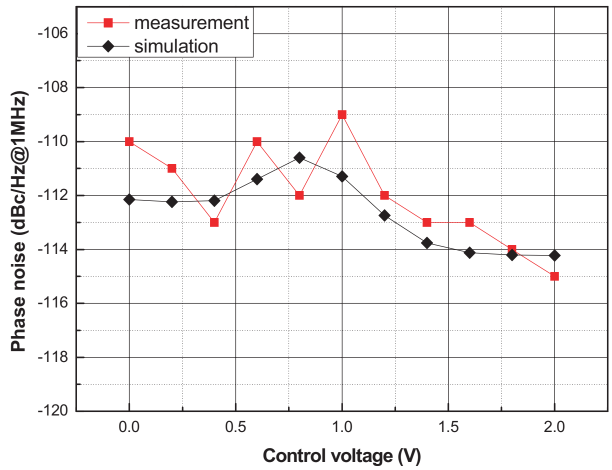

Figure 6: The phase noise versus control voltage.

The measured tuning range of this VCO is 9.92–10.22 GHz, i.e., 300 MHz under the controlled voltage was biased from 0 V to 2 V. The oscillator was measured with Agilent E4407B spectrum analyzer. Fig. 7 shows the phase noise versus offset frequency from 1 kHz to 10 MHz. The phase noise was measured as −111.16 dBc/Hz at 1-MHz frequency offset from a center frequency of 9.88 GHz.

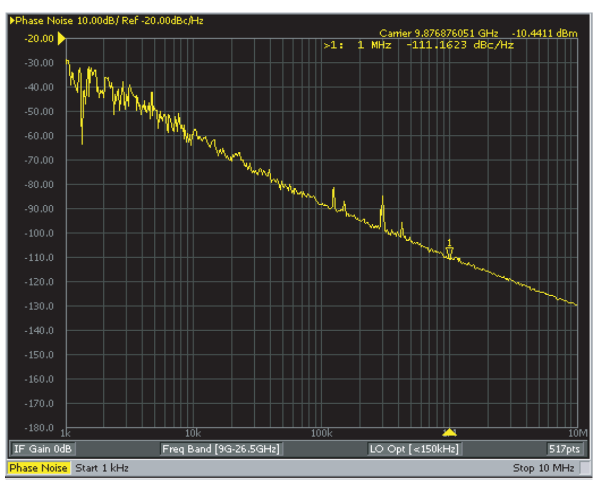

Figure 7: The phase noise versus offset frequency from 1 kHz to 10 MHz.

To evaluate the overall performance of the VCO, a common figure of merit (FOM) is used, which is given by [3]

$$FOM = L\{f_{offset}\} - 20\log\left(\frac{f_0}{f_{offset}}\right) + 10\log\left(\frac{P_{DC}}{1\,\text{mW}}\right) \tag{1}$$

where $L\{f_{offset}\}$ is the phase noise at a certain frequency offset (f_{offset}), f_0 is the oscillation frequency, and P_{DC} is the power dissipation. The simulated and measured results of FOM versus variable voltage is shown in Fig. 8. With a supply voltage of $V_{DD} = 1.6\,V$ and $V_b = 0.8\,V$, the value of FOM is from -179.1 dBc/Hz to -184.1 dBc/Hz under the controlled voltage was biased from 0 V to 2 V.

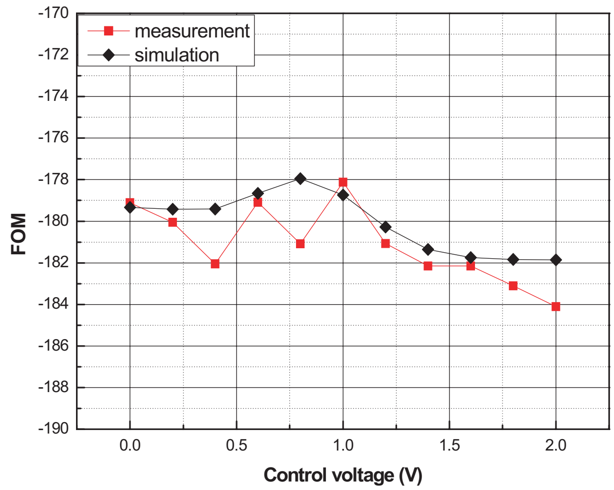

Figure 8: The figure of merit (FOM) versus control voltage.

4. CONCLUSION

A 10-GHz differential Colpitts VCO using transformer coupling technology in TSMC 0.18 μm 1P6M CMOS process has been presented. Due to replacing the converters (switches) by transformers, the circuit achieves a good performance in low power consumption and low phase noise. By adding the output buffers, the parasitic effects are reducing and the performance of whole circuit is not influenced.

ACKNOWLEDGMENT

The authors are grateful to the Construction Industry Council (CIC) for supporting the TSMC 0.18 μm 1P6M CMOS process. This work is financially supported by the National Science Council, ROC (NSC 94-2215-E-182–005).

REFERENCES

1. Smerzi, S. A. and G. Girlando, "A Ku-band monolithic receiver for DVB-S applications," *IEEE Communications Magazine*, August 2004.
2. Lee, C.-Y., "RF quadrature voltage-controlled oscillator," Thesis of Master of Science, Department of Electrical Engineering, National Cheng-Kung university, Tainan, Taiwan, R.O.C, June 2003.
3. Tsang, T. K. K. and M. N. El-Gama1, "A high figure of merit and area-efficient low-voltage (0.7–1 V) 12 GHz CMOS VCO," *IEEE Radio Frequency Integrated Circuits Symposium*, 2003.

Error Analysis and Compensation Algorithm for Digital Predistortion Systems

Jianing Zhao, **Jianyi Zhou**, **Ningde Xie**, **Jianfeng Zhai**, **and Lei Zhang**
Department of Radio Engineering, Southeast University, Nanjing, China

Abstract— Baseband Digital Predistortion based on the LUT is a popular method to improve the performance of high power amplifiers. The feedback loop is the key unit to obtain the sample signals based on which the model of the PA is built. The imperfectness of the modulator and demodulator will limit the improvement of the predistortion. In this paper, error items of the demodulator in the feedback path are analyzed and the compensating algorithm is derived.

1. INTRODUCTION

Advanced mobile communications require high data rates to achieve high-speed applications. Meanwhile, to enhance the spectrum efficiency, complicated digital modulation techniques such as 16QAM, 64QAM are adopted in the design of the modern mobile communications. Thus, power amplifiers built in basestations of those systems are required to have high linearity and efficiency in order to suit the large peak-to-average ratio character of the high order digital modulated signals. In the last decade, baseband predistortion techniques based on the LUT (Look Up Table) are developed to solve these problems.

A simplified block diagram of a typical digital pre-distortion system is shown in Fig. 1.

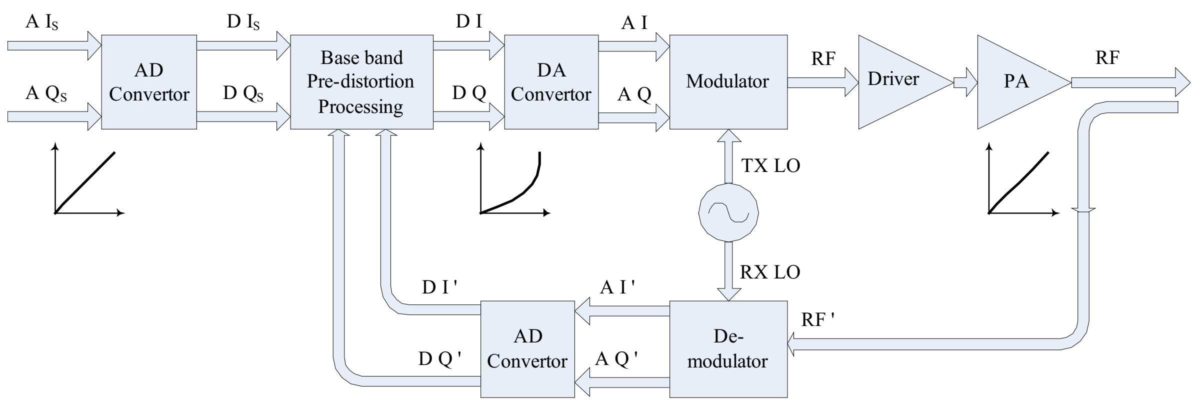

Figure 1: Baseband digital pre-distortion diagram.

Digital I and Q data of training signals are converted to the analog I and Q signals by the DACs. After that I and Q signals are modulated to the RF band by a quadrature direct modulator. The modulated signal is sent to the driver amplifier and the power amplifier under the test. The amplified and distorted signal is coupled into the downconverter and then is demodulated to base band I' and Q' signals. ADCs are used to digitalize the I' and Q' signals. By comparing the original I and Q data and the digitalized I' and Q' data, the nonlinearity of the power amplifier can be estimated, based on which the digital pre-distortion can be realized. The purpose of the pre-distortion is to change the characteristics of the baseband signals to compensate the distortion caused by the power amplifier in advance. It's obvious that the modulator and the demodulator are very important devices in the pre-distortion loop. Imperfect modulators and demodulators will cause some additional distortions to such system. Some of those distortions aroused in the feedback route should not be regarded as the congenital characteristics of the power amplifier.

In this paper, the effect of the modulation and demodulation errors on the modeling of the power amplifiers is analyzed. To overcome the effect of those errors, an algorithm is derived for ideal demodulation.

2. ANALYSIS AND DERIVATION

The quadrature modulation and demodulation process in the Fig. 1. can be simplified as Fig. 2. Here, Ψ stands for the signal phase shift on the RF channel.

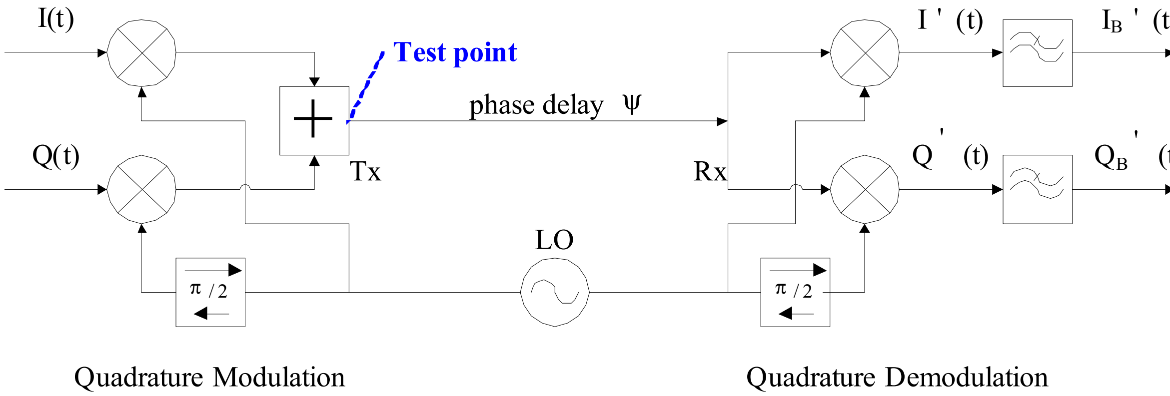

Figure 2: Analog quadrature modulation and demodulation.

The modulated signal from the ideal modulator can be expressed as

$$R(t) = A_1 I(t)\cos(\omega_c t + \varphi_1) + A_1 Q(t)\sin(\omega_c t + \varphi_1) \tag{1}$$

Here A_1 is the amplitude gain of the quadrature modulator and φ_1 is the phase shift caused by the modulator. After the radio frequency channel, the modulated signal changes to

$$R'(t) = A_1 I(t)\cos(\omega_c t + \varphi_1 + \Psi) + A_1 Q(t)\sin(\omega_c t + \varphi_1 + \Psi) \tag{2}$$

The output of the ideal demodulator is

$$\begin{aligned} I'(t) &= A_2 R'(t)\cos(\omega_c t + \varphi_2) \\ &= A_2 \left[A_1 I(t)\cos(\omega_c t + \varphi_1 + \Psi) + A_1 Q(t)\sin(\omega_c t + \varphi_1 + \Psi)\right]\cos(\omega_c t + \varphi_2) \\ &\xrightarrow{LPF} \frac{A_1 A_2}{2}\left[I(t)\cos(\varphi_1 - \varphi_2 + \Psi) + Q(t)\sin(\varphi_1 - \varphi_2 + \Psi)\right] = I'_B(t)_{\text{ideal}} \end{aligned} \tag{3}$$

$$\begin{aligned} Q'(t) &= A_2 R'(t)\sin(\omega_c t + \varphi_2) \\ &= A_2 \left[A_1 I(t)\cos(\omega_c t + \varphi_1 + \Psi) + A_1 Q(t)\sin(\omega_c t + \varphi_1 + \Psi)\right]\sin(\omega_c t + \varphi_2) \\ &\xrightarrow{LPF} \frac{A_1 A_2}{2}\left[-I(t)\sin(\varphi_1 - \varphi_2 + \Psi) + Q(t)\cos(\varphi_1 - \varphi_2 + \Psi)\right] = Q'_B(t)_{\text{ideal}} \end{aligned} \tag{4}$$

Here A_2 is the amplitude gain of the quadrature demodulator and φ_2 is the phase shift caused by the demodulator.

However, normal quadrature modulators and demodulators are not ideal devices. Amplitude errors and phase errors of modulators and demodulators will cause the distortion of the modulated and demodulated signals. Assume that the amplitude difference between the in-phase and quadrature paths of the modulator is ΔA_1 and the amplitude difference between the in-phase and quadrature paths of the demodulator is ΔA_2. The phase difference between the in-phase and quadrature local oscillators of the modulator is $\Delta\varphi_1$ and the phase difference between the in-phase and quadrature local oscillators of the demodulator is $\Delta\varphi_2$.

Therefore, (2), (3) and (4) can be rewritten as (5), (6) and (7)

$$R'(t) = A_1 I(t)\cos(\omega_c t + \varphi_1 + \Psi) + (A_1 + \Delta A_1) Q(t)\sin(\omega_c t + \varphi_1 + \Delta\varphi_1 + \Psi) \tag{5}$$

$$\begin{aligned} I'(t) &= A_2 R'(t)\cos(\omega_c t + \varphi_2) \\ &= A_2 \left[A_1 I(t)\cos(\omega_c t + \varphi_1 + \Psi) + (A_1 + \Delta A_1) Q(t)\sin(\omega_c t + \varphi_1 + \Delta\varphi_1 + \Psi)\right]\cos(\omega_c t + \varphi_2) \\ &\xrightarrow{LPF} \frac{A_1 A_2}{2} I(t)\cos(\varphi_1 - \varphi_2 + \Psi) + \frac{(A_1 + \Delta A_2) A_2}{2} Q(t)\sin(\varphi_1 + \Delta\varphi_1 - \varphi_2 + \Psi) \\ &= I'_B(t) \end{aligned} \tag{6}$$

$$\begin{aligned} Q'(t) &= (A_2 + \Delta A_2) R'(t)\sin(\omega_c t + \varphi_2 + \Delta\varphi_2) \\ &= (A_2 + \Delta A_2)\left[A_1 I(t)\cos(\omega_c t + \varphi_1 + \Psi) + (A_1 + \Delta A_1) Q(t)\sin(\omega_c t + \varphi_1 + \Delta\varphi_1 + \Psi)\right] \end{aligned}$$

$$\begin{aligned}&\sin(\omega_c t+\varphi_2+\Delta\varphi_2)\xrightarrow{LPF}-\frac{A_1(A_2+\Delta A_2)}{2}I(t)\sin(\varphi_1-\varphi_2-\Delta\varphi_2+\Psi)\\&+\frac{(A_1+\Delta A_1)(A_2+\Delta A_2)}{2}Q(t)\cos(\varphi_1+\Delta\varphi_1-\varphi_2-\Delta\varphi_2+\Psi)=Q'_B(t)\end{aligned}\tag{7}$$

$$\begin{aligned}\varepsilon_I&=I'_B(t)-I'_B(t)_{\text{ideal}}\\&=\frac{A_2}{2}\left[(A_1+\Delta A_1)\sin(\varphi_1+\Delta\varphi_1-\varphi_2+\Psi)-A_1\sin(\varphi_1-\varphi_2+\Psi)\right]Q(t)\end{aligned}\tag{8}$$

$$\varepsilon_Q = Q'_B(t)-Q'_B(t)_{\text{ideal}}$$

$$\begin{aligned}&=\frac{A_1}{2}\left[A_2\sin(\varphi_1-\varphi_2+\Psi)-(A_2+\Delta A_2)\sin(\varphi_1-\varphi_2-\Delta\varphi_2+\Psi)\right]I(t)\\&=\frac{1}{2}\left[(A_1+\Delta A_1)(A_2+\Delta A_2)\cos(\varphi_1+\Delta\varphi_1-\Delta\varphi_2+\Psi)-A_1A_2\cos(\varphi_1-\varphi_2+\Psi)\right]Q(t)\end{aligned}\tag{9}$$

Error items ε_I and ε_Q in (8) and (9) include the nonideal characters of the modulator and demodulator, which will cause the unbalance of the received $I'_B(t)$ and $Q'_B(t)$. Since building the PA model is essentially based on the feedback loop of the system, the ε_I and ε_Q will affect the accuracy of the model in some degree and will eventually limit the improvement of the linearity of the PA. The normal signal path includes the modulator, driver and PA while the path of training series includes the modulator, driver, PA, demodulator and the low-band pass filters. The imperfectness of the demodulator in the ε_I and ε_Q is the certain error to be eliminated when building the PA model.

To eliminate the nonideal characters of the demodulator, a test signal should be input to the feedback path to calculate the ΔA_2 and $\Delta\varphi_2$. Assume a RF continuous wave signal $S_{\text{test}}(t)=\cos(\omega_c t-\omega_s t)$ is fed to the feedback path at test point indicated in Fig. 2. Equations (5), (6) and (7) will be changed to

$$R'_{\text{test}}(t) = A_{\text{test}}\cos(\omega_c t-\omega_s t+\Psi)\tag{10}$$

$$\begin{aligned}I'(t)&=A_2R'_{\text{test}}(t)\cos(\omega_c t+\varphi_2)\\&\xrightarrow{LPF}\frac{A_2A_{\text{test}}}{2}\cos(\omega_s t+\varphi_2-\Psi)=I'_{B\text{test}}(t)\\I'_{B\text{test}}(t)&=A'_{IB\text{test}}\cos\left(\omega_s t+\alpha'_{IB\text{test}}\right)\\A'_{IB\text{test}}&=\frac{A_2A_{\text{test}}}{2},\qquad \alpha'_{IB\text{test}}=\varphi_2-\Psi\end{aligned}\tag{11}$$

$$\begin{aligned}Q'_t&=(A_2+\Delta A_2)R'_{\text{test}}(t)\sin(\omega_c t+\varphi_2+\Delta\varphi_2)\\&\xrightarrow{LPF}\frac{(A_2+\Delta A_2)A_{\text{test}}}{2}\sin(\omega_s t+\varphi_2+\Delta\varphi_2-\Psi)=Q'_{B\text{test}}(t)\\Q'_{B\text{test}}(t)&=A'_{Q\text{test}}\cos\left(\omega_s t+\alpha'_{QB\text{test}}\right)\\A'_{QB\text{test}}&=\frac{(A_2+\Delta A_2)A_{\text{test}}}{2},\qquad \alpha'_{QB\text{test}}=\varphi_2+\Delta\varphi-\Psi\end{aligned}\tag{12}$$

The value arrays of $I'_{B\text{test}}(t)$ and $Q'_{B\text{test}}(t)$ can be obtained from AD converters in the feedback path, from which $A'_{IB\text{test}}(t)$, $A'_{QB\text{test}}(t)$, $\alpha'_{IB\text{test}}$, $\alpha'_{QB\text{test}}$ can be regarded as knowns. Therefore, ΔA_2 and $\Delta\varphi_2$ can be calculated as

$$\left\{\begin{array}{ll}A'_{IB\text{test}}=\dfrac{A_2A_{\text{test}}}{2}, & \alpha'_{IB\text{test}}=\varphi_2-\Psi\\ A'_{QB\text{test}}=\dfrac{(A_2+\Delta A_2)A_{\text{test}}}{2}, & \alpha'_{QB\text{test}}=\varphi_2+\Delta\varphi_2-\Psi\end{array}\right.\Rightarrow\left\{\begin{array}{l}\Delta A_2=\dfrac{2}{A_{\text{test}}}\left(A'_{QB\text{test}}-A'_{IB\text{test}}\right)\\ \Delta\varphi_2=\alpha'_{QB\text{test}}-\alpha'_{IB\text{test}}\end{array}\right.\tag{13}$$

Knowing the ΔA_2 and $\Delta\varphi_2$, a compensating unit can be added in the feedback path after the AD converters as shown in Fig. 3. Here, $I''_{B\text{test}}(t)$ and $Q''_{B\text{test}}(t)$ are compensated signals.

According to (6) and (7), the relations among $I'_B(t)$, $Q'_B(t)$, $I''_B(t)$ and $Q''_B(t)$ are expressed in

(12).

$$\begin{cases} I'_B(t) = \dfrac{A_1A_2}{2} I(t)\cos(\varphi_1 - \varphi_2 + \Psi) + \dfrac{(A_1 + \Delta A_1)\,A_2}{2} Q(t)\sin(\varphi_1 + \Delta\varphi_1 - \varphi_2 + \Psi) = I''_B(t) \\ Q'_B(t) = Q''_B(t)\cos(\Delta\varphi_2) + I'_B(t)\sin(\Delta\varphi_2) + \dfrac{\Delta A_2}{A_2} Q''_B(t)\cos(\Delta\varphi_2) + \dfrac{\Delta A_2}{A_2} I'_B(t)\sin(\Delta\varphi_2) \\ \qquad\quad = \left(1 + \dfrac{\Delta A_2}{A_2}\right)\left[Q''_B(t)\cos(\Delta\varphi_2) + I'_B(t)\sin(\Delta\varphi_2)\right] \end{cases} \tag{14}$$

Therefore, compensated signals $I''_B(t)$ and $Q''_B(t)$ can be obtained from $I'_B(t)$ and $Q'_B(t)$.

$$\begin{cases} I''_B(t) = I'_B(t) \\ Q''_B(t) = \dfrac{A_2Q'_B(t) - (A_2 + \Delta A_2)\,I'_B(t)\sin(\Delta\varphi_2)}{(A_2 + \Delta A_2)\cos(\Delta\varphi_2)} \end{cases} \tag{15}$$

Here, ΔA_2 and $\Delta\varphi_2$ are knowns. It is obvious that after the compensation, the imperfectness of the demodulator has been eliminated. A more accurate model of PA can be built based on the corrected data.

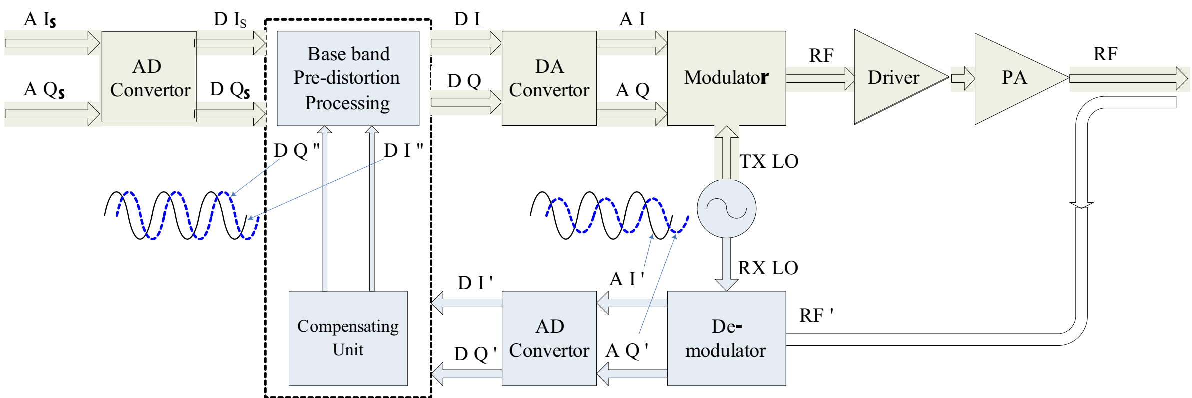

Figure 3: Modified baseband digital pre-distortion diagram.

3. CONCLUSIONS

In this paper, modulated and demodulated signal components are analyzed. It is indicated that the performance of the modulator and demodulator will affect the effect of the baseband digital predistortion. Unbalanced items in amplitude and phase of the demodulator ΔA_2 and $\Delta\varphi_2$ are calculated and relations among $I''_B(t)$, $Q''_B(t)$ and $I'_B(t)$, $Q'_B(t)$ are derived. According to the analysis and derivation above in the paper, error items caused by the imperfect demodulator in the feedback path can be eliminated and the corrected demodulated data can be obtained. Based on the algorithm, the experiment can be completed on practical platforms.

REFERENCES

1. Li, M. Y., J. X. Deng, L. E. Larson, and P. M. Asbeck, "Nonideal effects of reconstruction filter and I/Q imbalance in digital predistortion," *Radio and Wireless Symposium, 2006 IEEE*, 259–262, 17–19 Jan., 2006.
2. Shi, M., M. Chen, L. Zhang, and J. Zhou, "A new baseband digital predistortion system," *Microwave Conference Proceedings, APMC 2005*, Vols. 2, 3, SuZhou, China, 4–7 Dec., 2005.

Interaction Mechanism of a Field Emission Based THz Oscillator

M. C. Lin[1] **and P. S. Lu**[1,2]

[1]NanoScience Simulation Laboratory, Department of Physics, Fu Jen Catholic University
Taipei County 24205, Taiwan, China
[2]Institute of Optoelectronic Sciences, Taiwan Ocean University, Taiwan, China

Abstract— We proposed a vacuum electronic device based on field emission mechanism for the generation of terahertz (THz) waves in a previous work [JVST B 23(2), 849, 2005]. The preliminary simulation results showed that an electronic efficiency up to 4% can be achieved with no external magnetic fields applied. However, the interaction mechanism is not clear. In the present work, the interaction mechanisms are studied. The MAGIC code is used to investigate the interactions between the electrons and the THz waves. To understand the interaction mechanism, the cathode has been trimmed to emit electrons. The simulation results show that the efficiency of the case corresponding to the trimmed cathode is higher than that of the original planar cathode. The interaction regions are located among the gaps between the cathode and the anode. The AC electric fields of the THz waves not only velocity-modulate the electron beam but also cause the density modulation of the field emission current. This pre-bunching effect provides the feedback loop as required by an oscillator.

1. INTRODUCTION

Terahertz (THz) waves, electromagnetic (EM) radiation in the frequency extending from 0.1 to 10 THz (wavelengths of 3 mm down to 0.03 mm), have been used to characterize the electronic, vibrational and compositional properties of solid, liquid and gas phase materials during the past decade. The millimeter and sub-millimeter gap in the electromagnetic spectrum had been recognized for a long time. The well-known electron cyclotron masers (ECM) provide the solution [1]. In the past four decades, the ECM has undergone a remarkably successful evolution from basic research to device implementation, almost filling the gap. However, degradation of power generation in THz band is still present. Many rotational and vibrational spectra of various liquid and gas molecules lie within the THz frequency band, and their unique resonance lines in the THz wave spectrum allow us to identify their molecular structures. More and more applications in imaging science and technology call for the well development of THz wave sources.

Amplification and generation of a high frequency electromagnetic wave are a common interest of field emission array (FEA) based devices [2]. It is well known that a transition radiation is emitted when an electron passes through an ideally conducting screen in vacuum and a diffraction radiation is emitted when an electron of a constant velocity passes by a metallic structure [3–5]. We proposed a vacuum electronic device based on field emission mechanism for the generation of THz waves in a previous work [6]. The preliminary simulation results showed that an electronic efficiency up to 4% can be achieved with no external magnetic fields applied. However, the interaction mechanism is not clear.

In the present work, a two-dimensional (2D) finite-difference time-domain (FDTD) particle-in-cell (PIC) code MAGIC (developed by ATK Mission Research, VA, US) [7, 8] is used to investigate the interactions between the electrons and the THz waves. To understand the interaction mechanism, the cathode has been trimmed to emit electrons. Three types of cathodes including the untrimmed (original) planar, on-gap trimmed, and off-gap trimmed cathodes are considered for comparisons, as shown in Figure 1. The energy distribution of the electrons throughout the interaction structure has been observed for studying the interaction mechanism involved. The feedback mechanism of an oscillator is also discussed.

2. SIMULATION MODELS AND FIELD EMISSION

2.1. Simulation Models

Figure 1(a) shows the schematic of the field emission based THz wave generator we proposed. The anode consists of six coupled cavities and the cathode is some kind of field emission array. Three types of cathodes including the untrimmed (original), on-gap trimmed, and off-gap trimmed cathodes are considered for comparisons, respectively, as shown in Figure 1. These trimmed cathodes can be easily fabricated via today's technologies such as MEMS.

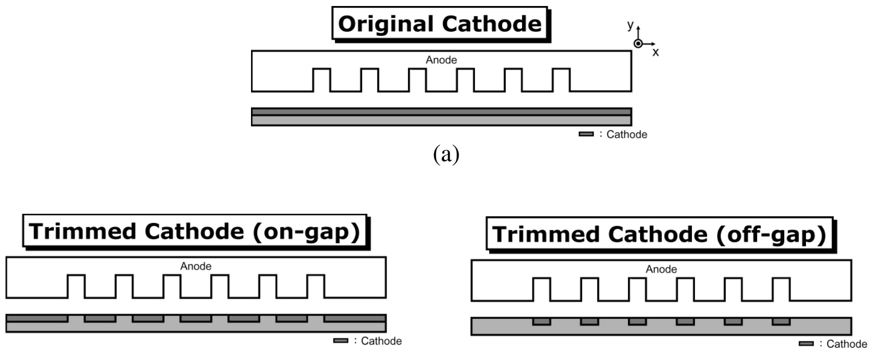

(a)

(b) (c)

Figure 1: Schematics of the simulation models including (a) the case of the original planar cathode, (b) the case of the on-gap trimmed cathode, and (c) the case of the off-gap trimmed cathode.

2.2. Field Emission

The field emission is described by the Fowler-Nordheim equation [9–17],

$$J = \frac{AE_s^2}{\phi t(y)^2} \exp\left(\frac{-Bv(y)\phi^{3/2}}{E_s}\right), \tag{1}$$

where A and B are the Fowler-Nordheim constants, and ϕ is the effective work function assumed to be a constant allowed dependence on material and surface roughness [18, 19]. The normal electric field at the cathode surface, E_s, is computed from the application of Gauss's law to the half-cell immediately above the emitting surface, or $E_s = (E_c A_c - q/\varepsilon_0)/A_s$. The Nordheim elliptic functions $t(y)$ and $v(y)$, with Nordheim parameter, $y = 3.79 * 10^{-5} E_s^{1/2}/\phi$, can be approximated by $t(y)^2 = 1.1$ and $v(y) = 0.95 - y^2$, respectively [20].

3. SIMULATION RESULTS AND DISCUSSION

The simulation results of MAGIC code for the three cases have been obtained. The last case corresponding to the trimmed cathode off-gap is failed to achieve oscillations. In the following, we discuss only the first two cases, the original planar cathode and the on-gap trimmed cathode. In the simulations, an input voltage $V_{\text{in}}(t) = V_{\max} * [1 - \exp(-t/T_{\text{rise}})]$, where $V_{\max}$ is 1 kV and T_{rise} is 0.25 ns, is superposed on the structure between the anode and the cathode for each case. For the field emission, the effective work function is set as $\phi = 0.2$ eV which might be due to the high applied electric fields and the local field enhancements [18, 19]. Figure 2(a) shows our monitored time evolution of diode voltages for the two cases. The diode voltages are almost the same. The average of the data is also shown in the figure. Figure 2(b) shows our monitored diode current

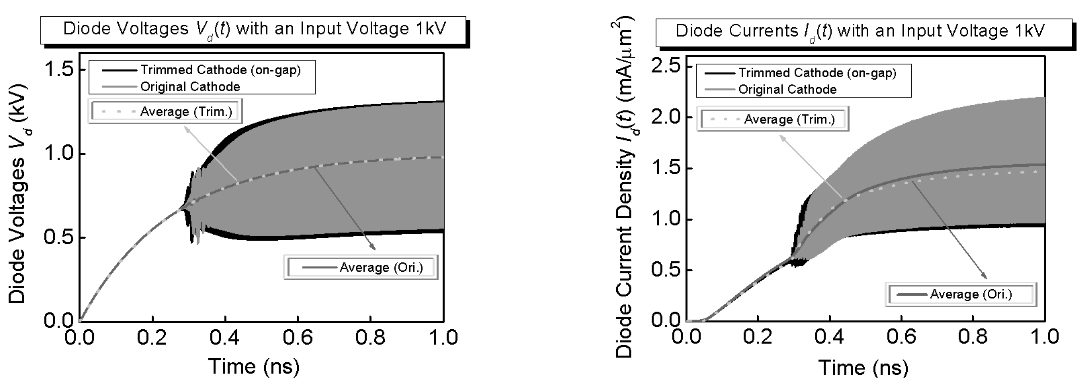

(a) (b)

Figure 2: (a) Monitored diode voltages, $V_d(t)$ curves, corresponding to the case of the original planar cathode and that of the on-gap trimmed cathode, respectively, with an input voltage 1 kV and (b) the corresponding diode current density, $I_d(t)$ curves. I_d stands for the total current divided by the cathode area.

per cathode area for the two cases. The average current of the case corresponding to the trimmed cathode is smaller than that of the original planar cathode.

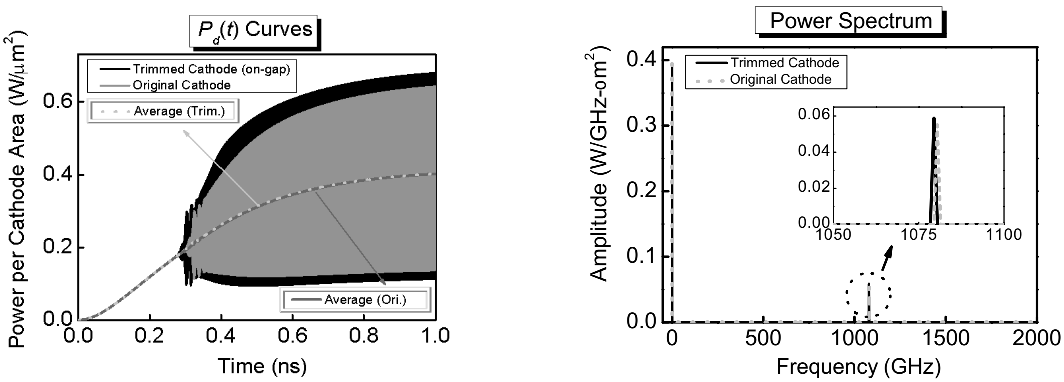

(a) (b)

Figure 3: (a) Monitored power, $P_d(t)$ curves, corresponding to the case of the original planar cathode and that of the on-gap trimmed cathode, respectively, and (b) the corresponding radiation power spectra, $P_d(f)$ curves. The resonant frequency is peaked at 1.076 THz. P_d stands for the output power divided by the cathode area.

The output power of the devices is also monitored. Figure 3(a) shows our monitored power per cathode area for the two cases. The output power includes low frequency electromagnetic waves as well. It is difficult to separate the component of THz waves from the monitored output power in the time domain, so that the results of the two cases are similar. However, it is easy to analyze the THz waves with the EM power spectrum, as shown in Figure 3(b). The resonant frequency of the case corresponding to the original cathode is about 1.076 THz and that corresponding to the on-gap trimmed cathode is the same. The amplitude of the former case is smaller than that of the latter case. The output peak power of the THz wave for the case corresponding to the original cathode is about 0.055 W/μm^2 and that for the trimmed cathode is 0.059 W/μm^2. The estimated values of the corresponding beam power are about 1.600 W/μm^2 and 1.524 W/μm^2, respectively. The electronic efficiency of the devices, i.e., the output power divided by the beam power, can be easily estimated to be 3.44% and 3.87%, respectively. The efficiency of the case corresponding to the trimmed cathode is higher than that of the original design. The efficiency of state of the art THz devises based on a quantum cascade laser or free electron laser is less than 2%. In comparison, an efficiency of 3–4% is relatively high and this motivates us to further study the interaction mechanisms.

From the above simulation results, we can conclude that the interaction regions are located among the gaps between the cathode and the anode. Figure 4(a) and Figure 4(b) show the phase space diagrams of the cases corresponding to the original and trimmed cathodes, respectively. The

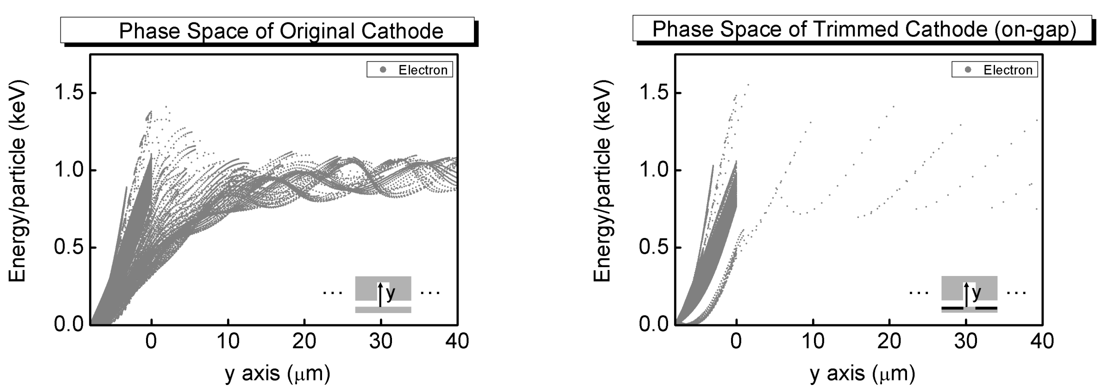

(a) (b)

Figure 4: (a) Phase space diagram of the case of the original planar cathode. The downstream current is oscillating with THz radiation. (b) Phase space diagram of the case of the on-gap trimmed cathode. The "y axis" is designated in the inset of the figure.

difference of these two diagrams is the downstream current. There is almost no downstream current in the trimmed case, but the corresponding efficiency is higher than that of the original case shown in Figure 4(a). This indicates that the bunching electrons between the gaps contribute most of the generation of THz waves and the interaction mechanism is strongly related to the gaps. In the gaps, the interactions of the field emission current and the THz waves cause the velocity modulation. As one can see from Figure 4(b), the most of electrons arrive at the anode with the correct phases at which the electrons have lower energy compared to the DC beam energy to lose energy to the THz radiation.

The density modulation of the beam due to the pre-bunching effect can be seen in both Figure 4(a) and Figure 4(b). In Eq. (1), the field emission current can be modulated by the surface electric fields that contain both the DC and AC components of the THz waves. This provides the required feedback loop for the system to be an oscillator. To confirm this, we observe the space-charge density of the system at different phases of the AC electric fields, as shown in Figure 5. As one can see in Figure 5(a) and Figure 5(b), the two bright regions indicated with white arrows in Figure 5(a) are corresponding to the highest negative electric fields and two dark regions indicated with black arrows at the same gaps in Figure 5(b) are corresponding to the highest charge densities. Similarly, in Figure 5(c) and Figure 5(d), after one half period, the fields in the other three gaps become negative and the corresponding charge densities become very large. The process will be continued and repeated. The AC electric fields of the THz waves cause the density modulation of the field emission current. This pre-bunching effect provides the feedback loop as required by an oscillator.

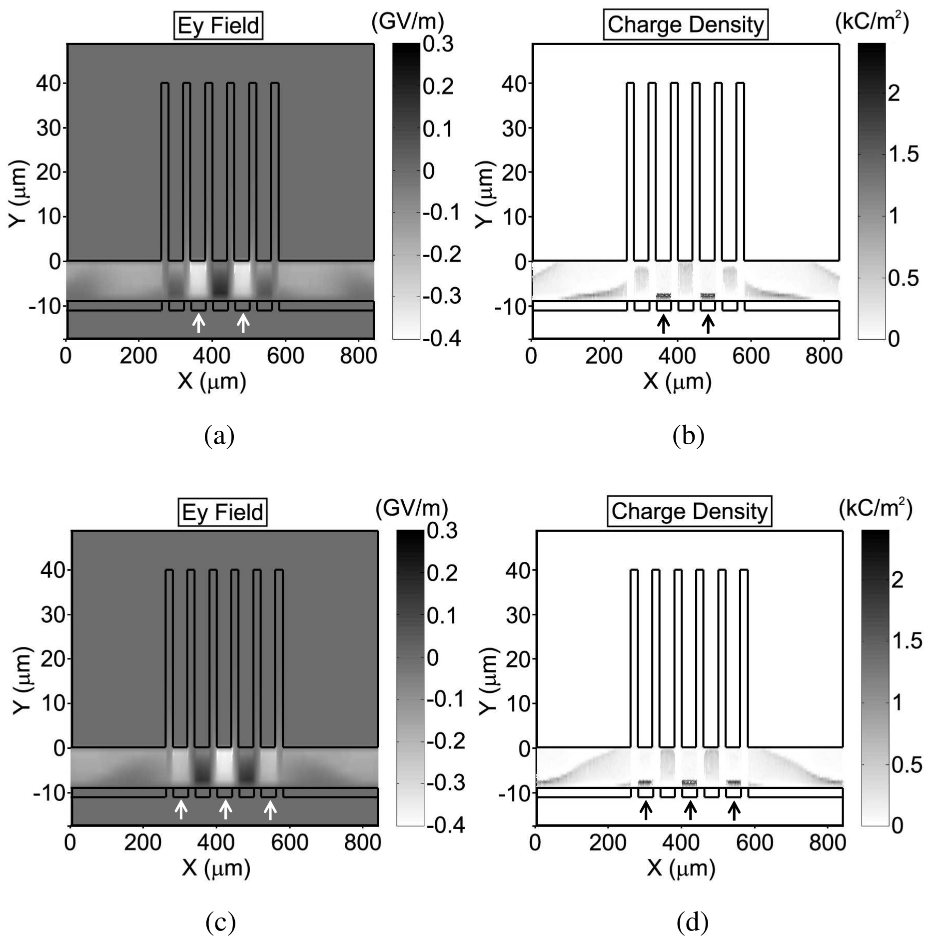

(a) (b)

(c) (d)

Figure 5: Distributions of the electric field patterns, (a) and (c), and the space-charge densities, (b) and (d). The cases (a) and (b) are observed at the same time step. Similarly with the cases (c) and (d) but with one-half period delay.

4. CONCLUSIONS

We proposed a vacuum electronic device based on field emission mechanism for the generation of THz waves. The interaction mechanisms are studied. The MAGIC code is used to investigate the interactions between the electrons and the THz waves. To understand the interaction mechanism, the cathode has been trimmed to emit electrons. The simulation results show that the interaction regions are located among the gaps between the cathode and the anode. The efficiency of the case corresponding to the trimmed cathode is higher than that of the original planar cathode. In addition, the AC electric fields of the THz waves not only velocity-modulate the electron beam but also cause the density modulation of the field emission current. This pre-bunching effect provides the feedback loop as required by an oscillator.

ACKNOWLEDGMENT

This work was partially supported by the National Science Council, Taiwan, R. O. C., under Grant No. NSC 95-2112-M-030-002 and the National Center for High-performance Computing, Taiwan, R. O. C. which provides the MAGIC code and the computing resources.

REFERENCES

1. Chu, K. R., *Rev. Mod. Phys.*, Vol. 76, No. 1, 1, 2004.
2. Yokoo, K. and T. Ishihara, *Conf. Digest of IVMC'95*, 123, 1995.
3. Bass, F. G. and V. M. Yakovenko, *Usp. Fiz. Nauk*, Vol. 86, 189, 1965.
4. Bolotovskii, B. M. and G. M. Voskresenskii, *Usp. Fiz. Nauk*, Vol. 88, 209, 1966.
5. Van den Berg, P. M. and A. J. A. Nicia, *J. Phys. A*, Vol. 9, 1133, 1976.
6. Lin, M. C., et al., *J. Vac. Sci. Technol. B*, Vol. 23, No. 2, 849, 2005.
7. Goplen, B., L. Ludeking, D. Smithe, and G.Warren, *Computer Phys. Comm.*, Vol. 87, No. 1 & 2, 54, 1995.
8. Goplen, B., L. Ludeking, D. Smithe, and G. Warren, *MAGIC User's Manual*, Mission Research Corp., MRC/WDC-R-409, 1997.
9. Fowler, R. H. and L. W. Nordheim, *Proc. R. Soc.*, *Ser. A*, Vol. 119, 173, London, 1929.
10. Nordheim, L. W, *Proc. R. Soc.*, *Ser. A*, Vol. 121, 626, London, 1928.
11. Nordheim, L. W., *Z. Phys.*, Vol. 30, 177, 1929.
12. Schottky, W., *Z. Phys.*, Vol. 14, 63, 1923.
13. Frank, N. H. and L. A. Young, *Phys. Rev.*, Vol. 38, 80, 1931.
14. Guth, E. and C. J. Mullin, *Phys. Rev.*, Vol. 61, 339, 1942.
15. Gogate, D. V. and D. S. Kothari, *Phys. Rev.*, Vol. 61, 349, 1942.
16. Gasiorowicz, S., *Quantum Physics*, 2nd edition, Wiley, New York, 1996.
17. Lin, M. C. and D. S. Chuu, *Appl. Phys. Lett.*, Vol. 80, No. 22, 4262, 2002.
18. Kim, C. and B. Kim, *Phys. Rev. B*, Vol. 65, 165418, 2002.
19. Nation, J. A., et al., *Proceedings of the IEEE*, Vol. 87, No. 5, 865, 1999.
20. Spindt, C. A., I. Brodie, L. Humphrey, and E. R.Westerberg, *J. Appl. Phys.*, Vol. 47, 5248, 1976.

A Small Multi-band MEMS Switched PIFA

K. R. Boyle[1] **and P. G. Steeneken**[2]

[1]NXP Semiconductors, Research, UK
[2]NXP Semiconductors, Research, The Netherlands

Abstract— This paper presents the design of a small MEMS switched planar inverted F antenna capable of operation in five cellular radio frequency bands. Both simulated and measured results are presented. The MEMs devices used in the measurements are fabricated in an industrialized process based on high-ohmic silicon.

1. INTRODUCTION

Planar inverted F antenna (PIFAs) are widely used in mobile phones. They suffer from a problem that is common to all electrically small antennas — they have limited bandwidth for a given size. This is a constant challenge for antenna designers, since there is a continual trend towards operation within more bands (for global "roaming") and a constant desire to reduce the antenna volume. Figure 1 shows the five UTRA (UMTS Terrestrial Radio Access) FDD and GSM bands used in Europe and America (and also many other countries worldwide).

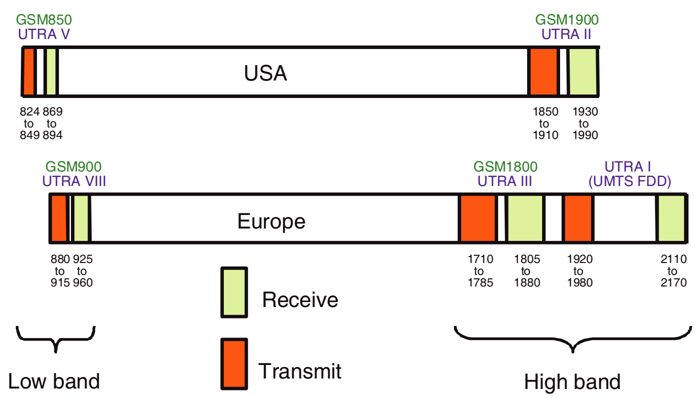

Figure 1: Common cellular frequency bands used in Europe and the USA (MHz).

Simultaneous operation is not required in all bands: the antenna can be switched to operate in a subset of the total number of bands at any given time. However, though MEMS switched antennas have been reported previously [1–3], none have been shown to be capable of operation over five mobile phone frequency bands.

To achieve switching over a bandwidth of approximately one octave without significantly reducing efficiency, high quality microelectromechanical systems (MEMS) switches have been developed [4–7]. Capacitive switches, fabricated in the industrialized Philips PASSI™ process, are reported here.

2. ANTENNA GEOMETRY AND MEMS CIRCUITRY

The antenna geometry and MEMS circuitry is shown in Figure 2. The antenna has dimensions $40 \times 12 \times 8$ mm, whereas the PCB has dimensions $40 \times 100 \times 0.8$ mm and is metalized on the back surface to provide an RF ground. All circuitry is on the PCB rather than the antenna and the slot in the antenna is located such that it is unlikely to be perturbed when the phone is held [8, 9].

The MEMS devices (shown as variable capacitors in Figure 2) require an actuation voltage of between 30 V and 50 V. MEMS Die 1 controls the antenna impedance and Die 2 controls the antenna resonant frequency. The circuit values for each operational mode are given in Table 1. The matching inductor, L1 is fixed and is realized as a meander line on the PCB. L2 is for DC biasing and is realized using a surface mount device (SMD) of value 10 nH. Capacitors CB1 and CB2 are used for DC blocking, whereas CD1-CD4 are for decoupling. All are 200 pF. Finally, resistors R1-R4 have a resistance of 10 kΩ. and are for decoupling the DC actuation voltages of the MEMS switches applied at terminals VDC1-VDC4.

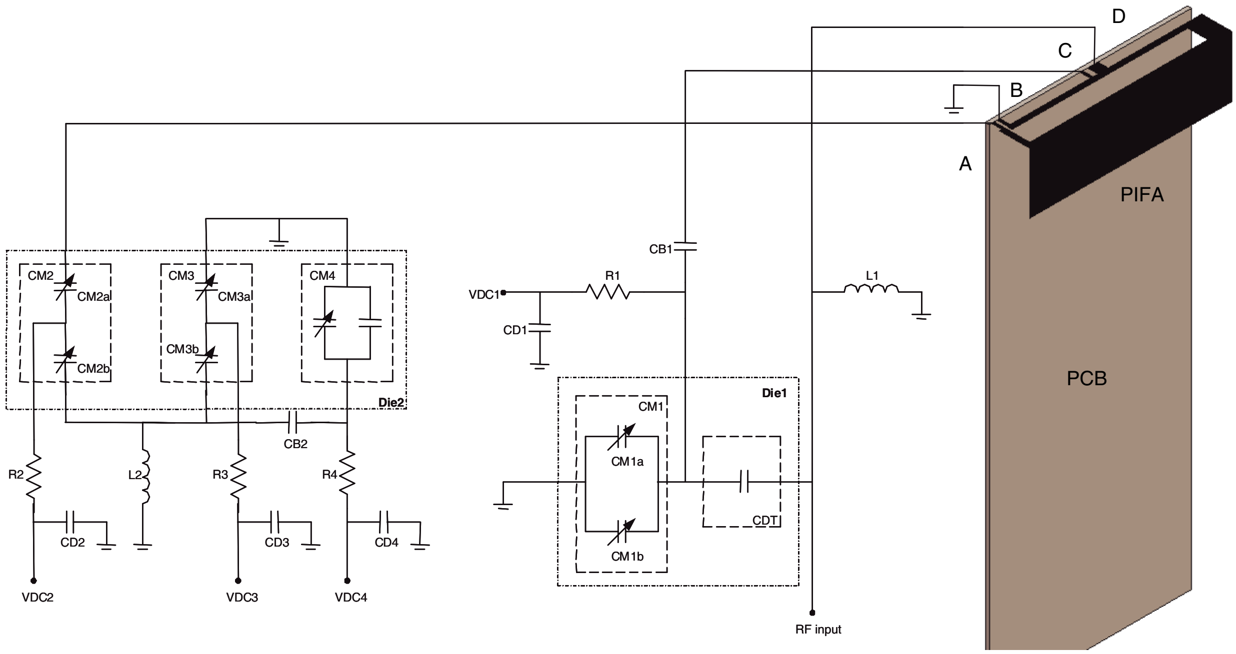

Figure 2: MEMS switched PIFA and circuit.

Table 1: MEMS capacitor values (pF) with operational mode.

Mode	CDT	CM1a CM1b	CM2A CM2B	CM3A CM3B	CM4
GSM850/900	12	10	0.2	3.4	5.7
GSM1800	12	10	4.0	3.4	5.7
GSM1900	12	.5	4.0	3.4	0.57
UMTS	12	.5	4.0	0.17	0.57

The MEMS capacitors CM2 and CM3 are series combinations of two capacitive switches in order both to reduce the OFF state capacitances and to improve voltage handling. CM1 is a parallel combination of two capacitive switches to increase the ON capacitance and CM4 is the combination of a fixed and a MEMS capacitor. CDT is a fixed capacitor that is used to double-tune the antenna in the lowest frequency mode. It is realized on the MEMS die to allow the use of non-preferred values.

3. SIMULATED RESULTS

The antenna and interconnects are modeled using Ansoft HFSS with all component positions represented as lumped ports. This allows a multi-port s-parameter file to be generated and subsequently imported into the Agilent ADS circuit simulator. Components can then be placed at the ports of the s-parameter network and the input impedance, circuit efficiency etc simulated. The simulated impedance in the four operational modes is shown in Figure 3. All modes have are capable of an S_{11} of -6 dB or better (referred to 50 Ohms) — the UMTS mode is deliberately designed to have a resonant frequency that is too high in order to allow DC tuning to lower frequencies.

4. IMPLEMENTATION

A photograph of the MEMS switched antenna is shown in Figure 4.

The antenna is fabricated from a polyimide flexible PCB that is folded over a Rohacell block. The antenna/PCB combination is fed via a coaxial cable at a central point on the PCB to avoid excessive perturbation from the feeding cables [10]. The MEMS capacitors are placed on two dies under the antenna, as shown in Figure 5. It can be seen that the bond wires used to connect from

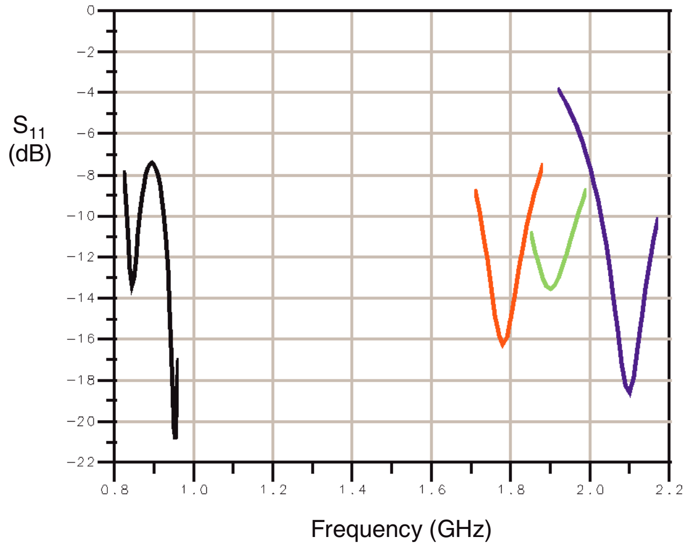

Figure 3: Simulated S_{11}: 824–960 MHz (black), 1710–1880 MHz (red), 1850–1990 MHz (green), 1920–2170 MHz (blue).

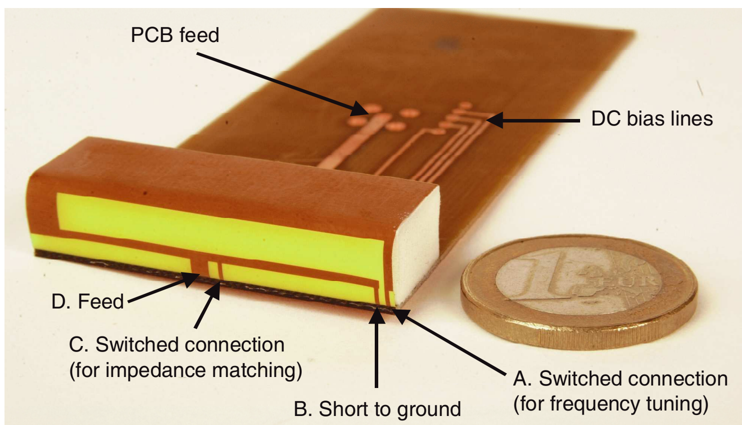

Figure 4: MEMS switched PIFA and PCB.

the MEMS dies to the PCB interconnects are rather long, in part due to the solder used to connect the SMDs. To compensate for device and assembly uncertainties, MEMS devices with slightly varying layouts are implemented.

5. MEASUREMENTS

Measured results are shown in Figure 6.

In the UTRA band V/VIII mode, the S_{11} is below -6 dB between 765–950 MHz, showing that a wide bandwidth resonance is obtained. The centre frequency is somewhat lower than that simulated at 830 MHz, but the bandwidth is approximately 180 MHz (fractionally, 22%), which is slightly better than simulated. For the high frequency bands, the resonant frequencies are somewhat higher than simulated. The -6 dB bandwidths are 1930–2062 MHz, 1941–2071 MHz and 2005–2117 MHz for the UTRA bands III, II and I respectively. These bandwidths are less than simulated. However this is largely due mismatch. With inductive matching, bandwidths of approximately 300 MHz — slightly higher than those simulated — can be achieved. Resonant frequency shifts are clearly observed in the high frequency modes, though the magnitudes of the shifts are less than simulated. The differences between simulation and measurement are attributed predominantly to uncertainties in the capacitance density of the MEMS devices and the long (un-simulated) bond wires used.

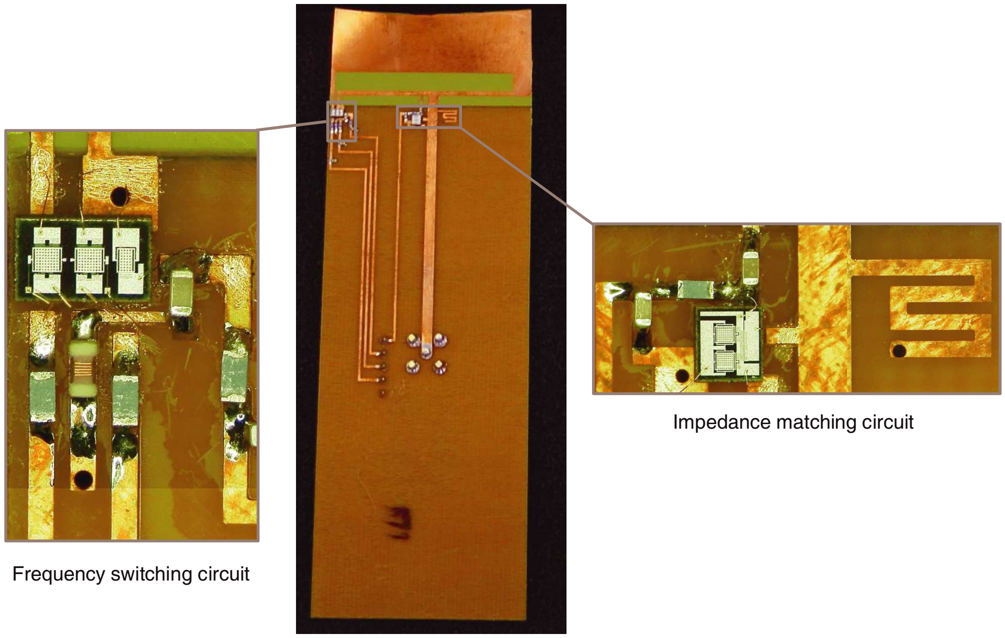

Figure 5: Unfolded antenna and details of MEMS dies and surrounding components.

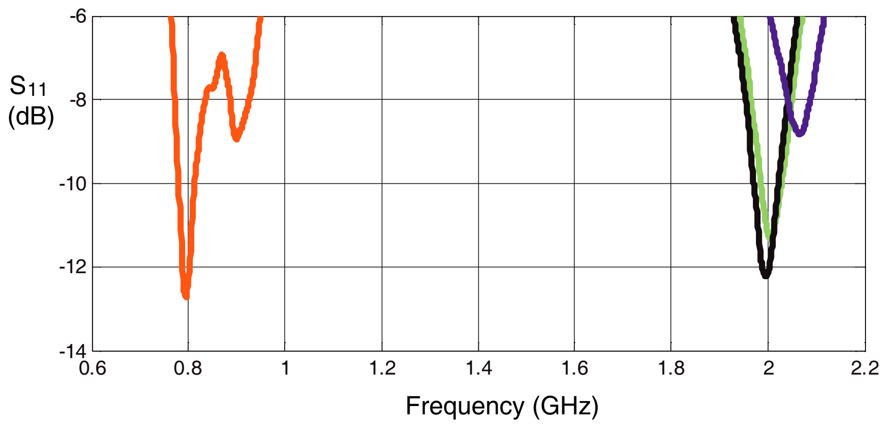

Figure 6: Measured S_{11} (below -6 dB): 765–960 MHz (red), 1930–2062 MHz (black), 1941–2071 MHz (green) and 2005–2117 MHz (blue). Low and high frequency results are measured with slightly different MEMS devices.

6. CONCLUSIONS

A five-band MEMS switched antenna, utilizing capacitive MEMS switches is demonstrated. The measured prototype confirms that the antenna is capable of operating in several modes over a bandwidth of greater than one octave. It is also confirmed that wide bandwidths are feasible (in each mode) from an antenna that is smaller than conventional. In the future, the use of directly soldered, packaged MEMS with improved capacitance density tolerances, will lead to closer agreement between simulations and measurement.

REFERENCES

1. Kiriazi, J., H. Ghali, H. Ragaie, and H. Haddara, "Reconfigurable dual-band dipole antenna on silicon using series MEMS switches," *Proceedings of the IEEE Antennas and Propagation Society International Symposium*, Vol. 1, 403–406, 22–27 June 2003.
2. Panaia, P., C. Luxey, G. Jacquemod, R. Staraj, G. Kossiavas, L. Dussopt, F. Vacherand, and C. Billard, "MEMS-based reconfigurable antennas," *Proceedings of the IEEE International Symposium on Industrial Electronics*, Vol. 1, 175–179, 4–7 May 2004.
3. Onat, S., M. Unlun, L. Alatan, S. Demir, and T. Akin, "Design of a re-configurable dual

frequency microstrip antenna with integrated RF MEMS switches," *Proceedings of the IEEE Antennas and Propagation Society International Symposium*, Vol. 2A, 384–387, 3–8 July 2005.

4. Rijks, T. G. S. M., et al., "Passive integration and RF MEMS: a toolkit for adaptive LC circuits," *Proceedings of the 29th European Solid-State Circuits Conference*, 269–272, 16–18 Sept. 2003.
5. Van Beek, J. T. M., et al., "High-Q integrated RF passives and micromechanical capacitors on silicon," *Proceedings of the Bipolar/BiCMOS Circuits and Technology Meeting*, 147–150, 28–30 Sept. 2003.
6. De Graauw, A. J. M., P. G. Steeneken, C. Chanlo, J. Dijkhuis, S. Pramm, A. van Bezooijen, H. K. J. ten Dolle, F. van Straten, and P. Lok., *Proc. BCTM2006*, 2006.
7. Van Beek, J. T. M., P. G. Steeneken, G. J. A. M. Verheijden, J. W. Weekamp, A. den Dekker, M. Giesen, A. J. M. de Graauw, J. J. Koning, F. Theunis, P. van der Wel, B. van Velzen, and P. Wessels, "MEMS for wireless communication: application, technology, opportunities and issues," *Proceedings of MEMSwave2006*, session 5, paper 17, 2006.
8. Boyle, K. R. and L. P. Ligthart, "Radiating and balanced mode analysis of PIFA antennas," *IEEE Transactions on Antennas and Propagation*, Vol. 54, Issue 1, 231–237, Jan. 2006.
9. Boyle, K. R. and L. P. Ligthart, "Radiating and balanced mode analysis of user interaction with PIFAs," *Proceedings of the IEEE Antennas and Propagation Society International Symposium*, Vol. 2B, 511–514, Washington DC, July 4th–8th, 2005.
10. Massey, P. J. and K. R. Boyle, "Controlling the effects of feed cable in small antenna measurements," *Proceedings of ICAP 2003*, 31 Mar.–3 Apr. 2003.

Three-band Modified Transmission Line Antennas for Mobile Communication

Takehiko Tsukiji and Yasunori Kumon
Department of Electronics and Computer Science, Faculty of Engineering
Fukuoka University
814-0180, Nanakuma, Jounan-ku, Fukuoka, Japan

Abstract— In order to respond to recent increases in the number of mobile telephone users, three frequency bands are currently used for mobile telephone systems. We herein propose a three-frequency-band antenna that is useful for mobile telephone base stations. We first developed a two-band antenna called the Double Modified Transmission Line Antenna (DMTLA) that consists of two simplified MTLA of different lengths. By attaching a parasitic element to the DMTLA based on the multi-band technique using parallel transmission line loading, we realize the three-band Double Modified Transmission Line Antenna (3-B DMTLA) for the base station antenna of a mobile telephone system.

1. INTRODUCTION

We previously developed the Modified Transmission Line Antenna (MTLA) and have reported several applications of the MTLA to the mobile telephone antenna [1]. The MTLA provides a low-profile antenna with good impedance characteristics that is suitable for mobile communication.

The present approach is to design a simplified MTLA, as indicated in Figure 1, where the total element length of this antenna $L + 2(H + W)$ is designated as a half wavelength of the resonant frequency. This simplified MTLA can reduce antenna space without losing the characteristics of the originally developed MTLA. Using two simplified MTLAs of different lengths, we developed the Double Modified Transmission Line Antenna (DMTLA) for two-frequency-band operation.

We also developed the multi-band monopole antenna for the portable telephone using the transmission-line loading technique and reported the double-folded monopole antenna in previous studies [2, 3].

A parasitic element parallel to the main antenna element works as a loading impedance for the main antenna. The position of the impedance element is located at the open-end position of the main element. When the length of the parasitic element is a quarter wavelength of higher frequency than the resonant frequency of the main antenna, the impedance of the parallel transmission line becomes infinity. This antenna can be then separated at the loading point of the parasitic element and can resonate at two frequencies: the frequency of the main antenna and the frequency of the parasite [4].

By utilizing this parallel line loading technique to the DMTLA, we can realize the multi-band antenna for a base station of a mobile telephone system.

2. DOUBLE MTLA

Figure 2 shows the fundamental structure of the DMTLA for two frequency bands of $f_1 = 900\,\mathrm{MHz}$ and $f_2 = 1.5\,\mathrm{GHz}$. The simplified MTLA drawn by the broad line in the figure, with a total length

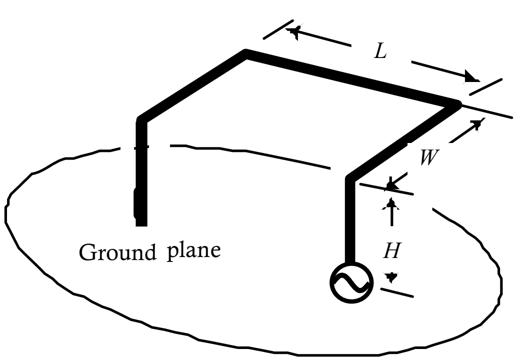

Figure 1: Simplified MTLA.

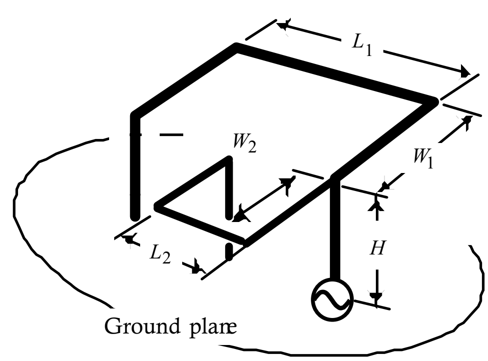

Figure 2: Double MTLA.

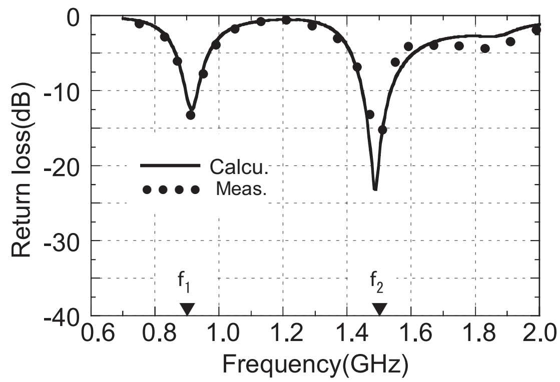

Figure 3: Return loss of DMTLA.

of $L_1 + 2(H + W_1)$, is the MTLA designed for f_1. Whereas the other simplified MTLA drawn by the thin line, with a total length of $L_2 + 2(H + W_2)$, is the simplified MTLA for f_2.

Figure 3 shows the return loss characteristics of the DMTLA for a characteristic impedance of $Z_0 = 50\,\Omega$. The parameters of the DMTLA are $H = 2.0\,\text{cm}$, $L_1 = 6.0\,\text{cm}$, $W_1 = 4.0\,\text{cm}$, $L_2 = 2.0\,\text{cm}$, and $W_2 = 2.5\,\text{cm}$, and the wire radius is $a = 0.5\,\text{mm}$.

This DMTLA can clearly operate on two frequency bands of 900 MHz and 1.5 GHz. This result was obtained using the Method of Moment computer program. Initially, the total length of $L_1 + 2(H + W_1)$ was adjusted until the antenna resonated at 900 MHz. Then, $L_2 + 2(H + W_2)$ was adjusted to meet the 1.5 GHz resonance.

This DMTLA radiates mainly a vertically polarized electric field around the driving element, and its radiation pattern is omni-directional.

3. THREE-BAND DMTLA

In this section, we explain how to add a new frequency band to the DMTLA using the parallel line loading technique introduced in Section 1. Figure 4 shows the parallel-line-loaded three-band

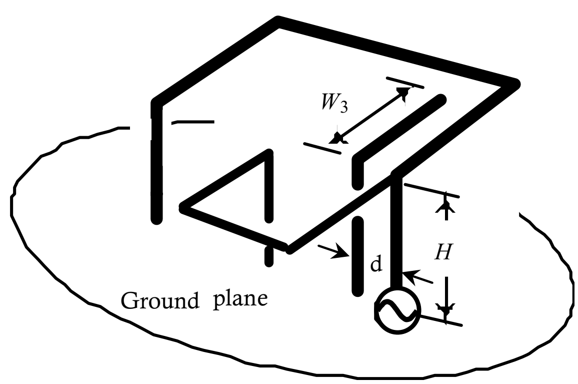

Figure 4: 3-B Double MTLA.

DMTLA, in which a parasitic element of length $H + W_3$ is attached along with the element of the DMTLA for parallel line loading. Note that the parasitic element must be constructed such that the distance d between the parasitic element and the element of the DMTLA remains constant. Since, along with a part of the element of the DMTLA, this parasitic element constitutes the parallel transmission line, it is considered that equivalent lumped impedance is loaded at the open end point of DMTLA. When the length of the parasitic element is equal to a quarter wavelength of frequency f_3, the impedance of the transmission line with a short-circuited end becomes infinity at f_3. This parasitic element then electrically cuts off the element of DMTLA at point W_3 from a corner, and this antenna resonates at a new frequency of f_3.

Figure 5 shows the rerun loss characteristics of the three-band DMTLA, where the length of the attached parasitic element is $W_3 = 1.6\,\text{cm}$ and the distance is $d = 0.5\,\text{cm}$. It is clear from the figure that this three-band DMTLA has three resonant frequencies. $f_1 = 900\,\text{MHz}$ and $f_2 = 1.5\,\text{GHz}$ are the resonant frequencies of the original DMTLA without parasitic elements, and $f_3 = 2.0\,\text{GHz}$ is the resonant frequency due to the parasitic elements.

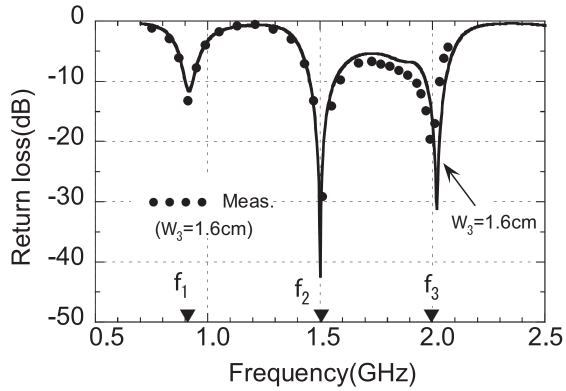

Figure 5: Return loss of the 3-B DMTLA.

In the figure, the dots indicate the measured results, and the calculated results are confirmed experimentally.

4. CONCLUSIONS

We proposed the DMTLA using two simplified MTLAs to reduce the space of the two-band antenna for a mobile telephone system. We first realized a two-band antenna with 900 MHz and 1.5 GHz. For these frequencies, the bandwidth of the return loss of less than — 10 dB are 5.6% and 6.3%, respectively.

Our approach was to use the parallel transmission line for the loading element of the DMTLA in order to add an additional frequency band to the DMTLA. We completed the three-band DMTLA by attaching a simple parasitic element with an inverted-L shape.

Without affecting a significant change in the return loss of the original two-band DMTLA, we obtained a bandwidth of 4.7% for the new frequency.

We realized a three-band antenna for a mobile telephone system with a relatively simple structure. It is expected that this three-band antenna will be applied as a base station antenna of a mobile telephone system.

REFERENCES

1. Tsukiji, T. and Y. Kumon, "Modified transmission line type antenna for mobile communication," *Ieice Trans. Commun.*, Vol. E75-B, No. 8, August 1992.
2. Tsukiji, T. and Y. Kumon, "A Double folded monopole antenna for the portable telephone," *Proceedings of the 1998 IWTS*, 184–187, 1998.
3. Tsukiji, T., Y. Kumon, and M. Yamasaki, "Double-folded monopole antenna using parallel line or coaxial cable," *IEE Proc. Microw. Antenna Propag.*, Vol. 149, No. 1, 17–22, 2002.
4. Tsukiji, T., Y. Kumon, and M. Yamasaki, "Reduced-size and multi-band modified transmission line antennas for wireless LAN or BlueTooth systems," *2nd ICONIC*, Barcelona, Spain, June 2005.

A Novel Compact Artificial Magnetic Conductor Based on Multiple Non-grounded Vias

Seyed Mohammad Amjadi and Mohammad Soleimani

Iran University of Science and Technology, Iran

Abstract— In this paper a novel compact artificial magnetic conductor based on multiple non-grounded vias (MNGV) is introduced. This structure has more bandwidth in comparison with other compact structures neither use magnetic materials nor NICs presented recently and exhibits an acceptable stability of resonance frequency for the complete angular spectrum of incident plane waves. The unit cell size is decreased 81.6% by MNGV-AMC with single grounded via compared with the similar Sievenpiper AMC structure. Therefore antennas and microwave integrated circuits performance can be improved by increasing the number of cells in a finite space, especially in mobile communications.

1. INTRODUCTION

In order to miniaturize mobile communication devices, it is necessary to incorporate the antenna with the printed circuit board. Because the substrate thickness is usually much smaller than the wavelength in dielectric medium, the ground plane destroys the antenna performance. To overcome this problem, in the late 1990s, Sievenpiper proposed a mushroom-like high impedance surface or AMC structure that reflects the plane wave in-phase and suppresses surface wave [1–3]. Consequently it can be placed very close to the antenna instead of the ground plane. But for low frequency band, i.e., wireless communication band (GSM, PCS and ISM), the unit cell size is large and it is not possible to use AMC in low profile and low frequency devices. Magnetic loading of AMC [4] and NICs [5] are used for decreasing the resonance frequency and enhancing the bandwidth. Multi-layer AMC structures are proposed for GSM applications [6–8]. However these methods are very difficult to implement and not applicable with conventional two-layer printed circuit boards with dielectric substrates. Some methods for reducing the cell size of two-layer AMC structures are introduced [9], but none of them can decrease the cell size better than 40%. An IE-AMC [10] is presented with about 70% reducing the cell size, but its bandwidth is 2.3%. This paper introduces a new compact MNGV-AMC structure having stable resonance with respect to polarization and incidence angle. The size of the unit cell is decreased 81.6% in MNGV-AMC with single grounded via compared with Sievenpiper AMC and the bandwidth is increased by a factor of 1.52 in MNGV-AMC without grounded via in comparison with IE-AMC.

2. STRUCTURE DESIGN

The conventional Sievenpiper AMC and its equivalent circuit are shown in Figs. 1(a) and (b) respectively. The resonance frequency is determined by $1/2\pi\sqrt{LC}$ and the bandwidth is proportional to $\sqrt{LC}$. Increasing the inductance or the capacitance of the structure leads to lower resonance frequency. But if the capacitance is increased, the bandwidth suffers. Therefore it is favorable to increase the structure inductance rather than the capacitance. As for Sievenpiper AMC and IE-AMC, the inductance $L = \mu h$, but in IE-AMC the capacitance is increased greatly and the bandwidth is decreased consequently. In order to increase the inductance without changing the capacitive layer, a thicker substrate must be used. But a thicker substrate occupies more space and makes the device enlarged. One way to increase the structure inductance is using a frequency selective surface with a series LC equivalent circuit instead of a conventional patch. Now the resonance frequency is determined by $1/2\pi\sqrt{(L+L_s)\,C_s}$. In other words, the surface inductance is added to the previous inductance and the total structure inductance is increased. Therefore a high inductance FSS is required to be placed as the top layer instead of the patch which acts as a capacitive surface. A well-known structure which has this kind of equivalent circuit with high inductance is a square-loop shown in Fig. 2. It is notable that there are other frequency selective surfaces with series LC equivalent circuit and high inductance. But Most of them are complicated. For simplicity the so-called structure is chosen. Since the inductance of the square loop is inversely proportional to the loop width, a narrow loop is used.

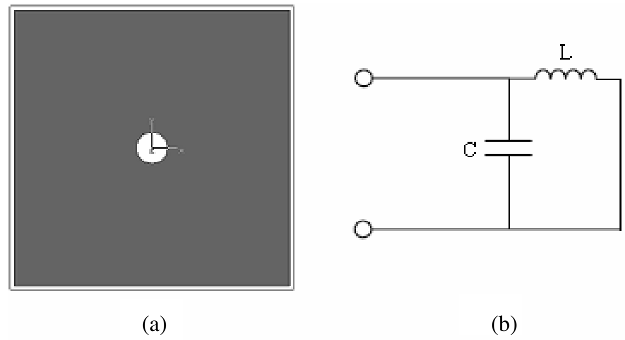

Figure 1: (a) Top view of conventional Sievenpiper AMC and (b) its equivalent circuit.

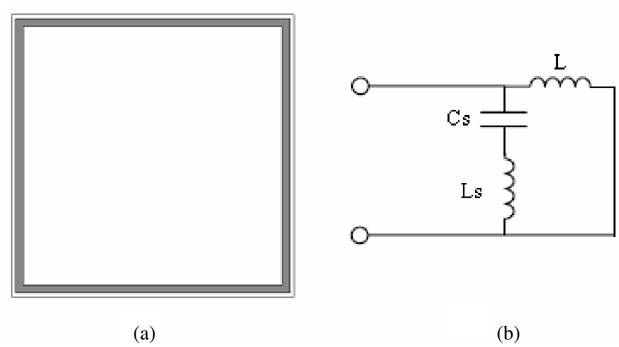

Figure 2: (a) Top view of AMC with the Square loop as the top FSS and (b) its equivalent circuit.

However because the square loop capacitance isn't high, the structure capacitance is not changed greatly. By adding new capacitive layers the structure capacitance can be increased. It is important to note that adding a new inductive surface between the ground and the top surface reduces the total structure inductance because it is parallel with the top surface inductance. If the microwave integrated circuit is a two-layer structure, it is difficult to integrate a multi-layer structure with a two-layer one. Also any change in the top surface configuration leads to the surface inductance reduction. Therefore an alternative approach is to create multiple non-grounded vias on the square-loop as shown in Fig. 3(a). The capacitance between the adjacent cells vias and between the vias in a cell is very high and the resonance frequency decreases without reducing the total structure inductance. So the bandwidth is more than IE-AMC. The more the vias, the more the resonance frequency reduction. Also if the length of the vias is taken larger, the capacitance is higher. Because of the narrow bandwidth, the resonance frequency stability in different incidence angles is very important. For a good performance, the maximum shift in resonance frequency at various incidence angles must be lower than half of the bandwidth. Since the vias are not grounded, the structure exhibits an acceptable stability of resonance frequency for the complete angular spectrum of incident plane waves.

If the single grounded via in Sievenpiper AMC structure which is in the center of the unit cell

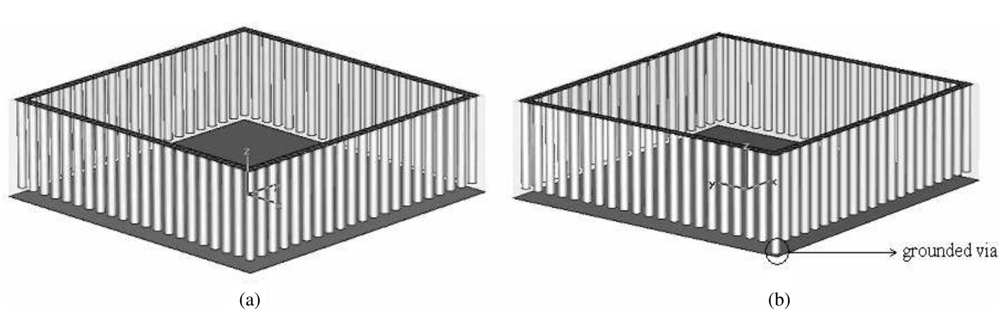

Figure 3: (a) Geometry of MNGV-AMC structure (b) MNGV-AMC structure with single grounded via.

is shifted to the corner of the cell, the resonance frequency is decreased about 30%. Applying this technique to the MNGV-AMC structure shows the similar effect. It means that if only one corner via in MNGV-AMC is grounded as shown in Fig. 3(b), the resonance frequency is reduced about 30% compared with MNGV-AMC with no grounded via. But the bandwidth and resonance frequency stability suffers a little in this case.

For creating non-grounded vias in fabrication process, an easy method is dividing the dielectric substrate into two layers. The top layer thickness is equal to vias length and the bottom layer is without via as shown in Fig. 4. In other words, first, the vias are created in the top layer and then the two layers are connected to each other. Finally the vias are metalized.

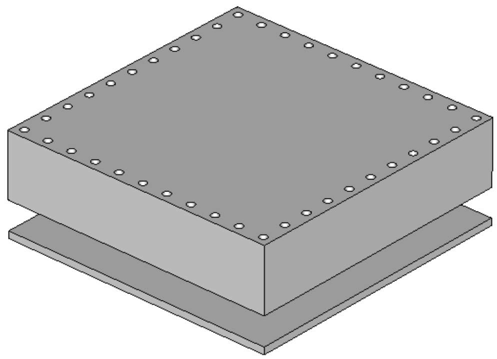

Figure 4: Dividing the dielectric substrate into two layers to provide an easiness of fabrication.

3. RESULTS AND DISCUSSIONS

We consider a unit cell size of $7.2 \times 7.2\,\mathrm{mm}^2$ with a substrate thickness of 2 mm for comparing the results with the analogous Sievenpiper and IE-AMC structures. The relative permittivity of the dielectric slab is 2.65. The diameter and the length of vias are 0.2 mm and 1.8 mm respectively. The distance between the centers of two adjacent vias is 0.335 mm. The width of the squar loop is 3 mm. Finite difference time domain method is used for the structure simulation. Fig. 5 shows the reflection phase of MNGV-AMC structure for various incidence angles. The resonant frequency of the analogous Sievenpiper AMC is 6.15 GHz. By applying this structure the resonant frequency is reduced to 1.66 GHz with 3.5% bandwidth at normal incidence and the maximum shift in resonance frequency ($\Delta f/f_0$) in different plane wave incidence angles is 0.8%. It means that the bandwidth is increased by a factor of 1.52 in comparison with the analogous IE-AMC that is 2.3% at 1.7 GHz. In other words, the total structure inductance is approximately doubled.

If only one of the corner vias is grounded, the resonance frequency is reduced to 1.13 GHz at

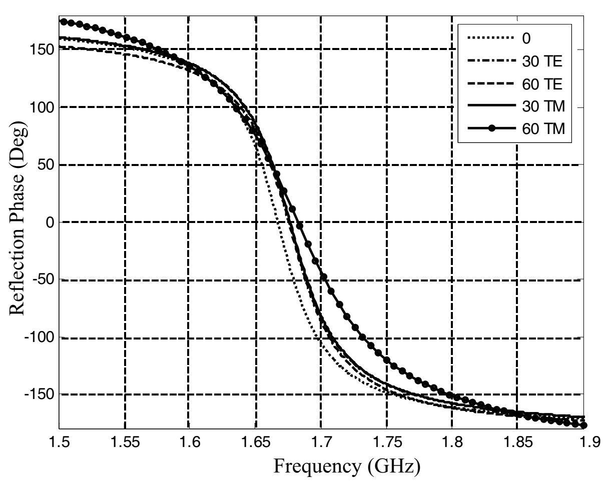

Figure 5: Reflection Phase of MNGV-AMC shown in Fig. 3(a) for different incidence angles.

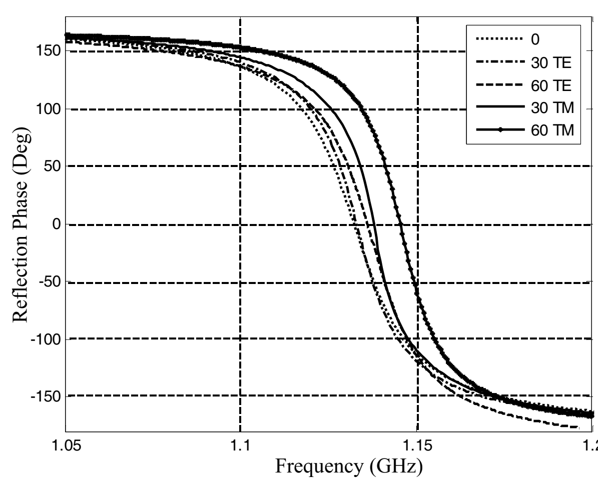

Figure 6: Reflection Phase of MNGV-AMC with single grounded via shown in Fig. 3(b) for different incidence angles.

normal incidence, which is 81.6% and 31.95% lower than Sievenpiper AMC structure and MNGV-AMC respectively. Fig. 6 illustrates the reflection phase of MNGV-AMC structure with single grounded via for different incidence angles. As it shows, the bandwidth is decreased to 1.9% at normal incidence and stability to resonance angle suffers a little in TM case which was predictable because of the grounded via. The maximum shift in resonance frequency ($\Delta f/f_0$) in MNGV-AMC with single grounded via is 1.1%.

4. CONCLUSIONS

In this paper a novel compact two layer MNGV-AMC structure and a MNGV-AMC with single grounded via are presented. Through applying these configurations not only the resonance frequency is decreased 81.6% and 10% compared with Sievenpiper and IE-AMC structures respectively but also the bandwidth is increased by a factor of 1.52 in comparison with IE-AMC structure. Also the maximum shift in resonance frequency is 0.8% for MNGV-AMC that is acceptable for 3.5% bandwidth. The MNGV-AMC with single grounded via is more compact but suffers from bandwidth and resonance frequency stability. This problem can be solved by a thicker substrate. Therefore this structure can be used in low-frequency and low-profile mobile communication devices with narrow bandwidth to improve the antenna performance by using more unit cells in a finite space, especially in mobile cell phones.

REFERENCES

1. Sievenpiper, D., et al., "High-impedance electromagnetic surfaces with a forbidden frequency band," *IEEE Trans. Microw. Theory Tech.*, Vol. 47, No. 11, 2059–2074, Nov. 1999.
2. Sievenpiper, D., "High-impedance electromagnetic surfaces," Ph.D. Dissertation, Univ. Calif., Los Angles, 1999.
3. Sievenpiper, D. F. and E. yablonovich, "3D metallo-dielectric photonic crystals with strong capacitive coupling between metallic islands," *Phys. Rev. Lett.*, Vol. 80, 2829–2832, Jul. 1998.
4. Diaz, R. E. V., C. Sanchez, E. Caswell, and A. Miller, "Magnetic loading of artificial magnetic conductors for bandwidth enhancement," *IEEE Ant. Prop. Inter. Symp.*, Columbus, OH, 431–434, Jun. 2003.
5. Kern, D. J., D. H. Werner, and M. J. Wilhelm, "Active negative impedance loaded EBG structures for the realization of ultra-wideband artificial magnetic conductors," *IEEE Ant. Prop. Symp.*, Columbus, OH, June. 2003.
6. Du, Z., J. S. Fu, B. Gao, and Z. Feng, "A compact planar inverted-F antenna with a PBG-type ground plane for mobile communications," *IEEE Trans. Vehicular Tech.*, Vol. 52, 483–489, May 2003.
7. Mckinzie III, W. E. and R. R. Fahr, "A low profile polarization diversity antenna built on an artificial magnetic conductor," *IEEE Antennas Propagat. Soc. Int. Symp.*, Vol. 1, 762–765, 2002.
8. Rogers, S., J. Marsh, W. McKinzie, and G. Mendolia, "AMC edge treatments enable high isolation between 802.11b and bluetooth TM antenna on laptop computers," *IEEE Antennas Propagat. Soc. Int. Symp.*, Vol. 2, 38–41, 2003.
9. Fu, Y., N. Yuan, and G. Zhang, "A very compact electromagnetic bandgap structure for suppressing surfacewaves in integrated circuits," *Microwave Opt. Technol. Lett.*, Vol. 41, 455–457, Jun. 2004.
10. Yan, D., Q. Gao, C. Wang, and N. Yaun, "Novel compact inter-embedded AMC structures for suppressing surface wave," *Progress in Electromagnetics Research Symp.*, 695–698, August 22–26, 2005.

Gain Enhancement for Reflectarray

The Nan Chang
Tatung University, Taipei, Taiwan, China

Abstract— A method to enhance gain of a reflectary by adjusting thickness of an air-layer is presented. Two circularly polarized arrays composed of gapped ring elements having variable rotation angles were studied. We found that gain of a reflectarray can be increased by adding a superstrate layer. The effect of an air layer is evaluated by studying radar cross section of a single element of the array. It is shown that radar cross section (RCS) varies as the thickness of the air layer is changed and there is an optimum thickness which results in a maximum RCS. Experiments show that gain of a reflectarray is also air thickness dependent and it also yields a maximum gain with the afore-mentioned optimum thickness.

1. INTRODUCTION

The conventional high-gain antennas most often used are parabolic reflectors. Although they are efficient radiators, parabolic reflectors are generally bulky in size and large in mass, due to their curved reflecting surfaces. As a result, a flat reflector using printed circuit technology is being proposed as a future candidate for high-gain antenna.

To achieve a high-gain reflectarray, several issues may draw our attention. For example, it was studied in [1] that efficiencies of a reflectarray can be improved by avoiding high losses associated with substrate materials. In [2] and [3], reflectarrays were made on FR4 materials at x band. It was demonstrated an efficiency of 25% to 32% due to high dielectric losses. However, FR4 material is cheap for the cost consideration. In [4], a technique to boost gain of an antenna by adding an air layer to an FR4 substrate was demonstrated. In this paper, we demonstrate that for a reflectarray, it is still possible to boost its gain by adding an air layer with an optimum thickness.

We use gapped ring elements combined with a variable rotation technique to achieve proper phasing between elements to construct the reflectarray. This configuration had been studied in [5] and [6]. However, no attention was focused on gain improvement in their papers. They also did not treat reflectarray with a superstrate layer.

Circularly polarized wave can easily be generated using ring elements. Adding gaps in the ring enables the direction of propagation to be reversed so that the reflected wave has the same polarization as the incident wave.

2. GEOMETRY OF THE REFLECTARRAY

Two configurations shown in Figs. 1(a) and (b) were studied. Fig. 1(a) is the normal arrangement where the rings are in front of the FR4 substrate viewing toward z-direction. While in Fig. 1(b), we place the rings on the backside of the FR4 by revolving the dielectric and rings 180 degrees on its own axis (parallel to z-axis). Geometry of each element is shown in Fig. 2. Adjacent spacing between elements is 15 mm in both x and y directions. Each reflectarray is composed of 137 elements in a 19.6 cm by 19.6 cm rectangular board.

3. RCS STUDY OF THE PROPOSED STRUCTURE

For a single element of the reflectarray shown in Fig. 1(a), we can simulate its radar cross section (RCS) value scattering from a right hand circularly polarized plane wave by varying the air thickness. For each fixed air thickness, we sweep frequency from 8 to 12 GHz. It results in a maximum RCS value of −20.5 dBsm at 9 GHz for an optimum air thickness of 2.5 mm. Optimum thickness to yield maximum RCS can also be verified by study of scattering fields from a group of four elements shown in Fig. 3. For the structure of Fig. 1(a), these elements are in front of the FR4 substrate viewing toward the z-axis. We arrange four elements sequentially rotated by 45 degrees. Since relative phase difference at a focal point duce to a relative rotation angle of φ is 2φ. Scattering fields from the four elements are equivalent to radiation fields of four elements directly fed with 90 degrees phase difference. The technique introduced here is based on a sequential rotation method to improve CP performance [7]; however, it is applied to scattering fields for the first time. It was studied that axial ratio at bore-sight is less than 4 dB from 9 to 11 GHz after scattering from the four-element model. In a reflectarray, there are many elements. However, rotation angle between adjacent elements is determined with an aim to achieving phase coherence, instead of improving CP performance. In our experiment, a CP horn is used to illuminate the array. We found that axial ratio of the whole reflectarray can be made less than 3 dB even if the reflectarray is collocated with a feed horn which has an axial ratio greater than 3 dB. Therefore, the rotation variable technique for phase coherence design in a reflectarray does have value-added effect on improving CP performance.

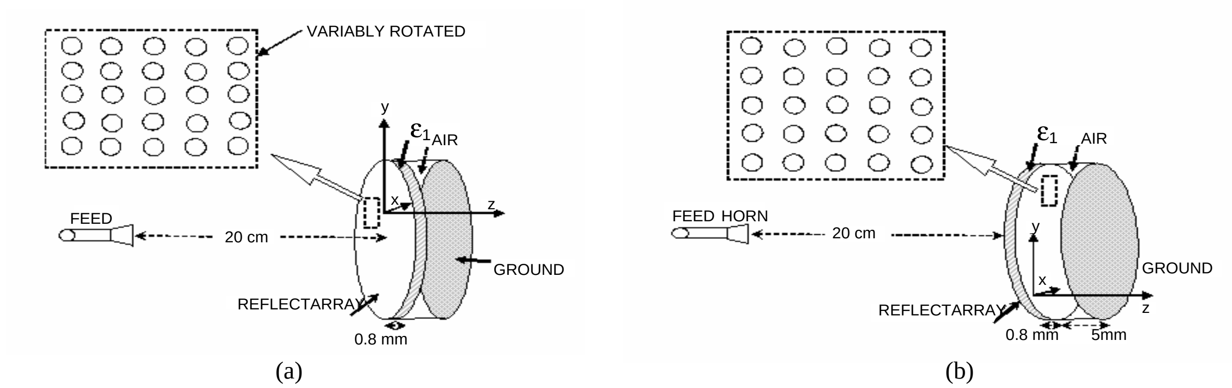

Figure 1: Two reflectarray topologies: (a) a RHCP array, (b) a LHCP array.

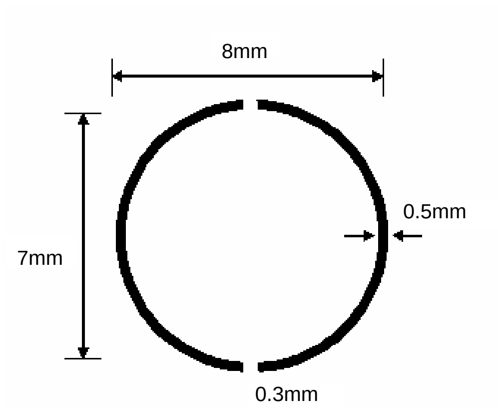

Figure 2: Geometry of the single element.

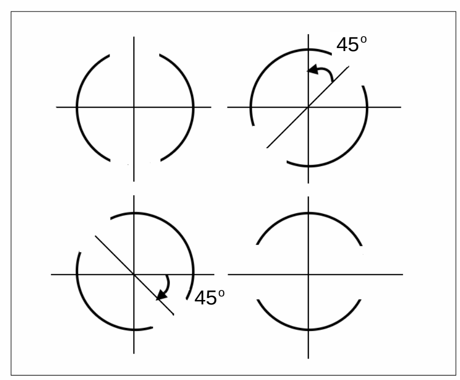

Figure 3: Model for RCS simulations.

Simulated maximum RCS values while varying the air thickness can be seen from the first and the second column of Table 1. Again, the optimum thickness is 2.5 mm. RCS value increases around 6 dB compared to that of a single element due to the enlarged area. In a reflectarray, elements are illuminated by a feed horn at a near distance instead of a far-away uniform plane wave. However, our experiments verify that optimum distance obtained by this approach is useful to determine a suitable distance to enhance gain of a reflectarray.

For the structure of Fig. 1(b), the model used for simulation contains the aforementioned four elements placed on backside of the FR4 material by revolving its own axis by 180 degrees. In this case, RCS is simulated assuming incident field being a left hand circularly polarized wave. Results are shown on the first and the third columns of Table 1. It is shown that optimum distance is 3 mm in this case. We also note that the maximum RCS value for a RHCP array is larger than that for a LHCP array.

To achieve phase coherence as is required to focus beam to the bore-sight direction, the gapped-ring elements are rotated. The centermost element has zero rotation as a reference. As the rings are placed away from the center, rotation angle increases accordingly as described in [5, 6]. The gaps in the ring are also used as a mark to identify the rotation. With these gaps, the reflected wave is a right-hand or a left-hand CP wave, as is of the same sense as the incident wave from the feed horn.

Table 1: Air-thickness dependent RCS values of four elements.

Thickness of air (mm)	RHCP RCS (dBsm)	LHCP RCS (dBsm)
1	−18.28	−13.18
1.5	−15.41	−11.35
2	−14.83	−10.90
2.5	−14.68	−10.71
3	−14.75	−10.65
3.5	−14.75	−10.70
4	−15.40	−10.87
4.5	−15.95	−11.17
5	−16.59	−11.58
5.5	−18.08	−12.08
6	−18.08	−12.68
6.5	−18.88	−13.33
7	−19.71	−14.03

4. MEASUREMENT RESULTS

Although our RCS simulation was based on only four elements, it was confirmed from experiment that this approach can be used to predict air-thickness effect on gain of a reflectarray.

Figure 4 shows measured gains by varying air-thickness of reflectarrays. The trace marked with "*o*" signs is for the RHCP reflectary. The trace with "*x*" signs is for the LHCP reflectarray. It is seen that maximum measured gain for the RHCP array occurs when the air thickness is 2.5 mm, and for the LHCP array, it occurs at 3 mm. We also found that maximum gain for the LHCP array is larger than that for the RHCP array. In Table 1, we also note that the LHCP array can provide more gain. The air thickness to yield maximum gain for both arrays is therefore predictable from Table 1. It also suggests that reflectarray with a superstrate layer has more gains.

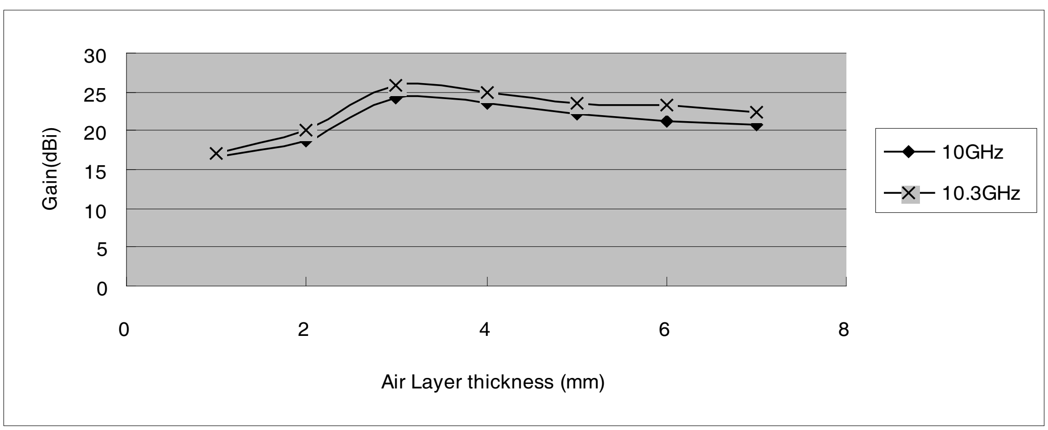

Figure 4: Measured gains of two arrays.

Maximum gain for RHCP array occurs at a frequency of 10 GHz, while for the LHCP array, it occurs at 10.3 GHz. Gains were measured by comparison with a standard liner horn antenna and were measured at the receiving end. In transmitting side, two circularly polarized transmitting antennas, one is a RHCP antenna and another is a LHCP one, were used so that we can measure both co- and cross-polarized receiving patterns of our arrays. Fig. 5 shows the measured H-plane pattern for the LHCP array at 10.3 GHz. The gain is 25.85 dBi. Cross polarization levels are greater than 20 dB. Since we use a linear polarized horn as a standard for comparison, we expect that maximum gain for the LHCP array would be 22.85 dBi if a very good circularly polarized horn is employed as a standard for comparison. Based on this data, the efficiency of our array is 35.23%, which is higher than that of reflectarrays we had made before using FR4 material.

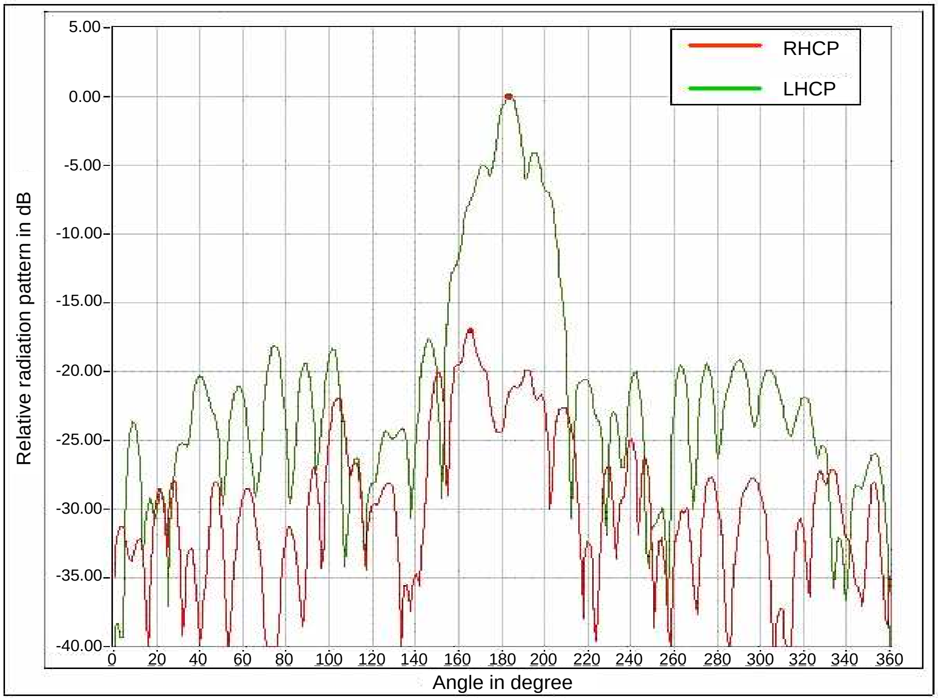

Figure 5: Measured H-plane pattern for the LHCP array at 10.3 GHz.

5. CONCLUSION

Effect of air thickness on gain of a reflectarray is studied. Aside from its conventional form shown in Fig. 1(a), we can also arrange a reflectarray by rotating its own axis to yield a configuration shown in Fig. 1(b). Fig. 1(b) displays a reflectarray using air-layer as its substrate and there is equivalent to have a superstrate. It is studied that gain is dependent on the air thickness for both configurations. Between them, array having a superstrate dielectric can result in more gain.

We also present RCS simulation results using few elements of a reflectarray as the scattered body. For a CP wave, we use 4 sequential rotated elements with an adjacent rotation angle of 45 degrees. It is studied that there is also an optimum thickness to yield a maximum RCS value. This optimum thickness can be used in a reflectarray design to enhance its gain.

REFERENCES

1. Pozar, D. M., S. D. Targonski, and H. D. Syrigos, "Design of millimeter wave microstrip reflectarrays," *IEEE Trans. Antennas Propagat.*, Vol. 45, 287–295, Feb. 1997.
2. Chang, T. N. and R. S. Hong, "Microstrip reflectarray with QUAD-EMC element," *IEEE Trans. on Antena and Propagation*, Vol. 53, No. 6, 1993–1997, June 2005.
3. Chang, T. N. and Y. C. Wei, "Proximity-coupled microstrip reflectarray," *IEEE Trans.on Antena and Propagation*, Vol. 52, 631–635, Feb. 2004.
4. Chang, T. N. and H. H. Sun, "A dual-band antenna with coplanar ring and patch," *Microwave and Optical Technology Letters,* Vol. 48, No. 9, September 2006.
5. Strassner, B., C. Han, and K. Chang, "Circularly polarized reflectarray with microstrip ring elements having variable rotation angles," *IEEE Trans. Antennas Propagat.*, Vol. 52, No. 4, 1122–1125, April 2004.
6. Han, C., C. Rodenbeck, J. Huang, and K. Chang, "A C/Ka dual frequency dual layer circularly polarized reflectarray antenna with microstrip ring elements," *IEEE Trans. on Antena and Propagation*, Vol. 52, No. 11, 2871–2876, Nov. 2004.
7. Lu, K. H. and T. N. Chang, "Circularly polarized array antenna," *IEEE Trans. on Antenna and Propagation*, Vol. 53, No. 10, 3288–3292, Oct. 2005.

Signal Attenuation of Ka Band Noise due to Rain from Small Aperture Antenna

Pongputhai Udomareyasap, **Donekeo Lakanchanh**, **Nipha Leelaruji**, **and Narong Hemmakorn**

Faculty of Engineering and Research Center for Communications and Information Technology
King Mongkut's Institute of Technology Ladkrabang (KMITL), Bangkok 10520, Thailand

Abstract— For individual reception of the digital satellite broadcasting in Ka-band, small-aperture antennas about 80 cm diameter is used. As the radiation patterns are wide in small aperture antennas and the noise temperature of antennas tend to rise. This effect is large when the receiver with lower noise factor is used. We propose the attenuation due to rain from the noise signal by measured Ka band antenna noise level at KMITL and convert to signal attenuation by noise. The measurement result indicates the rainfall rate 90 mm/hr cause to signal attenuation about 12 dB.

1. INTRODUCTION

In the tropical zone, air temperature and humidity are high throughout the year and the amount of water vapour contained in the atmosphere is higher all the time than that in the temperate zone. The noise level is high in Southeast Asia region. The atmosphere eventually contains much water vapor. Therefore, effects of attenuating media in the atmosphere received by the antenna can not be neglected. Some publications have emphasized the contributions of cosmic noise, and noise due to oxygen and water vapor absorption in the atmosphere to sky noise, but neglected the noise due to rain.

In the recent years, noise figure (NF) of LNB has been improved to $0.5 \sim 0.6$ dB level. Since NF of the receiver is improved, a slight atmospheric loss existing on the propagation path increases. Then the antenna noise temperature can reduce the CN ratio of the receiver [1]. The propagation impairments affecting on Ka band satellite links include gaseous absorption, cloud attenuation and rain attenuation on troposphere [2].

This paper is to study the attenuation of ka band signal due to rain by received the clear sky noise and rainny noise on small aperture antenna and calculate to attenuation. It is noticed that rate of receiver noise increase with lower noise figure even if atmospheric noise is reasonably low.

2. EXPERIMENTAL METHOD

The experiment parameters of Ka band noise signal and parameters of receiving system at KMITL in Bangkok are listed in Table 1.

Table 1: Parameter of receive Ka band noise.

Down link frequency	20 GHz
IF frequency from LNB	1.949 GHz
Elevation angle	62.62°E
Antenna diameter aperture	0.8 m
Rain gauge Type	Tipping bucket 0.5 mm/tip

The configuration of the propagation experiment system is illustrated in Fig. 1. The pulse numbers of rain gauge is counted to data logger and recorded by the computer parallel with the Ka band noise signal.

3. EFFECT OF ATMOSPHERIC NOISES

Radio wave absorption due to atmospheric gas in Ka-band is caused by oxygen [4], water vapour molecules, and clouds. Absorbed substances generate thermal noises and therefore added to the signal as antenna noise. As a result, rainfall attenuation, clouds, and atmospheric gas absorption

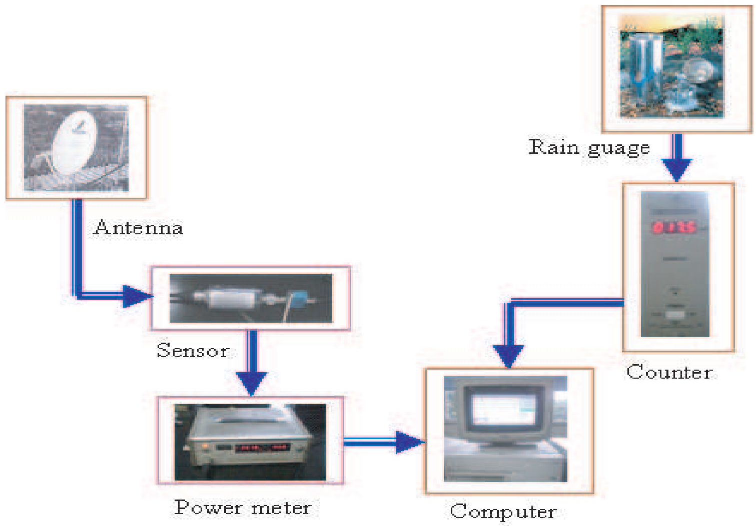

Figure 1: The experiment block diagram of receiving Ka band noise signal and rainfall rate at KMITL.

act as causes for increasing antenna noises of the receiver. In the countries close to the equator, effects of the atmosphere in Ka-band can not be ignored. Therefore, attenuation due to atmospheric noise results in reduction in CN ratio.

This experiment focus on investigate the signal attenuation of Ka-band by using radiometer method to find the signal attenuation by noise and finally analysis the collective data by new developing indirect equation that is radiometer equation. According to analysis equation, the signal attenuation of Ka-band frequency depends on the different of noise signal between clear sky condition and rain condition. The result reveals clearly that the signal attenuation of Ka-band frequency is divided into3 stages as follows: (1) noise level in clear sky condition, (2) noise level in rain cloud condition and (3) noise level in raining condition.

The clear sky noise temperature we determine on day time while the sky has no cloud and the aerosol load and moisture content in the atmosphere are low. The clear sky noise temperature given by the following equation:

$$N_{\text{clearsky}} = KT_B B \tag{1}$$

where K is Boltz'sman constant, T_B is noise temperature on antenna and noise bandwidth is B.

In raining day condition include the noise from rain cloud. Therefore increasing of noise signal level due to rain cloud absorbing and discharging. The rain also acts as a strong noise source. The noise from rain is usually higher than noise in clear sky. We calculate the noise from rain given by following equation:

$$N_{\text{rain}} = KT_B B + \left(1 - \frac{1}{L}\right) KT_M B \tag{2}$$

where N_{rain} is noise level in raining condition, L is the loss factor, T_M is equal to $1.12T_g - 50$, T_g is the surface temperature in $^\circ K$.

4. DATA ANALYSIS

In the implementing, the noise signal received from power sensor and power meter quipments has been changed to voltage level. The receiving antenna is face to the surface, that we can obtained the back body noise level higher than clear sky noise and raining noise. We can measure the signal level in none clouds day. The aerosol load and humanity content in the atmosphere are low and the noise signal in case of after raining condition, then take that result to be find signal attenuation in the next step.

The atmospheric attenuation A (dB) along a slant path from ground can calculation by.

$$A = 10 \log L \tag{3}$$

where A is attenuation, L is loses factor.

The loss factor is

$$L = \left[\frac{T_M - T_0}{T_M - T_b}\right] \tag{4}$$

where T_M is partially absorbing medium at uniform temperature, the temperature behind absorbing medium T_0 and equivalent black body temperature T_b.

In the calibration method of the signal from the measured data as $V_{(\text{blackbody})} = 0.38\,\text{V}$, and $V_{(\text{clearsky})} = 0.122\,\text{V}$ that are reference noise level and $V_{(\text{rain})}$ is depend the raining condition. We can find out signal attenuation as consider in each day then we can find any results to be replaced from related equation.

$$L = \left[\frac{T_M - T_0}{T_M - T_b}\right] = \frac{V(\text{blackbody}) - V(\text{clearsky})}{V(\text{blackbody}) - V(\text{rain})} \tag{5}$$

where $V(\text{blackbody})$ is average maximum noise level, $V(\text{clearsky})$ is noise level in clear sky condition, $V(\text{rain})$ is the noise in condition cloud and rain event.

5. MEASUREMENT RESULTS

For the rain cloud event in Fig. 2 the variance of attenuation depend on rain cloud event cause to signal attenuation peak about 1.5 dB. The estimation of cloud attenuation is not an easy subject.

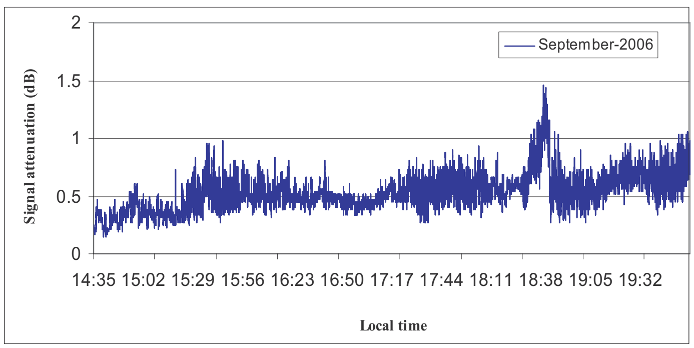

Figure 2: Signal attenuation in rain cloud event day.

As sky noise temperatures are measured in a slant path there is always the possibility that any fade event is caused by precipitation also and not only by clouds, even if information from nearby measurements of rain rate is available. Also even if a precipitating event can be detected the starting and ending time can not be fully identified. It is also expected that rain events also have some cloud contribution.

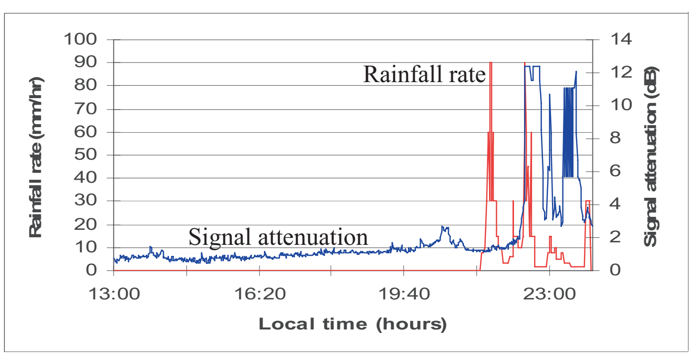

Figure 3: Signal attenuation cause by rain on 29-Aug-2006.

Figure 3 is indicated signal attenuation cause by rain, we found that on 29-Aug-2006 the high rainfall rate is 90 mm/hr cause to signal attenuation about 12 dB. This attenuation may cause fading in the communication link along the propagation path.

In Fig. 4 signal attenuation cause by rain on 12-September-2006 the rain intensity is 60 mm/hr cause to signal attenuation about 7 dB. In case of small rainfall rate 6 mm/hr cause to signal attenuation 3.2 dB in Fig. 5. It probably occur because the rain fall in the slant path is higher than in the experiment site.

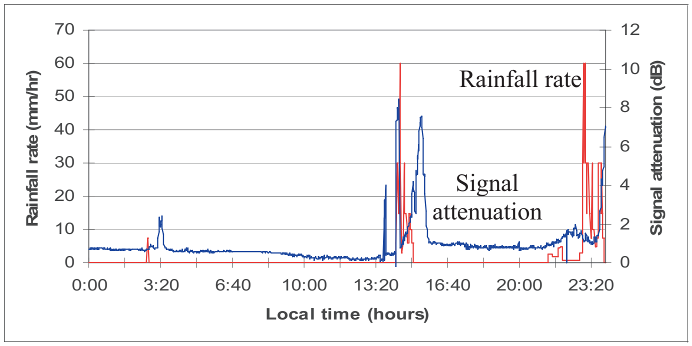

Figure 4: Signal attenuation cause by rain on 12-Sep-2006.

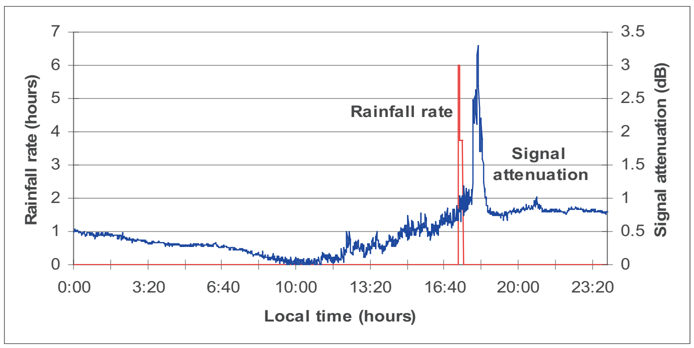

Figure 5: Signal attenuation cause by rain on 18-Sep-2006.

The performance of a communication satellite link is influenced by the fact that rain is not only attenuates the signal but also adds thermal noise to the other sources of sky noise. The influence of sky noise on the choice of communication satellite system parameters has been studied for some time.

6. CONCLUSION

This paper indicated the effect of noise in Ka band satellite signal. The effects of attenuating media in the atmosphere received by small aperture antenna such as cloud and rain is major of propagation loss in satellite communication links especially in tropical area. We propose the measurement of noise in clear sky, cloud and rain events to analyze the signal attenuation by small aperture antenna. Such as result before raining the attenuation due to cloud about 1.5 dB and the signal attenuation increase to 12 dB during 90 mm rainfall rate

ACKNOWLEDGMENT

The authors are grateful thanks to AUN/SEED - Net and King Mongkut's Institute of Technology Ladkrabang for technical support.

REFERENCES

1. Paungma, T., E. Shibuya, T. Kamimura, Y. Iituka, and Y. Moriya, "Comparison of measurements of carrier to noise ratios of small-aperture antenna satellite-broadcast reception," Vol. ITE 49, No. 3, 366–374, 1995.
2. Altshuler, E. E., Falconne, Jr., and K. N. Wulfsberg, "Atmospheric effects on the propagation at millimeter wavelengths," *IEEE Spectrum*, 83–90, July 1968.
3. Recommendation ITU-R P.618-7, "Propagation data and prediction methods required for the design of earth-space telecommunication system," ITU-R P. 618-7, 2001.

4. Smith, E. K., "Centimeter and millimeter wave attenuation and brightness temperature due to atmospheric oxygen and water vapor," *Radio Science*, Vol. 17, No. 6, 1455–1464, Nov.–Dec. 1982.
5. Hall, M. P. M., M.Sc, C.Eng, M.I.E.E. M.Inst.P., "Effects of the troposphere on radio Communication," 74–77, 1979.

On Analysis of Planar Antennas Using FDTD Method

K. Niikura[1], **R. Kokubo**[1], **K. Southisombath**[2], **H. Matsui**[1], **and T. Wakabayashi**[3]

[1]Graduate School of Engineering, Tokai University, Japan
[2]Faculty of Engineering, National University of Laos, Lao PDR, Laos
[3]School of Information Science and Engineering, Tokai University, Japan

Abstract—The FDTD method is a powerful method for analysis of electromagnetic fields in microwave circuits and devices, antennas, optical devices and transmission lines. In this paper, numerical conditions in analysis of planar antennas using the FDTD method are considered and found for a planar dipole antenna. The obtained results are compared with other and experimental results.

1. INTRODUCTION

The planar antennas that are useful for mobile communications have been developed for many researchers. The FDTD method is a powerful method for analysis of planar antennas that are defined as antennas that have planar shapes. We have analyzed several kinds of planar antennas for mobile communications.

In this paper, numerical conditions in analysis of planar antennas using the FDTD method [3] are considered and found for a planar dipole antenna. In order to use the method, it is important to decide the number of layers of the PML and the distance between the antenna and the wall of the analytical area. If they are decided appropriately, the computational time and memories are saved. Therefore, the relation between them is discussed precisely. The FDTD method which used their numerical values are applied to several planar antennas [1, 2]. The obtained results are compared with other and experimental results.

2. FDTD METHOD

Figure 1 shows an analytical area in the FDTD method. The cell size is assumed to be $dx = dy = dz = \Delta$ mm. The PML that has M layers is assumed as the absorbing boundary. The time step dt is decided by the following Courant stability condition, where c is the velocity of light in the free space.

$$dt \leq \frac{1}{c\sqrt{\left(\frac{1}{dx}\right)^2 + \left(\frac{1}{dy}\right)^2 + \left(\frac{1}{dz}\right)^2}} \tag{1}$$

The Gaussian pulse is used as an input pulse to analyze. The feeding method is 1cell delta gap feed.

The distance D between the antenna and the wall of analytical area is assumed in each direction as shown in Fig. 1. In Fig. 1, D includes the number of layers M of the PML.

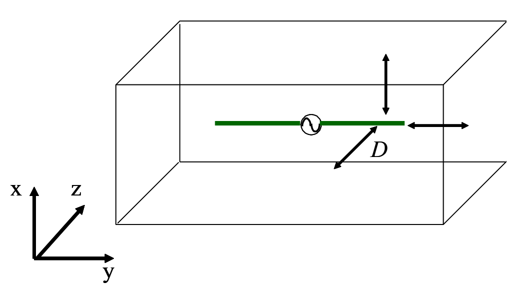

Figure 1: Analytical area.

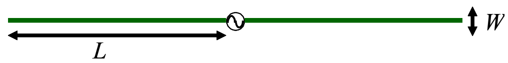

Figure 2: Structure of planar dipole antenna.

3. ANALYTICAL PARAMETERS OF THE FDTD METHOD

Let's consider a planar dipole antenna in free space as shown in Fig. 2 as an example of consideration of analytical parameters of the FDTD method. An element of planar dipole antenna (PDA) is assumed to be $2L$ mm in length, W mm in width and infinitesimal thin.

The element is also assumed to be a lossless conductor. The PDA is placed in the analytical area to analyze as shown in Fig. 1. In this case, the PML as the absorbing boundary is included in the D. Since it is seemed that the accuracy of the numerical result depends on the distance D and the operating wavelength of the PDA, the numerical analysis is implemented for several lengths of antenna elements.

We select that $\Delta = 1$ mm, $L = 90$ mm, and W is infinitesimal small as a numerical example. The design frequency of PDA is 0.833 GHz. Fig. 3 shows the convergence of first resonance as a function of the number of layers (M) with the numerical parameter D. The parameter D is the same distance along the three axes x, y, z. From Fig. 3, the first resonance frequency converges with increasing M, even if D is any kind of value more than 20. And when $D = 20$ and $D = 100$, the first resonance frequency converges even if M is any kind of value more than 8. Table 1 shows an illustration of the rate of convergence for the resonance frequency. When $D = 20$ and $D = 100$ the convergent frequency is 0.784 GHz. From the above results, it is clear that $D = 20$ is the satisfied distance even if M is more than 8. When $\Delta = 0.5$ mm, the first resonance frequency is 0.800 GHz. This frequency is close to 0.833 GHz.

Figure 4 shows return loss of PDA for $M = 8$ and $D = 20$. It has three resonance frequencies between 0 GHz and 5 GHz. The current distributions of each resonance frequencies are shown in Fig. 5. It is shown that the resonance points exist at 0.5λ, 1.5λ and 2.5λ in length of PDA. Fig. 6 shows the radiation patterns at the resonance frequencies. The radiation patterns analyzed by our

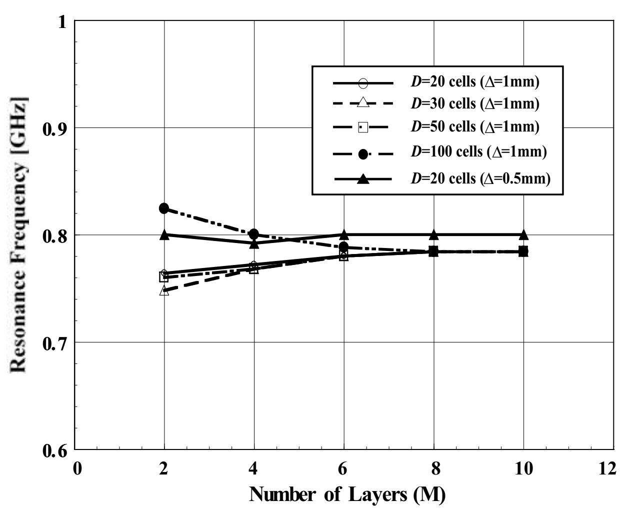

Figure 3: Convergence of the first resonance frequency.

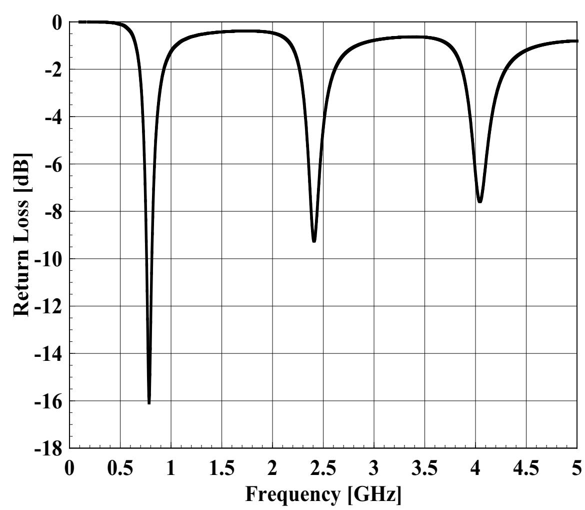

Figure 4: Characteristic of return loss.

Table 1: An illustration of the rate of convergence for the resonant frequency.

Δ [mm]	M [Layers] / D [cells]	2	4	6	8	10
1	20	0.76431	0.77231	0.78032	0.78432	-
	30	0.74830	0.76831	0.78032	0.78432	0.78432
	50	0.76031	0.76831	0.78032	0.78432	0.78432
	100	0.82433	0.80032	0.78832	0.78432	0.78432
0.5	20	0.80032	0.79232	0.80032	0.80032	-

(a) (b) (c)

Figure 5: Current distributions at each wavelength. (a) 0.5λ (0.784 GHz), (b) 1.5λ (2.409 GHz), (c) 0.5λ (4.041 GHz).

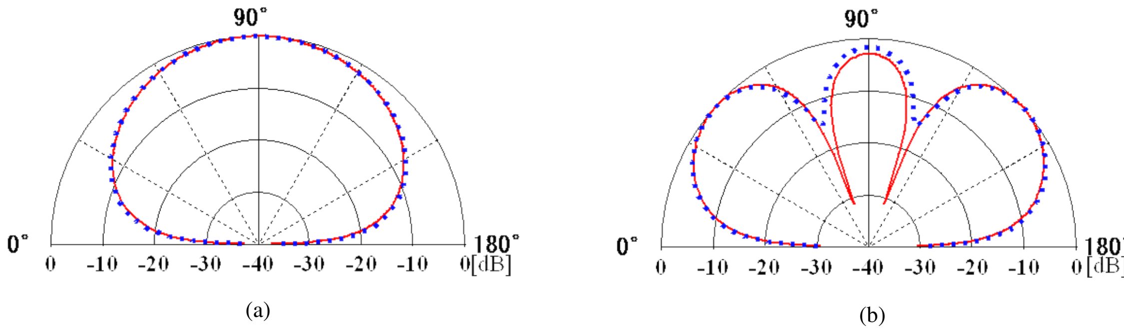

Figure 6: Characteristics of radiation patterns at each wavelength. (a) 0.5λ (0.784 GHz), (b) 1.5λ (2.409 GHz).

method are compared with the radiation patterns obtained by assuming an ideal sinusoidal current distribution with zero current at the end points of the dipole antenna [4]. Those results are in good agreement.

4. NUMERICUL APPLICATIONS AND EXPERIMENTS

Numerical applications are described for several planar antennas. Their experimental results are shown in figures.

4.1. Planar Dipole Antenna (PDA) on the Dielectric Substrate

Figure 7 is the structure of the planar dipole antenna on the dielectric substrate ($L_d = 225$ mm, $W_d = 70.0$ mm, $h = 3$ mm, $\varepsilon_r = 6.68$). Fig. 8 shows return loss for a planar dipole antenna that is printed on the dielectric substrate. In this figure, three resonance frequencies are shown in

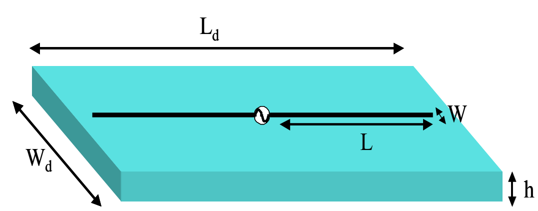

Figure 7: Structure of PDA on the dielectric substrate.

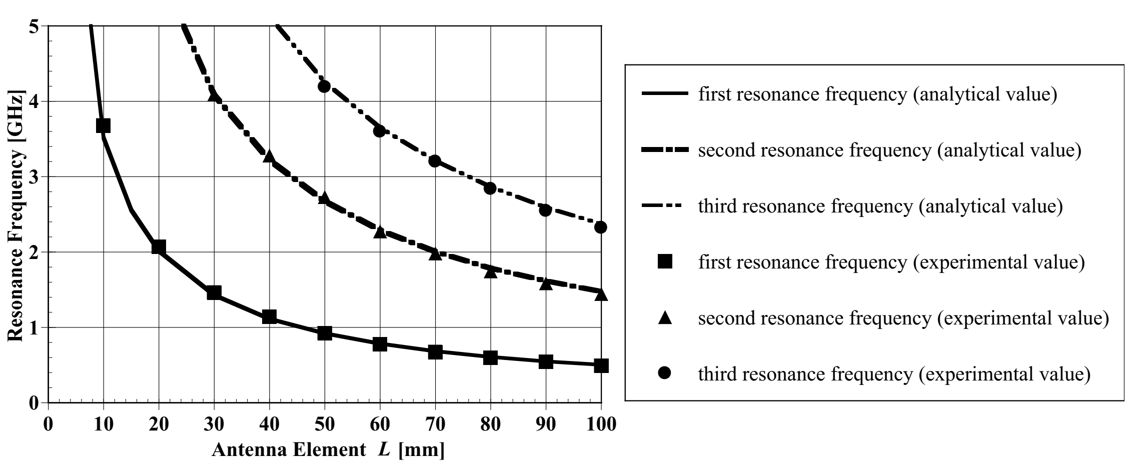

Figure 8: Analytical and experimental results of resonance frequency.

three kinds of lines, respectively and their experimental results are plotted. Analytical results are coincident with experimental results.

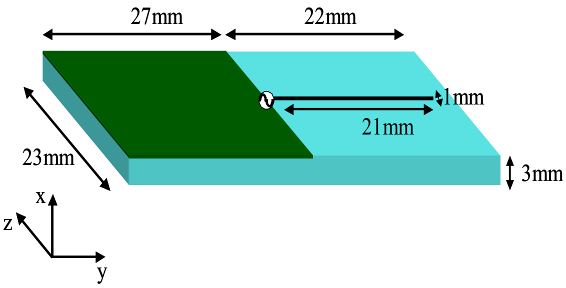

Figure 9: Structure of DMA on the dielectric substrate.

4.2. Planar Monopole Antenna (PMA) on the Dielectric Substrate

Figure 9 shows a structure of a planar monopole antenna, which consists of a monopole element and ground plane (27.0 mm×23.0 mm) on the dielectric substrate (49.0 mm×23.0 mm, $h = 3$ mm, $\varepsilon_r = 6.68$). An illustration of the rate of convergence of the first resonance frequency is shown as a function of the number of layers M in Fig. 10. The return loss of the first resonance frequency is shown in Fig. 11 and also compared with experimental result.

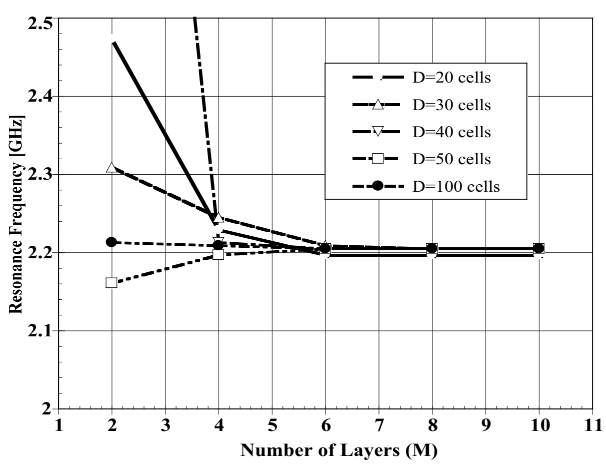

Figure 10: Convergence of the first resonance frequency.

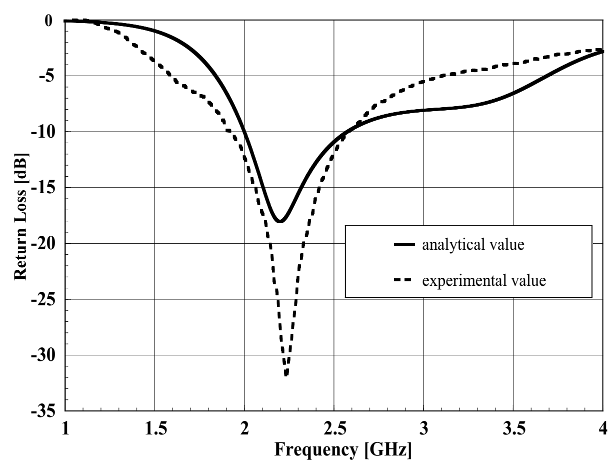

Figure 11: Characteristics return loss of PMA on the dielectric substrate.

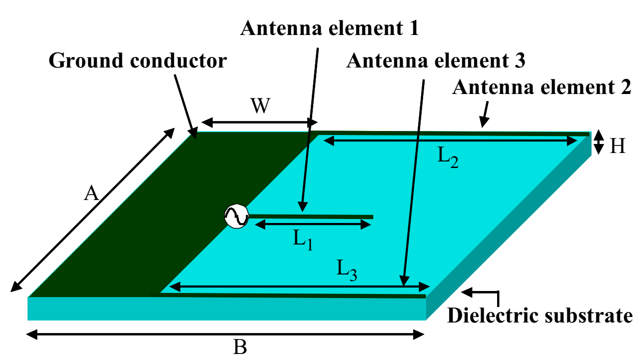

Figure 12: Structure of BEPA.

4.3. Basic E-type Planar Antenna (BEPA)

A structure of a basic E-type planar antenna (BEPA) is shown in Fig. 12. In Fig. 12, the BEPA has three antenna elements and the ground conductor that are printed on dielectric substrate ($A \times B$).

Table 2: Numerical examples of parameters.

Parameter	[mm]	Parameter	[mm]
L_1	19.0, 23.0, 27.0	H	3.0
L_2	67.5	A	55.0
W	19.0	B	86.5
ε_r	6.68	-	-

Their antenna element i ($i = 1 \sim 3$) has a length L_i ($i = 1 \sim 3$) and a width W_i ($i = 1 \sim 3$), respectively. The ground conductor has a width W and a length A.

Characteristics return loss of the BEPA that are shown in Fig. 13 as parameter of L_1. Resonance frequencies f_{B1}, f_{B3}, and f_{B4} are constant for different values of L_1 (Fig. 13). However, resonance frequency f_{B2} changes according to the length of the antenna element L_1. Fig. 14 shows the analytical and experimental results. Both of them are in good agreement.

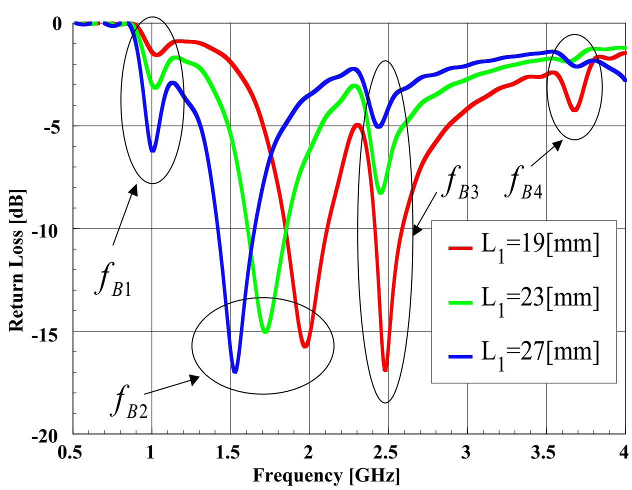

Figure 13: Return loss of BEPA for parameter L_1.

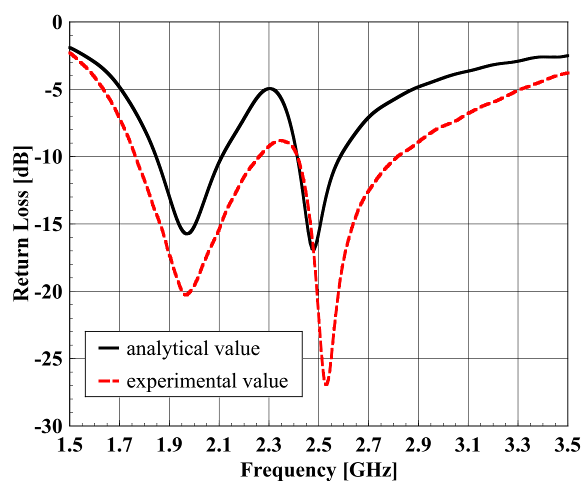

Figure 14: Analytical and experimental results.

5. CONCLUSIONSPARAMETERS

in analysis of planar antennas using the FDTD method are considered. From analytical results, the value of the distance D between the antenna and the wall of analytical area and the number of layers M were found for the cell size. By using them we could obtain reasonable results for several applications. Their results agreed with experimental results.

In future our analytical method using the FDTD method will be applied for many applications.

REFERENCES

1. Wakabayashi, T., K. Southisombath, et al., "Miniaturization and broadband characteristics of E-type planar antennas for mobile communications," *WEAS Trans. on Communications*, Vol. 5, Issue 9, Sep. 2006.
2. Kokubo, R., et al., "Consideration of analytical parameters in FDTD method for planar antenna analysis," *KJJC2006*, Vol. EMT4-12, 417–420, Sep. 2006.
3. Uno, T., *Finite Difference Time Domain Method for Electromagnetic Field and Antennas,* Corona Publishing, 1998.
4. Balanis, C. A., *Antenna Theory*, John Wiley & Sons Inc, 1982.

Design Narrow Slot Antenna for Dual Frequency

C. Chulvanich[1,2], **J. Nakasuwan**[1], **N. Songthanapitak**[1]
N. Anantrasirichai[3] **and T. Wakabayashi**[4]

[1]Department of Electronic and Telecommunication Engineering, Faculty of Engineering
Rajamangala University of Technology Thanyaburi (RMUTT) Klong 6
Thanyaburi, Pathumthanee, Thailand
[2]Department of Electronic and Telecommunication Engineering, Faculty of Engineering
Rajamangala University of Technology Phra Nakhon (RMUTP) North Bangkok
Bangkok 10800, Thailand
[3]ReCCIT, Faculty of Engineering, King Mongkut's Institute of Technology Ladkrabang
Bangkok 10520, Thailand
[4]School of Information Science and Technology, Tokai University
Hirasuka, Kanagawa 259-1292, Japan

Abstract— The narrow slot loop antenna and linear slot antenna fed by microstrip line are designed for dual frequency at 2.44 GHz and 5.25 GHz on the standard of IEEE 802.11b/g (2.4–2.4835 GHz), IEEE 802.11j/a (5.15–5.35 GHz), and IEEE 802.16d (5.7–5.9 GHz). These structures are easy to adjust the length of slot antenna for dual frequency band. It can control the higher frequency band around 4.9 GHz to 5.8 GHz by linear slot antenna. Adjusting some parameters of narrow slot loop antenna will influence on the resonance frequency and bandwidth. By using IE3D software [1], the characteristics of antenna are investigated and analyzed, including instance input impedance, return loss and far field radiation patterns.

1. CONCEPT OF LINEAR NARROW SLOT ANTENNA

The slot antennas in this paper are designed on FR4 (dielectric constant $\varepsilon_r = 4.5$) with thickness of 1.6 mm. The simple slot antenna is linear narrow slot antenna which is easy to control the resonance frequency by adjusting the length of slot antenna. The simple structure of single linear slot antenna is shown in Figure 1.

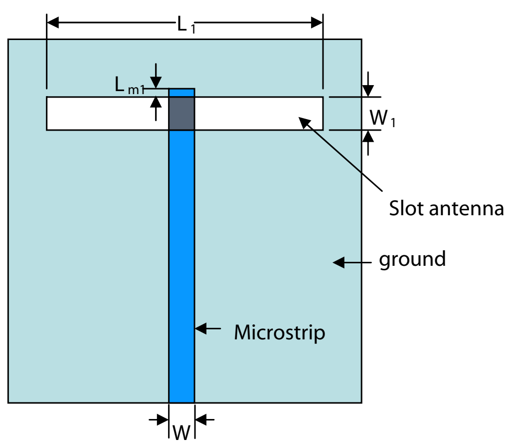

Figure 1: Simple structure of linear slot antenna.

The length of linear slot antenna L_1 is designed for 2.44 GHz which referred with wavelength in the substrate λ_g that can be calculated by following:

$$\lambda_0 = \frac{c}{f} \tag{1}$$

$$\lambda_g = \frac{\lambda_0}{\sqrt{\varepsilon_{eff}}} \tag{2}$$

where ε_{eff} is the effective dielectric constant

$$\varepsilon_{eff} = \frac{\varepsilon_r + 1}{2} + \frac{\varepsilon_r - 1}{2}\left[1 + 12\frac{h}{w}\right]^{-1/2} \tag{3}$$

In this case, $\lambda_g = 74.14$ mm at frequency 2.44 GHz.

The width of microstrip line is designed for match impedance with the characteristic impedance of transmission line 50 ohms which can be calculated by following:

$$\frac{w}{h} = \frac{2}{\pi}\left\{B - 1 - \ln(2B-1) + \frac{\varepsilon_r - 1}{2\varepsilon_r}[\ln(B-1)] + 0.39 - \frac{0.61}{\varepsilon_r}\right\} \tag{4}$$

where $B = \frac{60\pi^2}{Z_0\sqrt{\varepsilon_r}}$ and Z_0 is characteristic impedance.

In this case, width of microstrip line: $W = 3.0$ mm.

At designed frequency of 2.44 GHz, the length of slot antenna $L_1 = 35.8$ mm $(0.48\lambda_g)$. The width of linear slot antenna W_1 is varied in five values beginning from 2.5 mm to 5 mm by step up 0.5 mm, and L_{m1} is adjusted for match impedance. The simulation results of return loss S_{11}, resonance frequency, frequency range and bandwidth are tabulated in Table 1. It shows that the changing in width of slot antenna will affect on the resonance frequency. When the width of slot is increased, the resonance frequency will decrease and bandwidth is wider. Therefore, if we increase the width of slot, the length of slot should be decreased in order to achieve the same resonance frequency and wider bandwidth.

Table 1: The simulation results of slot antenna by adjusting W_1.

W_1 (mm.)	Resonance Freq. (GHz)	Freq. Range (GHz)	Bandwith (MHz)	Return Loss S_{11} (dB)
2.5	2.52	2.46–2.58	120	−20.9
3.0	2.49	2.425–2.56	135	−27.9
3.5	2.46	2.39–2.54	150	−41.5
4.0	2.43	2.355–2.51	155	−27.1
5.0	2.40	2.325–2.48	155	−21.7

2. ANTENNA STRUCTURE OF NEW DESIGN

The new design for low frequency is done by developing linear slot antenna as refer in Figure 1 to narrow slot loop antenna, as shown in Figure 2. There are six parameters in this structure used to control frequency and match impedance, namely L_1, L_3, W, W_1, s, and Lm_1. In this research, we fixed the value of L_1, W, W_1, s, and Lm_1 to 35.8 mm, 3.0 mm, 2.5 mm, 0.5 mm and 0.5 mm, respectively. When varying the value of L_3 from 0.25 mm to 10.0 mm, it will affect on the range of bandwidth. Therefore, some value of L_3 can achieve the frequency band in the standard of IEEE 802.11 b/g; 2.4–2.4835 GHz, as shown in Table 2. This table shows that the adjusting of L_3 will affect on the frequency band, so the parameter L_3 is sub-control and W_1 is the main control for finding the required frequency bandwidth.

Table 2: The simulation results of single narrow slot loop antenna by vary L_3.

L_3 (mm.)	Resonance Freq. (GHz)	Freq. Range (GHz)	Bandwith (kHz)	Return Loss S_{11} (dB)
0.25	2.48	2.42–2.54	125	−32.9
0.5	2.475	2.415–2.54	125	−31.9
1.0	2.465	2.405–2.525	120	−30.4
3.0	2.44	2.385–2.5	115	−29.6
3.9	2.435	2.38–2.495	115	−29.1
5.0	2.425	2.37–2.485	115	−25.9
6.0	2.425	2.37–2.48	110	−27.4
10.0	2.425	2.37–2.48	110	−25.9

Table 2 shows various lengths of L_3 between 0.25 mm–10.0 mm. The length of L_3 will affect on resonance frequency, bandwidth and return loss. It can be seen that the resonance frequency, bandwidth and return loss will decrease when L_3 is increased.

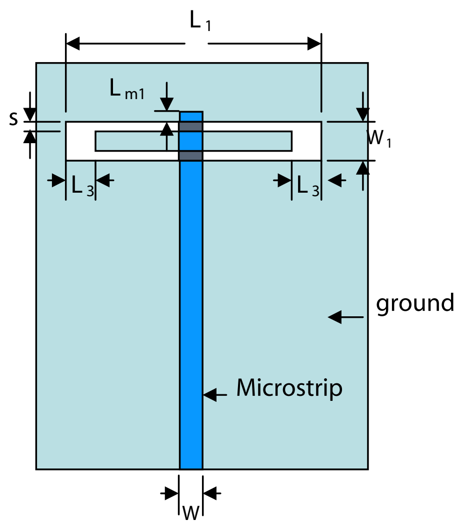

Figure 2: Structure of slot loop antenna for single low frequency.

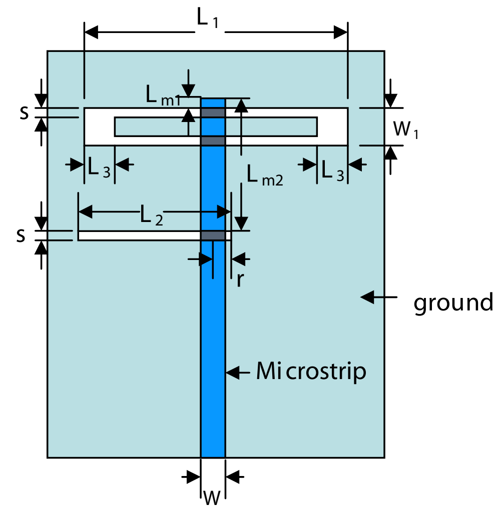

Figure 3: Structure of slot antennas for dual frequency.

Finally, a novel slot antenna for the dual frequency is proposed by inserting short linear narrow slot antenna below narrow slot loop antenna as illustrated in Figure 3. The new parameters of this structure are: L_2, Lm_2, and r. The parameter L_2 is the length of the linear narrow slot which use for achieving the higher resonance frequency in order to support the standard of IEEE 802.11j/a (4.90–5.091/5.15–5.35 GHz) or IEEE 802.16d (5.7–5.9 GHz). In this case, the length of linear narrow slot L_2 depends on the desired frequency. For the good results of S_{11}, we will set the parameter r to 2.0 mm and adjust L_{m2} for match impedance of 50 ohms.

3. RESULTS AND DISCUSSION

The simulation results in various different lengths L_2 and adjusts L_{m2} for matching impedance of 50 ohms at low frequency and high frequency are shown in Table 3.

Table 3: Simulation results by adjust L_2, L_{m2}.

Paramenter		Lower Frequency (GHz)			Upper Frequency (GHz)		
L_2 (mm)	L_{m2} (mm)	Resonance Freq.	Freq. Range	Return Loss S_{11} (dB)	Resonance Freq.	Freq. Range	Return Loss S_{11} (dB)
20.18	11.68	2.44	2.38–2.505	−38	4.945	4.84–5.11	−38
20.00	11.58	2.44	2.38–2.505	−38.9	4.995	4.86–5.155	−48.9
18.95	10.8	2.44	2.38–2.505	−43.6	5.25	5.125–5.39	−61.4
17.3	8.08	2.435	2.375–2.5	−40.5	5.8	5.53–5.965	−40.2

Table 3 shows the return loss, resonance frequency, and frequency range by fixing the L_3 to 3.9 mm, and adjusting the length L_2 and L_{m2} for dual frequency at lower resonance frequency 2.44 GHz and higher frequency from 4.945 GHz to 5.8 GHz. When the length of L_2 is decreased, the distance L_{m2} which is used for match impedance will be decreased, and the resonance frequency of the upper frequency will increase. However, the resonance frequency and frequency range of the lower frequency are slightly changed. The return loss of the lower frequency and the higher frequency are also shown in Table 3.

The simulation result of the return loss S_{11} of Figure 3 with different length of L_2 is shown in Figure 4.

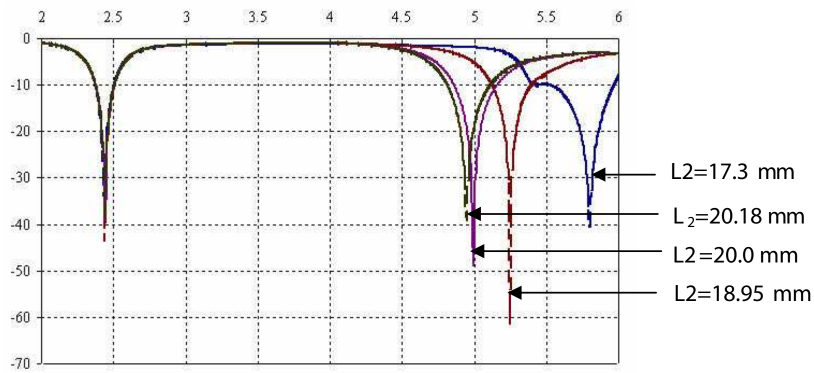

Figure 4: Return loss for dual resonance frequency of difference L_2.

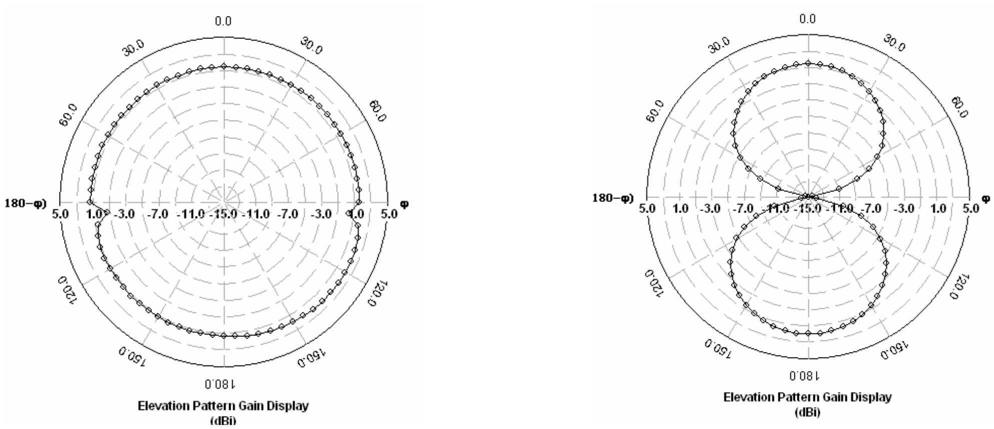

(a) (b)

Figure 5: Radiation pattern of E-total at 2.44 GHz, (a) yz plane ($\phi = 90°$), (b) xz plane ($\phi = 0°$).

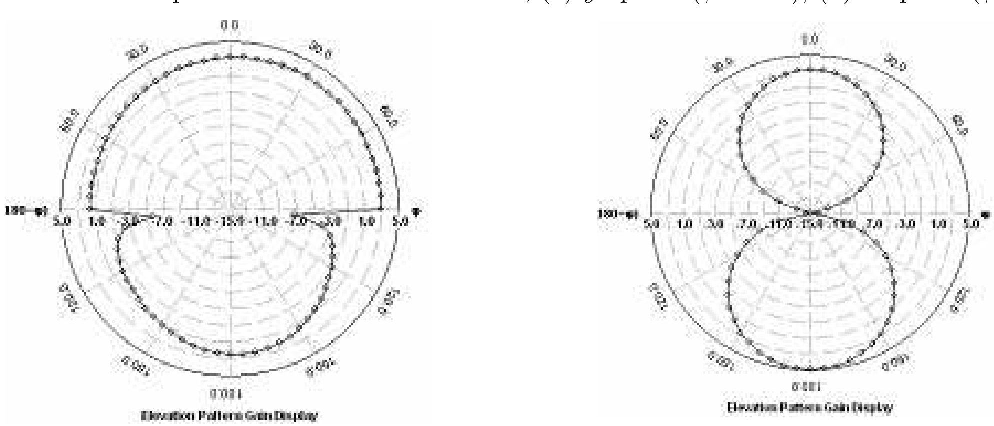

(a) (b)

Figure 6: Radiation pattern E-total at 5.25 GHz, (a) yz plane ($\phi = 90°$), (b) xz plane ($\phi = 0°$).

4. RADIATION PATTERN

The radiation pattern on yz-plane and xz-plane at frequency 2.44 GHz and 5.25 GHz are shown in Figure 5 and Figure 6.

5. CONCLUSIONS

In this paper, a narrow slot loop antenna and linear slot antenna were designed for dual frequency. The former was accomplished at the lower frequency on standard frequency by IEEE 802.11b/g and the latter was done at the higher frequency on standard frequency by IEEE 802.11j/a and IEEE 802.16d. The new design of narrow slot loop antenna with using the technique of adjusting L_3 can achieve the good match impedance for lower and higher resonance frequency.

REFERENCES

1. IE3D User's Manual Release 9, Zeland software, Inc., U.S.A., 2002.
2. Balanis, C. A., *Antenna Theory Analysis and Design*, John Wiley & Sons, Inc., 1997.
3. Benson, F. A. and T. M. Benson, *Fields Waves and Transmission Line*, Chapman & Hall, 1991.
4. Anantrasirichai, N., P. Rakluea, and T. Wakabayachi, "Slot antenna coupled by microstrip line for dual frequency," *ISITA/NOLTA 2002*, 635-638, October 7–11, 2002.

A Recursive Street Canyon Model for Low Height Terminal System

S. Kang and C. Tzaras
Centre for Communication Systems Research, University of Surrey, UK

Abstract— A novel recursive street canyon model is proposed for propagation in low height terminal system. This model combines a street canyon method and a recursive method together, describing the path loss of all street types (LOS, NLOS1, NLOSn) with a unified expression. Related parameters in the expression, such as recursive distance, street intersection number, street intersection orientation, street intersection separating distances, are achieved by a simplified ray tracing platform which considers only one ray along each street. Compared with present street canyon model and recursive model, this proposed model not only has a much simpler expression but also shows a higher prediction precision.

1. INTRODUCTION

The concept of relaying and multi-hop [1, 2] brings the research on propagation models between low height terminals. Usually, in simulating such relaying link with low height transmitter, it's better to differentiate line-of-sight (LOS) and non-line-of-sight (NLOS). Further, for NLOS, it can be classified as one-corner type (NLOS1), two-corner type (NLOS2) and n-corner type (NLOSn, $n > 2$), with NLOS1 and NLOS2 are the most concern. In [3], street canyon models are proposed for both LOS and NLOS but with different expressions. What's more, this NLOS model and also some other physical models in [4] considers actually only the NLOS1 case. The recursive model in [5, 6] can trace any street type with arbitrary crossings but shows an over estimation in case of a big number of corners.

This paper combines the idea of street canyon method and that of recursive method, putting forward a recursive street canyon model. This model has a simple but unified expression and is suitable for all street types. It's easy to use in simulation and in reality.

2. STREET CANYON METHOD

In [3], both LOS and NLOS are considered as propagating in street canyons when transmitter and receiver are both below roof-top level. Different models are proposed for LOS and NLOS. The LOS is modelled by two bounds, a lower one and an upper one, each is represented by a dual-slope.

$$L_{LOS,l} = -6 + 20\log_{10}\left(\frac{4\pi}{\lambda}\right) + \begin{cases} 20\log_{10}(d) & d \le d_b \\ 20\log_{10}(d_b) + 40\log_{10}(d/d_b) & d > d_b \end{cases} \tag{1}$$

$$L_{LOS,u} = 14 + 20\log_{10}\left(\frac{4\pi}{\lambda}\right) + \begin{cases} 20\log_{10}(d_b) + 25\log_{10}(d/d_b) & d \le d_b \\ 20\log_{10}(d_b) + 40\log_{10}(d/d_b) & d > d_b \end{cases} \tag{2}$$

$$d_b = 4h_t h_r/\lambda \tag{3}$$

where $L_{LOS,l}$ and $L_{LOS,u}$ are the lower and upper bound path loss, d is the distance from transmitter [m], d_b is the breakpoint distance, h_t and h_r are transmitter and receiver height, and λ is the wavelength. The NLOS is modelled by a sum of reflection and diffraction components.

$$L_{NLOS} = -10\log_{10}\left(10^{-L_r/10} + 10^{-L_d/10}\right) \tag{4}$$

$$L_r = 20\log_{10}\left(\frac{4\pi}{\lambda}\right) + 20\log_{10}(d_1 + d_2) + \frac{d_1 d_2}{w_1 w_2}\frac{3.86}{\theta^{3.5}} \tag{5}$$

$$L_d = -29 + 20\log_{10}\left(\frac{4\pi}{\lambda}\right) + 10\log_{10}(d_1 d_2 (d_1 + d_2)) + \frac{18\theta}{\pi} + \frac{40}{\pi}\left(\mathrm{tg}^{-1}\left(\frac{d_1}{w_1}\right) + \mathrm{tg}^{-1}\left(\frac{d_2}{w_2}\right)\right) \tag{6}$$

where L_r and L_d are the reflection and diffraction component, w_1 and w_2 are the LOS and NLOS street width, θ, d_1 and d_2 are the orientation [arc] and separating distances at the street crossing, $d_1 + d_2$ means a recursive distance from the transmitter.

Comparing expression (4)–(6) with (1)–(3), we can simply say that for street canyon method, NLOS considers an extra component relative to LOS. This extra component relates to the street orientation, separating distances and street widths.

3. RECURSIVE METHOD

In [5, 6], a computer efficient ray tracing platform is performed which considers only one single ray propagating along each street, as shown in Figure 1. An illusory distance is achieved by the

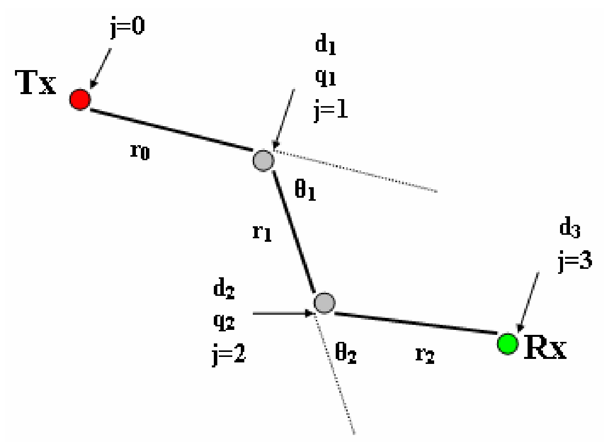

Figure 1: Recursive method with simple ray tracing platform.

following recursive expression

$$d_n = \sum_{j=0}^{n-1} r_j + \sum_{i=0}^{n-2} r_i \sum_{j=i+1}^{n-1} r_j \sum_{k=i}^{j-1} q_k + \sum_{i=0}^{n-3} r_i \sum_{j=i+1}^{n-2} r_j \sum_{k=j+1}^{n-1} r_k \sum_{h=i}^{j-1} q_h \sum_{l=j}^{k-1} q_l + \cdots \tag{7}$$

$$d_r = \sum_{j=0}^{n-1} r_j \tag{8}$$

where d_n is the illusory distance of the nth node, d_r is the recursive distance of the nth node, r_j is the physical distance at the jth node, q_j is a function for the street orientation θ_j. A dual-slope model is built based on the illusory distance and the recursive distance.

$$L = 20\log\left(\frac{4\pi}{\lambda}\right) + \begin{cases} 20\log_{10}(d_n) & d_r \le d_b \\ 20\log_{10}(d_n d_r/d_b) & d_r > d_b \end{cases} \tag{9}$$

From formula (7)–(9), we can see that this recursive model has an over estimation at large distances with multiple crossings, because the illusory distance increases exponentially with the recursive distance and the crossing number. Approximately, for zero street crossing, namely LOS, the path loss exponent will be about 4; for one street crossing, namely NLOS1, the path loss exponent will be about 6; for two street crossings, namely NLOS2, the path loss exponent will be about 8; and for n street crossings, namely NLOSn, the path loss exponent will be about $2(n+2)$.

4. PROPOSED MODEL

The proposed model tries to combine the idea of above street canyon method and recursive method but avoid their disadvantages. It has the following characteristics:

(1) It is a dual-slope model.
(2) It has a unified expression for LOS and all types of NLOS streets.
(3) For LOS, only recursive distance from transmitter is considered.
(4) For NLOS1, an extra path loss relative to LOS is considered. This extra path loss is a function of the crossing orientation and separating distances.
(5) For NLOS2, a weighted extra path loss relative to NLOS1 is considered.

(6) Similarly, for NLOSn, a weighted extra path loss relative to NLOSn-1 is considered.
(7) The weighted value decreases with the crossing number.

This proposed model is expressed as

$$L = c_1 + 20\log\left(\frac{4\pi}{\lambda}\right) + \sum_{j=1}^{n-1} W_j \cdot L_{extra}\left(r_{j-1},\, r_j,\, \theta_j\right) + \begin{cases} 10n_1\log_{10}(d_r) & d_r \le d_b \\ 10n_1\log_{10}(d_b) + 10n_2\log_{10}(d_r/d_b) & d_r > d_b \end{cases} \tag{10}$$

$$L_{extra}\left(r_{j-1},\, r_j,\, \theta_j\right) = c_2\log_{10} r_{j-1} + c_3\log_{10} r_j + c_4\log_{10}\theta_j \tag{11}$$

$$W_j = \begin{cases} 0 & j \le 0 \\ 1 & j = 1 \\ c_5 e^{-j} & j > 1 \end{cases} \tag{12}$$

where L is the predicted path loss, $L_{extra}\left(r_{j-1},\, r_j,\, \theta_j\right)$ is the extra path loss [dB] at the jth street crossing with orientation θ_j [arc] and separating distances r_{j-1}, r_j, W_j is the weighting function, n_1, n_2 are path loss exponents, and c_1, c_2, c_3, c_4, c_5 are constants.

According to formula (10), for LOS, NLOS1 and NLOS2 streets, the path loss can be simplified as

$$L_{LOS} = c_1 + 20\log\left(\frac{4\pi}{\lambda}\right) + \begin{cases} 10n_1\log_{10}(d_r) & d_r \le d_b \\ 10n_1\log_{10}(d_b) + 10n_2\log_{10}(d_r/d_b) & d_r > d_b \end{cases} \tag{13}$$

$$L_{NLOS1} = L_{LOS} + L_{extra}\left(r_0,\, r_1,\, \theta_1\right) \tag{14}$$

$$L_{NLOS2} = L_{NLOS1} + W_2 \cdot L_{extra}\left(r_1,\, r_2,\, \theta_2\right) \tag{15}$$

That is, the path loss of the nth crossing is a recursive expression based on the former $n-1$ crossings. Each former crossing can be regarded as the source of a following crossing.

5. PERFORMANCE

Here, we evaluate the performance of this proposed model and compare it with the street canyon model in [3] and the recursive model in [5]. The main street types, LOS, NLOS1 and NLOS2 are evaluated separately.

The measurement was taken in the Kingsland region of London city, with transmitter and receiver height are both 1.5 meters above the ground and the frequency is 2.1 GHz. Figure 2 shows the Geographic Information System (GIS) data with recorded measurement points. The street types of these points are got by a simplified ray tracing platform. For this scenario, the calculated

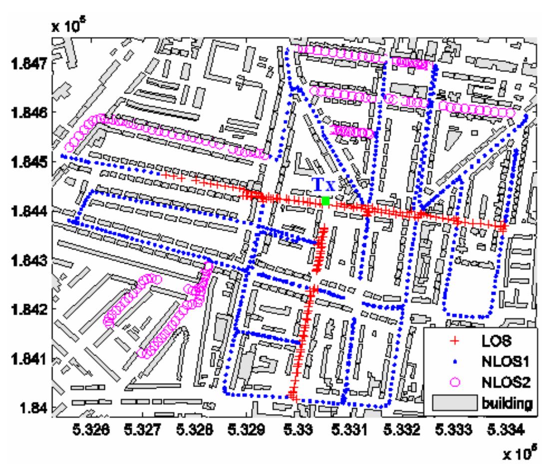

Figure 2: The GIS data with recorded measurement points.

parameters for the proposed model are the following: $n_1 = 2.3$, $n_2 = 4$, $c_1 = 1.9$, $c_2 = 5.9$, $c_3 = 2.2$, $c_4 = 9.9$, $c_5 = 5.1$.

Table 1: Comparison of prediction error statistics [dB] for different models.

Model	LOS		NLOS1		NLOS2	
	mean	std	mean	std	mean	std
Proposed	-0.8	5.0	-0.2	4.2	0.6	3.7
Street Canyon in [3]	--	--	-13.8	8.4	--	--
Recursive in [5]	-8.0	5.1	-2.2	6.3	7.5	8.7

Table 1 shows the error statistics with above three models compared with measurement results. From this table we can see that the proposed model has much better performance than the other two models for all street types. The mean error is within ± 1 dB and the standard deviation error is within 5 dB. Combining all points, Figure 3 shows the plots of predicted path loss with measured results according to the travelling process. From this figure, the proposed model can match the measurement very well. The calculated mean error is -0.3 dB and the standard deviation error is 4.4 dB.

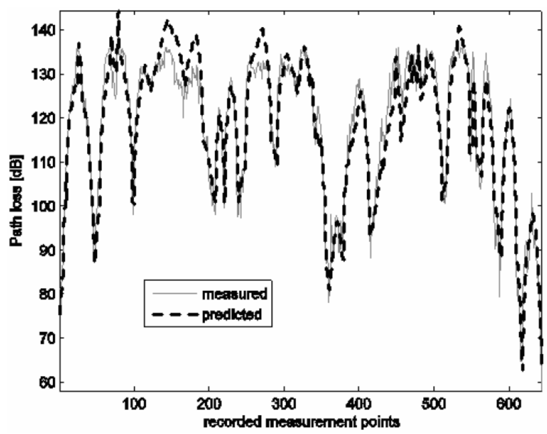

Figure 3: Comparison of predicted path loss with measured results.

6. CONCLUSION

In this paper, we proposed a novel recursive street canyon model which combines the idea of street canyon method and recursive method. This model has a simple and unified expression and can describe any street type. By simulation, the proposed model shows much higher prediction accuracy than present street canyon model and recursive model, with the mean error is within ± 1 dB and the standard deviation error is within 5 dB.

REFERENCES

1. Lin, P. and W. Lai, "Modeling opportunity driven multiple access in UMTS," *IEEE Transactions on Wireless Communications*, Vol. 3, Issue 5, 1669–1677, Sept. 2004.
2. Rouse, T., S. McLaughlin, and I. Band, "Congestion-based routing strategies in multihop TDD-CDMA networks," *IEEE Journal on Selected Areas in Communications*, Vol. 23, Issue 3, 668–681, March 2005.
3. Rec. ITU-R P.1411-3, "Propagation data and prediction methods for the planning of short-range outdoor radiocommunication systems and radio local area networks in the frequency range 300 MHz and 100 GHz," 2005.
4. COST 231 final report, Chapter 4 "Propagation Prediction Models," 1999.
5. Berg, J. E., "A recursive model for street microcell path loss calculations," *Proc. IEEE International Symposium on Personal, Indoor and Mobile Radio Communications (PIMRC'95)*, Vol. 1, 140–143, 1995.
6. Saunders, S., *Antenna and Propagation for Wireless Communication Systems*, John Wily & Sons, Inc., New York, 1999.